Preliminary sizing of critical electromechanical actuators for the primary flight control systems of helicopters

Jérémy Roussel

THÈSE

En vue de l'obtention du

DOCTORAT DE L'UNIVERSITÉ DE TOULOUSE

Délivré par : *l'Institut National des Sciences Appliquées de Toulouse (INSA de Toulouse)*

Présentée et soutenue le *22/09/2022* **par :**

Jérémy ROUSSEL

Dimensionnement préliminaire d'actionneurs électromécaniques critiques pour les commandes de vol primaires d'hélicoptères

(manuscrit: version finale publique)

École doctorale :
MEGEP : Génie mécanique, mécanique des matériaux
Unité de Recherche :
Institut Clément Ader (ICA, Toulouse)
Entreprise :
AIRBUS Helicopters (Marignane)
Directeur de Thèse :
Mr Marc BUDINGER

JURY

Mme Olivia PENAS	Ing. de Recherche HDR Laboratoire Quartz	Rapporteuse
Mr Tom VERSTRATEN	Professeur VUB Bruxelles	Rapporteur
Mr Jean-Charles MARE	Professeur INSA Toulouse	Président/Examinateur
Mr Marc BUDINGER	Professeur INSA Toulouse	Directeur de thèse
Mr Bruno CHADUC	Ingénieur Airbus H. Marignane	Invité
Mr Boris GROHMANN	Docteur Airbus H. Donauwörth	Invité
Mr Laurent RUET	Docteur Airbus H. Marignane	Invité

To my Parents & closed ones,

Manuscript written with LaTeX.
Version of October 2022.

FEDERAL UNIVERSITY OF TOULOUSE

Degree of Doctor of Mechanical Engineering

Delivered by INSA Toulouse the 2022/09/22

Abstract

Preliminary sizing of critical electromechanical actuators for the primary flight control systems of helicopters

by JEREMY ROUSSEL

in collaboration with AIRBUS HELICOPTERS (Marignane) and the laboratory INSTITUT CLÉMENT ADER (ICA, Toulouse)

Helicopter dronization is expanding nowadays. The VSR700 project is a relevant example of this expansion. This leads to the design and integration of electromechanical actuators (EMA) into the primary flight control system (PFCS). The PFCS is in charge of controlling the helicopter flight over its 4 axis (roll, pitch, yaw, vertical). It controls the blade pitch through dedicated mechanical kinematics and actuators. For more than 60 years, the actuators have been conventionally using the hydraulic technology. The EMA technology introduction involves the reconsideration of design practices. Indeed, EMA is multidisciplinary. Each of its components introduces new design drivers, and new inherent technological imperfections (friction, inertia, losses).

To address this topic, this thesis states firstly its position within the helicopter & actuation context and the fast changing digital world. Secondly, a methodology is established to understand better the need met by the EMA. The specification of the EMA is developed using flight data records. Thirdly, a first level modelling of the rotor dynamic load is developed to precise the actuator specification with reflected inertia limitations. Fourthly, a preliminary sizing tool gets prepared by the modelling of each actuator component and its main design drivers. Finally, the last chapter uses the MDO (Multidisciplinary Design Optimization) in order to solve numerical design issues (especially couplings). A GUI (Graphical User Interface) is done to easily enter specification, hypothesis and appreciate sizing results. Then, this sizing tool is applied on some real cases.

UNIVERSITÉ FÉDÉRALE DE TOULOUSE

Diplôme de Docteur en Ingénierie Mécanique

Délivré par INSA Toulouse le 22/09/2022

Résumé

Dimensionnement préliminaire d'actionneurs électromécaniques critiques pour les commandes de vol primaires d'hélicoptères

par JÉRÉMY ROUSSEL

en collaboration avec AIRBUS HELICOPTERS (Marignane) et le laboratoire INSTITUT CLÉMENT ADER (ICA, Toulouse)

La dronisation des hélicoptères se développe, comme par exemple avec le projet VSR700. Cela conduit à la conception et à l'intégration d'actionneurs électromécaniques (EMA) dans le système de commande de vol primaire (PFCS). Le PFCS est chargé de contrôler le vol de l'hélicoptère sur ses 4 axes (roulis, tangage, lacet, altitude). Il contrôle le pas des pales par le biais de cinématiques mécaniques et d'actionneurs dédiés. Depuis plus de 60 ans, les actionneurs utilisent conventionnellement la technologie hydraulique. L'introduction de la technologie EMA implique de reconsidérer les pratiques de conception. En effet, l'EMA est multidisciplinaire. Chacun de ses composants introduit de nouveaux critères de conception, et de nouvelles imperfections technologiques inhérentes (friction, inertie, pertes).

Pour aborder ce sujet, la thèse précise d'abord sa position dans le contexte de l'actionnement, des hélicoptères et de l'évolution rapide du monde numérique. Deuxièmement, une méthode est établie pour mieux comprendre le besoin auquel doit répondre l'EMA. La spécification de l'EMA est générée en exploitant les données issues des enregistrements en vol. Troisièmement, un modèle approximatif de premier ordre de la charge dynamique du rotor est établi pour préciser la spécification de l'actionneur avec des limitations d'inertie refléchie. Quatrièmement, un outil de dimensionnement préliminaire est préparé par la modélisation de chaque composant de l'actionneur et de ses principaux critères de conception. Enfin, le dernier chapitre utilise le MDO (Multidisciplinary Design Optimization) afin de résoudre les problèmes de conception numérique (notamment des couplages). Une interface utilisateur graphique (GUI) permet de saisir facilement les spécifications, les hypothèses et d'apprécier les résultats du dimensionnement. Ensuite, cet outil de dimensionnement est appliqué sur quelques cas réels.

Acknowledgements

What a chance to enter the helicopter world, its design and especially its flight control! My engineering degree internship was a first step into it. In parallel, I observed the design office environment and saw where and how I could bring my long-term added value. Therefore, I decided to write down and suggest this PhD thesis topic to answer one of the current main needs of the design office: build up and capitalize a know-how around electromechanical actuators and their preliminary sizing. Once this topic was defended at company level, the budget negotiated, the academic collaboration agreed, the company procedures performed, the recruitment accepted, the beginning of a long and energy-consuming work started. I integrated the department of Hydraulic, Actuation & Flight control systems (ETMH and later ETIRH) in Marignane. I worked there at 95% and 5% in the *Institut Clément Ader (ICA)* laboratory (group MS2M, Modelling of Mechanical Systems & Microsystems).

In the following lines, I would like to express acknowledgments to persons that contributed effectively, in different ways and at different moments, to this thesis achievements and this manuscript, to my technical and scientific training and to my understanding of the industrial context.

I thank Mr Bruno CHADUC (head of ETMH) for defending with me this thesis project in Airbus Helicopters innovation committee and fighting to unlock company budgets. His perseverance made this thesis project possible. Also, I'm grateful to him for forwarding me, most of the time, the best opportunities for the development of my knowledge and experience.

I dedicate a special thank to my thesis director, Mr Marc BUDINGER. I was happy to collaborate with him and benefit from his scientific and technical expertise, his talent, his generosity and his human values. Many thanks for his all-time availability, his support, his advice and his permanent supervision of my work from the start to the end of my thesis. I'm very grateful to him to have actively participated in enriching me with key qualities to evolve successfully during my future career of doctor.

I thank Mr Laurent RUET for supervising, at industrial level, my thesis project during its second half. Thanks for his feedback regarding my work and his advice regarding my oral presentations.

I thank Ms Olivia PENAS and Mr Tom VERSTRATEN to have accepted to review this manuscript. I thank them for having taken part of the thesis defense jury and to have shared their precious comments.

Now, in the following lines, I would like to express acknowledgments to persons who brought me, in different ways and during different short moments, some technical and scientific knowledge, a better understanding of the industrial context and its history.

First, I dedicate greetings to all the persons I met in the ICA laboratory and the friendly moments we shared. Among them, I especially thank the following persons.

I thank Mr Jean-Charles MARE for sharing his on-field experience, knowledge and point of view with me. I admire his background, his pedagogy and the clearness of his oral and written expression. I wish our timetables and our tasks coincided more often to meet and discuss.

I thank Mr Alain DEDIER and Mr Folly ABEVI for their time at guiding my development of a detailed code to estimate Hertz contact pressures in a planetary roller screw mechanism.

I thank Mr Dimitri LERAY for the exchanges regarding actuator architecture recommendations, actuator mechanical assembly difficulties and kinematic studies.

I thank Ms Céline LAMBERT for her efficient help and reactive explanations to set up a server.

I thank Mr Aitor OCHOTORENA for our exchanges around Python programming. Unfortunately, the Covid crisis obliged him to go back definitely to his native country.

Second, I dedicate greetings to all the persons I met in Airbus Helicopters.

I especially thank the members of the department ETMH/ETIRH (French and German teams) for welcoming me among them, for their kindness and the friendly moments we shared. All of them, by daily relevant exchanges enlightened my vision of the helicopter industry, its design and the on-field technical reality. They taught me a strong background in mechanical and hydraulic flight control systems (design, operation, standards, and legacy). They shared with me daily difficulties, in-service incidents and new development (prototypes). Also, they answered my questions and provided me their technical return-experience, their lessons learnt from previous developments and already operated helicopters.

I thank Mr Christophe TEMPIER, Mr Christophe PUJOL, Mr Nicolas AVRIL, Mr Jean-Ives AGRESTA, Mr André LE-GALL, Mr Stéphane MAZET, Mr Jean-François MANIERRE, Mr Michel LECLERC, Mr Christophe KILHOFFER, Mr Nicolas SADEGHI, Mr William PORTE-ANEZIN, Mr Sylvain BORNES and Mr Anthony CAILA for dedicating generously moments to improve my knowledge about mechanical and hydraulic flight control systems.

I thank Mr Serge BRAMATO for sharing with me his pragmatism and extended experience in production/assembly of helicopter systems. I really appreciated joining him for regular assembly line visits in the scope of checking parts or solving non-conformities and mounting difficulties on flight control systems.

I thank Mr Benoit GENOT for sharing with me his expertise in using the lumped parameter software Amesim and his expertise in flight control system sizing. I thank him for his good-heartedness and the friendly atmosphere he generated within the team.

I thank Mr Guillaume CHARRIER for the exhanges and the collaboration we had during the development of the on-site test bench and the assessment of the actuators at development stage (DEMA, DARS). This gave me a first experience in test bench set up and lab testing campaign follow-up. Also, during post-processing phase, I could correlate test bench results with simulation results from my Amesim actuator model.

I thank Mr Boris GROHMANN for dedicating, in his busy schedule, some time to exchange technically and advice me directions on my thesis work.

I thank the nice and reactive support from Mr Daniel GEMIGNANI. He enhanced my understanding of features implemented in the flight data analyzer softwares (SANDRA, EXTRACT). Also, it was enriching exchanging around software solutions and potential new code implementations.

I thank the nice team of Amesim support (Mr Sylvain PLUCHART, Mr Quentin NOHARET, Ms Diana CHITIC) to have enhanced with reactivity my understanding of some specific features applied to Amesim V16.

I thank Mr Célien NARBEY for his expertise in using specific features on CATIA V5. Also, it was great exchanging together around aeronautical topics during our free time.

From other Airbus departments (ETG, ETZ, ETIT previously ETMA), I would like to mention other persons.

I thank Mr Antoine MAUSSION for sharing his expertise in automatism and electrical science. I thank him for his practically proved explanations. I thank him for our exchanges around actuator development difficulties found on the lab test bench. I thank him for inviting me discovering other related topics to widen my technical vision.

I thank Mr Mounir AMOKRANE for sharing his expertise in electromechanical actuators and electrical motors. I thank him for sharing with me his return-experience on test benches. I thank him for encouraging me and providing me additional bibliography items.

I thank Mr Alexandre MADEIRA for the pleasure we had to exchange our passion for helicopters. I thank him for our exchanges regarding flight loads, piloting scenarios and flight mechanics.

I thank Mr Bernard-René MICHEL for his help related to helicopter blades.

I thank Mr Marc SALESSE for his availability, expertise and pleasure in exchanging around flight control system history and automatic flight control laws.

I thank Mr Laurent ZAMPONI for his expertise in gearboxes, this was helpful in recommending actuator bearing architectures and assemblies.

Further to the tasks involved by the PhD research, this experience at Airbus Helicopters included operational tasks for the design office in interactions with many persons.

This PhD–CIFRE period aroused my awareness of the key role entailed by a doctor in industry. It definitely prepared me and launched me to a thrilling career of research & development. In this way, I will add my stone to this existing scientific and technical world. This manuscript is a starter.

Last but not least, I will never thank enough my Parents, my Family and my Friends for their constant love and support that have been following me during all my years of scholarship until this end of thesis. I dedicate this manuscript to them.

Contents

List of Abbreviations

AAO	All–At–Once
ACC	Actuator Control Computer
ACME	American Trapezoidal thread
ACT	actuator
AEA	All–Electric Aircraft
AFCS	Automatic Flight Control System
AK	Antirotation Key
ATC	Analytical Target Cascading
BB1	double row angular contact Ball Bearing
BB2	single row deep groove Ball Bearing
BEMF	Back Electro Motive Force
BFGS	Broyden–Fletcher–Goldfarb–Shanno
BLDC	Brushless Direct Current
BLISS	Bilevel Integrated System Synthesis
CAD	Computer Aided Design
CFD	Computational Fluid Dynamics
CO	Collaborative Optimization
CON-MON	Controlled–Monitored
CMA-ES	Covariance Matrix Adaptation Evolution Strategy
CSM	Computational Structural Mechanics
CSO	Concurrent Subspace Optimization
CSP	Constraint Satisfaction Problem
DDV	Direct Drive Valve
DIRECT	Dividing Rectangles
DoE	Design of Experiment
DSM	Design Structure Matrix
EASA	European Aviation Safety Agency
ECU	Electronic Control Unit
EHA	Electro Hydrostatic Actuator
EHSV	Electro Hydraulic Servo Valve
EGO	Efficient Global Optimization
EM	Electrical Motor

EMA	Electromechanical Actuator
EMB	Electromagnetic Brake
EMI	Electromagnetic Interferences
eVTOL	electric Vertical Take–Off and Landing
FCC	Flight Control Computer
FCL	Flight Control Links
FEA	Finite Element Analysis
FEM	Finite Element Modelling
FH	Flight Hour
FMI	Functional Mock–up Interface
FOC	Field Oriented Control
GA	Genetic Algorithms
GEMS	Generic Engine for MDO Scenarios
GEMSEO	Generic Engine for Multidisciplinary Scenarios, Exploration and Optimization
GUI	Graphical User Interface
H	Housing
HIRF	High Intensity Radiated Field
HSA	Hydraulic Servo Actuator
HUMS	Health Usage Monitoring Systems
IBC	Individual Blade Control
ICA	Institut Clément Ader
IDF	Individual Discipline Feasible
IFI	In-Flight Instrumentation
KDD	Key Design Driver
KKT	Karush–Kuhn–Tucker
LB	Linear Bushing
LHS	Latin Hypercube Sampling
MCE	Motor Control Electronics
MDA	Multidisciplinary Design Analysis
MDF	MultiDisciplinary Feasible
MDO	Multidisciplinary Design Optimization
MEA	More Electric Aircraft
MFE	Maximum Functional Evaluation
MGB	Main Gear Box
MOET	More Open Electrical Technologies
MOO	Multi–Objective Optimization
MPE	Motor Power Electronics
MRA	Main Rotor Actuator

MSDO	Multidisciplinary System Design Optimization
NVH	Normalized Variable Hybrid
OOP	Object–Oriented Programming
OPV	Optionally Piloted Vehicle
OR	Output Rod
PFCS	Primary Flight Control System
PbW	Power–by–Wire
PMSM	Permanent Magnet Synchronous Motor
POA	Power Optimised Aircraft
PRS	Planetary Roller Screw
RE	Rod End
RMS	Root Mean Square
RSM	Response Surface Model
SA	Simulated Annealing
SAND	Simultaneous Analysis and Design
SFCS	Secondary Flight Control System
SIA	Smart Interface Actuator
SLSQP	Sequential Least Square Quadratic Programming
SM	Screw Mechanism
SNOPT	Sparse Nonlinear OPTimizer
SRM	Standard Reluctance Motor
SSBJ	Super Sonic Business Jet
STORM	Simulation Tool for Overall Rotorcraft Modelling
THSA	Trimmable Horizontal Stabilizer Actuator
TRA	Tail Rotor Actuator
TVC	Thrust Vector Control
UAM	Urban Air Mobility
UAS	Unmanned Aerial System
UAV	Unmanned Aerial Vehicle
VPLM	Variable Power Law Metamodel
VTOL	Vertical Take Off and Landing
WebApp	Web Application
XDSM	Extended Design Structure Matrix

Chapter 1

Introduction

1.1 The helicopter

1.1.1 Air vehicle classification

The helicopter is classified among the aerodyne and more especially in the category of spinning wings. The aerodyne is an aeronautic navigation machine, heavier than the air. Its flight is ensured thanks to aerodynamic forces. There are mainly two types of aerodyne: the fixed wing and the spinning wing [Raletz, 2010] [Mermoz and FFG, 2022]. The diagram in fig. 1.1 sums them up.

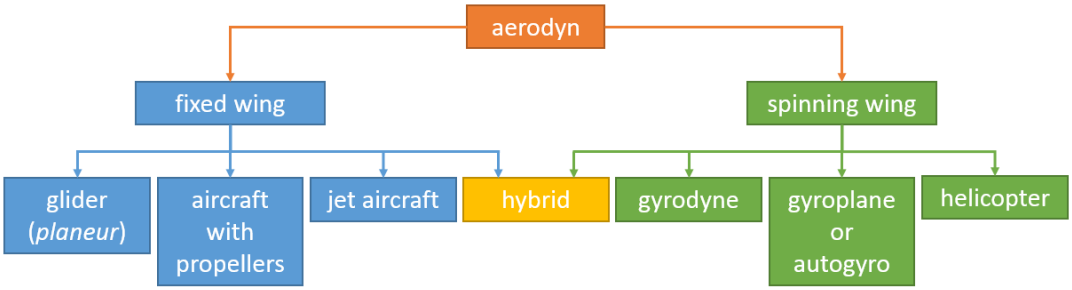

FIGURE 1.1: *Aerodyne classification*

Among the spinning wing category, four vehicles point out.

The *autogyro* is lifted by the main rotor made of several blades. The main rotor does not consume any engine power, the relative air speed in the rotor makes it spin. This generates aerodynamic forces. The autogyro propulsion is ensured by a propeller in a vertical plane powered by a small engine. The autogyro requires a runway to take-off and land.

The *helicopter* is based on two rotors, both powered by an engine. The main rotor generates a lift vector controlled in direction and intensity. The tail rotor generates a vector, usually controlling the helicopter on the yaw axis.

The *gyrodyne* is the combination of the *autogyro* and the *helicopter*. The main rotor is powered by an engine during the take-off and landing phases. The flight propulsion is ensured such as the autogyro i.e. with a propeller in the vertical plane.

The *hybrid* has the possibility to change its flight mode during a flight. Indeed, it takes spinning wings during the take-off, landing and hover phases, and turns to fixed wind during forward flight. There are several concepts of *hybrid*: tilt rotor [Boeing, 2022], tilt-wing [Airbus, 2022d].

1.1.2 Main components

The helicopter is equipped with components necessary to generate lift and control the flight. The main components are presented in fig. 1.2.

The *blades* turn a mechanical power of rotation into a lift force. It is precisely this force that propels the helicopter to take off from the ground and maintain it in flight.

The *power plant* produces the mechanical power of rotation by fuel combustion. Light helicopters are usually equipped with a single turbine or a piston engine. Medium and heavy helicopters fly with a minimum of two turbines.

Because of the gap between the required rotor speed and turbine nominal speed, the *Main Gear Box (MGB)* converts the speed and torque levels and provides it to the rotor mast. The helicopter Super Puma, one of the biggest Airbus product, is an example where the reduction ratio is huge: one turbine delivers 28000 RPM, the main rotor spins at 270 RPM, and the tail rotor spins at 1300 RPM. On light helicopter using a piston engine, the reduction ratio is less important. It is the case of the Cabri G2, a 2-passenger light helicopter with a 4-cylinder engine delivering 2650 RPM, the main rotor spins at 530 RPM, and the tail rotor spins at 5150 RPM.

The *rotor mast* is the intermediate part connecting the main gearbox to the blade. The set of rotor mast and blades is named the *main rotor*. It ensures the helicopter lift, and the control regarding the altitude, the pitch and the roll axis. The *main rotor* generates a reaction torque making the helicopter airframe turn around its yaw axis.

The *tail rotor* generates a force at the tip of the tail boom. It counters the reaction torque of the main rotor. It controls the helicopter on its yaw axis (fig. 1.3).

The *primary flight control system* controls the amplitude and the intensity of the force generated by both rotor blades (the main and the tail). It connects the pilot to the blades and allows her/him to control the helicopter flight on its four axis (fig. 1.3).

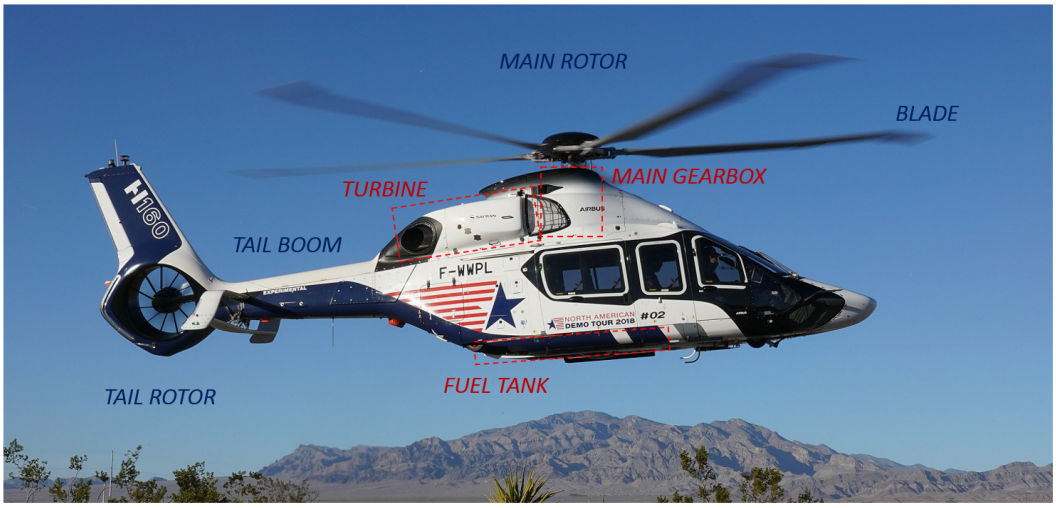

FIGURE 1.2: *Helicopter main components (example of H160, picture from [Airbus, 2022b])*

1.1.3 Flight principle

The helicopter flight is based on four axis. Fig. 1.3 illustrates them.

FIGURE 1.3: *Helicopter flight axis (example of H145 in search & rescue operation, picture from [Airbus, 2022c])*

The *roll axis* is the axis passing through the helicopter nose and the tail rotor. The *pitch axis* is the transversal axis of the helicopter. The *yaw axis* is the axis orthogonal to the plane described by the roll and pitch axis. The yaw axis goes through the gravity center.

The interaction of the helicopter components is summed up into fig. 1.4 (left). They generate a lift resultant F_N and a counter torque force F_{CT}. The flight control system offers the pilot the possibility to control these forces i.e. the direction and magnitude of F_N, and the magnitude of F_{CT}.

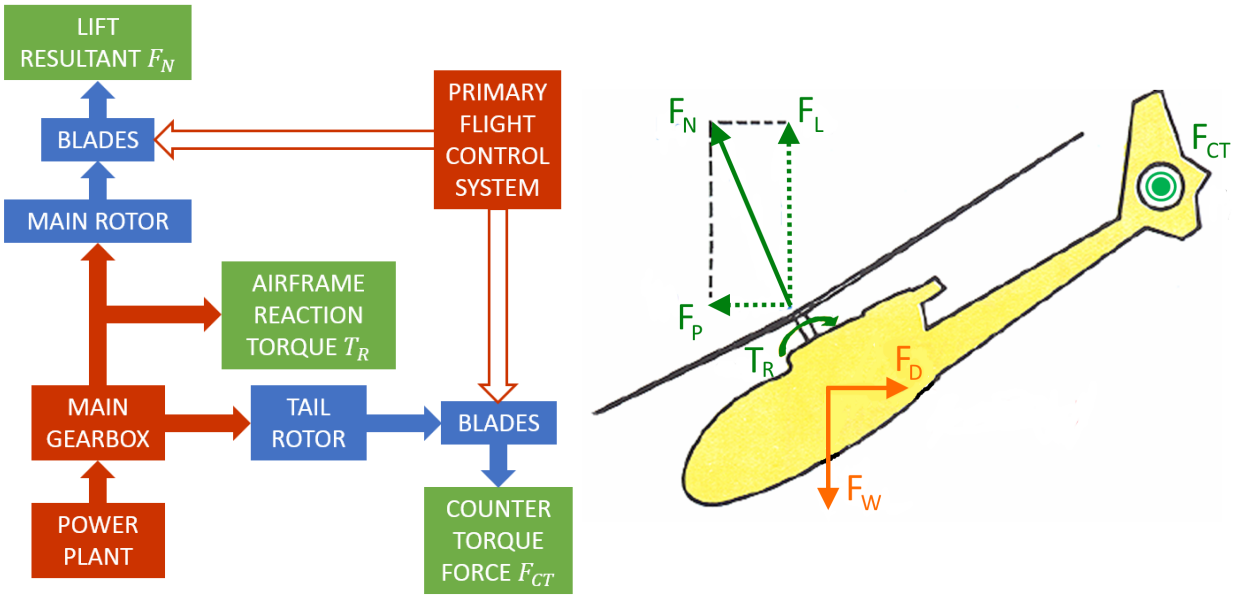

FIGURE 1.4: *Helicopter component interactions and working principle: (left) block diagram of main components, (right) helicopter force status*

The helicopter moves forward thanks to the horizontal component of F_N named the propulsive force F_P (fig. 1.4, right). While moving into the air, the aerodynamic effect applies a drag force F_D with the same direction and an opposite sense than F_P. The vertical component of F_N is the lift force F_L, it balances the helicopter weight F_W. The counter torque force F_{CT} balances the reaction torque T_R and orientates the helicopter around its yaw axis.

1.1.4 Main rotor & tail rotor

The control of the direction and the amplitude of the main rotor resultant F_N is performed controlling the angle of attack of each blade according to the rotor azimuth. This is possible thanks to the swashplate and the pitch rods (fig. 1.5). The swashplate is linked to the rotor mast with a kinematic similar to an annular joint. It transfers the position of a fixed reference plane to a rotating plane in order to induce a blade angle of attack through pitch rods. The rotating part spins with the rotor mast thanks to the scissor. The fixed reference is kept away from any rotor rotation thanks to another scissor located underneath the swashplate and attached to the top of the main gearbox.

The swashplate is controlled by three actuators named critical actuators because of the application they are in charge of (see fig. 1.5).

As far as the tail rotor is concerned, only the amplitude of the generated force F_{CT} is controlled. The swashplate is substituted by a plane, translating along the axis of the rotor hub. This controls the blades with a same angle of attack whatever the rotor azimuth is. The control requires only a single actuator.

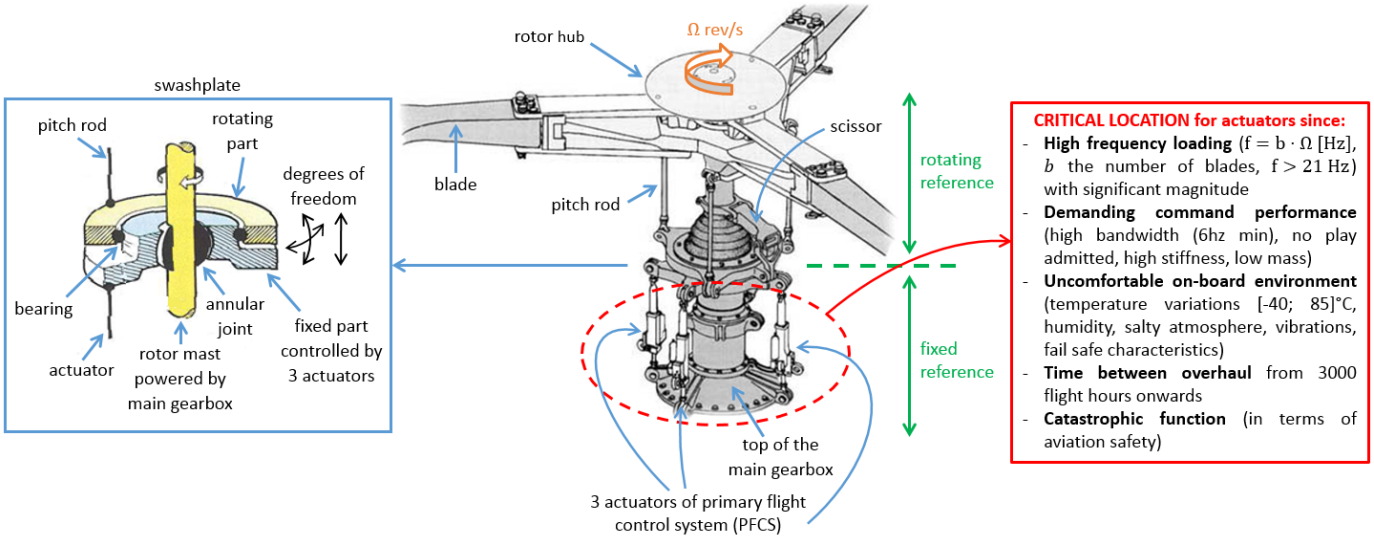

FIGURE 1.5: *Main rotor description: example of the H125 main rotor (row pictures from [Airbus, 2022c] & [Raletz, 2010])*

1.1.5 Flight in operation

Standardized helicopter flight scenarios are: take-off, cruise (at different horizontal speeds, altitudes and climb rates), landing, hard turns, and autorotation. The flight scenarios are difficult to predict, they depend on the customer need. Each customer operates differently and in miscellaneous environments. For instance, in the civil field operation, there are the Search & Rescue (SAR), the passenger transportation, the freight, the VIP use, the tourism, the offshore (passenger transportation, repair, prospection), the high voltage line control, the movie shooting, the coastguard,... In the military field, there are mainly the attack and the tactical approach on battle fields, the troops or the equipment transportation, the sea operations in sea with landing on Navy ships,...

1.2 Electrification trend

1.2.1 Global observation

On one hand, it is clear that the climate change awareness is a catalyser of the air transport evolution. In 2019, the *Aeronautics Strategic Implementation Plan* of NASA listed the solutions to reduce the air transport GHG emissions. They are a combination of the following: "*more efficient operations, improved vehicle fuel efficiency, increased electrification of aircraft and, in the longer term, new propulsion concepts and alternative sustainable jet fuels to incentivize emission reductions*" [NASA, 2019]. The aim is to respect the objectives defined by the Advisory Council for Aeronautics Research in Europe (ACARE): the Flightpath 2050 suggests to reduce CO_2 emissions by 75%, nitrogen oxides by 90% and noise by 65% in comparison to a 2000's aircraft [Dareck et al., 2011] [Zaporozhets et al., 2021]. This initiated a global industrial fever to develop demonstrators. For instance, there is the distributed propulsion hybrid aircraft demonstrator, named the NASA x-57 or the EcoPulse™, developed by Daher, Airbus and Safran. This project develops an architecture with high-voltage eletric motors powered by high-energy-density batteries and an auxiliary power unit (eAPU) coupled to an electric generator [Arpiany and Michon, 2021]. The first flight test is planned for mid 2022.

On the helicopter sector, the industry contributes in the same development fever.

Already, in June 2022, Airbus Helicopters celebrated the first flight powered solely with 100% of SAF (Sustainable Aviation Fuel) on the two turbines of the Super Puma H225 Mk2+ [Airbus, 2022a].

In addition, the RACER project in collaboration with Safran develops a propulsive eco-mode strategy to turn off one turbine out of two during steady and standard cruise flights [Lagarde and Orlandini, 2019]. The RACER first flight is expected end of 2022.

What is more, Airbus Helicopters celebrated the successful first flight test of an engine back-up system (EBS) installed on a H125 helicopter [Airbus, 2021]. It includes an electric motor powered by a supercapacitor. Connected to the main gearbox, it provides the mechanical power to fly for 30 seconds after the turbine failure. The EBS enhances the flight safety of a single engine light helicopter. It is a technological brick validated, opening the way to a future hybridised propulsion system for light helicopters.

It is clear that already flying vehicles and future ones are required to develop new functionalities to be more autonomous and to be safer. Reducing pilots' working load is part of current helicopter development roadmaps for enhanced safety.

Thus, today's market trend is globally facing a technological watershed towards more electrical solutions. Aircraft makers aim at *More Electric Aircraft (MEA)* and *All–Electric Aircraft (AEA)* achievement [Qiao et al., 2018].

1.2.2 Dronization

As the time goes by, a fast increase in the number of projects of *Optionally Piloted Vehicle (OPV)*, *Unmanned Aerial Vehicle (UAV)*, *Unmanned Aerial System (UAS)*, *Urban Air Mobility (UAM)*, and *Vertical Take Off and Landing (VTOL)* is observed. For instance, Ehang 184, Vahana, CityAirbus, Boeing's self-piloted passenger drone can be seen on the civil range; the aerial fighter Northrop Grumman X-47B, Airbus VSR700 (Figure 1.6), Leonardo AWHero can be seen on the military range. Furthermore, the market of aerial delivery already grows with vehicles carrying parcels, weighing less

than 10kg (DPD France drones in rural areas) up to 100kg (Kawasaki K-Racer X1 drone).

The drone concept comes progressively by the implementation of new electrical solutions on already existing vehicles [Cochoy et al., 2007]. This thesis was born in the context of the VSR700 project development. It is a light and stealth helicopter, fully autonomous for tactical applications around modern Navy ships. It aims at supporting search & rescue power too. Its payload capability allows the installation of long-range and high-performance sensors. It takes basis on the French Cabri G2 helicopter from Guimbal Industry [Guimbal, 2022].

FIGURE 1.6: *VSR700, the multi-mission naval UAS [Airbus, 2022e]*

1.3 Primary flight control system

1.3.1 Conventional architectures

As mentioned in section 1.1, the *Primary Flight Control System (PFCS)* Figure 1.7 is in charge of controlling the four flight axis of the helicopter (fig. 1.3).

In fig. 1.7, the PFCS is presented from a pilot seat view. To control the yaw axis, the pilot puches on the pair of *yaw pedals*. To control the pitch and roll axis, the pilot moves back and forward or side to side the *cyclic stick*. To control the altitude, the pilot pulls up or pushes down the *collective stick*.

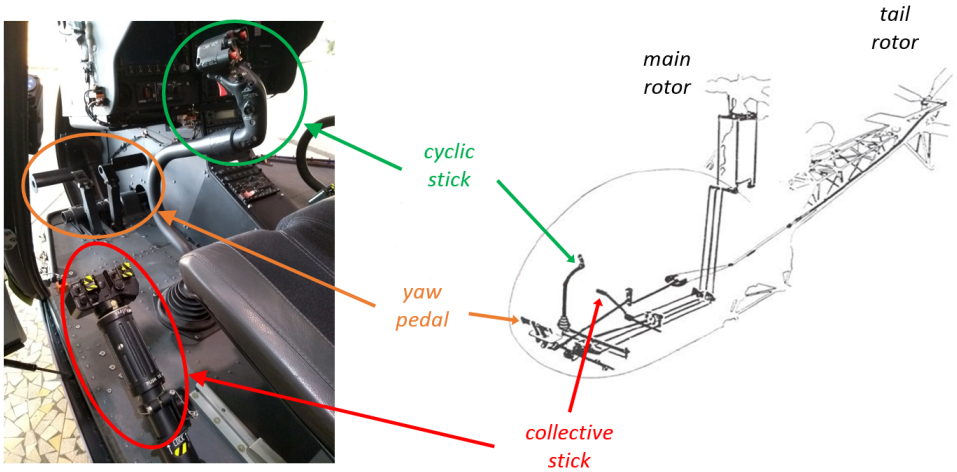

FIGURE 1.7: *PFCS pictures. (**a**) Cockpit of EC130 B4 (**b**) FCS of Alouette II AS313B*

Conventional PFCS architecture includes *Flight Control Links (FCL)* and, for high loads and automatic pilot option, actuators (Figure 1.5, Figure 1.8 (a)). The FCL connects the pilot to the actuators. Attached to the kinematics, the actuator supplies

the power to give and maintain the blade's angle of attack of the helicopter's rotors (the main and the tail). The conventional actuators are hydraulic. The FCL is mainly made out of mechanical links including rods, levers and bearings. The automatic pilot function is ensured through *Electromechanical Actuators (EMAs)*, located in series and in parallel with the mechanical links of the FCL (Figure 1.8 (a)).

They actually control the helicopter in a hands off mode, such as following a GPS destination or performing a strategic approach to ground in a special operative mission. Only one helicopter of Airbus fleet (NH90) does not have any FCL, the hydraulic actuators (*Direct Drive Valve (DDV)*) are commanded directly by 4 electrical torque-motors connected to the *Flight Control Computer (FCC)* as shown in Figure 1.8 (b).

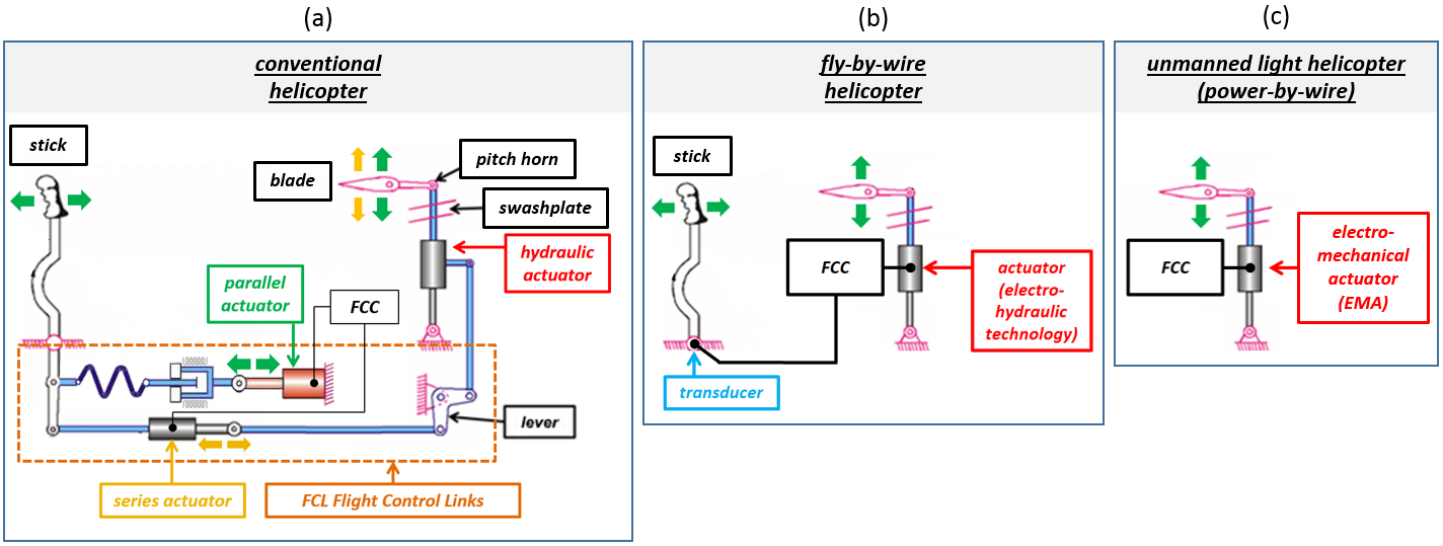

FIGURE 1.8: *PFCS architectures on the way to autonomy: sketches of principle. Note: In (**a**), removing the components of assistance makes a purely mechanical architecture. (**b**) and (**c**) are electrical architectures*

1.3.2 Electrical architectures

The hydraulic technology has been conventionally used in actuators for more than 60 years [Maré, 2017] [Qiao et al., 2018]. A new trend uses EMAs as substitutes to hydraulic actuators in PFCS of actual helicopters or as part of Fly-By-Wire PFCS of new autonomous helicopters (Figure 1.8 (c)). This requires the reconsideration of design practices, right at the preliminary design phase. It is the case with the VSR700 (Figure 1.6), an already proved light helicopter (Cabri G2) turned into a drone by the integration of electrical components. These components include four EMAs in the PFCS.

In fig. 1.8, (**a**) to (**c**) shows basically the evolution of PFCS architectures as it goes to autonomous helicopters. This evolution clearly shows that the helicopter mass can be significantly reduced with the reduction of part numbers. As long as the actuation control loop is concerned, this part number reduction decreases the response delay sources. The quid pro quo for it, is the increase of the actuator critical level, since it gathers nearly all piloting functions.

Another helicopter PFCS architecture is possible with the *Individual Blade Control (IBC)* controlling directly the angle of attack [Maré, 2017]. This opens the way to a potential application of EMA. In the 2000's, a project emerged to install EMA

actuators directly at the blade neck. This was done on the 6-blade main rotor of Sikorsky CH-53G [Fuerst and Neuheuser, 2007], a 19-tone helicopter. This architecture removes all the mechanical kinematic linked to the swashplate. The IBC introduces difficulties to reach a sufficient safety level. For each blade of the rotor, the actuation system is made of a triplex electrical system (*Permanent Magnet Synchronous Motor (PMSM)* motor and power control unit) and a mechanical reductor. The triplex redundant topology involves an important mass.

The actual entire Airbus fleet is turned towards a blade control through a swashplate solution. This thesis follows the same choice and focuses on actuators with a linear displacement installed under the swashplate.

1.3.3 Level of requirement of the functions

As tackled previously with the IBC, the function of a flight control system goes with the following important properties:

- *reliability*: system ability to perform its function during a given amount of time, in a given environment and for a given purpose. In the aeronautic field, the failure rate λ is commonly used. It defines the probability of failure expressed with respect to the provided service quantity. Therefore, it is expressed per *Flight Hour (FH)*.
- *safety*: system capability to shield from a failure occurence
- *maintenance*: system capability to repairs and evolutions (retrofit).
- *failure tolerance*: system capability to detect a failure and to behave accordingly, either by *reconfiguration* or by compensation thanks to a *redundancy*. The *reconfiguration* defines a system capability to find a new running state from which the system function is still satisfied despite the failure. The *redundancy* defines a system made of two or more component sets ensuring the same function. If one set fails, another one keep ensuring the system function.

Each equipment of an helicopter is usually specified according to its critical level and its failure probability per FH (table 1.1). According to in-service experience feedback over 10 years, the maximum tolerated failure rate for a catastrophic event is $\lambda_{cat} = 10^{-9}\ FH^{-1}$. This quantifies a threshold of acceptability, making the event extremely unlikely. Then, λ_{cat} is increased hundred-fold to define the successive degrees of gravity as presented in table 1.1.

As far as the PFCS is concerned, the loss of its function has a criticity qualified as 'catastrophic'. Indeed, the helicopter control can be lost and the landing can be uncontrolled. This corresponds to a failure probability of $\lambda_{PFCS} < 10^{-9}\ FH^{-1}$.

To reach this safety level, the PFCS must follow redundant topologies. The redondancy allows, in the case of a system failure, to maintain the system function by a second system. For instance, the hydraulic actuators equipping most of the helicopters have two separate chambers, totally independent from each other. Each of them develops the required performance to ensure the function of actuation in case one of them struggles from a hydraulic pressure loss, a pipe rupture, a distributor jamming... Also, the redundancy applies in the case of electrical PFCS. There are many redundant topology options to undertake so as to satisfy the safety requirements. They are presented later in section 1.5.5, table 1.5.

Quantitative probability	Qualitative probability	Gravity	Consequences on the airplane and its passenger
$\lambda < 10^{-9}$	extremely improbable	catastrophic	Many dead, loss of aircraft
$10^{-7} < \lambda < 10^{-9}$	extremely remote	hazardous	Heavily reduced safety margins, increased workload for the crew, serious or deadly injuries to a number of passengers
$10^{-5} < \lambda < 10^{-7}$	remote	major	Significantly reduced safety margins, crew experiences difficulties handling the situation, injury to passengers
$10^{-3} < \lambda < 10^{-5}$	probable	minor	Operational limitations, emergency procedures
$10^{-3} < \lambda$	frequent	minor	nuisance

TABLE 1.1: *Failure acceptability thresholds and consequences (data from [FAA, 2014] [Maré, 2016]), λ $[FH^{-1}]$ is the failure rate*

1.4 Actuators

The first light helicopters ever built, such as Aérospatial's Alouette 2 (1955) use levers, cables and pulleys to control the rotor blades. The pilot arm muscles are the power source of the actuation system. This actuation architecture is purely mechanical (fig. 1.9). Today, small helicopters keep using pure mechanical PFCS such as Guimbal's Cabri G2 or the Robinson's R22. The development of the hydraulic power allowed to develop heavy helicopters while managing the confort and the flight precision of the pilot. Right now, the whole fleet of Airbus Helicopters in operation, is equipped with a PFCS using the hydraulic power (fig. 1.9). This section overviews the actuator technologies classified in fig. 1.9.

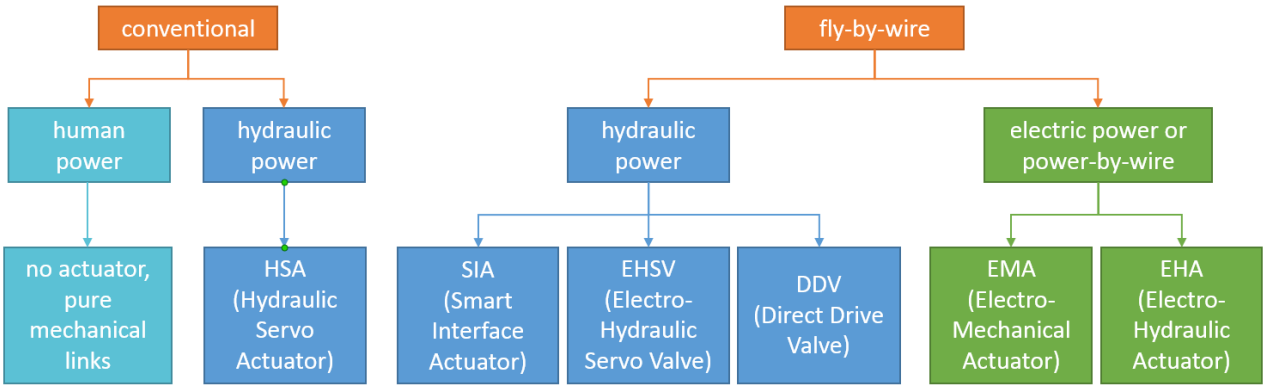

FIGURE 1.9: *Actuator technology classification*

1.4.1 Hydraulic powered technology

1.4.1.1 with mechanical input

Today's Airbus Helicopters fleet mainly flies using hydraulic powered PFCSs with mechanical inputs. The technology is named *Hydraulic Servo Actuator (HSA)*. Fig. 1.10 shows the HSA of the helicopter Tigre with its main components. The *control lever* is connected to the pilot and allows the control of the actuator position. The *control valves* are constantly supplied with hydraulic pressure. They control the hydraulic power, sent to the actuator *chambers*, according to the position of the *control lever*. Inside the *chamber*, a *piston* converts the hydraulic power into mechanical power. The actuator *housing* attached to the airframe, transmits the mechanical power to the load,

thanks to the *output rod*. The *position feedback link* acts on the valve opening according to the position of the *control lever* and the *output rod*.

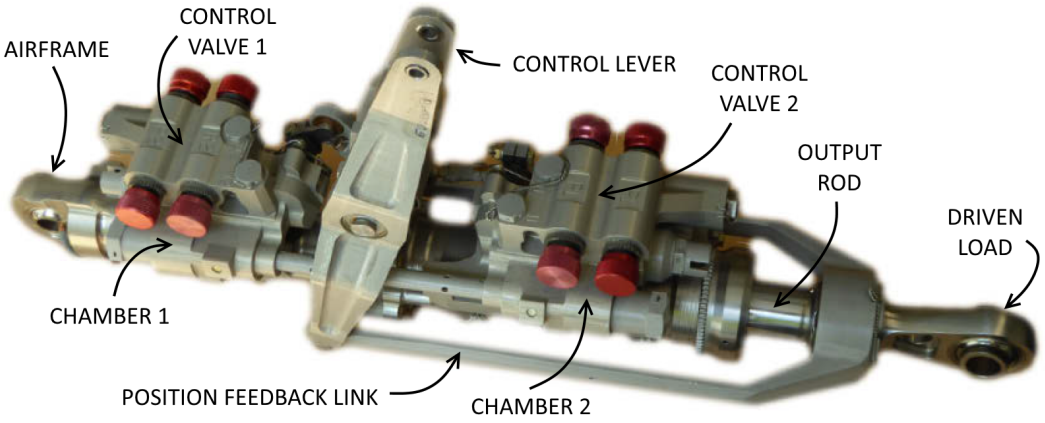

FIGURE 1.10: *Duplex HSA of Tigre PFCS [Maré, 2016]*

1.4.1.2 with electrical input

The successive development of actuators came to implement electrical inputs i.e. the fly-by-wire technologies. The aim is to remove the mechanical links connecting the pilot to the actuator (FCL, fig. 1.8, (**a**)) by electrical signals. There are mainly three types of hydraulic powered actuators with electrical inputs (fig. 1.9).

A first one is the *Direct Drive Valve (DDV)* presented in fig. 1.11 (*left*). Its valves are controlled by electromechanical actuators (electrical motors), located on the actuator housing. Linear position sensors are installed on the output rod for the control and the monitoring of the actuator. The closed control loop is global. This actuator type equips only one helicopter of the Airbus fleet: the NH90.

A second one is the *Electro Hydraulic Servo Valve (EHSV)* presented in fig. 1.11 (*right*). Its valves are controlled by a force from an hydraulic source, controlled by electrical coils. A hydraulic amplification device allows the electrical coils to work with a very low current intensity. Similarly to the DDV, the EHSV controls the output rod position with a global closed control loop.

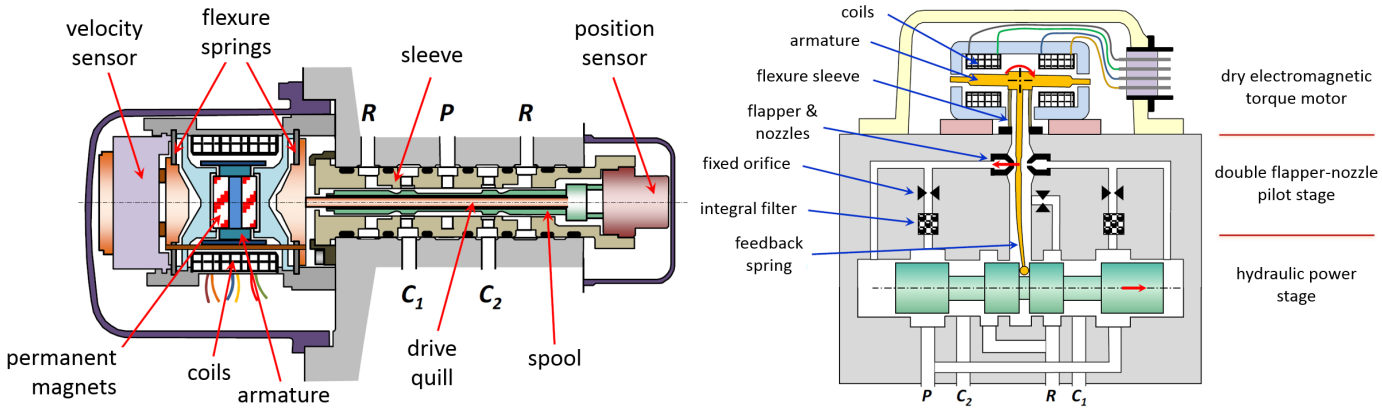

FIGURE 1.11: *DDV and EHSV examples [Maré, 2017]: (left) Moog DDV with linear motor, (right) EHSV servovalve with double flopper-nozzle pilot stage, (terminology: P = pressure supply, R = return, C_1 and C_2 correspond to chambers on both side of the hydraulic ram piston)*

A third one is the *Smart Interface Actuator (SIA)* presented in fig. 1.12. This technology is made of a device controlling the HSA input lever through mechanical connections (rods and levers). To control the output rod position of the HSA, the SIA technology takes advantage of the HSA mechanical loop (position feedback link). It does not use any global electric regulation loop. The SIA technology applied in helicopter PFCS has been studied and prototyped by [Estival, 2015].

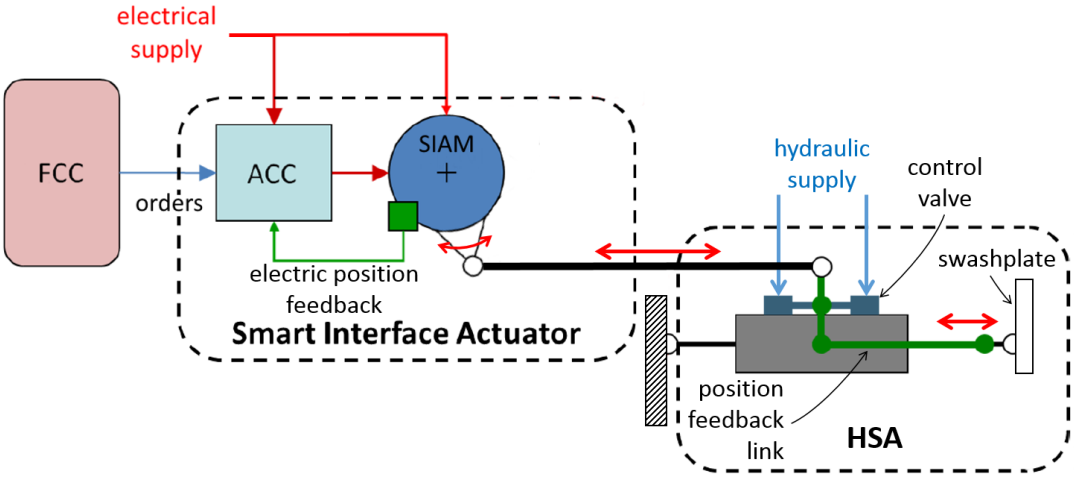

FIGURE 1.12: *SIA command diagram (terminology: FCC, Actuator Control Computer (ACC))*

1.4.2 Electric powered technology

With the ambition to remove hydraulic pipes going through the airplanes and to improve the maintenance task, actuators powered by electricity emerged [Botten et al., 2000] [Maré, 2017]. Among them, there are mainly the *Electro Hydrostatic Actuator (EHA)* and the EMA (fig. 1.9). These technologies are not installed on helicopters yet, although, the EMA has already done a step forward with the VSR700 project.

The EHA is an actuator with a hydraulic power whose pressure is brought by a hydraulic pump coupled to an electric motor. All these components are integrated into the actuator. In other words, the EHA is an electric powered actuator with a local hydraulic circuit.

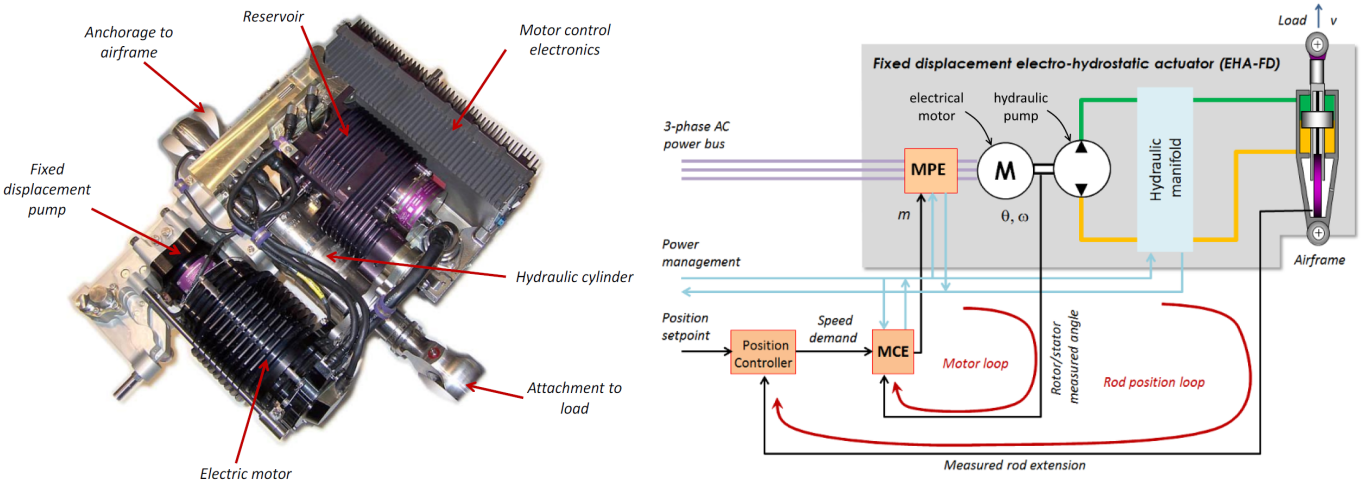

FIGURE 1.13: *EHA actuator example and sketch of principle: (left) EHA for the Airbus A400M, (right) EHA simplified sketch, precisions: Motor Power Electronics (MPE), Motor Control Electronics (MCE)*

The EMA actuator includes components from multiple disciplines, however there is no longer hydraulic technology. The main components are mechanical (rod ends, bearings and screw mechanisms, clutch), electrical (motor, brake, clutch) and electronic (for power & control). Fig. 1.14 shows an example of EMA. The motor with its bearings converts the electrical energy input into a mechanical energy of rotation. The gears adapt this energy in terms of a speed and a torque. The screw mechanism (ball screw in fig. 1.14) converts this last energy into a mechanical energy of translation.

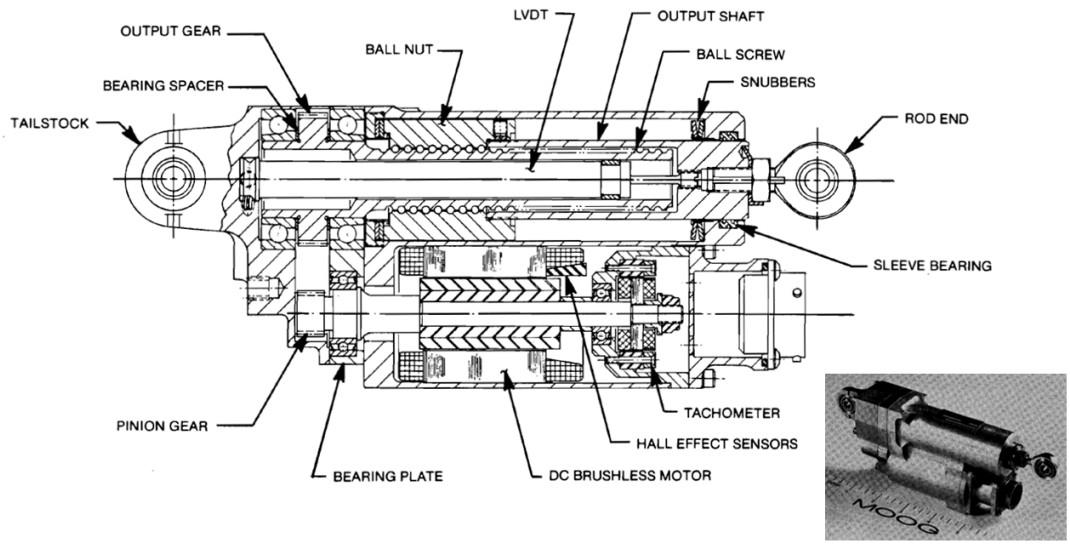

FIGURE 1.14: *EMA example, MOOG model 17E373 (section view from moog.com)*

This thesis will focus on the EMA technology. Section 1.5 comes with further details.

1.4.3 Technology summary

All these different technologies can be summed up into table 1.2. The thesis focus corresponds to the grey row.

technology	command input	power source	energy transporter	conversion	output
pure mechanical	mechanical	mechanical		mechanical	
hydro-mechanical (HSA)	mechanical	hydraulic	pipes		mechanical
electro-hydro-mechanical (DDV, EHSV, SIA)	electrical	hydraulic	pipes		mechanical
electro-hydraulic EHA	electrical	electrical	wires	'in-situ' hydraulic	mechanical
electro-mechanical EMA	electrical	electrical	wires	mechanical	mechanical

TABLE 1.2: *Actuation technology classification for aerodyne*

1.4.4 From hydraulic power to electric power

Table 1.3 gives a brief comparison of the hydraulic powered technology with the electric powered technology such as the EMA.

There are three main motivations to go on for an EMA: the energy efficiency, the power networks, and the environment. Indeed, the average efficiency of the power generation and the control through throttling is poor. The hydraulic power networks are heavy and impose strong constraints at all levels (design, production, operation, vulnerability in a battle field context). The hydraulic fluid is aggressive for people and the natural environment.

The EMA technology already exists in the field of civil and military aviation for auxiliary functions (non-critical in the sense of aviation safety) and/or back up functions (in case of failure of the critical primary function) and in various industrial sectors for positioning workpieces or laboratory tools. Except for low-power and less safety-critical applications (flaps, slats, spoilers, trim horizontal stabilizer), the EMAs are rather immature for primary flight controls [Maré, 2017]. This is essentially because of their lack of accumulated return of experience. The statistical database on components fault modes is poor [Mazzoleni et al., 2021]. The EMAs entail some concerns in terms of reliability, risk of failures due to jamming in mechanical transmission components, health monitoring (HM) & assessment, and thermal management. Some research activities or development efforts can be cited e.g. *Power Optimised Aircraft (POA)*, *More Open Electrical Technologies (MOET)*, DRESS European projects [Iordanidis and Dellac, 2010], and VEGA space launcher (*Thrust Vector Control (TVC)* actuator). The EMA applicability in aerospace has been proved in terms of dynamic performances [Mazzoleni et al., 2021]. In addition, the EMAs offer interesting perspectives in terms of maintenance, integration, reconfiguration in case of failure, ease of operation, harsh running environment ($[-50, 125]^{\circ}$C) and management of power [Maré, 2017, Qiao et al., 2018]. The EMA energetic efficiency is particularly convenient for the landing gears and the flight control since actuation systems are one of the main energy consumers onboard. The reference [Guidi et al., 2021] written by Umbra's group members raises the benefits and challenges of EMA actuation on landing and braking systems of aircrafts. It presents the first EMA, ever certified by *European Aviation Safety Agency (EASA)*, equipping the landing gear of the helicopter H160.

Merits	Hydraulic	Electric
Power density at the level of the actuators	Excellent	Average
Power density at the level of the power network	Poor (tubes, fasteners, fluid)	Good (3-phase)
Efficiency of control of power	Generally low (throttling losses)	Excellent (power-ondemand)
Direct mechanical power transmission to the load (direct-drive)	Easy with linear actuators	Mechanical reducer generally mandatory
Evacuation of the heat generated by energy losses in the actuator	Excellent, due to the hydraulic fluid returning to the reservoir	Poor, local exchange with the ambient
Power management functions (clutch, brake, damping, force limitation)	Easy, compact, lightweight and efficient in the hydraulic field	Often inefficient if applied to the field of electrics. Heavy or bulky in the mechanical field
Inertia reflected by the actuator	Low	High
Options and ease of command	Average	Excellent
Dynamic reconfiguration of power paths (redundancy)	Difficult	Easy
Integration and operation constraints (segregation,installation, maintenance)	Strong (fire, leaks, pollution, bleeding)	Moderate (EMI*, HIRF**), Built-in test options
Technology maturity level	Excellent	Low return of operational experience
Potential evolution	Moderate to weak	Strong
Environment and human friendliness	Poor	Good

*Electromagnetic Interferences (EMI); **High Intensity Radiated Field (HIRF)*

TABLE 1.3: *Comparison of hydraulic and electrical power technology [Maré, 2017]*

1.5 EMA

1.5.1 Different architecture options

There are mainly two groups of EMA architectures: the rotary one, and the linear one. The rotary EMAs output an angular position and a torque. The linear EMAs with rotative electrical motors are the architecture of interest in this thesis. Thanks to a screw mechanism, they output a linear position and a force. The different architecture options are presented in fig. 1.15.

Thanks to the modularity of gearboxes and the screw mechanism configurations, the EMA can be designed with miscellaneous forms.

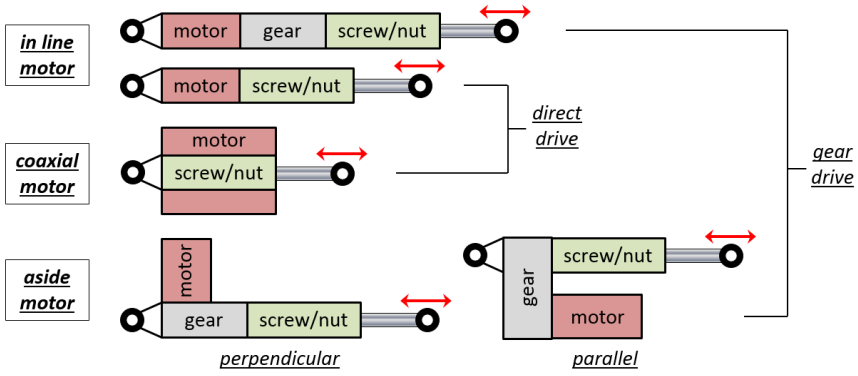

FIGURE 1.15: *Different EMA architectures*

1.5.2 Electrical motor

A broad range of electrical motor technology is available, it can be divided in six categories: synchronous machines, induction machines, continuous current machines, reluctance machines, torque machines and other special machines (such as piezo-electrical ones or machines, combining parts of the technology, used in different categories).

At first glance, for aeronautic application, only two technologies stand out: the PMSM, and the *Standard Reluctance Motor (SRM)*. The step by step motor stands out too by its fundamental technology. However, it delivers a discontinuous output torque which doesn't match with flight control system requirements. What is more, all electrical machines with brushes are excluded because of their high level of maintenance and their lack of reliability. The piezo-electric motor technology is excluded too. Their motion involves dry friction and wear.

The SRM technology is interesting but remains at prototype level in the aeronautic field because of its low power and torque density.

The PMSM technology answers all aeronautic criterias, therefore it is the only one to be used in PFCS. These criterias check that the motor guarantees the following: high torque density; high torque to volume ratio (compact design); high torque to current ratio (K_t); high torque to rotor inertia ratio; high thermal efficiency (high motor constant K_m $[N \cdot m \cdot W^{-0.5}]$); low maintenance; long lifespan; good electrical, thermal and magnetic insulations; high level of safety during operation; correct performance during degraded scenarios; and abilities to integrate failure resistance concepts such as a redundancy of phases [Cros and Viarouge, 2002].

The PMSM technology (fig. 1.16) depends on an electronic drive system producing a rotating magnetic field which makes the rotor spin [Electropaedia, 2005]. The rotor is polarized with permanent magnets. This rotating field is obtained thanks to an inverter with commutations, triggered by a pulse-width modulation (PWM). Each stator phase is sequentially energized by a current according the rotor instantaneous angular position. The motor runs under a closed loop system. Therefore, it requires the installation of a rotor angular sensor.

The PMSM exists with 3 types of rotor [Multon et al., 2005]: radial, axial and linear flux. The radial flux rotors are the most interesting ones in this actuation context. Indeed, it has a low rotor inertia and an interesting torque to volume ratio.

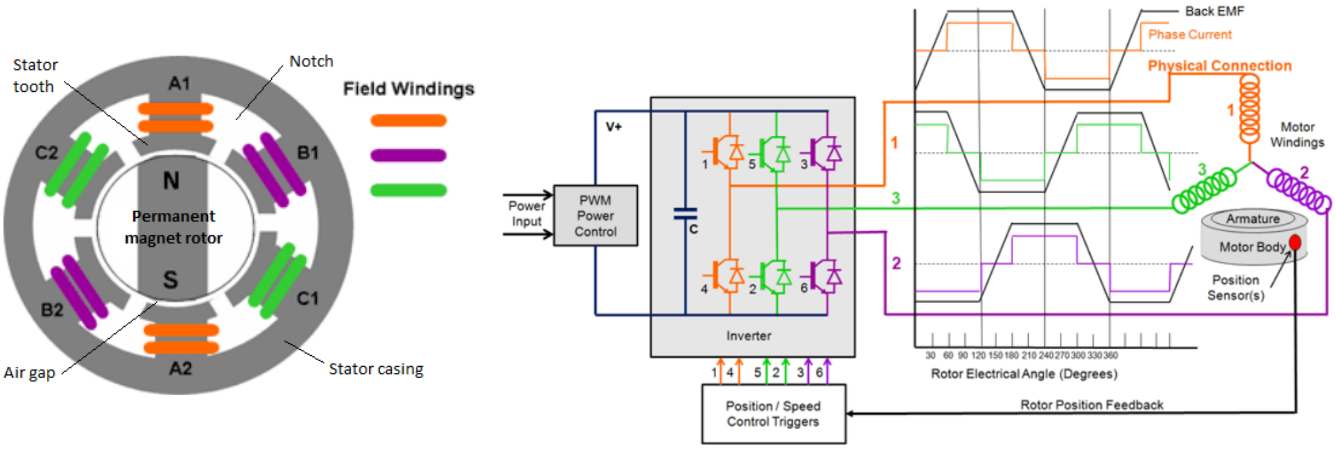

FIGURE 1.16: *Permanent Magnet Synchronous Motor (PMSM) [Electropaedia, 2005]: (left) motor section view, sketch of principle, (right) diagram of principle of motor control*

The PMSM has drawbacks. It involves high manufacturing costs especially due to the permanent magnets (Rare Earth element such as in Neodymium alloys) and the necessary protections to install around the magnets for high rotating speed applications. Another drawback is the parasitic torque generated due to the interaction of the rotor magnets with stator teeth. This parasitic torque is named *cogging* (also known as detent or no-current torque, [Muljadi and Green, 2009], [Flankl et al., 2017]). It is dependent on the rotor position. Its periodicity per revolution depends on the number of magnetic poles and the number of stator teeth. It results in a torque ripple or speed ripple.

Finally, another type of PMSM are the torque motors (named the annular motor too). They follow the same principle than PMSM but they have hollowed rotors and bigger diameters. Their important torque density avoids the use of reducers or gearboxes and allows to use them in highly dynamic applications.

1.5.3 Screw mechanism

A screw mechanism converts a rotary motion into a linear one.

There are three possible screw mechanisms: the lead-screw (e.g. trapezoidal thread), the ball-screw mechanism or the roller-screw mechanism.

The lead screw is by far the cheapest and the easiest to produce but it has the poorest efficiency. Table 1.4 provides orders of magnitude of the dynamic friction coefficents and efficiencies praticed by each technology.

technology	dynamic friction coefficient	efficiency
lead-screw	0.03 to 0.3	$\approx 40\%$
roller-screw	0.01 to 0.038	$75 - 90\%$
ball-screw	0.0008 to 0.0065	$85 - 95\%$

TABLE 1.4: *Friction in the screw mechanisms [Chevalier, 2004] [SKF, 2008] [SKF, 2014] [MOOG, 2022]*

The ball-screw technology is already implemented on aircrafts and broadly used. The *Trimmable Horizontal Stabilizer Actuator (THSA)* on A350 is an example [Todeschi M, 2014]. There is a big offer from the ball-screw supplier, this allows negociating prices. It reaches the best performance in terms of efficiency. Regarding the lead, the product range is limited by the ball minimum size (manufacturing constraints).

The roller-screw mechanism is based on rollers moving as planetaries, hence its name: *Planetary Roller Screw (PRS)*. The PRS is presented in fig. 1.17.

The standard PRS (fig. 1.17, left) involves a long direct-drive actuator design (fig. 1.15, in line motor).

The inverted PRS (fig. 1.17, right) involves a compact direct-drive actuator design (fig. 1.15, coaxial motor). It requires a hollowed motor rotor. Usually, torque motors are suitable for it. In addition, the screw is not threaded all along, this enables the direct installation of lip seals on the screw.

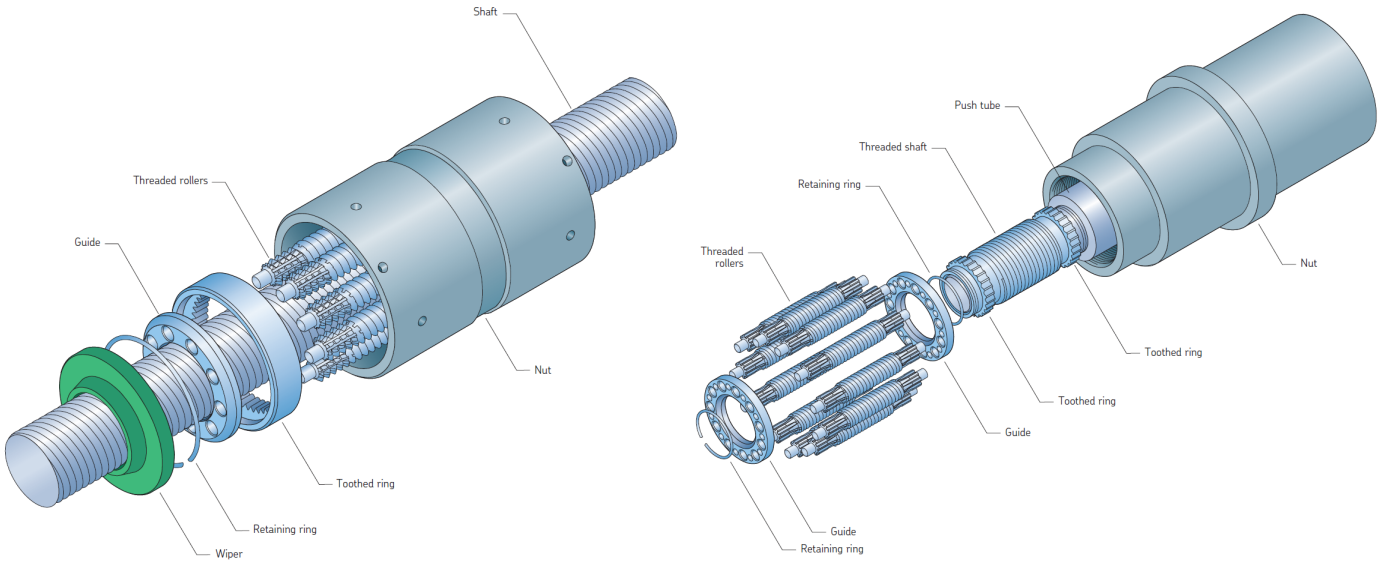

FIGURE 1.17: *Planetary roller screw mechanism [SKF, 2014]: (left) standard, (right) inverted*

Both PRS types, inverted and standard, provide four EMA design options (fig. 1.18): the nut translates when the screw spins or the screw translates when the nut spins.

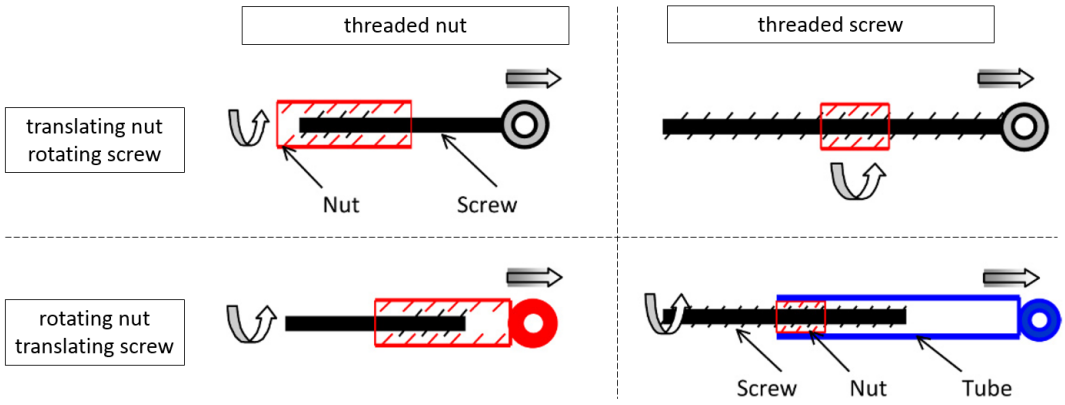

FIGURE 1.18: *Driving configurations of screw mechanisms [Karam, 2007] [Maré, 2017]*

Also, the roller screw mechanism allows a broad modularity in terms of integration. The nut can be either purely cylindrical or flanged. Fig. 1.19 illustrates it.

FIGURE 1.19: *Standard roller screw mechanism: some integration options [ROLLVIS, 2019]*

In fig. 1.20, the manufacturer [MOOG, 2022] offers a qualitative comparison of the three screw mechanism. Data comes from systems deriving from Moog's own

actuation design experience as well as data provided by other manufacturers. The roller-screw mechanism clearly points out from the other.

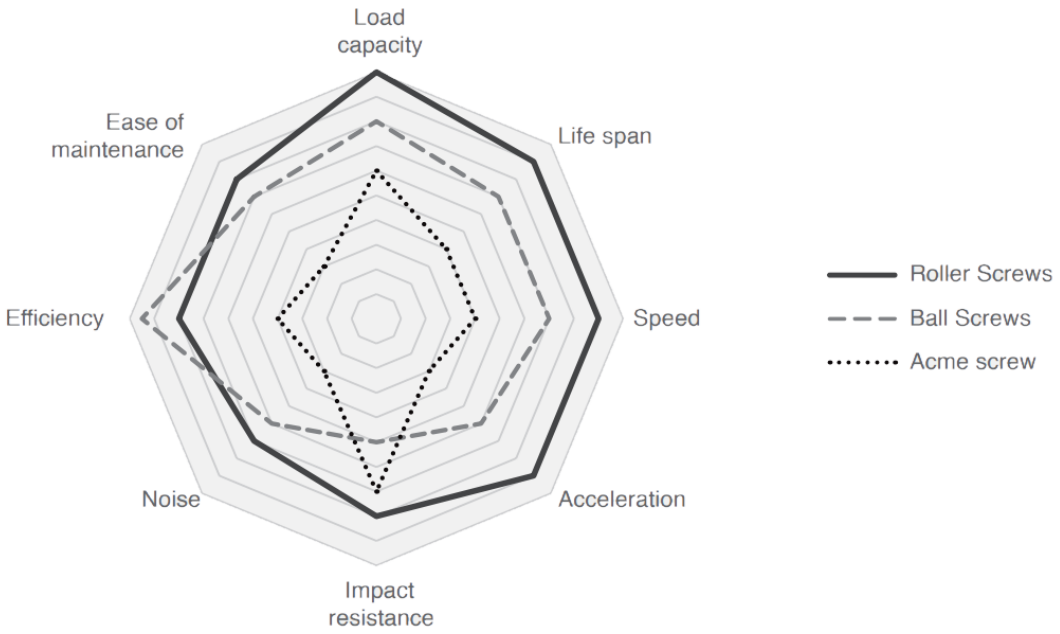

FIGURE 1.20: *Qualitative comparison of screw mechanism [MOOG, 2020b]*

Ball screws should be considered for drive mechanisms that give priority to smoothness or efficiency; whereas the PRS mechanisms are suitable when high load capacity, long service life, and high speed are required [MOOG, 2022]. Also, rollers have roughly four times as many contact points as balls, the load is spread over an area that is roughly four times larger [MOOG, 2022]. This results in longer service life and a load capacity that is more than 10 times higher in favor of a planetary roller screw. Increased contact area also improves the rigidity and impact resistance of planetary roller screws. In addition, PRS mechanisms are indicated for their positioning accuracy and motion repeatability [MOOG, 2020b].

Finally, from a design point of view, PRS mechanism is interesting since the catalog product offer, presents a wide range of leads including small ones (smaller than those ones offered in a ball screw catalog).

To conclude, the PRS technology is the most promising screw mechanism to develop critical EMA in helicopter applications.

1.5.4 Electromagnetic brake

As in any system, the current supply shortage is a potential failure scenario. In helicopter PFCS, the actuator must be locked in motion if not active. Therefore, the electromagnetic brake is a key component for safety.

There are many brake designs. Only one technology is presented. For a direct drive actuator, the interest is for a brake architecture with an axial contact and a single disc. It has to be actively braking when no current is supplied. This corresponds to a power-off brake (named spring-applied single-disc brake too).

Fig. 1.21 presents the principle of a power-off brake. The disk is interposed between two friction-pad plates, ones till, the other mobile. The movable plate is forced against the rotating disc by means of a set of pre-tensioned coil springs, arranged at the center of the brake, around the rotor shaft. The plate is released by a magnetic effect using an annular solenoid coil attracting element.

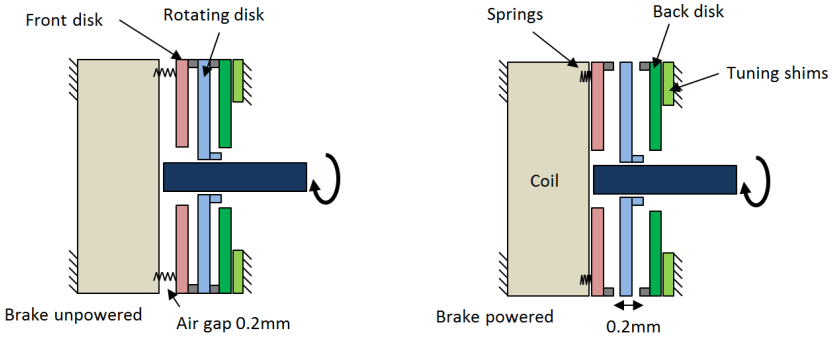

FIGURE 1.21: *Power-off brake: a type of electromagnetic brake*

1.5.5 Redundancy configurations

To comply with high safety level requirements (section 1.5, e.g. $\lambda = 10^{-9}\ FH^{-1}$), a redundancy topology of actuation is often mandatory to remove failure nods.

failure mode	configuration	sketch	known applications
free or declutched	**Force summation** - 2 actuation physical units (2 simplex actuators), - unique load, load path redundancy	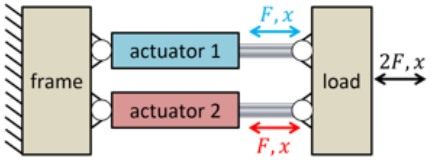	largely used on PFCS of commercial aircrafts [*]
	Force summation - 1 actuation physical unit (1 duplex actuator) - unique load, no load path redundancy	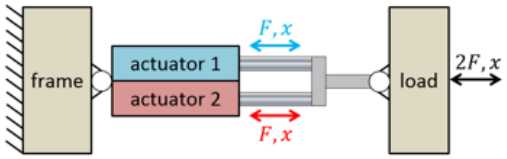	PFCS fighter aircraft, helicopters, secondary FCS of commercial aircrafts (except spoiler) [*]
blocked	**Position summation** - 1 tandem actuator - unique load	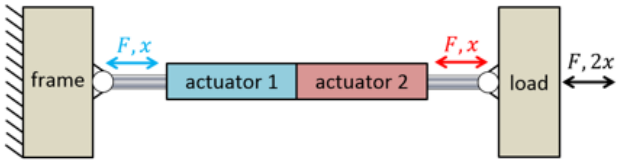	PFCS fighter aircraft, helicopters, secondary FCS of commercial aircrafts (except spoiler) [*]
	Position summation - 2 simplex actuators linked by a cross bar - unique load	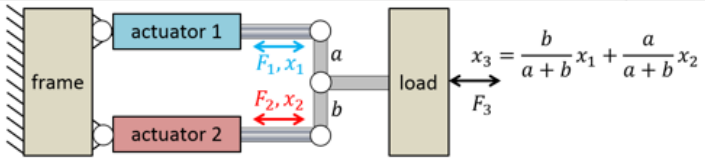	
	Speed summation - 1 duplex actuator with velocity-summing differential system - unique load	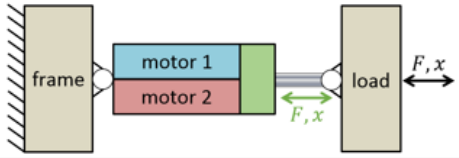	EPAD EMA applied on F18 aircraft [**]
blocked or damped	**Multiple loads** - 2 simplex actuators - 2 loads	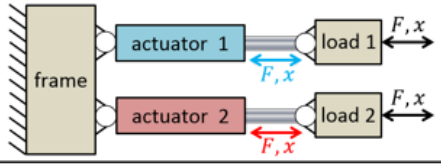	spoiler of commercial aircrafts [*]

TABLE 1.5: *PFCS redundant topologies of actuation. [*]: [Maré, 2017], [**]: [Jensen et al., 2000]*

In mechanical power transmission, redundancy can be applied by force summing (or torque summing) or position summing (linear or angular). Table 1.5 provides an

overview of possible redundancy options classified according to the failure mode specified by the application. In any case, the entire system must include additional functions and components to have a fail-operational behavior. In force summing, the faulty path unabled to generate motion (jamming, for instance) has to be let free. The installation of a clutch does the job. In position summing, the faulty path that cannot generate force (breakage, for example) has to be blocked. The installation of a brake does the job.

1.5.6 Architectures of reference

In the case of the VSR700, a direct-drive solution, with an in-line motor, a standard roller-screw mechanism and a power-off brake have been selected. The design office estimated that these choices made an EMA architecture the most likely to be certified by the EASA. Also, it is the most convenient to introduce in the reduced volume of the VSR700. This EMA architecture with all its components is presented in fig. 1.22 in its simplex topology. The selected redundancy topology is the position summation (fourth row of table 1.5) presented in fig. 1.23.

This thesis work is based on this actuator architecture. Throughout the manuscript, this architecture is named the architecture of reference.

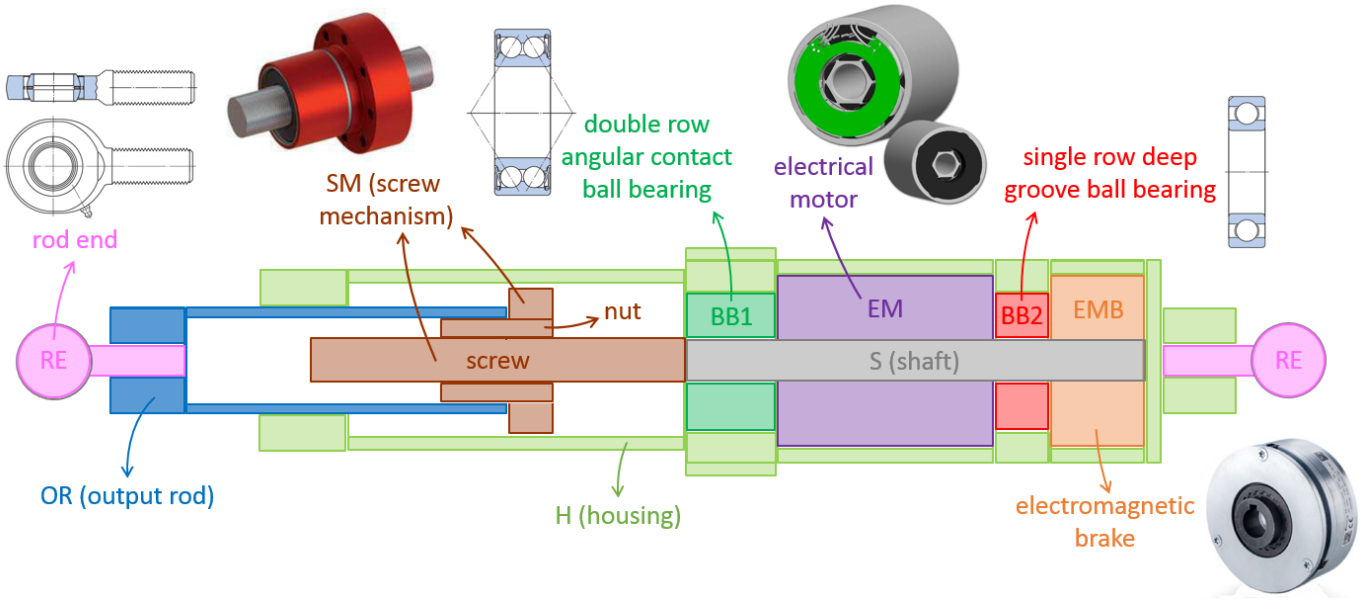

FIGURE 1.22: *EMA architecture of reference*

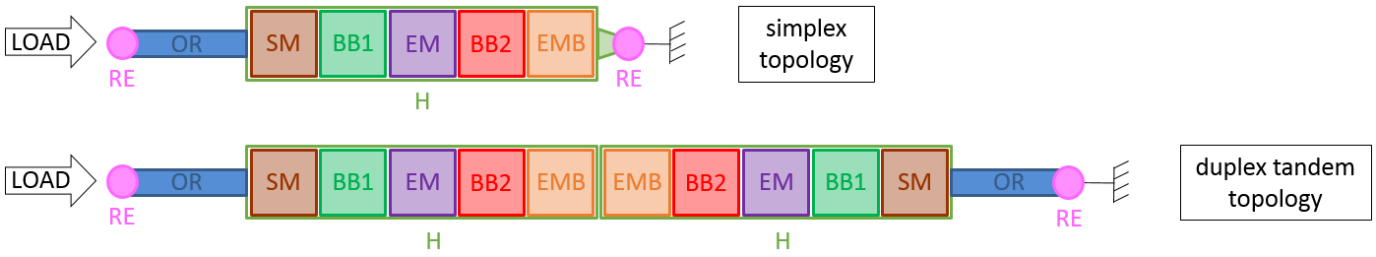

FIGURE 1.23: *Redundant topology of the architecture of reference*

1.6 Thesis environment

1.6.1 Position in the company

At Airbus Helicopters design office, this thesis came up in the department of Hydraulic, Flight control, Actuation & Auxiliary systems. This department is in charge of all helicopter PFCS regarding assembly line non-conformities, in-service incident investigations, modifications after customer delivery, and development of innovations.

At the time of the thesis, the company was developing four new autonomous and enhanced vehicles. A first and a second one are the Vahana and the CityAirbus developed in the USA and in Germany. They are all-electric and full-scale demonstrators that focus on remote piloted *electric Vertical Take–Off and Landing (eVTOL)* flights. They are single-seat and four-seat respectively. Their last take-off took place in Nov. 2019 and July 2021 respectively. A third vehicle is the high speed helicopter RACER prototype going to fly soon. It is being developed in Marignane. RACER means Rapid & Cost-Effective Rotorcraft. It is the successor of the technological proof of concept named Eurocopter X^3, winner of the world helicopter speed record in 2013 (255 knots i.e. 472 km/h). A fourth vehicle is the Navy UAS named VSR700 as mentioned in section 1.2.2. It is partially developed in Marignane, it is the closest project to this thesis since it involved the development of PFCS actuators.

The business need is to perform EMA preliminary studies and learn more about this technology. Further to an application in *Primary Flight Control System (PFCS)* (main rotor and tail rotor), the EMA technology finds interest in many other helicopter applications such as the automatic pilot actuators or the *Secondary Flight Control System (SFCS)*. This includes the actuation of landing gears and wing flaps, and the propellers' pitch control (for high speed helicopters such as the RACER helicopter).

A previous PhD candidate [Estival, 2015] of the design office worked on the detailed sizing of the electrical motor involved in the SIA as presented in section 1.4.1.2. An optimization loop is implemented to find the motor component geometries so as to satisfy helicopter requirements and optimize the magnetic and thermal responses from FEM simulations.

Also, a flight test data tool analyser, developed by Eurocopter, can be cited. Its name is *Sandra* and it is deployed at Airbus Group level. It is a software program used mainly for flight test data analysis and plotting. It clearly separates data from its representation for layout reuse. It supports many input formats. The user interface uses Javascript language. This tool will be useful for the helicopter flight test data analysis, developed in Chapter 2. Since this tool was developed, following real-time stream data display and user needs mainly, some features are missing unless coded by hand in a python script. Finally, the thesis will use *Sandra* only for its spectral analysis features.

1.6.2 Position in the laboratory

At the ICA laboratory, this thesis came up in the department of MS2M (Modelling of Systems and Mechanical Microsystems). The scientific activities of this department are focused on the development of models (in the broadest sense) and multi-tool methodologies for the multi-disciplinary and multi-scale study of mechanical structures and systems. This is from the conceptual phase to the verification & prediction phase of their behaviour.

Three previous PhD works are worth mentioning in this introduction. They will be more precisely mentioned throughout the manuscript (Chapters 2, 4 & 5).

In Laplace laboratory, [Jaafar, 2011] worked on a methodological approach aiming at analyzing and processing mission profiles to produce compact profiles. This is to work with in a context of system design requiring a wide number of system simulations and an optimization. This methodology is applied on the real use case of a hybrid locomotive, devoted to shunting and switching missions.

In the ICA laboratory, [Reysset, 2015] created a Simulink toolbox bringing a mechatronic system design methodology. This methodology offers a simplification of mission profile for design specification and validation steps. The tool applies in a context of a collaborative multi-partner design i.e. an airframer and a system-supplier. It includes an optimization process with constraints. Also, it includes response surfaces (surrogate models) that accelerate the optimization process. The toolbox is finally applied to perform some preliminary sizing studies of landing gear actuation systems and primary flight control surfaces (aileron & spoiler).

Finally, [Delbecq, 2018] (ICA laboratory) focuses on the sizing problem formulation. He offers a new *Multidisciplinary System Design Optimization (MSDO)* formulation allowing fast and robust analysis along with the reusability of models. Also, he offers a graph approach using symbolic manipulation to assist engineers in formulating multidisciplinary problems with important number of variables, constraints and interdependencies. A benchmarking is provided to compare different formulation options. The methodology is applied on two aircraft actuation systems: an electromechanical PFCS and an electrical thrust reverser.

1.6.3 Position in the scientific community

The preliminary design methodologies can be divided into two phases. The first phase is the system architecture choice, commonly guided by reliability studies, such as those presented in [Liscouët et al., 2012, Andersson et al., 1998, Jiao et al., 2019]. At this level, there are difficulties in taking into account the entire set of design criteria, important to evaluate an architecture. A study with a higher level of details is necessary, especially in the case of the EMA as it includes many constraints and interdisciplinary couplings between components. This is up to the second phase: the preliminary sizing. This phase is mainly based on multidisciplinary optimizations. The models used are usually analytical models or *Response Surface Model (RSM)* to facilitate the design space exploration and the design optimization.

Some already existing preliminary sizing methodologies can be cited. The references [Roos, 2005, Roos et al., 2006] present a methodology to select the motor and gearhead of the actuators in the automotive field. The methodology includes a selection based on scaling laws. It outputs graphs showing all feasible motor/gear ratio combinations. In the aeronautic field and regarding the secondary flight control actuators, the paper [Pfennig et al., 2010] presents a methodology for the preliminary design of mechanical transmission systems. It is formalized as a *Constraint Satisfaction Problem (CSP)* with an automated consistency checking and a pruning of the solution space. The mechanical components are modeled by scaling laws. In addition, the paper [Andersson et al., 1998] presents a simulation and an optimization strategy to evaluate two concepts of actuation systems: the conventional hydraulic actuators and the EHAs. Moreover, the paper [Wu et al., 2017] describes a preliminary design method of EHAs based on *Multi–Objective Optimization (MOO)* with Pareto dominance. Two objectives are set: the minimization of the mass and the maximization of the efficiency. The weight prediction is achieved using scaling laws, and the efficiency

is calculated by a static energy loss model. The method outputs the design parameter, leading to a Pareto front in mass and efficiency.

The scaling laws are good candidates for preliminary design. They are an example of analytical models. They are interesting because they require few data to build them and validate them (existing industrial product ranges). In aerospace, the scaling laws are broadly used in the conceptual design of aircraft, especially regarding aerodynamics, propulsion, structure, and mass [Raymer, 2012]. Moreover, the propellers are often described by scaling laws [Budinger et al., 2020, Massachusetts, 2022, McCormick et al., 1979]. Furthermore, the scaling laws can be used in the field of robotic actuators where low speeds and high torques are usually required [Saerens et al., 2019].

This thesis suggests a preliminary sizing methodology applied in the aeronautic field, on helicopters, and on critical EMAs. It contains similar concepts as found in the previously cited literature. Indeed, it includes scaling laws and a RSM. It includes an optimization where the component selection must satisfy a specification and design constraints while minimizing the actuator total mass. Further to an extended study around scaling laws, this thesis adds a value by the introduction of three elements not considered in the literature yet. The first element concerns a data-driven specification. It includes the consideration of the motor heating based on dynamic criteria extracted from an equivalent representation applied on complex real mission profiles (flight test records). The helicopter application is more dynamic than the aircraft application, as highlighted in the paper [Roussel et al., 2022]. The second element is the consideration of the hammering load into the fatigue design driver of mechanical components. The third element is the vibratory environment taken into account through the actuator housing sizing. Finally, this thesis methodology is applicable to any EMA architectures from light to heavy helicopters. It finds an extension to the design of multi–rotor drones such as presented in the paper [Delbecq et al., 2020b].

1.6.4 Digital revolution

Today's industry is facing a digital revolution. At engineering level, the working technics and habits must evolve to enhance work efficiency. This is to contribute in reducing time-to-market and increasing company competitiveness.

The digital revolution leads to implement new engineering practices i.e. new ways of thinking and organizing exchanges in a system design flow. The trend grows towards more collaborative and knowledge-based engineering tool developments. Nowadays, the key factor in the success of an industrial company lies in its ability to innovate while mastering a growing complexity. Usually, companies are ill-equipped in these regards [DPS, 2022]. Most of the time, companies can not afford to spend the time and the funds required to enhance their IT and software resources [DPS, 2022].

Mainly three locks come back within companies [DPS, 2022]. The first one is the significant amount of time spent researching and detangling data. The second one is the heterogeneity of languages, tools and cultures. The third one is the cycles of convergence or verification of design options that are too slow. What is more, this complexity combined with the specialization produced a *silo effect* that fragments and detains the information. This produces *silos of information* making decision-making more difficult and reducing dramatically the efficiency of the engineering phases. The main challenge of an engineering office is to embed all disciples and make them exchange.

To answer this need, the offer of the digital tool market has been thriving towards web collaborative platforms (fig. 1.24).

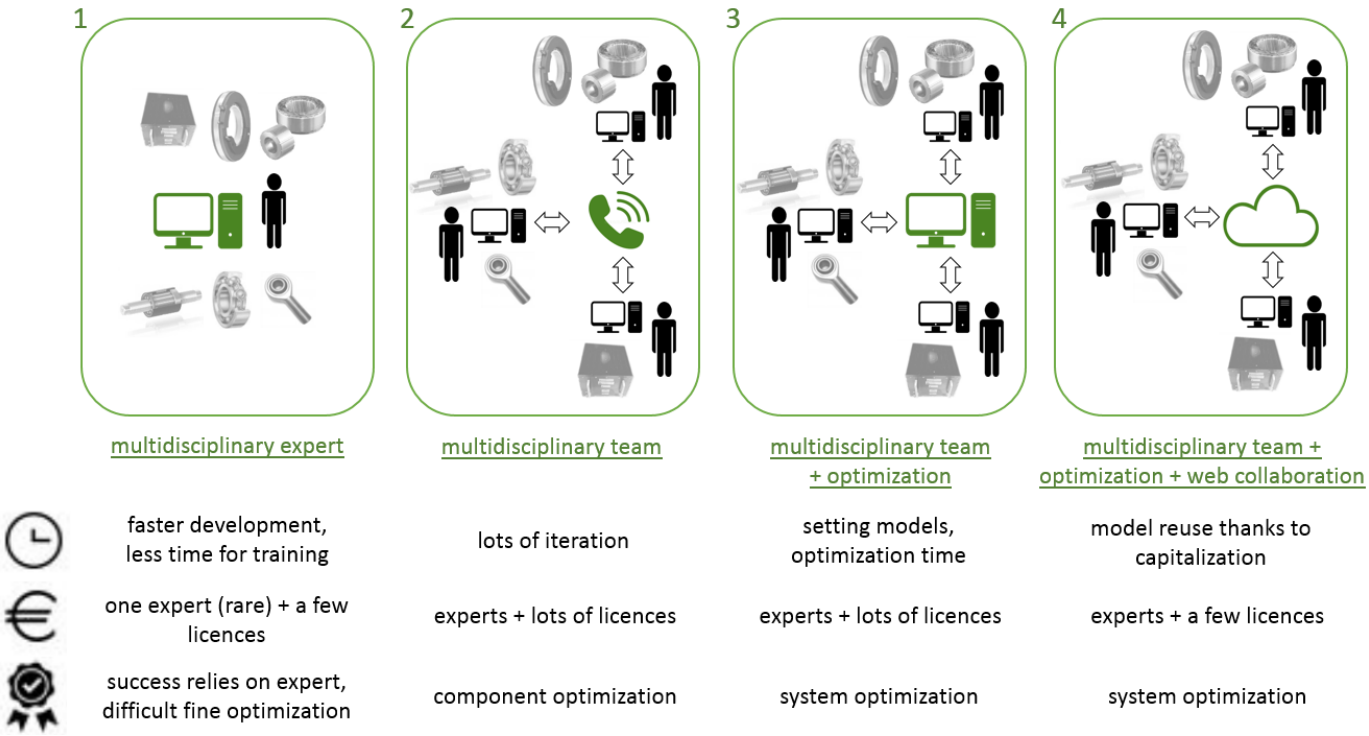

FIGURE 1.24: *On the way to web collaboration*

A first tool example from [Eynard et al., 2005] can be cited. This paper was born in a context of mechanical design where product data sharing is needed between two separate disciplines: the *Computer Aided Design (CAD)* and the *Finite Element Analysis (FEA)*. This reference addresses this need offering a software named *Teamproject*. It is an asynchronous Web Computer Supported Cooperative Work (CSCW) oriented toward the sharing and viewing of 3D data (CAD and FEA) based on the Virtual Reality Modeling Language (VRML). It opens to CAD and FEA data viewing through a Java3D read by the most used web navigator with the aid of a free plug-in. This strongly contributes at improving working collaboration and efficiency. Indeed, it increases the information access and its availability to team members in a remote mode. It simplifies the information access by removing software installation locks (any computer has got a web browser).

Other examples of collaborative platforms can be cited.

The *Karren* platform from the company DPS (Digital Product Simulation) [DPS, 2022]. This platform focuses on integrating disciplines with a global vision and converging towards an unique and optimum design proposal.

The *ID8* platform solution offered by NOESIS [NOESIS, 2022]. It is a collaborative platform that leverages engineering data from miscellaneous sources and deploys prediction models among users.

A last example concerns the *Skywise* platform created by Airbus Commercial in Toulouse and managed by Palantir Technologies. It is a modern data ecosystem which receives, extracts, transforms data to and from any source regardless of size and format. It can handle long term increases in data size and user account. Its deployment at Airbus Helicopters started in automn 2021. This platform aims at being the future Airbus group database of the company. It collects all helicopter data

and allows postprocessing it using implemented interfaces and features. A company user requires only a basic computer with a web browser and a reading access. For advanced user, coding is possible to implement new features.

Furthermore, the Covid health crisis accelerated IT tool developments too.

Indeed, the crisis increased the demand for online tools to perform collaborative engineering design by geographically separated team members. In some companies, the IT services strove to accelerate the migration towards Google Suit in order to provide a wider bandwidth to visio-conference daily used by homeworking and on-site team members.

During this crisis, [Anderson et al., 2022] intended to rapidly identify the available platforms for remote collaboration so that engineering teams could employ them immediately. Through first-person testing of 18 candidates filtered among 100 web-based collaborative tools, *Conceptboard*, *Limnu*, and *Vibe*, were the highest rated tools owing to their low-latency and rich feature set.

What is more, [Anderson et al., 2022] indicates that e-brainstorming is superior to face-to-face methods. This reference suggests that a cleverly designed platform could surely enhance team workflows and increase effectiveness. This emerges to an investigation axis: how best to use computer-based design tools to enhance a design process?

1.6.5 The mechatronic product

The mechatronic product design is at the heart the digital revolution. According to the norme NF E 01-010 (2008), the mechatronic is an approach aiming at the synergic integration of mechanics, electronics, automation and computer science in the design and manufacture of a product, in order to increase and/or optimise its functionalities. Thanks to the mechatronic, the existing system functionalities evolves, and even, many new functionalities are created. Mechatronic systems involve a high number of components. This leads to strong interactions between different physical and technological domains.

In [Penas et al., 2013], the authors define some good practices to follow. The product design success is based on the multidisciplinary collaborations integrated into a unique design framework considering the product life cycle. An example of the product design of an electrical gate is presented in [Plateaux et al., 2009]. A framework based on a single environment (Dymola) offers the integration of each design step of the downward side of the V-cycle (fig. 1.25).

Another example can be cited: the *Simcenter System Architect* plateform provided by Siemens [SIEMENS, 2022]. It accelerates system design with an architecture-driven simulation approach. The framework distributes roles in levels of expertise (architect, model builders, analysts). It opens access to diverse localized parameter simulation tools and FMI. It ensures the continuity of models without changing the toolchain. The models can be reused within the working entity, this helps to maximize return on initial invested efforts. Also, [Penas et al., 2013] raises some concerns regarding the reuse by capitalisation of previous studies to gain in design reactivity. In addition, [Penas et al., 2013] clearly mentions the importance of collaborative tools as soon as a project starts. This is to facilitate the exchanges (data, knowledge) between the different teams (multidomain & multilevel).

1.6.6 Digital thesis choices

The design office need is to develop skills around EMA preliminary sizing. This must be done without dependency regarding any new software licences.

According to the digital context previously mentioned and the design office needs, we made the following choices for the thesis tasks.

The thesis tasks mainly include the development of a flight data analysis code (Chapter 2), a code for studying scaling laws (Chapter 4) and a preliminary sizing tool (Chapter 4 & 5).

Since the engineering need is very specific and do not require advanced computational power, self-programming and Open Source solutions were estimated as the most suitable and reliable for the future. This thesis is the beginning of a preliminary sizing tool that is going to evolve as time goes by.

Python language was a first choice. This language is extending progressively. A key asset of a thesis work is to be continuously improved and easily handled by new persons. Today, high school calculators already include python features for coding initiations. This is to say that future young newcomers of the company (e.g. trainees) will come with python in their pencil case. What is more, a report from a company of developers named AVISTO, drew a language state-of-art prior starting developments, around the tool named *Simulation Tool for Overall Rotorcraft Modelling (STORM)*. This report states that, among all other languages on the market, Python was the best choice in technical aspects and on a long term basis.

Regarding knowledge capitalization, the *Jupyter Notebooks* were used for the flight data analysis and scaling law study. The *notebooks* gather in the same file written explanations (Markdown language, LaTeX) and documentation (pictures, pdf), along with the execution of python code cells.

As far as the preliminary sizing tool is concerned, we wanted it to be as light, as fast and as handy as possible for the user. A *Web Application (WebApp)* available on a server has been introduced. The user-friendly standalone App is generated using *Voilà* dashboarding [Voilà, 2020] and *ipywidgets*. The access on server allows the user to enjoy the App without struggling with any software installation or package update. The only thing required is a web browser and a password. The *Voila* dashboarding enables a successful use of the App on different devices (laptop, tablet, smartphone). In addition, the availability of this App on a server, allows sharing it easily across the company to the benefits of other employees with similar interests.

The Open Source is proactive in finding solutions to convert a script into a Python web application so the script is usable for a broad audience. Many initiatives came up. Further to *Voilà*, another example of solution is provided by *RealPython* courses [Darren, 2022]. They teach the way to go from a local Python script to a fully deployed *Flask web application* that can be shared to anybody with *Google App Engine*. The industrial context obliged the consideration of confidentiality and IT restrictions. It drastically limited the development opportunities with Open Source solutions.

Finally, Skywise platform offers open interface capabilities that allow developing new applications, it should be the most relevant platform to implement this thesis preliminary sizing tool. Unfortunately, this opportunity emerged at the end of the thesis. Transferring the thesis preliminary sizing tool onto this platform required many days of coding which did not fit into this thesis planning.

1.7 Thesis chapters into design cycle

Chapter 1 ending by this paragraph stated the thesis position within the helicopter & actuation context and the fast changing digital world.

To give a better view of the content offered by other thesis chapters and their contribution into the actuator design, we propose to locate each thesis chapter into the well-known design cycle. This is presented in fig. 1.25.

Within the whole product development process, the purpose of a preliminary design phase is to evaluate architecture feasibility, compare technologies, select components and define component high-level specifications based on the whole product requirements and operational scenarios. This is what this thesis intends to provide for critical EMA applied in the PFCS of helicopters.

Prior to any study, the need must be well understood. The mission profile analysis methodology developed in Chapter 2, supports this engineering task. This Chapter results in an actuator specification that will serve as an input of Chapters 4 & 5.

Chapter 3 presents a first order approximative study around the helicopter rotor dynamic load modelling. It helps understanding the complex load withstood by the PFCS actuators. This Chapter comes to precise the specification of Chapter 2 in terms of equivalent reflected inertia.

Finally, Chapters 4 & 5 develop all the knowledge gathered and discovered for the actuator preliminary sizing tool. Chapter 4 focuses on the models established to describe each actuator component. Chapter 5 focuses on the arrangement of these different models into an optimization process aiming at minimizing the actuator mass. The numerical design issues and couplings are highlighted too. A section of Chapter 5 shows the final preliminary sizing tool implemented as a Web *Graphical User Interface (GUI)*. The specification, the hypothesis are entered and the sizing results are appreciated. The end of Chapter 5 shows some preliminary sizing tool results applied on real cases. Part of the real cases come from the real flight data analysis performed in Chapter 2.

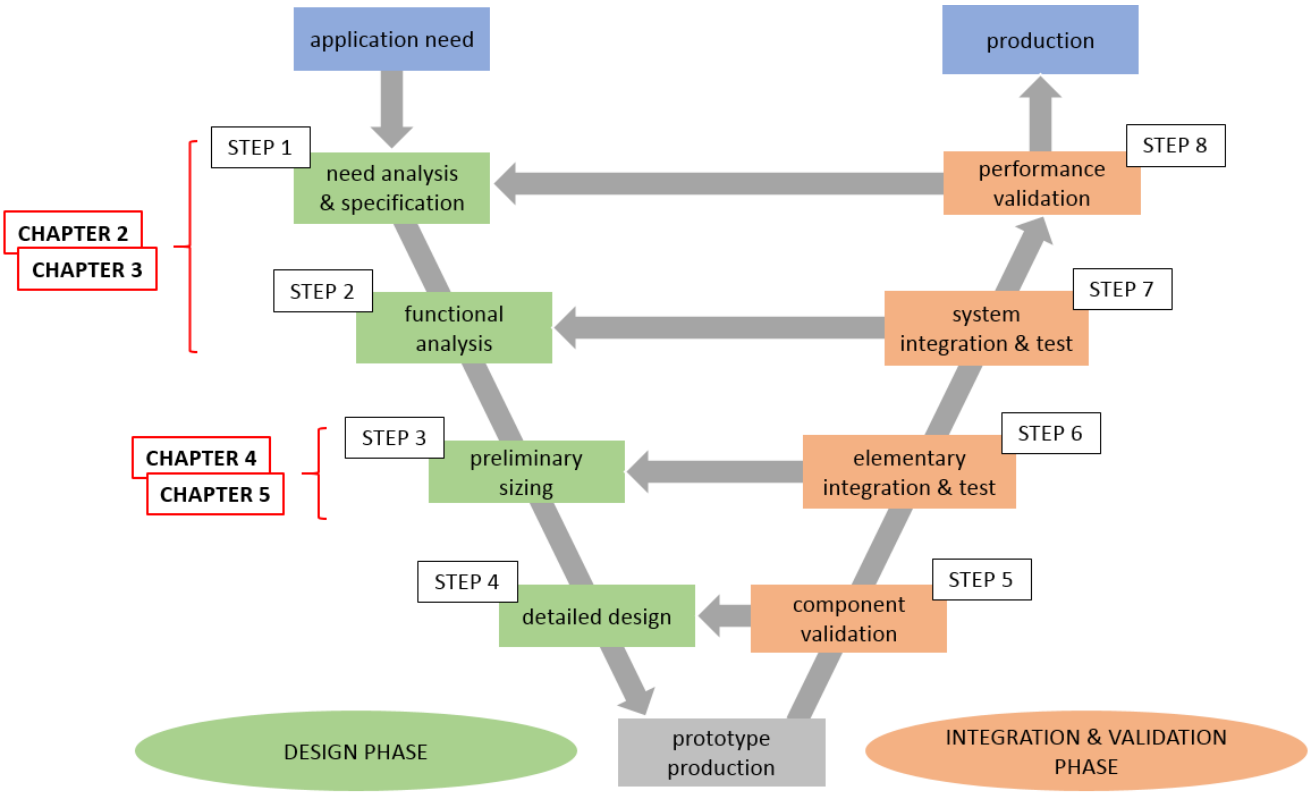

FIGURE 1.25: *Thesis Chapters into engineering V-cycle*

Chapter 2

Actuator specification assistance by mission profile analysis

2.1 Introduction

To reach the first-time-right objective of a design office, the requirements of any application must be well understood. In that way, the specification gets fully representative and the design is well guided. The EMA application in the PFCS of helicopter combines 3 types of difficulties which impedes writing down easily its specification. These difficulties are:

- a set of multidisciplinary design drivers due to the different technologies of components;
- an external loading spectrum, coming from rotor spinning in air, difficult to model;
- operational piloting scenarios difficult to predict.

The industrial context comes to a digital twin. There is an increase of the quantity of flight data recordings during helicopter life cycle, especially with the implementation of the *Health Usage Monitoring Systems (HUMS)*. Today, the HUMS does not contain any data about the actuator loads and positions. In the future and with the implementation of the EMA technology, these data might be found in the HUMS database. This digital context raises the need to develop data analysis methodologies based on synthetic values.

The VSR700 project is a special case where the technological bricks being developed are implemented on an already running helicopter. Some data are available, recorded during a flight test campaign by a specific instrumentation installed on board. These data are mission profiles. They are the most reliable elements, representative of the application requirements. This chapter suggests to set up an EMA specification based on the analysis of these mission profiles.

What is more, the industrial trend is to reduce the number of helicopter flight tests in order to shrink development costs. Consequently, the methodology must extract as much added value as possible from any available data sample.

The objective of this Chapter is to build the specification whilst simplifying the data analysis for the engineer and keeping her/him as the decision-maker. The methodology shown in fig. 2.1 contains 4 main steps:

1. Considering the actuator architecture and components to extract a list of key parameters driving the design named key design drivers in this chapter.

2. Preparing the data to be analyzed (mission profiles) by filtering and transformation within the temporal or frequency domains.

3. To link the data to the component key parameters, setting up of mathematical indicators to estimate over mission profiles. Each design driver has got its own representative indicator(s).

4. Evaluation of indicators over mission profile to develop the final EMA specification

The structure of this chapter follows these steps. Some indicators linked to fatigue and motor performance are addressed in more details. Also, some statistical analysis are presented to see how they can help to specify. Furthermore, the EMA specification synthesis is presented with indicators estimated out of real mission profiles of VSR700 prototype. The VSR700 flight control system is presented in Appendix C. Finally, a comparison between the main rotor and the tail rotor applications is done through ratios of indicators derived in order to emphasize the difference between both applications.

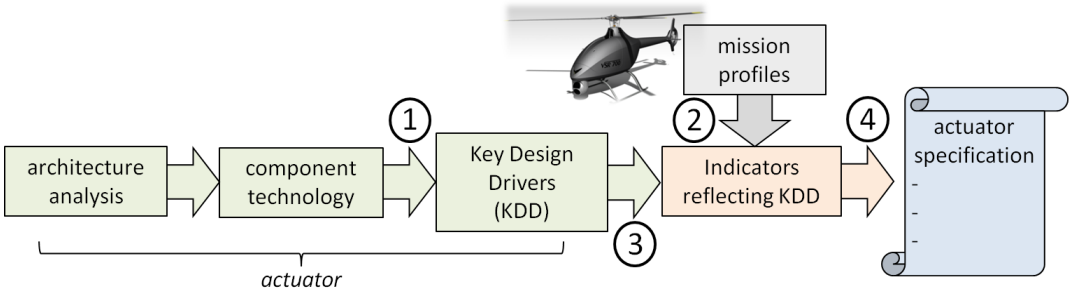

FIGURE 2.1: *Proposed methodology for specification set up*

2.2 From key design drivers & corresponding indicators to actuator specification

In preliminary sizing, the interest is focused on *Key Design Driver (KDD)* since they are the main physical phenomena guiding the EMA components design. A component has got one or several design drivers which are representatives of 4 types of criteria:

- *Performance*: it defines a degradation which damages the component over a short period of time (e.g. a single flight), it comes from intense and/or transient power requirements (e.g. high load creating plastic strain).

- *Endurance*: it defines a degradation which damages the component over a long period of time (e.g. a cumulation of flights) and diminishes the component life span (e.g. mechanical fatigue involved by a dynamic fluctuating load).

- *Imperfection*: it states any intrinsic component characteristic (e.g. inertia, friction) evolving against the overall component performance. It influences the selection of the component itself and/or another component of the actuator.

- *Environment*: it defines any component characteristic evolving according to environmental conditions (e.g. motor continuous torque influenced by ambiant temperature)

For the sake of terminology, a sizing scenario is the running conditions activating a given design driver. A mission profile is a data set coming from onboard measurements during flight tests. An indicator is a mathematical tool worked out on mission profiles, its value quantifies the design driver it has been set up for.

2.2.1 Mechanical components

To identify the design drivers of mechanical components [Budinger, 2021], the following points shall be considered:

- *Performance*: a significant load generates local damage (a plastic strain or failure). Plastic deformation is unacceptable, only a limited linear elastic behavior is allowed. The corresponding maximum stress can be represented at application level by the maximum transient load.
- *Endurance*: any repeated fluctuating mechanical stresses result in formation of micro cracks. The cracks propagate along lines of weakness, which act as stress contractors. The design is driven by the fatigue (mainly rolling). For components with rolling elements, these degradations come essentially from rolling and pitting fatigue.
- *Imperfection*: friction is the main intrinsic imperfection of mechanical components, it alters the overall performance (power transmission). Stiffness and inertia can take part but with less importance.
- *Environment*: depending on the vibratory level, it involves failure due to fatigue or mechanical overstress, wear, lossening of fasteners (e.g. screw, bolts) at resonance frequency. The design is driven by the maximum stress seen in a given section of the actuator housing.

In table 2.1, the retained KDD for the 4 categories of mechanical components found in EMAs are listed.

Component	**KDD**	**Component**	**KDD**
BEARINGS	max stress rolling fatigue pitting fatigue ** ball speed * friction	SCREW-NUT MECHANISM	max stress rolling fatigue pitting fatigue ** ball speed *** friction resonance frequency buckling
HOUSING	max stress fatigue stress resonance modes machining constraints	ROD ENDS	max stress friction

* *for internal heating due to centrifugal forces and friction;*
** *motionless varying stress;*
*** *for outer recirculation limitation on ball screw technology*

TABLE 2.1: *KDD for mechanical components*

To link the KDD with data, the main mechanical KDDs (table 2.1) are associated to indicators. Some of these indicators are estimated on mission profiles expressed by evolution with time of load F(t) and position x(t), others come from the application itself such as the top level specification). Their value is either the extrema of the flight data variables or it comes from a combination of them (section 2.4 details it).

The table 2.2 gathers these indicators whose values make the EMA specification of the mechanical components.

KDD	Indicator over mission profile	Mathematical relation	Deduced specification	Units
component stress	max load	$F_{max} = \max[\|F(t)\|]$	max static load F_{max}	N
pitting fatigue			load frequency f_{load}	Hz
			total lifespan T_{life}	hour
	equivalent pair (static load, dynamic load peak-to-peak)	Rainflow matrix (*)	pair (F_{static}, $F_{dyn,ptp}$)	(N, N)
rolling fatigue	equivalent rolling fatigue load (*)	$F_{rmc} = \sqrt[3]{\frac{1}{L_{eq}} \int \|F(t)\|^3 \cdot \|\dot{x}(t)\| \cdot dt}$	equivalent rolling fatigue load F_{rmc}	N
	equivalent distance travelled (*)	$L_{eq} = \int \|\dot{x}(t)\| \cdot dt$	equivalent distance travelled L_{eq}	m
			total lifespan T_{life}	hour
ball speed	max speed	$v_{max} = \max[\|\dot{x}(t)\|]$	max speed v_{max}	m/s
stroke	max position amplitude	$L_s = \|\max[x(t)] - \min[x(t)]\|$	stroke L_s	m

* *see section 2.4*

TABLE 2.2: *KDD (mechanical components) & their corresponding indicators*

2.2.2 Electrical components

This study is reduced to a brushless DC motor ignoring its electronic powering system and sensors.

Herebelow, the design drivers of the electrical motor are identified:

- *Performance*: Current induces excessive magnetic field which:
  - involves magnet demagnetization i.e. it decreases the magnetic characteristics of permanent magnets. Nowadays, this risk is reduced with the Rare Earth magnets such as the magnets of samarium–cobalt ($SmCo_5$) or neodymium–iron–bore ($Nd_2Fe_{14}B$) (fig. 2.2).
  - saturates magnetically the steel sheets especially at the teeth level of the notches where the winding is (magnetic saturation in fig. 2.3)

The retained KDD is the magnetic saturation of iron sheets that happens when reaching a given maximum transient current flow or peak torque.

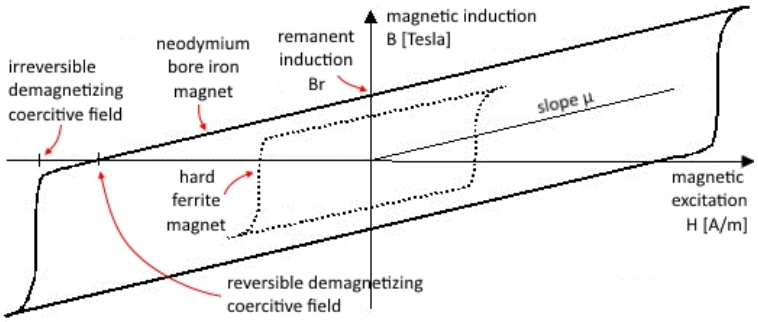

FIGURE 2.2: *Permanent magnet induction B limits under external magnetic excitation H*

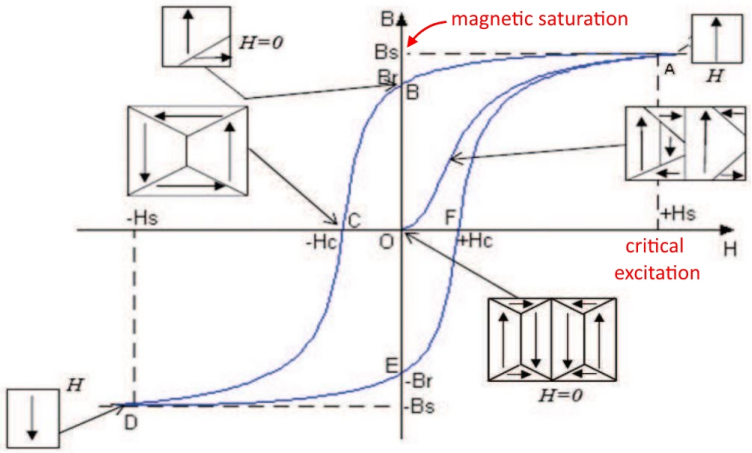

FIGURE 2.3: *Curve of first magnetization (OA) and hysteresis cycle (ABCDEF) of a ferromagnetic material [Bui, 2011]*

- *Performance*: The electrical behaviour of Permanent Magnet Synchronous (PMS) machines can be represented by a RLE circuit (Benh-Eschenburg's model, [Multon, 2010], see Appendix O):

$$V_s = E_b + \mathscr{L} \cdot \frac{di}{dt} + \mathscr{R} \cdot i \; with \; E = f(\omega) \tag{2.1}$$

  where V_s $[V]$ is the motor voltage supply, E_b $[V]$ the electromotive force, $\mathscr{L}$ $[H]$ the winding inductance, $\mathscr{R}$ $[Ohm]$ the winding resistance, i $[A]$ the current intensity, and ω $[rad/s]$ the rotor speed. As the voltage supply V_s is limited, the speed creating the electromotive force E_b is limited. Also, there is a centrifugal force limit for keeping the magnets attached to the rotor.

  The KDD is the rotor maximal speed.

- *Endurance*: Current generates Joules losses which heats up the motor. The consequences are:
  - excessive temperatures alter component performance (magnets, wire resistivity)
  - reductions of the life span of wire insulation: the higher is the temperature, the lower is the life span of insulators. An insulator aging is likely to create short circuits.

  The KDD is the average motor overheating i.e. the continuously applied Joules losses Q_J $[W]$ which are involved in the winding continuous temperature. Since $Q_J = \mathscr{R} \cdot I^2 = K_t \cdot T^2$, an equivalent continuous torque, the *Root Mean Square (RMS)* torque, is classically chosen [Budinger, 2014].

- *Imperfection 1*: the rotor inertia J_m $[kg.m^2]$ acts as an energy storage which:
  - increases drastically, in dynamic applications, the electromagnetic torque peak T_{motor} and in some extent the motor heat generation:

$$T_{motor} = T_{load} + J_m \cdot \frac{\dot{\omega}}{p} \tag{2.2}$$

  - induces a very high reflected mass $M_{eq} = J_m/p^2$ (p the lead $[m/rad]$) involving high stress when jamming or hitting into actuator end stops.

The rotor inertia is a KDD which takes part in two previous KDD (max continuous temperature & magnetic saturation). It is linked to an equivalent continuous acceleration and a max power rate (section 2.5.2.2).

- *Imperfection 2*: the iron losses heat up the motor. They are critical in high speed applications. They come from magnetic variation (more details in section 2.5.1) as hysteresis loss or Eddy current.

  The iron losses are a KDD, they are involved in the continuous temperature of the motor.

Fig. 2.4 gives a torque-speed diagram reminding the limitations of brushless motors (cylindrical & annular). The diagrams are concretely illustrated with curves from two different motor suppliers.

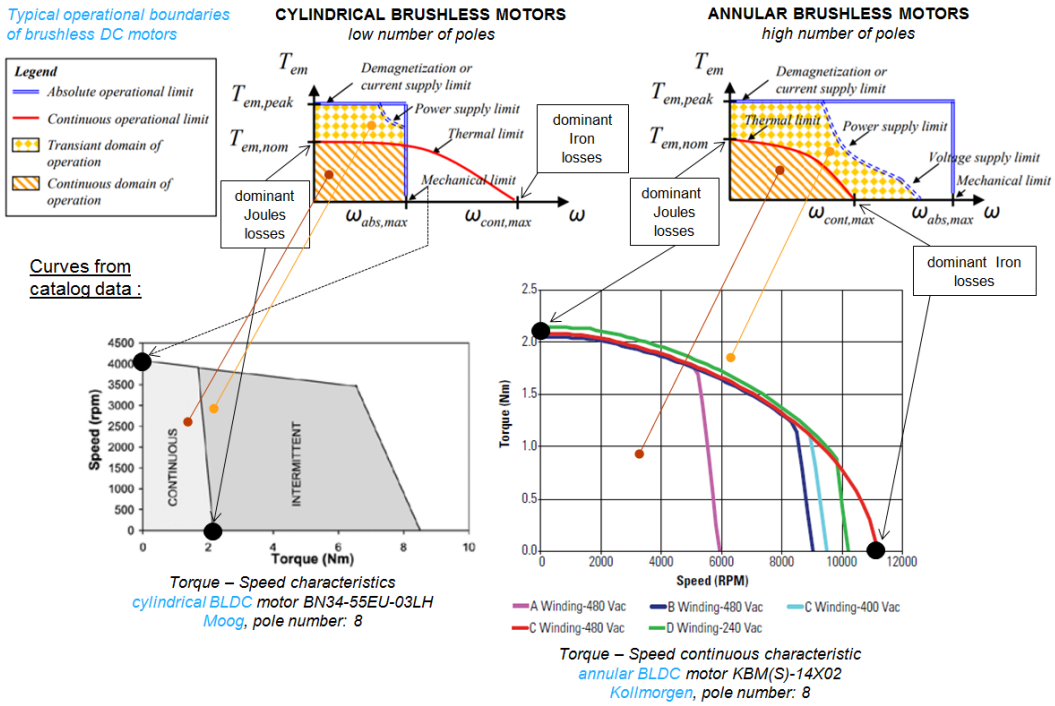

Remark 1: Depending on the cooling technologies, the continuous operating area can be extended.
Remark 2: In annular motors, the thermal boundary is the first operational boundary met whereas in cylindrical motors, this boundary involves 2 KDDs (thermal & mechanical aspects).

FIGURE 2.4: *Motor operating area global overview (adapted from [Liscouet, 2010])*

In table 2.3, the retained KDDs for the electrical motor are listed.

Component	KDD
ELECTRICAL MOTOR	max continuous temperature (Joules & iron losses) magnetic saturation (peak torque) max voltage & magnet attachment resistance (max rotor speed)

TABLE 2.3: *KDD for electrical components*

To link the KDD with data, the main electrical KDDs (table 2.3) are associated to indicators. Their value is either the extrema of the flight data variables or it comes from a combination of them (section 2.5 details it).

Table 2.4 gathers these indicators which values make the EMA specification of the electrical components.

KDD	Indicator over mission profile	Mathematical relation	Deduced specification	Units
motor max speed	max speed	$v_{max} = \max[\lvert\dot{x}(t)\rvert]$	max speed v_{max}	m/s
motor magnetic saturation	max load	$F_{max} = \max[\lvert F(t)\rvert]$	max static load F_{max}	N
	max acceleration	$a_{max} = \max[\lvert\ddot{x}(t)\rvert]$	max acceleration a_{max}	m/s²
	max power rate (inertia effect) (**)	$PR_{max} = \max[\lvert F(t)\cdot\ddot{x}(t)\rvert]$	(a_{PRmax}, F_{PRmax}), pair maximizing PR	(m/s², N)
continuous motor temperature	RMS load (**)	$F_{rms} = \sqrt{\frac{1}{T}\cdot\int F(t)^2\cdot dt}$	RMS load F_{rms}	N
	RMS acceleration (**)	$a_{rms} = \sqrt{\frac{1}{T}\cdot\int \ddot{x}(t)^2\cdot dt}$	RMS acceleration a_{rms}	m/s²
	mean power rate (**)	$\overline{PR} = \left\lvert\frac{1}{T}\cdot\int F(t)\cdot\ddot{x}(t)\cdot dt\right\rvert$	mean power rate $\overline{PR}$	W/s
	mean value of speed representative of iron losses (**)	$v_{iron} = \sqrt[1.5]{\frac{1}{T}\cdot\int\lvert\dot{x}(t)\rvert^{1.5}\cdot dt}$	iron speed v_{iron}	m/s
			ambient temperature θ_{amb}	°C

** *see section 2.5*

TABLE 2.4: *KDD (electrical components) & their corresponding indicators*

2.2.3 Specification

From tables 2.2 & 2.4, the final specification is filled up. The layout is presented in table 2.5. This specification is used in the actuator sizing process described in section 5.4 and 5.5. The power rate is not appearing in table 2.5 but its analysis allows to get the sizing pair (a_{PRmax}, F_{PRmax}). Chapter 3 will complete this specification by a maximum reflected inertia. This latter criteria can not be obtained through the analysis of flight test data. It will need the development of a loading dynamic model.

	Indicators	Units		Indicators	Units
TO EVALUATE ON MISSION PROFILS	STROKE L_s	m	PROJECT INPUTS	equivalent load mass M_{load}	kg
	equivalent distance travelled L_{eq}	m		ambient temperature θ_{amb}	°C
	SPEED max v_{max}	m/s		max skin temperature $\theta_{max,skin}$	°C
	SPEED iron v_{iron}	m/s		load frequency f_{load}	hz
	ACCELERATION max a_{max}	m/s²		total lifespan t_{life}	flight hours
	ACCELERATION rms a_{rms}	m/s²		current max supply I_{max}	A
	LOAD max F_{max}	N		voltage max supply $V_{dc,bus}$	V
	LOAD rms F_{rms}	N			
	LOAD rmc F_{rmc}	N			
	LOAD pitting $(F_{static}, F_{dyn,ptp})$	(N, N)			
	POWER RATE mean $\overline{PR}$	W/s			
	pair (a_{PRmax}, F_{PRmax}) at PR_{max}	(m/s², N)			

TABLE 2.5: *EMA specification (layout)*

2.3 Mission profile data pre-process

2.3.1 Available data

For the present thesis, available data are load, position and actuator commands over a complete mission profile in time coming from onboard measures during flight tests

on a given applicative helicopter.

As a preliminary approach, the sizing scenarii as being the basic flight phases of take-off, cruise and landing are considered. Transient flight phases should be distinguished from permanent flight phases in the estimation of the indicators. Fig. 2.6 sums it up. The final values for the specification are taken as the maximum occuring among all consistent flight phases.

Indicators	Units	TAKE OFF	CRUISE	LANDING
STROKE L_s	m			
equivalent distance travelled L_{eq}	m			
SPEED max v_{max}	m/s			
SPEED iron v_{iron}	m/s			
ACCELERATION max a_{max}	m/s²			
ACCELERATION rms a_{rms}	m/s²			
LOAD max F_{max}	N			
LOAD rms F_{rms}	N			
LOAD rmc F_{rmc}	N			
LOAD pitting (F_{static}, $F_{dyn,ptp}$)	(N, N)			
POWER RATE mean $\overline{PR}$	W/s			
pair (a_{PRmax} , F_{PRmax})	(m/s², N)			

TABLE 2.6: *Specification: considered phases*

The helicopter rotors are presented in fig. 2.5 with pictures from the Cabri G2. The main rotor and the tail rotor are two different actuation applications. Their working principle is illustrated in fig. 2.6. In fig. 2.5 & 2.6, the positions of the *Main Rotor Actuator (MRA)* and the *Tail Rotor Actuator (TRA)* are identified.

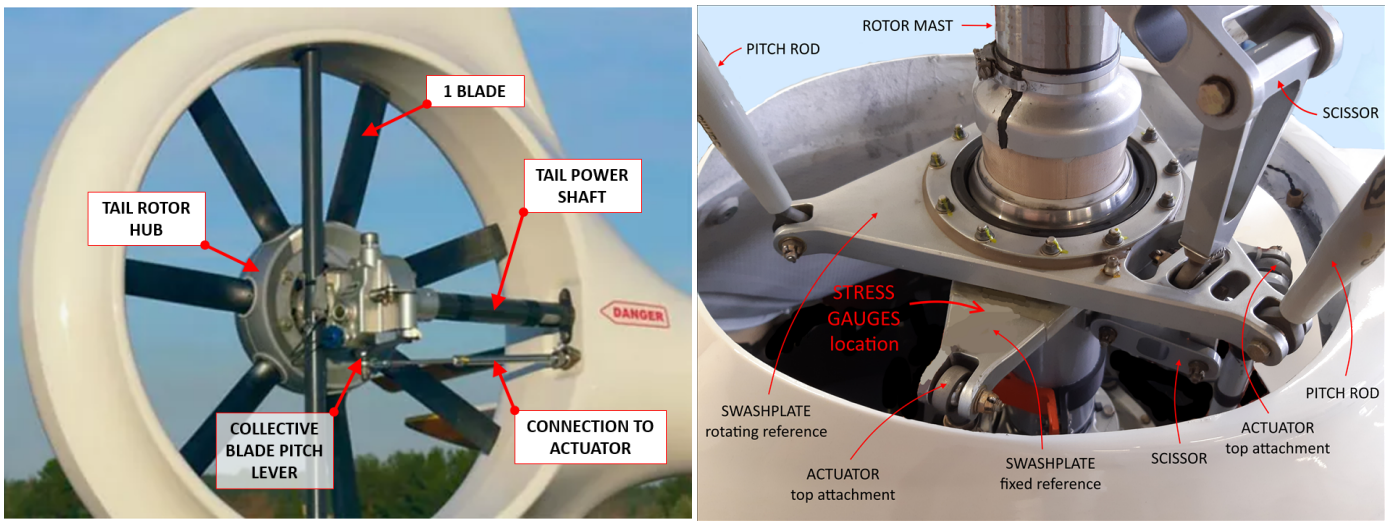

FIGURE 2.5: *Presentation of the CABRI G2 rotors for position and stress gauges localisation: (left) tail rotor, (right) main rotor*

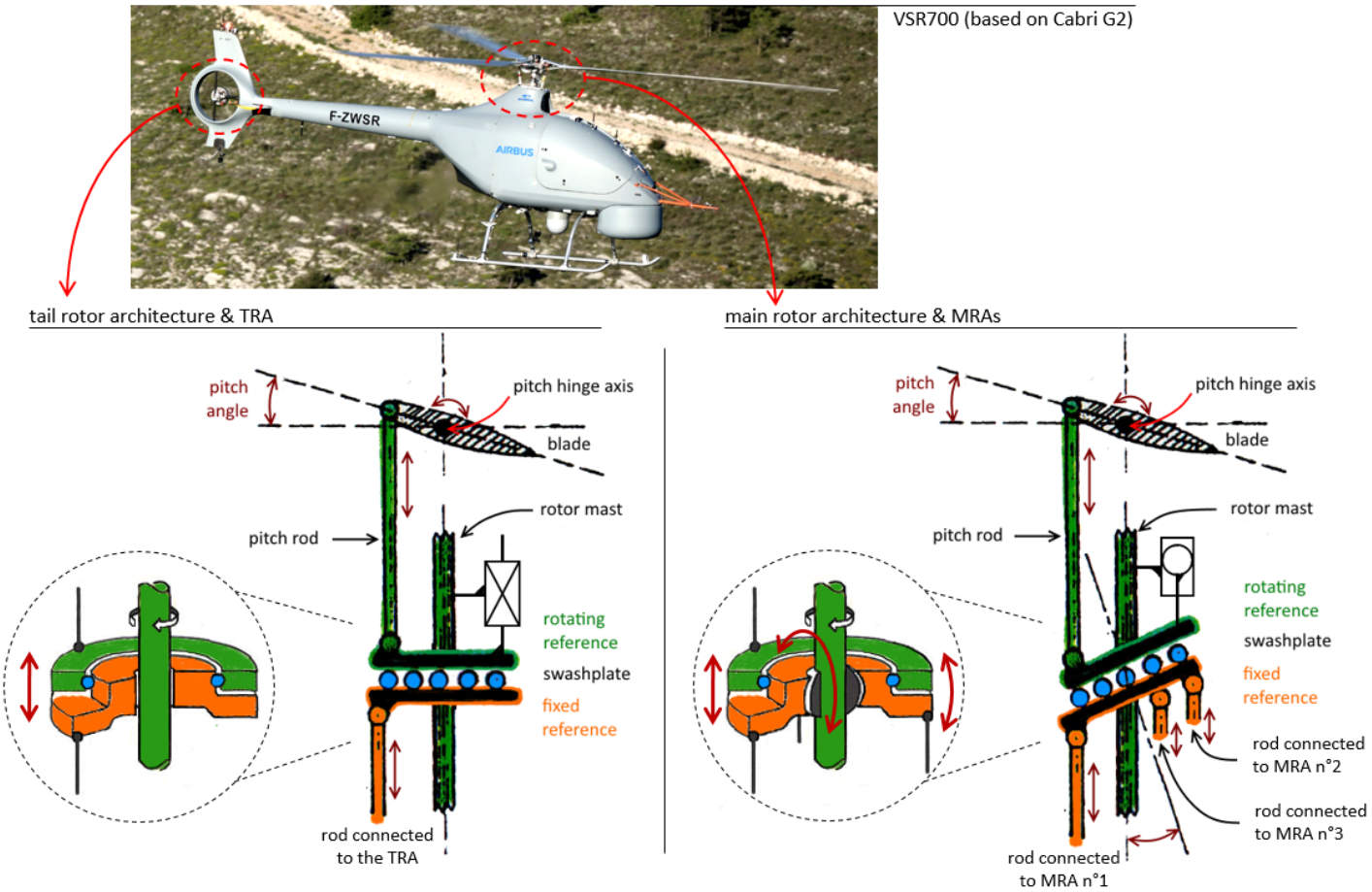

FIGURE 2.6: *Sketches of principle of helicopter rotors and positions of TRA & MRAs: (left) tail rotor, (right) main rotor*

The load recordings regarding the MRA come from stress gauges (fig. 2.5, right) stuck on the swashplate close to the actuator attachment points. Regarding the TRA, the gauges are installed on the levers connecting the actuator to the pitch lever of the tail rotor hub (fig. 2.5, left).

As far as the position recordings are concerned, the data records come from different sources (fig. 2.7):

1. rotative potentiometers with levers installed in parallel of the actuator output rods. Flight test card records it at 2048hz.

2. the linear sensor installed in parallel of the actuator output rod to monitor position. Flight test card records it at 125hz.

3. the rotary sensor installed close to motor to measure and control motor position. Flight test card records it at 125hz.

4. position commands[1] picked on the bus linking a *Flight Control Computer (FCC)* to an *Electronic Control Unit (ECU)*. A flight test card records it at 83hz.

5. position commands picked after the ECU pre-treatment. Flight test card records it at 125hz.

[1]Position commands are precious data since they are additional position sources, only available on helicopters with *Automatic Flight Control System (AFCS)*

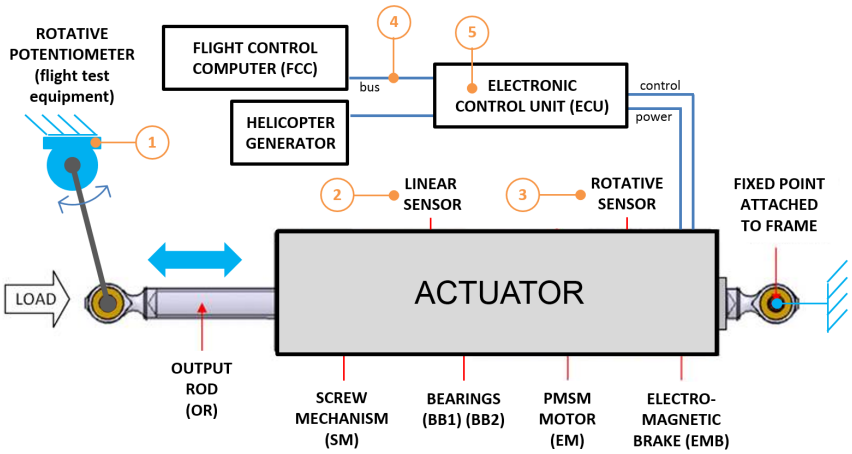

FIGURE 2.7: *Localisation of all position data sources*

2.3.2 Data pre-processing

2.3.2.1 Load

The loads given by stress gauges do not need specific treatment if the sample frequency enables to capture the current bandwidth dynamic. Indeed, usually actuators count a ratio of 5-10 [Lacroux, 1985] between the position & the speed bandwidths and between the speed & the current bandwidths. For a position bandwidth of 6hz, the current bandwidth (i.e. the load bandwidth) would be of 600hz. The stress gauges of the VSR700 sample at a minimum of 1024hz. In this case, applying a filter would be over the Nyquist frequency of this signal. Consequently, no signal treatment is required.

2.3.2.2 Position

The position data and their derivatives need more attention as they are involved in most of the indicators which make combination with the load data. The quality of the data guarantees a representative specification. Quality means that there is no captured noise and a relevant choice of sample frequency regarding environmental perturbations (dominant aliasing phenomena). In practice and as described previously, there are several possible position data configurations and they are summarized in table 2.7.

	Helicopter type	Position sources	Limits	Solutions
CASE 1	with pure mechanical PFCS (e.g. Cabri G2)	position sensor (potentiometers) in parallel of PFCS kinematic	very noisy data, flight not representative of an Airbus stabilized helicopter	extrapolation from other similar helicopters
CASE 2	with automatic pilot (e.g. VSR700)	position sensors (potentiometers) in parallel of PFCS kinematic	very noisy data, position derivatives (speed/acceleration) not representative of reality	Savitzky-Golay filter
CASE 3		actuator sensors (rotary, linear)	noisy data	Savitzky-Golay filter
CASE 4		position command from FCC (bus) or ECU	data is not what is effectively performed by the actuator	filter representative of actuator (3rd order filter with actuator bandwidths)

TABLE 2.7: *Different available position data sources & their possible exploitation*

The first case refers to light helicopters whose stabilization relies only on the pilot's skills. Data are partially useful, they can give an order of magnitude about the stroke value. For speed and acceleration, we only suggest a linear extrapolation from other similar helicopters, proportional to the stroke (one full stroke per time unit and squared time unit, the design office know-how provides the time unit value).

In the second case, the position data from rotational potentiometers includes an important level of noise (from rotor & engine vibrations) and their derivatives (speed, acceleration) are inconsistent. Applying conventional filtering methods is not convenient since the noise removal introduces delays which are not acceptable with the load data. A solution is the Savitzky-Golay filter [Savitzky and Golay, 1964] which has two main advantages:

- it does not introduce any delay in filtered data
- its polynomial approach easily gives derivatives up to the 5th order

In the third case, as in the second case, Savitzky-Golay's filter is suitable too.

In the fourth case, the command has to go through a filter which is representative of the actuator dynamism. We suggest to apply a 3rd order filter in order to represent the position loop bandwidth. The classical ratio between the position and the speed loop bandwidths is 5-10 [Lacroux, 1985]. This 3rd order filter is detailed in Appendix A. The difference between data from FCC and ECU lies into the signal treatment operated by the ECU on the FCC commands.

Furthermore, the table 2.8 shows the diversity of order of magnitude encountered with the different available data sources.

		CASE 2 potentiometer		CASE 3 rotary sensor		CASE 3 linear sensor		CASE 4 ECU	
Recording sampling frequency [hz]		1024		125		125		125	
Treatment		raw	SAVGOL (-3dB@6hz)	raw	SAVGOL (-3dB@6hz)	raw	SAVGOL (-3dB@6hz)	3rd order TF (R=10)	3rd order TF (R=5)
Position [-]	stroke	0,9	0,9	1,0	1,0	1,0	1,0	1,0	1,0
Speed [-]	max	11	2,9	2,0	1,0	2,3	1,0	1,3	1,3
	iron	8,0	2,5	1,6	1,0	2,0	1,0	1,1	1,1
Acceleration [-]	max	923	44	16	1,0	29	0,9	5,2	5,1
	RMS	794	49	21	1,0	37	0,1	3,9	4,0

TABLE 2.8: *Position, speed & acceleration estimations on different position sources for a given flight test and actuator, results are normalized using the filtered results from the rotary sensor*

Table 2.8 highlights that potentiometers do not provide suitable data for speed and acceleration estimation. Indeed, even filtered, they give a speed and acceleration higher than the raw signal from the rotary and linear sensors. If the position was not studied combined with load, another filter (e.g. butterworth) with high order could be applied. In this context, we suggest choosing the ECU commands (case 4) as position data sources for the specification as it does not embbed any noise. In addition, it results in conservative speed & acceleration values compared to the rotary and linear sensors. Also, it takes into account further expectations (actuator dynamism).

2.4 Analysis for mechanical fatigue

This section comes with more details regarding some of the indicators presented previously in table 2.2.

2.4.1 Rolling fatigue

Fatigue is a phenomenom illustrated as in fig. 2.8 where elementary test samples are loaded periodically with a monotonically increasing magnitude. Smoothing up the experimental points gives the endurance curve or curve of Wöhler. This quantifies the fatigue resistance of the material.

Three different fatigue domains can be noticed [Duprat, 1997]:

- *oligocyclic fatigue* (low number of cycles, $N < 10^4$), a domain where the stress level is around the elastic limit.
- *limited endurance* ($10^4 < N < 10^6$): a domain where the cracks occur after the application of a limited number of cycles. Working structures under volume and mass constraints (especially aeronautic airframes) belong to this domain.
- *unlimited endurance* ($N > 10^6$): under a given level of stress (named fatigue limit), whatever the number of cycles, no crack appears.

The reference [Duprat, 1997] mainly gives 4 models expressing partially or entirely the three endurance domains:

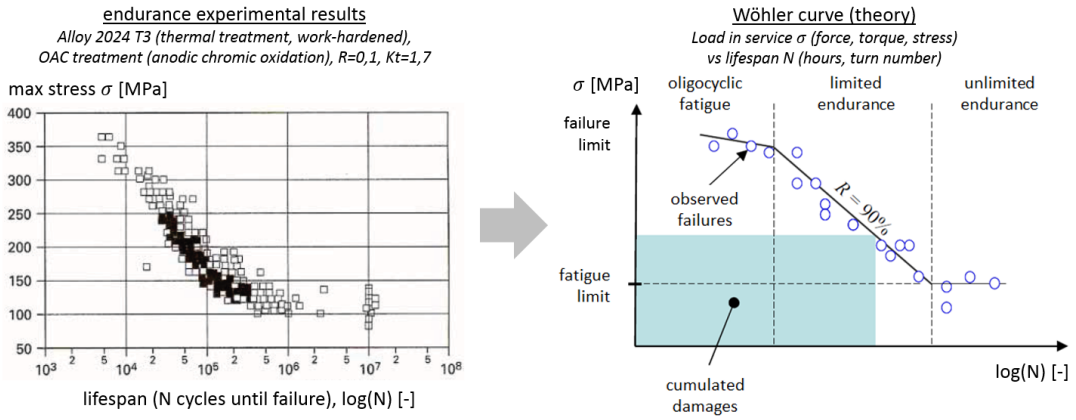

FIGURE 2.8: *Fatigue endurance curve (experimental & theoretical)) [Duprat, 1997]*

Wöhler:	$log(N) = k_1 - k_2 \cdot \sigma_{max}$
Basquin:	$log(N) = k_1 - k_2 \cdot log(\sigma_{max})$
Palmgren:	$log(N + k_a) = k_1 - k_2 \cdot log(\sigma_{max} - \sigma_f)$
Basténaire:	$log(N + k_b) = k_1 - k_2 \cdot log(\sigma_{max} - \sigma_f) + k_3 \cdot (\sigma_{max} - \sigma_f)$

N	life rating in number of cycles	$[-]$
k_1, k_2, k_3, k_a, k_b	empirical constant in $[0; +\inf[$	$[Pa]$, $[-]$
σ_{max}	max nominal stress in service	$[Pa]$
σ_f	fatigue limit	$[Pa]$

The present interest is focused on the limited endurance domain since the context is with mass/volume reduction constraints combined with flight safety. The Basquin model is fairly representative of it. [Budynas et al., 2008] states a load-life function at 90% reliability such as:

$$\sigma^{k_2} \cdot N = C^{st} = D \tag{2.3}$$

with the following empirical values:

$k_2 = 3$	for ball bearing	$[-]$
$k_2 = 10/3$	for roller bearings (cylindrical & tapered rollers)	$[-]$
D	cumulated damage quantity leading to failure with 90% reliability	$[Pa^{k_2}]$

The manufacturer SKF defines similarly the life rating of its components [SKF, 2008, SKF, 2018a]. SKF uses the empirical formula of Lundberg-Palmgren:

$$N_{10} = (\frac{C_d}{F})^3 \tag{2.4}$$

with N_{10} the life rating in million of revolutions (10^6), C_d the basic dynamic load rating in $[N]$ (a catalog data) and F the dynamic load of the application in $[N]$.

In addition, the hypothesis of Palmgren-Miner [Duprat, 1997] states that the damage is linear and cumulative. Therefore, the damage can be broken down as the sum of each single damage:

$$D = \sigma^{k_2} \cdot N = \sum_k D_k = \sum_k \sigma_k^{k_2} \cdot N_k \tag{2.5}$$

2.4.1.1 Equivalent load F_{RMC}

Adapting eq. 2.5 to the available flight data measures (position, load), the equivalent rolling fatigue load F_{RMC} (fig. 2.9) combined with the cumulative distance travelled L_{eq} re-define a damage D such as:

$$D = F_{RMC}^3 \cdot L_{eq} = \sum_{1}^{t_T/\Delta t} F_k^3 \cdot L_k \tag{2.6}$$

$$L_k = \Delta t \cdot \dot{x}_k \tag{2.7}$$

with $L\ [m]$ the distance travelled and $\dot{x}\ [m/s]$ the linear speed during the sampling time period $\Delta t\ [s]$. $t_T\ [s]$ is the total mission duration.

Thus, it follows:

$$F_{RMC}^3 \cdot \int_0^{t_T} |\dot{x}(t)| \cdot dt = \int_0^{t_T} |F(t)|^3 \cdot |\dot{x}(t)| \cdot dt \tag{2.8}$$

which gives :

$$F_{RMC} = \sqrt[3]{\frac{1}{L_{eq}} \int_0^{t_T} |F(t)|^3 |\dot{x}(t)| dt} \tag{2.9}$$

and

$$L_{eq} = \int_0^{t_T} |\dot{x}(t)| dt \tag{2.10}$$

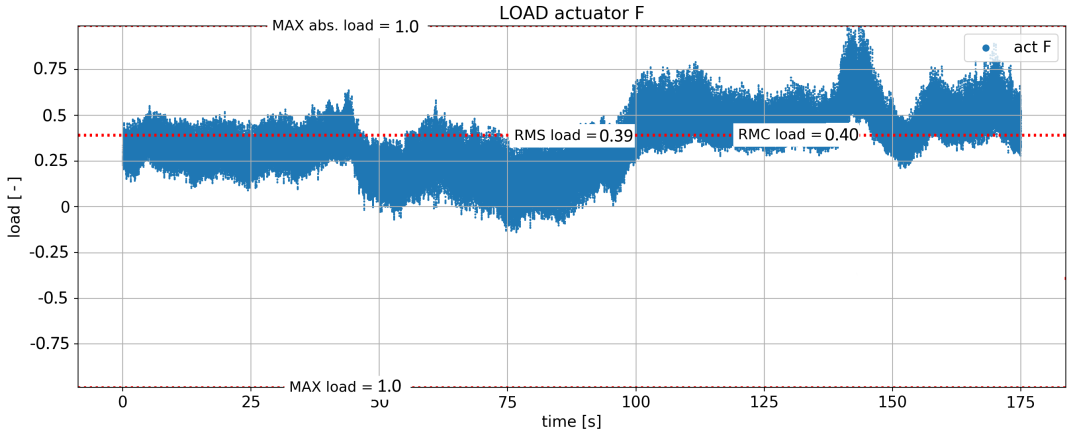

FIGURE 2.9: *Example of an actuator loading during a CRUISE flight, values normalized by the absolute maximum load*

2.4.1.2 Equivalent distance L_{eq}

Defined in eq. 2.10, L_{eq} provides a cumulative distance travelled. When displayed over time, it gives the equivalent speed steps over which an actuator on test bench has to be launched to reach the distance L_{eq} (fig. 2.10). This is relevant to specify an endurance test for instance.

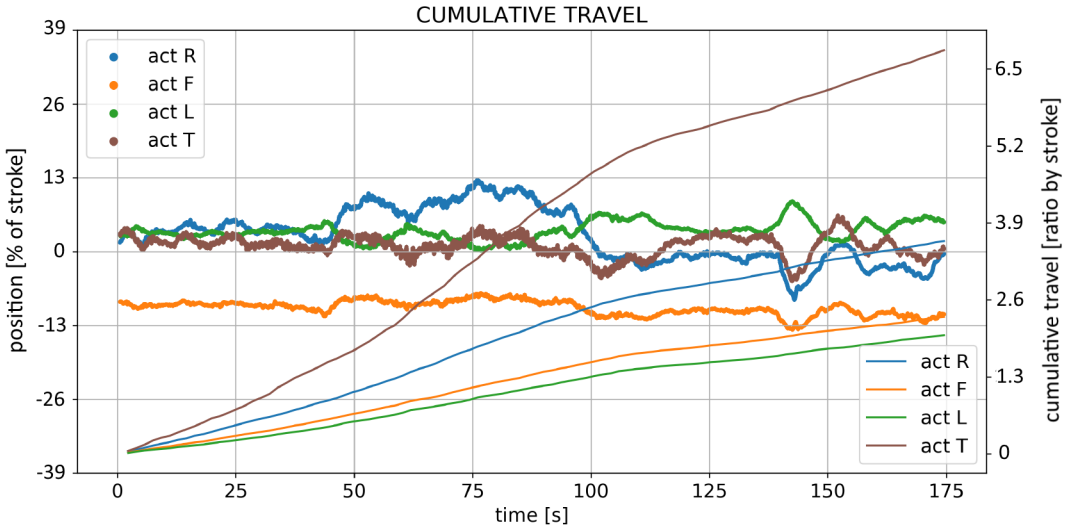

FIGURE 2.10: *Example of cumulative distance travelled by an actuator during a CRUISE flight (175s), values normalized with the application stroke*

2.4.1.3 Fatigue distribution

In flight control actuation applications and especially during cruise flight phases, the rolling fatigue might be concentrated around a given position.

The distribution of cumulated damages per stroke area is important to display. This distribution is a useful tool for the actuator designer when it comes to choose the screw mechanism lead and/or the gear reduction ratio. Considering the mechanical transmission lifespan only, the ideal design is the one with damages evenly spread along the entire stroke.

The spacial distribution is based on a total amount of damage D provided by the application of duration t_T $[s]$. D is broken down into the damages D_j occuring in each stroke area j of range 1 mm.

$$D = F_{RMC}^3 \cdot L_{eq} = \sum_{j=0}^{j=stroke,max} D_j \tag{2.11}$$

$$D_j = \sum_{s=1}^{s=t_T/\Delta t} D_{j,s} \;\; with \; t_s = s \cdot \Delta t \tag{2.12}$$

$$D_{j,s} = \begin{cases} |F(t_s)|^3 \cdot |\dot{x}(t_s)| \cdot \Delta t & : \; if \; x(t_s) \subset [x_j - 0.5; x_j + 0.5] \; [mm] \\ 0 & : \; if \; x(t_s) \not\subset [x_j - 0.5; x_j + 0.5] \; [mm] \end{cases}$$

Δt $[s]$ is the sampling time period used by the flight test equipment, s $[-]$ is the number of time periods within the total mission duration t_T. The fatigue distribution is normalized by the total amount of damage D. Fig. 2.11 illustrates the fatigue distribution. Δt $[s]$ and t_T rely on the available flight data sets. To ensure good representativeness of fatigue phenomena, long mission durations are preferred.

The helicopter application (fig. 2.11) show that the rolling fatigue is concentrated on a small part of the total stroke. This is an important information for the next steps of the actuator predesign. Indeed, it will be necessary to check that this identified fatigue area corresponds to, at least, a full shaft rotation. This will depend on the

reduction ratio. If a full shaft rotation is not done, the components will have to be oversized regarding rolling fatigue.

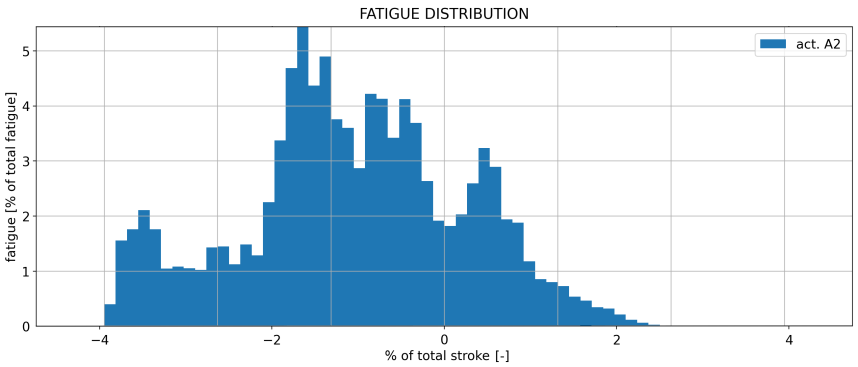

FIGURE 2.11: *Example of fatigue distribution during a CRUISE flight (175s), x-axis values normalized by the actuator stroke*

2.4.2 Pitting fatigue

The pitting fatigue takes place when a dynamic loading is applied onto motionless parts (high ratio of load frequency versus position frequency).

To capture the phenomenon, one can proceed through a rainflow method to count the loading cycle content of the mission profile (see Appendix B). This outputs a rainflow matrix providing a classification of the loading cycles by numbers of occurrences for different classes of static and dynamic loads.

Fig. 2.12 shows the rainflow heatmap of a CRUISE flight phase with a colour gradient corresponding to loading occurrences. This highlights a loading spectrum with 3 classes: a big load amplitude with a low number of occurrences, a medium load amplitude with a medium number of occurrences and a low load amplitude with a high number of occurrences.

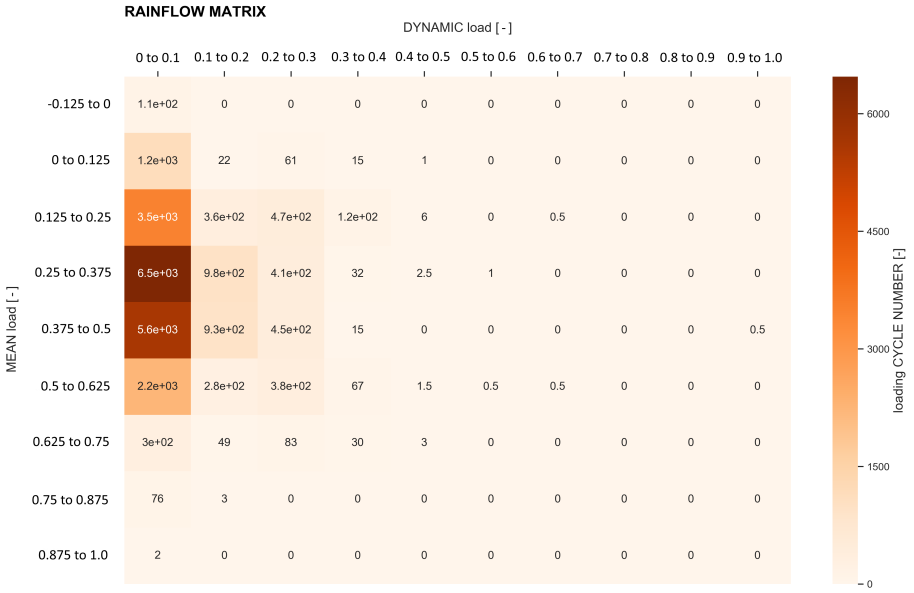

FIGURE 2.12: *Example of a Rainflow matrix applied on an actuator loading during a CRUISE flight (175s), x-axis values normalized by the maximum dynamic load (half peak-to-peak) recorded, y-axis values normalized by the maximum static load recorded*

2.5 Analysis for motor performance

This section comes with more details regarding some of the indicators presented previously in table 2.4.

2.5.1 Continuous performance

The continuous operation is the critical scenario for an EMA. As said in [Maré, 2017], the EMA can not take advantage of the fluid flowing inside it (such as in hydraulic actuators) to improve the heat exchange with the outside. However, the good thermal capacity of its metallic components allows absorbing the power peaks. Built with winding and steel sheets, the electrical motor shows a significant thermal capacity. Its temperature is often controled by the continuous loading applied.

2.5.1.1 Copper & Iron losses

Fig. 2.13 shows the link suggested between one of the motor KDD (continuous temperature) and the mission profile.

As previously mentioned, copper and iron losses take part in the motor maximum continuous temperature.

The iron losses evolve following the electrical speed [Grellet, 1989] such as:

$$Q_{iron} \propto \omega_e^b \text{ with } b \in [1,2] \tag{2.13}$$

where ω_e $[rad/s]$ is the electrical speed and b $[-]$ a constant. The value of b depends on the motor design which can be in favor of either hysteresis ($b = 1$) or Eddy current ($b = 2$) losses [Grellet, 1989]. For a preliminary study, a mean value of $b = 1.5$ is chosen. What's more, an obvious and direct variable of mission profile reflecting the

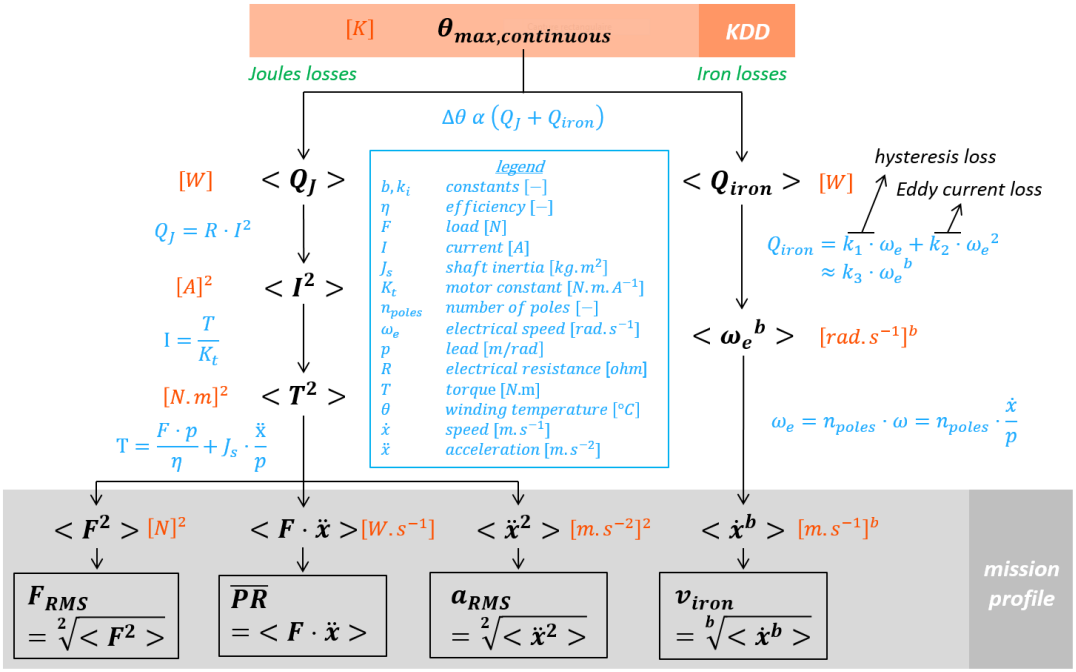

FIGURE 2.13: *Indicators dedicated to motor max continuous temperature*

electrical speed is the linear speed. Thus, we suggest the equivalent averaging speed v_{iron} as the representative indicator:

$$v_{iron} = \sqrt[1.5]{\frac{1}{t_T}\int_0^{t_T} |\dot{x}(t)|^{1.5} dt} \tag{2.14}$$

with $x(t)$ the position $[m]$. This variable is displayed in fig. 2.14

Joules' losses evolve, following the continuous electromagnetic torque performed by the motor T_{RMS}:

$$\begin{aligned} T_{RMS}^2 =< T(t)^2 > =< \left(\frac{F(t)\cdot p}{\eta_B} + J\cdot\frac{\ddot{x}(t)}{p}\right)^2 > \\ = \underbrace{\left(\frac{F_{RMS}\cdot p}{\eta_d}\right)^2}_{1} + \underbrace{\left(J\cdot\frac{a_{RMS}}{p}\right)^2}_{2} + \underbrace{2\cdot\frac{J}{\eta_d}\cdot < F(t)\cdot\ddot{x}(t) >}_{3} \end{aligned} \tag{2.15}$$

where p $[m/rad]$ is the screw lead, η_d, η_i $[-]$ are the screw efficiencies (direct, indirect), J $[kg\cdot m^2]$ is the rotating inertia. η_d $[-]$ is kept to ensure upper margins on final estimations. η_B $[-]$ is the Boolean function of the screw efficiency depending on the load sens and defined by:

$$\eta_{\mathscr{B}} = \eta_d(\mathscr{B} > 0) + \eta_i(\mathscr{B} < 0) \begin{cases} \mathscr{B} = 1 & \text{if } F(t) > 0 \\ \mathscr{B} = -1 & \text{if } F(t) < 0 \end{cases} \tag{2.16}$$

1. On one hand, this torque is linked to the load the actuator shall fight against. In this case, as indicator on mission profile, an equivalent continuous loading

value, the RMS load, makes sense:

$$F_{RMS} = \sqrt[2]{\frac{1}{t_T}\int_0^{t_T} |F(t)|^2\, dt} \tag{2.17}$$

This variable is displayed in fig. 2.9.

2. On a second hand, this torque is linked to a motor KDD: the rotor inertia. In this case, the variable at stake is the acceleration. As an indicator on mission profiles, we suggest an equivalent continuous acceleration value resumed by the RMS value of the acceleration:

$$a_{RMS} = \sqrt[2]{\frac{1}{t_T}\int_0^{t_T} |\ddot{x}(t)|^2\, dt} \tag{2.18}$$

with $x(t)$ the position $[m]$. This variable is displayed in fig. 2.15.

3. On a third hand, this torque is linked to the mean value of the combination of the load with the acceleration named the power rate. We suggest to use it as an indicator:

$$\overline{PR} = |<PR(t)>| = |<F(t)\cdot\ddot{x}(t)>| = |\frac{1}{t_T}\int_0^{t_T} (F(t)\cdot\ddot{x}(t))\, dt| \tag{2.19}$$

The mean power rate takes an absolute value as a design margin.

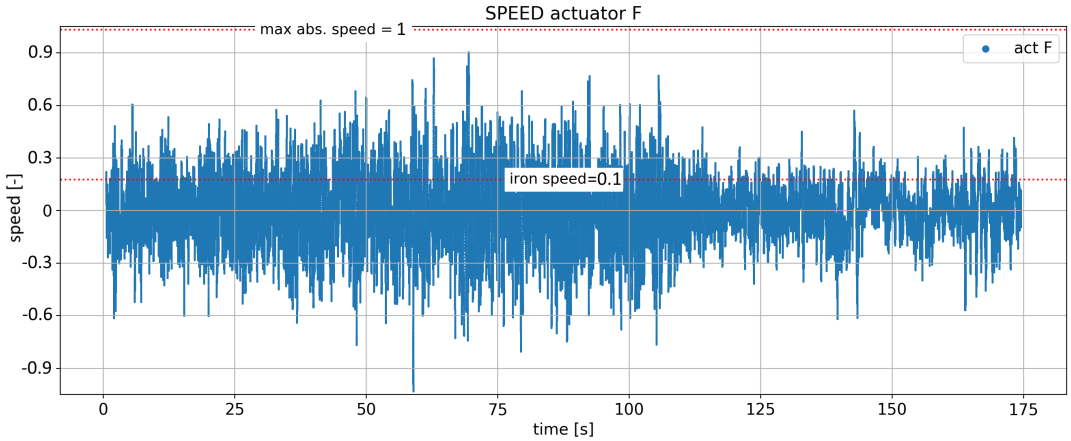

FIGURE 2.14: *Example of an actuator speed during a CRUISE flight (175s), the y-axis values are normalized by the maximum speed recorded*

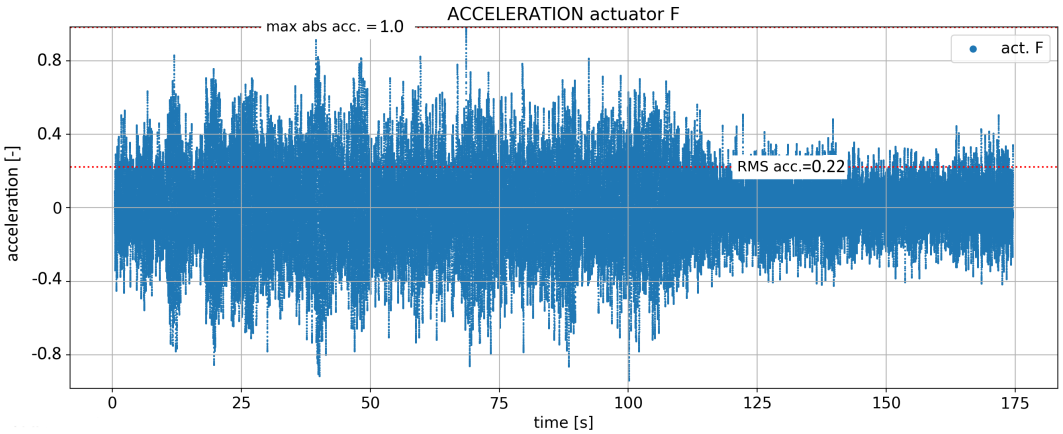

FIGURE 2.15: *Example of an actuator acceleration during a CRUISE flight (175s), y-axis values normalized by the maximum acceleration recorded*

2.5.1.2 Thermal distribution

In this section, the thermal behaviour of the electrical motor is represented to justify the consistency of the use of the RMS averaged load (F_{RMS}). The mission profile (a time varying force $F(t)$) of any non-transient flight phase is filtered through a simplified thermal model of the motor (see Fig. 2.16). The model is a transfer function with the same time response as a typical brushless motor. The objective is to check if the simulated temperature evolution can be assimilated to a continuously applied load of F_{RMS}.

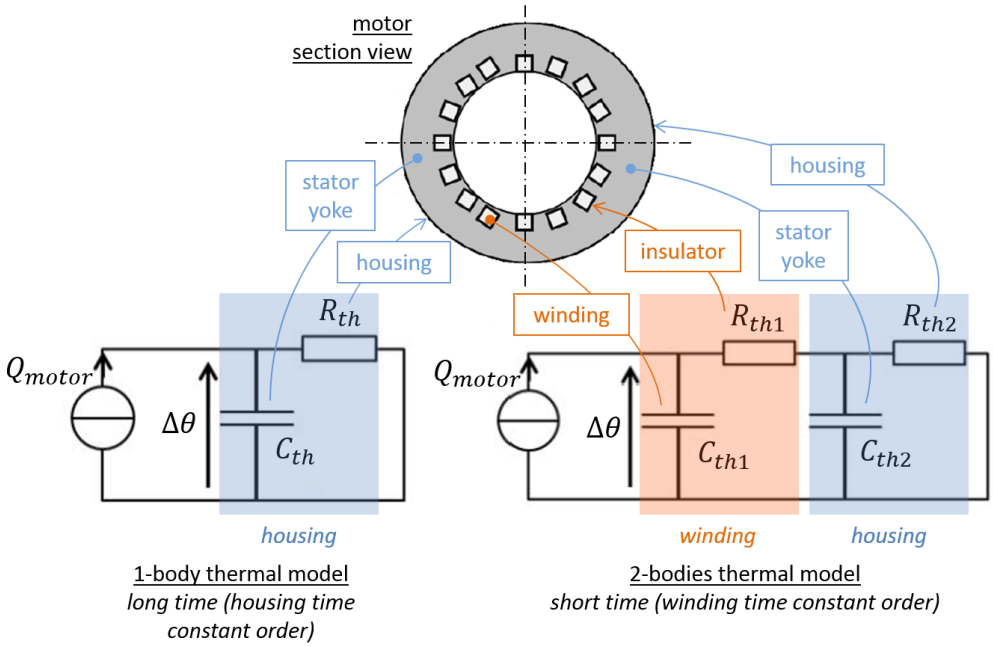

FIGURE 2.16: *Thermal model consideration*

Two modelling levels have been developed depending on the mission profile length. For short periods of time (winding time constant magnitude), the 2-bodies model is the most suitable. For longest periods of time (housing time constant magnitude), the 1-body model should be used. In a steady state, a pure resistant model suits too.

The model is based on the following hypothesis:

- The inertial torque is not considered since the future rotor inertia can not be predicted.
- The heat source comes only from Joules losses: $Q_{motor}(t) = Q_J(t)$. Passing over the screw-nut efficiency and the reduction ratio of the actuator, the heat source appears being proportional to the squared load:

$$Q_{motor}(t) = \mathscr{R} \cdot I(t)^2 = \mathscr{R} \cdot \left(\frac{T(t)}{K_t}\right)^2 \approx \underbrace{\left(\frac{\mathscr{R} \cdot p^2}{K_t^2 \cdot \eta^2}\right)}_{k} \cdot F(t)^2 \approx k \cdot F(t)^2 \quad (2.20)$$

  where $\mathscr{R}$ $[Ohm]$ the motor resistance, I $[A]$ the motor current intensity, T $[m \cdot N]$ the motor torque, K_t $[m \cdot N/A]$ the motor torque constant, p $[m/rad]$ the screw lead, η $[-]$ the screw-nut efficiency, $F(t)$ $[N]$ is the measured linear force of the actuator, k is any constant representative of the proportionality between $Q_{motor}(t)$ $[J]$ and $F(t)^2$ $[N^2]$.

The transfer function $G_i(s)$ is worked out by the impedance method between the winding temperature $\Delta\theta$ and the motor heat generated Q_{motor} (fig. 2.16), and according to the two modelling levels. This gives the following expressions of the thermal transfer function:

- 1-body model :

$$G_1(s) = \frac{\Delta\theta}{k \cdot F^2} = \frac{R_{th}}{1 + \tau_{th} \cdot s} \quad (2.21)$$

$$\tau_{th} = R_{th} \cdot C_{th} \quad (2.22)$$

  where τ_{th} $[s]$ is the thermal time constant. The authors in [Budinger et al., 2014] & [Reysset, 2015] provide an order of magnitude:

$$G_1(s)\ parameter\ range : \left\{ \tau_{th} \subset [10;25] \quad [minutes] \right.$$

- 2-bodies model :

$$G_2(s) = \frac{\Delta\theta}{k \cdot F^2} = \frac{(R_{th1} + R_{th2}) \cdot \left(1 + \left(\frac{\tau}{k_R(1+k_C)(1+1/k_R)^2}\right) \cdot s\right)}{1 + \left(\frac{\tau(1+k_C+k_Ck_R)}{k_Ck_R(1+1/k_C)(1+1/k_R)}\right)s + \left(\frac{\tau^2}{k_Ck_R(1+1/k_C)^2(1+1/k_R)^2}\right)s^2} \quad (2.23)$$

  where k_R $[-]$, k_C $[-]$ and τ $[s]$ are coefficients defined such as:

$$k_R = \frac{R_{th1}}{R_{th2}};\ k_C = \frac{C_{th1}}{C_{th2}};\ \tau = (R_{th1} + R_{th2}) \cdot (C_{th1} + C_{th2})$$

  The authors in [Budinger et al., 2014] & [Reysset, 2015] provide their order of magnitude:

$$G_2(s)\ parameter\ ranges : \left\{ \begin{array}{lll} \tau & \subset [10;25] & [minutes] \\ k_R & \subset [0.25;1] & [-] \\ k_C & \subset [0.25;0.5] & [-] \end{array} \right.$$

The transfer function provides temperatures which values depend on unknown constants (R_{th}, R_{th1}, R_{th2}, k). Since the future design is ignored, these constants can not be known. The exact temperature can not be predicted anyhow. However, the temperature evolution can be predicted. We propose to display it as dimensionless values thanks to the transfer functions $\widetilde{G_1}$ and $\widetilde{G_2}$. They are the respective transfer functions G_1 and G_2 without the gains R_{th}, $(R_{th1} + R_{th2})$ and k:

$$\widetilde{\Delta\theta}(t) = \frac{\Delta\theta(t)}{[\Delta\theta(t)]_{max}} = \frac{(\widetilde{G}_i * F^2)(t)}{[(\widetilde{G}_i * F^2)(t)]_{max}} \ [-] \tag{2.24}$$

Furthermore, the evolution of the filtered load $F_{filtered}$ is interesting to display.

$$F_{filtered}(t) = \sqrt{(\widetilde{G}_i * F^2)(t)} \ [N] \tag{2.25}$$

Indeed, it represents a simplified equivalent load profile that leads to the same motor thermal behaviour as the initial profile. Visually, on graphs (fig. 2.17), its evolution around the RMS value of the initial load profile is visually meaningful. Some acceptable boundaries can be set ($\pm$20%).

Fig. 2.17 presents a thermal analysis onto the concrete case of a cruise mission profile of the VSR700 PT1. The 2-bodies model was the most suitable regarding the mission profile duration. Since the exact thermal time constant can not be known, the motor thermal model can be set between the possible extreme values of its parameters in order to observe any possible behaviour. Therefore, fig. 2.17 shows an upper thermal estimation (the lowest time constant τ, the lowest thermal capacity k_C, the highest thermal resistance k_R) along with a lower thermal estimation (the highest time constant τ, the highest thermal capacity k_C, the lowest thermal resistance k_R).

For having a conservative approach, an initial condition has been supposed: the actuator has no time to cool down before performing the considered mission profile. Thus, the filter starts with an initial temperature corresponding to the RMS average load F_{RMS} of the considered mission profile.

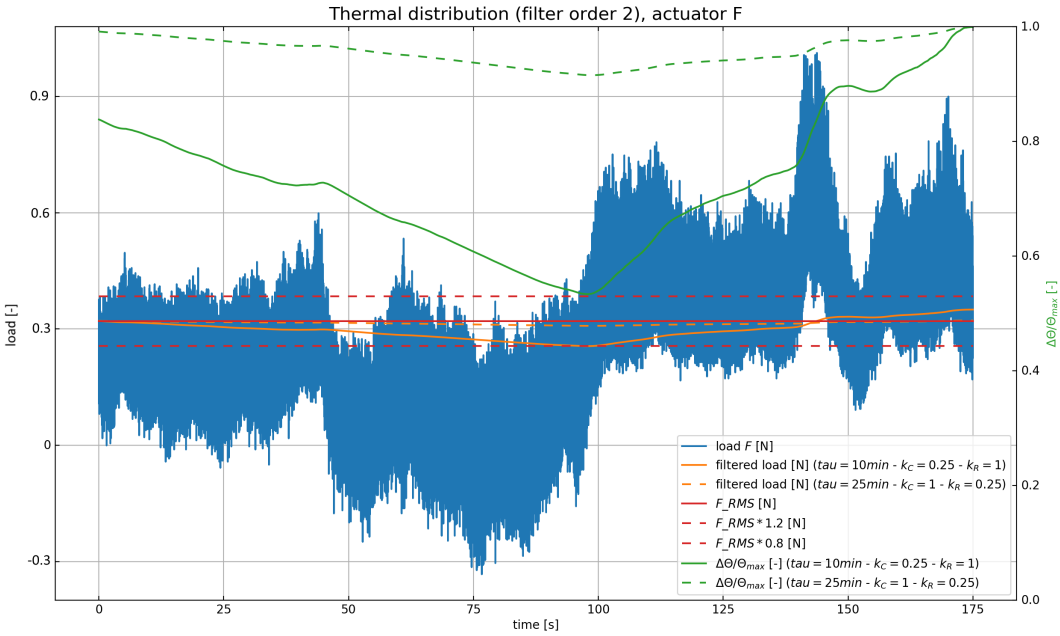

FIGURE 2.17: *Example of a thermal distribution (order 2) during a CRUISE flight (175s), y-axis (load) normalized by the maximum load recorded*

This analysis illustrated by fig. 2.17 states that a safety margin up to 20% on the value F_{RMS} can be taken so as to take into account the uncertainties linked to the dynamic evolution of the motor temperature.

2.5.2 Maximum performance

2.5.2.1 Scenarii

During helicopter operations, the motor maximum performance meets the 3 following scenarii:

- The motor spins with important accelerations and under very low external loads $(\dot{\omega}_{max}, T_{load} = 0)$ $[rad/s^2, N.m]$: the indicator of interest is a_{max} $[m/s^2]$;
- The motor spins under important external loads and with very low accelerations $(\dot{\omega} = 0, T_{load,max})$ $[rad/s^2, N.m]$: the indicator of interest is F_{max} $[N]$;
- The motor spins with accelerations combined with external loads $(\dot{\omega}, T_{load})$ $[rad/s^2, N.m]$: the indicator of interest is the maximum power rate PR_{max} and the corresponding pair (a_{PRmax}, F_{PRmax}).

In the two first cases, the indicators of interest are a_{max} and F_{max}. Here, finding on flight test measures the third case is challenging i.e. the pair $(\ddot{x}(t_i), F(t_i))$ $[m/s^2, N]$, at a given time t_i $[s]$, which maximizes the motor torque. a_{max} and F_{max} do not occur obviously simultaneously at the same time. Also, a Pareto front method applied on data is not sufficient to shortlist one single pair $(\ddot{x}(t_i), F(t_i))$ $[m/s^2, N]$. We propose to proceed through the estimation of the maximum power rate $PR_{max} = a_{PRmax} \cdot F_{PRmax}$ (fig. 2.19). This variable has the interest to remain constant whatever its location into the entire mechanical transmission power chain assuming a mechanical efficiency of 1 (fig. 2.18).

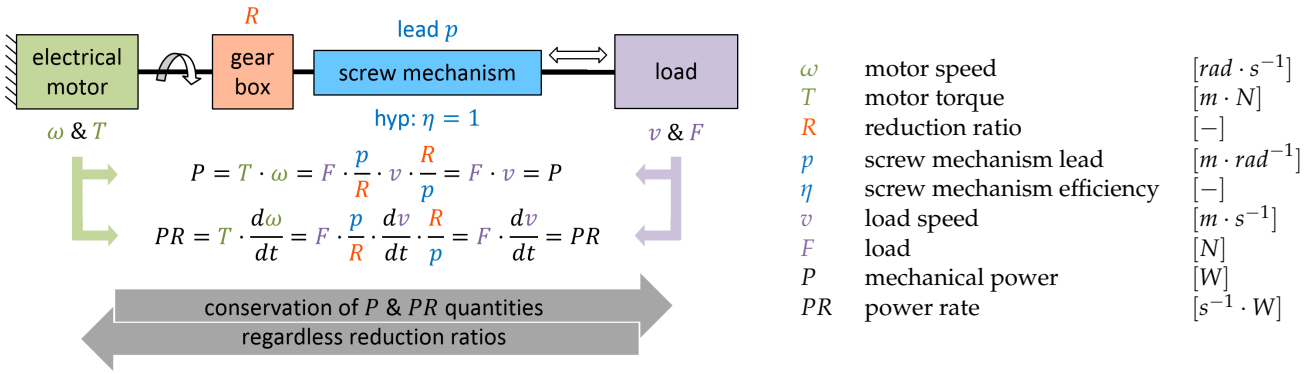

FIGURE 2.18: *Power rate: a conservative quantity through actuator*

2.5.2.2 Max torque at max power rate

We suggest proving by derivation the link between the motor torque and the application power rate. For this, a basic actuator is considered. It includes an electrical motor connected to mechanical components of reduction ratio R. The actuator moves with an acceleration $\dot{\omega}$ under a fluctuating load T_{load}. The power rate is derived from a choice of reduction ratio R minimizing the torque of a given motor in operation:

$$T_{motor} = \frac{T_{load}}{R} + J_{motor} \cdot \dot{\omega} \cdot R \tag{2.26}$$

Eq. 2.26 is minimized if :

$$\frac{\partial T_{motor}}{\partial R} = 0 \implies -\frac{T_{load}}{R^2} + J_{motor} \cdot \dot{\omega} = 0 \tag{2.27}$$

Thus, the optimum reduction ratio is:

$$R = \sqrt{\frac{T_{load}}{J_{motor} \cdot \dot{\omega}}} \tag{2.28}$$

Also, eq. 2.27 gives

$$\frac{T_{load}}{R} = J_{motor} \cdot \dot{\omega} \cdot R \tag{2.29}$$

leading to:

$$T_{motor} = 2 \cdot \frac{T_{load}}{R} \tag{2.30}$$

Furthermore, the torque and the inertia can be linked using a scaling law (see Chapter 4) which is generalised by:

$$J_{motor} = k_{SLr} \cdot T_{motor}^{k_{SLp}} \tag{2.31}$$

where k_{SLp} $[-]$ is the power law constant of the scaling law ($k_{SLp} \subset [1;2[$), $k_{SLr} \subset \mathbb{R}^+$ is a constant linked to components of reference. Eq. 2.30 & eq. 2.31 in eq. 2.29 results in a formulation of the reduction ratio R:

$$\frac{T_{load}}{R} = R \cdot \dot{\omega} \cdot k_{SLr} \cdot \left(2 \cdot \frac{T_{load}}{R}\right)^{k_{SLp}} \tag{2.32}$$

$$R = \left(T_{load}^{1-k_{SLp}} \cdot \dot{\omega}^{-1} \cdot k_{SLr}^{-1} \cdot 2^{-k_{SLp}}\right)^{\frac{1}{2-k_{SLp}}} \tag{2.33}$$

Eq. 2.33 in eq. 2.30 results in:

$$T_{motor} = 2^{\frac{2}{2-k_{SLp}}} \cdot k_{SLr}^{\frac{1}{2-k_{SLp}}} \cdot (\dot{\omega} \cdot T_{load})^{\frac{1}{2-k_{SLp}}} \tag{2.34}$$

Finally, the power rate is defined as $P_{rate} = T_{load} \cdot \dot{\omega}$:

$$T_{motor} = 2^{\frac{2}{2-k_{SLp}}} \cdot k_{SLr}^{\frac{1}{2-k_{SLp}}} \cdot (P_{rate})^{\frac{1}{2-k_{SLp}}} \tag{2.35}$$

This equation can be reduced to the following:

$$T_{motor} = k_{PR1} \cdot (P_{rate})^{k_{PR2}} \tag{2.36}$$

where $k_{PR1} \subset [0;+\inf[$ and $k_{PR2} \subset [1;+\inf[$ are positive constants. $|T_{motor}| = f(P_{rate})$ is maximum when $|P_{rate}|$ is maximum. The maximum power rate $P_{rate,max} = max(|P_{rate}|)$ and its corresponding pair $(|\dot{\omega}|, |T|)$ are representative of one of the critical dynamic scenarii of the application. The pair $(\ddot{x}_{PRmax}, F_{PRmax})$ should be extracted from the mission profiles.

2.5.2.3 Power rate use on mission profiles

Fig. 2.19 illustrates the interest of using an approach based on the power rate. Applying a level of 99% occurrences, it helps mapping data (fig. 2.21).

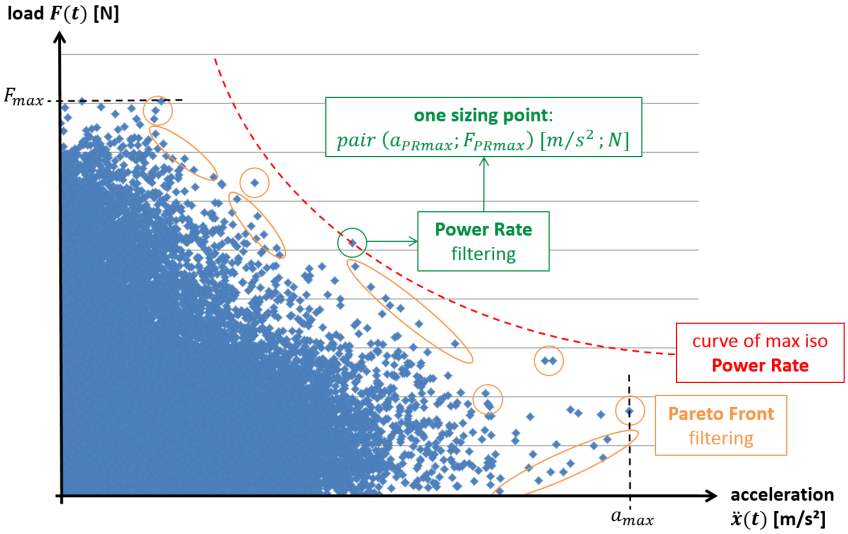

FIGURE 2.19: *Force vs acceleration: determination of critical pair using the power rate*

Fig. 2.19 provides three key information for the actuator: the maximum acceleration without load specified by F_{max}, the maximum load at a standstill specified by a_{max} and the critical dynamic point specified by the pair (a_{PRmax}, F_{PRmax}).

2.6 Complementary analysis

The previous sections were based on temporal analysis. In this section, the mission profile study is completed by a frequency and statistical analysis.

2.6.1 Frequency content

When looking at the load frequency content (FFT, fig. 2.20), a few remarks can be listed. Firstly, the observation of the mean frequency levels clearly highlights a difference of rotor type (see fig. 2.6). Indeed, as reminder, on tail rotors, there are lower load levels and higher speed levels than for the main rotor. Secondly, the observation of the main frequencies highlights the following points.

- The main frequencies show the main rotor speed and its harmonics (530 rpm (8.8 hz), 3 blades).
- The frequency content is biased for the tail rotor (5148 rpm (86 hz), 7 blades) because of the measuring equipment location into the tail rotor actuation system.
- The tail rotor actuation system is different from the one of the main rotor. A flexball is installed going through an important part of the helicopter length (tail boom, motor and gear box area) from the actuator top lever to the tail rotor hub. Since the tail rotor actuation has low load amplitude levels, the high frequency load content is cancelled out by the effect of friction into the long flexball transmission.

- The plot shows an eigenfrequency of the tail rotor actuator at around 65hz. This data is consistent with actuator data from test bench. The main rotor frequency with its 3 blades gives the 27hz with its lower and upper frequencies (e.g. 9hz, 54hz). The helicopter engine frequency is at 125hz.
- A dissimetry in load intensity is seen among the main rotor actuators (R: right, F: front, L: left), the front actuator globally sees higher intensities.
- The load frequency content drops at 500 hz. The sampling frequency of load records can be adjusted accordingly to optimize data storage.

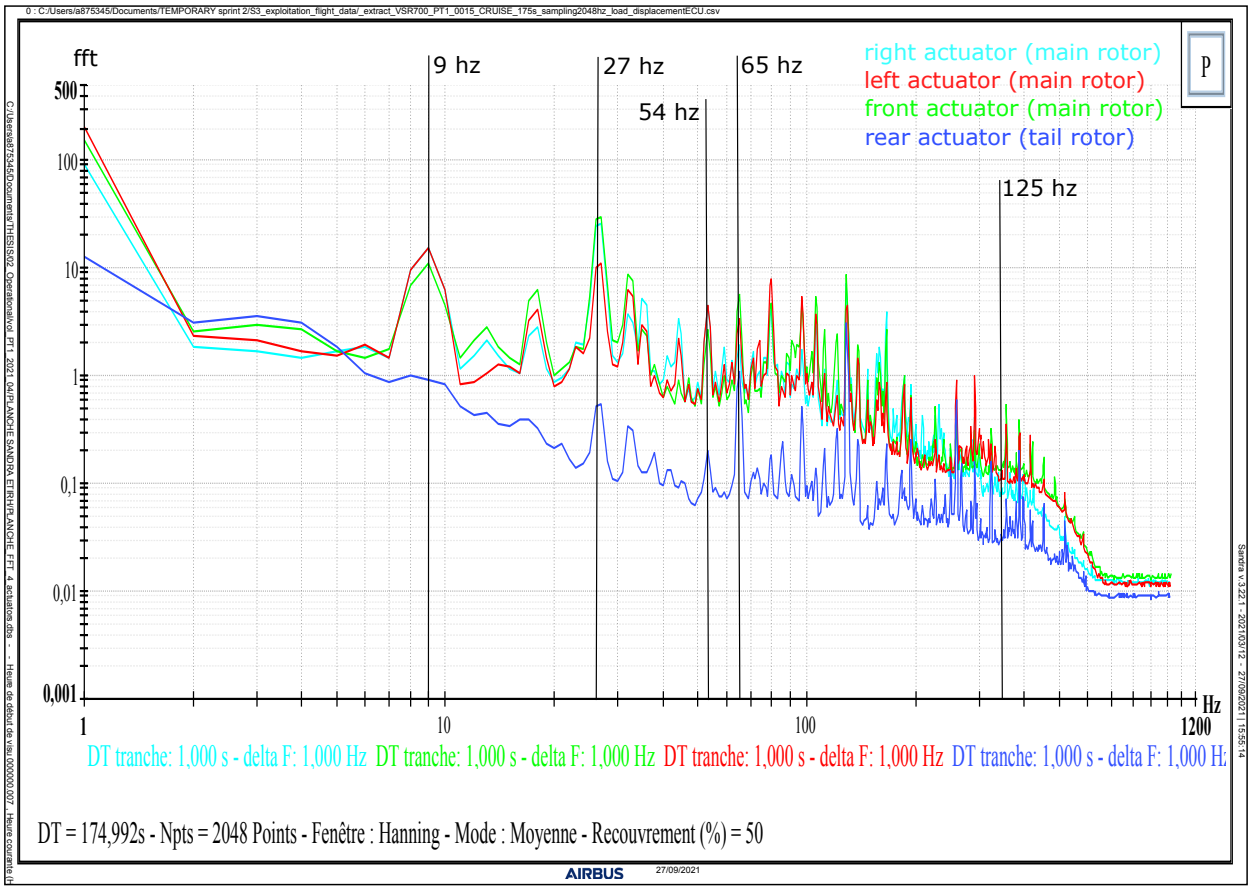

FIGURE 2.20: *Frequency content per rotorcraft actuators (cruise flight, 175s)*

2.6.2 Statistics

In non-transient phases such as cruise phases, we noticed that load, speed and acceleration mission profiles fit Gauss' statistical laws (fig. 2.21). Statistics are a tool for trends. Therefore, their use gets an interest for extrema estimations when the considered mission profiles are non-representative of the helicopter lifespan. In this case, an important extrema might be missed and the future EMA design might be undersized. Consequently, we propose setting up some safeguards for load/speed/acceleration using statistical values based on Gauss' law applied on data. The safeguard is set as it follows:

$$\mathcal{N}(\mu, \sigma) \qquad X_s = \mu \pm k_r \cdot \sigma \tag{2.37}$$

with $k_r = 4.75$ such that $P(X > X_s) = 10^{-6}$. X being the variable of speed, acceleration and load; μ the mean value of X and σ the standard deviation of X. Considering a design with a 10^4 flight hours lifespan, the probability 10^{-6} becomes 10^{-10} per flight hour.

For the application, the maximum picked up on mission profile and the statistical value given by $X_s = \mu + k_r \cdot \sigma$ are compared, and the maximum out of both is kept.

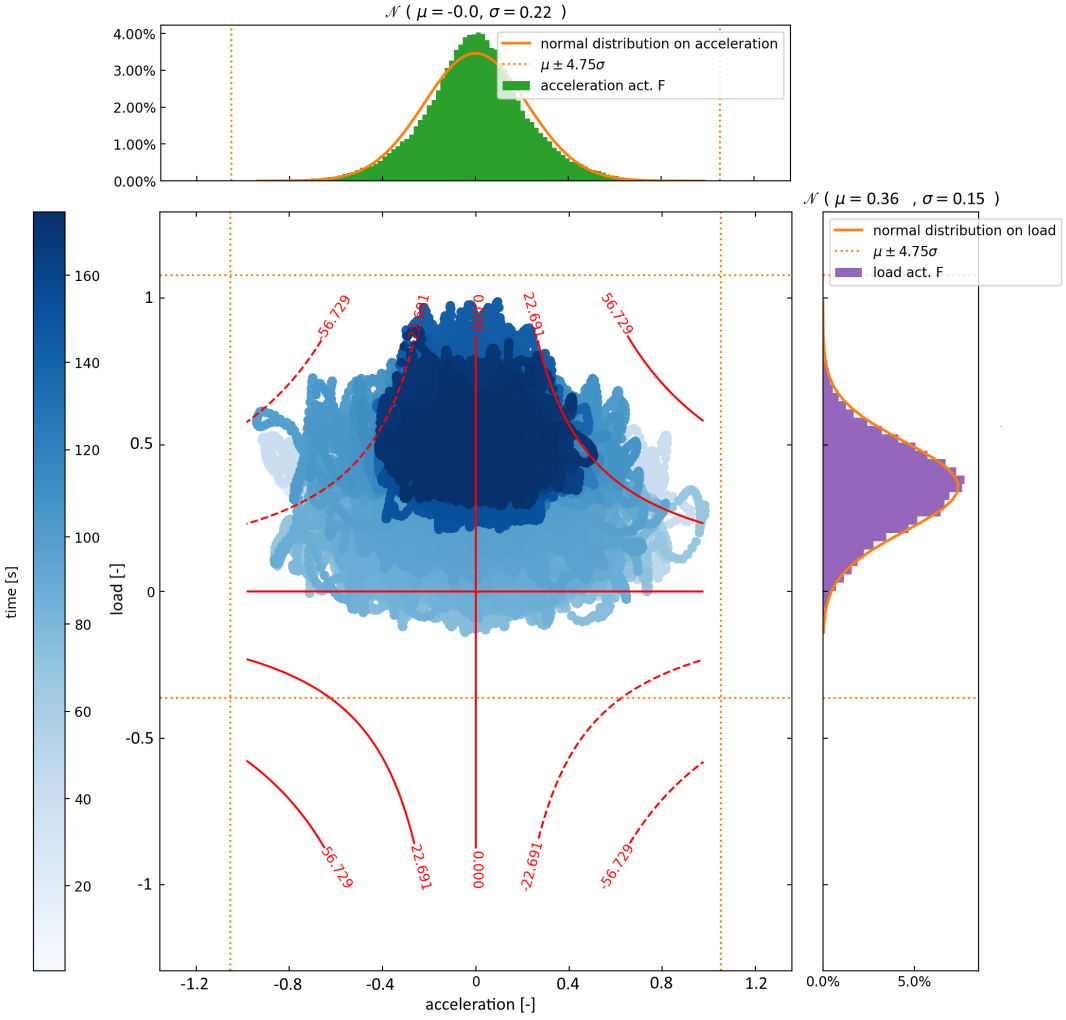

The red dashed lines are the iso 99% occurence power rate & max power rate

FIGURE 2.21: *Example of load vs acceleration with power rate (PR) & statistics during a CRUISE flight (175s): acceleration values normalized by the maximum acceleration recorded, load values normalized by the maximum load recorded*

Note: The flight test operator might not provide the resolution used to record. For the statistical distribution, speed, acceleration and load values are divided into classes. The number of classes has to be chosen so as to contain an equal number of variable states.

2.7 Study status & comparison MRA vs TRA

This section shows the results from the analysis of mission profiles recorded on a single helicopter flight test (VSR700). In addition, we suggest to compare the main

rotor and the tail rotor applications with the same data.

2.7.1 Helicopter analysis

Three mission profiles from the VSR700 flight test campaign have been analysed: a take-off of 25 seconds, a cruise of 175 seconds and a landing of 88 seconds. An overview of the CRUISE mission profile is available in Appendix C.

The values of indicators are presented in table 2.9. The values are normalized for confidentiality reasons. Some orders of magnitude regarding the MRAs can be given: loads $\sim 1\ kN$, speeds $\sim 10^{-2}\ m/s$, accelerations $\sim 1\ m/s$.

			TAKE-OFF				CRUISE				LANDING			
	Indicators	Units	R	F	L	T	R	F	L	T	R	F	L	T
position	STROKE max L_s	-	1,0	1,6	1,2	1,6	1,8	0,6	0,8	1,0	1,3	1,1	1,2	1,5
	equivalent distance travelled L_{eq}	-	0,0	0,0	0,0	0,1	0,5	0,3	0,3	1,0	0,1	0,1	0,1	0,4
	SPEED max v_{max}	-	0,5	0,5	0,4	0,9	0,7	0,6	0,4	1,0	1,1	0,8	0,8	1,0
	SPEED iron v_{iron}	-					0,5	0,3	0,3	1,0				
	ACCELERATION max $\ddot{x}_{max}$	-	0,6	0,4	0,3	0,7	0,6	0,4	0,3	1,0	0,5	0,5	0,4	1,0
	ACCELERATION rms $\ddot{x}_{rms}$	-					0,7	0,5	0,4	1,0				
load	LOAD max F_{max}	-	2,7	9,8	7,2	1,8	6,4	11	8,5	1,0	5,2	12	6,0	1,5
	LOAD rms F_{RMS}	-					7,0	12	15	1,0				
	LOAD rmc F_{RMC}	-					7,1	10	13	1,0				
	LOAD pitting $(F_{static}, F_{dyn,ptp})$	(-, -)					(5,0; 12)	(7,5; 17)	(10; 6,7)	(1,0; 1,0)				
position & load	POWER RATE mean $\overline{PR}$	-	3,5	2,0	1,0	1,0	2,0	5,0	2,0	1,0	1,0	0,2	0,3	2,0
	POWER RATE max PR_{max}	-	1,3	2,4	1,5	1,6	6,0	5,1	4,0	1,0	1,8	4,1	2,2	2,0
	pair $(\ddot{x}_{PRmax}, F_{PRmax})$	(-, -)	(0,4; 3,9)	(0,4; 7,3)	(0,3; 4,9)	(0,6; 2,2)	(0,6; 9,9)	(0,4; 13)	(0,3; 15)	(1,0; 1,0)	(0,2; 8,7)	(0,5; 8,4)	(0,2; 9,9)	(1,0; 2,0)

R (right), F (front), L (left) are the Main Rotor Actuators (MRAs), T (tail) is the Tail Rotor Actuator (TRA)

TABLE 2.9: *VSR700 indicator values evaluated for the 4 actuators and considering 3 flight phases, values are normalized by the values obtained for the TRA during the CRUISE flight*

When analysing table 2.9, different actuator needs are observed:

- between the main and the tail rotors: the tail rotor actuator is globally much more dynamic. Indeed, it roughly performs 2-3 times more speed, 2-3 times more acceleration while withstanding 7-15 times less load. Also, there is nearly a ratio of 10 between both applications regarding the pitting load (static & dynamic).

- among the main rotor: the right actuator has got the highest acceleration, the front actuator has got the highest load.

The specification will be the maximum of each line considering separetely main and tail rotor actuators (table 2.10).

Furthermore, the load sense is different. The mission profile analysis clearly shows that the actuators R, L and T are under a compressive loading meanwhile the actuator F is under tensile load.

Notes: the difference of actuator needs on main rotors is even more preponderant on german helicopters (Tiger, H145, H135). In this helicopter configuration, the actuators are connected to the swashplate through a combinator. This makes each actuator play on pure flight axis (collective, roll, pitch).

2.7.2 Rotorcraft specificities

To conclude this study, we suggest to emphasize the specificity of the rotorcraft PFCS for EMA application by comparing the MRA and the TRA specifications. Based on table 2.9, the specifications are displayed in table 2.10 with ratios of the values found in the MRA specification to the values found in the TRA specification. Table 2.10 shows clearly the scale difference of both applications. At first sight, the MRA application has got the heaviest load spectrum.

	Indicators	Ratio of values MRA/TRA [-]
position	STROKE max L_s	1,1
	equivalent distance travelled L_{eq}	0,5
	SPEED max v_{max}	1,1
	SPEED iron v_{iron}	0,5
	ACCELERATION max $\ddot{x}_{max}$	0,6
	ACCELERATION rms $\ddot{x}_{rms}$	0,7
load	LOAD max F_{max}	6,4
	LOAD rms F_{RMS}	15
	LOAD rmc F_{RMC}	13
	LOAD pitting (F_{static}, $F_{dyn,ptp}$)	(10; 17)
position & load	POWER RATE mean $\overline{PR}$	2,5
	POWER RATE max PR_{max}	3,0
	pair ($\ddot{x}_{PRmax}$; F_{PRmax})	(0,6; 6,6)

TABLE 2.10: *Final specification of the MRA and the TRA (VSR700)*

To simplify the comparison, we suggest creating other indicators, based on the ratios of the previously mentioned indicators.

R_a, R_{Frms} and R_{Frmc} are introduced and correspond respectively to the following ratios:

$$R_a = \frac{\text{continuous inertia load}}{\text{max inertia load}} \tag{2.38}$$

$$R_{Frms} = \frac{\text{continuous external load}}{\text{max external load}} \tag{2.39}$$

$$R_{Frmc} = \frac{\text{equivalent rolling fatigue load}}{\text{max external load}} \tag{2.40}$$

What is more, to characterise better the inertia impact, we suggest 2 indicators making the ratio of the load produced by the inertia effect out of the external load.

The first one is R_{jmax}. It defines the ratio of the load produced by the max acceleration out of the max external load to fight against. For this indicator, the max acceleration and the max load might not appear at the same time.

The second one is R_{JPR}. It is based on the pair (a_{PRmax},F_{PRmax}) which is the acceleration and the load maximizing the power rate. It gives the load produced by the acceleration a_{PRmax} normalized by the external load F_{PRmax}. In this case, a_{PRmax} and F_{PRmax} appear at the same time on the mission profile.

One would thus expect those 2 indicators (R_{jmax}, R_{JPR}) to be close to each other if the max acceleration and load occur at the same time, but could be significantly different if the peak acceleration occurs while the external load is smaller or the other way around.

In addition, to characterize the motor losses, the following indicators are introduced.

The first one is R_{IL}. It makes the ratio of the iron losses produced by v_{iron} and the ones produced by the max transient speed v_{max}. R_{IL} gives an idea of the importance of iron losses during operation (fig. 2.4).

The two following indicators comes from the RMS averaging which reflects the averaged motor heating over a mission profile. The load seen by the motor $F_{m,rms}$ can be extended as developed in fig. 2.22. To identify better the inertia impact on motor heating (Joules losses), 2 indicators can be defined: R_{PR} and R_{aRMS} (fig. 2.22). R_{aRMS} reflects the inertial load alone meanwhile R_{PR} reflects the coupling of the inertial and external load. R_{PR} uses the Power Rate which reflects the level of synchronism between the external load and the acceleration demand.

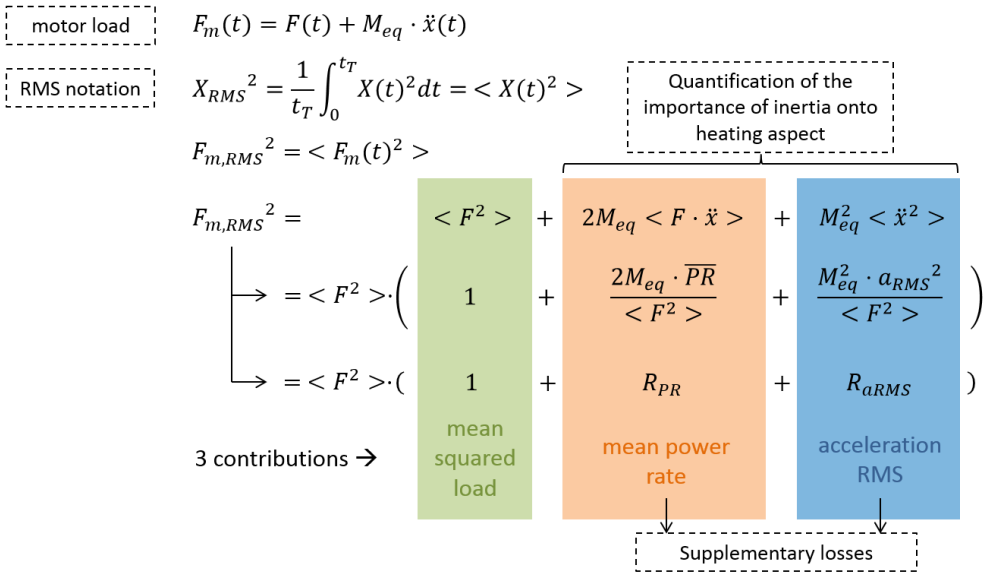

FIGURE 2.22: *Indicators of inertia impact*

In fig. 2.22, M_{eq} represents a reflected mass. For the helicopter, already proved values of rotational inertia and reduction ratio provide a reflected mass of $M_{eq,rotorcraft} = 355\ kg$.

Finally, to characterize pitting fatigue, the indicator R_p is introduced. It provides a view on the continuous load generated by the high frequency load components, normalized by the continuous load generated by its entire frequency content.

Based on results from table 2.10, all the dimensionless indicators mentioned previously are estimated and gathered in table 2.11. This facilitates the comparison of both applications.

			TAKE OFF		CRUISE		LANDING	
	Ratio of indicators	**Units**	**main**	**tail**	**main**	**tail**	**main**	**tail**
continuous /transitory loading	$R_a = \ddot{x}_{rms}/\ddot{x}_{max}$	%			25	18		
	$R_{Frms} = F_{rms}/F_{max}$	%			66	40		
rolling fatigue	$R_{Frmc} = F_{rmc}/F_{max}$	%			68	46		
inertia impact	$R_{Jmax} = \frac{M_{eq} \cdot \ddot{x}_{max}}{F_{max}}$	%	130	250	57	650	63	400
	$R_{JPR} = \frac{M_{eq} \cdot \ddot{x}_{PRmax}}{F_{PRmax}}$	%	250	280	71	730	62	510
loss analysis	$R_{IL} = v_{iron}/v_{max}$	%			21	29		
	$R_{PR} = \frac{2M_{eq} \cdot \overline{PR}}{{F_{rms}}^2}$	%			0,3	9,1		
	$R_{aRMS} = \frac{{M_{eq}}^2 \cdot {\ddot{x}_{rms}}^2}{{F_{rms}}^2}$	%			10	870		
pitting fatigue	$R_p = \frac{[butter_{HP}[F(t)]]_{rms}}{[F(t)]_{rms}}$	%			28	5,0		

TABLE 2.11: *Comparison of MRA and TRA specifications (VSR700)*

Analysing Table 2.11, a few points are showcased as it follows.

In both applications, loads have to be maintained all along flight phases, so it is expected to observe roughly same levels of equivalent heating (ratio R_{Frms}) and fatigue (ratio R_{Frmc}).

The speed & acceleration differences between MRA and TRA shown in Table 2.10 are not clearly found in Table 2.11 through the ratios R_{IL} & R_a. However, the indicators of loss analysis (R_{PR} and especially R_{aRMS}) highlight much higher induced losses linked to a high dynamism. The equivalent continuous acceleration a_{RMS} of the TRA has an important impact on the induced losses.

What's more, the ratios R_{Jmax} and R_{JPR} show that the TRA suffers much more from dynamism than the MRA. The difference of dynamism contribution is significant. This involves higher losses, hence R_{PR} is significative and R_{aRMS} is very high on TRA compared to MRA. Obviously, the TRA design will have to be driven by a small rotor inertia.

During transient flight phases such as the take-off & landing, the inertia effect takes a significant part as much for MRA than TRA. During these transient periods of time, the inertia effect is cancelled out by the EMA thermal time constant.

In addition, the gap observed between R_{PR} and R_{aRMS} on a single application, means that there is a more significant level of coupling between the external load and the inertia load on MRA compared to TRA.

Finally, the indicator R_p shows a higher level of pitting load in the MRA. This result is understood considering the helicopter rotor architectures. As a piece of information, the MRA controls selectively the rotor blade's angle of attack during one rotor azimuth. Meanwhile, the TRA controls simultaneously the angle of attack of all the blades whatever the azimuth is.

2.8 Conclusion

This chapter presented a data driven specification generation which makes a parallel between measurement data on flight and EMA technologies using indicators to estimate over mission profiles.

It emphasized the *Key Design Driver (KDD)* of an EMA. Through indicators, it showed that the dynamism of the application is involved in many KDDs.

Processing data from potentiometers showed that the position recorded on board needs important data treatment to remove perturbations and finally get the acceleration levels. This is not consistent when it comes to combine acceleration with load data. The use of accelerometers, although expensive, might be a good *In-Flight Instrumentation (IFI)* solution to measure directly the acceleration.

Then, this chapter highlighted four interesting precautions:

- the application of Savitzky-Golay's filter in case of noisy data,
- the use of statistics as safeguards for peak values in the case of a set of mission profiles not representative,
- the use of a thermal filter to check motor temperature evolution,
- the use of damage distribution to address fatigue potential issues

In addition, the use of the third order filter brings an added value to the publication [Maré, 2020] where a top-level model of EMA is proposed with a 2nd order transfer function. This 2nd order model is thought to run with a reduced set of parameters. It is a good representative of the poursuit dynamism, however it misses fidelity in load perturbation rejection. The third order transfer function fills this gap and adds only one parameter (ratio between position & speed control loop pulsations).

Finally, the comparison of the MRA and TRA specifications clearly showed the difference of dynamism contribution between the main and the tail rotor applications. Thus, this analysis points the importance of taking into account speed and acceleration within the preliminary sizing of the EMA.

Chapter 3

Dynamic rotor model

3.1 Introduction

3.1.1 Context & objectives

This chapter develops a first level model to simulate the dynamic loads applied on the PFCS actuators. These loads stem from the helicopter blade spinning and flows through the pitch rod and the swashplate. The need of such model raises in a context of an actuator preliminary design where no data can be reached. The actuator loading levels and the flight operations are unknown.

The objective is not to predict the helicopter rotor loads. Indeed, as developed in the following state-of-the-art, it is a long and hard job based on many years of experience. Besides, it gets away from the flight control system skills. Ideally, the objective would be to find a simple way to represent these rotor loads in order to support the flight control system design and, potentially, the control command elaboration. In [Lebel, 2012], this need is formulated too.

The previous chapter clearly highlights the necessary care dedicated to inertia. In helicopter PFCS actuators, inertia highly contributes into the actuator heat losses. The required dynamic position control required by the helicopter obliges this inertia to be as low as possible. With the increase of the actuator loading, the actuator sizing will converge towards solutions with an increased motor size, and also an increased rotor inertia. According to the transmission ratio, the reflected rotor inertia can be significantly important. On aircraft application, the actuation specification requests a maximum reflected motor inertia. This is for structural resistance reasons when actuator failure modes are activated. Also, it requests a given mechanical stiffness. In the helicopter context, there might be some values of reflected inertia and actuator stiffness that results in some actuator instabilities.

In this Chapter, we propose to perform a simplified study of the dynamic rotor loads applied on the main rotor actuators. We aim at: - identifying the hammering load levels, - observing the load distribution among the actuators, - studying the actuator stability with respect to its fundamental characteristics. The stability study is a way of specifying more precisely the actuator specification in terms of behaviour especially the admissible range of reflected motor rotor inertia and the actuator stiffness.

In such a context, we suggest a system level modelling with a low number of parameters. The simulation software named *OpenModelica* will be used. In fig. 3.15, the model architecture is presented with a sketch of diagrams and with the OpenModelica interface.

3.1.2 State of the art

The helicopter principle is presented in theory in [Raletz, 2010] and with more details in [FAA, 2019]. The first Chapter of this thesis showed the flight control system principle to control the helicopter flight. Thanks to the swashplate and the pitch rods, each blade is controlled individually according to the rotor azimuth. Now, the attention is focused on the kinematic of the rotor hub and especially the blade connection to the rotor mast (see fig. 3.1). Basically, it relies on three degrees of freedom:

- The *pitch* controls the blade lift.
- At the blade root, the *flap* removes the important alternated flexion stress due to the lift dissimetry over one rotor azimuth. The blade going forward has a higher relative speed, a higher lift and it goes up meanwhile the blade going backward has a lower relative speed, a lower lift and then, it goes down.
- At the blade root, the *drag* or *lag* removes the alternated stress due to the fluctuating blade drag over one rotor azimuth and the Coriolis force appearing when flapping. A damper is installed on the lag axis to avoid too large amplitudes where the blade would hit an end stop.

Fig. 3.1 presents these three axis.

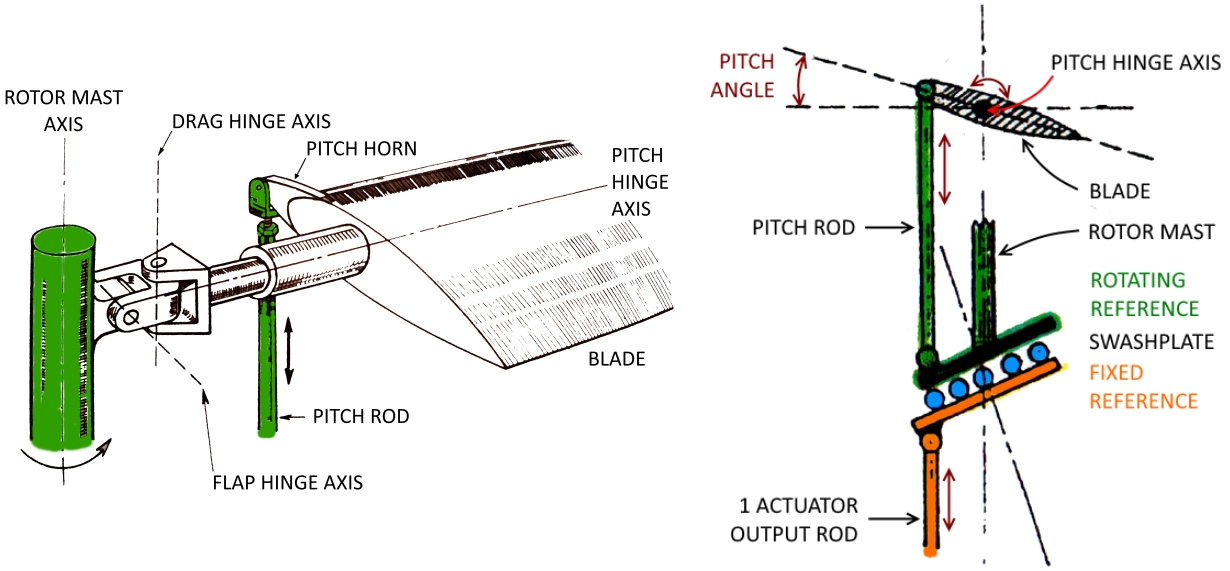

FIGURE 3.1: *Sketch of principle of an articulated rotor with its three degrees of freedom: lag, flap and pitch (only one blade is represented), (right) main rotor hub, (left) swashplate and blade pitch*

The rotor loading mainly comes from four sources: the blade aerodynamism, the blade inertia, the stiffness and the damping of elastomers installed on each axis depending on the rotor architecture (see section 3.2.1). These loads flow through the pitch horn, the pitch rod and the swashplate to apply on the three actuators fixed on the airframe.

Through this short overview, it can be understood that the helicopter rotor produces a very specific loading which requires a very detailed analysis.

Nowadays, the helicopter actuator loading prediction is, in practice, based on a detailed simulation using tools with high computational costs. A workflow connects together different modelling levels (*Computational Fluid Dynamics (CFD)*, *Finite*

Element Modelling (FEM), solid-body kinematic, and flight mechanics laws). The simulation runs over a single stabilized flight scenario. The rotor loads are broken down into aerodynamic and elastodynamic contributions. The aerodynamic models estimate the induced rotor speeds and determine the distribution of aerodynamic forces on the rotor. In solving the equations of the solids dynamics, for a mechanical system, the code of flight mechanics named HOST considers an elastic blade model to determine the force torsor. Using the pitch rod and the swashplate, the actuation control loads are estimated. The non-linear behaviour of the drag damper located between the blades is taken into account too.

In [Lebel, 2012], the author reminds the steps of this calculation methodology applying it to an innovative helicopter blade study (BlueEdge® blade). This illustrates as well the modelling difficulty level engaged to estimate rotor dynamic loads only validated experimentally in given stabilized flights.

The context of frequency modes search or vibratory response analysis gives some references to be inspired of. On helicopters, vibrations are important and they affect particularly the mechanical parts in terms of fatigue and the comfort level of passengers.

In [Boudon, 2014], the author focuses on the assembly of the main gearbox with the helicopter structure. He highlights the lack of tools and methodologies to model such complex mechanical systems. These skills are necessary to study semi-active solutions performing filtration according to real-time frequencies. In this context, the author proposes a modelling methodology based on the multi-bond graph (MGB) providing a global and modular vision on the helicopter systems. Furthermore, the performance combination of these vibration-enhancing devices deserves a helicopter ride quality assessment. This is the work offered by [Tamer et al., 2019]. Lumped parameter models of seat-cushion and human biodynamics are dynamically coupled to a medium weight helicopter numerical model. This provides an estimation of the actual vibratory level experienced by the occupants. The multiphysics modeling with lumped parameters are at the heart of the development of mechatronic systems. The dynamic behaviour requires to be simulated before any detailed CAD geometry is available. The book [Budinger et al., 2019] presents the fundamental concepts of it.

In [Krysinski and Malburet, 2007a], the authors study the helicopter rotor vibration to understand the main dynamic phenomena. This allows them to propose relevant solutions for reducing vibration levels in cabin. A simplified and generic modelling method is developed to have access to the analytical expressions of the moment at the blade hinge. This moment is caused by the inertial and the aerodynamic loads applied on the blades. This approach mainly uses Lagrange's equations with the flap and the lag blade angles, the latters being the only degrees of freedom. In technical reports from the NASA ([Jenkins Jr, 1967] and [Chen, 1987]), the same approach is developed. Appendix E reminds the principle of Lagrange's equations and the interest to use them.

In [Chellil, 2008], the author studies the dynamic behaviour of a helicopter rotor spinning with unbalancing masses. Despite the FEM of the blade, the undertaken approach considers Lagrange's equations with flap and drag angles and virtual works.

3.1.3 Approach

The formalism offered by the approach of [Krysinski and Malburet, 2007a] allows to reduce the number of parameters while expressing the main dynamic phenomena at stake. Inspired from it, we offer to develop an approach mainly based on Lagrange's

equations. In [Krysinski and Malburet, 2007a], the equations of motion consider a system with two degrees of freedom: the flap and the drag blade angles. We suggest to add in this approach an additional degree of freedom, the pitch angle, in order to finally have access to the actuator loading levels.

The study is limited to the elementary aerodynamic and inertial forces applied on the blade taken as a solid body with a rectangular section.

The differential equation expressions are determined analytically on one hand. On the other hand, a symbolic mathematical Python library is used to check them and develop a second part with many variable combinations [Sympy, 2021]. The final set of equations is implemented into a lumped parameter model (OpenModelica) simulating a three-blade helicopter with three degrees of freedom per blade.

The study is based on the Provençal two-seat helicopter named Cabri G2 produced by Guimbal's Industry [Guimbal, 2022] and equiped with a three-blade main rotor [Bazzani, 2018].

The presentation of the study is split in four sections. Firstly, the technical context is introduced with the helicopter components and the variables at stake. Secondly, a modelling of the swashplate is proposed. Its study brings some information about the "hammering load" applied on the flight control actuators. Thirdly, the dynamic model of a blade is presented. The last part assembles this model with the other helicopter rotor hub components. A study about stability with respect to the actuator reflected inertia and actuator stiffness, concludes this chapter.

3.2 Architectures & kinematics

3.2.1 Generalities

Helicopter rotors have evolved historically. Based on the implemented design technologies, they can be divided into three categories [FAA, 2019] [Krysinski and Malburet, 2007b].

1. The *articulated rotors* is one category. It includes the *conventional articulated rotor* installed on Puma, SuperPuma MK1 and Gazelle helicopters. Also, it includes the *Starflex® rotor* and the *Spheriflex® rotor* installed on the Colibri EC120, the Ecureuil range, the Dauphin range, the SuperPuma MK2, the EC725 and the NH90. The *Starflex® rotor* and the *Spheriflex® rotor* reduce drastically the rotor maintenance.

The *conventional articulated rotor* uses conventional bearings as the pitch, the flap and the lag hinges. The bearings require a constant lubricant supply. The drag dampers are initially hydraulic and finally simplified into viscoelastic dampers which use elastomer to dissipate energy and provide stiffness.

The *Starflex® rotor* is an articulated hub which does not have hinge axes. It works thanks to the flexibility of a laminated composite star, a viscoelastic damper, a self-lubricating ball and a laminated spherical bearing.

The *Spheriflex® rotor* gathers the pitch, the lag and the drag freedom in a single point. This is possible thanks to a laminated spherical bearing. Fig. 3.2 presents it.

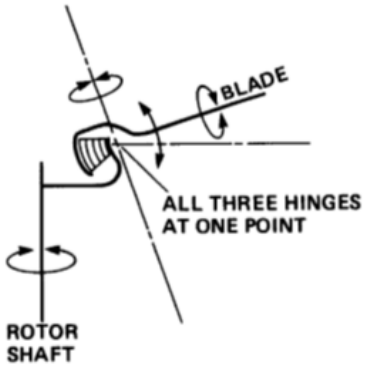

FIGURE 3.2: *Spheriflex® rotor, sketch of principle [Raletz, 2010]*

2. The *rigid rotors* (named *hingeless rotors* too) are another category where the flapping and the drag hinges have been replaced by the elasticity of the material. The Tiger main rotor is a good example. Drag and flap motions are possible thanks to the flexibility of the blade neck made of composites. The eccentricity of the flap axis is important, this improves the control of the helicopter. Pitch control is obtained by a pivot type elastomeric pitch hinge. The drag damper is hydraulic.

3. The *bearingless rotors*: this is the last developed rotor. It is installed on EC135 and EC145. The pitch, the flap and the lag hinges are replaced by flexible elements.

This chapter will focus on the *Spheriflex® rotor* since it equips the Cabri G2 helicopter.

3.2.2 Presentation of the different components

The *Spheriflex® rotor* of the Cabri G2 is presented with its components in fig. 3.3 & 3.4.

Compared to the *conventional articulated rotors*, the *Spheriflex® rotor* design brings a reduced maintenance, weight saving, improved reliability and reduced vibration levels. This rotor is compact so it reduces its aerodynamic impact. The helicopter flight speed is slightly increased. Pilots usually say this rotor gives an excellent manoeuvrability and stability [Bazzani, 2018].

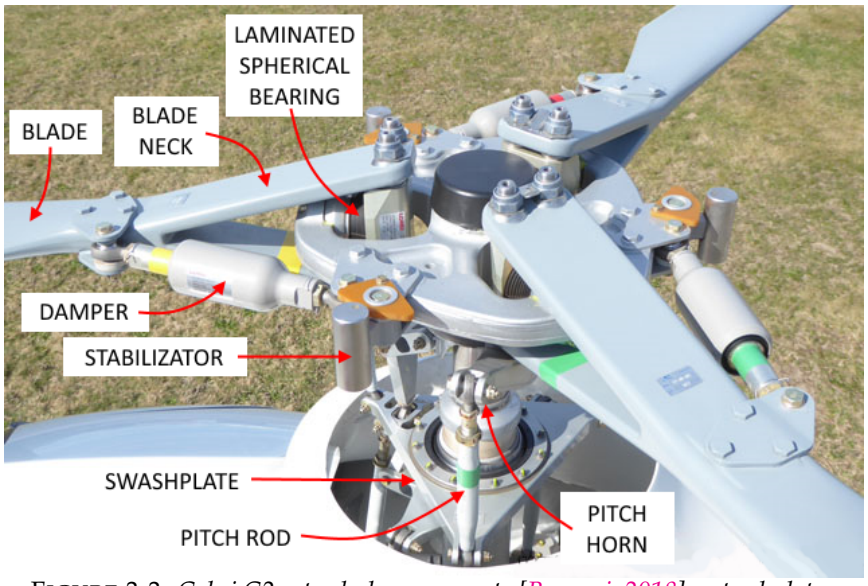

FIGURE 3.3: *Cabri G2 rotor hub components [Bazzani, 2018]: rotor hub top side view*

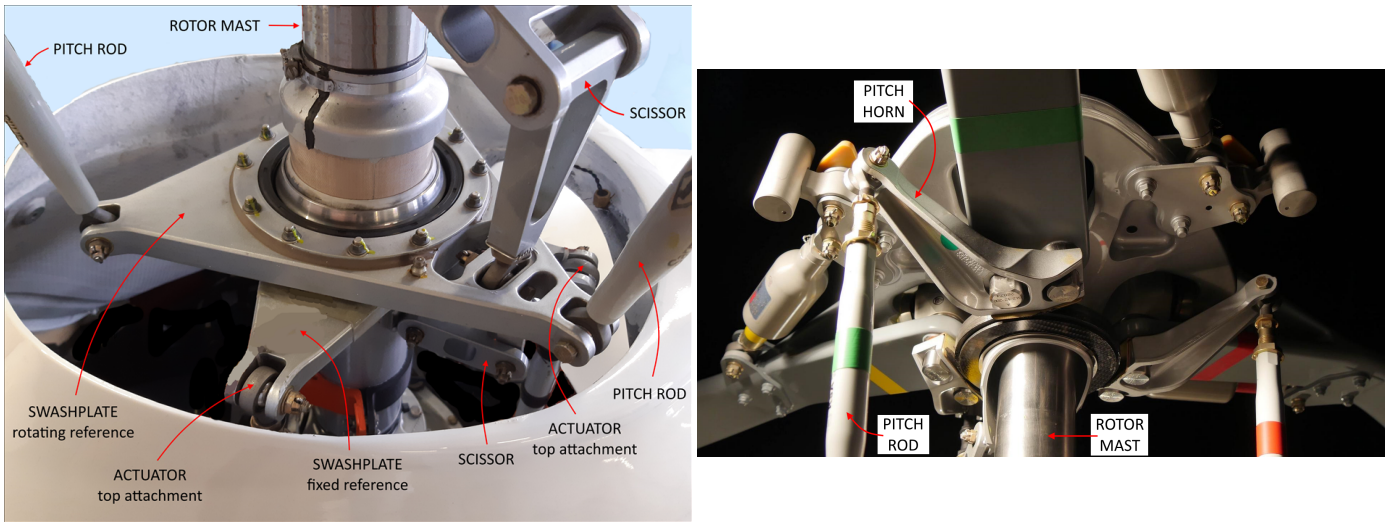

FIGURE 3.4: *Cabri G2 rotor hub components [Bazzani, 2018]: (left) zoom on swashplate, (right) zoom on pitch horn*

The *rotor mast* is driven in rotation by the MGB. The *blades* are connected to it thanks to a *laminated spherical bearing*. The fork shape of the *blade neck* allows this connection. Also, it enables the pitch, the flap and the drag freedoms of the *blade*. The drag movement is damped thanks to a *damper* attached between the *blade* and the *rotor mast* disk. The blade pitch is controlled with the *pitch rod* attached between the *swashplate rotating reference* and the *pitch horn*. The *swashplate fixed reference* welcomes the three *actuator* attachments. The *swashplate* is mounted according to an annular joint with the *rotor mast*. This allows the swashplate to move up and down and rotate the two orthogonal axis with the *rotor mast*.

3.2.3 Kinematics and settings

This section presents the sketches of reference and the angles used in the equations developed in the chapter.

3.2.3.1 Notations & available data

β	flap angle $(\overrightarrow{X_2};\overrightarrow{X_3})$	$[rad]$	a	blade chord	$[m]$
e	blade eccentricity (OA dist.)	$[m]$	b	blade equivalent width	$[m]$
I_p	blade inertia in flap and drag	$[kg \cdot m^2]$	δ	drag angle $(\overrightarrow{X_1};\overrightarrow{X_2})$	$[rad]$
I_θ	blade inertia in rotation around its longitudinal axis	$[kg \cdot m^2]$	δ_0	neutral drag angle	$[rad]$
K_β	stiffness in flapping	$[N \cdot m/rad]$	γ	Lock number*	$[-]$
K_θ	stiffness in pitch	$[N \cdot m/rad]$	K_δ	stiffness in drag	$[N \cdot m/rad]$
l	blade equivalent thickness	$[m]$	l_{arm}	drag damper lever arm	$[m]$
λ_δ	coef. of viscous drag moment from damper	$[N \cdot m/rad]$	m_p	blade mass	$[kg]$
λ_β	coef. of viscous pitch moment of bearing	$[N \cdot m/rad]$	m_s	static moment	$[kg \cdot m]$
λ_θ	coef. of viscous flap moment of bearing	$[N \cdot m/rad]$	Ω	$= \dot{\psi}$, rotor mast speed	$[rad/s]$
ψ	rotor mast rotation angle $(\overrightarrow{X_0};\overrightarrow{X_1})$	$[rad]$	r	blade length (AM dist.)	$[m]$
ρ	air density	$[kg \cdot m^{-3}]$	R	rotor radius at blade tip	$[m]$
θ_0	neutral pitch angle	$[rad]$	θ	pitch angle $(\overrightarrow{Z_3};\overrightarrow{Z_4})$	$[rad]$

* *constant representing the ratio between the aerodynamic forces and the inertia forces.*

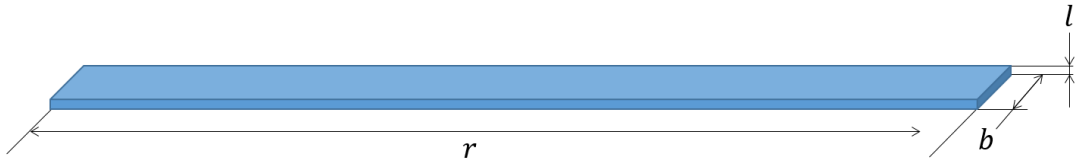

FIGURE 3.5: *Blade geometry considerations*

For the sake of confidentiality concerning the Cabri G2 helicopter, most of its characteristics are not provided with real values.

3.2.3.2 Sketch of reference

The blade motion can be described by five sketches of reference ($\mathscr{R}_g$, $\mathscr{R}_1$, $\mathscr{R}_2$, $\mathscr{R}_3$, $\mathscr{R}_4$) as suggested in fig. 3.6. $\mathscr{R}_g = (O, X_0, Y_0, Z_0)$ is supposed to be galilean. $\mathscr{R}_4 = (A, X_4, Y_4, Z_4)$ is the sketch linked to the blade. Hereafter, the rotation matrices are presented with the sketches they refer to.

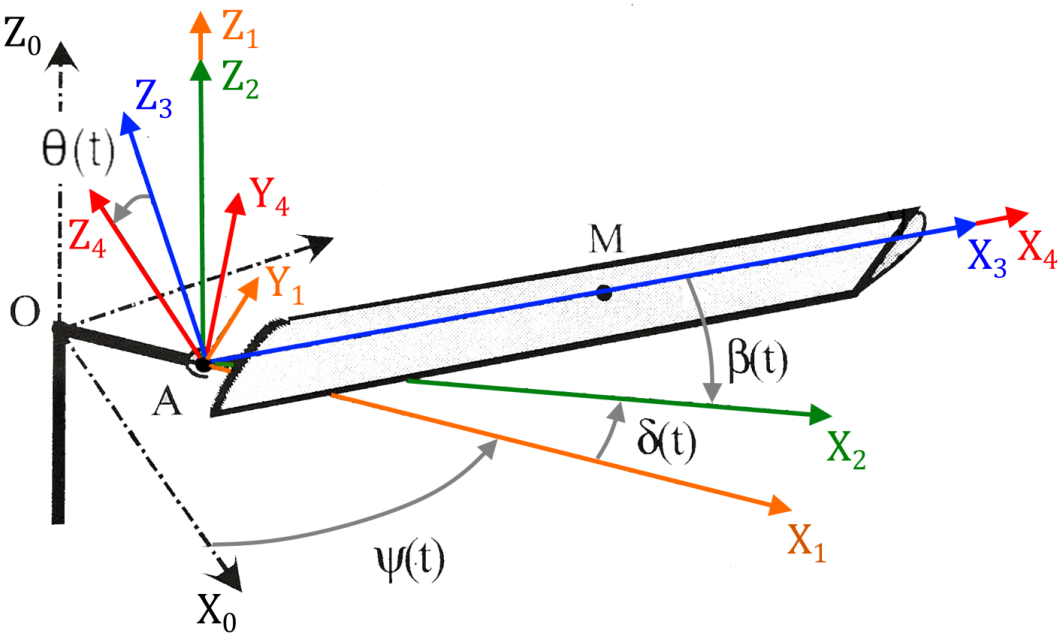

FIGURE 3.6: *Parametric description of the blade motion*

$\mathscr{R}_g \Longrightarrow \mathscr{R}_1 \ (Z_0 = Z_1)$	$\mathscr{R}_1 \Longrightarrow \mathscr{R}_2 \ (Z_1 = Z_2)$
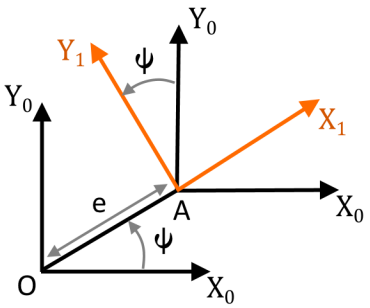	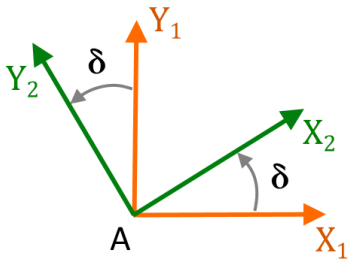
$\begin{pmatrix} X_1 \\ Y_1 \\ Z_1 \end{pmatrix} = \begin{pmatrix} \cos\psi & \sin\psi & 0 \\ -\sin\psi & \cos\psi & 0 \\ 0 & 0 & 1 \end{pmatrix} \begin{pmatrix} X_0 \\ Y_0 \\ Z_0 \end{pmatrix}$	$\begin{pmatrix} X_2 \\ Y_2 \\ Z_2 \end{pmatrix} = \begin{pmatrix} \cos\delta & \sin\delta & 0 \\ -\sin\delta & \cos\delta & 0 \\ 0 & 0 & 1 \end{pmatrix} \begin{pmatrix} X_1 \\ Y_1 \\ Z_1 \end{pmatrix}$
$\mathscr{R}_2 \Longrightarrow \mathscr{R}_3 \ (Y_2 = Y_3)$	$\mathscr{R}_3 \Longrightarrow \mathscr{R}_4 \ (X_3 = X_4)$
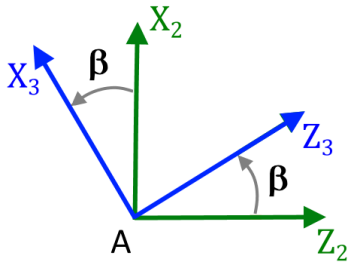	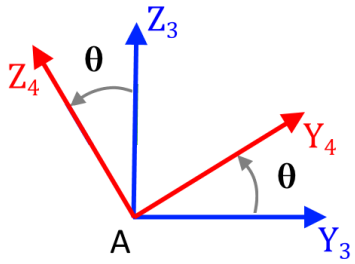
$\begin{pmatrix} X_3 \\ Y_3 \\ Z_3 \end{pmatrix} = \begin{pmatrix} \cos\beta & 0 & -\sin\beta \\ 0 & 1 & 0 \\ \sin\beta & 0 & \cos\beta \end{pmatrix} \begin{pmatrix} X_2 \\ Y_2 \\ Z_2 \end{pmatrix}$	$\begin{pmatrix} X_4 \\ Y_4 \\ Z_4 \end{pmatrix} = \begin{pmatrix} 1 & 0 & 0 \\ 0 & \cos\theta & \sin\theta \\ 0 & -\sin\theta & \cos\theta \end{pmatrix} \begin{pmatrix} X_3 \\ Y_3 \\ Z_3 \end{pmatrix}$

TABLE 3.1: *Sketches of reference with their respective rotation matrix*

3.3 Swashplate modelling & hammering phenomena

This section focuses on the swashplate component. A modelling approach based on virtual work is suggested. This model provides a first explanation of the origin of the hammering load phenomena applied on actuators.

3.3.1 Swashplate: representation by virtual work method

3.3.1.1 Geometrical conventions

In fig. 3.7, the swashplate is presented with a top view. The fixed part is separated from the rotating one.

On the fixed reference, the actuator R (right), F (front) and L (left) are attached. The height position of the actuator attachments is marked by the labels z_R, z_F and z_L.

On the rotating reference, the pitch rods a, b et c are attached. Their height position is defined according to the rotor mast angle ψ with the labels z_a, z_b et z_c.

The swashplate is considered as a plane described by a height of reference z_0 and two angles α_x et α_y. Actuator and pitch rod attachments are considered to be at a radius R_s.

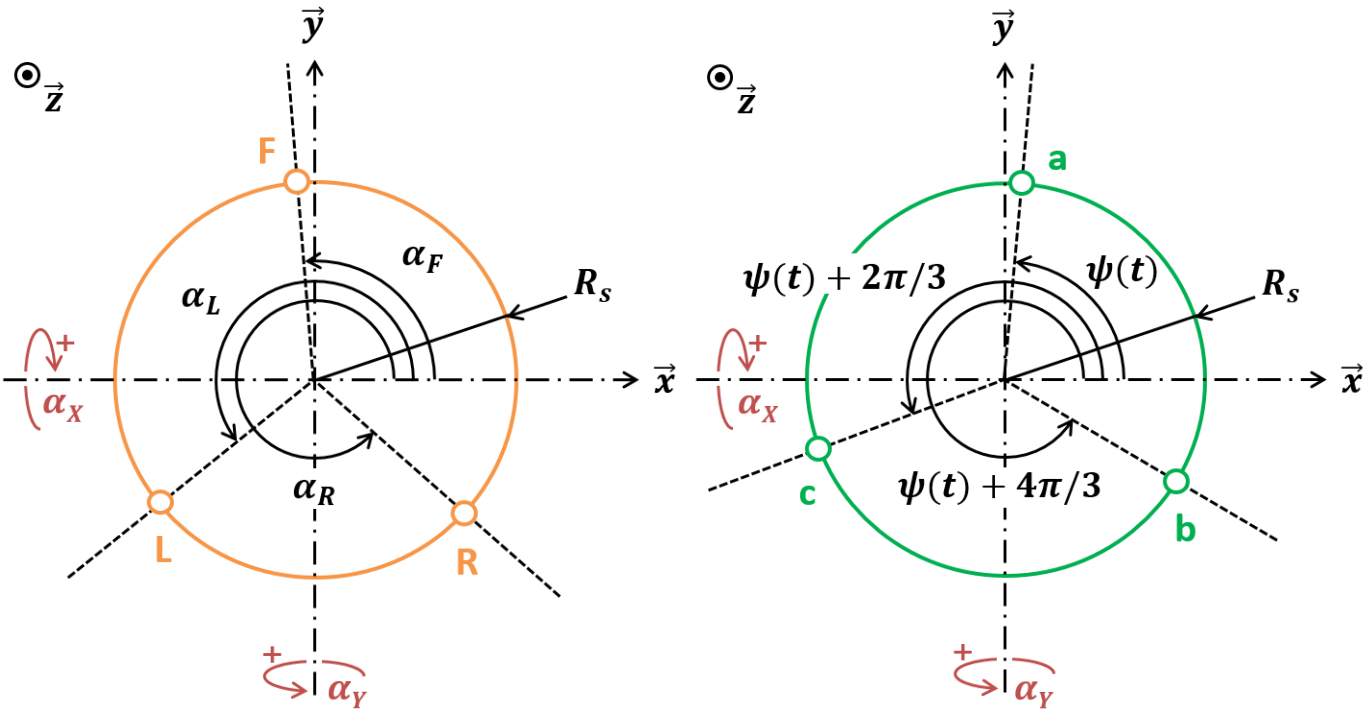

FIGURE 3.7: *Cabri G2 swashplate, sketch of principle: (left) fixed reference, (right) rotating reference. The y-axis points the helicopter front.*

Each actuator height can be defined by:

$$z_R = z_0 + \alpha_x \cdot R_s \cdot \sin(\alpha_R) - \alpha_y \cdot R_s \cdot \cos(\alpha_R) \tag{3.1}$$

$$z_F = z_0 + \alpha_x \cdot R_s \cdot \sin(\alpha_F) - \alpha_y \cdot R_s \cdot \cos(\alpha_F) \tag{3.2}$$

$$z_L = z_0 + \alpha_x \cdot R_s \cdot \sin(\alpha_L) - \alpha_y \cdot R_s \cdot \cos(\alpha_L) \tag{3.3}$$

Each pitch rod height position can be defined such as:

$$z_a = z_0 + \alpha_x \cdot R_s \cdot \sin(\psi) - \alpha_y \cdot R_s \cdot \cos(\psi) \tag{3.4}$$

$$z_b = z_0 + \alpha_x \cdot R_s \cdot \sin(\psi + \frac{2\pi}{3}) - \alpha_y \cdot R_s \cdot \cos(\psi + \frac{2\pi}{3}) \tag{3.5}$$

$$z_c = z_0 + \alpha_x \cdot R_s \cdot \sin(\psi + \frac{4\pi}{3}) - \alpha_y \cdot R_s \cdot \cos(\psi + \frac{4\pi}{3}) \tag{3.6}$$

3.3.1.2 Virtual work method

To apply the virtual work method, we assume that the swashplate works without any loss. On both sides of the swashplate, the work is expressed such as

$$\mathscr{W}_a = F_a \cdot z_a \qquad \mathscr{W}_R = F_R \cdot z_R \tag{3.7}$$

$$\mathscr{W}_b = F_b \cdot z_b \qquad \mathscr{W}_F = F_F \cdot z_F \tag{3.8}$$

$$\mathscr{W}_c = F_c \cdot z_c \qquad \mathscr{W}_L = F_L \cdot z_L \tag{3.9}$$

The work provided by the actuators balances the work required for blade pitch control. The sum of the virtual works vanishes such as:

$$\sum_{a,b,c} \mathscr{W}_i = \sum_{R,F,L} \mathscr{W}_i \qquad \Longrightarrow \qquad \mathscr{W}_{total} = \sum_{a,b,c} \mathscr{W}_i - \sum_{R,F,L} \mathscr{W}_i = 0 \tag{3.10}$$

Now, it comes to project this virtual work sum onto each degree of freedom of the swashplate. Derivatives according to z_0, α_x, α_y gives the following set of three equations:

$$\text{on } z_0 : F_1 + F_2 + F_3 + F_a + F_b + F_c = 0 \tag{3.11}$$

$$\begin{aligned} \text{on } \alpha_x : & F_R \cdot \sin(\alpha_R) + F_F \cdot \sin(\alpha_F) + F_L \cdot \sin(\alpha_L) \\ & + F_a \cdot \sin(\psi) + F_b \cdot \cos(\psi + \frac{\pi}{6}) - F_c \cdot \sin(\psi + \frac{\pi}{3}) = 0 \end{aligned} \tag{3.12}$$

$$\begin{aligned} \text{on } \alpha_y : & - F_R \cdot \cos(\alpha_R) - F_F \cdot \cos(\alpha_F) - F_L \cdot \cos(\alpha_L) \\ & - F_a \cdot \cos(\psi) + F_b \cdot \sin(\psi + \frac{\pi}{6}) + F_c \cdot \cos(\psi + \frac{\pi}{3}) = 0 \end{aligned} \tag{3.13}$$

3.3.2 Modelling of loading harmonics & hammering origin

With the previous equation set formulated (eq. 3.11, 3.12 & 3.13), a swashplate model is created under the software OpenModelica environment. In order to explain the generation of load pulsation frequencies at the actuator level, a model test is set (fig. 3.8).

The test consists in injecting load excitations of a given harmonic number into the pitch rod attachments (swashplate upper part, rotating reference). The actuator positions are such that the swashplate is horizontal. The test aims at observing the load response at the actuator level.

The blade is a source of complex loading broken down into different harmonics [Krysinski and Malburet, 2007a]. The blocks in the upper part of the model (fig. 3.8) allow to choose the harmonic to be tested. These blocks simulate the load flowing through the pitch rods. Therefore, they inject in the swashplate model, three sources

of load with the following shape:

$$F_i = A \cdot \sin(k_h \cdot (\dot{\psi} \cdot t + \phi_i)) + B \qquad i \in [a, b, c] \tag{3.14}$$

where A and B are the constants $[N]$ which provide, under an excitation of harmonic 1, an actuator loading level corresponding to a real case (mission profile), taken as the reference. $\dot{\psi}$ $[rad/s]$ is the rotor mast angular frequency. ϕ $[rad]$ is the loading phaseshift separating the three blades according to their relative position i.e. $[0, 2\pi/3, 4\pi/3]$ $[rad]$. The constant k_h $[-]$ is the number of the harmonic to be tested.

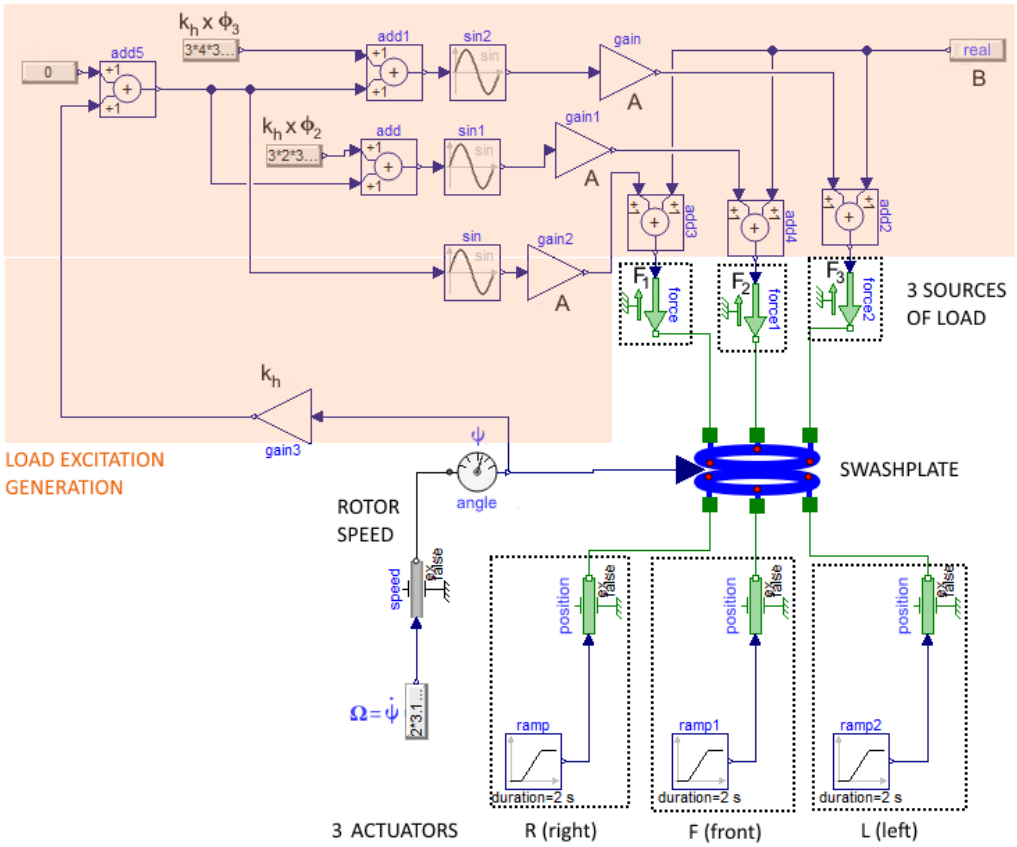

FIGURE 3.8: *Swashplate model with harmonic test (OpenModelica)*

Harmonic number	Load frequency
1	static
2	27hz
3	27hz
4	27hz
5	54hz

TABLE 3.2: *Actuator load frequency according to the harmonic number of the pitch rod load*

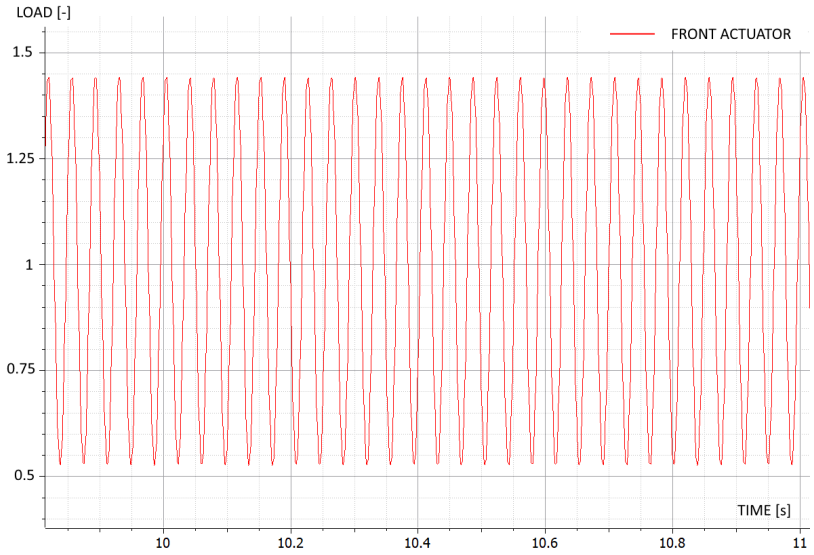

FIGURE 3.9: *Swasplate model tested with a harmonic 4: load of the actuator F (front)*

The test is run on five harmonics, the results are presented in table 3.2. It is observed that the harmonic 1 provides a constant loading level. The harmonics 2, 3, and 4 involve a loading level at 27 hz. This frequency corresponds to the rotor mast frequency multiplied by the number of blades. The harmonic 5 generates a 54 hz loading level, a multiple of rotor mast frequency. The first harmonics are the most important in terms of intensity. Indeed, the frequency spectrum of a real mission profile shows effectively the biggest loading level at 27 hz (see fig. 2.20 of Chapter 2).

When adding supplementary phaseshift to the ϕ-triplet ($[0, 120, 240]^\circ$), we observed harmonics at 9 hz and 18 hz appearing in the actuator loading. These frequency levels are noticed in the real mission profile too. [Krysinski and Malburet, 2007a]'s literature brings some relevant information at that stage. The lift load is a function of the lift coefficient and of the relative speed blade/air.

The lift coefficient C_p varies all along the blade length. C_p depends on the attack angle and on the Mach number. The angle of attack varies according to the blade twist. The Mach number relies on the relative speed blade/air. Ignoring this consideration leading to complex calculations, it is possible to show that each blade section undergoes alternate aerodynamic loads due to the pure functionning principle of the rotor.

Contrary to the hover flight where each blade undergoes the same air flow, in forward flights, the speed of a blade point, relative to the air, evolves following the blade angular position (fig. 3.10). If $0 \leq \psi \leq \pi$, the blade is in its advancing area, if it is not, the blade is in its retreating area. Thus, the blade experiences loads of variable intensity during one azimuth. This is named alternate aerodynamic loads. What is more, supposing the blade as non-deformable and ignoring the effects of the induced speed, [Krysinski and Malburet, 2007a] shows that the lift load has dynamic components in 1Ω, 2Ω and 3Ω (where Ω is the rotor mast speed). The consideration of a deformable blade involves a dynamic torsion of the blade acting directly on the lift and on the dynamic flapping. This consideration, combined with a variation in the field of the induced speed, results in a dynamic excitation on the blade for all higher harmonics.

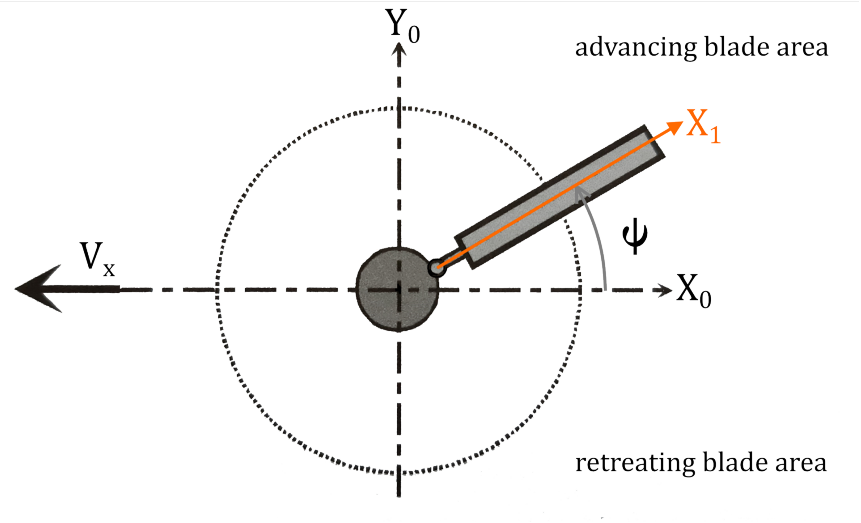

FIGURE 3.10: *Definition of the advancing and retreating blades*

The hammering loads or alternate aerodynamic loads are observed at the actuator level when the swashplate is excited through loads with harmonics greater than 1. According to the simplifications undertaken in this chapter (non-deformable blade, hover flight), the hammering load will not be considered. Consequently, the following sections will deal with first harmonic load cases.

3.4 Blade dynamism

This section starts gathering the hypothesis applied in the equation derivations presented in the further subsections. The hypothesis are reminded all along the derivation too.

3.4.1 Modelling hypothesis

The modelling takes into account a hovering flight phase ($\overrightarrow{V_x} = \overrightarrow{0}$).

The blade motion is described by the angles already mentioned in fig. 3.6 i.e. $\psi(t)$ the rotation angle of the rotor mast, $\delta(t)$ the lag angle, and $\beta(t)$ the flap angle. The coordinate system $\mathscr{R}_g = (O, \overrightarrow{X_0}, \overrightarrow{Y_0}, \overrightarrow{Z_0})$ considers an inertial frame (Galilean reference) and the coordinate system $\mathscr{R}_3 = (A, \overrightarrow{X_3}, \overrightarrow{Y_3}, \overrightarrow{Z_3})$ is linked to the blade. The rotor mast speed Ω $[rad/s]$ is considered as constant.

The blade is considered as a non-deformable blade of rectangular section for mass and inertia estimations. The blade eccentricity $e = \|\overrightarrow{OA}\|$ is ignored compared to the blade radius R: $R \gg e$. The eccentricity in the lag and the flap motions is neglected. Also, the flap and lag angles follow the hypothesis of small angles:

$$\cos(\beta) \approx 1 \qquad \sin(\beta) \approx \beta \tag{3.15}$$

$$\cos(\delta) \approx 1 \qquad \sin(\delta) \approx \delta \tag{3.16}$$

The lag speed is neglected compared to the rotor mast speed: $\Omega \gg \dot{\delta}$.

The lift coefficient variation according to the attack angle i is considered as constant along the blade ($\partial C_p / \partial i = c^{st}$). The aerodynamic loads are considered to be applied on the blade rotation axis $\overrightarrow{X_4}$. Therefore, they do not generate any moment according to $\overrightarrow{X_4}$. Also, in a forward flight phase, the flap motion over one rotor

azimuth generates forces of Coriolis. Further to the aerodynamic drag variations, these fluctuating forces contribute to the lead-lag motion of the blade. Lagrange's equations take these forces into account as far as the kinetic energy and the centrifugal forces [Hrabovsky and Susskind, 2020].

3.4.2 Study case with system of two degrees of freedom

Following the approach stated by [Krysinski and Malburet, 2007a], the method of Lagrange's equations is applied to find the equation of the blade motion. The calculation steps are given below. In this section, the blade is free regarding only 2 axes, the flap and the drag. The following section, section 3.4.3, makes the same study with an additional degree of freedom: the pitch axis.

3.4.2.1 Estimation of the blade speed relative to the air

To estimate the speed of a blade point M relative to the air, the vector $\overrightarrow{V_{M,blade/air}}$ must be determined. Fig. 3.11 presents it.

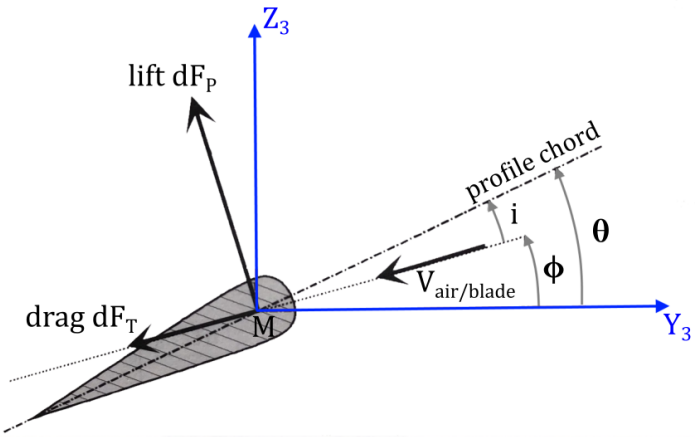

FIGURE 3.11: *Diagram of the air speed & angle of attack for a blade in hovering flight*

$\overrightarrow{V_{M,blade/air}}$ can be broken down into three speeds:

$$\overrightarrow{V_{M,blade/air}} = \overrightarrow{V_{M,blade/rotor}} + \overrightarrow{V_{M,rotor/airframe}} + \overrightarrow{V_{M,airframe/air}} \tag{3.17}$$

$$= -\left(r \cdot \dot{\beta} + V_i\right) \cdot \overrightarrow{Z_1} + \left(e + r \cdot \cos(\beta)\right) \cdot \Omega \cdot \overrightarrow{Y_1} - V_x \cdot \overrightarrow{X_0} \tag{3.18}$$

[Krysinski and Malburet, 2007a] states that, as a first level approach, the induced speed carried by $\overrightarrow{Z_3}$ can be neglected: $V_i = 0$. In hover flight, the air speed with respect to the airframe is vanished: $V_x = 0$. What is more, the small angles hypothesis ($\beta \ll 1$) and the eccentricity neglected compared to the blade length ($e \ll R$) lead to the following approximation of the relative speed of the wind:

$$\overrightarrow{V_{M,blade/air}} \approx -r \cdot \dot{\beta} \cdot \overrightarrow{Z_1} + r \cdot \Omega \cdot \overrightarrow{Y_1} \tag{3.19}$$

3.4.2.2 Estimation of the aerodynamic moments

The Cabri G2 is equiped with a blade which profile section NACA evolves from the blade neck to the blade tip. As a first approximation, a simple symmetric profile is

considered. This profile type is one of the most used in the helicopter world [Doat, 2016]. In addition, the center of pressure where the aerodynamic resultant applies is nearly stationary whatever the attack angle is [Doat, 2016] [Avi, 2020]. Its location is approximately at a distance of 25% of the profile chord from the leading edge. This is the point where the pitch axis is. Thus, the lift is applied on the blade rotation axis.

The lift can be defined such as:

$$\overrightarrow{dF_P} = \frac{1}{2} \cdot \rho \cdot a \cdot C_p(M,i) \cdot \overrightarrow{V_{M,air/blade}}^2 \cdot dr \tag{3.20}$$

The aerodynamic moment due to the lift can be broken down into two degrees of freedom: the flap moment $M_{aero,\beta}$ and the lead-lag moment $M_{aero,\delta}$.

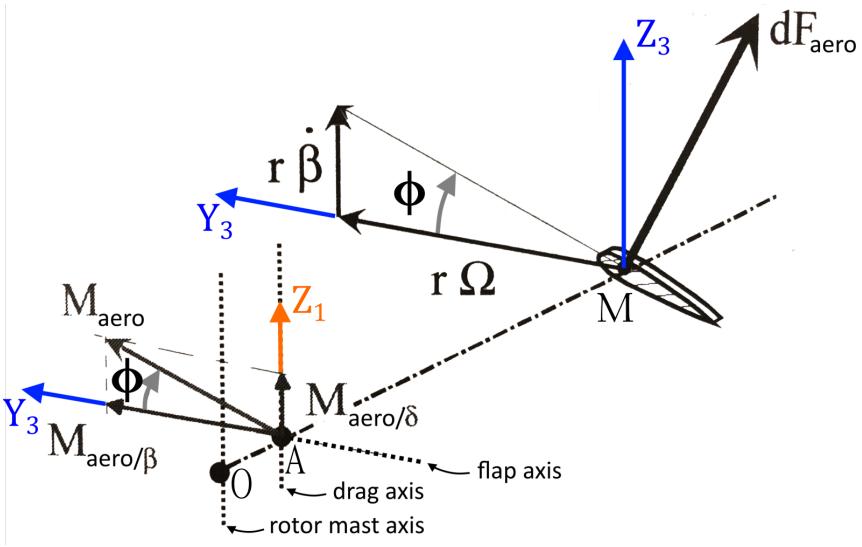

FIGURE 3.12: *Relationship between drag and flapping moments*

3.4.2.3 Flapping moment

The flapping moment in point A, associated to the aerodynamic loads, is presented in fig. 3.12 and calculated by the following projection:

$$M_{aero/\beta} = \overrightarrow{M_A}(aero \rightarrow blade) \cdot \overrightarrow{Y_3} \tag{3.21}$$

The hypothesis of small angles leads to the following approximation:

$$\overrightarrow{M_A}(aero \rightarrow blade) \cdot \overrightarrow{Y_3} = \int_{blade} \overrightarrow{AM} \wedge \overrightarrow{dF_{aero}} \cdot \overrightarrow{Y_3} = -\int_{blade} r \cdot \overrightarrow{Z_3} \cdot \overrightarrow{dF_{aero}} \tag{3.22}$$

$$= -\int_{blade} r \cdot \left(\cos(\phi) \cdot dF_p - \sin(\phi) \cdot dF_t\right) \tag{3.23}$$

$$\approx -\int_{blade} r \cdot dF_p \tag{3.24}$$

Combining the eq. 3.19 and 3.20 and neglecting the flapping speed as suggested by [Krysinski and Malburet, 2007a], the moment at point A gives:

$$\overrightarrow{M_A}(aero \rightarrow pale) \cdot \overrightarrow{Y_3} = -\frac{1}{2} \cdot \rho \cdot a \cdot \Omega^2 \cdot \int_0^R r^3 \cdot C_{zp}(r) \cdot dr \tag{3.25}$$

[Krysinski and Malburet, 2007a] assumes that the local lift coefficient C_{zp} is, within the running condition, a linear function of the angle of attack i such as:

$$C_{zp} = \frac{\partial C_p}{\partial i} \cdot i \qquad \frac{\partial C_p}{\partial i} = C^{st} \tag{3.26}$$

Fig. 3.13 illustrates this linearity. Also, in Appendix F, this linearity is checked on real blade profile data. In addition, the aerodynamic forces could have been considered through the coefficient of moment C_m. Appendix F shows that the lift coefficient is the best choice.

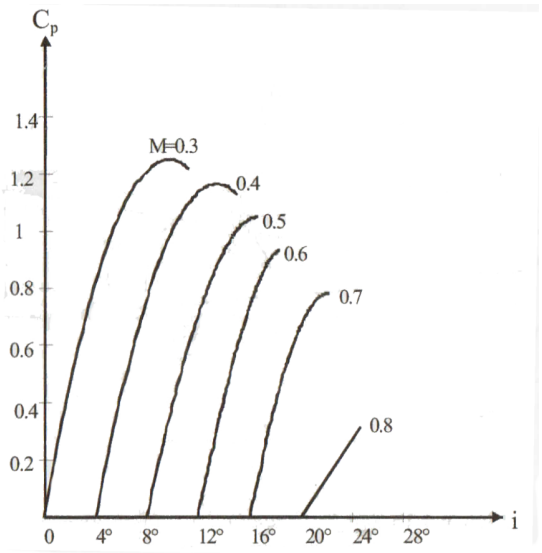

FIGURE 3.13: *Lift coefficient of a NACA0012 profile according to the angle of attack [Krysinski and Malburet, 2007a]*

Fig. 3.11 and 3.12 define the angle of attack i such as:

$$i = \theta - \phi \approx \theta - \frac{\dot{\beta}}{\Omega} \tag{3.27}$$

Finally, combining the previous results from eq. 3.21, 3.25, 3.26 and 3.27, the flapping moment takes the following shape:

$$M_{aero/\beta} = \frac{1}{2} \cdot \rho \cdot a \cdot \frac{\partial C_p}{\partial i} \cdot \left(\theta - \frac{\dot{\beta}}{\Omega}\right) \cdot \Omega^2 \cdot \frac{R^4}{4} \tag{3.28}$$

[Krysinski and Malburet, 2007a] introduces Lock's number, corresponding to the ratio between the aerodynamic loads and the inertia loads. It is a key full-scale parameter, it varies within $[6, 12]$ depending on the helicopter size [Singleton and Yeager Jr, 2000]. Its expression is:

$$\gamma = \frac{\rho \cdot a}{I_p} \cdot \frac{\partial C_p}{\partial i} \cdot R^4 \tag{3.29}$$

To conclude, the flapping moment in point A, associated with the aerodynamic loads is expressed by:

$$M_{aero/\beta} = \frac{\gamma \cdot I_p \cdot \Omega^2}{8} \cdot \left(\theta - \frac{\dot{\beta}}{\Omega}\right) \tag{3.30}$$

where I_p is the blade inertia in flap and drag.

3.4.2.4 Dragging moment

The moment in point A stemming from the aerodynamic loads and associated to the drag aerodynamic loads is expressed by:

$$M_{aero/\delta} = |\overrightarrow{M_A}(aero \rightarrow pale) \cdot \overrightarrow{Z_1}| \tag{3.31}$$

With fig. 3.12, this moment is reduced to an expression with respect to $M_{aero/\beta}$:

$$M_{aero/\delta} = -M_{aero/\beta} \cdot \frac{\dot{\beta}}{\Omega} \tag{3.32}$$

3.4.2.5 Kinetic energy

3.4.2.5.1 Blade speed in $\mathscr{R}_g$ The segment $\overrightarrow{OM}$ is defined by:

$$\overrightarrow{OM} = e \cdot \overrightarrow{X_1} + r \cdot \overrightarrow{X_3} \tag{3.33}$$

By derivative, the speed is:

$$\overrightarrow{V_M} = e \cdot \Omega \cdot \overrightarrow{Y_1} + r \cdot \frac{d\overrightarrow{X_3}}{dt} \tag{3.34}$$

One equation member requires to be developed further:

$$\begin{aligned} \frac{d\overrightarrow{X_3}}{dt} &= \overrightarrow{\Omega_{3/0}} \wedge \overrightarrow{X_3} = \left((\dot{\delta} + \Omega) \cdot \overrightarrow{Z_2} + \dot{\beta} \cdot \overrightarrow{Y_3}\right) \wedge \overrightarrow{X_3} \\ &= (\dot{\delta} + \Omega) \cdot \cos(\beta) \cdot \overrightarrow{Y_2} - \dot{\beta} \cdot \overrightarrow{Z_3} \end{aligned} \tag{3.35}$$

Finally, the speed of a blade point in $\mathscr{R}_g$ is defined by:

$$\overrightarrow{V_{M,blade/\mathscr{R}_g}} = e \cdot \Omega \cdot \overrightarrow{Y_1} + r \cdot (\dot{\delta} + \Omega) \cdot \cos(\beta) \cdot \overrightarrow{Y_2} - r \cdot \dot{\beta} \cdot \overrightarrow{Z_3} \tag{3.36}$$

The same relation is mentioned in [Krysinski and Malburet, 2007a].

3.4.2.5.2 Blade kinetic energy The galilean kinetic energy of the blade is defined by:

$$\mathscr{E}_c(blade/\mathscr{R}_g) = \int_{blade} \frac{1}{2} \cdot \|\overrightarrow{V_{M,blade/\mathscr{R}_g}}\|^2 \cdot dm \tag{3.37}$$

The previous formulation from eq. 3.36 is used to develop the kinetic energy. The definition of the blade inertia in flap and drag $I_p = \int_{blade} r^2 \cdot dm$ and the definition of the static moment $m_s = \int_{blade} r \cdot dm$ simplifies the expression and provides the following expression of the kinetic energy:

$$\begin{aligned} \mathscr{E}_c =& \frac{1}{2}\left[e^2\Omega^2 m_p + I_p(\dot{\delta} + \Omega)^2 \cos(\beta)^2 + I_p\dot{\beta}^2\right] \\ &+ m_s e\Omega(\dot{\delta} + \Omega)\cos(\beta)\cos(\delta) - m_s e\Omega\dot{\beta}\sin(\beta)\sin(\delta) \end{aligned} \tag{3.38}$$

[Krysinski and Malburet, 2007a] mentions the same relation.

3.4.2.6 Potential energy

The potential energy gathers the stiffnesses found on the two degrees of freedom.

$$\mathscr{E}_p = \frac{1}{2} \cdot K_\beta \cdot \beta^2 + \frac{1}{2} \cdot K_\delta \cdot \delta^2 \tag{3.39}$$

where K_β and K_δ are stiffnesses $[N \cdot m/rad]$ respectively around the flap and drag axis.

3.4.2.7 Flapping equation

3.4.2.7.1 Derivation To determine the equation describing the flapping motion, the previous results are reused and Lagrange's method is applied. The Lagrangian is determined by eq. 3.38 and 3.39:

$$\mathscr{L} = \mathscr{E}_c - \mathscr{E}_p \tag{3.40}$$

$$\frac{\partial \mathscr{L}}{\partial \beta} = -I_p(\dot{\delta} + \Omega)^2 \cos(\beta)\sin(\beta) - em_s\Omega(\dot{\delta} + \Omega)\sin(\beta)\cos(\delta) - em_s\Omega\dot{\beta}\cos(\beta)\sin(\delta) - K_\beta\beta \tag{3.41}$$

$$\frac{\partial \mathscr{L}}{\partial \dot{\beta}} = I_p\dot{\beta} - em_s\Omega\sin(\beta)\sin(\delta) \tag{3.42}$$

$$\frac{\partial}{\partial t}\left(\frac{\partial \mathscr{L}}{\partial \dot{\beta}}\right) = I_p\ddot{\beta} - em_s\Omega(\dot{\beta}\cos(\beta)\sin(\delta) - \sin(\beta)\dot{\delta}\cos(\delta)) \tag{3.43}$$

Now, the necessary equation members (eq. 3.43, 3.41 & 3.30) are determined to estimate Lagrange's equation of motion:

$$\frac{\partial}{\partial t}\left(\frac{\partial \mathscr{L}}{\partial \dot{\beta}}\right) - \frac{\partial \mathscr{L}}{\partial \beta} = M_{aero/\beta} \tag{3.44}$$

Applying the hypothesis regarding the small angles ($\delta \ll 1$), the neglected lag speed compared to the rotor mast speed ($\dot{\delta} \ll \Omega$) and the neglected eccentricity compared to the rotor radius ($e \ll R$), eq. 3.44 becomes:

$$\ddot{\beta} + \frac{\gamma \cdot \Omega}{8} \cdot \dot{\beta} + \omega_\beta^2 \cdot \beta = \frac{\gamma \cdot \Omega^2}{8} \cdot \theta \tag{3.45}$$

where ω_β^2 is the flapping angular frequency of the blade obtained such as:

$$\omega_\beta^2 = \underbrace{\left(1 + \frac{e \cdot m_s}{I_p}\right) \cdot \Omega^2}_{1} + \underbrace{\frac{K_\beta}{I_p}}_{2} \tag{3.46}$$

A numerical application of the equation members of eq. 3.46 shows that the member 2 is $3 \cdot 10^{-3}$ % of the member 1. This makes the member 2 negligeable compared to member 1. [Krysinski and Malburet, 2007a] agrees with this hypothesis too. In addition, the ratio $e \cdot m_s / I_p$ is negligeable. Indeed, m_s and I_p (expressions in Appendix G) are estimated considering a blade supposed as a uniform volume of a rectangular

section, thus the mass is constant per unit of length. Applying the hypothesis $e \ll R$ leading to $e/R \ll 1$, the following statement is formulated:

$$\frac{e \cdot m_s}{I_p} = \frac{3}{2}\left(\frac{e}{R-e}\right) \ll 1 \tag{3.47}$$

As a result, $\omega_\beta \approx \Omega$ meaning that the flapping angular frequency is close to the rotation speed of the rotor. Indeed, during one azimuth, the blade performs a flapping movement (ascent and descent), which is named a flapping cyclic motion.

Finally, the flapping equation is reduced to:

$$\ddot{\beta} + \frac{\gamma \cdot \Omega}{8} \cdot \dot{\beta} + \Omega^2 \cdot \beta = \frac{\gamma \cdot \Omega^2}{8} \cdot \theta \tag{3.48}$$

3.4.2.7.2 Damping & natural frequency The eq. 3.48 can be formulated on the following way:

$$\ddot{\beta} + 2 \cdot \lambda \cdot \omega_\beta \cdot \dot{\beta} + \omega_\beta^2 \cdot \beta = \frac{\gamma \cdot \Omega^2}{8} \cdot \theta \tag{3.49}$$

Since the lock number evolves within $[6, 12]$ according to the helicopter size, the value of $\lambda = \gamma/16$ evolves within $[0.38, 0.75]$. This means that the flapping movement is very damped (Appendix H). Moreover, since $w_\beta = \Omega$, the rotor works in flapping motion at the natural frequency. This is possible thanks to a strong aerodynamic damping. Therefore, $K_\beta \approx 0$ is a consistent assumption.

3.4.2.8 Drag equation

3.4.2.8.1 Derivation The flapping equation development, previously presented, is applied in the same way, in the drag equation development (angle δ). Lagrange's quantity is:

$$\begin{aligned}\mathscr{L} = \frac{1}{2}\Big[e^2\Omega^2 m_p + I_p(\dot{\delta}^2 + 2\dot{\delta}\Omega + \Omega^2)\cos^2(\beta) + I_p\dot{\beta}^2\Big] \\ + em_s\Omega(\dot{\delta} + \Omega)\cos(\beta)\cos(\delta) - em_s\Omega\dot{\beta}\sin(\beta)\sin(\delta) - \frac{1}{2}K_\beta\beta^2 - \frac{1}{2}K_\delta\delta^2\end{aligned} \tag{3.50}$$

$$\frac{\partial \mathscr{L}}{\partial \delta} = -em_s\Omega(\dot{\delta} + \Omega)\cos(\beta)\sin(\delta) - em_s\Omega\dot{\beta}\sin(\beta)\cos(\delta) - K_\delta\delta \tag{3.51}$$

$$\frac{\partial \mathscr{L}}{\partial \dot{\delta}} = (I_p\dot{\delta} + I_p\Omega)\cos^2(\beta) + em_s\Omega\cos(\beta)\cos(\delta) \tag{3.52}$$

$$\begin{aligned}\frac{\partial}{\partial t}\left(\frac{\partial \mathscr{L}}{\partial \dot{\delta}}\right) = I_p\ddot{\delta}\cos^2(\beta) - 2I_p\dot{\delta}\dot{\beta}\sin(\beta)\cos(\beta) - 2I_p\Omega\dot{\beta}\sin(\beta)\cos(\beta) \\ - em_s\Omega\dot{\delta}\cos(\beta)\sin(\delta) - em_s\Omega\dot{\beta}\cos(\delta)\sin(\beta)\end{aligned} \tag{3.53}$$

Lagrange's equation of motion is defined by:

$$\frac{\partial}{\partial t}\left(\frac{\partial \mathscr{L}}{\partial \dot{\delta}}\right) - \frac{\partial \mathscr{L}}{\partial \delta} = M_{aero/\delta} \tag{3.54}$$

The first equation members are provided by eq. 3.53 & 3.51. The expression of $M_{aero/\delta}$ is obtained from the eq. 3.32 using $M_{aero/\beta}$ taken from a formulation of eq. 3.44 such

as:

$$M_{aero/\beta} = I_p \cdot \ddot{\beta} + I_p \cdot \Omega^2 \cdot \beta \tag{3.55}$$

Applying the hypothesis regarding the small angles ($\beta \ll 1$), the neglected lag speed compared to the rotor mast speed ($\dot{\delta} \ll \Omega \implies \dot{\delta} + \Omega \approx \Omega$) and the neglected eccentricity compared to the rotor radius ($e \ll R$), eq. 3.54 becomes:

$$\ddot{\delta} - 2 \cdot \dot{\beta} \cdot \beta \cdot \Omega + \frac{e \cdot m_s \cdot \Omega^2 + K_\delta}{I_p} \cdot \delta = -\left(\ddot{\beta} + \Omega^2 \cdot \beta\right) \cdot \frac{\dot{\beta}}{\Omega} \tag{3.56}$$

The same expression is found back into [Krysinski and Malburet, 2007a]. Furthermore, this expression can be rewritten to highlight the natural frequency such as:

$$\ddot{\delta} + \omega_\delta^2 \cdot \delta = \Omega \cdot \beta \cdot \dot{\beta} - \frac{\ddot{\beta} \cdot \dot{\beta}}{\Omega} \tag{3.57}$$

where

$$\omega_\delta = \sqrt{\frac{e \cdot m_s \cdot \Omega^2 + K_\delta}{I_p}} \tag{3.58}$$

3.4.2.8.2 Damping & natural frequency The eq. 3.57 shows that the drag is excited by the blade flapping.

[Krysinski and Malburet, 2007a] shows that the blade is subjected to loads in 1Ω and 2Ω on the drag axis. Following the technology of rotors, there is a possibility to set the drag angular frequency ω_δ according to the speed of the rotor mast Ω (fig. 3.14). The drag axis must avoid the resonance in both 1Ω and 2Ω, in order to avoid very high drag loads. Therefore, a drag damper is installed and chosen to locate the resonant frequency of the first drag mode under 1Ω in the context of an articulated rotor type. Here, in the case of the Cabri G2, the value of the stiffness K_δ $[N.m/rad]$ must verify $0 \ll \omega_\delta \ll \Omega$.

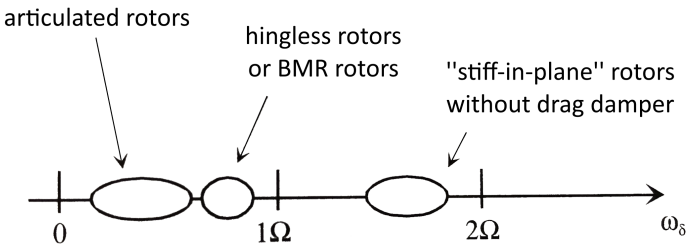

FIGURE 3.14: *Rotor type according to the drag stiffness [Krysinski and Malburet, 2007a]*

3.4.3 Study case with system of three degrees of freedom

Further than the approach presented in the previous subsection 3.4.2, we propose to consider that the flight control system introduces a torque on the blade pitch angle θ which becomes a third degree of freedom. Therefore, an additional reference sketch $\mathscr{R}_4 = (A, \overrightarrow{X_4}, \overrightarrow{Y_4}, \overrightarrow{Z_4})$ is introduced in fig. 3.6. The calculation steps to go through are the same than in the previous section, they will not be written entirely. The differential equations are obtained by a python script using Sympy's symbolic mathematical library [Sympy, 2021].

3.4.3.1 Kinetic energy

3.4.3.1.1 Blade speed in $\mathscr{R}_g$ A point M of the blade is described such as:

$$\overrightarrow{OM} = e \cdot \overrightarrow{X_1} + r \cdot \overrightarrow{X_3} + h \cdot \overrightarrow{Y_4} \tag{3.59}$$

where $r \in [0, R]$ is the rotor disk radius, Y_4 belongs to the additional sketch of reference $\mathscr{R}_4$, $h \in [-3/4 \cdot a, 1/4 \cdot a]$ gives the position on the blade profile chord. The speed is basically expressed by:

$$\overrightarrow{V_M} = e \cdot \Omega \cdot \overrightarrow{Y_1} + r \cdot \frac{d\overrightarrow{X_3}}{dt} + h \cdot \frac{d\overrightarrow{Y_4}}{dt} \tag{3.60}$$

where

$$\frac{d\overrightarrow{X_3}}{dt} = \overrightarrow{\Omega_{3/0}} \wedge \overrightarrow{X_3} = (\dot{\delta} + \Omega) \cdot \cos(\beta) \cdot \overrightarrow{Y_2} - \dot{\beta} \cdot \overrightarrow{Z_3} \tag{3.61}$$

$$\frac{d\overrightarrow{Y_4}}{dt} = \overrightarrow{\Omega_{4/0}} \wedge \overrightarrow{Y_4} = (\dot{\delta} + \Omega)(\sin(\theta)\sin(\beta)\overrightarrow{Y_2} - \cos(\theta)\overrightarrow{X_2}) + \dot{\beta}\sin(\theta)\overrightarrow{X_3} + \dot{\theta}\overrightarrow{Z_4} \tag{3.62}$$

With eq. 3.60, 3.61 & 3.62, the speed of point M is expressed by:

$$\begin{aligned}\overrightarrow{V}_{M,blade/\mathscr{R}_g} = e\Omega\overrightarrow{Y_1} + (r(\dot{\delta} + \Omega)\cos(\beta) + h(\dot{\delta} + \Omega)\sin(\theta)\sin(\beta))\overrightarrow{Y_2} - r\dot{\beta}\overrightarrow{Z_3} \\ - h(\dot{\delta} + \Omega)\cos(\theta)\overrightarrow{X_2} + h\dot{\beta}\sin(\theta)\overrightarrow{X_3} + h\dot{\theta}\overrightarrow{Z_4}\end{aligned} \tag{3.63}$$

3.4.3.1.2 Blade kinetic energy The kinetic energy formula is given in eq. 3.37. The speed is taken from eq. 3.63. The kinetic energy is developed and simplified using $I_p = \int_{blade} r^2 dm$ and $m_s = \int_{blade} r dm$. The final expression of the kinetic energy is given in Appendix G.

3.4.3.2 Potential energy

The potential energy gathers the stiffnesses found on the three degrees of freedom.

$$\mathscr{E}_p = \frac{1}{2} \cdot K_\beta \cdot \beta^2 + \frac{1}{2} \cdot K_\delta \cdot (\delta - \delta_0)^2 + \frac{1}{2} \cdot K_\theta (\theta - \theta_0)^2 \tag{3.64}$$

where K_β, K_δ and K_θ are elasticity modulus $[N \cdot m/rad]$ respectively around the flap, the drag and the pitch axis. δ_0 and θ_0 are neutral drag and pitch angles when the rotor is not rotating.

3.4.3.3 Flapping, drag & pitch equations

With the previous results from eq. G.7 & 3.64, Lagrange's quantity $\mathscr{L} = \mathscr{E}_c - \mathscr{E}_p$ is determined. Then, with respect to each degree of freedom, the differential equations are estimated. To be brief, these equations are presented in Appendix G.

A viscous damping is taken into account for the 3 degrees of freedom. This choice is motivated since a viscous contribution is provided by the drag damper. At blade attachment, the laminated spherical bearing made of elastomers is based on the same technology than the drag damper. It obviously contributes to a viscous damping in flap and pitch motions, however with a viscous coefficient much lower

than the one involved by the drag damper. We could get the drag viscous coefficient λ_δ $[N \cdot m/rad]$. Assuming that the elastomers intalled in the spherical bearing and in the drag damper have the same composition, a constant ratio between the viscous stiffness and the linear stiffness can be considered. Knowing the linear stiffnesses of both components, we can deduce λ_θ $[N \cdot m/rad]$ and λ_β $[N \cdot m/rad]$. These damping contributions are included into the Lagrange's equations.

Lagrange's equation according to β is based on:

$$\frac{\partial}{\partial t}\left(\frac{\partial \mathscr{L}}{\partial \dot{\beta}}\right) - \frac{\partial \mathscr{L}}{\partial \beta} = M_\beta \tag{3.65}$$

$$\text{where } M_\beta = M_{aero/\beta} + M_{act/\beta} + M_{viscous/\beta} \tag{3.66}$$

$$= \frac{\gamma I_p \Omega^2}{8}\left(\theta - \frac{\dot{\beta}}{\Omega}\right) + M_{act/\beta} - \lambda_\beta \cdot \dot{\beta} \tag{3.67}$$

Because of the pitch horn, the pitch rod acts on the flap and the pitch angles of the blade (details in section 3.5). This is taken into account through the equation member $M_{act/\beta}$.

Lagrange's equation according to δ is based on:

$$\frac{\partial}{\partial t}\left(\frac{\partial \mathscr{L}}{\partial \dot{\delta}}\right) - \frac{\partial \mathscr{L}}{\partial \delta} = M_\delta \tag{3.68}$$

$$\text{where } M_\delta = M_{aero/\delta} + M_{viscous/\delta} = -M_{aero/\beta} \cdot \frac{\dot{\beta}}{\Omega} - \lambda_\delta \cdot \dot{\delta} \tag{3.69}$$

This is similar to the system with 2 degrees of freedom.

Lagrange's equation according to θ is based on:

$$\frac{\partial}{\partial t}\left(\frac{\partial \mathscr{L}}{\partial \dot{\theta}}\right) - \frac{\partial \mathscr{L}}{\partial \theta} = M_\theta \tag{3.70}$$

$$\text{where } M_\theta = M_{act/\theta} + M_{viscous/\theta} = M_{act/\theta} - \lambda_\theta \cdot \dot{\theta} \tag{3.71}$$

where $M_{act/\theta}$ is the equation member considering the action of the pitch rod onto the blade (details in section 3.5). It is assumed a symmetric profile with a nearly fixed center of pressure located on the pitch axis. The aerodynamic resultant is considered to be applied on the blade pitch axis, it does not involve any moment $M_{aero/\theta}$.

3.5 Global system modelling & stability study

This section brings the additional models necessary to loop the global system modelling from the swashplate to the blade. A stability study with respect to two actuator characteristics is suggested as a last part.

3.5.1 Architecture of the global model

As already mentioned, the undertaken approach is a modelling at the system level. The implementation is done using *OpenModelica*®. This software solution is acausal, it offers the opportunity to work directly with equations. Fig. 3.15 sums up the different modelling bricks and their interactions.

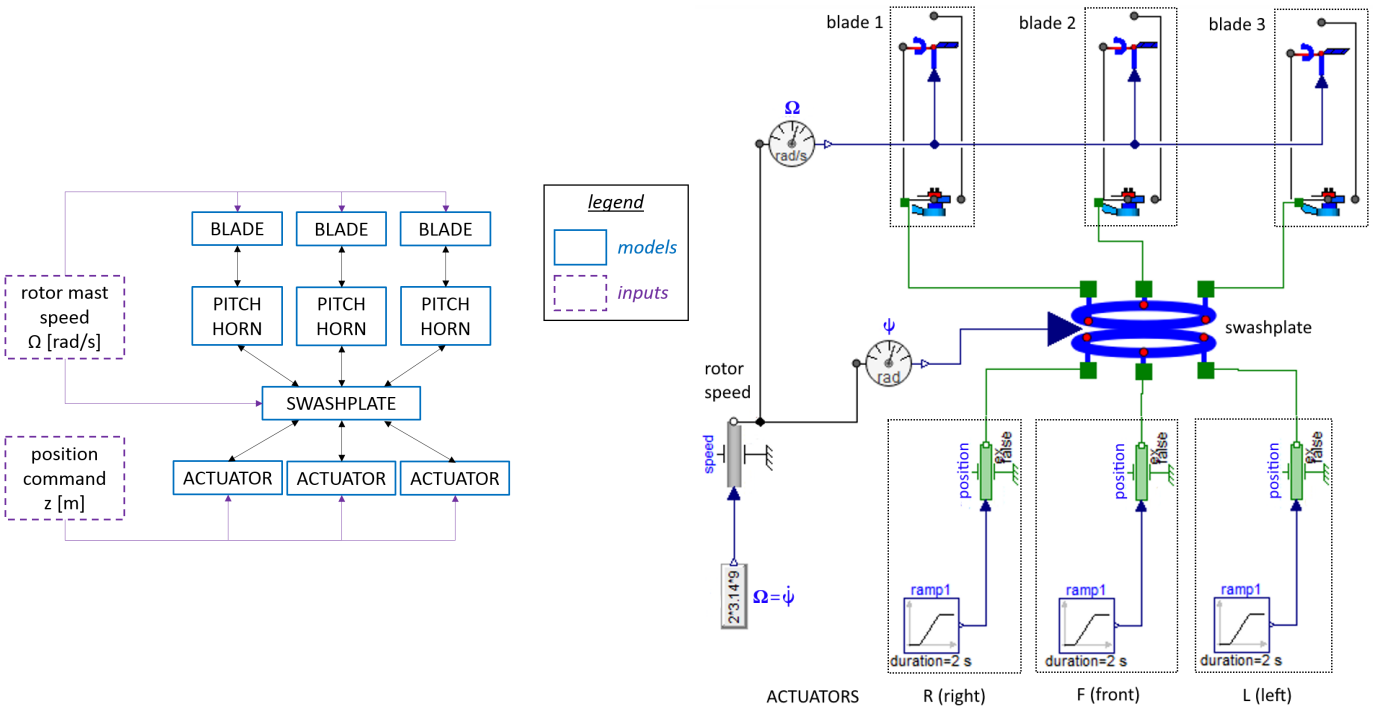

FIGURE 3.15: *Rotor model architecture: (left) diagram of model bricks, (left) model view from OpenModelica*

The *blade* brick is the heart of the problem where the dynamic is generated. It contains all the parameters, variables, and equations linked to the blade (see section 3.4.3) and the components made of elastomers (see section 3.5.5). The 3 differential equations describing the blade motion according to its three degrees of freedom (β, δ, θ) are in this brick. Since the Cabri G2 is three-bladed helicopter, there are three *blade* bricks and three *pitch horn* bricks.

The *pitch horn* brick makes the link between the swashplate and one blade (see section 3.5.3).

The *swashplate* brick makes the link between the rotating reference and the fixed reference where the actuators are attached (see section 3.5.2).

The *actuator* brick includes different models depending on the study to perform. If the focus is only on the rotor, this brick set only a fixed vertical position. If the focus is linked to the actuator technology as it is in section 3.5.7, the brick models with a strickly reduced number of parameters the actuator characteristics at stake. Three *actuator* bricks are necessary to consider the three actuators orientating the swashplate.

The positions of reference of the actuators have been adjusted according to the effective blade pitch angle of the helicopter.

The modelling bricks of the blade, the swashplate and the actuators are fed with four input values: the helicopter rotor speed value, and the three actuator vertical positions.

3.5.2 Swashplate model

The swashplate is presented on the helicopter in fig. 3.3 & 3.4. Its modelling is presented en details in section 3.3.

3.5.3 Pitch horn model

The pitch horn (*liaison k* in french, fig. 3.3 & 3.4) is a system commonly installed on helicopter to reduce the flapping amplitude on rotors spinning [Doat, 2016]. This contributes in keeping low the vibratory level.

The pitch horn is actually a coupling between flapping and pitch. Indeed, the rod end attachement is not on the flap axis but phaseshifted from an angle φ. Therefore, when the blade is flapping up, its pitch angle decreases and vice versa.

The pitch horn is sketched in fig. 3.16 where the flap and pitch lever arms are highlighted.

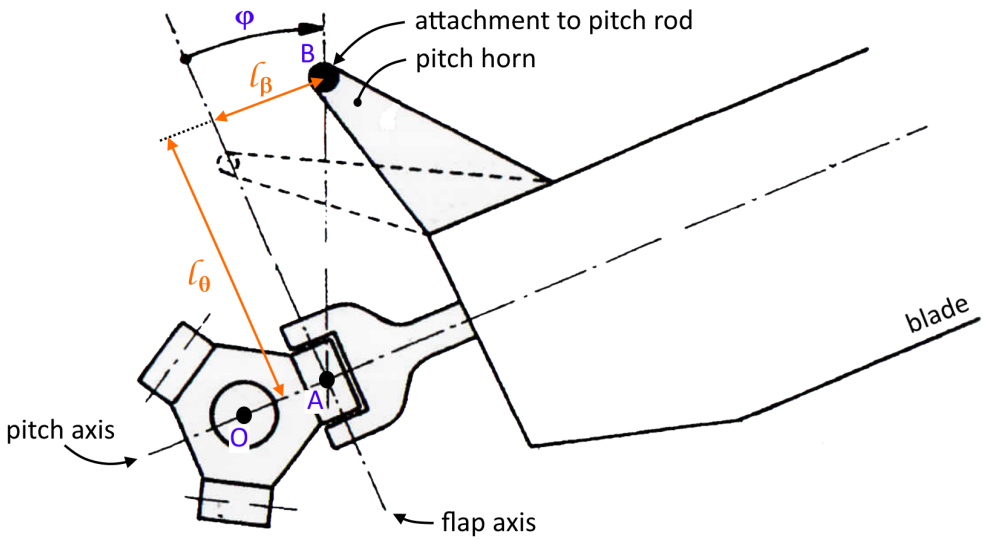

FIGURE 3.16: *Pitch horn & lever arms for the pitch angle θ and the flap angle β*

The application of the virtual works generate the three necessary equations describing the motion involved by the pitch horn.

Considering the two degrees of freedom presented in fig. 3.16, the vertical displacement z_{ph} of the pitch rod can be written by:

$$z_{ph} = l_\theta \cdot \theta + l_\beta \cdot \beta \tag{3.72}$$

The pitch rods are supposed to be vertical (along $\overrightarrow{Z_0}$). This is a first equation. At the junction (point B, fig. 3.16), a work status gives:

$$\mathscr{W}_{total} = F_{pitch,rod} \cdot z_{ph} + C_\beta \cdot \beta + C_\theta \cdot \theta = 0 \tag{3.73}$$

$$= F_{pitch,rod} \cdot (L_\theta \cdot \theta + L_\beta \cdot \beta) + C_\beta \cdot \beta + C_\theta \cdot \theta = 0 \tag{3.74}$$

The two other equations come from the derivatives of the total work regarding each degree of freedom:

$$\frac{\partial \mathscr{W}_{total}}{\partial \theta} = F_{pitch,rod} \cdot L_\theta + C_\theta = 0 \tag{3.75}$$

$$\frac{\partial \mathscr{W}_{total}}{\partial \beta} = F_{pitch,rod} \cdot L_\beta + C_\beta = 0 \tag{3.76}$$

3.5.4 Blade model

The blade evolves with respect to the application of three main forces: the aerodynamic forces, the inertia forces and the weight. The two first ones have been taken into account in Lagrange's approach presented in sections 3.4.2 & 3.4.3.

The blade weight is taken into account in the potential energy $\mathscr{E}_p$. In the particular case of a gravity field perfectly uniform, the blade potential energy of gravity $\mathscr{E}_{pp}$ is estimated at the inertia center, with a mass equal to the blade solid. According to the hypothesis concerning the blade geometry, a uniform mass repartition is considered. Thus, the moment involved by the gravity considers the inertia center and the center of gravity as the same point.

The distance to the point G where the weight applies is defined by:

$$\overrightarrow{AG} = \frac{R}{2} \cdot \overrightarrow{X_3} - \frac{b}{4} \cdot \overrightarrow{Y_4} \tag{3.77}$$

where R $[m]$ is the blade length, b $[m]$ is the blade equivalent width. Its projection onto the axis $\overrightarrow{Z_1}$ is:

$$z_G = \overrightarrow{AG} \cdot \overrightarrow{Z_1} = -\frac{R}{2} \cdot \sin(\beta) - \frac{b}{4} \cdot \sin(\theta) \cdot \cos(\beta) \tag{3.78}$$

This results in the following potential energy of gravity:

$$\mathscr{E}_{pp} = m_{blade} \cdot g \cdot z_G = m_{blade} \cdot g \cdot \left(\frac{R}{2} \cdot \sin(\beta) - \frac{b}{4} \cdot \sin(\theta) \cdot \cos(\beta) \right) \tag{3.79}$$

3.5.5 Elastomer model

The rotor gathers two components made out of elastomers: the drag damper (fig. 3.3 & 3.17) and the spherical bearing (fig. 3.18). Both components are based on a 'sandwich' architecture where the elastomer is located between two metallic parts.

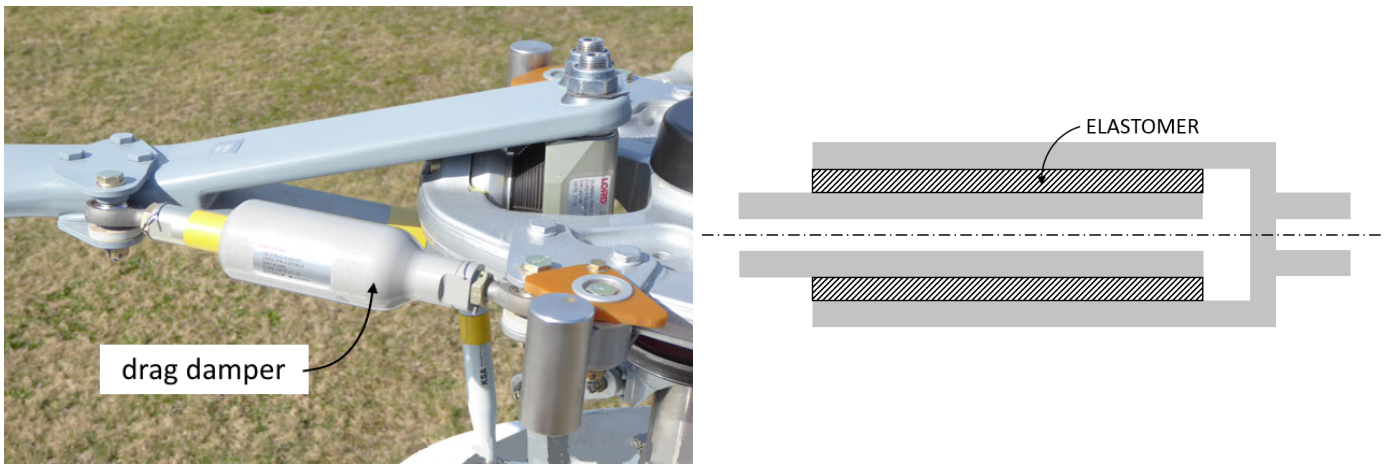

FIGURE 3.17: *Drag damper [Bazzani, 2018]: (left) view of integration in rotor, (right) section view (sketch of principle)*

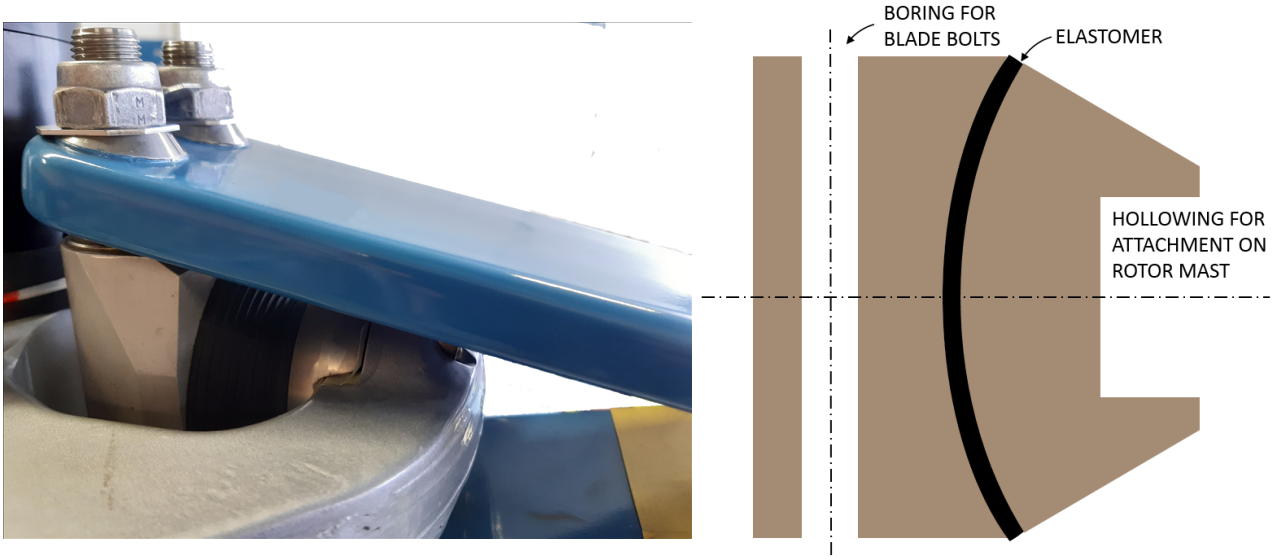

FIGURE 3.18: *Laminated spherical bearing [Bazzani, 2018]: (left) view of integration in rotor, (right) section view (sketch of principle)*

3.5.5.1 Visco-elastic behaviour

The rotor elastomers are dynamically qualified through lab tests. Indeed, the dynamic loading of the rotor spinning requires a description of the visco-elastic behaviour in the frequency domain [Long, 2005]. In this context, a description of the material characteristics based on complex numbers is convenient [Jrad, 2014] [Boukamel, 2006]. The real part of the characteristic is linked to the elastomer elasticity meanwhile the imaginary part corresponds to the elastomer dissipation. The real part is named the storage modulus. It is linked to a measure of the energy stored up and released during one cycle. The imaginary part is named the loss modulus. It is linked to a measure of energy dissipated as a heat during one cycle.

We suggest introducing Kelvin-Voigt's model presented in fig. 3.19. It considers a simple approach based on a complex stiffness K_c with K' $[N \cdot m^{-1}]$ the storage modulus and K'' $[N \cdot m^{-1}]$ the loss modulus.

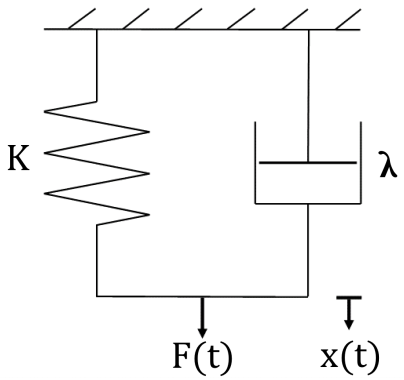

$$
\begin{aligned}
K_c &= K' + j \cdot K'' && (3.80)\\
F(t) &= -K_c \cdot x(t) \\
&= -K' \cdot x(t) - j \cdot K'' \cdot x(t) \\
&= -K' \cdot x(t) - j \cdot w \cdot \frac{K''}{w} \cdot x(t) \\
&= -K' \cdot x(t) - \frac{K''}{w} \cdot v(t) \\
F(t) &= -K' \cdot x(t) - \lambda' \cdot v(t) && (3.81)
\end{aligned}
$$

FIGURE 3.19: *Kelvin-Voigt model for a system of translation*

The only lab test data available for this elastomer study are: the elasticity property K_β $[N \cdot m \cdot rad^{-1}]$ of the spherical bearing on the flap axis, the elasticity property K'_{dd} $[N \cdot m^{-1}]$ and the dissipative property K''_{dd} $[N \cdot m^{-1}]$ of the drag damper.

We suggest modelling the elastomer of the drag damper as an elastic torque of elasticity modulus $K_{\delta,dd}$ $[N \cdot m \cdot rad^{-1}]$ and a viscous torque of coefficient $\lambda_{\delta,dd}$ $[N \cdot$

$m \cdot rad^{-1} \cdot s]$ applied at point A.

We suggest converting the elastic and viscous properties of the drag damper from a linear kinematic to a rotative kinematic at the spherical bearing level (point A, fig. 3.20). The conversion ratio regarding the elasticity modulus is obtained assuming a conservation of the elastic energy $\mathscr{E}_{elastic}$ $[J]$ such as:

$$\mathscr{E}_{elastic} = \frac{1}{2} \cdot K'_{dd} \cdot x_{dd}^2 = \frac{1}{2} \cdot K'_{dd} \cdot (l_{arm} \cdot \delta)^2 = \frac{1}{2} \cdot K_{\delta,dd} \cdot \delta^2 \tag{3.82}$$

where K'_{dd} $[N \cdot m^{-1}]$ is the elasticity modulus in translation of the drag damper, x_{dd} $[m]$ its linear strain during the drag motion δ (fig. 3.20), $K_{\delta,dd}$ $[N \cdot m \cdot rad^{-2}]$ is an equivalent elasticity modulus in rotation applied at point A and defined by:

$$K_{\delta,dd} = K'_{dd} \cdot l_{arm}^2 \tag{3.83}$$

The conversion ratio regarding the viscous coefficient is obtained assuming a conservation of the dissipated power $\mathscr{P}_{dissipated}$ $[W]$ such as:

$$\mathscr{P}_{dissipated} = F_{viscous,dd} \cdot v_{dd} = \lambda'_{dd} \cdot v_{dd}^2 = \lambda'_{dd} \cdot (l_{arm} \cdot \dot{\delta})^2 = \lambda_{\delta,dd} \cdot \dot{\delta}^2 \tag{3.84}$$

where λ'_{dd} $[N \cdot m^{-1} \cdot s]$ is the viscous coefficient in translation of the drag damper, $\lambda_{\delta,dd}$ $[N \cdot m \cdot rad^{-1}]$ is an equivalent viscous coefficient in rotation applied at point A and defined by:

$$\lambda_{\delta,dd} = \lambda'_{dd} \cdot l_{arm}^2 = \frac{K''_{dd}}{\Omega} \cdot l_{arm}^2 \tag{3.85}$$

where Ω $[rad \cdot s^{-1}]$ is the rotor mast speed.

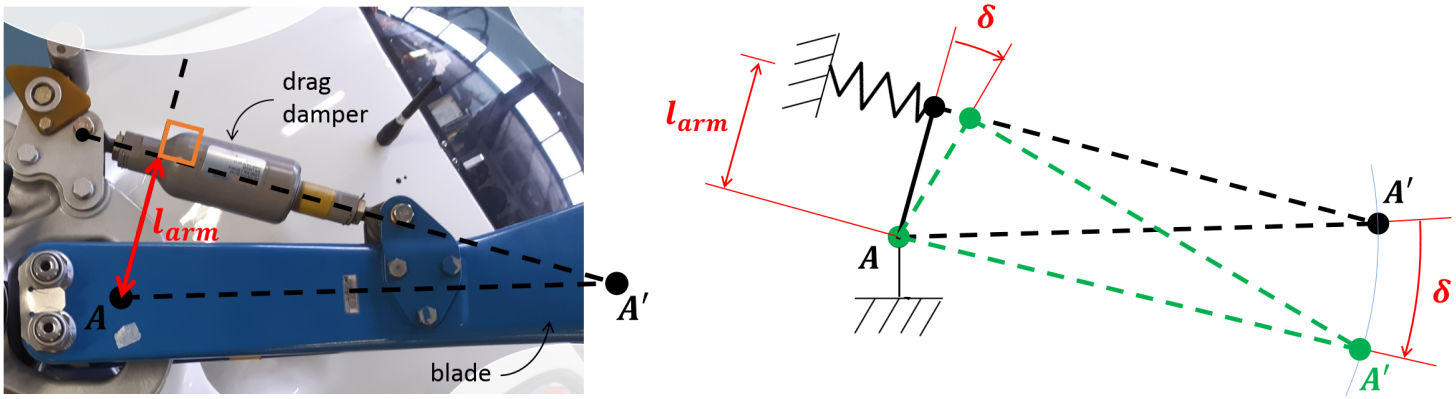

FIGURE 3.20: *Drag damper lever arm [Bazzani, 2018]: (left) helicopter top view, (right) sketch of principle*

The drag damper adds, for the drag axis, an additional elastomer in parallel at point A. Thus, its equivalent elasticity modulus $K_{\delta,dd}$ and viscous coefficient $\lambda_{\delta,dd}$ is summed up to the one provided by the spherical bearing:

$$K_\delta = K_{\delta,sb} + K_{\delta,dd} \tag{3.86}$$

$$\lambda_\delta = \lambda_{\delta,sd} + \lambda_{\delta,dd} \tag{3.87}$$

We suggest to model the elastomer of the spherical bearing as an elastic torque of the elasticity modulus K_i $[N \cdot m \cdot rad^{-1}]$ and a viscous torque of the coefficient λ_i $[N \cdot m \cdot rad^{-1} \cdot s]$ applied at point A.

It is assumed that the spherical bearing has the same characteristics K'_{sb} and K''_{sb} for the three angular motions β, δ and θ. Thus, $K_\theta = K_\beta = K_{\delta,sb}$ and $\lambda_\theta = \lambda_\beta = \lambda_{\delta,sb}$ at the spherical bearing.

As reminder, the only data available are K_β $[N \cdot m \cdot rad^{-1}]$ (spherical bearing, flap axis), K'_{dd} $[N \cdot m^{-1}]$ and K''_{dd} $[N \cdot m^{-1}]$ (drag damper).

From these data, it is possible to workout the variables necessary for the modelling of the elastomer. Nevertheless, the dissipative property K''_{sb} of the spherical bearing requires to be known. An additional hypothesis must be formulated. In [De and White, 2001] [Ferry, 1980] and [Wikipedia, 2022], it is taught that elastomers can be classified with a loss factor defined such as:

$$\eta = \frac{K''}{K'} \; [-] \tag{3.88}$$

The loss factor and elastomer modulus can be ajusted to comply with a given application. This is possible, modifying the elastomer chemical composition e.g. adding a hardener or a plasticizer. For a 'sandwich' structure of elastomer material such as a three-layer metal/polymer/metal (as it is for the spherical bearing), the loss factor is commonly defined with an order of magnitude of $\eta = 0.1$ at ambiant temperature and for frequencies $[10, 10^4]$. From this data and the previous results, the λ_i are estimated.

$$\lambda_i = \frac{K''_{sb} \cdot l_{eq}^2}{\Omega} = \frac{0.1 \cdot K'_{sb} \cdot l_{eq}^2}{\Omega} = \frac{0.1 \cdot K_\beta}{\Omega} \tag{3.89}$$

where $i \in [\beta, \delta, \theta]$, and l_{eq} $[m]$ is an equivalent lever arm.

3.5.5.2 End stops

As already seen in fig. 3.18, the spherical bearing is made of an assembly of thin spherical layers of metallic sheets separated by thin layers of elastomer. This architecture provides the equivalent kinematic of a spherical joint with limitations in terms of angular stroke.

The necessary angular freedom in the flap is assumed to be $\pm 10°$ (value taken from an Airbus light helicopter). Outside these bounds, we suggest to apply a spring and damping effect connected in parallel. The constants linked to them must be determined. Therefore, we consider and assume a spring-damper model is implemented with a damping coefficient $\xi > 1$ (to avoid overshoot) and a high natural frequency i.e. $\omega_0 \approx 1$ khz (order of magnitud far from rotor mast frequency). The second order transfer function is:

$$T(s) = \frac{1}{c + d \cdot s + I_p \cdot s^2} = \frac{\frac{1}{c}}{1 + \frac{d}{c} \cdot s + \frac{I_p}{c} \cdot s^2} \tag{3.90}$$

where c $[N \cdot m \cdot rad^{-1}]$ is the spring constant, d $[N \cdot m \cdot s \cdot rad^{-1}]$ is the damping constant, and I_p $[kg \cdot m^2]$ is the blade inertia in flapping.

From eq. 3.90, two equation members are identified (Appendix H):

$$\omega_0 = \sqrt{\frac{c}{I_p}} \qquad\qquad \frac{d}{c} = \frac{2 \cdot \xi}{\omega_0} \tag{3.91}$$

The constants necessary to model the end stops are finally defined by:

$$c = I_p \cdot \omega_0^2 \qquad d = \frac{2 \cdot \xi \cdot c}{\omega_0} \tag{3.92}$$

3.5.6 Simulation results

To check the model consistency, two simulations are run considering the Cabri G2 nominal rotor speed (fig. 3.21). A first simulation considers a hover flight phase where the helicopter is stationary in the air and balances its own weight (fig. 3.21, *left*). This flight phase involves equal actuator displacement commands so as to move vertically the swashplate. Another simulation is run with different actuator displacements (fig. 3.21, *right*) as if the helicopter was leaving from its hover phase to an advancing flight phase.

Fig. 3.21 presents the simulation results with normalized y-axis for the sake of confidentiality. The blade lift force is normalized by the helicopter weight. The actuator displacement is normalized with an actuator position of reference. The actuator loads are normalized by the maximum load simulated for the actuator L (left).

As reminder, the model ignores the helicopter advancing speed, this is for a first modelling approach. Also, the model considers the aerodynamic characteristics of the blade through a single coefficient, Lock's number γ (eq. 3.29). This coefficient value is set with the mean value of an interval in practice for rotorcraft models found in [Singleton and Yeager Jr, 2000]. The model considers the real geometries of the Cabri G2 rotor. However, the blade is considered as a uniform rectangular section volume. Therefore, the results can not really be compared with real flight test measures. However, the order of magnitude can be checked. The simulated actuator loading belongs to the loading spectrum found on flight tests and for similar flight phases. The model parameters were not adjusted to fit results with flight data, there is still a future model fitting work to provide.

In addition, the consistency of the dynamic behaviour representation can be commented. As expected, in hover flight (fig. 3.21, *left*), the total lift generated allows to balance the helicopter weight. The lift generated by the blades is constant whatever the rotor azimuth is. The actuator loads are steady and lower than during any other flight phase where the swashplate is tilted. In the simulation of fig. 3.21 (*right*), the swashplate is tilted. In this case, higher loads are noticed indeed. The low frequency dynamic of 9hz linked to rotor speed appears in the aerodynamic forces. However, the actuator loading levels do not show clearly a fluctuating load which should be of 27 hz. 27 hz is the product of the rotor speed by the number of blades (3 blades).

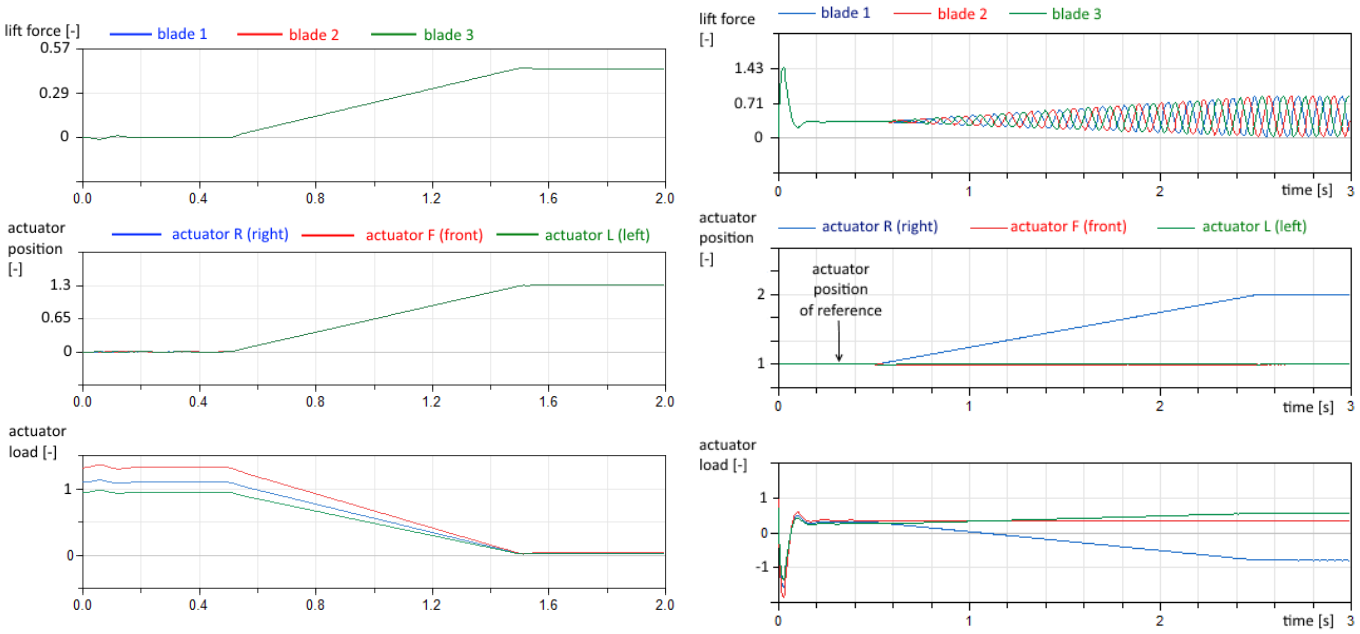

FIGURE 3.21: *Simulation results of blade lift force and actuator load according to actuator position, hover flight, nominal rotor speed: (left) pure collective command (3 actuators move the same), (right) other flight scenario with actuator positions leaving the hover to a forward flight*

The lift force is estimated with the following eq. 3.93 coming from a combination of eq. 3.20 & 3.19 with previous hypothesis and a projection onto the vertical axis $\overrightarrow{Z_1}$.

$$F_P = \frac{\gamma \cdot I_p}{6 \cdot \Omega \cdot R} \cdot \left(\Omega^2 + \dot{\beta}^2\right) \cdot \left(\Omega \cdot (\theta - \theta_0) - \dot{\beta}\right) \tag{3.93}$$

3.5.7 Stability study

3.5.7.1 State-of-the-art

In 2012, Airbus A320 fly-by-wire architecture included ailerons actuated by EMAs. Each aileron was actuated by one EMA in the active mode whilst the other remained free in motion and in damping mode [Todeschi, 2012]. The damping mode prevents from the appearance of a flutter phenomenon if multiple failures occur. An actuator failure scenario is the loss of its control or its power supply.

For a conventional hydraulic actuator, there are two intrinsic behaviours: one comes from a hydraulic stiffness force due to the fluid compressibility and the airframe compliance; the other one comes from a dissipative or damping force. The actuator damping behaviour is achieved easily, simply connecting the two actuator chambers through a hydraulic flow restriction [Todeschi, 2012]. With the aerodynamic surface inertia and the anchorage stiffness, the system behaviour is known.

According to the flutter certification rules (FAR25), the flutter clearance has to be covered whatever the actuator technology [Todeschi, 2012].

The introduction of the EMA technology involves parameters, different from the hydraulic. The Airbus A320 flight test campaign, equipped with a linear EMA in the scope of the MEA, drew the following conclusion [Todeschi, 2012]. The reflected inertia of an EMA becomes an important parameter in the definition of its damping performance requested for the failure scenario in a free mode. Consequently, Airbus specifies the domain of possible parameter pairs (the EMA rotor inertia and its

damping coefficient). This specified domain corresponds, in the failure scenario, to the acceptable flutter levels in compliance with the flutter certification rules (FAR25).

Literature provides two solutions to ensure the EMA damping behaviour in the failure scenario. A first solution is the passive damping. This solution can apply the patent registered by J. Piaton working for Sagem defense [Piaton, 2010]. It consists of a steel tube-shaped frame envelopping the EMA motor stack laminations. This arranges the single internal electromagnetic circuit of the stator in a manner that directly produces, by magnetic induction, a friction phenomenon that is both dry, through magnetic hysteresis, and viscous, through eddy currents. A second solution is the active damping. This introduces a position control loop based on the dynamic force feedback from force sensors installed in the actuator attachment points. The TVC of the European launcher VEGA made this choice [Vanthuyne, 2009].

3.5.7.2 Suggestion

The failure mode where the actuator remains free is not really expected in this thesis context. Indeed, it corresponds to an extremely impossible event where, both the actuator current supply and the power-off brake fail simultaneously. However, this failure mode could occur considering another EMA architecture, different from this thesis architecture of reference. Furthermore, such study could be a starting point for designers of actuator controllers in helicopters. Indeed, a closed loop control acts as a viscous friction [Budinger et al., 2019].

So far, the dynamic rotor load model considered the actuators on a simple way i.e. as perfect sources of position. The actuator strictly maintained the position entered as input.

In this section and as a first level approach, we suggest to substitute the ideal actuator model by an impedance. The impedance is specifically chosen according to the considered actuator technology. The hydraulic technology impedance is a resistance. The electromechanical technology impedance is a reflected rotor inertia i.e. an equivalent mass. As mentioned in the previous subsection 3.5.7.1, a viscous damping will be introduced to tackle this technology.

The rotor model is run for each technology separately. This is to check if any sign of instability could be initiated at the swashplate level. It is clear that any instability raises some concerns in such critical and dynamic application.

3.5.7.3 Hydraulic actuator

Section 3.5.7.1 mentioned the two intrinsic behaviours of a conventional hydraulic actuator. We consider the worst–case failure scenario where the actuator behaves such as a pure stiffness without damping. The hydraulic actuator is basically a piston located into a hollowed cylinder. An oil pressure ensures the motion of the piston. For a given quantity of oil, the piston moves within the oil compressibility, it provides to the actuator an impedance of stiffness summed up to the anchorage compliance. As a first order approximation, we suggest to implement between the imposed position and the swashplate, a stiffness coefficient K_{hyd} (fig. 3.22, left). The actuator is modelled with an opened loop control.

Varying this coefficient $K_{hyd} \in [10^3, 10^9]$ $[N \cdot m^{-1}]$ with different possible actuator positions and over 100 seconds of simulation, no position instability has been noticed. Implementing a speed closed loop control and a viscous friction heighten this conclusion.

As a first approximation, the hydraulic actuator does not raise any concern regarding a position instability at the swashplate level.

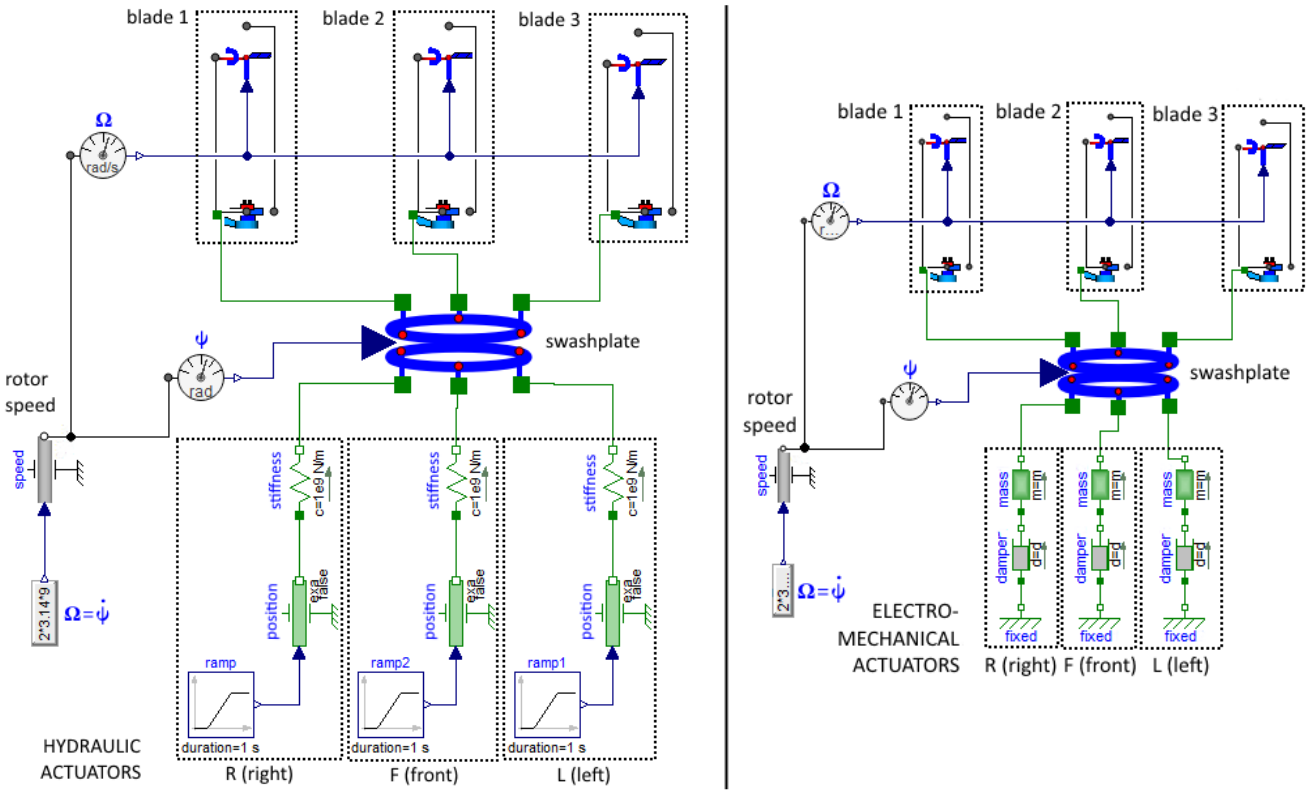

FIGURE 3.22: *Block diagram of rotor model in OpenModelica®: (left) with equivalent hydraulic actuators, (right) with equivalent EMA actuators*

3.5.7.4 Electromechanical actuator

The EMA technology is described in Chapter 1. Its architecture includes a rotating inertia and a mechanical transmission converting a rotating reference to a linear one. In free mode, this architecture gives the actuator the behaviour of a mass: the reflected inertia. Depending on the component sizing, the reflected inertia can be very high. This can affect position stability under the swashplate. We intend to bound this reflected inertia M_{rJ} $[kg]$ within an interval. These bounds could be applied further as an actuator design constraint and guide the design of the electrical motor and the mechanical transmission. As mentioned previously (subsection 3.5.7.1), the reflected inertia goes with a viscous damping.

As a first level approximation, we suggest to model the actuator with an equivalent mass M_{rJ} and a linear viscous friction c_{vf} (fig. 3.22, right). M_{rJ} and c_{vf} will be the parameters to vary so as to check the system stability (fig. 3.23). Launching multiple simulation runs (similarly to a full factorial *Design of Experiment (DoE)*), some pairs (M_{rJ}, c_{vf}) lead to the actuator position stability (fig. 3.23, *right*), other pairs lead to position instabilities (fig. 3.23, *left*). The set of the acceptable pairs (M_{rJ}, c_{vf}) draws an actuator design domain (fig. 3.24).

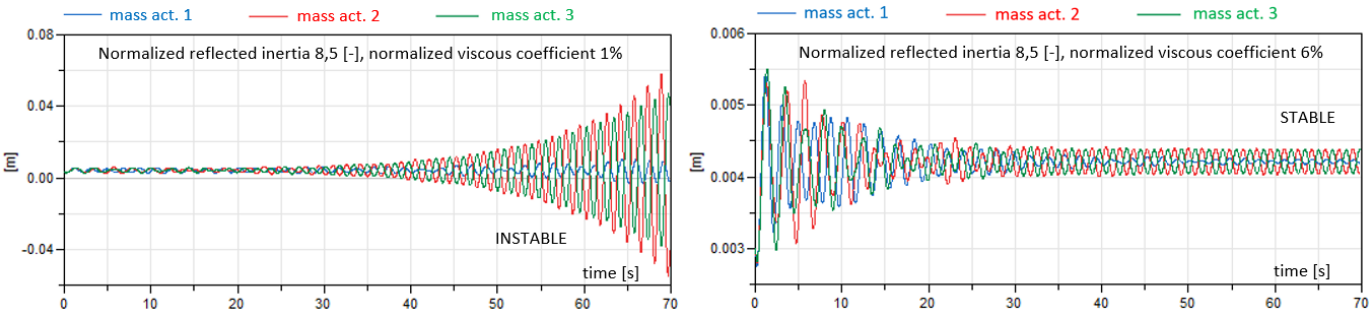

FIGURE 3.23: *Example of two pairs (M_{rJ}, c_{vf}) leading to an unsteady system (left) or a steady system (right)*

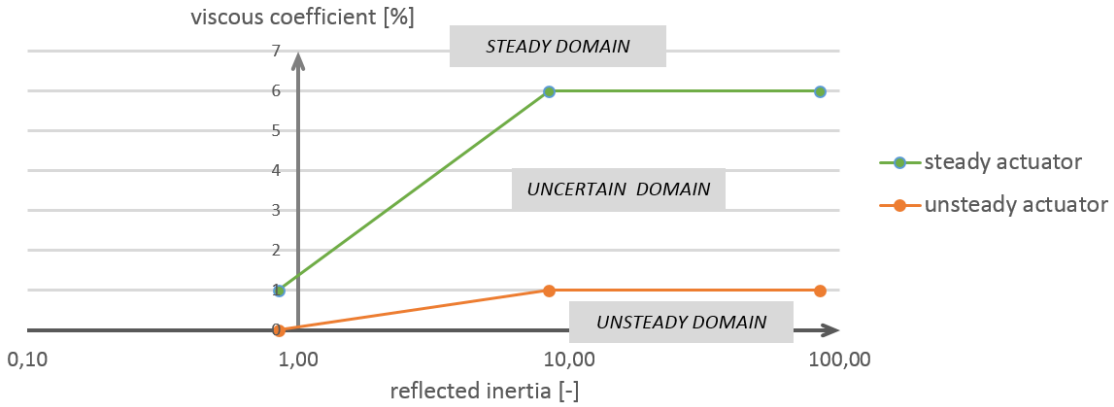

FIGURE 3.24: *Actuator stability analysis: domain of acceptable design characteristics*

From flight test data analysis in Chapter 2, the nominal load and the maximum speed of the actuators can be known. The ratio of this load to this speed defines a reference with a viscosity unit $[N/(m/s)]$. A percentage of this reference ratio is applied as a viscosity coefficient in the actuator model of fig. 3.22 (right). It is this percentage that is displayed on the y-axis of fig. 3.24. The x-axis of fig. 3.24 is normalized by the real actuator reflected inertia of the helicopter VSR700.

The simulation test points defines three design domains for this application: the steady, the uncertain, and the unsteady domains. The pairs (M_{rJ}, c_{vf}) belonging to the steady domain (the ones upper the green line) are the actuator characteristics that do not introduce an actuator instability risk.

Fig. 3.24 shows that, in the failure scenario where the actuator is in a free mode, the VSR700 actuators require a continuous damping whose resulting energy dissipated is on the order of $[1-2]\%$ of the nominal energy the helicopter rotor is providing. The patent [Piaton, 2010], used in a similar application, states its design to ensure a continuous damping whose order is $[2-10]\%$. We can suggest that the actuator is capable to provide through its own mechanical losses a damping of order $[1-2]\%$ [Maré, 2015]. Therefore, the VSR700 actuators do not need any further concern regarding the stability risk.

3.6 Conclusion & discussion

This chapter brings a brief overview of the helicopter rotor and its running principle. It gives a clearer view on the origin of the 'hammering' load which flight control actuators have to withstand under the swashplate.

A first level approach of rotor load modelling is presented. It is inspired from the approach suggested by [Krysinski and Malburet, 2007a] and developed with an additional degree of freedom (the blade pitch angle). The modelling level is a system level. Therefore, a lumped parameter modelling software is used to run the different equations describing the system. Lagrange's approach is developped to work out the equations of the blade motion. The blade is considered as a rectangular section volume. The induced speed is not taken into account. These hypothesis are open to criticism. Obviously, the considered blade model provides a very limited representation since the aero-elasticity of the blade contributes into the rotor dynamism [Lebel, 2012] [Krysinski and Malburet, 2007b].

Initially, this model was developed in order to: - estimate the actuator load spectrum, - observe the load distribution among the swashplate actuators, - identify the actuator stability to define a new design driver guiding the electrical motor sizing (rotor inertia).

The actuator load results presented in this Chapter are globally and reasonably representative in terms of order of magnitude. However, the assymetric distribution of the rotor load among the three actuators lacks representativity. Finally, the actuator load spectrum can be obtained using another way than modelling: the flight test analysis. This way is expensive in money, in time and lacks reactivity.

Identifying the actuator stability with different motor rotor inertia is impossible to carry on experimentally. The need of modelling is compulsory. The last part of the chapter tackles this topic. The results shows that in the case of the VSR700 and its actuators, there is not any instability risk.

The complexity of the problem, the time spent in searching for data (helicopter characteristics, flight measures), the unavailibility of skillful support jeopardized this rotor model development. This chapter offers a first milestone in the elaboration of a preliminary rotor load model. Such model represents an unvaluable tool in a context where helicopter data are missing to predesign PFCS actuators.

As a perspective, the suggested model of this chapter requires to take into account the advancing speed to consider a simple advancing flight phase. Additional time shall be spent to fit better the results to the flight test measures. Indeed, the assymetric load distribution among actuators is not explained yet. Finally, to take into account the aerodynamic load harmonics, an opportunity could be to take benefit from the CFD simulations performed during other helicopter developments.

Chapter 4

Actuator modelling for preliminary sizing

The purpose of this chapter is to provide the different types of models, necessary to select the components of an actuator as it is presented in section 1.5.6.

4.1 Modelling needs for sizing activities

The electromechanical actuator includes multidisciplinary components. Each of them has multiple and different key design drivers and operational scenarios. The selected components should comply with the actuator specification and ensure the minimization of the actuator total mass.

Therefore, this chapter answers this need of component selection. It develops a methodology providing the necessary knowledge regarding the actuator component modelling. This chapter is divided into two parts covering the two following levels [Hehenberger et al., 2010]:

1. The *component level* deals with the determination of component characteristics from a reduced number of parameters facilitating the optimization. The involved models are the *estimation models* (fig. 4.1).

2. The *system level* deals with interactions between components, operational scenarios and operational limits. The involved models are *simulation models* and *evaluation models* (fig. 4.1).

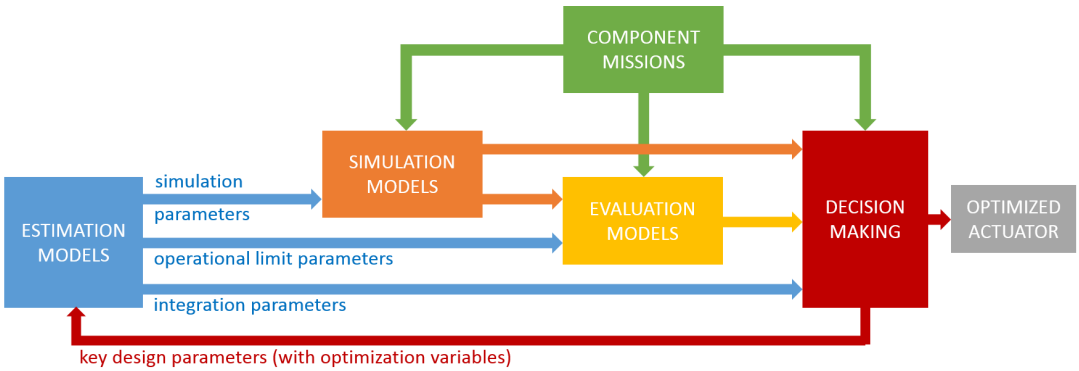

FIGURE 4.1: *Structure of a model-based preliminary design*

4.2 Estimation models

4.2.1 Need & approach

As shown in fig. 4.1, to start a first iteration in the sizing loop, the main characteristics of each component has to be identified from a reduced set of key parameters. The *estimation models* are introduced for this purpose. They directly link the primary characteristics, which define the component functionally, to secondary characteristics, which can be seen as the dimensions and features of imperfections (see part "a" of Fig. 4.2). Thus, the *estimation models* provide the necessary parameters for the integration study, *simulation models* and *evaluation models*.

Generally, at component level, the models link the physical dimensions and the characteristics of in use materials to the primary and secondary characteristics (see part "b" of Fig. 4.2). The design, at component level, is an inverse problem which requires the primary characteristics as inputs.

In such context of multidisciplinary problems with optimization, a unified modelling approach is required. The dimensional analysis and the Vaschy-Buckingham's theorem are good candidates for it [Van Groesen and Molenaar, 2007] [Holmes, 2019]. Indeed, they are extensively used in aerodynamics and fluid mechanics since they provide a more physical and unified framework with a reduced number of parameters. This section shows how they can be extended to other domains such as all the components of an EMA.

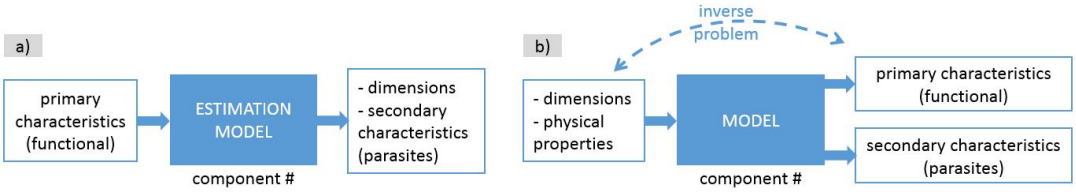

FIGURE 4.2: *Component modelling: a) for system level design b) for component level design [Budinger et al., 2012a]*

The development steps of an estimation model are presented in fig. 4.3. The starting point is the expression of one component characteristic y as an algebraic function f depending of geometrical dimensions and material/physical properties P_i. l is a length and d_i is an other dimensions.

$$y = f(\underbrace{l, d_1, d_2, ...}_{\text{dimensions}}, \underbrace{P_1, P_2, ...}_{\text{properties}}) \tag{4.1}$$

Then, applying the dimensional analysis and Vaschy-Buckingham's theorem (theorem 1), the problem is rewritten into a reduced number of dimensionless parameters [Sanchez et al., 2017].

Theorem 1 (Vaschy-Buckingham's theorem)**.** *Any physical equation dealing with n physical variables depending on k fundamental units (mass, length, time, temperature, charge) can be formulated as an equivalent equation with $q = n - k$ dimensionless variables named "π-numbers" built from the initial variables.*

$$\pi_y = g(\underbrace{\pi_{d_1}, \pi_{d_2}, ..., \pi_{P_1}, \pi_{P_2}, ...}_{q \text{ variables}}) \text{ with } \begin{cases} \pi_y = y^{c_y} \cdot l^{c_L} \cdot \prod_i P_i^{c_{P_i}} \\ \pi_{d_i} = \frac{d_i}{l} \\ \pi_{P_i} = l^{c_{P_i,0}} \cdot \prod_j P_i^{c_{P_i,j}} \end{cases} \tag{4.2}$$

It is clear that thanks to dimensional analysis and Buckingham theorem, the number of input parameters of the problem is reduced. The computational cost will be reduced in the same way.

The next step is to develop the estimation models based on the π-groups.

Scaling law formulations (section 4.2.2) are undertaken when π_{d_i} and π_{P_i} remain constant around a given component product range. This means that the geometrical and/or material similarities are checked. This is applicable for the mechanical and electrical components of the actuator as detailed in section 4.2.2.

In the case the dimensionless numbers π_{d_i} and π_{P_i} are not considered as constant, the approximation of the function g can be achieved by performing data regressions [Lacey and Steele, 2006] [Sanchez et al., 2017]. The data can come from manufacturer product data, test measurements or finite element simulation results based on a DoE as presented in section 4.2.4 for the housing vibratory sizing.

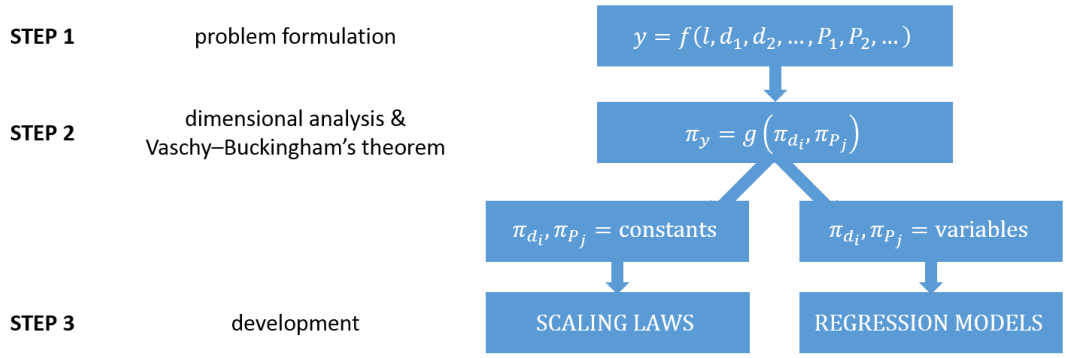

FIGURE 4.3: *Estimation model development steps*

4.2.2 Scaling laws

4.2.2.1 Fundamentals

In literature, scaling laws are also defined as *similarity laws* or *allometric models* [Budinger et al., 2012a]. They estimate the component main characteristics requested for their selection without requiring a detailed design.

Scaling laws are based on 3 hypothesis:

- Geometric similarity: all the dimensions of the considered component to all the lengths of the component used for reference are constant. Thus, all corresponding aspect ratios are constant: $\pi_{d_i} =$ constant.
- Uniqueness of design drivers: only one main dominant physical phenomenon drives the evolution of the component secondary characteristic y ('a' fig. 4.2). Thus, in most cases, there is not anymore dependency with any π_{P_i} (function g eq. 4.2).
- Material similarity: all material properties are assumed to be identical to those of the component used for reference. Thus, all corresponding scaling ratios are equal to 1: $\pi_{P_i} = 1$.

Once these assumptions are satisfied, π_y is stated to be constant since it depends on constant variables.

$$\pi_y = g(\pi_{d_1}, \pi_{d_2}, \dots, \pi_{P_1}, \pi_{P_2}, \dots) = \text{constant} \tag{4.3}$$

This gives the standard power law shape of a scaling law:

$$\pi_y = y^{c_y} \cdot l^{c_L} \cdot \prod_i P_i^{c_{P_i}} = \text{constant} \implies y \propto l^c \tag{4.4}$$

with c a constant. Then, as proposed by [Jufer, 1996], the 'star' notation is introduced. It indicates the scaling ratio of a desired component characteristic y by the same characteristic y_{ref} of a component taken as a reference: $y^* = y/y_{ref}$. This component of reference is picked up into the supplier range of the considered product.

Thus, eq. 4.4 becomes:

$$y^* = l^{*c} \iff \frac{y}{y_{ref}} = \left(\frac{l}{l_{ref}}\right)^c \tag{4.5}$$

From a single component of reference and a reduced number of parameters (no detailed design required), scaling laws extrapolate quickly the main characteristics y_{ref} of a known component towards the one y of a possible component of the same technology:

$$y = y_{ref} \cdot \left(\frac{l}{l_{ref}}\right)^c \tag{4.6}$$

Consequently, the scaling laws level down the complexity of the inversion problem ('b' part fig. 4.2). For an estimation model ('a' part fig. 4.2), it is easy then to express all the useful relations as a function of a single *key design parameter* (also named *definition parameter*) associated with its component (fig. 4.1).

Finally, there are other interests of using them:

- They are useful for the exploration study of a design domain: integration study (mass, dimensions), sizing, scenario analysis, optimization, and technology & architecture comparison.
- They replace the use of catalog data when unavailable.
- They are easy enough to exchange with suppliers and especially to challenge suppliers.

4.2.2.2 Building a scaling law

To illustrate section 4.2.2.1, the scaling law approach is applied herebelow on the case of an electrical brushless motor. The aim is to state the mass evolution of the motor.

The study is based on the following hypothesis: the main design driver is the maximum continuous winding temperature; the natural convection is the dominant thermal phenomenon; the average induction in the airgap is constant for a given magnet technology; the geometric similarities are verified, the number of poles is constant, the similarities in the material and the design limits are satisfied. In fig. 4.4, the scaling law expression describing the motor torque is developed following step by step the approach mentioned in section 4.2.2.1.

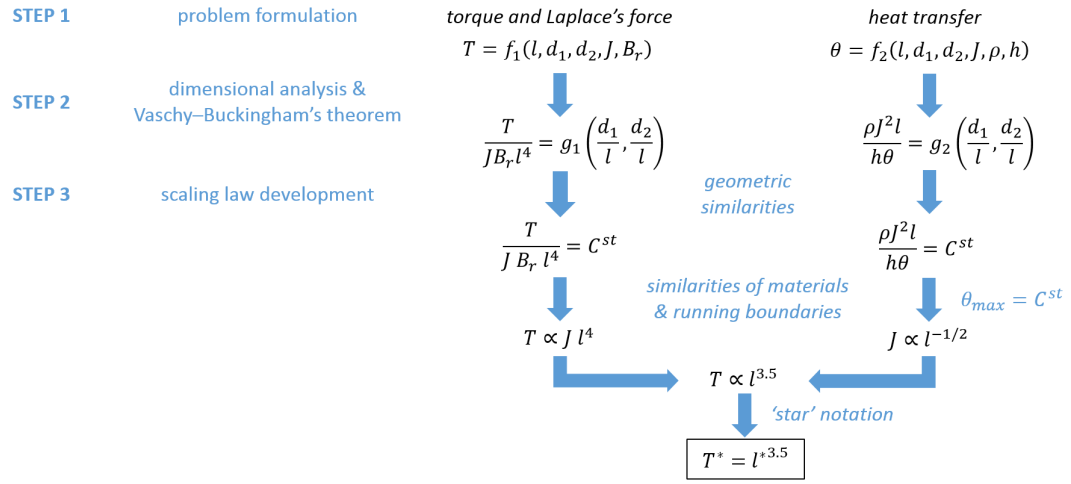

B_r	remanent induction of permanent magnets	$[T]$	θ	max admissible temperature rise for winding insulation	$[°C]$
d_i	other motor dimensions	$[m]$	h	convection heat exchange coef.	$[J \cdot K^{-1} \cdot m^{-2}]$
J	current density	$[A \cdot m^2]$	l	motor length	$[m]$
ρ	copper resistivity	$[ohm \cdot m]$	T	electromagnetic torque	$[N \cdot m]$

FIGURE 4.4: *Electrical motor torque formulation*

Supposing the diameters and lengths evolving similarly ($d^* = l^*$, fig. 4.5), the mass $\mathscr{M}$ of the motor is basically approximated by:

$$\mathscr{M} = \int \rho_{eq}\, dV \implies \mathscr{M}^* = l^{*3} \tag{4.7}$$

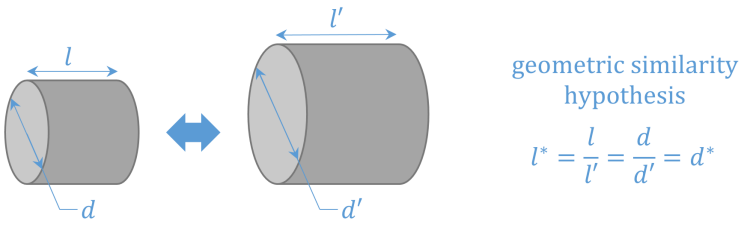

FIGURE 4.5: *Electrical motor: homothety hypothesis*

Using the torque expression (prerequisite of fig. 4.4), the motor mass $\mathscr{M}$ becomes:

$$\mathscr{M}^* = T^{*3/3.5} \implies \mathscr{M} = \mathscr{M}_{ref} \cdot \left(\frac{T}{T_{ref}}\right)^{3/3.5} \tag{4.8}$$

Fig. 4.6 compares the evolution of this law (eq. 4.8) to real data from two manufactured motors: Parvex NX [PARKER, 2022b] and Kollmorgen RBE [KOLLMORGEN, 2003]. It is observed that a single motor reference allows to rebuild the evolution of the motor mass for a broad range of torque. And this is possible with less than 10% of relative error.

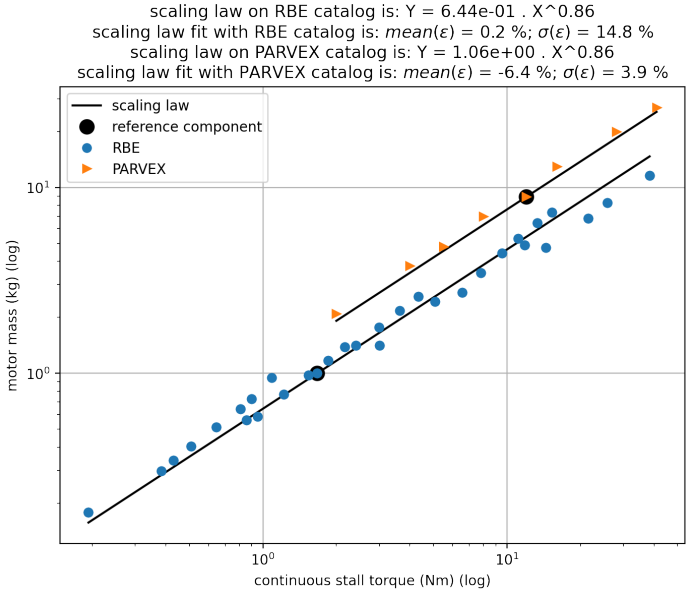

FIGURE 4.6: *Motor mass: scaling law prediction compared to manufacturer catalogs (Parvex NX, Kollmorgen RBE)*

4.2.2.3 Established laws

The tables 4.1 and 4.2 present per component all the established scaling laws. Each law prediction has been compared to supplier catalogues. The fitting quality is quantified using the mean of relative errors ϵ_r and the standard deviation of the relative errors σ_r.

The main hypothesis taken into account to establish these scaling laws are: a constant maximum stress, for mechanical components; a constant maximum temperature and a constant mean induction field in the airgap for the electrical components.

The laws presented in the tables 4.1 and 4.2 are derived in detail in Appendix J (for mechanical components), Appendix K (for electrical components) and in section 4.2.3 (electrical & mechanical components). Each component derivation is followed by a validation based on graphs comparing supplier catalog data and their regressions with scaling law predictions.

Some other applicative cases of scaling laws (construction, validation) can be found in [Budinger et al., 2012a], [Budinger et al., 2012b] and [Budinger et al., 2013].

4.2.2.3.1 Mechanical components

Component characteristics	Units	Scaling law expressions		ϵ_r	σ_r	
ROD END (RE), spherical bearing						
Key design parameter						
max static load	N	$C_0 = d^{*2}$		-	-	
Integration parameters						
dimensions	m	$l^* = d^* = C_0^{*1/2}$		4%	6%	
mass	kg	$\mathscr{M}^* = d^{*3} = C_0^{*3/2}$		19%	26%	(1)
Operational limit parameter						
max dynamic load	N	$C_d^* = d^{*2} = C_0^*$		16%	23%	
Error estimations done using SKF catalog range ($C_0 \in [8.15; 585]$ kN, 44 components) and component of reference of $C_0 = 42.5$ kN						
(1) impact of standardization						
BALL BEARING (BB)						
Key design parameter						
max static load	N	$C_0 = d^{*2}$		-	-	
Integration parameters						
dimensions	m	$l^* = d^* = C_0^{*1/2}$	BB1	0.2%	2.5%	
			BB2	4.4%	10%	
mass	kg	$\mathscr{M}^* = d^{*3} = C_0^{*3/2}$	BB1	8.8%	17%	
			BB2	15%	39%	(1)
Operational limit parameters						
max dynamic load ($d_{ball} \leq 25.4$ mm)	N	$C_d^* = d^{*1.8} = C_0^{*1.8/2}$	BB1	0.2%	7.6%	
			BB2	6.3%	21%	
number of balls	$-$	$n_{ball}^* = 1$	BB1	0%	0%	
			BB2	0%	0%	
max speed (mechanical limit)	$rad \cdot s^{-1}$ or RPM	$\omega_{max,mechanical}^* = d^{*-1} = C_0^{*-1/2}$	BB1	2.1%	5.8%	
			BB2	18%	45%	(2)
max speed (thermal limit)	$rad \cdot s^{-1}$ or RPM	$\omega_{max,thermal}^* = d^{*-1} = C_0^{*-1/2}$	BB1	1.1%	6.5%	
			BB2	11%	19%	
Error estimations done using SKF catalog:						
BB1: double row angular contact ball bearing (range: $C_0 \in [4.3; 140]$ kN, 30 components, component of reference: $C_0 = 28$ kN)						
BB2: deep grooved single row ball bearing (range: $C_0 \in [0.18; 430]$ kN, 377 components, component of reference: $C_0 = 8.3$ kN)						
(1) two sets of product with different design concepts ; (2) sets of product to distinguish						
SCREW MECHANISM (SM), standard PRS						
Key design parameters						
max static load	N	C_0		-	-	
stroke	m	s		-	-	
lead	$m \cdot rad^{-1}$	p		-	-	
Integration parameters						
nut diameter (in, out)	m	$d_n^* = C_0^{*0.37} \cdot p^{*1/6}$		4.6%	8.8%	
nut length	m	$l_n^* = C_0^{*0.37}$		1.8%	7.7%	
nut mass	kg	$\mathscr{M}_n^* = d_n^{*2} \cdot l_n^* = C_0^{*1.11} \cdot p^{*1/3}$		7.5%	23%	
nut flange dimensions	m	$l_f^* = d_f^* = C_0^{*0.37}$		1%	7%	
screw diameter	m	$d_s^* = C_0^{*1/2}$		1.9%	10%	
screw length	m	$l_s = l_{n,ref} \cdot (C_0/C_{0,ref})^{0.37} + s$				
screw mass	$kg \cdot m^{-1}$	$\mathscr{M}_s^* = d_s^{*2} = C_0^*$		2.7%	20%	
roller number	$-$	$n_{roller}^* = 1$		-%	-%	(1)
Simulation parameter						
inertia (screw)	$kg \cdot m$	$\mathscr{J}_s^* = d_s^{*4} = C_0^{*2}$		1.6%	39%	(2)
Operational limit parameter						
max dynamic load	N	$C_d^* = C_0^{*0.74} \cdot p^{*1/3}$		7.1%	11%	
Error estimations done using SKF & ROLLVIS catalog ranges ($C_0 \in [8.4; 4320]$ kN, 60 & 201 components), and the components of reference ($C_0 = 294$ kN and $C_0 = 334$ kN)						
(1) hypothesis (see section 4.2.3.1)						
(2) propagation of error due to high law exponent, reducing the exploration domain (C_0 range) improves the prediction quality						

TABLE 4.1: *Scaling law recap and prediction quality on catalog data for mechanical components*

In Appendix L, a study onto the Hertz contact has been carried out to extract potentially interesting scaling laws around roller, ball and thread contacts. It is always useful to keep in mind such laws, especially for stress - load transfers.

Component characteristics	Units	Scaling law expressions	ϵ_r	σ_r	
ELECTRICAL MOTOR (EM), brushless, cylindrical					
Key design parameters					
continuous torque	Nm	$T^* = d^{*3.5} = K_m^{*3.5/5}$	-	-	
motor constant	$(Nm)^2/W$	$K_m^* = d^{*5} = T^{*5/3.5}$	-	-	
Integration parameters					
dimensions ($l^* = d^*$)	m	$d^* = T^{*1/3.5} = K_m^{*1/5}$	0.0%	8.5%	(1)
mass	kg	$\mathscr{M}^* = d^{*3} = T^{*3/3.5} = K_m^{*3/5}$	8.8%	9.9%	(1)
Simulation parameters					
inertia	$kg \cdot m^2$	$\mathscr{J}^* = d^{*5} = T^{*5/3.5} = K_m^*$	0.1%	21%	(1)
copper coef.	$W/(Nm)^2$	$\alpha^* = d^{*-5} = T^{*-5/3.5} = K_m^{*-1}$	5.0%	18%	(1)
Joules' losses	W	$\mathscr{P}_J^* = d^{*2} = T^{*2/3.5} = K_m^{*2/5}$	5.0%	18%	(1)
iron loss coef.	$W/(rad/s)^{1.5}$	$\beta^* = d^{*3} = T^{*3/3.5} = K_m^{*3/5}$	2.8%	24%	(1)
resistance	$\Omega/(Nm/A)^2$	$\mathscr{R}^*/\mathscr{K}_t^{*2} = d^{*-5} = T^{*-5/3.5} = K_m^{*-1}$	18%	13%	(1)
inductance	$H/(Nm/A)^2$	$\mathscr{L}^*/\mathscr{K}_t^{*2} = d^{*-3} = T^{*-3/3.5} = K_m^{*-3/5}$	2.0%	21%	(1)
number of pole pair	-	$n_{poles}^* = 1$	0%	0%	(1,4)
Operational limit parameters					
peak torque	Nm	$T_p^* = d^{*3.5} = T^* = K_m^{3.5/5}$	0.4%	2.5%	(1,2)
		$T_{p,mag}^* = d^{*3} = T^{*3/3.5} = K_m^{*3/5}$	-%	-%	(3)
		$T_{p,th}^* = d^{*4} = T^{*4/3.5} = K_m^{*4/5}$	13%	6.5%	(4,5)
max speed (mechanical limits)	RPM	$\Omega_{max}^* = d^{*-1} = T^{*-1/3.5} = K_m^{*-1/5}$	1.6%	4.5%	(4)
Error estimations done using PARVEX NK & KOLLMORGEN RBE catalogue ranges ($T \in [0.5; 41]$ Nm, 9 & 32 components)					
(1) validation on Parvex; (2) Parvex specificity; (3) definition based on a magnetic saturation criteria (see section 4.2.3.2), missing data for validation; (4) validation on Kollmorgen; (5) definition based on a thermal criteria (see section 4.2.3.2)					
ELECTROMAGNETIC BRAKE (EMB)					
Key design parameter					
static torque	Nm	T_s	-	-	
Integration parameters					
dimensions	m	$d^* = T_s^{*1/4}$	5%	9%	
mass	kg	$\mathscr{M}^* = d^{*3} = T_s^{*3/4}$	11%	26%	
Simulation parameters					
disk inertia	$kg.m^2$	$\mathscr{J}^* = d^{*5} = T_s^{*5/4}$	21%	60%	(1)
resistance	Ω	$\mathscr{R}^* = \mathscr{U}^{*2} \cdot d^{*-2} = \mathscr{U}^{*2} \cdot T_s^{*-2/4}$	16%	30%	
Joules' losses	W	$\mathscr{P}_J^* = d^{*2} = T_s^{*2/4}$	4%	64%	(1)
Error estimations done using RS, KENDRION, MIKIPULLEY catalog ranges ($T_s \in [0.113; 130]$ Nm, total of 14 components) and component of reference of $T_s = 4$ Nm					
(1) important error propagation since high law exponent, limited extrapolation capabilities, reference component to choose accordingly, low consequence on final actuator sizing.					

TABLE 4.2: *Scaling law recap and prediction quality on catalog data for electrical components*

4.2.2.3.2 Electromagnetic components Parvex is a motor serie following the geometrical similarities ($l^* = d^*$). The laws describing this motor type are presented in table 4.2. The cylindrical motor type is chosen as the component of reference for this thesis. Kollmorgen RBE is a motor serie not following the geometrical hypothesis ($l^* \neq d^*$). This motor type involves some scaling laws different from the one presented in table 4.2, they are presented in Appendix K.

4.2.2.3.3 Further components Beyond the scope of this thesis, another direct-drive actuator architecture may be of the utmost relevance. The involved components would be the inverted PRS and the annular *Brushless Direct Current (BLDC)* motor.

Component characteristics	Units	Scaling law expressions	ϵ_r	σ_r	
SCREW MECHANISM (SM), inverted PRS					
Key design parameter					
max static load	N	C_0	-	-	
stroke	m	s	-	-	
lead	$m \cdot rad^{-1}$	p	-	-	
Integration parameters					
nut diameter	m	$d^*_{nut} = C^{*1/2}_0$	0.1%	4.1%	
roller set length	m	$l^*_{rs} = C^{*0.37}_0$	0.5%	3.1%	
nut length	m	$l_{nut} = l_{rs,ref} \cdot (C_0/C_{0,ref})^{0.37} + s$			
nut mass	kg/m	$\mathscr{M}^*_n = d^{*2}_{nut} = C^*_0$	-%	-%	(1)
screw diameter	m	$d^*_s = C^{*1/2}_0$	0.1%	4.1%	
screw mass	$kg \cdot m^{-1}$	$\mathscr{M}^*_s = d^{*2}_s = C^*_0$	-%	-%	(1)
Simulation parameters					
inertia (nut)	$kg \cdot m$	$\mathscr{J}^*_s = d^{*4}_s = C^{*2}_0$	-%	-%	(1)
Operational limit parameters					
max dynamic load	N	$C^*_d = C^{*0.74}_0 \cdot p^{*1/3}$	3.7%	9.2%	

Error estimations done using SKF & ROLLVIS catalog ranges ($C_0 \in [21;1226]$ kN, 30 & 110 components), and components of reference of $C_0 = 194$ kN and $C_0 = 214$ kN
(1) *missing data*

TABLE 4.3: *Scaling law recap and prediction quality on catalog data for inverted PRS*

Component characteristics	Units	Scaling law expressions	ϵ_r	σ_r	
ELECTRICAL MOTOR (EM), brushless, annular					
Key design parameters					
continuous torque	Nm/m	$T^*/l^* = d^{*2} = K^{*2/3}_m \cdot l^{*-2/3}$	-	-	
motor constant	$(Nm)^2/W$	$K^*_m = d^{*3} \cdot l^*$	-	-	
Integration parameters					
dimensions ($d^* \neq l^*$)	m	$d^* = (T^* \cdot l^{*-1})^{1/2} = K^{*1/3}_m \cdot l^{*-1/3}$	1%	14%	(1)
mass	kg/m	$\mathscr{M}^*/l^* = d^* = (T^*/l^*)^{1/2} = K^{*1/3}_m \cdot l^{*-1/3}$	9%	12%	
Simulation parameters					
inertia	$kg \cdot m^2/m$	$\mathscr{J}^*/l^* = d^{*4} = T^{*2} \cdot l^{*-2} = K^{*4/3}_m \cdot l^{*-4/3}$	21%	39%	(2)
copper coef.	$W/(Nm)^2$	$\alpha^* = d^{*-3} \cdot l^{*-1} = T^{*-3/2} \cdot l^{*-5/2} = K^{*-1}_m$	14%	45%	(2)
Joules' losses	W	$\mathscr{P}^*_J = d^* \cdot l^* = T^{*1/2} \cdot l^{*1/2} = K^{*1/3}_m \cdot l^{*2/3}$	4.7%	15%	
iron loss coef.	$W/(rad/s)^{1.5}$	$\beta^* = d^{*2} \cdot l^* = T^* = K^{*2/3}_m \cdot l^{*5/3}$	-%	-%	(3)
resistance	$\Omega/(Nm/A)^2$	$\mathscr{R}^*/\mathscr{K}^{*2}_t = d^{*-3} \cdot l^{*-1} = T^{*-3/2} \cdot l^{*1/2} = K^{*-1}_m$	15%	30%	(2)
inductance	$H/(Nm/A)^2$	$\mathscr{L}^*/\mathscr{K}^{*2}_t = d^{*-3} \cdot l^{*-1} = T^{*-3/2} \cdot l^{*1/2} = K^{*-1}_m$	1%	8.6%	
number of pole pair	-	$n^*_{poles} = d^*$	1.0%	3.7%	
Operational limit parameters					
peak torque	Nm	$T^*_p = T^*$	16%	7.8%	
max speed (mechanical limits)	RPM	$\Omega^*_{max} = d^{*-1/2} = T^{*-1/4} \cdot l^{*1/4} = K^{*-1/6}_m \cdot l^{*1/6}$	-%	-%	(3)

Error estimations done using TECNOTION catalogue range ($T \in [0.29;100]$ Nm, 14 components) and component of reference of $T = 3.2$ Nm
(1) *regression tends to* $d^* = (T^* \cdot l^{*-1})^{0.3}$; (2) *propagation of error due to high law exponent and introduction of* l^* *(additional error source);*
(3) *missing data*

TABLE 4.4: *Scaling law recap and prediction quality on catalog data for annular motors*

4.2.3 Special focus

Further to scaling law derivation, checks and validation performed for the previous section, this section offers to focus onto some added values.

The first part deals with the introduction of the lead into roller screw scaling laws.

The second part explains the different definitions of the motor peak torque. This highlights the need to have a universal parameter as the motor constant K_m.

The third part introduces the motor constant K_m and the role it can play into motor selection.

A last part would be for the electromagnetic brake since it is a key component to comply with actuator safety criteria. The formulation of its laws and the validation with different manufacturer catalog represents an added value to [Budinger et al., 2013]. In brief, this part has been integrated in Appendix K.

4.2.3.1 Screw mechanism: fatigue load & nut dimensions

The screw mechanism is a key component in the actuation system. The technology of interest is the PRS (fig. 4.7). This section is dedicated to study its dynamic load capabilities and its nut dimensions. New scaling laws are formulated. This brings an added value to what is already established in [Budinger et al., 2013]. Standard and inverted PRS are studied in parallel. Appendix J.3 completes this study.

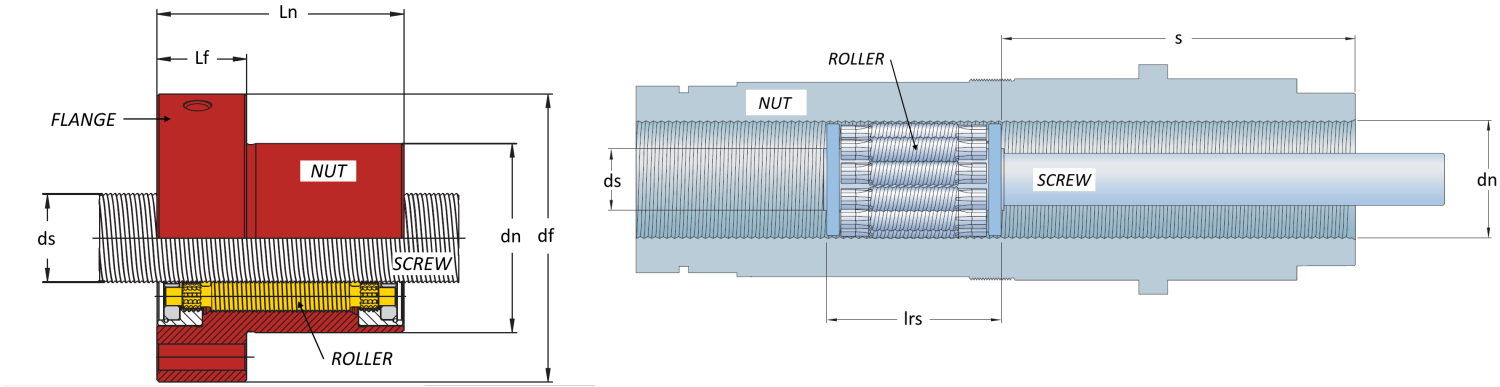

FIGURE 4.7: *PRS section view with dimensions: (**left**) standard PRS from [ROLLVIS, 2019], (**right**) inverted PRS from [SKF, 2014]*

4.2.3.1.1 Dynamic load Similarly to bearings, a screw mechanism has a limited lifespan depending of running conditions. As far as the running conditions consider protections, lubrication and maintenance, the main origin of mechanism failures is the material fatigue. This is generated by the repeated loading from the rolling elements. Therefore, the number of screw revolution realized before any crack initiation relies on the load withstood by the mechanism. The nominal dynamic load C_d $[N]$ is defined such that 90% of screw mechanisms reach or exceed 10^6 revolutions under this load.

According to [Budinger et al., 2013], the roller screw dynamic load evolves with:

$$C_d^* = C_0^{*1.8/2} \tag{4.9}$$

This law comes from the standard ISO 3408 [AFNOR, 2006]. For a ball screw technology, this standard provides the estimation of the dynamic axial load based on a rolling element apparent diameter, the thread characteristics, shape factors and coefficients linked to materials and surface treatments. When considering geometrical similarities

($d_i^* = l_i^*$), the evolution of the dynamic load can be expressed as: $C_d^* = d^{*1.8}$ with d a dimension characterizing the screw mechanism (i.e. the screw diameter). As any mechanical components, the roller screw mechanism sizing is based on a constant maximum mechanical stress σ_{max}. This is induced by the maximum static load C_0 $[N]$. As a result, the evolution of the dimensions evolves according to:

$$\sigma_{max}^* = 1 \implies d^* = C_0^{*1/2} \tag{4.10}$$

This leads to eq. 4.9.

When displaying C_d with respect to C_0 using supplier catalog [SKF, 2014] & [ROLLVIS, 2019], the data cloud is widely spread. The prediction of the scaling law (eq. 4.9) results in important relative errors (as much on the mean value than on the deviation value).

To improve the dispersion of the data cloud and improve the prediction of C_d^*, we suggest to reformulate the law taking basis on fatigue law fundamentals. From Palmgren Miner's damage law, a constant ratio can be stated (eq. 4.11).

$$\sum \sigma_i^3 \cdot N_i = k_1 \implies \left(\frac{C_d}{S}\right)^3 \cdot N_{10} = k_2 \implies \frac{C_d^*}{d^{*2} \cdot p^{*1/3}} = 1 \tag{4.11}$$

where k_i are constants, σ_i are the stress withstood during N_i revolutions, p the lead, C_d is the dynamic load defined for the standardized revolution number $N_{10} = 10^6$. The number of revolution evolves according to the inverse of the lead: $N_{10} = L_{10}/p$.

The correlation matrix is an efficient tool to point out the dependencies between the variables of a dataset. The correlation study is performed on the logarithm of the different characteristics available in the supplier catalogs [SKF, 2014] [ROLLVIS, 2019]. The correlation matrix is shown in fig. 4.8. This highlights that the static load C_0 and the fatigue load C_d are the most correlated variables with screw and nut dimensions.

	lead_mm	Cd_kN	C0_kN	eta_d	eta_i	ds_mm	dn_mm	Ln_mm	df_mm	Lf_mm	Ms_kgbym	Tmax_Nm	Tdyn_Nm
lead_mm	1.000000	0.679022	0.640837	0.250420	0.237821	0.643263	0.626430	0.541672	0.594478	0.561875	0.643263	0.880302	0.904072
Cd_kN	0.679022	1.000000	0.991462	0.047069	0.040662	0.987708	0.989373	0.969053	0.981507	0.958730	0.987708	0.941542	0.927632
C0_kN	0.640837	0.991462	1.000000	-0.006077	-0.009509	0.986433	0.995588	0.981232	0.990523	0.965449	0.986433	0.928326	0.903234
eta_d	0.250420	0.047069	-0.006077	1.000000	0.986988	-0.005234	-0.002481	0.016651	-0.006218	0.006865	-0.005234	0.117516	0.154807
eta_i	0.237821	0.040662	-0.009509	0.986988	1.000000	-0.011606	-0.005839	0.014969	-0.007333	0.009919	-0.011606	0.109294	0.144668
ds_mm	0.643263	0.987708	0.986433	-0.005234	-0.011606	1.000000	0.990580	0.957666	0.978600	0.953884	1.000000	0.921117	0.902284
dn_mm	0.626430	0.989373	0.995588	-0.002481	-0.005839	0.990580	1.000000	0.983370	0.994436	0.969062	0.990580	0.918623	0.894689
Ln_mm	0.541672	0.969053	0.981232	0.016651	0.014969	0.957666	0.983370	1.000000	0.985883	0.964610	0.957666	0.868705	0.839737
df_mm	0.594478	0.981507	0.990523	-0.006218	-0.007333	0.978600	0.994436	0.985883	1.000000	0.977054	0.978600	0.907457	0.881284
Lf_mm	0.561875	0.958730	0.965449	0.006865	0.009919	0.953884	0.969062	0.964610	0.977054	1.000000	0.953884	0.876143	0.851409
Ms_kgbym	0.643263	0.987708	0.986433	-0.005234	-0.011606	1.000000	0.990580	0.957666	0.978600	0.953884	1.000000	0.921117	0.902284
Tmax_Nm	0.880302	0.941542	0.928326	0.117516	0.109294	0.921117	0.918623	0.868705	0.907457	0.876143	0.921117	1.000000	0.996005
Tdyn_Nm	0.904072	0.927632	0.903234	0.154807	0.144668	0.902284	0.894689	0.839737	0.881284	0.851409	0.902284	0.996005	1.000000

FIGURE 4.8: *Correlation matrix of the standard PRS from ROLLVIS & SKF catalogs*

The ratio from eq. 4.11 can be expressed according to a dimension d^*, closely linked to the static load C_0^* such as:

$$\frac{C_d^*}{p^{*1/3}} = d^{*2} = C_0^{*E} \implies C_d^* = C_0^{*E} \cdot p^{*1/3} \tag{4.12}$$

The unknown power E is estimated by regression with the data provided by two supplier catalogs on two product ranges. Table 4.5 presents it.

supplier	roller screw type	value of E $[-]$
SKF (SRC/BRC serie, [SKF, 2014])	standard	0.73
	inverted	0.82
ROLLVIS ([ROLLVIS, 2019])	standard	0.72
	inverted	0.69
	MEAN value	0.74

TABLE 4.5: *Regression on supplier catalogs to determine the value of E*

The value of the coefficient E is retained to be 0.74. As a result, the scaling law giving the dynamic load is expressed by:

$$C_d^* = C_0^{*0.74} \cdot p^{*1/3} \tag{4.13}$$

Fig. 4.9 compares 4 component ranges from 2 suppliers with the new scaling law prediction (eq. 4.13). Now, the supplier data set follows a linear trend. The average and deviation of the relative error are far below 20%. The law is validated.

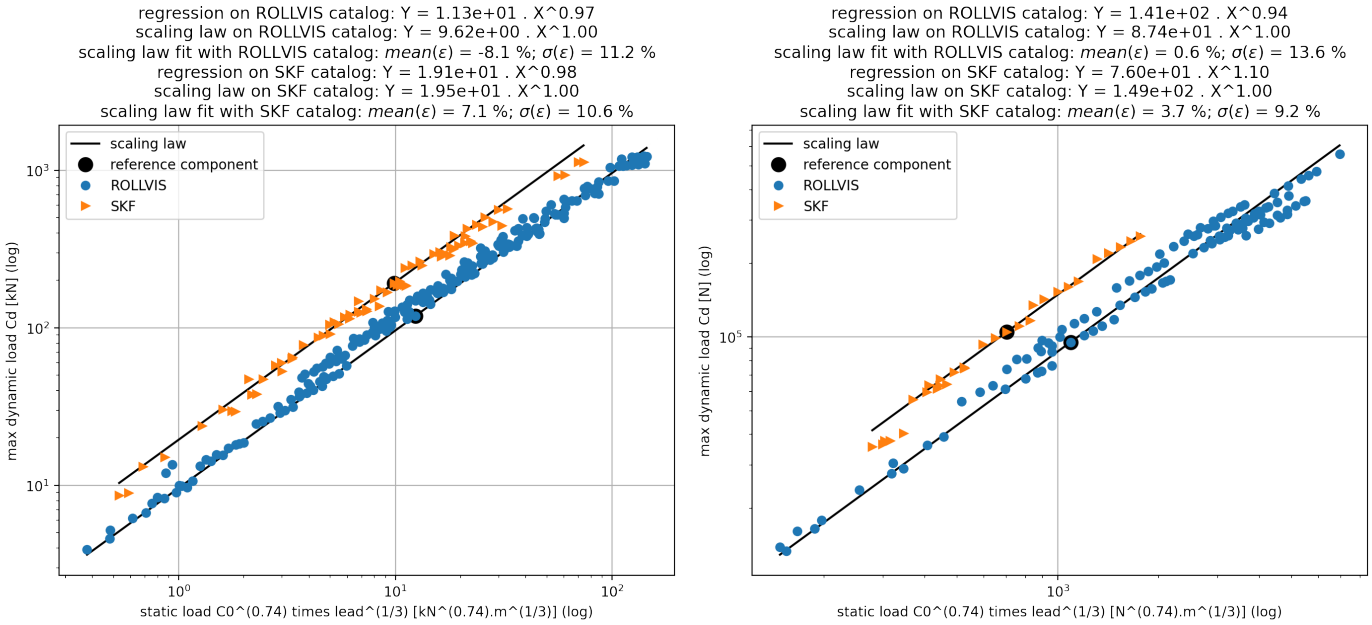

FIGURE 4.9: *Scaling law validation, PRS, dynamic load capability Cd with respect to* $C_0^{0.74} \cdot lead^{1/3}$ *and scaling law prediction (eq. 4.13), data from [SKF, 2014] and [ROLLVIS, 2019]: (**left**) standard roller screw, (**right**) inverted roller screw*

This new formulation of the dynamic load (eq. 4.13) involves the introduction of a new parameter: the lead. The shorter is the lead, the smaller is the dynamic load capability. Eq. 4.13 brings an added value in terms of sizing. The actuator component selection will penalize the solutions with a small lead.

4.2.3.1.2 Dimensions In [Budinger et al., 2013] and for the standard roller screw, the nut and screw dimensions are defined based on a constant Hertz stress level and a maximum static load C_0 such as:

$$\sigma_{Hertz,max}^* = 1 \implies \frac{F_{max}^{*1/3}}{d^{*2/3}} = 1 \implies d^* = C_0^{*1/2} \tag{4.14}$$

where d^* is a dimension. The Hertz contact scaling laws are detailed in Appendix L.

The scaling law defined in eq. 4.14 is verified on several parameters: – the screw diameter for both standard and inverted PRS (Appendix J.3), – the screw linear mass of standard PRS (Appendix J.3, nut linear mass data are missing on inverted PRS) – the nut diameter of the inverted PRS (fig. 4.11, *right*).

The diameter, the length and the mass of the standard PRS nut catch the attention. Through a regression on the supplier data, we observed that eq. 4.14 requires to be reformulated to describe better the nut characteristics.

The relation developed in eq. 4.12 (left side) suggests that the dimensions (diameters, lengths) evolve according to:

$$l_n^* = C_0^{*0.37} \tag{4.15}$$

Fig. 4.10 shows that this scaling law describes, with a good prediction level, the nut length of the standard PRSs and the roller set length of the inverted PRSs. In addition, this scaling law similarly describes the length and the diameter of the nut flange (see validation in fig. J.20 of the Appendix J.3). The nut flange is the part protruding from the outer nut diameter and welcoming fasteners.

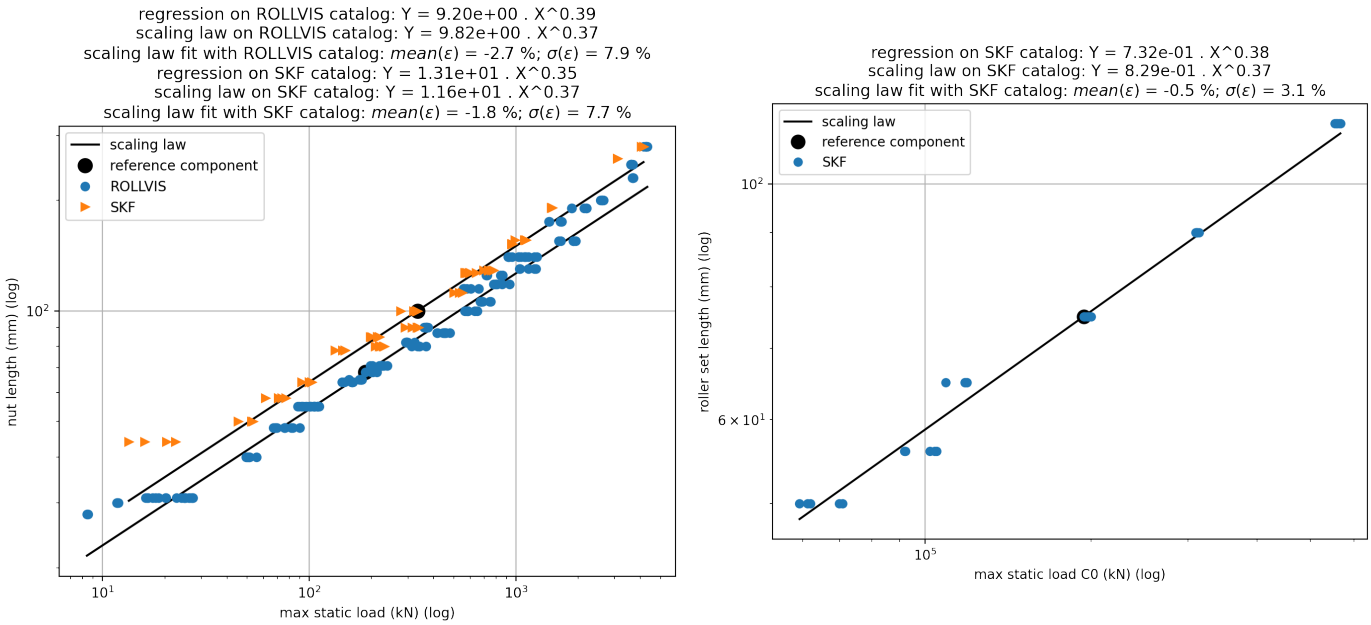

FIGURE 4.10: *Scaling law validation, PRS, nut length L with respect to static load C_0, scaling law prediction (eq. 4.15; (**left**) standard roller screw, (**right**) inverted roller screw; data from [SKF, 2014] and [ROLLVIS, 2019]*

As far as the diameter of the standard PRS nut is concerned, we observed that the scaling law deserves to be reformulated. Going through data displays, it seems that the nut is sized regarding a different design criteria from the one guiding the screw. We suggest that this criteria is the Hertz stress involved by the fatigue load C_d instead of the one involved by the static load C_0. Supposing a constant Hertz stress level throughout a given product range, the following scaling law is worked out:

$$\sigma^*_{Hertz,fatigue} = 1 \implies \frac{F^{*1/3}_{fatigue}}{d^{*2/3}} = 1 \implies d^* = C_d^{*1/2} \tag{4.16}$$

This new scaling law can be combined with a previous formulation from eq. 4.13 to give:

$$d_n^* = C_0^{*0.37} \cdot p^{*1/6} \tag{4.17}$$

This statement can be understood in a way that the nut of a standard roller screw suffers more from the roller passing than the screw does. Indeed, the threaded part of the screw is longer than the one of the nut. The screw thread experiences fatigue cycles spread all along its length if the application uses the entire stroke.

The inner and outer diameters of the standard PRS nuts verify the scaling law given in eq. 4.17 (see validation in fig. 4.11 (*left*), fig. J.21 (*left*) of Appendix J.3). In contrast, the inner and outer diameters of the inverted PRS nuts follow the same design criteria than the standard PRS screws, i.e. eq. 4.10. This is validated in fig. 4.11 (*right*) and fig. J.21 (*right*) of Appendix J.3.

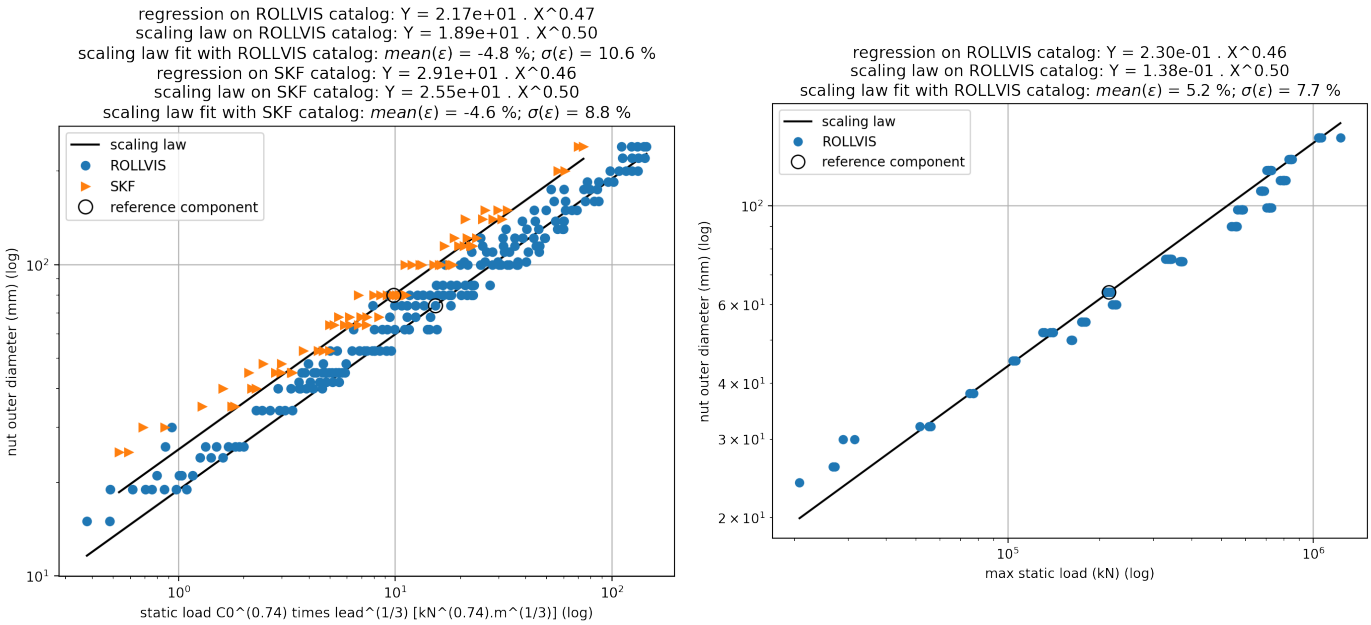

FIGURE 4.11: *Scaling law validation, PRS, nut outer diameter d with respect to: (**left**) $C_0^{0.74} \cdot lead^{1/3}$ for standard roller screw, (**right**) C_0 for inverted roller screw; scaling law prediction (eq. 4.14 and 4.17); data from [SKF, 2014] and [ROLLVIS, 2019]*

Finally, the nut mass must be determined. It is supposed to follow geometrical similarities ($d_{in}^* = d_{out}^*$). This hypothesis is checked on [SKF, 2014] & [ROLLVIS, 2019]. The nut mass scaling law is defined by the volume of a ring with a given density ρ_{nut} such as:

$$\mathscr{M}_{nut} = \rho_{nut} \cdot \pi \left[\left(\frac{d_{out}}{2} \right)^2 - \left(\frac{d_{in}}{2} \right)^2 \right] \cdot l \tag{4.18}$$

The dimensions d^* and l^* are substituted by their respective formulation from eq. 4.17 & 4.15:

$$\mathscr{M}_{nut}^* = d^{*2} \cdot l^* = C_0^{*1.11} \cdot l^{*1/3} \tag{4.19}$$

Due to missing data in Rollvis catalog, the mass of the nut can only be checked on SKF supplier. Fig. 4.12 compares the scaling law prediction (eq. 4.19) with SKF standard roller screw catalog (SRC/BRC serie, [SKF, 2014]). The regression performed on these data shows that the scaling law describes correctly the evolution of the nut mass. As expected, the high power of the scaling law generates dispersion in data. The prediction level remains satisfying. The scaling law tends to underestimate the

mass of small roller screws. This has to be kept in mind. The choice of the component of reference can be ajusted accordingly too.

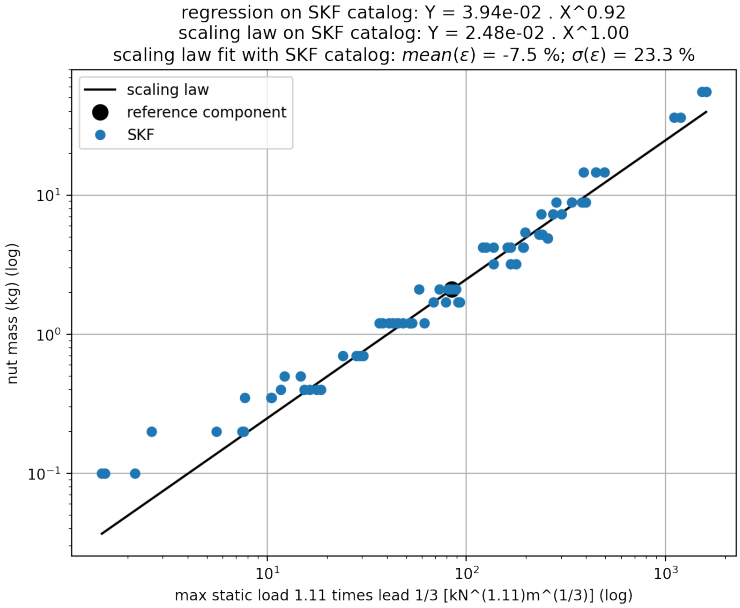

FIGURE 4.12: *Scaling law validation, standard PRS, dynamic load vs static load & pitch (SKF)*

4.2.3.1.3 Rollers Data regarding the roller characteristics are missing in the supplier catalogs [SKF, 2014] [ROLLVIS, 2019]. The roller-screws are not subject to any standard and the product ranges are created so as to allow a maximum reuse of subcomponents (roller, screw, nut).

In addition, the geometrical similarity hypothesis is followed by the screw and the nut of the inverted PRSs ($d^*_{nut} = d^*_{screw}$). This is checked on supplier catalogs. The evolution of the number of rollers can be assumed to be invariable. However, regarding the standard PRSs, we have just shown that the screw and the nut dimensions were not following the same power law.

As first approximation, we could estimate the roller diameters d_r $[m]$ using the scaling laws of the other dimensions i.e. the nut inner diameter and the screw diameter such as:

$$d_r = 0.5 \cdot \left(d_{in,nut} - d_s\right) \tag{4.20}$$

Thus, the number of roller could be defined by the number of roller diameters fitting into the perimeter drawn by the mean diameter of the roller-screw mechanism such as:

$$n_{roller} = \frac{\pi \cdot d_{mean}}{d_{roller}} \qquad d_{mean} = 0.5 \cdot \left(d_{in,nut} + d_s\right) \tag{4.21}$$

In practice, due to the accumulation of scaling law uncertainties, this geometrical estimations (eq. 4.20 and 4.21) does not lead to realistic roller numbers for some parts of a catalog product range.

Furthermore, in an ancient catalog version from [SKF, 2005], roller number intervals are mentioned for each product. A roller number interval $[9, 11]$ globally fits the full product range (screw diameters within $[8, 210]$ mm). Consequently, we suggest

that the evolution of the number of rollers is invariable:

$$n^*_{roller} = 1 \tag{4.22}$$

The number of rollers is only used for estimating the fatigue capability of the PRS (section 4.3.1.3). For a first actuator sizing, the choice of a component of reference with $n_{roller} = 10$ is a relevant choice.

4.2.3.2 Different max torque definitions

4.2.3.2.1 Introduction The maximum torque has got different definitions depending on manufacturer choices:

- **CASE 1:** The manufacturer defines it as the torque leading to magnetic circuit saturation (e.g. [KOLLMORGEN, 2003]'s catalog defines a maximum torque for which Kt will be greater than 90% of Kt at low torque)
- **CASE 2:** The manufacturer defines it as the torque leading to a given temperature increase $\Delta\Theta$ [°C] or a given maximum current density over a period of time Δt [s] (e.g. [KOLLMORGEN, 2003]'s catalog defines 10 seconds maximum)

We propose to study each case with a scaling law approach. For cylindrical and annular motors, a current density is defined. These definitions are used to develop a specific expression of the motor maximum torque.

4.2.3.2.2 Law formulations CASE 1:
In the case of a solenoid, the theorem of Ampere states for free space that:

$$\oint_{\mathscr{C}} \vec{B}(M) \cdot d\vec{l} = \mu_0 \cdot \sum I_{embraced,i} = \mu_0 \cdot \iint_S \vec{j}(P) \cdot \vec{n}\, dS = \mu_0 \cdot n_{turn} \cdot I \tag{4.23}$$

with $\vec{B}(M)$ the induction magnetic field ($[T]$ or $[kg \cdot s^{-2} \cdot A^{-1}]$) at a point M of a contour $\mathscr{C}$, μ_0 the magnetic constant (or vacuum permeability) $\mu_0 = 4.10^{-7}\ H \cdot m^{-1}$, $\vec{J}(P)$ the embraced current flux $[A.m^{-2}]$ through point P of the surface S surrounded by $\mathscr{C}$, $\vec{n}$ the unitary normal vector of the surface at this point, n_{turn} the number of solenoid turns, and I $[A]$ the intensity of a single wire.

- For cylindrical motors:

- On one hand, if the geometrical similarity is supposed ($d^* = l^*$), the eq. 4.23 becomes:

$$B^*_{max} \cdot d^* = J^*_{max} \cdot d^{*2} \implies J^*_{max} = d^{*-1} \tag{4.24}$$

The relations linking the torque, the current density and the dimension are defined such as:

$$T^* = J^* \cdot d^{*4} \quad ; \quad d^* = T^{*1/3.5}_{cont} \tag{4.25}$$

where T_{cont} $[Nm]$ is the continuous torque stated on a thermal criteria in a speed steady state. These relations are derived in Appendix K (eq. K.15, eq. K.16).

The corresponding maximum torque is then defined as:

$$\boxed{T^*_{max,mag} = d^{*3} = T^{*3/3.5}_{cont}} \tag{4.26}$$

In addition,

$$\frac{T^*_{max,mag}}{T^*_{cont}} = d^{*-0.5} \tag{4.27}$$

This ratio decreases along with the increase of motor size.

- On a second hand, if the geometrical similarity is not supposed ($d^* \neq l^*$), the eq. 4.23 becomes:

$$B^*_{max} \cdot d^* = J^*_{max} \cdot d^{*2} \implies J^*_{max} = d^{*-1} \tag{4.28}$$

The relations linking the torque, the current density and the dimension are defined such as:

$$T^* = J^* \cdot d^{*3} \cdot l^* \quad ; \quad d^* = \left(\frac{T^*_{cont}}{l^*}\right)^{1/2.5} \tag{4.29}$$

These relations are derived in Appendix K (eq. K.19, eq. K.21). The corresponding maximum torque is then defined as:

$$\boxed{\frac{T^*_{max,mag}}{l^*} = d^{*2} = \left(\frac{T^*_{cont}}{l^*}\right)^{2/2.5}} \tag{4.30}$$

In addition, the ratio $T^*_{max,mag}/T^*_{cont}$ gives the same result than in the previous consideration (eq. 4.27). This ratio decreases along with the increase of motor diameter.

- For annular motors:

The geometrical similarity is not supposed ($d^* \neq l^*$). The motor is supposed to be done by an assembly of the same elementary modules. This assumes that the contour $\mathscr{C}$ and the surface S do not evolve. The eq. 4.23 becomes:

$$B^*_{max} = J^*_{max} \implies J^*_{max} = 1 \tag{4.31}$$

The relations linking torque, current density and dimension are defined such as:

$$T^* = J^* \cdot d^{*2} \cdot l^* \quad ; \quad d^* = \left(\frac{T^*_{cont}}{l^*}\right)^{1/2} \tag{4.32}$$

These relations are derived in Appendix K, (eq. K.96, K.98). The corresponding maximum torque is then defined as:

$$\boxed{\frac{T^*_{max,mag}}{l^*} = d^{*2} = \frac{T^*_{cont}}{l^*}} \tag{4.33}$$

In addition,

$$\frac{T^*_{max,mag}}{T^*_{cont}} = \frac{l^* \cdot d^{*2}}{l^* \cdot d^{*2}} = 1 \tag{4.34}$$

Whatever the motor size, the gap between the maximum and the continuous torque remain constant.

In CASE 1 and for cylindrical motors, whatever the geometrical similarity consideration is, the increase of the motor diameter leads to a reduction of the motor

running margin in its limited operation domain (fig. 2.4). When it comes to annular motors, this motor running margin remains constant wathever the motor size is.

CASE 2:
The heat equality between Joules and thermal capacity at winding level gives:

$$\mathscr{P}_J \cdot \Delta t = C_{th} \cdot \Delta\Theta \tag{4.35}$$

The thermal capacity can be defined as $C_{th} = C_p \cdot M_{copper}$ with C_p the specific heat at constant pressure $[J/Kg/K]$ and $M_{copper} = \int \rho_{copper}\, dV$ the mass $[Kg]$ of copper involved into winding. What is more, it is supposed that the manufacturer defines a same specification ($\Delta\Theta$ [°C], Δt [s]) among its whole product range.

- <u>For cylindrical motors:</u>

- On one hand, the geometrical similarity is supposed ($d^* = l^*$). It is shown (Appendix K, eq. K.5, K.23) that Joules' losses $\mathscr{P}_J$ and winding mass $\mathscr{M}$ evolve according to:

$$\mathscr{P}_J^* = d^{*3} \cdot J^{*2} \quad ; \quad \mathscr{M}^* = d^{*3} \tag{4.36}$$

  Then, the eq. 4.35 gives the following maximum current density:

$$d^{*3} \cdot J_{max}^{*2} = d^{*3} \implies J_{max}^* = 1 \tag{4.37}$$

  Using the relations previously proved in case 1 (eq. 4.25), the corresponding maximum torque is expressed:

$$\boxed{T_{max,\Delta\Theta/\Delta t}^* = d^{*4} = T_{cont}^{*4/3.5}} \tag{4.38}$$

  In addition,

$$\frac{T_{max,\Delta\Theta/\Delta t}^*}{T_{cont}^*} = d^{*0.5} \tag{4.39}$$

  The ratio increases along with the increase of the motor size.

- On a second hand, the geometrical similarity is not supposed ($d^* \neq l^*$). It is shown (Appendix K, eq. K.6, K.25) that Joules' losses $\mathscr{P}_J$ and winding mass $\mathscr{M}$ evolve according to:

$$\mathscr{P}_J^* = d^{*2} \cdot l^* \cdot J^{*2} \quad ; \quad \mathscr{M}^* = d^{*2} \cdot l^* \tag{4.40}$$

  The eq. 4.35 provides the same maximum current density than in the previous considereation (eq. 4.37) Using the relations previously proved in case 1 (eq. 4.25), the corresponding maximum torque is expressed:

$$\boxed{\frac{T_{max,\Delta\Theta/\Delta t}^*}{l^*} = d^{*3} = \left(\frac{T_{cont}^*}{l^*}\right)^{3/2.5}} \tag{4.41}$$

  In addition, the ratio $T_{max,\Delta\Theta/\Delta t}^* / T_{cont}^*$ gives the same result than in the previous consideration (eq. 4.39). This ratio increases along with the increase of the motor diameter.

- For annular motors: The geometrical similarity is not supposed ($d^* \neq l^*$). It can be shown (Appendix K, eq. K.88, K.99) that Joules' losses $\mathscr{P}_J$ and winding mass $\mathscr{M}$ evolves according to:

$$\mathscr{P}_J^* = d^* \cdot l^* \cdot J^{*2} \quad ; \quad \mathscr{M}^* = d^* \cdot l^* \tag{4.42}$$

Then, the eq. 4.35 gives the maximum current density:

$$d^* \cdot l^* \cdot J_{max}^{*2} = d^* \cdot l^* \implies J_{max}^* = 1 \tag{4.43}$$

Using the same already proved relations than in case 1 (eq. 4.32), the corresponding maximum torque is expressed:

$$\boxed{\frac{T_{max,\Delta\Theta/\Delta t}^*}{l^*} = d^{*2} = \frac{T_{cont}^*}{l^*}} \tag{4.44}$$

In addition,

$$\frac{T_{max,\Delta\Theta/\Delta t}^*}{T_{cont}^*} = \frac{l^* \cdot d^{*2}}{l^* \cdot d^{*2}} = 1 \tag{4.45}$$

The ratio remains constant whatever the motor size is.

In **CASE 2** and for cylindrical motors whatever the geometrical similarity consideration is, the runnning margin in its limited operation domain increases proportionally with the diameter (fig. 2.4). For annular motors, the running margin remains constant whatever the motor size is.

Conclusion: Two max torque definitions have been studied: one following a magnetic saturation criteria and the other following a thermal criteria. These definitions lead to a different maximum torque expression for cylindrical motors. In the motor predesign process, using the torque as a *definition parameter* is a choice which might introduce confusions somehow. The motor constant K_m is more relevant to use instead, since it has a unique definition among manufacturers. The following section is dedicated to this constant.

4.2.3.2.3 Validation The previous formulated laws are compared with catalog data.

To illustrate the case of the cylindrical motors following the geometrical similarity hypothesis, the NK motor range from Parker is chosen [PARKER, 2022]. Fig. 4.13 displays its peak torque with respect to its equivalent continuous torque. A regression performed over this data set is plotted along with the scaling laws. Neither the scaling law from the magnetic criteria (CASE 1) nor the one from the thermal criteria (CASE 2) is validated. A piece of information is missing concerning the design concept of this motor range. As a result, the intermediate formulation that minimizes the error estimations is prefered. Thus, the peak torque law is defined as:

$$T_{max}^* = T_{cont}^* \tag{4.46}$$

The validation study is completed with another manufacturer. The cylindrical motors, from Kollmorgen RBE serie, are chosen [KOLLMORGEN, 2003]. In fig. 4.14, the scaling law based on a thermal criteria is compared to the catalog data. According to the logarithmic display, the law trend is validated. However, the plot in real values highlights the dependency of the continuous torque with respect to the thermal integration hypothesis. Therefore, there is an interest of using the motor constant K_m.

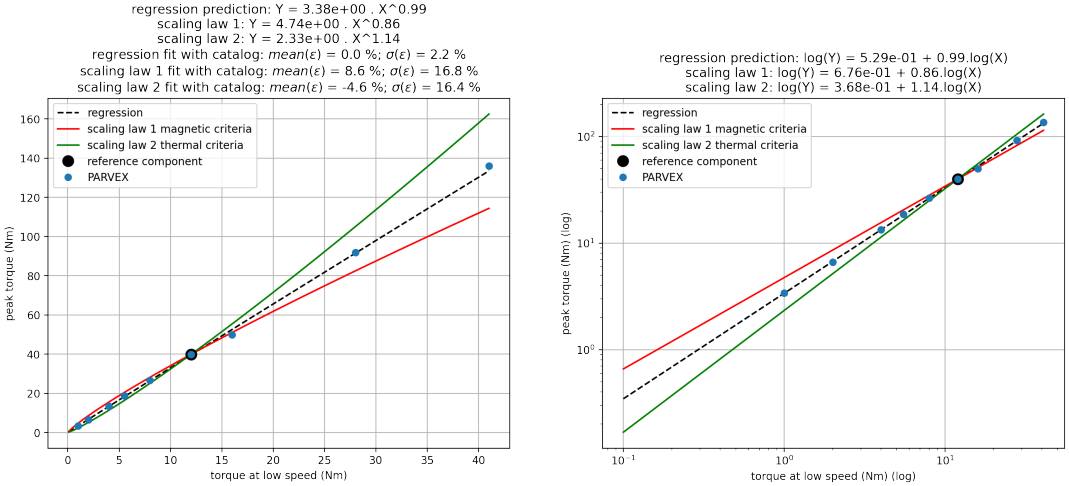

FIGURE 4.13: *Scaling law validation, cylindrical motor, peak torque (Parvex NK)*

It allows to avoid such uncertain parameter and check the motor continuous torque capabilities only through a thermal loss statement. The following section is dedicated to this constant K_m.

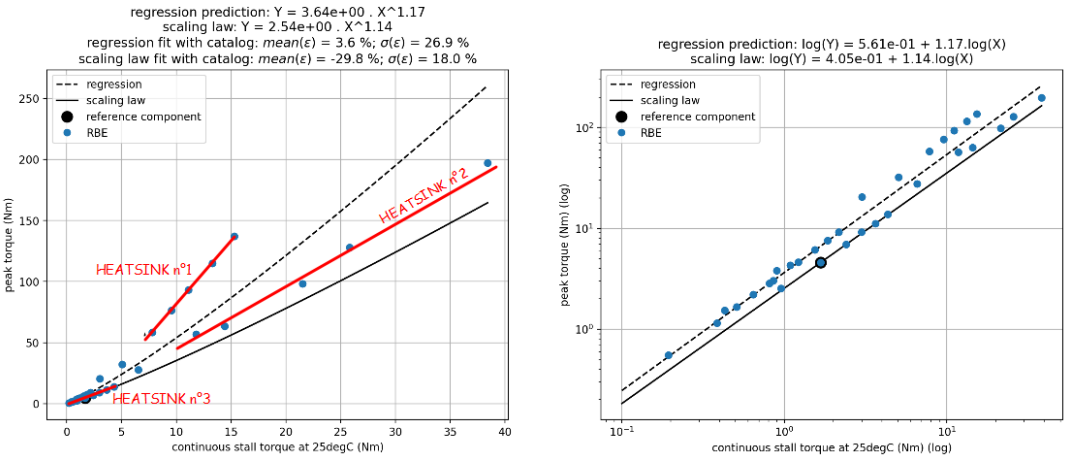

FIGURE 4.14: *Scaling law validation, cylindrical motor, peak torque at 25 degrees, thermal criteria (KOLLMORGEN, RBE serie)*

4.2.3.3 Motor performance

The motor constant K_m gives the relation between the dissipated electrical power (Joules' losses) and the torque. It can be defined such as:

$$K_m = \frac{T^2}{\mathscr{P}_J}\left[(N \cdot m)^2 \cdot W^{-1}\right] \qquad K'_m = \frac{T}{\mathscr{P}_J^{1/2}}\left[(N \cdot m) \cdot W^{-1/2}\right] \tag{4.47}$$

4.2.3.3.1 Introduction [MOOG, 2020a] manufacturer reports that K_m constant is a figure of merit commonly used to compare motor capabilities. It gets interesting

since it is independent of winding type as long as the same material properties are used for wires.

The winding independance can be shown easily. Since the torque constant K_t $[Nm/A]$ and Joules' losses $\mathscr{P}_J$ $[W]$ are expressed by $T = K_t \cdot I$ and $P_J = \mathscr{R} \cdot I^2$, the motor constant of eq. 4.47 can be written in another way:

$$K_m = \frac{K_t^2}{\mathscr{R}} \tag{4.48}$$

Then, studying each member of the ratio separately provides elements to conclude about.

- Supposing a constant maximum induction field B^*, Laplace's force can be expressed such as:

$$\overrightarrow{dF_{laplace}} = n_{turns} \cdot I \cdot d\overrightarrow{l} \wedge \overrightarrow{B} \implies F^*_{Laplace} = n^*_{turns} \cdot I^* \cdot l^* \tag{4.49}$$

  This leads to a torque defined with a given radius r following the geometrical similarity hypothesis $r^* = d^*$:

$$T^* = n^*_{turns} \cdot I^* \cdot l^* \cdot d^* = K^*_t \cdot I^* \implies K^*_t = n^*_{turns} \cdot l^* \cdot d^* \tag{4.50}$$

  The torque constant is dependent on the number of wire turn n:

$$\boxed{K^*_t = f(n^*_{turns})} \tag{4.51}$$

- The resistance is basically defined such as:

$$\mathscr{R} = \rho \cdot \frac{l_{wire}}{S_{wire}} \quad \begin{cases} l_{wire} = l_{1spire} \cdot n_{turns} \\ S_{wire} = S_{notch}/n_{turns} \end{cases} \tag{4.52}$$

  Turning into scaling laws:

$$l^*_{1spire} = l^* \qquad S^*_{notch} = d^{*2} \qquad \mathscr{R}^* = \frac{l^*}{d^{*2}} \cdot n^{*2}_{turns} \tag{4.53}$$

  The resistance is dependent on the squared power of the number of wire turn n:

$$\boxed{\mathscr{R}^* = f(n^{*2}_{turns})} \tag{4.54}$$

Using eq. 4.51 and eq. 4.54, K_m winding independance is clear then:

$$\boxed{K_m = \frac{K_t^2}{\mathscr{R}} \neq f(n_{turns})} \tag{4.55}$$

The same conclusion is drawn considering the geometrical similarity ($l^* = d^*$).

Consequently, at a given ambient temperature, a motor with a winding of n_{turns} of doubled parallel wires instead of $2 \cdot n_{turns}$ single wire doubles the velocity constant K_v meanwhile K_m remains unchanged (table 4.6).

K_m can be used for selecting the size of a motor to use in an application as long as no current and voltage limitations are specified. The torque to supply and the power to dissipate are the unique inputs. Therefore, the scaling laws mentioned in the table 4.2 are expressed with K_m.

The velocity and torque constants K_e or K_t are used to select the winding characteristics of the motor regarding the specified current and voltage limitations.

motor characteristics	unit	winding 1	winding 2	equations
wire section	m^2	S	$S/2$	
nbr of winding turn	$-$	n_{turns}	$2 \cdot n_{turns}$	
wire length	m	l	$2 \cdot l$	
torque	$N \cdot m$	T	T	
resistance	Ohm	$\mathscr{R}$	$4 \cdot \mathscr{R}$	$\mathscr{R} = \rho \cdot l/S$
current	A	I	$I/2$	$I = J \cdot S$
torque constant	$N \cdot m/A_{dc}$	K_t	$2 \cdot K_t$	$T = K_t \cdot I$
speed constant	$V_{dc}/(rad \cdot s^{-1})$	K_e	$2 \cdot K_e$	$K_t = K_e$
voltage	U_{peak}	U	$2 \cdot U$	$U = \mathscr{R} \cdot I$ if $\omega = 0$
Joules' losses	W	$\mathscr{P}_J$	$\mathscr{P}_J$	$\mathscr{P}_J = \mathscr{R} \cdot I^2$
motor constant	$(N \cdot m)^2/W$	K_m	K_m	$K_m = T^2/\mathscr{P}_J$

TABLE 4.6: *Motor characteristic evolution from one winding to another*

4.2.3.3.2 Formulation The motor constant is established for cylindrical and annular motors considering both motor constant definitions (K_m & K'_m).
- For cylindrical motor: the cited relations are detailed in Appendix K.1.

- If the geometrical similarity is considered ($d^* = l^*$), Joules' losses and torque expressions (eq. K.5 & K.15) give:

$$\frac{T^{*2}}{\mathscr{P}_J^*} = \frac{(J^* \cdot d^{*4})^2}{J^{*2} \cdot d^{*3}} \tag{4.56}$$

The current density being $J^* = d^{*-1/2}$ (eq. K.8), the motor constant becomes:

$$K_m = \frac{T^{*2}}{\mathscr{P}_J^*} = d^{*5} \qquad K'_m = \frac{T^*}{\mathscr{P}_J^{*1/2}} = d^{*5/2} \tag{4.57}$$

Using the mass relation $\mathscr{M}^* = d^{*3}$ (eq. K.23), the motor constant per unit of mass is:

$$\frac{K_m^*}{\mathscr{M}^*} = \frac{T^{*2}}{\mathscr{P}_J^* \cdot \mathscr{M}^*} = d^{*2} \qquad \frac{K_m'^*}{\mathscr{M}^*} = \frac{T^*}{\mathscr{P}_J^{*1/2} \cdot \mathscr{M}^*} = d^{*-1/2} \tag{4.58}$$

- If the geometrical similarity is not considered ($d^* \neq l^*$): Joules' losses and torque expressions (eq. K.6 & K.19) give:

$$\frac{T^{*2}}{\mathscr{P}_J^*} = \frac{(J^* \cdot d^{*3} \cdot l^*)^2}{J^{*2} \cdot d^{*2} \cdot l^*} \tag{4.59}$$

The current density being $J^* = d^{*-1/2}$ (eq. K.9), the motor constant becomes:

$$\frac{K_m^*}{l^*} = \frac{T^{*2}}{\mathscr{P}_J^* \cdot l^*} = d^{*4} \qquad \frac{K_m'^*}{l^{*0.5}} = \frac{T^*}{\mathscr{P}_J^{*1/2} \cdot l^{*0.5}} = d^{*2} \tag{4.60}$$

Using the mass relation $\mathscr{M}^* = d^{*2} \cdot l^*$ (eq. K.25), the motor constant per unit of mass is:

$$\frac{K_m^*}{\mathscr{M}^*} = \frac{T^{*2}}{\mathscr{P}_J^* \cdot \mathscr{M}^*} = d^{*2} \qquad \frac{K_m'^*}{\mathscr{M}^*} = \frac{T^*}{\mathscr{P}_J^{*1/2} \cdot \mathscr{M}^*} = l^{*-1/2} \tag{4.61}$$

- For annular motors: with the relations detailed in Appendix K.2, the motor constant is derived to be:

$$\frac{K_m^*}{l^*} = \frac{T^{*2}}{\mathscr{P}_J^* \cdot l^*} = d^{*3} \qquad \frac{K_m'^*}{l^{*1/2}} = \frac{T^*}{\mathscr{P}_J^{*1/2} \cdot l^{*1/2}} = d^{*3/2} \tag{4.62}$$

Per unit of mass, the motor constant becomes:

$$\frac{K_m^*}{\mathscr{M}^*} = \frac{T^{*2}}{\mathscr{P}_J^* \cdot \mathscr{M}^*} = d^{*2} \qquad \frac{K_m'^*}{\mathscr{M}^* \cdot l^{*-1/2}} = \frac{T^*}{\mathscr{P}_J^{*1/2} \cdot \mathscr{M}^* \cdot l^{*-1/2}} = d^{*1/2} \tag{4.63}$$

4.2.3.3.3 Validation Some of the previous scaling laws are compared to manufacturer catalogs.

Parvex NK motor serie [PARKER, 2022] is a cylindrical motor following the geometrical similarity hypothesis ($l^* = d^*$). The eq. 4.57 & 4.58 are validated by comparison with Parvex NK datasheets (fig. 4.15).

Kollmorgen RBE motor serie [KOLLMORGEN, 2003] is a cylindrical motor not following the geometrical similarity hypothesis ($l^* \neq d^*$). The eq. 4.60 & 4.61 are validated by comparison with RBE datasheets (fig. K.15 in Appendix K.1).

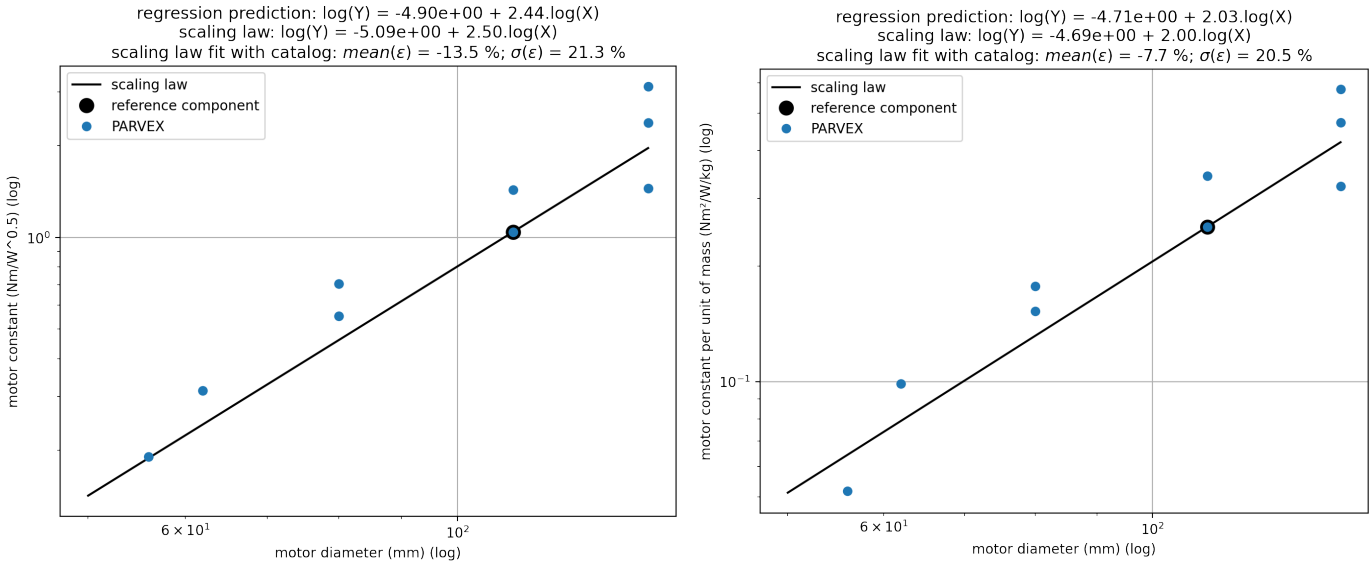

FIGURE 4.15: *Scaling law validation, cylindrical motor, motor constant vs diameter: (left) K_m, (right) K_m per unit of mass, data from [PARKER, 2022]*

In the case of the annular motor, the eq. 4.62 & 4.63 are compared to the catalog of [TECNOTION, 2019] and [ETEL, 2013]. Fig. 4.16 validates these scaling laws. Another representation with respect to the linear continuous torque is available in fig. K.26 of Appendix K.2.

In fig. 4.16 (left) and for a given diameter, the point with the higher linear K_m corresponds to the longest motor whereas the point with the lowest linear K_m corresponds to the shortest motor. The vertical dispersion is explained by the unconsidered thermal dissipation from the motor lateral surfaces. For short motors, these surfaces contribute in a significant thermal dissipation compared to the surface covered by the lamination stack. When the motor length increases, the lamination stack length increases and the contribution of these lateral surfaces gets less significant. This explains the observed variation of the thermal dissipation capability per unit of length for a given diameter.

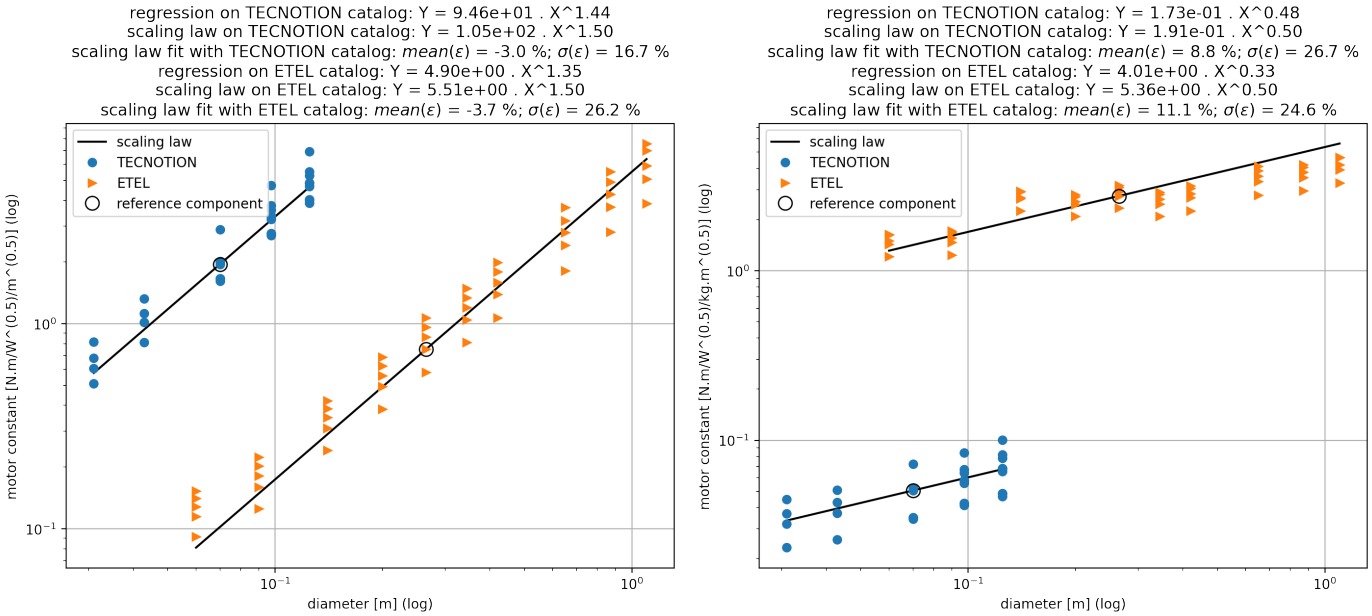

Notes: The prediction of the Etel catalog uses the rotor inner diameter. This prediction can be improved using the airgap diameter. Etel documentation does not provide 2D sketches to get such a data. The prediction of the Tecnotion catalog uses the airgap diameter.

FIGURE 4.16: *Scaling law validation, annular motor, motor constant vs diameter: (left) K_m, (right) K_m per unit of mass, data from [TECNOTION, 2019, ETEL, 2013]*

The same explanation apply for the linear K_m per unit of mass (fig. 4.16, right). In addition, the mass of the winding heads gives an offset to the total mass. When the motor length increases, the torque value increases and this mass offset per unit of torque decreases.

4.2.3.3.4 Conclusion This study shows that the motor constant K_m per unit of mass is similar whatever the motor technology (cylindrical, annular) is. This illustrates the universal property of this constant.

The motor is a converter of electrical power into mechanical power. The K_m constant points out the heart of the problem, it is a motor conversion factor. Unlike the continuous or peak torque where every supplier has got its own definition (as seen in section 4.2.3.2), the K_m constant takes a higher view at design level, it does not require any information about the motor winding or the thermal integration.

What is more, the K_m per unit of mass (eq. 4.58, 4.61 and 4.63) highlights the following points:

- It is an interesting coefficient allowing easy comparison of motors between technologies and suppliers. It can be seen as an indicator of supplier technical finishing level.
- It is not dependent on the motor length. Indeed, the length does not have any impact on the energy conversion, the torque has got one.
- The expression basically shows that the higher the motor diameter is, the higher the efficiency of energy conversion per unit of mass is.
- The definition of K_m leads to more direct interpretations than the other definition, K'_m.

4.2.4 Surrogate

In a helicopter context, the resonance frequencies and the stress under a vibratory environment is an unavoidable check to perform. The following subsections present a preliminary vibratory study of a simplified actuator housing. The approach goes through the synthesis of a surrogate model to implement into the actuator preliminary sizing loop.

4.2.4.1 Introduction

From a purely mechanical point of view, the design of the EMA housing has to focus on the elementary forces acting on the housing, which can be divided into two categories: the static stresses induced by the power transmission to the load, they have low frequencies; the vibratory stresses induced by vibratory environment, they have high frequencies ($f \in [5; 2000]hz$, [RTCA, 2005]).

The path of the various static or dynamic loads is represented for a generic actuator in fig. 4.17.

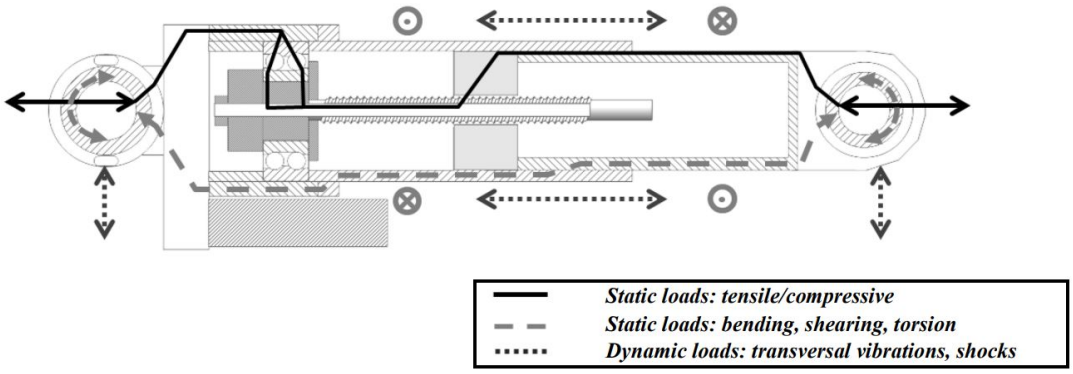

FIGURE 4.17: *Load path in generic EMA [Budinger et al., 2015]*

The most significant static loadings are the tensile, compressive, buckling forces. They are transmitted through the rod to the nut, the screw, the bearings and finally to the housing. The high number of cycles generally requires the fatigue limit of materials to be considered.

Other low frequency sollicitations are the shearing, torsion, bending stresses induced by the friction and the reaction torques from the motor, the reducer, the nut screw and the spherical bearings in anchorage points.

The dynamic stress is mainly generated by the transversal vibrations due to the vibratory environment which can generate important mechanical bending stresses. For long actuator, as considered in this thesis, these stresses can be prevailing.

4.2.4.2 Prior considerations

A high fidelity model of vibratory stress in the housing would be difficult to develop. Indeed, ball bearing stiffness, roller screw stiffness and plays are unknown and not supplied in datasheets. The contact at linear bushing level is unclear.

Therefore, we propose a simple model based on some simplifications. The first one concerns the potential plays in the actuator assembly and their effect with respect to excitation frequencies. The vibratory amplitude relies on the acceleration level as illustrated in table 4.7.

$$x = \frac{a}{w^2} \quad \begin{cases} x & \text{vibratory amplitude } [m] \\ a & \text{acceleration } [m \cdot s^{-2}] \\ w = 2\pi f & \text{angular speed } [rad \cdot s^{-1}] \end{cases} \tag{4.64}$$

number of g	-	6	6	20	20
acceleration a	$m \cdot s^{-1}$	58.8	58.8	196	196
frequency f	hz	250	50	250	50
vibratory amplitude x	μm	24	596	79	1986

TABLE 4.7: *Vibratory amplitudes for different accelerations and frequencies*

The vibratory amplitudes are estimated in table 4.7 with eq. 4.64 regarding commonly used accelerations, found in DO160 standard [RTCA, 2005] (6g for in-cabin equipment, 20g for under-swashplate location). The amplitudes can be lower and close to the typical plays. In this case, the vibratory phenomena gets even more complex. Typical plays at linear bushing level are roughly 100 μm.

To model the effect of the play, we propose a lumped-parameter simulation. It associates one or two mass–spring systems excited through an elastogap where the play is modelled as a non-linear stiffness (very low value into the play, and high value far from the play).

In fig. 4.18, the accelerations stated by the DO160 standard ([RTCA, 2005]) are plotted in terms of amplitude and frequency.

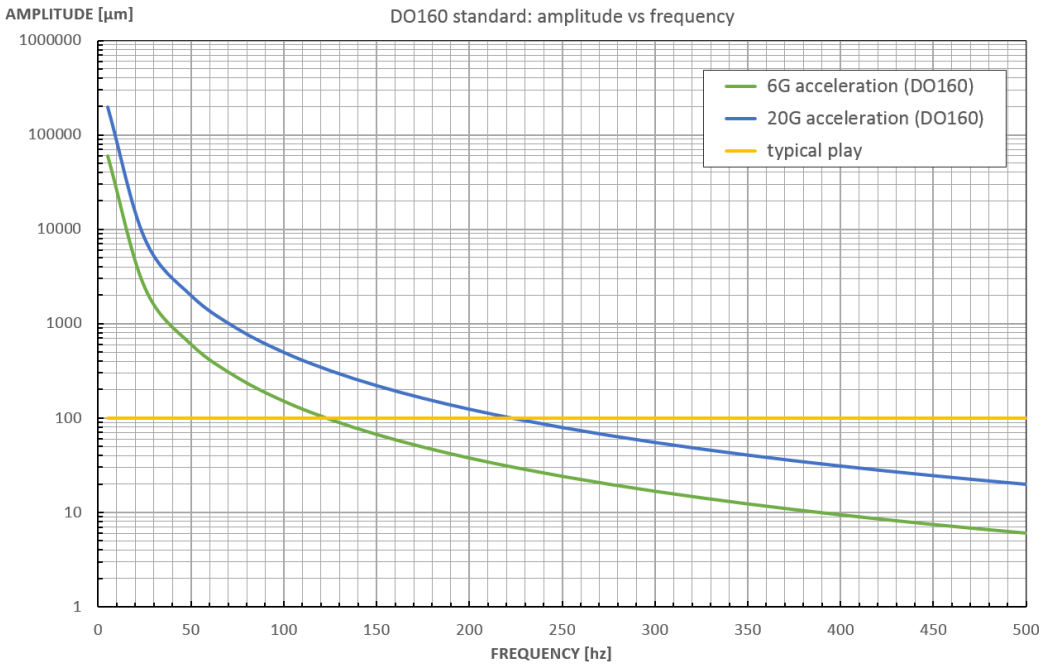

FIGURE 4.18: *DO160 accelerations: amplitude evolutions vs frequency*

Two cases are studied and illustrated thereafter: the **case 1** at 250 hz with $x \leq 100\ \mu m$ and the **case 2** at 50 hz with $x \geq 100\ \mu m$. Both cases consider an acceleration of 6 g.

First of all, the model considers only one mass–spring system.

Case 1 is simulated in fig. 4.19. The mass–spring resonance is set at 250 *hz* and the excitation is around this frequency. No resonance mode of the mass is observed, the vibratory excitation is 'filtered' by the play.

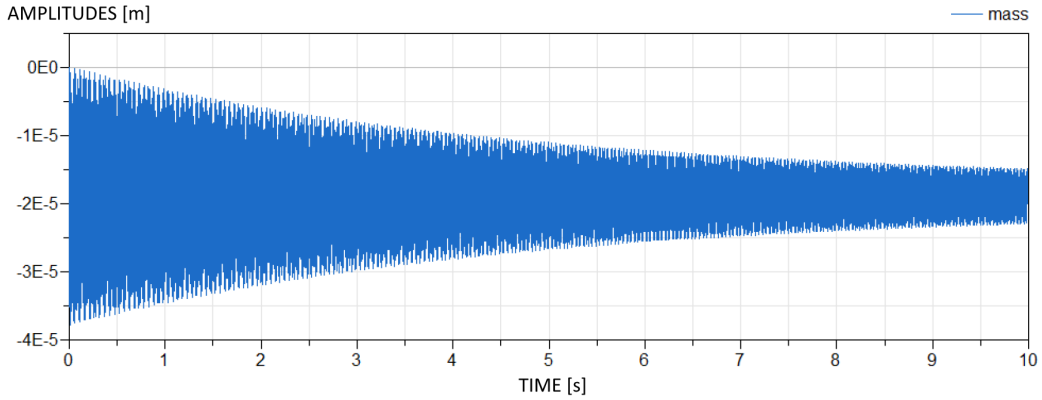

FIGURE 4.19: *Mass amplitudes of the simple mass–spring coupled with play (f=250hz)*

Case 2 is simulated in fig. 4.20. The mass–spring resonance is set at 50 *hz* and the excitation is around this frequency. The mass vibrations are more important and the resonance is observed.

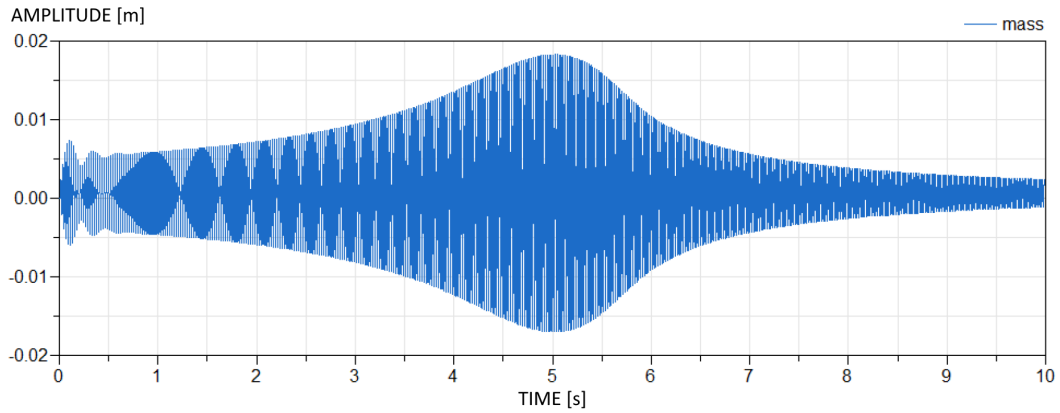

FIGURE 4.20: *Mass amplitudes of the simple mass–spring coupled with play (f=50hz)*

For the plays inside the actuator, the model considers two mass–spring systems linked by an elastogap. Using this model, the displacement of each mass is plotted (fig. 4.21). For a resonance frequency around 50 *hz*, the amplitudes are such that the vibrating parts interfaced by the play are considered as one and a single part.

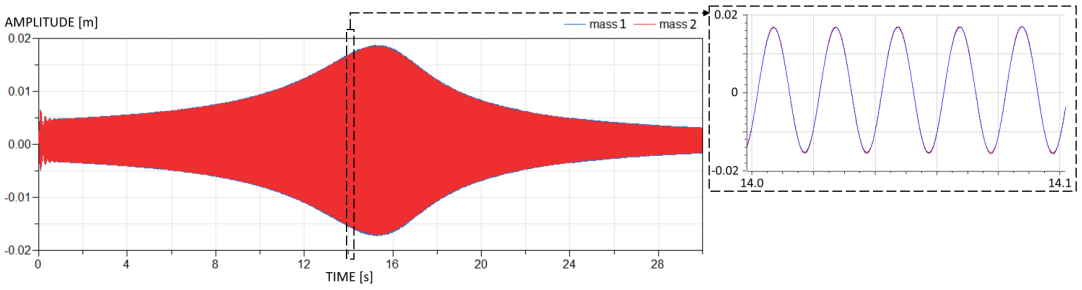

FIGURE 4.21: *Mass amplitudes of the double mass–spring coupled with play (f=50hz)*

For a resonance frequency around 250 hz, the vibratory amplitudes are much lower and the two masses evolve within the play.

As a result, to keep the vibratory amplitudes smaller than the play between parts, the resonance frequencies must be high (e.g. $\geq$ 200 hz, this limit depends on the amplitude of the acceleration). For long and narrow actuators such as the actuator of reference of this thesis, it is not the case. The resonance frequencies are low. A hammering impact lab test on the actuator of reference showed a resonance frequency of around 50hz.

Thus, some simplifications can be introduced into the stress estimations of the actuator housing under vibratory excitations. For housings with low resonance frequency, we can suppose that the plays are negligible compared to the vibratory amplitudes. Consequently, the contact with linear bushing is modelled as an infinitely rigid contact.

4.2.4.3 Hypothesis

Now, a FEM model of reduced parameters is developped in order to represent it by a surrogate model. Some more hypothesis are formulated then.

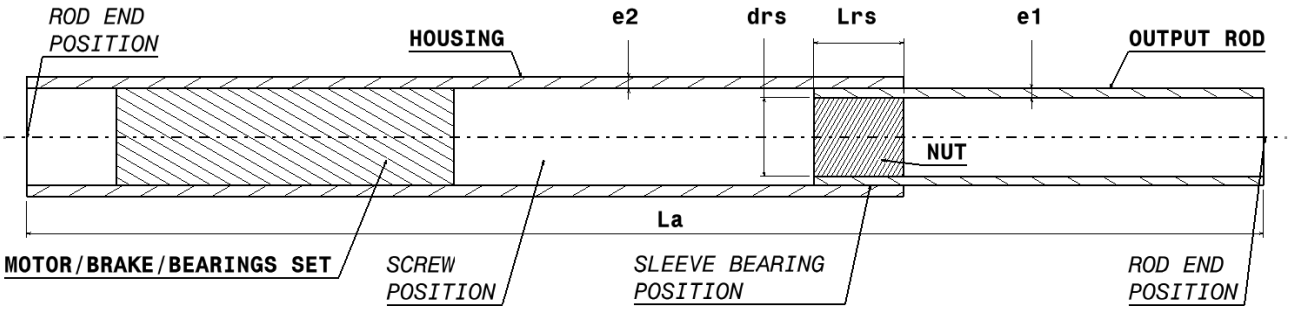

FIGURE 4.22: *Actuator simplified geometry for modal analysis*

A simplified geometry is considered (fig. 4.22): two hollowed cylinders one in the other. The connection between them is assumed to be perfect. The set (motor, brake, connectors, and bearings) is supposed to be a cylinder of 1/3rd of La with an equivalent density. This equivalent mass is modelled with Young's modulus of a low value (1/10th of aluminium modulus). This choice is conservative, it is so as not to impact the stiffness of the housing.

The housing and output rod are set with the same material properties (aluminium). Their length are respectively supposed to 2/3rd and 1/3rd of La.

The nut is modelled as a full cylinder with a density of 90% of steel density ($7000\ kg.m^{-3}$) to consider air content between rollers. The geometry of the nut evolves with a geometrical similarity assumption (scaling law). The cylinder representing the nut is modelled, using Young's modulus of a low value (1/10th of steel modulus) so as to not influence the stiffness of the global structure.

The rod ends allow rotations with no friction.

The antirotation key and the sealing leap at the interface output rod with housing are not modelled.

In the 3 following sections, a surrogate modelling technic inspired from the surrogate proposed in the paper [Sanchez et al., 2017] is developped.

4.2.4.4 Problem formulation

Under vibration, the system can be associated to a basic damped mass–spring model. Fig. 4.23 presents this model with U (m) the displacement of an equivalent mass M_{eq} (kg) evolving according to an excitation force F_e (N), a stiffness K_{eq} $(N \cdot m^{-1})$, and a damping C_{eq} $(N \cdot m^{-1} \cdot s)$.

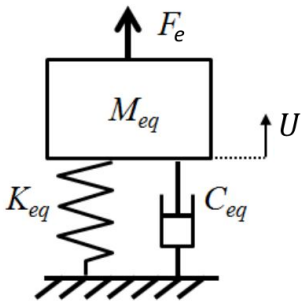

FIGURE 4.23: *Mass–spring model*

The stress σ is linearly linked to the displacement U:

$$\sigma = k_\sigma \cdot U \qquad\qquad k_\sigma = \frac{\sigma_0}{U_0} \tag{4.65}$$

with σ_0 $[Pa]$ and U_0 $[m]$, the maximum stress and the maximum displacement at resonance frequency.

Newton's second law applied to the moving body enables the Laplace function between the displacement $U(t)$ and the excitation load $F_e(t)$ to be estimated, such as:

$$\frac{U(p)}{F_e(p)} = \frac{1}{M_{eq} \cdot p^2 + C_{eq} \cdot p + K_{eq}} = \frac{1/K_{eq}}{p^2/\omega_r^2 + 2 \cdot \xi \cdot p/\omega_r + 1} \tag{4.66}$$

Considering an excitation of the mass with a sinusoidal force $F_e(t) = F_0 \cdot sin(\omega \cdot t)$, the maximum displacement at the first resonance mode is:

$$U_0 = \frac{1}{2 \cdot \xi} \cdot \frac{F_0}{K_{eq}} = \frac{Q_m \cdot F_0}{K_{eq}} \qquad\qquad \xi = \frac{C_{eq}}{2 \cdot \sqrt{K_{eq} \cdot M_{eq}}} \approx \frac{1}{2 \cdot Q_m} \tag{4.67}$$

where Q_m is the mechanical quality coefficient.

The article [Budinger et al., 2015] reports that tests performed on industrial prototypes show a wide range of practical values for the equivalent mechanical quality coefficient Q_m. In addition, it reports that experiments give typical values for Q_m between 10 and 50, depending on the application and boundary conditions.

For structural dynamic models, in the absence of better information, it is normally acceptable to assume a value of $Q_m = 30$ (according to [EASA, 2007]).

The equivalent force F_0 of the acceleration effect can be evaluated thanks to an equivalent work $\mathscr{W}_0$ [Moës, 2011, Spencer, 2004]:

$$\mathscr{W}_0 = F_0 \cdot U_0 = \iiint_{\mathscr{V}} u_0 \cdot a \cdot \rho \cdot d\mathscr{V} \tag{4.68}$$

with $u_0(x)$ the deflection of the actuator envelop, a the amplitude of the vibratory sinusoidal acceleration. A mass M_{acc} subjected to the acceleration can be defined:

$$F_0 = M_{acc} \cdot a \qquad\qquad M_{acc} = \frac{1}{U_0} \cdot \iiint_{\mathscr{V}} u_0 \cdot \rho \cdot d\mathscr{V} \tag{4.69}$$

The mass subjected to the acceleration is not identical to the mass expressing the kinetic energy, M_{eq}, defined such as [Moës, 2011, Spencer, 2004]:

$$\frac{1}{2} \cdot M_{eq} \cdot v_{0,M}^2 = \iiint_{\mathscr{V}} \frac{1}{2} \cdot \rho \cdot v_{0,a}^2 \cdot d\mathscr{V} \tag{4.70}$$

with, at the first mode resonance, $v_{0,M}$ the speed of M_{eq} and $v_{0,a}(x)$ the speed of each point of the actuator deflection. The speeds can be defined such as:

$$v_{0,M} = w_0 \cdot U_0 \qquad\qquad v_{0,a} = w_0 \cdot u_0 \tag{4.71}$$

Thus, we can easily define the equivalent mass such as:

$$M_{eq} = \frac{1}{U_0^2} \cdot \iiint_{\mathscr{V}} \rho \cdot u_0^2 \cdot d\mathscr{V} \tag{4.72}$$

The following ratio is introduced:

$$k_{acc} = \frac{M_{acc}}{M_{eq}} = \begin{cases} U_0 \cdot \frac{\iiint_{\mathscr{V}} u_0 \cdot d\mathscr{V}}{\iiint_{\mathscr{V}} u_0^2 \cdot d\mathscr{V}} & \text{if } \rho \text{ is constant} \\ U_0 \cdot \frac{\iiint_{\mathscr{V}} u_0 \cdot \rho \cdot d\mathscr{V}}{\iiint_{\mathscr{V}} u_0^2 \cdot \rho \cdot d\mathscr{V}} & \text{if } \rho \text{ is not constant} \end{cases} \tag{4.73}$$

and the maximum displacement at the resonance can be approximated as it follows:

$$U_0 = \frac{Q_m \cdot k_{acc} \cdot M_{eq} \cdot a_0}{K_{eq}} = \frac{Q_m \cdot k_{acc} \cdot a_0}{\omega_0^2} \tag{4.74}$$

with $\omega_0^2 = K_{eq}/M_{eq}$ the resonance angular frequency.

4.2.4.5 Dimensional analysis

As seen in Section 4.2.2, the use of a dimensional analysis and Buckingham's Theorem enable to reduce the number of variables expressing a physical problem. Here below, this approach is developed for the vibratory use case. By simplification and for a reduced number of parameters, a constant density ρ is assumed all along the actuator (eq. 4.73).

The link between stress and displacement evolves according to the following variables:

$$\frac{\sigma}{U} = k_\sigma = f(E, d_{rs}, L_a, e_1, e_2, L_{rs}) \tag{4.75}$$

which can be rewritten with the following dimensionless numbers:

$$\pi_{k_\sigma} = \frac{\sigma \cdot d_{rs}}{U \cdot E} = f(\frac{L_a}{d_{rs}}, \frac{e_1}{d_{rs}}, \frac{e_2}{d_{rs}}, \frac{L_{rs}}{d_{rs}}) \tag{4.76}$$

The resonance angular frequency evolves according to:

$$\omega_0 = g(E, \rho, d_{rs}, L_a, e_1, e_2, L_{rs}) \tag{4.77}$$

which can be rewritten with the following dimensionless numbers:

$$\pi_{\omega_0} = \omega_0 \cdot \left(\frac{\rho}{E}\right)^{1/2} \cdot d_{rs} = g(\frac{L_a}{d_{rs}}, \frac{e_1}{d_{rs}}, \frac{e_2}{d_{rs}}, \frac{L_{rs}}{d_{rs}}) \tag{4.78}$$

The stress under a vibratory acceleration can be expressed as:

$$\sigma = k_\sigma \cdot U = k_\sigma \cdot \frac{Q_m \cdot k_{acc} \cdot a}{\omega_0^2} = \sigma_0 \cdot Q_m \cdot a \cdot \frac{\iiint_{\mathscr{V}} u_0 \cdot d\mathscr{V}}{\iiint_{\mathscr{V}} u_0^2 \cdot d\mathscr{V}} \tag{4.79}$$

The stress evolves according to:

$$\sigma = h(k_\sigma, \omega_0^2, a, Q_m) \tag{4.80}$$

which can be rewritten as:

$$\pi_0 = \frac{\sigma}{Q_m \cdot a \cdot d_{rs} \cdot \rho} = h(\frac{L_a}{d_{rs}}, \frac{e_1}{d_{rs}}, \frac{e_2}{d_{rs}}, \frac{L_{rs}}{d_{rs}}) \tag{4.81}$$

The expression of the stress is thus only function of four aspect ratios. One of these aspect ratios, L_{rs}/d_{rs}, can be assumed to be constant because of the geometrical similarity assumption used for roller screw component sizing (scaling law).

The final expression of the stress is a function dependent of three dimensionless quantities:

$$\pi_0 = g(\pi_1, \pi_2, \pi_3) \begin{cases} \pi_0 = \sigma/(Q_m \cdot a \cdot d_{rs} \cdot \rho) \\ \pi_1 = L_a/d_{rs} \\ \pi_2 = e_1/d_{rs} \\ \pi_3 = e_2/d_{rs} \end{cases} \tag{4.82}$$

It remains to determine this function g. The following section does the job.

4.2.4.6 FEM software model

In a software of computation by finite elements (fig. 4.22), a model is parametrized according to previous considerations and hypothesis. It enables to get:

- the resonance frequency f_0 or the resonance angular frequency ω_0.
- the modal form characterised by a maximal displacement U_0.
- the corresponding maximum stress σ_0. The maximum stress is identified to be on the output rod tube (e_1 thickness).

The intersection of both cylinders has been cared by smooth and arced geometries to avoid numerical stress constraints. The boundaries are clamped at each extremity

of the actuator model. The deflection is allowed within the plane of the section presented in fig. 4.24.

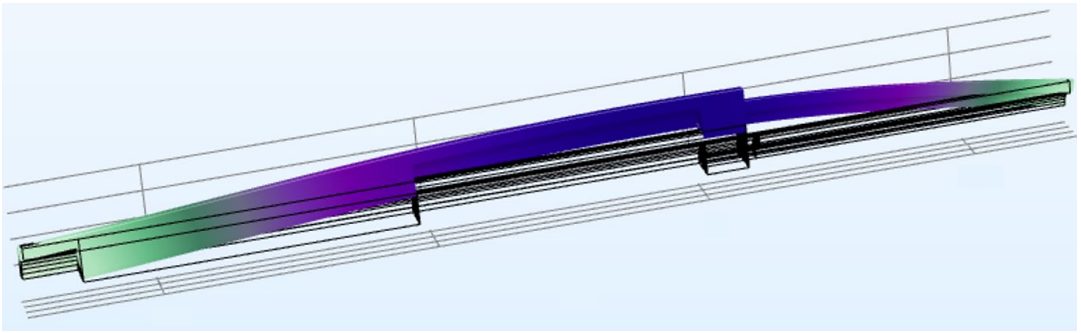

FIGURE 4.24: *Actuator modal analysis (COMSOL)*

As mentioned in Chapter 1 and table 1.5, the tandem topology of actuation is largely used in the aeronautic field since it complies with safety aviation rules. This topology involves 2 actuators stuck to each other at their basement (fig. 1.23), their extension is in opposite directions. This topology increases the total length of the actuation unit and reduces the diameter to total length ratio. To consider this use case, another surrogate model needs to be developed.

The FEM model for the single actuator is reused. The boundary conditions are changed. A symmetry constraint is applied on the CAD model to double it. The plane of symmetry is at actuator basement (next to the brake). The stress is picked up onto 2 critical points: at the interface between both actuators and at the interface between output rod and housing. Two surrogate models are expressed to determine the value of π_0 for each of these points.

4.2.4.7 DOE & surrogate synthesis

Once the dimensionless quantities are known (eq. 4.82), a *Design of Experiment (DoE)* is realized with e_1, e_2, d and L_a. The simulations (modal analysis) is carried out using the model presented in section 4.2.4.6 which finally allows to generate the variable of interest π_0.

The use of dimensionless numbers (or π-numbers) to set up a RSM or a surrogate model has several advantages. First, it decreases the number of variables to be manipulated and therefore it drastically decreases the number of physical or numerical experiments to be carried out. Secondly, it increases the regression robustness [Lacey and Steele, 2006] in particular if the RSM is built within the logarithmic space. [Budinger et al., 2020] mentions that logarithmic shows good results in interpolation and in extrapolation because of the power law form. This is the case for the *Variable Power Law Metamodel (VPLM)* methodology [Sanchez et al., 2017] used in this approach.

The dependant variable of the problem are approximated thanks to a linear regression (RSM) where the development takes into account a mean value, a first order member (which represents the main effects of the problem), a combined member (representing the interactions) and a second order member to consider further effects. The development takes the following form:

$$\pi_0 = \underbrace{a_0}_{\text{mean value}} + \underbrace{\sum a_i \pi_i}_{\text{main effect}} + \underbrace{\sum a_{ij} \pi_i \pi_j}_{\text{interactions}} + \underbrace{\sum a_{ii} \pi_i^2}_{\text{high order effect}} \tag{4.83}$$

A log transformation on variables is performed for the linearisation which gives the form:

$$log(\pi_0) = a_0 + \sum a_i log(\pi_i) + \sum a_{ij} log(\pi_i) log(\pi_j) + \sum a_{ii} log(\pi_i)^2 \tag{4.84}$$

and can be rewritten as:

$$\pi_0 = 10^{a_0} \prod_{i=1}^{n} \pi_i^{\,a_i + a_{ii} log(\pi_i) + \sum_{j=i+1}^{n} a_{ij} log(\pi_j)} \tag{4.85}$$

This power law form enables to deal with large variation range of dependent and independent variables.

The data set coming from the DoE is shared in two sets: one for the regression procedure so as to determine the coefficients a_i and a_{ij} (eq. 4.84) and the other for the test of the final surrogate.

The regression gives the following surrogate model which determines the value of π_0 for the housing of a single actuator:

$$\begin{aligned} log_{10}(\pi_0) = {} & 68 \cdot log_{10}\left(\frac{L}{d}\right)^2 \cdot \frac{1}{293} + 64 \cdot log_{10}\left(\frac{L}{d}\right) \cdot log_{10}\left(\frac{e_1}{d}\right) \cdot \frac{1}{973} \\ & + log_{10}\left(\frac{L}{d}\right) \cdot log_{10}\left(\frac{e_2}{d}\right) \cdot \frac{1}{1000} + 1099 \cdot log_{10}\left(\frac{L}{d}\right) \cdot \frac{1}{984} \\ & + 86 \cdot log_{10}\left(\frac{e_1}{d}\right)^2 \cdot \frac{1}{657} + 229 \cdot log_{10}\left(\frac{e_1}{d}\right) \cdot log_{10}\left(\frac{e_2}{d}\right) \cdot \frac{1}{884} \\ & - 101 \cdot log_{10}\left(\frac{e_1}{d}\right) \cdot \frac{1}{249} + 538 \cdot log_{10}\left(\frac{e_2}{d}\right)^2 \cdot \frac{1}{685} \\ & + 670 \cdot log_{10}\left(\frac{e_2}{d}\right) \cdot \frac{1}{359} + \frac{527}{551} \end{aligned} \tag{4.86}$$

with L the length L_a and d the diameter d_{rs}.

For the tandem actuation topology and at the interface between output rod and housing, the regression gives the following surrogate model:

$$\begin{aligned} log_{10}(\pi_0) = {} & 180 \cdot log_{10}\left(\frac{L}{d}\right)^2 \cdot \frac{1}{983} + 23 \cdot log_{10}\left(\frac{L}{d}\right) \cdot log_{10}\left(\frac{e_1}{d}\right) \cdot \frac{1}{243} \\ & + 43 \cdot log_{10}\left(\frac{L}{d}\right) \cdot log_{10}\left(\frac{e_2}{d}\right) \cdot \frac{1}{880} + 1187 \cdot log_{10}\left(\frac{L}{d}\right) \cdot \frac{1}{766} \\ & + 149 \cdot log_{10}\left(\frac{e_1}{d}\right)^2 \cdot \frac{1}{993} + 179 \cdot log_{10}\left(\frac{e_1}{d}\right) \cdot log_{10}\left(\frac{e_2}{d}\right) \cdot \frac{1}{712} \\ & - 175 \cdot log_{10}\left(\frac{e_1}{d}\right) \cdot \frac{1}{429} + 625 \cdot log_{10}\left(\frac{e_2}{d}\right)^2 \cdot \frac{1}{791} \\ & + 1229 \cdot log_{10}\left(\frac{e_2}{d}\right) \cdot \frac{1}{694} + \frac{922}{999} \end{aligned} \tag{4.87}$$

with L the length L_a and d the diameter d_{rs}.

For the tandem actuation topology and at the interface between both actuators, the regression gives the following surrogate model:

$$\begin{aligned} log_{10}(\pi_0) = {} & 96 \cdot log_{10}\left(\frac{L}{d}\right)^2 \cdot \frac{1}{899} + 25 \cdot log_{10}\left(\frac{L}{d}\right) \cdot log_{10}\left(\frac{e_1}{d}\right) \cdot \frac{1}{974} \\ & + 8 \cdot log_{10}\left(\frac{L}{d}\right) \cdot log_{10}\left(\frac{e_2}{d}\right) \cdot \frac{1}{223} + 1012 \cdot log_{10}\left(\frac{L}{d}\right) \cdot \frac{1}{585} \\ & - 8 \cdot log_{10}\left(\frac{e_1}{d}\right)^2 \cdot \frac{1}{819} - 43 \cdot log_{10}\left(\frac{e_1}{d}\right) \cdot log_{10}\left(\frac{e_2}{d}\right) \cdot \frac{1}{974} \\ & - 84 \cdot log_{10}\left(\frac{e_1}{d}\right) \cdot \frac{1}{811} + 2 \cdot log_{10}\left(\frac{e_2}{d}\right)^2 \cdot \frac{1}{15} \\ & - 259 \cdot log_{10}\left(\frac{e_2}{d}\right) \cdot \frac{1}{372} - \frac{175}{731} \end{aligned} \tag{4.88}$$

with L the length L_a and d the diameter d_{rs}.

4.2.4.8 Validation

In fig. 4.25 and 4.26, the elaborated surrogates are compared to the FEM simulation result data set. The prediction level is satisfying with $R^2 > 99\%$.

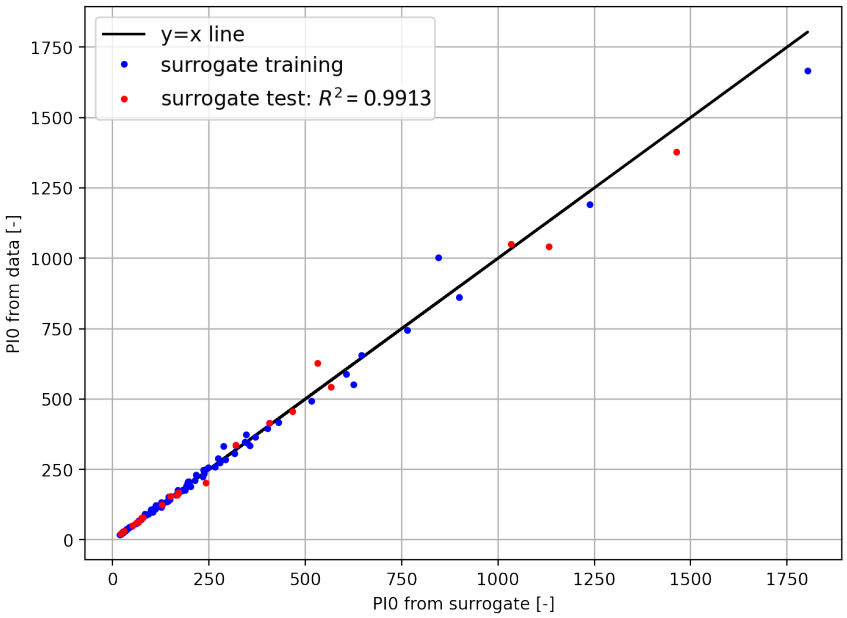

FIGURE 4.25: *Vibratory surrogate, single actuator: comparison π_0 results (eq. 4.86) with FEM simulation results*

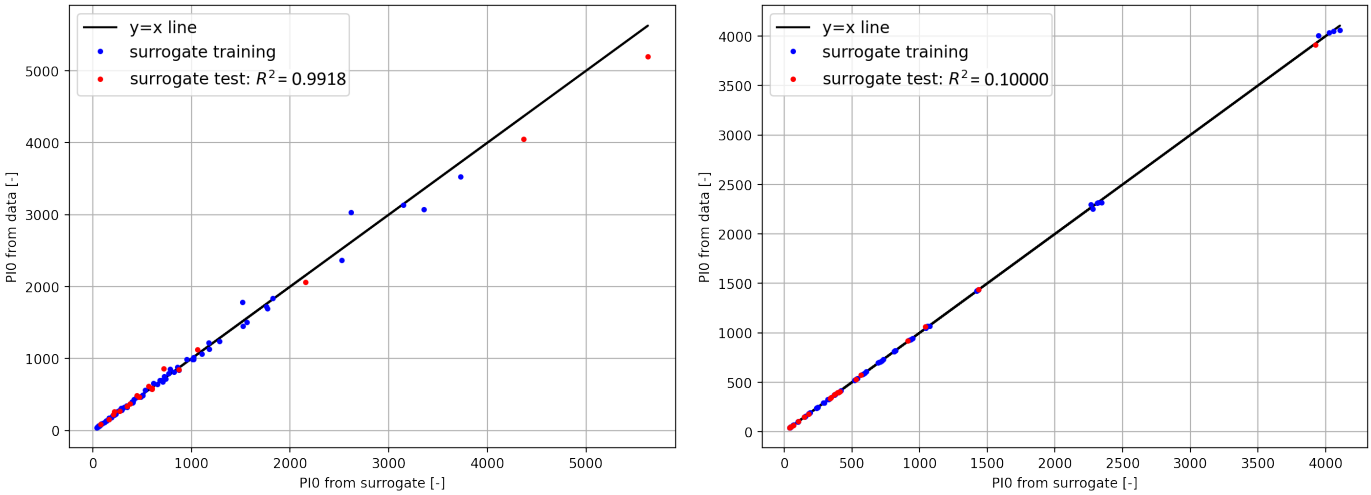

FIGURE 4.26: *Vibratory surrogate, double actuator, comparison π_0 results (eq. 4.87, 4.88) with FEM simulation results: (left) point at the intersection of housing with output rod, (right) point at the interface between both actuators*

4.3 Simulation & evaluation models

This section presents the simulation & evaluation models already introduced in section 4.1. According to the main sizing scenarios, these models are a link between the sizing parameters, the component characteristics and the constraints to satisfy during the design. These models quantify each component key design drivers (KDD) using the actuator specification and design hypothesis. As reminder, the KDDs cover four criterias: performance, endurance, imperfection and environment (section 2.2). This includes especially the transmission efficiencies and the heat losses that are of the upmost importance in such actuation technology and such application. The selected component capabilities and dimensions have to be compared according to these 4 criterias when they are applicable. The component characteristics come from the estimation models presented in section 4.2. This section is split into two parts. The first part deals with the mechanical components. The second part is for the electrical components. Fig. 4.27 basically reminds the actuator architecture.

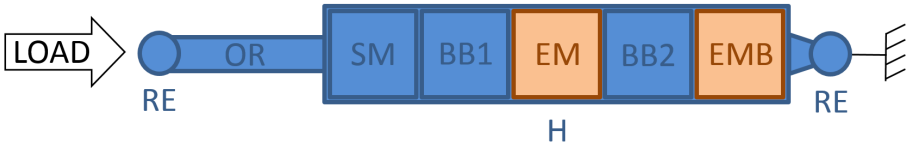

FIGURE 4.27: *Actuator architecture: mechanical components in blue, electrical components in orange*

4.3.1 Mechanical components

Section 2.2.1 of Chapter 2 introduces the key design drivers KDD of the mechanical components.

4.3.1.1 Rod end

A key design driver of the rod end is the maximum stress. The stress is directly linked to the load applied on the component.

Typically, in manufacturer catalogs, the first parameter of component selection is either the static load rating C_0 $[N]$ or the dynamic load rating C_d $[N]$ [SKF, 2011] [Shigley, 2006]. The first one corresponds to a rapid degradation i.e. an irreversible plastic deformation. The second one corresponds to a gradual degradation i.e. a given level of rolling fatigue cycles which limits the component lifetime. In the context of this thesis, the rod ends are spherical plain bearings that perform small angular amplitudes ($\ll 90°$). The gradual degradation is rather turned towards a wear than a rolling fatigue (C_d).

Thus, the selection of the rod end is reduced to a choice of static load rating C_0, higher than the maximum load given by the actuator specification:

$$C_{0,RE} \geq F_{max,spec} \tag{4.89}$$

where $C_{0,RE}$ is the key definition parameter of the rod end estimation models (scaling law, table 4.1). The rod end characteristics will be estimated, based on this parameter value.

The bore diameter of the spherical plain bearing must be greater than a given diameter $d_{axle,min}$. This diameter is an input of the design problem, a design hypothesis.

$$d_{in,spherical} \geq d_{axle,min} \tag{4.90}$$

With this inequation, the component selection is constrained to be of a minimum standard.

In appendix M, table M.1 sums up in detail the variables and relations involved for the rod end selection.

4.3.1.2 Ball bearing

This section focuses on two components: the *double row angular contact Ball Bearing (BB1)* and the *single row deep groove Ball Bearing (BB2)*. As reminder, the ball bearing design is driven by five design drivers: the maximum stress, the fatigue, the geometry, the inertia and the friction torque.

4.3.1.2.1 Loading statement First of all, before detailing the bearing selection, it is necessary to draw up a loading statement. Theoretically, only the bearing BB1 withstands all the axial load and there is no transverse load in the arrangement (architecture of reference in fig. 1.22, Chapter 1). This cannot be supposed since in reality, small misalignments, vibrations or friction in rod ends finally transfer a tranverse load and a torque to the actuator. Quantifying this additional load is difficult, as it depends on many unknowns. Therefore, the following worst-case scenario is supposed:

- the roller screw nut is jammed to its shaft.
- at the interface with the linear bushing, the output rod stands within its toleranced play. The linear bushing does not support any load.
- the actuator is fully spread out (maximum specified stoke applied).
- a transverse load is applied at the rod end of the actuator. This transverse load has a magnitude of 10% of the axial load. This value is a hypothesis involving margins. This value is in practice at the Airbus design office (aircraft actuators, Toulouse).

This scenario is summarized in fig. 4.28.

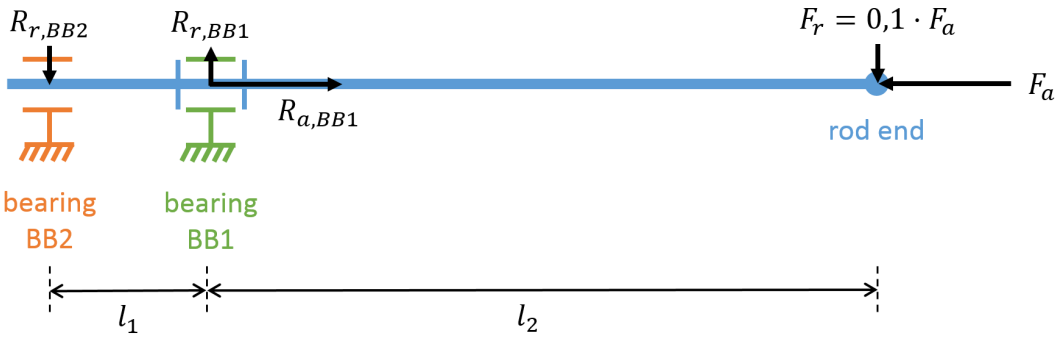

FIGURE 4.28: *Actuator ball bearing loading statement*

The torque sums, at the identified points, lead to the expression of reactions as a function of the transverse or radial load F_r $[N]$ and the axial load F_a $[N]$:

$$R_{a,BB1} = F_a \qquad R_{r,BB1} = \frac{l_1 + l_2}{l_1} \cdot F_r = k_{radial,BB1} \cdot F_a \tag{4.91}$$

$$R_{a,BB2} = 0 \qquad R_{r,BB2} = \frac{l_2}{l_1} \cdot F_r = k_{radial,BB2} \cdot F_a \tag{4.92}$$

where $F_r = 0.1 \cdot F_a$ and F_a corresponds to the specified maximum static load F_{max} $[N]$.

In the following paragrahs, the selection of the bearings BB1 and BB2 is detailed per design driver.

4.3.1.2.2 Maximum stress Firstly, two scenarios involve a critical level of stress in the component. The first scenario is an important static load application. BB1 withstands the entire actuator axial load. The maximum load given by the actuator specification must remain under the component static load capability C_0 $[N]$:

$$C_{0,BB1} \geq F_{max,spec} \tag{4.93}$$

As a reminder, the static load rating C_0 is defined in the standard ISO 76. This states that, for ball bearing, C_0 is the load that results in a contact stress of 4200 MPa at the contact of the most heavily loaded rolling element and raceway. This stress value produces a total permanent deformation roughly equal to 0.01% of the rolling element diameter [SKF, 2018a].

BB1 static sizing does not include the radial loading $R_{r,BB1}$. Indeed, in the case of a combined loading, the manufacturer indicates to use an equivalent static load P_0 $[N]$ such as $P_0 = R_r + 0.76 \cdot R_a$. This is not consistent for a particular sizing case where a long motor and a small stroke are required. The ball bearing static load capability would result to be undersized ($P_0 \leq F_a = F_{max}$).

BB2 withstands only a radial loading. Its static load capability should satisfy the specified maximum radial load:

$$C_{0,BB2} \geq F_{max,spec} \cdot k_{radial,BB2} \tag{4.94}$$

The second scenario of maximum stress is a high level of centrifugal forces which is proportional to speed. For ball bearings, the estimation models (scaling law, table 4.1) already offer a maximum speed based on a mechanical limitation

$\Omega_{max,mecha}$ $[RPM]$. This characteristic must remain higher than the maximum speed given by the actuator specification:

$$\Omega_{max,mecha} \geq \Omega_{max,spec} = \frac{v_{max}}{p} \cdot \frac{60}{2\pi} \tag{4.95}$$

where v_{max} $[m/s]$ is the specified linear speed, p $[m/rad]$ is the lead of the screw mechanism.

4.3.1.2.3 Fatigue Secondly, the mechanical fatigue drives the bearing design. It counts the rolling and pitting fatigue. The rolling fatigue is introduced in section 2.4.1. The damage due to rolling is defined as a function of a load and an equivalent number of revolutions (eq. 2.7). The rolling damage induced by the specification is estimated by:

$$D_{rolling,BB1} = F_{RMC}^3 \cdot N_{eq,rolling} \qquad N_{eq,rolling} = \frac{L_{eq}}{p \cdot 2\pi} \tag{4.96}$$

$$D_{rolling,BB2} = (F_{RMC} \cdot k_{radial,BB2})^3 \cdot N_{eq,rolling} \tag{4.97}$$

where p $[m/rad]$ is the screw mechanism lead, F_{RMC} $[N]$ and L_{eq} $[m]$ are values of the specification detailed in eq. 2.9 and eq. 2.10, $N_{eq,rolling}$ $[rev]$ is the number of revolutions representative of rolling fatigue. The pitting fatigue is introduced in section 2.4.2. It corresponds to a fluctuating load intensity applied on component without motion. This produces fatigue cycles at contact points inside the components. The pitting load is at stake in the rotating components of the actuator loading path: the ball bearing double row (BB1) and the *Screw Mechanism (SM)*. In the scope of a preliminary study, we propose to express the pitting fatigue in terms of fatigue cycles coming from an additional rolling fatigue. The fatigue cycles induced by pitting are associated to the fatigue cycles induced by the ball rolling. The number of equivalent bearing revolution must be chosen consequently to be representative of the pitting cycle number. Fig. 4.29 presents a ball bearing with the outer ring fixed to a reference.

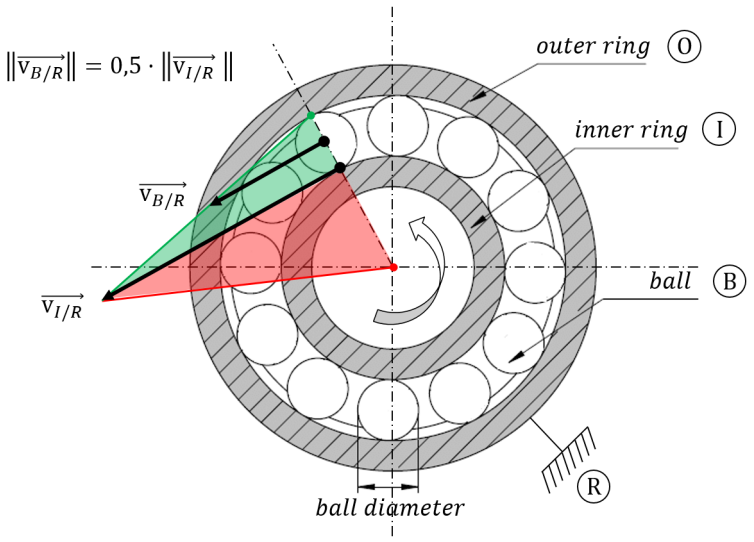

FIGURE 4.29: *Ball bearing kinematic sketch: highlight of speed fields*

It is graphically shown that the ball speed $\omega_{B/R}$ is half smaller than the inner ring speed $\omega_{I/R}$. This means that, for one ring turn, there are $n_{ball}/2$ ball passings where

n_{ball} is the number of balls. The pitting load produces a number of cycle $N_{c,pitting}$ depending on the load frequency f_{load} $[hz]$ and the actuator lifespan t_{life} $[s]$. The equivalent pitting revolution number is expressed such as:

$$N_{eq,pitting} = N_{c,pitting} \cdot k_{cycle} \quad \begin{cases} N_{c,pitting} = f_{load} \cdot t_{life} \\ k_{cycle} = \dfrac{1}{n_{ball}/2} \end{cases} \tag{4.98}$$

The pitting phenomena is identified as a fluctuating load around a static load level. The static and dynamic levels of the actuator loading are identified while analysing mission profiles from the helicopter flight tests. A maximum amplitude (peak to peak) can be determined for the dynamic level. To consider the pitting phenomena, this maximum amplitude is supposed to be applied for each pitting cycles. This amplitude value is a parameter of the actuator specification: $F_{max,pitting}$ $[N]$, named the maximum dynamic load amplitude. This choice is opened to criticism. Indeed, this choice does not consider the load static level. It is clear that a given dynamic load at a vanished static load or a given static load does not involve the same fatigue damage. The only way to consider the static load is to use Haigh's diagram. From a given static and dynamic stress level, it estimates an equivalent dynamic stress at a vanished static stress. This approach introduces a locking point since it requires to get into component stress values. We could use the scaling laws developed for elliptical Hertz contact in Appendix L and assumes a Hertz contact stress for the considered product range. Such approach will not be undertaken in this work since it is based on too many uncertainties. What is more, it gets away from the modelling complexity level of this thesis. The component stress calculation belongs to the detailed design. The supplier is entailed to perform it later in the design process cycle. In a preliminary phase, the choice is rather turned to let the engineer ajust the dynamic load value entered in specification ($F_{max,pitting}$) according to the static level if necessary.

Thus, the pitting damage stands as:

$$D_{pitting} = F^3_{max,pitting} \cdot N_{eq,pitting} \tag{4.99}$$

As a reminder from Miner's law (see eq. 2.5), the damage is linear and cumulative. The total damage from rolling and pitting is sumed up.

$$D_{total} = D_{rolling} + D_{pitting} = C^3_{d,spec} \cdot 10^6 \tag{4.100}$$

This sum leads to the expression of the specified equivalent dynamic load $C_{d,spec}$ $[N]$ given for an ISO 281 basic rating life of 10^6 revolutions.

$$C_{d,spec} = \left(\frac{D_{total}}{10^6 \cdot k_{rf}} \right)^{1/3} \tag{4.101}$$

A reliability factor k_{rf} $[-]$ is introduced to consider a survival probability upper than 90% (fig. 4.30). The selected ball bearing must verify that its dynamic load capability C_d $[N]$ remains greater than the specified dynamic load:

$$C_d \geq C_{d,spec} \quad [N] \tag{4.102}$$

Reliability	Failure probability n	Factor a_1
%	%	–
90	10	1
95	5	0,64
96	4	0,55
97	3	0,47
98	2	0,37
99	1	0,25

FIGURE 4.30: *Ball bearing reliability factor [SKF, 2018b]*

4.3.1.2.4 Geometry Thirdly, the assembly operation of the ball bearing onto the shaft has to be considered. This consists in a diameter limitation between the bore diameter of the ball bearing d_{in} $[m]$ and the screw diameter of the screw-mechanism $d_{screw,SM}$:

$$d_{in} \geq d_{screw,SM} \tag{4.103}$$

where d_{in} is the selected ball bearing characteristic.

4.3.1.2.5 Inertia Fourthly, the ball bearing contributes into the shaft rotating inertia. This contribution is mainly broken down into the inertia involved by the inner ring rotation, the inertia involved by the ball self-rotation and the inertia involved by the displacement of balls around the inner ring. The expression of the kinetic energy $\mathscr{E}_c$ enables to extract an equivalent value J_{eq} of the ball bearing inertia contribution such as:

$$\mathscr{E}_c = \mathscr{E}_{c,ring} + \mathscr{E}_{c,balls,r} + \mathscr{E}_{c,balls,t} = \frac{1}{2} \cdot J_{eq,ring} \cdot \omega_{ring}^2 \tag{4.104}$$

where

$$\mathscr{E}_{c,ring} = \frac{1}{2} \cdot J_{ring} \cdot \omega_{ring}^2 \qquad \mathscr{E}_{c,balls,r} = n_{ball} \cdot \frac{1}{2} \cdot J_{ball} \cdot \omega_{ball}^2 \tag{4.105}$$

$$\mathscr{E}_{c,balls,t} = n_{ball} \cdot \frac{1}{2} \cdot M_{ball} \cdot v_{ball}^2 \tag{4.106}$$

As a preliminary approach, we suggest to estimate the bearing inertia as the inertia of an equivalent inner ring. Its dimensions takes the bearing bore diameter as an inner diameter and the bearing mean diameter as an outside diameter. Its density is introduced as a design hypothesis. We propose to set it as the steel density.

$$J_{eq,ring} = \frac{M_{ring}}{2} \cdot \left[\left(\frac{d_{mean}}{2} \right)^2 + \left(\frac{d_{in}}{2} \right)^2 \right] \tag{4.107}$$

$$M_{ring} = \frac{\pi}{4} \cdot \left(d_{mean}^2 - d_{in}^2 \right) \cdot l \cdot \rho_{eq,ring} \tag{4.108}$$

$$d_{mean} = 0.5 \cdot \left(d_{in} + d_{out} \right) \tag{4.109}$$

where d_{in} $[m]$, d_{out} $[m]$, and l $[m]$ are the inner ring diameter, the outside diameter and width of the bearing. These dimensions are provided by the estimation models.

Using a supplier component (e.g. bearing 61804 from [SKF, 2018a]), this second approach has been compared to the first one (eq. 4.104). The comparison showed that the second approach was conservative of 28% on the estimation of the inertia $J_{eq,ring}$.

4.3.1.2.6 Friction & viscous torque Fifthly and lastly, the ball bearing contributes to motor no-load torque (fig. 4.35) with a resistant torque. This torque results

from friction and lubrication viscosity. In a preliminary study, the interest is for a reduced number of known parameters and expressions with physically meaningful expressions. This allows quantifying physical phenomena separately and make a study. Among the three manufacturers [NSK, 2013], [ScheafflerKG, 2009] and [SKF, 2018a], the set of equations from Schaeffler Group was selected. The main equation exponents has been checked to be consistent with [Maré, 2015] proposing some detailed modelling. The estimation of the total resistant torque is separated into two sets of equations.

The first set of equations is for viscosity, it depends on shaft speed taken as the specified maximum speed $\Omega_{max,spec}$ $[RPM]$ (defined in eq. 4.95). The kinematic viscosity ν_{grease} $[mm^2/s]$ is set as a design hypothesis. [ScheafflerKG, 2009] indicates that the viscosity to consider is the one of the oil basis of the grease at running temperature. Appendix Q helps in estimating an order of magnitude to this viscosity and its evolution regarding temperature. [ScheafflerKG, 2009] states the speed dependent friction as it follows:

$$\text{if } p_{vs} = \nu_{grease} \cdot \Omega_{max,spec} \geq 2000 \text{ then,} \tag{4.110}$$

$$T_{fs} = k_c \cdot p_{vs}^{2/3} \cdot d_{mean}^3 \tag{4.111}$$

$$\text{else } T_{fs} = k_d \cdot d_{mean}^3 \tag{4.112}$$

where k_c, k_d are two constants inherent to bearing type, d_{mean} $[m]$ is the mean diameter of the bearing as formulated in eq. 4.109.

The second set of equation is for dry friction, depending on loading. It consists in the estimation of a coefficient of friction μ_1 $[-]$ and a deterministic load F_1 $[N]$:

$$T_{fl} = \mu_1 \cdot F_1 \cdot d_{mean} \quad \begin{cases} \mu_1 = f(R_a, R_r, C_0) \\ F_1 = f(R_a, R_r) \end{cases} \tag{4.113}$$

where d_{mean} $[m]$ is the mean diameter as formulated in eq. 4.109. μ_1 and F_1 involve coefficients inherent to each bearing type. The manufacturer catalog [ScheafflerKG, 2009] provides them.

The total resistant torque is deduced consequently as:

$$T_f = T_{fs} + T_{fl} \tag{4.114}$$

4.3.1.2.7 Further In appendix M, tables M.2 and M.3 sum up the variables and detailed relations involved in the selection of the ball bearings BB1 and BB2.

4.3.1.3 Screw-nut mechanism

This section focuses on the SM selection. The component SM is driven by three design drivers: the maximum stress, the fatigue and the geometry. The screw inertia and the efficiency are parasitic characteristics to implement within the selection of the other components of the power transmission. The screw inertia is estimated by an estimation model (scaling law). The efficiency is the topic of the following section 4.3.1.4.

4.3.1.3.1 Maximum stress To start with the maximum stress design driver, four scenarios involve a critical level of stress in the component. An important static load application is a scenario. SM withstands the entire actuator axial load. The maximum

static load, given by the actuator specification, must remain under the component static load capability C_0 $[N]$:

$$C_{0,SM} \geq F_{max,static,spec} \tag{4.115}$$

Another scenario comes with the screw rotating at a resonance speed. The permissible critical speeds under 0 N load and under loads are provided by [ROLLVIS, 2019] with empirical equations such as:

$$\Omega_{r,0l,SM} = 3.456 \cdot 10^4 \cdot d_{s,SM} \cdot l_{s,SM}^{-2} \tag{4.116}$$

$$\Omega_{r,l,SM} = 1.6 \cdot 10^2 \cdot d_{s,SM}^{-1} \tag{4.117}$$

where $l_{s,SM}$ $[m]$ is the sum of the nut length and the application stroke. The screw rotation speed must remain under the resonance speeds:

$$\Omega_{r,0l,SM} > \Omega_{max,spec} = \frac{v_{max}}{p} \cdot \frac{60}{2\pi} \qquad \Omega_{r,l,SM} > \Omega_{max,spec} \tag{4.118}$$

where p $[m/rad]$ is the lead, Ω_i are angular speeds in $[RPM]$.

A last scenario comes with the buckling phenomena occuring for a small screw diameter, an important stroke and important loads. The supplier [ROLLVIS, 2019] provides an empirical equation to estimate the corresponding load limit:

$$F_{buckling,SM} = 2.122 \cdot 10^{10} \cdot d_{s,SM}^4 \cdot l_{s,SM}^2 \tag{4.119}$$

The maximum static load given by the actuator specification must remain under the component buckling resistance $F_{buckling}$ $[N]$:

$$F_{buckling,SM} \geq F_{max,static,spec} \tag{4.120}$$

4.3.1.3.2 Fatigue Secondly, the mechanical fatigue drives the SM design. It involves the rolling and pitting fatigue. The damage due to rolling is defined similarly to the ball bearing section 4.3.1.2 discussed previously. It is a function of a load and an equivalent number of revolutions (eq. 2.7). The rolling damage induced by the specification is estimated by:

$$D_{rolling,SM} = F_{RMC}^3 \cdot N_{eq,rolling} \qquad N_{eq,rolling} = \frac{L_{eq}}{p \cdot 2\pi} \tag{4.121}$$

where p $[m/rad]$ is the lead, F_{RMC} $[N]$ and L_{eq} $[m]$ are values of the specification detailed in eq. 2.9 and eq. 2.10.

In the scope of a preliminary study and similarly to the suggestion made for the ball bearing fatigue, we suggest to express the pitting fatigue in terms of fatigue cycles coming from an additional rolling fatigue. This suggestion keeps a homogeneous complexity level among component models. Further in the design cycle, a detailed calculation of contact stress will have to be carried out anyhow for validation. A thesis project is in progress on this fatigue concern.

Following this proposition, the corresponding number of equivalent screw revolution must be chosen consequently to be representative of the pitting cycle number. The total number of pitting cycle is given by the load frequency and the actuator lifespan. The equivalent number of revolution is:

$$N_{eq} = f_{load} \cdot t_{life} \cdot k_{cycle} \tag{4.122}$$

where k_{cycle} is the number of revolution per fatigue cycle. Now, the question is: how many fatigue cycles does a single revolution correspond to?

In the following paragraph, this question is answered for the screw mechanism.

For this purpose, it is necessary to deepen the PRS kinematic and some relevant literature concerning the PRS sizing [Sandu, 2018] [Kossi Abevi, 2013]. The diagram in fig. 4.31 presents the PRS kinematic. The different parts in relative motion are in different colors. For simplification, the roller is drawn with only 4 threads in contact with the nut and the screw.

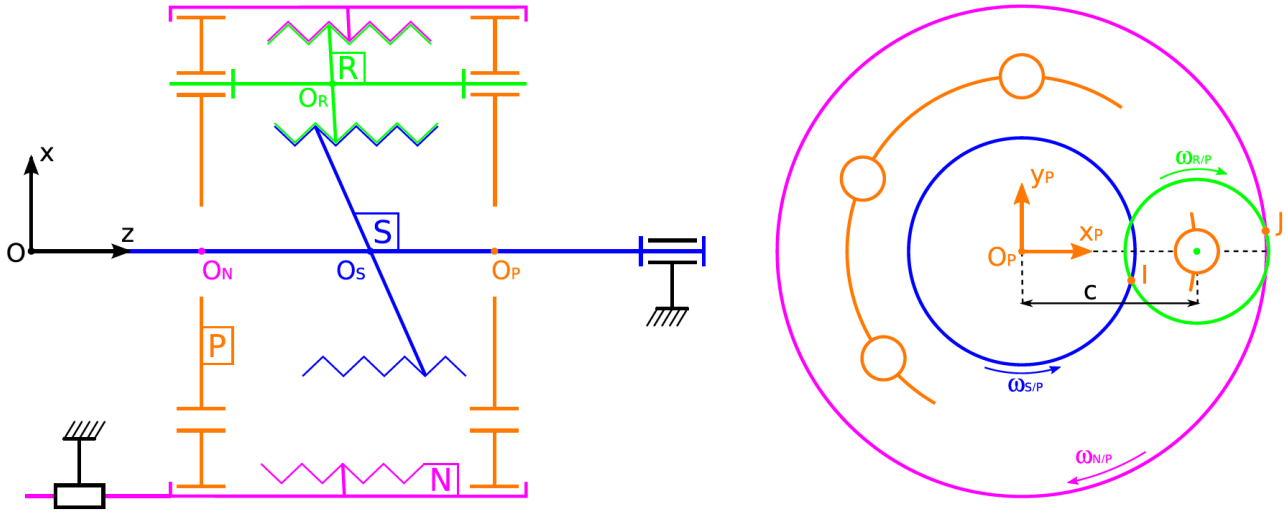

FIGURE 4.31: *Standard planetary roller screw kinematic diagram ([Sandu, 2018]) with respect to a test bench (**left**) and the planet carrier (**right**): **N**: nut, **P**: planet carrier, **R**: roller, **S**: screw*

[Sandu, 2018] suggests to characterize the PRS kinematic by mainly two coefficients: the gear (or overdrive) ratio Γ and the slip ratio ϵ. The gear ratio is defined such as:

$$\Gamma = \begin{cases} \dfrac{\omega_{N/P}}{\omega_{R/P}} = \dfrac{r_R}{r_N} & \text{if standard PRS} \quad (4.123c) \\ \dfrac{-\omega_{S/P}}{\omega_{R/P}} = \dfrac{r_R}{r_S} & \text{if inverted PRS} \quad (4.123d) \end{cases}$$

where r_i are the pitch radii of the PRS parts. The slip ratio is decribed by:

$$\epsilon = -\frac{\omega_{N/P}}{\omega_{S/N}} = \frac{\omega_{P/N}}{\omega_{S/N}} \tag{4.124}$$

The slip ratio ϵ expresses how fast the planet carrier (P) turns inside the nut (N), compared to the screw (S). In other words, it indicates how far a roller (R) goes when a full turn of screw (S) is performed. Since the planet carrier (P) never turns faster than the screw (S), the value of ϵ is within $[0, 1]$ in any case. For a standard PRS, $\epsilon = 0$ means that the planet carrier (P) does nut turn a rad with respect to the nut (N). Since the rollers (R) are geared to the nut (N), their rotation is blocked, the screw (S) is the only one to rotate. Consequently, $\epsilon = 0$ means there is no rolling occuring, the system is equivalent to a basic friction screw. When increasing ϵ, the planet carrier (P) starts to move and most of the pure sliding friction gets gradually transformed into rolling. This is one of the performance asset that makes the PRS standing out from friction

screws. ϵ is an indicator of this performance. The higher ϵ is, the more rolling and the less sliding occurs. However, the value $\epsilon = 1$ can not be physically reached. It exists a value of ϵ characterizing ideal running conditions for the mechanism where the sliding is reduced to a minimum. At that point, the value of ϵ is annotated ϵ'. Thus, the intervals become:

$$\begin{cases} \epsilon \in [0, \epsilon'] & \text{if standard PRS} \quad (4.125c) \\ \epsilon \in [\epsilon', 1] & \text{if inverted PRS} \quad (4.125d) \end{cases}$$

The inverted PRS follows the same approach but the other way around. [Sandu, 2018] suggests two methods of determining the value of ϵ': experimental or analytical. Both methods lead to the same result. The analytical method is quicker and simpler. It is based on a single formula offered by [Ma et al., 2015] and [Velinsky et al., 2009]:

$$\epsilon' = \frac{1 - 2 \cdot \Gamma}{2 \cdot (1 - \Gamma)} \tag{4.126}$$

The initial question is answered introducing the PRS variables into the eq. 4.122 such as:

$$N_{eq} = f_{load} \cdot t_{life} \cdot k_{cycle,SM} \qquad k_{cycle,SM} = \frac{1}{\epsilon' \cdot n_{roller}} \tag{4.127}$$

where n_{roller} is the number of roller.

Once the equivalent number of revolution is determined, the same set of equations already suggested for the component ball bearing are applied (eq. 4.101, 4.100 & 4.99). It leads to the expression of a specified equivalent dynamic load $C_{d,spec}$ $[N]$ given for an ISO 281 basic rating life of 10^6 revolutions. A reliability factor k_{rf} $[-]$ is introduced in the estimation to consider a survival probability upper than 90% (fig. 4.32).

The selected screw mechanism must verify that its dynamic load capability C_d $[N]$ remains greater than the specified dynamic load:

$$C_d \geq C_{d,spec} \quad [N] \tag{4.128}$$

Reliability %	f_r
90	1
95	0,62
96	0,53
97	0,44
98	0,33
99	0,21

FIGURE 4.32: *Screw mechanism reliability factor [ROLLVIS, 2019]*

4.3.1.3.3 Geometry Thirdly, the screw is subject to manufacturing constraint stemming from the assembly of the screw with the electrical motor *Electrical Motor (EM)*. The inner diameter of the motor inductor must remain bigger than the screw diameter. The following relation must be satisfied.

$$d_{out,rotor,EM} \geq d_{screw,SM} \tag{4.129}$$

4.3.1.3.4 Further In appendix M, table M.5 sums up the variables and detailed relations involved in the selection of the screw mechanism.

4.3.1.4 Efficiency

The mechanical efficiency is at the heart of the power transmission component selection since it directly drives the value of the motor torque.

Fig. 4.33 gives an overview of the EMA loss sources that impact its mechanical efficiency.

There are two sets of components to distinguish: a rotating one and translating one. The rotating set includes the motor rotor, the brake disk, the shaft, the inner races of ball bearings and the SM screw. The translating set includes the SM nut, the output rod and the rod end.

The pure tanslation is enabled by the antirotation key, making a prism pair between the SM nut and the EMA housing. It balances the nut torque that is transmitted by the screw. Consequently, it generates a friction force on the rod that depends on the torque driving the SM nut. The transverse loads at rod seal and linear bushing can be considered as negligible [Maré, 2020]. This makes their friction force nearly load-independent.

Similarly, the double row ball bearing BB1 balances the axial force produced by the nut on the screw. It generates a friction torque that depends on this axial load. Also, a transverse load applied on rod end is supposed. It results in a load dependent friction on the single row ball bearing BB2. The seals and grease of the bearings produce a load-independent friction on the rotating shaft (dry friction and viscous friction). The SM friction applies between the screw and the nut. The friction forces are reduced to their equivalent on the rotating part of the system.

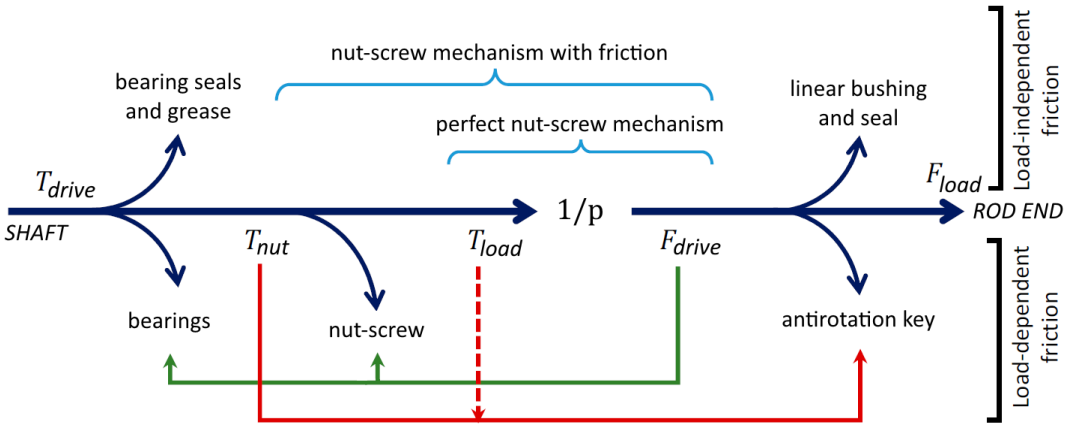

$p\ [m/rad]$: *screw lead*

FIGURE 4.33: *Mechanical loss sources on a direct drive EMA (adapted from [Maré, 2020]): arrows consider a countering load; arrows are reversed for an aiding load.*

This section focuses on the SM component efficiency.

4.3.1.4.1 Definition The efficiency has two values according to the considered running quadrant of a diagram presenting the motor torque with respect to the external load (fig. 4.35). These two values are:

- The *direct efficiency* η_d is applicable for countering loads, when the power is transmited from the motor to the external load. The screw rotation drives the nut translation.
- The *indirect efficiency* η_i is applicable for helping loads with a reversible transmission. It takes place when the power is transmitted from the external load to the motor which acts as a brake. The external load moves the rod in translation and drives the screw rotation.

Fig. 4.34 illustrates both efficiencies.

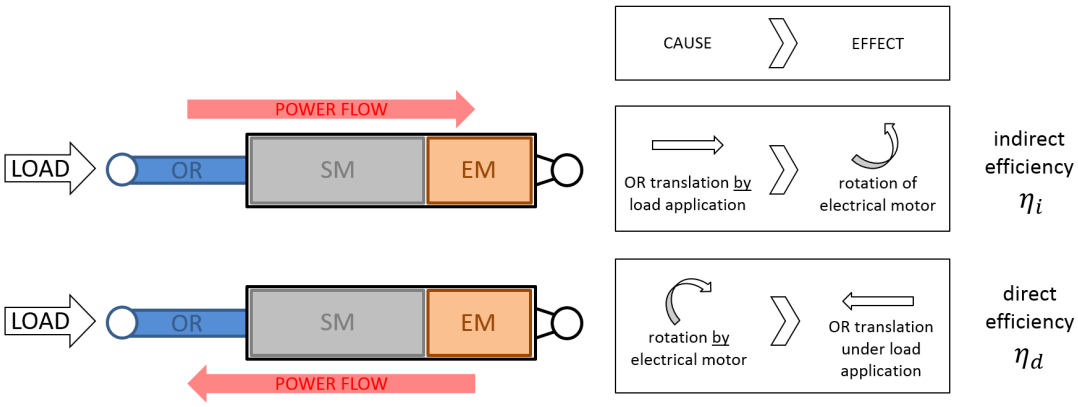

FIGURE 4.34: *Direct & indirect efficiency*

Fig. 4.35 shows, at actuator level, the evolution of the torque required for motion under an external loading. Four running zones are identified regarding torque and external load sens. The dashed white line represents the ideal case with 100% efficiency. The validity of this representation stands for a low speed and regardless inertia effects (acceleration nearly vanished). The x-axis has been normalized with the stall limit (*label 1*). The y-axis has been normalized with the motor peak torque (*red line*).

Four remarkable values can be highlighed. Fig. 4.35 displays them with labels from number 1 to 4. Each label corresponds to the following definition:

1. The **stall limit**, this is the maximum external load the actuator can move against. The speed and acceleration generated are low.
2. The **no-load torque**, this is the minimum torque required to move no load.
3. The **reversibility limit**, this is the external load required to move the actuator output rod when the electrical motor is not powered and the brake is released.
4. The **transparency limit** or reversibility with power on, this is the external load required to move the actuator output rod when the electrical motor is powered and controlled against this load.

All those 4 values have a positive and negative value. They may not be fully symmetrical. They depend on the actuator weight itself which is not taken into account in the figure. An offset can be applied to the external load too.

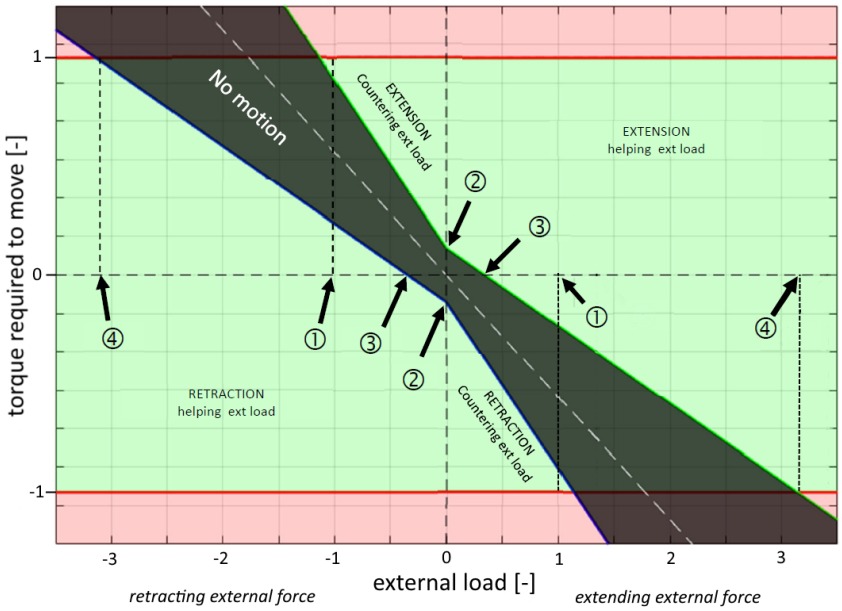

FIGURE 4.35: *Friction graph principle: required torque vs external loading*

The actuator sizing considers both efficiencies depending on the component or the discipline and the sizing scenario.

The electrical motor EM is selected with torques based on a worst-case scenario i.e. the motor motion goes with an antagonist load. The direct efficiency is considered to turn a specified load into a specified torque. Also, in any sizing case, the electrical motor must ensure a minimum torque supply. Indeed, the minimum performance expected from the actuator is to maintain its position under a maximum static load application. The torque, at stake is the one linked to the actuator reversibility limit. This running condition corresponds to the indirect efficiency.

The electromagnetic brake *Electromagnetic Brake (EMB)* is selected with a torque based on a worst-case scenario i.e. the shaft rotates with a helping load. This corresponds to an indirect efficiency.

The actuator transparency load is defined as a load stemming from the motor maximum torque capabilities converted through the lead and the indirect efficiency. The transparency load must remain higher than the specified maximum static load.

These different scenarios are illustrated in fig. 4.35.

4.3.1.4.2 Models The efficiency of the roller PRS mainly relies on the friction of the rolling elements [Karam, 2007] [Maré, 2015]. A static analysis of the screw and the nut shows that the efficiency depends of the contact friction between the screw, the rolling elements and the nut, along with the helix angle of the screw threads [Shigley, 2006]. Practically, an equivalent friction coefficient μ is identified from measures supposing a friction model of a standard friction screw (*American Trapezoidal thread (ACME)*). The helix angle λ $[rad]$ is expressed with the screw characteristics: the lead p $[m/rad]$ and the diameter $d_{s,SM}$ $[m]$.

$$\lambda = atan\left(\frac{p}{\pi \cdot d_{s,SM}}\right) \tag{4.130}$$

Thus, the direct and indirect efficiencies are formulated with respect to the friction coefficient, the pitch and the screw. [SKF, 2014] offers a set of equations presented in table 4.8. In addition, [SKF, 2008] usually considers the practical efficiency as it follows:

$$\eta_{d,p} = k_{s,\eta} \cdot \eta_d \qquad \eta_{i,p} = k_{s,\eta} \cdot \eta_i \tag{4.131}$$

where $k_{s,\mu,SM}$ $[-]$ is the safety coefficient on efficiency, taken as $0,9$. This value corresponds to an average value between the practical efficiency of a new screw and the one of a properly run-in screw.

The relations offered by [SKF, 2014] have been considered for this thesis since they come from the return-experience of a supplier. Going through some literature around actuator modelling [Karam, 2007] and [Maré, 2015], we observe that their consistency regarding this thesis modelling level is confirmed. Furthermore, we propose comparing them with the generic efficiency formulae (table 4.8, *third column*), offered by [Shigley, 2006]. They are based on a planar kinematic analogy. The comparison raises a validity criteria concerning the SKF efficiencies such as:

$$\left(\frac{1}{R}\right)^2 \gg 1 \iff \left(\frac{\pi \cdot d_0}{p}\right)^2 > 10 \iff \frac{d_0}{p} > \frac{\sqrt{10}}{\pi} \approx 1 \tag{4.132}$$

The condition must be verified when selecting the screw mechanism. The fourth column of table 4.8 gives the efficiency formulae if any thread type consideration is required.

efficiency	**SKF**	**SHIGLEY (1st level)**	**SHIGLEY (2nd level)**
direct η_d	$\dfrac{1}{1+\dfrac{\mu}{R'}}$	$\dfrac{1-\mu\cdot R}{1+\dfrac{\mu}{R}}$	$\dfrac{1-\mu\cdot R\cdot sec(\varphi)}{1+\dfrac{\mu\cdot sec(\varphi)}{R}}$
indirect η_i	$\dfrac{1}{\dfrac{\mu}{R'}-1}$	$\dfrac{1+\mu\cdot R}{\dfrac{\mu}{R}-1}$	$\dfrac{1+\mu\cdot R\cdot sec(\varphi)}{\dfrac{\mu\cdot sec(\varphi)}{R}-1}$

Notes: if T_0 is an ideal torque such as $T_0 = \dfrac{F\cdot p}{2\pi}$ $[N]$, then the real torques is defined by: $T = T_0/\eta_d$ and $T = T_0/\eta_i$. The expression of η_i might output negative values, it is required to apply an absolute value function.

TABLE 4.8: *Efficiency formulae from [Shigley, 2006] and [SKF, 2014], notation in table 4.9*

R	$[-]$	reduction ratio: $R = p/(\pi\cdot d_m)$	R'	$[-]$	reduction ratio: $R' = p/(\pi\cdot d_0)$
μ	$[-]$	equivalent friction coefficient	p	$[m/rev]$	thread lead: $p = p'\cdot n_{th}$
p'	$[m]$	thread pitch	n_{th}	$[-]$	number of thread starts
d_0	$[m]$	nominal diameter	d_m	$[m]$	pitch diameter
d	$[m]$	major diameter			$d_m = d - \frac{3\sqrt{3}}{8}\cdot\frac{p'}{2\pi} \approx d - 0.65\cdot\frac{p'}{2\pi}$
sec	$[-]$	secant: $sec(\varphi) = cos(\varphi)^{-1}$	φ	$[rad]$	half thread angle

TABLE 4.9: *Notation for efficiency formulae of table 4.8: dimensions concern the screw*

The equivalent friction coefficient μ can be modelled as a function of the helix angle (fig. 4.36). Indeed, the friction cone theory states a possible motion based on the helix angle value such as $\mu > tan(\lambda)$. This model has evolved throughout the years with SKF manufacturer [SKF, 2005, SKF, 2014]. Its first model includes a discontinuity

(fig. 4.36) and stands with a set of two equations with conditions:

$$\text{for } \lambda' < 7°,\ \mu = 0.010\ [-] \tag{4.133}$$

$$\text{for } \lambda' > 7°,\ \mu = 0.007 \cdot \lambda' - 0.040\ [-] \tag{4.134}$$

$$\lambda' = \lambda \cdot \frac{180}{\pi}\ [°] \tag{4.135}$$

Its last model is retained for this thesis since the continuous functions are always prefered in a context of optimization. This model is digitalized directly on the supplier catalog. The collected points are fitted with a polynomial function (fig. 4.36). The equation of this continuous friction model is:

$$\mu = 10^{-5} \cdot \lambda'^3 + 2 \cdot 10^{-5} \cdot \lambda'^2 + 7 \cdot 10^{-4} \cdot \lambda' + 8.8 \cdot 10^{-3}\ [-] \tag{4.136}$$

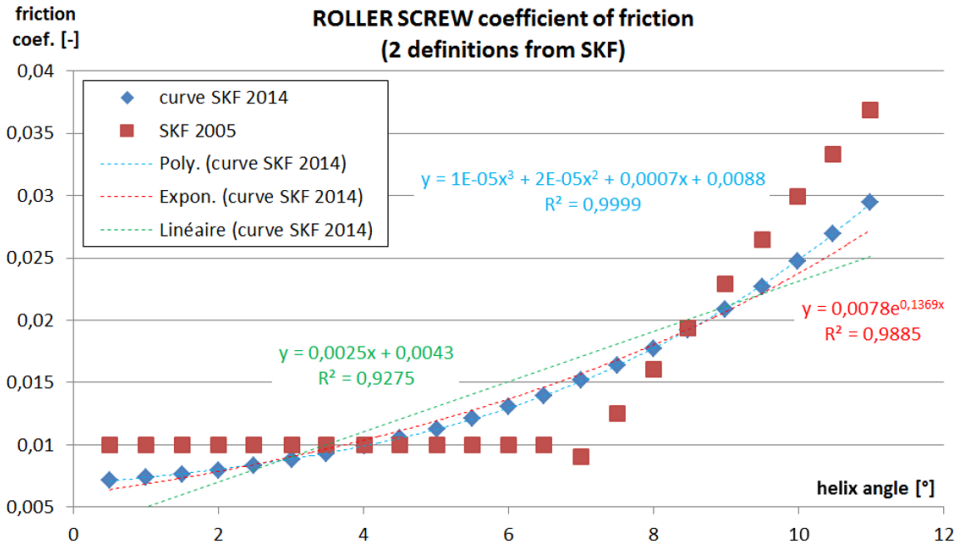

FIGURE 4.36: *Friction coefficient evolution vs helix angle*

A special attention shall be dedicated to the performance of the actuator command. Indeed, it is necessary to limit the efficiency gap between the running operations involved by the helping and countering loads. [Karam, 2007] suggests to choose a screw helix angle such as $\eta_i > 0.9 \cdot \eta_d$.

To go further in the control loop parameter concerns while keeping the preliminary design phase, we suggest the perspective introduced in the last section of Appendix A and the reference [Maré, 2022].

Finally, in [Maré, 2015], we understand that the friction coefficient varies according to three regimes of lubrication. Fig. 4.37 illustrates it. The figure links the friction coefficient to the service number SN. Sometimes, the Sommerfeld's number s can be used instead. These coefficients are defined by:

$$SN = \frac{\mu_l \cdot v_r}{P_l} \qquad\qquad s = \frac{h_l}{Ra} \tag{4.137}$$

where $\mu_l\ [Pa.s]$ is the lubricant dynamic viscosity, $v_r\ [m.s^{-1}]$ the relative velocity at contact, $P_l\ [Pa]$ the lubricant pressure at contact, $h_l\ [\mu m]$ the lubricant film thickness and $Ra\ [\mu m]$ the surface roughness (quadratic mean).

It is obvious that, for position-controlled actuators, contacts frequently operate in boundary or mixed lubrication regimes where the SN evolves dynamically in the whole domain of lubrication. We are aware that lubrication strongly impacts friction levels. However, lubrication domains still lack generic models [Maré, 2015] and involve uncertainties. This thesis will only consider dry contacts for the screw mechanism component.

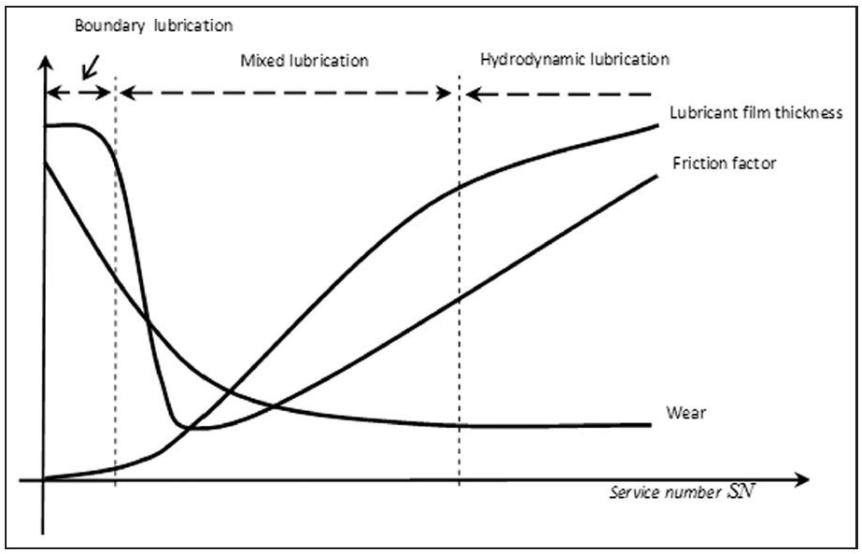

FIGURE 4.37: *Typical lubrication regimes [Maré, 2015]*

4.3.1.5 Pitting

4.3.1.5.1 First considerations The first level approach is the models described previously in the case of the ball bearing, subsection 4.3.1.2, and in the case of the screw mechanism, subsection 4.3.1.3. The pitting fatigue cycles are associated to an additional rolling fatigue i.e. an equivalent number of shaft revolutions. Each revolution corresponds to a respective number of fatigue cycles depending on the component geometry. For each component, a specified equivalent dynamic load $C_{d,spec,i}$ $[N]$ is expressed and compared to the selected component dynamic load $C_{d,i}$ $[N]$.

4.3.1.5.2 Full consideration We offer a higher modelling level in Appendix T. The methodology starts by reading a time varying load profile and extracts a rainflow matrix. The force is converted into component stress using a scaling law. The application of Haigh's diagram and Miner's law deduces an equivalent stress for a given life (e.g. 10^6 revolutions). This stress is compared to the infinite contact fatigue stress of the material. However, this last data is missing, it is an unknown to estimate with bench tests. This approach was not applied in this thesis.

4.3.1.6 Housing & output rod

This section focuses on two components: the *Housing (H)* and the *Output Rod (OR)*.

To start, the actuator housing and output rod are identified by elementary volumes as shown in fig. 4.38. This figure shows basically the actuator components. The volumes are generated to surround each component and assemble them.

The housing is identified by the volumes V4 to V12. The output rod is identified by the volumes V1 and V2. V3 is an added volume to the nut. Indeed, it allows fasteners to fix the volume V2 onto the nut.

The volumes V1 to V7 and volume V12 are hollowed cylinders. The volumes V8 to V10 are hollowed squares. The volume V11 is a squared plate.

For mass estimations, different densities are considered: steel density for volume V3 and aluminium density for the volumes V1, V2, and V4 to V12. These densities are design hypothesis.

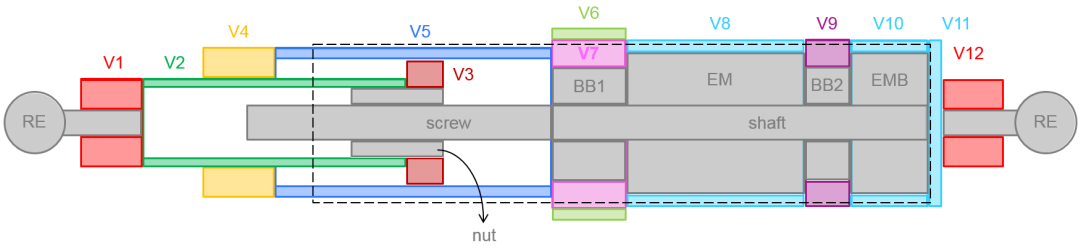

FIGURE 4.38: *Housing elementary volumes*

The structural component design is driven by two design drivers: the maximum fatigue stress, and the geometry.

Both components must check that the stress generated by the specified maximum stress is smaller than the fatigue limit $\sigma_{fatigue}\ [MPa]$ of the considered material with a safety margin $k_s\ [-]$:

$$\sigma_i \geq \sigma_{fatigue} \cdot k_s \tag{4.138}$$

The volumes V2, V7, V8 are checked regarding a traction stress. Volume V5 is checked regarding a torsion stress. The torsion moment is taken as the maximum rated torque provided by the electrical motor (EM). The thicknesses are initialized at a minimum value $e_{min}\ [m]$ set as a design hypothesis.

For the geometry, the housing and output rod volumes are driven as it follows:

- The volumes V6 to V11 are driven by the outside dimensions of the components it surrounds. The components are the bearings, the frameless motor and the brake.
- Volume V5 has its length driven by the nut length and the specified stroke. Its inner diameter is driven by the outer diameter of the nut flange (volume V3).
- Volume V4 is driven by the linear bushing length and the seal length set as a design hypothesis.
- Volume V2 is driven by the nut dimensions and the lengths of the volumes V4 and V5. When the actuator is fully retracted, the output rod and volume V4 flush.
- Volume V1 is driven by the rod end diameter $d_{RE}\ [m]$ with a design hypothesis $k_{thread}\ [-]$: $l_{V1} = d_{RE} \cdot k_{thread}$. This is for keeping sufficient in-hold threads. In practice, as a design rule in aeronautics, $k_{thread} = 1.9$ [Chevalier, 2004].

The thicknesses of these volumes might vary according to the actuator vibratory analysis presented later in section *Actuator* (section 4.3.1.8).

Finally, for the housing, the heat dissipation allowed by its skin, is a design driver too. The surface $S_{hd}\ [m^2]$ of an equivalent dissipation cylinder is used to quantify this

heat exchange. The equivalent cylinder is shown in fig. 4.38 by a black dashed line. Its length is defined by the length of the brake, the ball bearings, the electrical motor and the stroke value. Its diameter is defined by the motor diameter surrounded by the housing minimum thickness. The heat transfers are considered to be the convection and the radiation.

For convection, the following expression is used [Incropera et al., 2007]:

$$Q_{convection} = h_{conv} \cdot S_{hd} \cdot (t_{max,skin} - t_{amb}) \tag{4.139}$$

where h_{conv} $[W/m^2/K]$ is the heat transfer coefficient in convection (Appendix R offers different orders of magnitude), $t_{max,skin}$ $[^\circ K]$ is the maximum skin temperature set as a design hypothesis, and t_{amb} $[^\circ K]$ is the specified ambiant temperature.

For radiation, the following expression is used [Incropera et al., 2007]:

$$Q_{radiation} = \epsilon_{rad} \cdot \sigma_{SB} \cdot S_{hd} \cdot \left[(t_{max,skin} + 273)^4 - (t_{amb} + 273)^4\right] \tag{4.140}$$

where ϵ_{rad} $[-]$ is the emissivity set as a design hypothesis, and σ_{SB} $[W.m^{-2}.K^{-4}]$ Stefan-Boltzmann's constant.

The total housing dissipation is the sum of the dissipation by convection and radiation. In the worst-case scenario, this must balance the total heat generated by the actuator components:

$$Q_{convection} + Q_{radiation} \geq Q_{EM} + Q_{EMB} \tag{4.141}$$

where Q_{EM} $[W]$ and Q_{EMB} $[W]$ are the heat generated by the electrical motor and the electromagnetic brake.

In appendix M, tables M.4 and M.1 sum up the variables and detailed relations involved in the selection of the housing and the output rod.

4.3.1.7 Antirotation Key & linear bushing

This section focuses on two components: the *Antirotation Key (AK)* and the *Linear Bushing (LB)*.

Firstly, the antirotation key is considered for its parasitic contribution into the actuator performance. Indeed, the contact interface between nut and key creates a resistance by friction as the nut slides all along. This friction force is supposed to be applied at the furthest radial point it can be i.e. the inner radius of the housing volume V5. This force is estimated by the application of the motor maximum rated torque $T_{max,EM,rated}$ $[Nm]$. The friction force is expressed as the product of a friction coefficient and a normal force:

$$F_{f,AK} = \mu_{AK} \cdot \frac{T_{max,EM,rated}}{d_{in,V5}/2} \tag{4.142}$$

where μ_{AK} $[-]$ is a friction coefficient set as a design hypothesis. For instance, a contact between steel parts with basic greasing gives a value $\mu_{AK} = 0.1$ (other contacts are given in Appendix S). The torque induced by this friction force is:

$$T_f = \frac{F_{f,AK} \cdot p}{\eta_{d,SM}} \tag{4.143}$$

where the lead p $[m/rad]$ and the direct efficiency $\eta_{d,SM}$ $[-]$ are the characteristics of the screw mechanism. The efficiency is chosen direct to consider the worst-case running quadrant.

Secondly, the linear bushing is driven by its pU factor (pressure speed factor). It represents in fact a power by unit of surface. As mentioned into the introduction of a previous section 4.3.1.2, they are many uncertainties to estimate the force developed at the interface of linear bushing and output rod. Consequently, a normal force $F_{n,LB}$ $[N]$ is set as a design hypothesis. The bushing dimensions are given by the outer diameter of the output rod (volume V2) and a length taken as a function of this diameter:

$$l_{LB} = k_{rld,LB} \cdot d_{out,V2} \tag{4.144}$$

where $k_{rld,LB}$ $[-]$ is the ratio of the linear bushing length out of the linear bushing diameter. This ratio is set as a design hypothesis. Thus, the bushing inner surface S_{LB} $[mm^2]$ is known. Because of running clearance and strain, two cylinders, one in the other, never define a contact surface exceeding half of the surface at the interface. Therefore, the contact surface $S_{c,LB}$ $[mm^2]$ is $S_{c,LB} = S_{LB}/2$. The bushing pU factor is deduced by the product of the specific pressure and a linear speed chosen to be the specified maximum speed v_{max} $[m/s]$:

$$pU = \frac{F_{n,LB}}{S_{c,LB}} \cdot v_{max} \leq pU_{spec} \tag{4.145}$$

The pU capability depends on the material or coatings applied into it. There is a wide assortment fitting all application cases [GGB, 2015] [SKF, 2010]. The estimated pU factor must remain under its specified value linked to a bushing technology. This condition will not be part of the sizing constraints guiding the design. The engineer will be informed of the pU value to be aware of any risk threatening this component.

Furthermore, similarly to the antirotation key, a parasitic torque is induced by the friction force developed at the bushing interface. This force relies on the coefficient of friction which varies according to the bushing coating and grease [GGB, 2015] [SKF, 2010]. A coefficient of friction μ_{LB} is set as a design hypothesis for the calculation. The friction force is:

$$F_{f,LB} = \mu_{LB} \cdot F_{n,LB} \tag{4.146}$$

The conversion into torque $T_{f,LB}$ $[Nm]$ follows the same equation than eq. 4.143. This parasitic torque estimation is considered within peak and continuous motor torque estimations.

In appendix M, table M.6 sums up the variables and detailed relations involved in the selection of the antirotation key and the linear bushing.

4.3.1.8 Actuator

This section takes a back view and focuses onto the *actuator (ACT)* as a single component gathering all previously mentioned components. Three design drivers come up: the vibration stress, the transparency load and the reflected inertia.

Firstly, the stress induced under vibrations is a design driver for actuator housings. For a given level of vibration, the finer and the longer is the actuator, the higher are the induced stresses. To assess this design driver, the surrogate models detailed in the section 4.2.4 are used. They estimate dimensionless maximum stresses π_0 for a single actuator (model of eq. 4.86) and for a double actuator (model of eq. 4.87 & 4.88).

These models take the following variables as inputs: the output rod and housing thicknesses (volume V2 and V5), the output rod inner diameter (volume V2) and the actuator total length taken in full extension.

The stress results are brought back to their regular dimension with the eq. 4.82. This involves three other parameters set as design hypothesis: a quality factor Q_m $[-]$, a vibratory acceleration G_{vib} $[m/s^2]$ and a material density ρ_{vib} $[kg/m^3]$. This density shall be consistent with the material used in *Housing (H)* and *Output Rod (OR)*. The eq. 4.147 sums that all.

$$\sigma_{vib,i} = \pi_0(d_{in,V2}, L_{max,ACT}, e_{V2}, e_{V5}) \cdot Q_m \cdot G_{vib} \cdot d_{in,V2} \cdot \rho_{vib} \tag{4.147}$$

where $d_{in,V2}$ $[m]$ is the inner diameter of volume V2, $L_{max,ACT}$ $[m]$ is the distance between rod end centers when the actuator is fully deployed, e_{V2}, e_{V5} $[m]$ are the thicknesses of volumes V2 and V5.

The housing and the output rod shall be sized with margins regarding to an infinite fatigue limit. Thus, the sizing scenario follows the condition already set in the eq. 4.138.

Secondly, it is important to make sure that the tansparency load is not lower than the specified maximum static load F_{max} $[N]$. The tansparency load is explained in label 4 of fig. 4.35. This load induces a torque at motor level and the maximum motor torque should balance it. To increase design margin, the parasitic torques from the bearings, the antirotation key, and the linear bushing are not taken into account. They are braking torques to stop the motion induced by the load. In addition, the motor torque is considered with its reduced capabilities due to temperature (derating). The expression of the transparency load is:

$$F_{transparency} = T_{max,EM,derated} \cdot \frac{\eta_{i,SM}}{p} \geq F_{max} \tag{4.148}$$

where $\eta_{i,SM}$ $[-]$ is the inverse efficiency (fig. 4.34), p $[m/rad]$ is the lead of the screw mechanism.

Thirdly, the actuator is installed on-board and attached to structural elements. A maximum reflected inertia is usually specified to prevent overloading scenarios in case of degraded running conditions.

The actuator reflected inertia is an equivalent mass. Its formulation is deduced from the conservation of the kinetic energy expressed upstream and downstream the screw mechanism (a torque to force converter). The eq. 4.149 derives it:

$$\frac{1}{2} \cdot J_{total} \cdot \omega^2 = \frac{1}{2} \cdot M_{eq} \cdot \dot{x}^2 \implies M_{eq} = \frac{J_{total}}{(\dot{x}/\omega)^2} = \frac{J_{total}}{p^2} \tag{4.149}$$

where M_{eq} $[kg]$ is the actuator reflected inertia moving at a linear speed $\dot{x}$ $[m/s]$, J_{total} $[kg.m^2]$ is the total actuator inertia (eq. 4.150) spinning at a speed $\omega = \dot{x}/p$ $[rad/s]$. The total actuator inertia is the sum of the inertia from rotating parts (motor rotor, screw, braking disk, bearing rings) and the reflected inertia from parts moving linearly (nut, output rod, rod end, load mass):

$$J_{total} = \sum_i J_{rotative,part,i} + \sum_j M_{linear,motion,part,j} \cdot p^2 \tag{4.150}$$

The actuator reflected inertia M_{eq} must not exceed the specified value.

In appendix M, table M.6 sums up the variables and detailed relations involved in the selection of these specificities of the actuator.

4.3.2 Electrical components

Section 2.2.2 of Chapter 2 introduces the key design drivers KDD of the electrical components.

4.3.2.1 ELECTRICAL MOTOR

The motor technology considered in this section is a BLDC synchronous motor of cylindrical type.

The motor is selected according to 4 key design drivers: the continuous motor temperature, the magnetic saturation, the rotor magnet maximal stress and the electrical supply limitations. Some key motor characteristics correspond to each of these design drivers. The main motor characteristics come from the estimation models (scaling laws, table 4.2). The sizing scenarios assess the compliance of the motor characteristics with the specification. Therefore the specification is adapted at the motor level. The following paragraphs introduce by design driver, the relations formulating the motor characteristics, its specification and its selection.

In appendix M, table M.7 presents in details these relations. The relations are classified per key design driver with the specification and design hypothesis involved into them. The sizing scenarios are presented, they link by inequalities the parameters estimated for the motor and other components with the specification. To make it easier to read, the equation members linked to specification, design hypothesis, sizing scenarios and optimization are set in different colors. The colors are red, blue, orange and cyan respectively. The symbol $f_{SL}()$ refers to the scaling laws mentioned in section 4.2 (estimation models).

4.3.2.1.1 First consideration To ensure a motor design margin, the torque estimations consider an antagonist load. This is the worst-case scenario during the operation.

This scenario is represented in fig. 4.35 by the two slants, up and down initiated at the points marked by the label numbered 2.

4.3.2.1.2 Magnetic saturation As mentioned in Chapter 2 section 2.2.2, the motor peak torque is an indicator of the magnetic saturation design driver. From the specification inputs, three scenarios of peak torque are estimated. These scenarios are:

- a slow motion under loading (stall load F_{stall}),
- a motion at maximum acceleration a_{max} without any load application,
- a motion with an acceleration a_{PRmax} under a load F_{PRmax}.

The worst-case scenario is considered. The required peak torque is given, adding to it the parasitic torques: peak iron losses torque, friction and viscous torques from bearing, friction torques from antirotation key and linear bushing.

Thus, the motor peak torque $T_{peak,EM}$ must check:

$$T_{peak,EM} \geq T_{peak,spec} + T_{parasitic} \tag{4.151}$$

The motor peak torque is the key design parameter for the estimation models. The optimization loop acts on it. Its value is initialized with the reversibility limit i.e. the torque necessary to maintain the actuator position under the maximum static load F_{max}.

4.3.2.1.3 Continuous motor temperature As mentioned in Chapter 2 section 2.2.2, the motor continuous temperature is directly linked to continuous torque and heat generation. The specified continuous torque is determined by the RMS averaging of the motor torque $T(t)$. This,

$$T(t) = \frac{F(t) \cdot p}{\eta_B} + \frac{J_{total} \cdot a(t)}{p} \tag{4.152}$$

$$T_{RMS,spec} = \sqrt{\langle T(t)^2 \rangle} = \sqrt{\left(\frac{F_{RMS} \cdot p}{\eta_d}\right)^2 + 2 \cdot \frac{J_{total}}{\eta_d} \cdot \overline{PR} + \left(\frac{J_{total} \cdot a_{RMS}}{p}\right)^2} \tag{4.153}$$

$$\langle\,\rangle \text{ is a notation of average: } \langle X(t) \rangle = \frac{1}{t_T} \cdot \int_0^{t_T} X(t) \cdot dt \tag{4.154}$$

where p $[m/rad]$ is the screw lead, η_B $[-]$ is the Boolean efficiency considering the sign of $F(t)$ (see eq. 2.16). A direct efficiency is chosen in $T_{RMS,spec}$ for estimations with upper margins. J_{total} $[kg.m^2]$ is the total rotating inertia as expressed in eq. 4.150. This RMS expression is derived in eq. I.4 of Appendix I.

The required continuous torque must include the actuator parasitic torques: the mean iron losses torque, the friction and viscous torques from the bearings, the friction torques from the antirotation key and the linear bushing. Thus, the motor continuous torque $T_{RMS,EM}$ must check:

$$T_{RMS,EM} \cdot k_{derating} \geq T_{RMS,spec} + T_{parasitic} \tag{4.155}$$

To take into account the specified thermal environment, the motor torque capability is modified using a derating coefficient $k_{derating}$. Some details about this coefficient are given in Appendix N.

As mentioned by [Grellet, 1989] and [Jufer, 1996], the copper and iron losses bound the motor continuous operation domain (fig. 2.4). As a first simplification, the heat generated by iron and Joules' losses is supposed to have both the same effect on motor temperature despite their different location. Indeed, Joules' losses are based in the winding; meanwhile the iron losses take place into the iron lamination stacks. At steady state, the total heat generated by the electrical motor (EM) is the sum of Joules and iron losses such as:

$$Q_{EM} = Q_{Joules} + Q_{iron} = \alpha \cdot T^2 + \beta \cdot \omega_e^b \tag{4.156}$$

where α and β are respectively the Joules and iron losses coefficients, ω_e is the electrical speed. As mentioned in section 2.5.1.1 and detailed in Appendix K section K.1.8.3, a value of $b = 1.5$ can be taken. The scaling laws, presented in table 4.2 give α and β. Some details on these coefficients are given in Appendix K, section K.1.9.

The mean value of the generated heat can be expressed in terms of the specification input values:

$$\begin{aligned} < Q_{EM} > &= \alpha \cdot \langle T^2 \rangle + \beta \cdot \langle \omega_e^{1.5} \rangle \\ &= \alpha \cdot T_{RMS}^2 + \beta' \cdot \omega_{iron}^{1.5} \end{aligned} \tag{4.157}$$

where $\beta' = \beta \cdot n_{poles}^{1.5}$, T_{RMS} is the equivalent continuous torque as shown in eq. 4.153 and $\omega_{iron} = v_{iron}/p$. The definition of v_{iron} is introduced in Chapter 2 (eq. 2.14).

The total heat generation is the sum of the generated by the *Electrical Motor (EM)* and the *Electromagnetic Brake (EMB)*. This heat has to be dissipated by the *Housing (H)*. Thus, the following inequality stands:

$$Q_{EM} + Q_{EMB} \leq Q_{housing} \tag{4.158}$$

Further to an effect on the motor temperature, the iron losses have an effect on the motor output torque. Indeed, the iron losses induce an iron torque T_{iron} $[Nm]$ which can be determined by:

$$Q_{iron} = \beta' \cdot \omega^b = \beta' \cdot \omega^{b-1} \cdot \omega = T_{iron} \cdot \omega \implies T_{iron} = \beta' \cdot \omega^{b-1} \tag{4.159}$$

For the particular case of a motor with mainly Eddy's current losses ($b = 2$), the iron torque is $T_{iron} = \beta' \cdot \omega$. The value of β' becomes a coefficient of viscous friction $[Nm/(rad/s)]$. The iron losses act as a viscous friction.

This effect on the motor torque is not negligeable. The product catalog from SSD Drives Parvex NK confirms it. The catalog includes BLDC motors of motor constant $K_m \in [1.3 \cdot 10^{-2}; 9.2]$ $(Nm)^2 \cdot W^{-1}$, rated torque $T_{rated} \in [1.2; 22]$ Nm and rated speed $\Omega_{rated} \in [3200; 8400]$ RPM. The torque related to iron losses is estimated as $[1.5 - 4]\%$ of rated torque. This increase of torque has a bigger impact on the losses. A limited development highlights it:

$$(T \cdot (1 + 0.03))^2 = T^2 \cdot (1 + \underbrace{2 \cdot 0.03}_{} + \epsilon_e)$$

If the iron torque contributes at 3% of rated torque, its contribution on losses is doubled (6%). The iron torque contribution must be taken into account.

4.3.2.1.4 Rotor magnet maximal stress

As mentioned in Chapter 2 section 2.2.2, the motor rotor mechanical resistance is directly linked to maximum speed.

Using the lead of the screw mechanism, the specification gives the required maximum speed. The estimation model (scaling law, table 4.2) provides the motor maximal speed which must be greater than the specified maximum speed:

$$\Omega_{max,EM} \geq \Omega_{max,spec} \tag{4.160}$$

4.3.2.1.5 Electrical supply

The electrical supply limitations are part of motor design drivers. It is necessary to check that the motor remains with a voltage and current flow under the specified maximum values.

Firstly, the motor winding characteristics are determined. Since the specification provides a maximum torque $T_{peak,spec}$ and a maximum current flow I_{max}, the torque constant K_t $[Nm/A]$ is known. The winding resistance, inductance and the rotor pole number are obtained by the estimation model (scaling law, table 4.2). The motor characteristics are given assuming a *Field Oriented Control (FOC)* command.

Secondly, the maximum voltage is estimated. A simple motor model is chosen: Behn-Eschenburg's model [Multon, 2010]. It proposes to model the electrical motor as an equivalent circuit with a voltage supply, a resistance and a cyclic inductance. More details are available in Appendix O. The maximum motor voltage is estimated considering a conservative scenario: the specified maximum current flows in the winding whilst the rotor spins at the specified maximum speed. Each contributor of

voltage is estimated separetly. The voltage linked to *Back Electro Motive Force (BEMF)* V_{BEMF} is proportional to the rotor speed using the speed constant K_e. The voltage linked to resistance V_R is proportional to current using the resistance. The voltage linked to the inductance V_L is proportional to the current and rotor speed. Because of the use of a FOC command at minimized copper losses, the BEMF and the current are in phase meanwhile the term linked to inductance is in quadrature. The motor voltage results in:

$$V_{total} = \sqrt{(V_{BEMF} + V_R)^2 + V_L^2} \tag{4.161}$$

The motor voltage at bus level is obtained by conversions corresponding to a generic architecture of the power path for *Power–by–Wire (PbW)* actuators (Appendix P).

Finally, the estimated maximum motor bus voltage is checked to be smaller than the specified maximum bus voltage:

$$V_{dc,bus,EM} \leq V_{dc,bus,spec} \tag{4.162}$$

4.3.2.1.6 Cogging torque The cogging torque (also named "*couple de détente*" in French) is a torque disturbance based on the magnetic attraction of the magnets to the teeth of the inductor.

[KOLLMORGEN, 2003] states that the cogging torque is minimized in the motor design by a strategic selection of slot/pole combinations and by skewing the laminations in the armature.

Danaher's catalog [KOLLMORGEN, 2003] provides a value of max cogging torque peak to peak. The ratio with the continuous torque among the serie RBE(H) gives $[7-24]\%$ for motor diameters $d < 40mm$ and $[1-4]\%$ for diameters $d > 40mm$ up to $d = 240mm$.

Since the cogging torque either helps or counters the motor torque, its mean value is equal to zero. It is not worth considering it in the scope of a preliminary study. However, it is a relevant consideration if any study about resonance modes is carried out.

4.3.2.1.7 Air gap losses The air contained between the rotor and the stator has a damping effect on rotor spinning. The following estimation provides an order of magnitude of this effect.

Basically, a viscous torque is defined such as:

$$T_v = \frac{d_r}{2} \cdot F_{air} \qquad F_{air} = -\eta_{air} \cdot S_r \cdot \frac{dv}{dz} \tag{4.163}$$

where the rotor outer surface $S_r = \pi \cdot d_r \cdot l_r \ [m^2]$ is defined with the rotor dimensions $(d_r,\ l_r)\ [m]$. η_{air} is the dynamic viscosity $[kg \cdot m^{-1} \cdot s^{-1}]$, dv the circumference speed $[m/s]$ and dz the air gap $[m]$. η_{air} is given by [Nancy-Metz, 2021] and [Wikipedia, 2021] as an order of magnitude of $\eta_{air} = 2.10^{-5}\ [kg \cdot m^{-1} \cdot s^{-1}]$ for air at atmospheric pressure and temperature $[30-130]°C$.

Considering the characteristics of an electrical motor from Kollmorgen (RBE(H) 01215, 8 poles, the continuous torque $T_c = 0.6\ N.m$, $d_r = 30\ mm$, $l_r = 57\ mm$, $\Omega_{max} = 18000\ RPM$) and an air gap of $1\ mm$, the numerical application gives $T_v = 4.10^{-3}\ N.m$ i.e. $T_v \approx 0.7\% T_c$.

This effect can be neglected in a preliminary design context. However, it is important to take it into account when the cooling is based on oil flow (η_{oil} is 10^2 times higher than η_{air}) or when dealing with stability of a closed loop control.

In appendix M, table M.7 sums up the variables and detailed relations involved in the selection of the electrical motor.

4.3.2.2 ELECTROMAGNETIC BRAKE

The considered electromagnetic brake is the power-off brake as presented in Chapter 1.

The brake design is mainly guided by two design drivers: the continuous holding pressure the brake can apply on its disc and the heat the coil losses generate.

The brake main characteristics are determined by the estimation models (scaling laws, table 4.2). The characteristics of interest for the design drivers are the braking torque and the heat generation. These characteristics must be compared to the specified values.

To formulate the specified braking torque, the following scenario is chosen. The braking torque is applied when no current flows in the actuator anymore. The shaft is supposed to spin at the specified maximum speed and to be helped by the application of the specified maximum static load. The brake must stop the shaft within a short period of time t_{EMB} $[s]$. This sizing scenario involves design margins. A motor runaway with a motor maximum acceleration is not a possible scenario for a *Controlled–Monitored (CON-MON)* motor configuration. Moreover, the motor can behave as a generator which acts as an "additional brake" if a failure reconfiguration mode exists in the actuation system [Maré, 2017].

Thus, the electromagnetic brake design is driven by the following specified torque:

$$T_{max,EMB,spec} = T_{load} + T_{speed} \qquad T_{load} = \frac{F_{static,max} \cdot p}{\eta_i} \tag{4.164}$$

$$T_{speed} = J_{total} \cdot \frac{d\omega}{dt} = J_{total} \cdot \frac{v_{max}/p}{t_{EMB}} \tag{4.165}$$

where $F_{static,max}$ $[N]$ and v_{max} $[m/s]$ are the specification inputs, p $[m/rad]$ the lead of the screw mechanism, and η_i $[-]$ its indirect efficiency. The total inertia J_{total} $[kg.m^2]$ gathers the rotating inertia and the reflected mass as expressed in eq. 4.150. The time to stop t_{EMB} is a design hypothesis. Because of the safety function of the brake, the torque to stop does not include the friction torque induced by the bearings, antirotation key and the linear bushing.

The brake heat generation occurs continuously as long as the actuator is energized. With motor losses, it takes part of the heat the actuator housing must dissipate (eq. 4.158).

In appendix M, table M.8 sums up the variables and detailed relations involved in the selection of the electromagnetic brake.

4.4 Conclusion

This chapter mentioned all the necessary models chosen for the preliminary sizing of a direct drive actuator as presented in fig. 1.22 of Chapter 1.

The scaling law presented in the estimation models are interesting and precious tools in a preliminary design phase. Indeed, they limit drastically the number of design parameters while having good estimation capabilities based on a single reference component. What is more, the power law shape is pedagogically appreciated for interpreting results.

The estimation and evalutation models showed how the actuator specification was brought from a system level to a component level and specify each component. The component specification requires design hypothesis and the characteristics of other components.

The following chapter introduces how all these models can be assembled together to perform a sizing loop and optimize the actuator final mass.

Chapter 5

Sizing code

The previous Chapter focused on modelling the components. Now, this Chapter takes a back view at the system level. It shows how sorting out each model within a workflow to finally estimate a total actuator mass and minimize it. The *Electromechanical Actuator (EMA)* is a multidisciplinary system with inter-discipline couplings. The use of *Multidisciplinary Design Optimization (MDO)* methods is required.

This Chapter firstly addresses a brief overview of the MDO world. It mentions where the MDO problem of the actuator preliminary sizing is and the choices undertaken. Secondly, it shows the difficulties met in this MDO problem and how the chosen MDO architecture gets away with them. Thirdly, the design graph representation is introduced to study each component interaction in the whole sizing process. Fourthly, the entire sizing execution steps are presented. The fifth section shows how the preliminary sizing code was implemented into an user-friendly tool. The last sections bring some elements of validation and two applicative study cases.

5.1 MDO state of the art

This section draws an overview of the MDO field in order to see where the choices, made for the actuator preliminary sizing, stand.

5.1.1 Introduction

MDO appeared in the 80's, motivated by the necessity to tackle more and more complex design systems while reducing the lead-time and improving the robustness as well as the accuracy of final design data [Gazaix et al., 2017]. Also, there was an intention to explore more broadly the design space in order to generate innovative concepts and make significant breakthroughs with the current state-of-the-art. This was no more achievable in mono-discipline approaches. The implementation of a methodology from the very early steps and throughout the design process became necessary [Gazaix et al., 2017]. This enables system designers to handle interactions between multiple physical and technological disciplines, and to optimize them at the same time.

5.1.1.1 Optimization problem

The MDO problem is a standard constrained non-linear programming problem as presented in fig. 5.1. The problem must find the values of the design variables x that maximize or minimize a particular objective function f, subject to the constraints c_i. The design variables x are unknown in this problem. The constraints c_i are equalities or inequalities, bounding the design variables or the system functionalities.

The choice of the objective, the constraints, and even the variables to change in a given system is up to the system designer. The modeled behavior of each component, or discipline, within the system is up to the discipline designer. The disciplines have a broad range of complexity from analytical equations to highly detailed physics-based simulation.

An optimization problem always goes with an optimizer i.e. an optimization algorithm. It is an iterative procedure aiming at solving a numerical optimization problem (fig. 5.1). The starting point x_0 is usually provided by the user, it is named the *initial guess*.

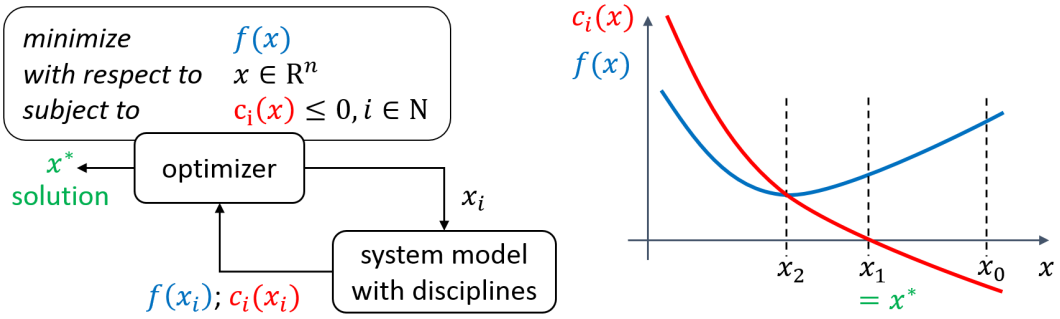

FIGURE 5.1: *MDO problem basics*

5.1.1.2 Coupling

One of the major challenges of MDO formulations is to deal with the multidisciplinary couplings, or algebraic loops, inherent to a design problem. The image of "the snake biting its tail" illustrates a coupling. Indeed, the problem disciplines are mutually interdependent: one discipline analysis requires the outputs of another as an input. Furthermore, the objective and constraint functions, in general, depend on both the design variables and the analysis outputs from multiple disciplines.

To illustrate the idea of coupling or coupled problem, the simple study case of an EMA electrical motor sizing is chosen. This problem is presented in eq. 5.1. The problem is set to minimize the motor mass while satisfying a required maximum rotating speed with an unique design variable: the screw mechanism lead. The dynamic component of the motor torque is dependent on the inertia whilst the motor inertia estimation is dependent on the motor torque. The difficulty stems from one coupling variable: the motor inertia J_{EM}.

$$
\begin{cases}
\text{minimize objective function} & M_{EM} = M_{EM,ref} \cdot \left(\frac{T_{EM}}{T_{EM,ref}} \right)^{3/3.5} & (5.1c) \\
\text{varying the design variable} & p\ (lead)\ [m/rad] & (5.1d) \\
\text{subject to bound constraint} & min \leq p \leq max\ [m/rad] & (5.1e) \\
\text{subject to global constraint} & c_1 = \Omega_{max,EM} - v_{max}/p \geq 0 & (5.1f) \\
\text{discipline 1 gives} & T_{EM} = \left[\left(\frac{F_{RMS} \cdot p}{\eta_d} \right)^2 + \frac{2 \cdot J_{EM} \cdot \overline{PR}}{\eta_d} + \left(\frac{J_{EM} \cdot a_{RMS}}{p} \right)^2 \right]^{0.5} & (5.1g) \\
\text{discipline 2 gives} & J_{EM} = J_{EM,ref} \cdot \left(\frac{T_{EM}}{T_{EM,ref}} \right)^{5/3.5} & (5.1h) \\
\text{discipline 3 gives} & \Omega_{max,EM} = \Omega_{max,EM,ref} \cdot \left(\frac{T_{EM}}{T_{EM,ref}} \right)^{-1/3.5} & (5.1i)
\end{cases}
$$

To quickly visualize graphically the problem organization and to identify couplings between disciplines, the N^2-diagram is very useful [Shishko and Aster, 1995]. It is a causal diagram made out of entities (the blocks) and interactions (the arrows) following the organization convention presented in fig. 5.2. The inputs of the blocks are represented by vertical arrows while the outputs must be horizontal arrows. The N^2-diagram of the EMA problem presented in eq. 5.1 is shown in fig. 5.3 under an *Extended Design Structure Matrix (XDSM)* representation [Lambe and Martins, 2012]. The coupled problem is highlighted by the black arrows making a loop.

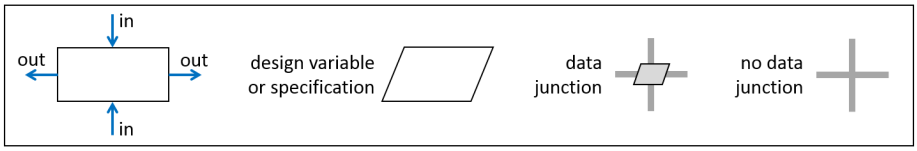

FIGURE 5.2: *N^2-diagram organization conventions*

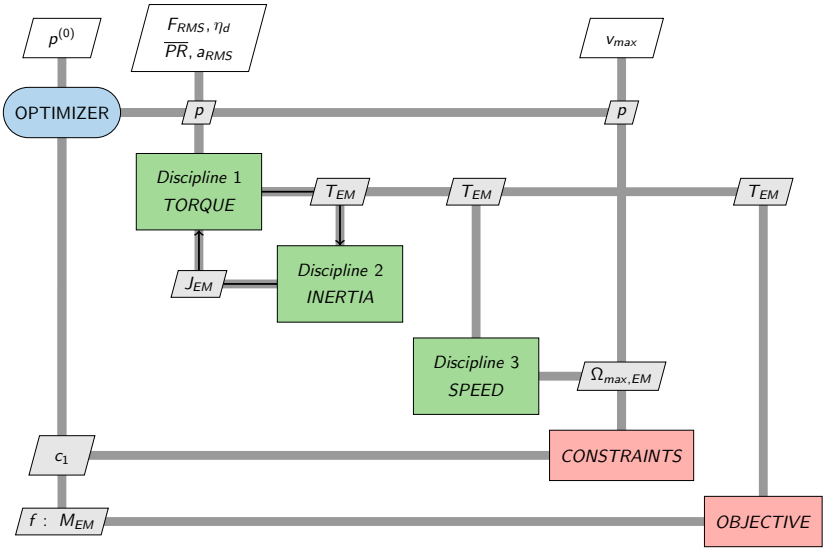

FIGURE 5.3: *Graphical representation of EMA problem eq. 5.1 and its coupling difficulty*

The MDO formulations answer this difficulty of interdependences by providing a formal setting to manage them. The following subsection 5.1.3 proposes 3 main solutions to solve this problem.

Furthermore, based on the same principle than the N^2-diagram, some tools are available to support the engineer in formulating the MDO solutions to a given design problem. On a manual basis, there is the XDSM [Lambe and Martins, 2012]. On a more assisted way, there is the *Design Structure Matrix (DSM)* [Browning, 2001]. On an automated manner, [Pate et al., 2014] offers an ordering automatically determined using graph based methods. In addition, *Multidisciplinary Design Analysis (MDA)*-MDO platforms, such as GEMSEO and Open-MDAO, integrates these functionalities. These tools are a must when the design problem includes many disciplines and many design variables.

5.1.2 MDO architectures

A survey on MDO from [Martins and Lambe, 2013] mentions that over the last two decades, mainly two families of MDO formulations (also referred to as MDO architectures in literature) have been suggested: the distributed architectures and the monolithic ones (fig. 5.4).

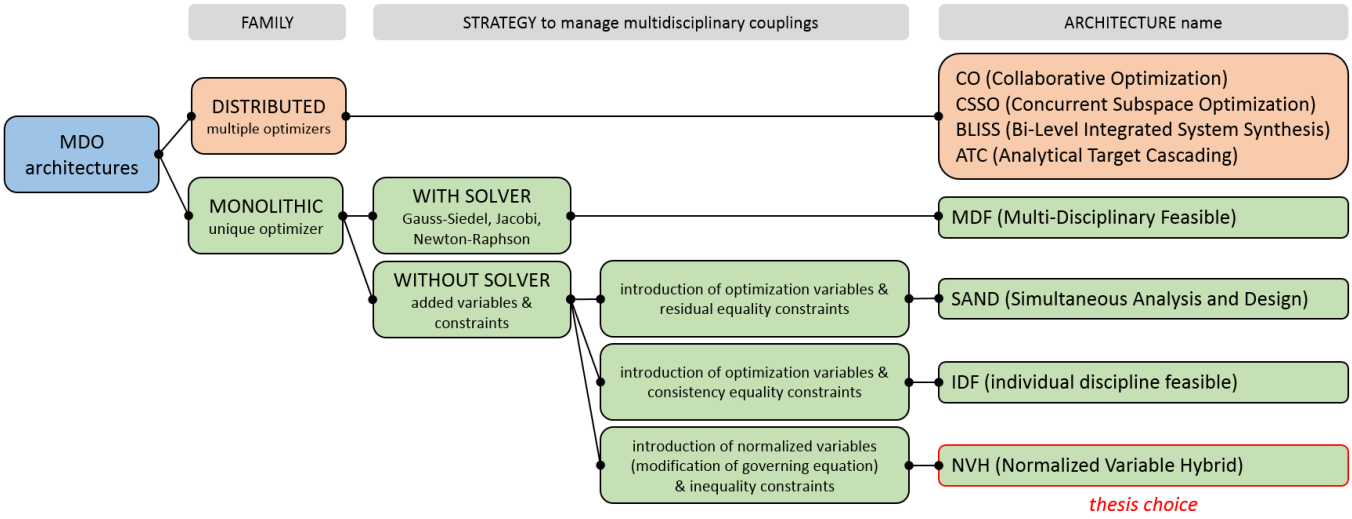

FIGURE 5.4: *MDO architecture overview*

The monolithic architectures solve the MDO problem by casting it as a single optimization problem according to different strategies. The most common monolithic architectures are *Simultaneous Analysis and Design (SAND)*, *Individual Discipline Feasible (IDF)* and *MultiDisciplinary Feasible (MDF)* [Martins and Lambe, 2013]. They are detailed in subsection 5.1.3.

The distributed architectures solve the MDO problem breaking it up into smaller problems. The main distributed architectures are *Collaborative Optimization (CO)*, *Concurrent Subspace Optimization (CSO)*, *Bilevel Integrated System Synthesis (BLISS)* and *Analytical Target Cascading (ATC)* [Martins and Lambe, 2013]. This MDO category is commented in subsection 5.1.4.

5.1.3 Monolithic architectures

The fundamental optimization problem in its most general form can be described as a generic problem known as the *All–At–Once (AAO)* problem [Martins and Lambe, 2013]. It is presented in fig. 5.5. It is the reference from which all other problem statements can be derived.

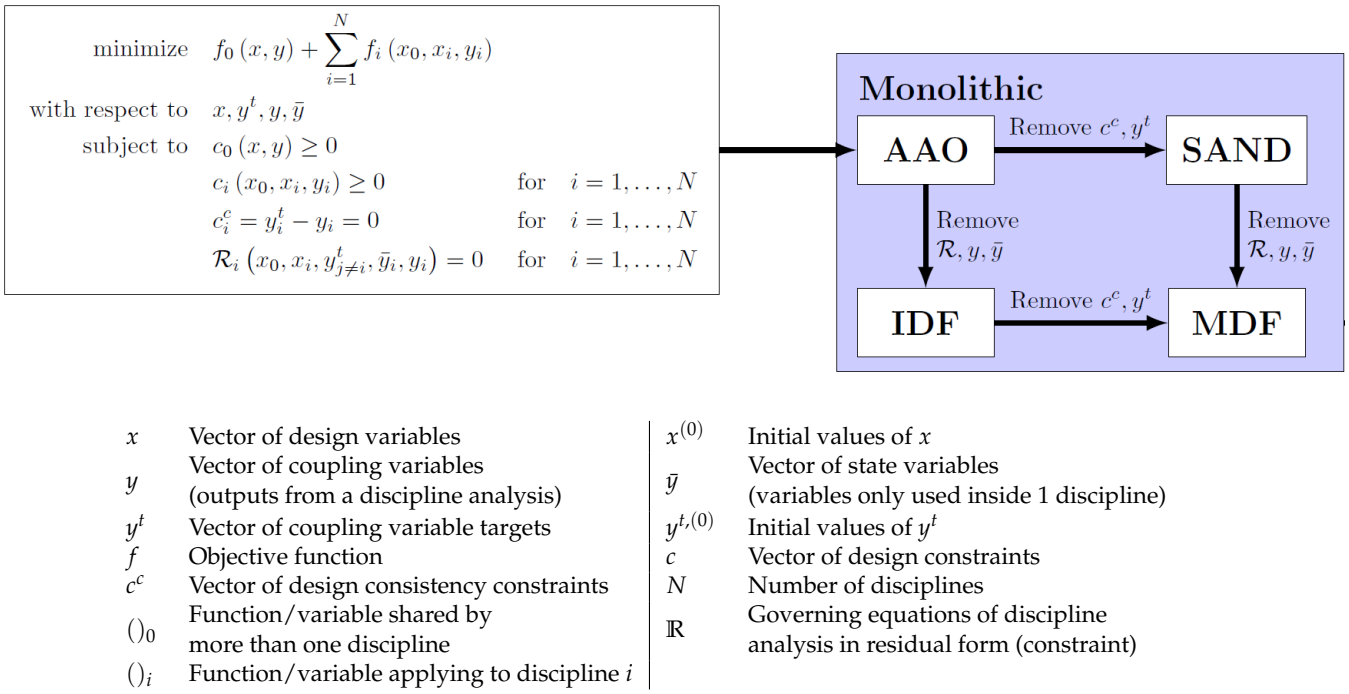

x	Vector of design variables	$x^{(0)}$	Initial values of x
y	Vector of coupling variables (outputs from a discipline analysis)	$\bar{y}$	Vector of state variables (variables only used inside 1 discipline)
y^t	Vector of coupling variable targets	$y^{t,(0)}$	Initial values of y^t
f	Objective function	c	Vector of design constraints
c^c	Vector of design consistency constraints	N	Number of disciplines
$()_0$	Function/variable shared by more than one discipline	$\mathbb{R}$	Governing equations of discipline analysis in residual form (constraint)
$()_i$	Function/variable applying to discipline i		

FIGURE 5.5: *Monolithic architecture classification according to [Martins and Lambe, 2013]*

In this section, the architectures will not be presented on a formal and generic way as shown in fig. 5.5 since it is already thoroughly provided in the paper [Martins and Lambe, 2013]. We suggest using, as a practical use case, the resolution of a simple EMA coupling example such as the one previously introduced (eq. 5.1, fig. 5.3). The considered architectures will be MDF, a solver based architecture, IDF, an optimizer based architecture, and *Normalized Variable Hybrid (NVH)*. These architectures are compared graphically in fig. 5.6 before being commented in further subsections.

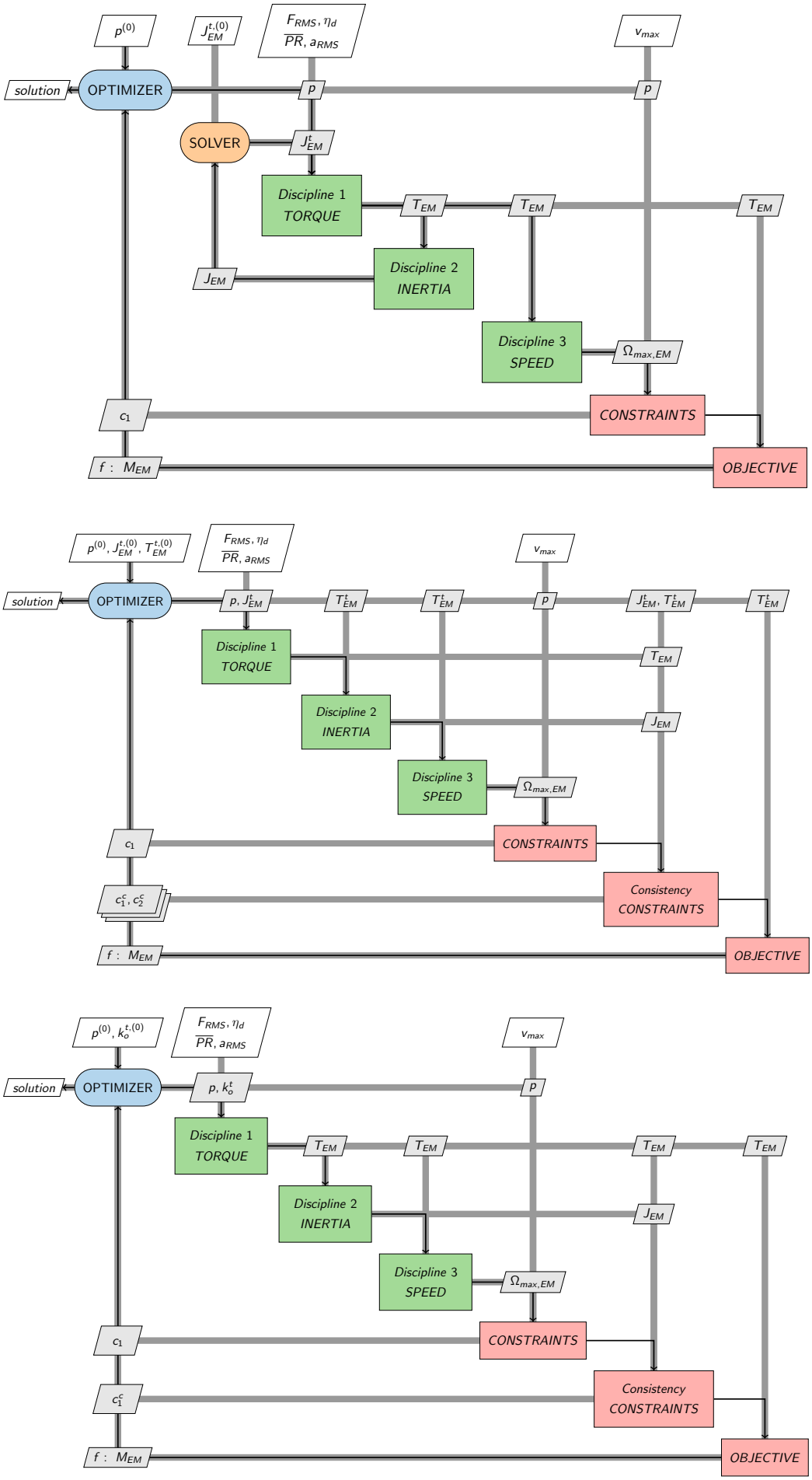

FIGURE 5.6: *Monolithic architectures solving the example of EMA coupling problem (presented in fig. 5.3): (**top**) MDF; (**middle**) IDF; (**bottom**) NVH*

5.1.3.1 MDF architecture

The MDF solving strategy is presented in fig. 5.6 (top). The problem formulation remains the same as the initial formulation (eq. 5.1) without additional design variable nor consistency constraint. There is a single optimizer. A solver or an analyzer is implemented to deal with the consistency of the coupling variable J_{EM} between the motor torque and the motor inertia determinations. The consistency is checked for every optimization iteration. Thus, the coupling variable consistency is evaluated independently of the optimizer iteration. The formulation delivers a consistent design even if the optimizer fails to satisfy the problem global constraint (eq. 5.1f) or reaches the maximum iteration limit. On the other way, the non-convergence of the analyzer results in an inconsistent design whatever the optimizer convergence is. The global formulation success relies on the analyzer effectiveness. The introduction of an analysis tool in the formulation is an important asset for further perspectives. Indeed, it provides modularity to implement a variety of methods for particular physical disciplines.

Most common methods are iterative ones such as Gauss-Seidel or Jacobi methods [Martins and Lambe, 2013]. The first one splits into lower and strictly upper triangular elements whereas the Jacobi method breaks up into a diagonal element and a remainder $\mathbb{R}$. In addition, better convergence rates can be achieved through the use of Newton-based methods such as the gradient based Newton-Raphson method [Martins and Lambe, 2013].

5.1.3.2 IDF architecture

The IDF solving strategy is presented in fig. 5.6 (middle). Contrary to the MDF method, there is no solver implementation. The optimizer deals with the coupling difficulty through the introduction of: two additional variables named the *coupling variables* $J^t_{EM}\ [kg.m^2]$, $T^t_{EM}\ [Nm]$; and two additional constraints named the *consistency constraints* c^c_1, c^c_2. The problem formulation becomes:

$$
\begin{cases}
\text{minimize objective function} & M_{EM} & \text{(5.2c)} \\
\text{varying the design variables} & \left[p\ (lead),\ J^t_{EM},\ T^t_{EM}\right] & \text{(5.2d)} \\
\text{subject to bound constraints} & min \leq p \leq max\ [m/rad] & \text{(5.2e)} \\
 & min \leq J^t_{EM} \leq max\ [kg.m^2] & \text{(5.2f)} \\
 & min \leq T^t_{EM} \leq max\ [N.m] & \text{(5.2g)} \\
\text{subject to global constraint} & c_1 = \Omega_{max,EM} - v_{max}/p \geq 0 & \text{(5.2h)} \\
\text{subject to consistency constraints} & c^c_1 = J^t_{EM} - J_{EM} = 0 & \text{(5.2i)} \\
 & c^c_2 = T^t_{EM} - T_{EM} = 0 & \text{(5.2j)}
\end{cases}
$$

Iteratively, the optimizer chooses the values of inertia and torque that is equal to the value obtained through the discipline estimations.

MDF raises some drawbacks. The introduction of equality constrained involves a considerable risk of numerical difficulties [Thareja and Haftka, 1986]. Also, the equalities give a consistent design once the solution is found, rather than on each iteration [Alexandrov and Lewis, 2000]. Finally, setting the coupling variable bounds is not very convenient for the user. Indeed, the user is likely to choose either too restrictive bounds that result in a biased optimization output or too broad bounds. In this case, the computational cost is impacted because of the large design space the optimizer covers.

5.1.3.3 NVH architecture

Further to the architectures presented in [Martins and Lambe, 2013], the paper [Reysset et al., 2015] offers a new architecture named NVH reformulating the design problem. The NVH solving strategy is presented in fig. 5.6 (bottom graph).

It manages the coupling implementing a normalized variable k_o $[-]$ inside the problem governing equation and introducing a single consistency inequality constraint c_1^c. Compared to the IDF formulation, NVH removes the equalities constraints and reduce the risk of numerical difficulties. Moreover, the design variable range is now reduced. [Reysset et al., 2015] specifies that, in the common basis, $k_o \in [1; 10]$.

The NVH formulation involves a specificity: it requires to reformulate the design problem and enter into a discipline to modify the equations. Indeed, the governing equation (eq. 5.1g) providing the motor torque (discipline 1) is modified into the equation 5.3j. Its initial expression is kept and used into the inequality constraint c_1^c (eq. 5.3h) to check consistency. The problem formulation becomes:

$$
\begin{cases}
\text{minimize objective function} & M_{EM} & \text{(5.3c)} \\
\text{varying the design variables} & [p\ (lead),\ k_o] & \text{(5.3d)} \\
\text{subject to bound constraints} & min \leq p \leq max\ [m/rad] & \text{(5.3e)} \\
 & 1 \leq k_o \leq 10\ [-] & \text{(5.3f)} \\
\text{subject to global constraints} & c_1 = \Omega_{max,EM} - v_{max}/p \geq 0 & \text{(5.3g)} \\
 & c_1^c = T_{EM} - T_{EM,c} \geq 0 & \text{(5.3h)} \\
 T_{EM,c} & = \left[\left(\frac{F_{RMS} \cdot p}{\eta_d} \right)^2 + \frac{2 \cdot J_{EM} \cdot \overline{PR}}{\eta_d} + \left(\frac{J_{EM} \cdot a_{RMS}}{p} \right)^2 \right]^{0.5} & \text{(5.3i)} \\
\text{Discipline 1 gives} & T_{EM} = \left(\frac{F_{RMS} \cdot p}{\eta_d} \right) \cdot k_o & \text{(5.3j)}
\end{cases}
$$

5.1.3.4 Architecture benchmarking

[Vanaret et al., 2017] develops a generic methodology for the MDO architecture comparison (benchmarking). This methodology applies to any potentially expensive design optimization problem. It generates a scalable analytic replacement function that can be quickly computed. It captures the structure and behavior of an equivalent high-fidelity problem. The number of inputs and outputs can be set independently. The methodology is applied to two academic MDO test cases: the *Super Sonic Business Jet (SSBJ)* design problem and a propane combustion problem. MDF and IDF are benchmarked on various instances to prove the dependency between the architecture performance and the problem dimension. The study finally concludes that the "no free lunch" theorem (theorem 2) applies to the choice of the best suited MDO architecture for a scalable dimension problem.

Theorem 2 ("no free lunch" theorem of optimization)**.** *No particular optimization algorithm holds an advantage over another when considering all possible problems [Wolpert and Macready, 1997].*

Furthermore, [Delbecq, 2018, Delbecq et al., 2020a] offers a benchmark which compares MDF, IDF and NVH formulation performances in terms of design optimization and design exploration. The study is done using the Open-MDAO platform on a problem of optimization, similar to the one previously mentioned (eq. 5.1). Firstly, the study assesses the performance of a single run: the proximity of the result with a

known solution, the total function evaluations, and the convergence characteristics. The NVH formulation stands out from the other.

Secondly, the study performs a *Latin Hypercube Sampling (LHS)* DoE on 4 key variables with 50 samples. The 3 formulations succeed 100% in solving the coupling variable consistency in the current design problem.

The robustness to scale change is assessed then. In each DoE sample set, the success percentage in solving coupling variable consistency is estimated at a new load requirement. The loading scale change factor is chosen to be 5, which can be found similarly on one actuator product range. Indeed, the higher load increases the stiffness of the coupling. The NVH formulation shows 100% of success compared to the others, showing more than 40% of failure.

Table 5.1 sums up the main results of this study.

	MDF	**IDF**	**NVH**
Design optimization			
proximity to know solution	accurate	accurate	accurate
total function evaluations	100	20	5
number of derivative evaluations	5	11	5
iteration number to convergence	5	22	5
convergence characteristics (1)	error decreasing with steep slant	error decreasing slower with irregular slants	error decreasing with steep slant
Design exploration			
success in load scale change (2)	15%	60%	100%

(1) *relative error evolution with respect to iteration number;* (2) *percentage of coupling solving success among all samples and considering an increased load requirement*

TABLE 5.1: *MDO architectures benchmark sum up (results from [Delbecq, 2018])*

5.1.4 Distributed architectures

Early in the history of optimization, the motivation for decomposition methods was to exploit the structure of the problem to reduce solution time [Martins and Lambe, 2013]. Many large optimization problems, such as network flow problems and resource allocation problems, exhibit such a special structure [Lasdon, 1970].

As previously detailed, the monolithic MDO architectures solve a single optimization problem. Many more architectures have been developed and break down the optimization problem into a set of smaller optimization problems, or subproblems, that have the same solution when reassembled [Martins and Lambe, 2013]. These are the distributed MDO architectures. Each of them differs from the workflow structure, the discipline analysis workflow, the number of design variables and constraints they involve.

The survey from [Martins and Lambe, 2013] offers a classification of the distributed architectures based on their monolithic analogs: MDF, IDF, or SAND. This classification provides a framework to help developing new distributed architectures. It considers that the starting point of a distributed architecture is always a monolithic architecture.

Distributed architectures can be used when disciplines are high-fidelity models, with important amount of design variables, constraints and when their MDA is

difficult to perform. This can be illustrated with the study case of the Airbus XRF-1 transport aircraft re-engine performed by the *Institute of Technology IRT Saint Exupéry* [Gazaix et al., 2017]. It actually performs an aero-structural optimization of the engine pylons to maximize the aircraft range. This design problem is mainly built from three highly coupled disciplines: structure, aerodynamic, and propulsion. It involves tools of CFD and *Computational Structural Mechanics (CSM)* and many manufacturing constraints.

Furthermore, the distributed architectures are prefered for its interesting flexibility stemming from the separation of system-level and disciplinary-level in the problem resolution. This flexibility mostly provides:

- the possibility of using simultaneously different optimizers. The optimization is broken down into parallel disciplinary optimization tasks coordinated by a system-level optimizer [Delbecq, 2018, Gazaix et al., 2017].
- the possibility to use gradient-based algorithms for solving the disciplinary optimization problems, and derivative-free algorithms for solving the system-level optimization problem for which the number of design variables is reduced [Gazaix et al., 2017].
- the possibility to make use of different levels of fidelity
- the possibility to elaborate a strategy in terms of constraints handling, depending on the considered level.
- the suitability for a direct industrial use since the architectures preserve a partial autonomy of each discipline [Defoort et al., 2012, Gazaix et al., 2017], especially from a software point of view.

Distributed architectures will not be detailed any further. The following section 5.1.5 explains that, in preliminary phase, they are not the best candidate to focus on.

5.1.5 Architecture selection

[Gray et al., 2010] mentions that there is no universal method answering all the design problems. The range of possible multi-disciplinary decomposition methods is large, and defining the best one is not straightforward. It depends on the structure of the design optimization problem, the dimension of the design space, the type and the number of the objective function, the constraints, and the design variables.

To choose the best MDO architecture, a trial-and-error approach is not really practiced due to the high cost of the overall optimization and the complexity of each implementation [Vanaret et al., 2017].

Some tools are required to perform architecture benchmarkings, they are listed hereafter.

- The platform π-MDO presented by [Martins et al., 2009] is shown to be an invaluable tool which rapidly implements multiple MDO architectures for a given problem.

- The Open-MDAO library presented by [Gray et al., 2010, Gray et al., 2019] and available at [Gray et al., 2022] offers an open-source framework for a multidisciplinary design, analysis, and optimization.

- Inspired from π-MDO and Open-MDAO, the *Generic Engine for MDO Scenarios (GEMS)* is developed and presented in [Gazaix et al., 2017, Gallard et al., 2018]. GEMS brings an important progress in MDO automation. It provides an automatic

generation of MDO processes with an easiness of reconfiguration and a MDO formulation engine. Furthermore, it focuses on: 1. the integration of algorithms for optimization, design of experiments, surrogate models and coupled analyses; 2. the postprocessing with automation of MDO result analysis; 3. the deployment in heterogeneous and distributed industrial simulation environments. The GEMS software is now available as a full open source Python 3 library named *Generic Engine for Multidisciplinary Scenarios, Exploration and Optimization (GEMSEO)* [Gallard et al., 2022].

The analytic *Sellar problem* is commonly used for benchmarking architectures. Indeed, it is a typical simple MDO test case introduced by [Sellar et al., 1996, Sellar and Batill, 1996] in 1996. It is presented in eq. 5.4 with arbitrary variables. Although is has low dimensionality, it exhibits characteristics of larger MDO problems and allows each of the MDO architecture implementations to be verified prior to further testing [Martins et al., 2009].

$$\text{Sellar problem} \begin{cases} \text{minimize the objective function} & f_{obj} = x_2^2 + x_3 + y_1 + e^{-y_2} \\ \text{varying the design variables} & x_1, x_2, x_3 \\ \text{subject to global constraints} & c_1 = y_1/8 - 1 \geq 0 \\ & c_2 = 1 - y_2/10 \geq 0 \\ \text{subject to bound constraints} & -10 \leq x_1 \leq 10 \\ & 0 \leq x_2 \leq 10 \\ & 0 \leq x_3 \leq 10 \\ \text{discipline 1 gives} & y_1 = x_1^2 + x_2 + x_3 - 0.2 \cdot y_2 \\ \text{discipline 2 gives} & y_2 = y_1^{0.5} + x_1 + x_3 \end{cases} \tag{5.4}$$

Firstly, [Delbecq, 2018] runs with Open-MDAO the *Sellar problem* with different monolithic architectures and distributed ones. The total function evaluation counts showed to be much greater for the distributed formulations (BLISS, BLISS-2000, CO) than for the monolithic formulations (MDF, IDF). [Delbecq, 2018] finally focuses on the monolithic architectures to deal with the design problem of aerospace EMAs.

Secondly, in the article of [Martins et al., 2009], the authors present a similar performance comparison of architectures with the *Sellar problem* and complete it with a scalable problem. This problem was designed to allow examining the effects of increasing dimensionality while keeping manageable computational requirements. Fig. 5.7 shows convergence results with respect to each problem. The authors concluded that IDF consistently outperformed MDF and CO. The performance of SAND was close to that of IDF, but it was not very robust: SAND did not manage to solve problems of certain dimensionalities. CO usually was the least efficient method, but it was not affected by an increase in the number of local design variables.

Thirdly, the report of [Gazaix et al., 2017] offers a performance comparison between monolithic and distributed architectures on a large scale problem e.i. the academic SSBJ test case firstly introduced by [Sobieszczanski-Sobieski et al., 1998]. The study concludes that both architectures appear as appropriate for large-scale design problems.

5.1.6 Optimization algorithms

A wide range of numerical optimization algorithms enables to tackle most of optimization problems. The fundamentals to select an algorithm is to understand how it works and to identify the problem to optimize. The optimization problems can

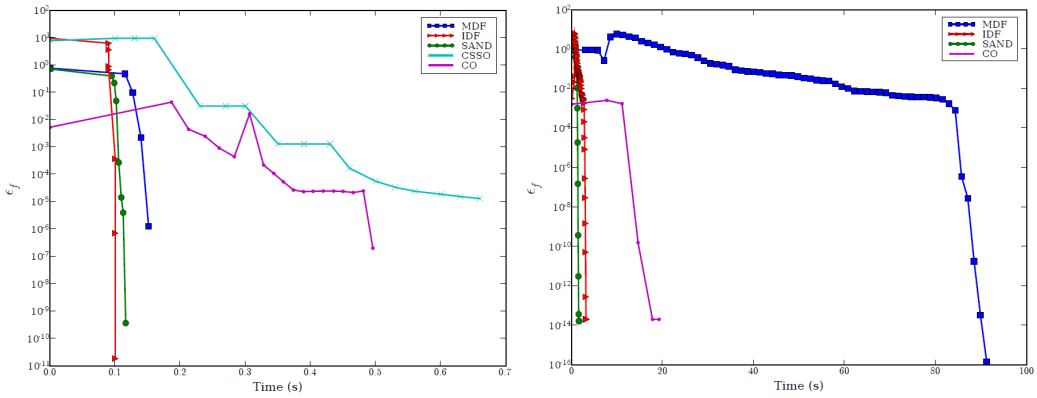

FIGURE 5.7: *Convergence history [Martins et al., 2009]: (**left**) Sellar problem includes 2 disciplines and global variables, 1 local design variable, 2 coupling variables, 2 constraints; (**right**) scalable problem includes 3 disciplines and global variables, 24 local design variables, 21 coupling variables, 21 constraints*

be identified mainly by: the number of variable; the variable type (continuous, discrete, mixed); the linear or non-linear functions; the constrained or un-constrained singularities; the function with consistent derivatives; the local or global minima to find.

Fig. 5.8 clearly shows that there is not a unique optimal technique for every problem (Theorem 2). Combinaison of techniques is possible. For instance, in fig. 5.8 and function f_2, combining gradient-based optimizers and multi-starting point capabilities increases the chances to find the global optimum.

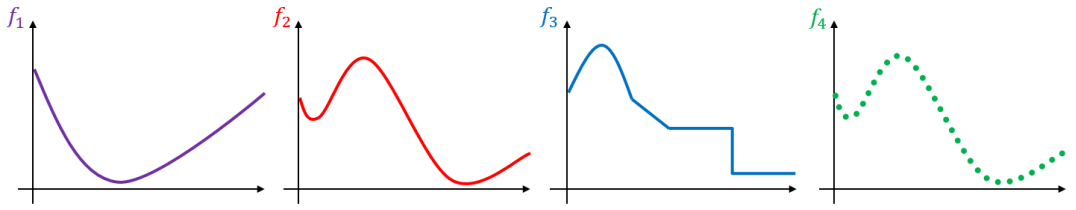

FIGURE 5.8: *Different possible strategies for different function minimum: f_1 gradient-based/free, f_2 gradient-based/free, f_3 gradient-free, f_4 gradient-free*

When the design problem has continuously differentiable functions and constraints with respect to design variables, a gradient-based method is the right solution. If the derivatives are not available, gradient-free techniques are the only recourse. When multiple optima is suspected, gradient-free techniques are effective to get close to the global optimum, and then a switch to a local gradient method should be done. This is often the most effective global optimization strategy [Papalambros and Wilde, 2017].

Gradient-based methods are very effective for optimization problems composed of a large number of design variables (fig. 5.9). They are not very robust for multimodal or non-convex problems (e.g. the eggholder function [Surjanovic and Bingham, 2013]) as they tend to terminate on a local minima.

The gradient-based algorithms basically work estimating the partial derivatives of the objective function f_i (and constraints) with respect to n design variables x_i. This defines the objective n-rows vector and the (nxn) Hessian's matrix (eq. 5.5).

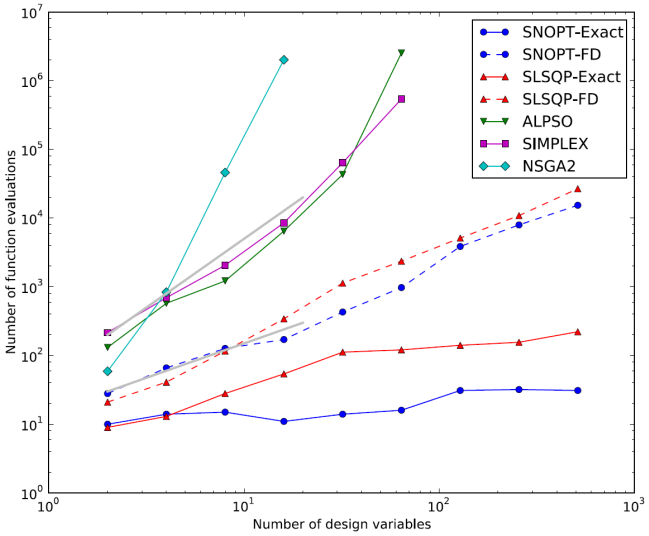

FIGURE 5.9: *Gradient-based (SNOPT, SLSQP) versus gradient-free (ALPSO, SIMPLEX, NSGA2) iteration level with respect of variable number [Martins, 2012]*

$$\nabla f(x) = \frac{\partial f}{\partial x_i} \qquad (\mathcal{H}_f)_{i,j} = J(\nabla f(x)) = \frac{\partial^2 f}{\partial x_i \partial x_j} \tag{5.5}$$

The minimum x^* is reached when $\|\nabla f(x)\| = 0$ and $\mathcal{H}_f(x^*)$ is positive semi-definite [Luenberger et al., 1984].

As far as unconstrained optimization problems are concerned, the most simple method that uses derivatives of objective function is the steepest method (fig. 5.10). It usually converges with a high computational cost. Another method is the Newton's one. It uses the second-order Taylor series expansion which improves the convergence rate. Moreover, the Quasi-Newton methods such as *Broyden–Fletcher–Goldfarb–Shanno (BFGS)* use only the first-order derivative information and estimate numerically the Hessian along the iterations [Nocedal and Wright, 2006].

As far as constrained optimization problems are concerned, the approach takes basically the gradient of the objective and constraint functions and iterates until satisfying the *Karush–Kuhn–Tucker (KKT)* optimality conditions [Kuhn, 2014, Luenberger et al., 1984, Martins, 2012]. Well known and efficient gradient-based methods for constrained optimizations are the *Sequential Least Square Quadratic Programming (SLSQP)* [Kraft et al., 1988] and the *Sparse Nonlinear OPTimizer (SNOPT)* [Gill et al., 2005].

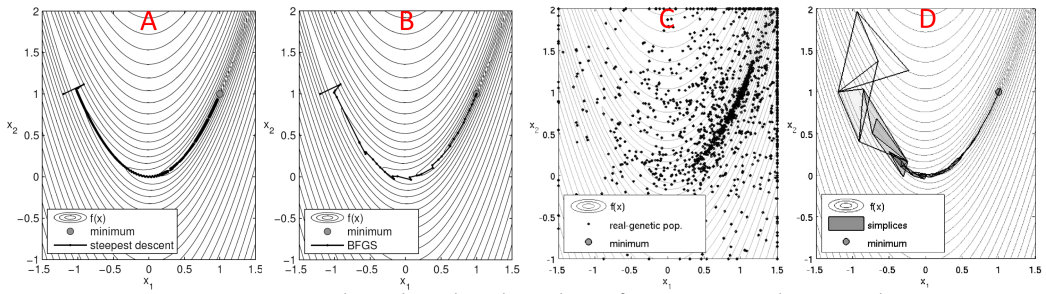

FIGURE 5.10: *Gradient-based and gradient-free iteration plots on a basic resolution example: **A** steepest descent (1st order); **B** BFGS (2nd order); **C** genetic algorithm; **D** Nelder-Mead simplex*

The gradient-free algorithms generally work by sampling the design space for good points, and most of them use this information to decide where to sample next [Papalambros and Wilde, 2017]. The problem of these algorithms is limited by the problem size i.e. the number of variable (fig. 5.9). Their computational effort increases dramatically as the number of design variables becomes large (ie. more than 20 or 30 variables [Papalambros and Wilde, 2017]). Table 5.2 briefly gives an overview of the gradient-free algorithms.

The heuristic methods are easy to implement but difficult to use for problems with expensive function calls because of their sampling methods closer to brute-force search.

The *Simulated Annealing (SA)* is suitable for both discrete and continuous optimization problems. SA is not designed to explore the design space, this makes it efficient at finding a region that contains local optima. Nevertheless, once the region is found, SA can take an extremely large number of function calls to converge to the optimal solution as the steps are random. According to [Papalambros and Wilde, 2017], the parameter tuning is cumbersome.

The *Genetic Algorithms (GA)* (fig. 5.10) are versatile, they require no mathematical knowledge, and they are easy to program. They allow to choose a variety of different crossover and operators as well as a variety of different methods for parent selection. The initial population is usually generated randomly, but it can be seeded with known good points, thus providing the algorithm a partial ability to be restarted. A variety of stopping criteria can be set (convergence to a single point, reached minimum improvement tolerance, reached number of generation). The drawback is that this versatility makes the algorithm specific to a given problem. Similarly to SA, at start, the global search of GA finds efficiently points around local minima. However, GA do not quickly converge to the given minima. If the functions of the problem are costly to compute, a parallel computing scheme is the only reliable way to use GA [Papalambros and Wilde, 2017].

Black-box methods, such as *Efficient Global Optimization (EGO)* and *Dividing Rectangles (DIRECT)*, are designed for expensive functions. They arise in engineering design simulations where the functions, which may be smooth, have a possible numerical noise content. EGO and DIRECT require essentially no parameter tuning and work efficiently as long as the number of variables is small [Papalambros and Wilde, 2017].

Further to Table 5.2, two additional algorithm types are worth mentioning. The pattern search algorithms are used for continuous, discrete, and mixed-discrete problems, as well as discontinuous, non-smooth, or noisy functions. They have rigorous convergence proofs and are widely applied [Papalambros and Wilde, 2017]. The evolutionary algorithms are developed combining the contribution of GAs and evolutionary strategies influenced from biological evolutions. The evolutionary strategies such as the *Covariance Matrix Adaptation Evolution Strategy (CMA-ES)* [Hansen, 2006] are used for non-linear continuous problems. They are stochastic methods avoiding combinatorial explosion for finding the global optimum.

Algorithms	**Constraint handling**	**Number of function calls per iteration**	**Stochastic nature**
Direct-search methods			
Coordinate search (also named *Compass search* or *Coordinate descent*) GPS (*Generalized Pattern Search*) MADS (*Mesh-Adaptive Direct Search*) *Nelder-Mead*	filter, progressive barrier	close to problem size	search step can be stochastic
Heuristic methods			
SA (*Simulated Annealing*)		one	yes
GA (*Genetic Algorithm*), MOGA (*Multiobjective Genetic Algorithm*)	penalty (1)	population size	yes
PSO (*Particle Swarm Optimization*)		swarm size	yes
Black-Box methods			
EGO (*Efficient Global Optimization*)	kriging	one	can be stochastic (3)
DIRECT (*Dividing Rectangles*)	penalty (2)	increases	no

Notes: (1) *for GA/MOGA, also: augmented Lagrangian, custom operators;* (2) *with inequality constraints;* (3) *for maximizing the expected improvment*

TABLE 5.2: *Gradient-free algorithm recap [Papalambros and Wilde, 2017]*

5.1.7 Thesis choices

In a context of preliminary design, the important criterias to select a MDO architecture are:

- the *overall performance* (time to convergence, number of iteration)

- the *robustness to scale change* since it should be applicable as much on a small helicopter as a bigger one.

- the *reuse* since the actuator preliminary design will evolve in terms of complexity. This evolution will lead to the implementation of new low-fidelity disciplines, involving new design variables, new constraints and new inter-disciplinary couplings to solve.

The scope of the actuator preliminary sizing gathers low-fidelity models i.e. analytical models (algebraic equations) and response surface models (surrogate). In addition, the size of the engaged numerical problem is reduced (small number of design variables and constraints). Since the monolithic architecture shows good performance and robustness, the use of the distributed MDO architectures for the actuator preliminary sizing problem is not justified.

The reported monolithic benchmark highlights that the NVH stands out from the other formulations with good performances. What is more, it is the formulation the most robust to scale changes. However, its formulation is intrusive to the design problem discipline. This makes it suitable only for preliminary sizing problems where the user manages all the disciplines on her/his own.

The choice of the thesis is to implement the NVH monolithic architecture.

As far as the optimization algorithm is concerned, the sizing tool is equiped of 2 resolution algorithms that the user can select:

- A heuristic algorithm such as the differential evolution introduced by [Storn and Price, 1997]. The library is available on [SciPy, 2022]. This algorithm is based on a GA and follows an evolutionary strategy. It has been done for minimizing non-linear and non-differentiable continuous space functions. It requires a few control variables, it is easy to use and it is robust [Storn and Price, 1997].

- An efficient gradient-based algorithm for constrained optimization such as the SLSQP introduced by [Kraft et al., 1988]. The library is available on [SciPy, 2022].

As presented previously in subsection 5.1.5, the frameworks GEMS and OpenMDAO offer a considerable potential at supporting efficiently an optimization problem (architecture and algorithm choices, formulation, solving, postprocessing). In this thesis, we didn't use these frameworks since they become available too late in the thesis progress. Initially, the industrial choice was to not rely on any framework and licence. This thesis took its way with Open Source solutions (Python) and limited the packages to the standard ones (Sympy, Scipy, Numpy, Matplotlib).

5.2 Singularities & algebraic loops

The MSDO formulation basically follows 3 main steps:

1. *the definition*: per component, the variables, parameters, equations, constraints describing the problem are gathered on a design graph (similarly presented in section 5.3).

2. *the orientation*: a first workflow is drawn linking equations with their supposed inputs and outputs. This highlights over-constrained singularities, under-constrained singularities and algebraic loops (couplings). The N^2-diagram can be done beforehand to check the interfaces between several disciplines.

3. *the formulation*: the problem is re-organized according to the selected MDO architecture. The final MDO process can be checked using the XDSM representation.

For large scale design problems, the formulation is not straightforward. Removing the problem difficulties by adding/removing variables or reordering discipline analysis may be a hardwork and time consuming.

To support designers in going through these steps, [Delbecq, 2018] offers an automated way through a graph-based approach. It is implemented in the Python programming language. It is build on top of the NetworkX graph library [Hagberg et al., 2008] and the Sympy symbolic computation library [Sympy, 2021].

In the scope of the actuator MSDO problem, this section focuses on each coupling and singularity (fig. 5.11) found into the design graphs and provides the formulations removing these difficulties. As reminder, the formulation follows the chosen formulation strategy (NVH). The final design graphs per component are presented in section 5.3 with the MDO difficulties solved.

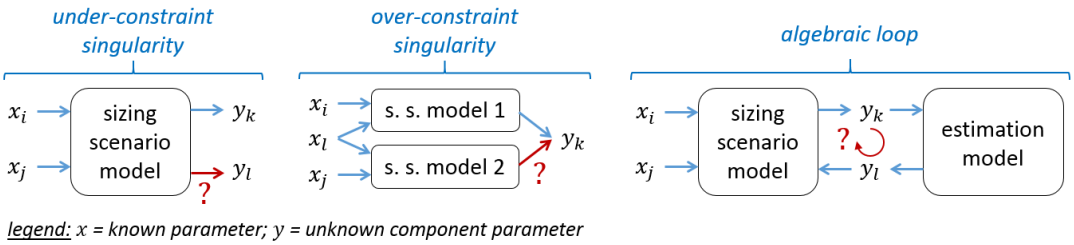

FIGURE 5.11: *Singularities & algebraic loops*

Some conventions have been set in the following equations. $f(x_i)$ means a dependency on with the variable x_i. $f_{SL}(x)$ indicates the use of the relevant scaling law function of generic form: $f_{SL}(x) = A \cdot x^B$. c_i and c_i^c are the constraints and the consistency constraints (optimizer setting) linked to a component i. The variable subscript contains different information: in the first positions, a precision regarding the variable; in the last position, the component ownership. When there is no component ownership, it means that the variable comes from a combination of different component characteristics or comes directly from the specification inputs. Each component has its respective abbreviation as illustrated in Chapter 1 (architecture of reference, fig. 1.22): *Rod End (RE)*, BB1, BB2, SM, EM, EMB, ACT, H, OR. No safety coefficient appears in any equation sets, this is to facilitate the reading.

5.2.1 Algebraic loops

The principle of coupling or algebraic loop has been presented and illustrated in section 5.1.1.2. This difficulty is found in the electrical component sizing (EM, EMB). Indeed, the shaft inertia is known once the components are determined. However, the component determination requires the shaft inertia as an input parameter. This describes an algebraic loop.

5.2.1.1 Electromagnetic brake

The EMB component model takes the static braking torque as key parameter. All brake characteristics are determined from this parameter requiring the total shaft inertia J_{total}. This variable is unknown at this step of sizing since it requires a brake characteristic: the disk inertia J_{EMB}. Consequently, the disk inertia becomes the coupling variable of the problem. The difficulty is overcome adding one normalized variable $k_{o,EMB}$ and one consistency constraint c^c_{EMB} as presented in the frame below. An intermediate value of inertia J' is estimated with the other components contribution. This is for the oversizing coefficient exploration depth to be reduced.

Initial problem:

↦ sizing scenario(s):

$$T_{s,EMB} = \frac{F_{max} \cdot p_{SM}}{\eta_{i,SM}} + J_{total} \cdot \frac{v_{max}}{p_{SM} \cdot t_{EMB}}$$

↦ model(s):

$$J_{EMB} = f_{SL}(T_{s,EMB})$$
$$J_{total} = \sum_i J_i + J_{EMB}$$

Formulated problem:

↦ sizing scenario(s):

$$J' = \sum_i J_i$$
$$T_{s,EMB} = \left(\frac{F_{max} \cdot p_{SM}}{\eta_{i,SM}} + J' \cdot \frac{v_{max}}{p_{SM} \cdot t_{EMB}} \right) \cdot k_{o,EMB}$$
$$T_{s,EMB} \geq \frac{F_{max} \cdot p_{SM}}{\eta_{i,SM}} + J_{total} \cdot \frac{v_{max}}{p_{SM} \cdot t_{EMB}} \implies c^c_{EMB}$$

↦ model(s): *the same than initial problem*

Note(s): $i \in [BB1, BB2, SM, EM, M_{reflected}]$; the lead l_{SM} of the screw mechanism is an optimization variable

5.2.1.2 Electrical motor

Similarly to the EMB, the EM states an algebraic loop based on the rotor inertia J_{EM}. This is overcome by the introduction of an oversizing coefficient $k_{o,EM}$ and an inequality consistency constraint c^c_{EM}. What is more, the RMS torque is determined by 2 equations (overconstrained problem, see subsection 5.2.2). The extra equation involving the specification is turned into an inequality constraint c_{EM}.

Initial problem:
$\mapsto$ sizing scenario(s):

$$T_{peak,EM} = f_{scen}(J_{total}, p_{SM}, \eta_{d,SM})$$

$$T_{RMS,EM} = \sqrt{\left(\frac{p_{SM} \cdot F_{RMS}}{\eta_{d,SM}}\right)^2 + 2 \cdot \frac{J_{total}}{\eta_{d,SM}} \cdot \overline{PR} + \left(\frac{J_{total} \cdot a_{RMS}}{p_{SM}}\right)^2}$$

$\mapsto$ model(s):

$$T_{RMS,EM} = f_{SL}(T_{peak,EM}); \quad J_{EM} = f_{SL}(T_{peak,EM}); \quad J_{total} = \sum_i J_i + J_{EM}$$

Formulated problem:
$\mapsto$ sizing scenario(s):

$$T_{peak,EM} = \left(\frac{F_{max} \cdot p_{SM}}{\eta_{i,SM}}\right) \cdot k_{o,EM}$$

$$T_{peak,EM} \geq f_{scen}(J_{total}, p_{SM}, \eta_{d,SM}) \implies c^c_{EM}$$

$$T_{RMS,EM} \geq \sqrt{\left(\frac{p_{SM} \cdot F_{RMS}}{\eta_{d,SM}}\right)^2 + 2 \cdot \frac{J_{total}}{\eta_{d,SM}} \cdot \overline{PR} + \left(\frac{J_{total} \cdot a_{RMS}}{p_{SM}}\right)^2} \implies c_{EM}$$

$\mapsto$ model(s): *the same than initial problem*

Note: f_{scen} indicates the scenario function providing the maximum torque among 3 defined peak scenarios (Chapter 4, paragraph 4.3.2.1.2); $i \in [BB1, BB2, SM, EMB, M_{reflected}]$; the lead p_{SM} $[m/rad]$ of the screw mechanism is an optimization variable

Other difficulties challenge the MDO formulation, they are the over-constrained singuralities and under-constrained singularities.

5.2.2 Over-constrained singularity

An over-constrained singularity takes place when more than one equation yields to the same output (fig. 5.11). To solve the difficulty, a known parameter named over-sizing coefficient $k_o \subset [1; +\inf[$ is introduced on the deterministic equation and all extra equations are replaced by inequality constraints in the optimizer settings. This is detailed in the following paragraphs.

5.2.2.1 Rod end

The component RE involves an over-constrained singularity. Indeed, the component key parameter (the static load capability, $C_{0,RE}$) is driven by 2 sizing scenarios: the specified max static load F_{max} and a limitation, the referenced minimum axle diameter $d_{axle,min,ref}$. To overcome this difficulty, an over-sizing coefficient k_o is introduced to

drive the value of the model key parameter. The problem and its formulation are presented hereafter.

Initial problem:	*Formulated problem:*
↦ sizing scenario(s):	↦ sizing scenario(s):
$C_{0,RE} = F_{max}$	$C_{0,RE} = F_{max} \cdot k_{o,RE}$
$d_{axle,RE} \geq d_{axle,min,ref,RE}$	$d_{axle,RE} \geq d_{axle,min,ref,RE} \implies c_{RE}$
↦ model(s):	↦ model(s): *the same than initial problem*
$d_{axle,RE} = f_{SL}(C_{0,RE})$	

5.2.2.2 Ball bearing 1 & screw mechanism

The components BB1 and SM involve an over-constrained singularity. Indeed, their component key parameter (the static load capability, C_0) is driven by 2 sizing scenarios: the specified max static load F_{max} and the specifiied dynamic load $C_{d,spec}$. To overcome this difficulty, the set of the 2 equations is turned into an inequation constraint and the introduction of an over-sizing coefficient k_o driving the value of the model key parameter. The problem and its formulation are presented hereafter.

Initial problem:	*Formulated problem:*
↦ sizing scenario(s):	↦ sizing scenario(s):
$C_{0,i} = F_{max}$	$C_{0,i} = F_{max} \cdot k_{o,i}$
$C_{d,i} = C_{d,spec,i}$	$C_{d,i} \geq C_{d,spec,i} \implies c_i$
↦ model(s):	↦ model(s): *the same than initial problem*
$C_{d,i} = f_{SL}(C_{0,i})$	

Note(s): $i \in [BB1, SM]$

5.2.3 Under-constrained singularities

It can happen that several parameters to determine participate in a single equation, the system is undetermined (fig. 5.11). This is named an under-constrained singularity. It usually happens when the design problem has not enough design drivers.

The way to deal with it is to formulate a design assumption (e.g. a maximum reachable value) and associate it with an under-sizing coefficient $k_u \subset [0;1]$. The unknown parameter becomes a design variable bounded by independent limits far from any particular specification.

The actuator problem does not include such a singularity.

5.3 Design graphs

The design graph is a graphical and handmade tool to study the coordination between MDO problem variables and components. The design graph method is introduced in [Budinger, 2014]. Here, we suggest to rework it differently: it includes colors, a unidirectional reading and it is applied to each component separately. It basically provides an overview of the component execution sequence. The design graph principle is explained and illustrated with the simple example of the rod end in the following subsection 5.3.1. Further, the design graphs of the screw mechanism and

the electromagnetic brake are displayed to show the principle with more variables at stake. All other design graphs are available in Appendix U.

The design graph color legend is given in fig. 5.12.

FIGURE 5.12: *Design graph color legend*

The design graph is read from left to right and top to bottom. The parameters dealing with safety coefficients, components of reference or design hypothesis are not mentioned to improve the clearity of the presentation.

5.3.1 Rod End

A specification parameter (F_{max}) and an oversizing parameter ($k_{o,RE} \in [0;10]$) are required to estimate the rod end key parameter. A rod end estimation model provides the parameter necessary for the sizing procedure $d_{axle,RE}$. At mechatronic level, the scenarios sizing the rod end are: - the static load capability $C_{0,RE}$ should be higher than the specified maximum static load F_{max}; - the axle diameter $d_{axle,RE}$ should be bigger than a minimum referenced standard specified in the design hypothesis. Thanks to the introduction of the oversizing coefficient, the first scenario des not need to be set as a constraint in the optimizer settings. The second scenario is set as an optimization constraint $c_{axle,BB1}$.

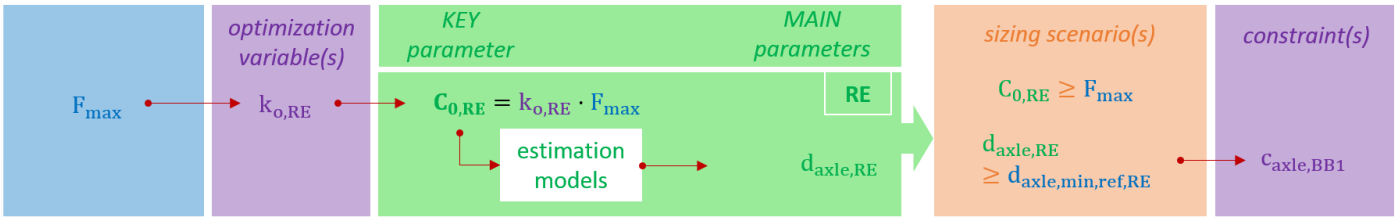

FIGURE 5.13: *Design graph of component Rod End (RE)*

5.3.2 Screw mechanism

The same principle than for RE is applied for the SM component (fig. 5.14). Visually, the graph shows that this component does not need other component parameter to be determined. This component will be among the first disciplines to be executed in the sizing. This component has 7 sizing scenarios. Among them, there are the component capabilities regarding the static load $C_{0,SM}$ and the fatigue load $C_{d,SM}$ to be compliant with the application requirements, respectively F_{max} and $C_{d,spec,SM}$. Thanks to the introduction of the oversizing coefficient $k_{o,SM} \in [0,10]$, only the fatigue load limitation is set as an optimization constraint $c_{Cd,SM}$.

In addition, the component counts 3 running limitations regarding the buckling resistance $F_{buckling,SM}$, the resonance speed without loading $\Omega_{res,noload,SM}$, and the resonance speed with loading $\Omega_{res,load,SM}$. These limitations are set as optimization constraints.

Futhermore, the component is subject to an assembly constraint dealing with the electrical motor inner diameter. This is set as an optimization constraint $c_{d,screw,SM}$.

Finally, the screw efficiency formula has a domain of validity to respect. Also, the direct and indirect efficiency values must remain close. This enters the optimization settings as two constraints: $c_{eta,val,SM}$ and $c_{eta,gap,SM}$.

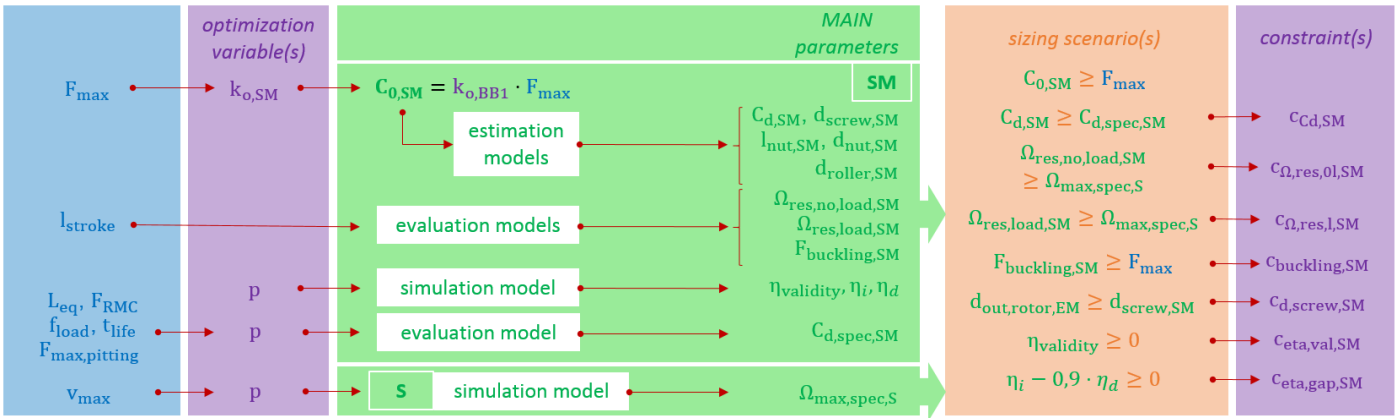

FIGURE 5.14: *Design graph of component Screw Mechanism (SM); abbreviations used on discipline: Shaft (S)*

5.3.3 Electromagnetic brake

The design graph of the EMB component is presented in fig. 5.15. To get its key parameter $T_{s,EMB}$ defined, this component requires the outputs from different disciplines (efficiency and inertia). The EMB estimation model provides the disk inertia. The discipline I gathers all contributing inertia and ouputs the total rotating inertia J_{total}. Finally, given this value, the discipline RT estimates the required braking static torque $T_{s,spec,EMB}$.

Due to the chosen MDO formulation (section 5.2.1.1), the consistency between the EMB key parameter (carrying the oversizing coefficient) and the application requirement must be checked. This corresponds to a sizing scenario implemented as an optimization constraint $c^c_{Ts,EMB}$.

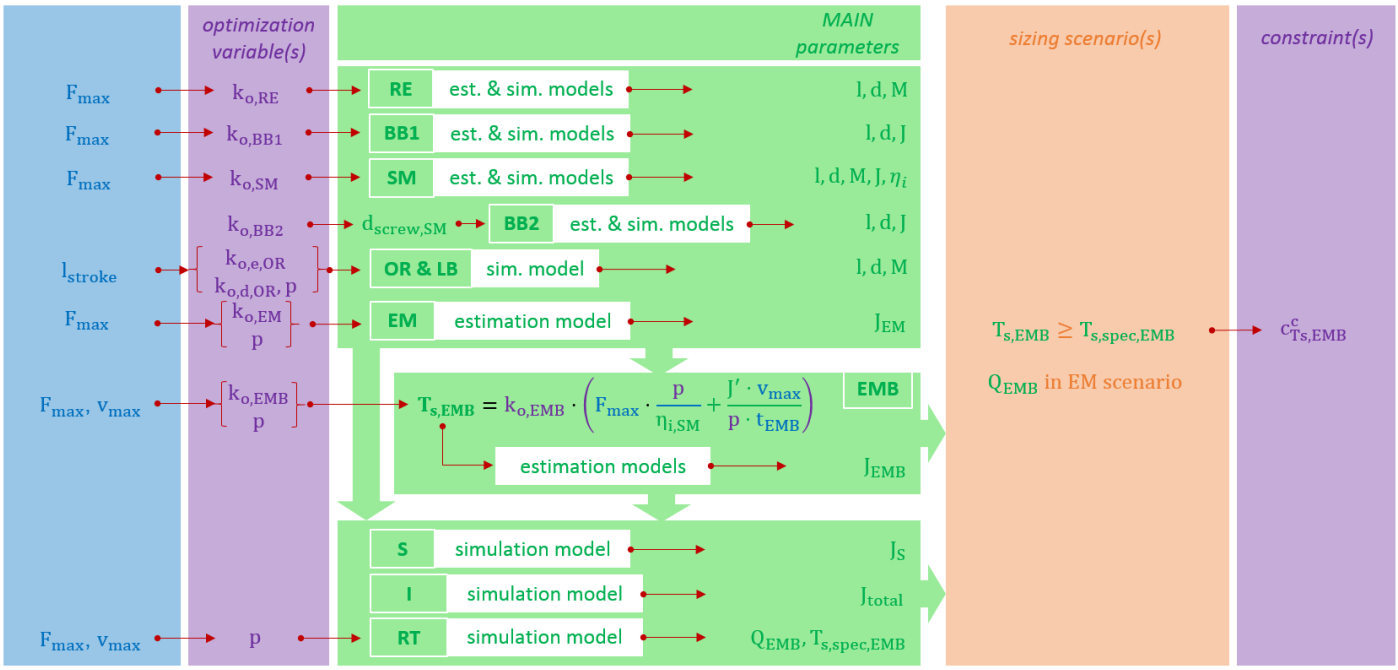

FIGURE 5.15: *Design graph of component Electromagnetic Brake (EMB); abbreviations used on disciplines: Shaft (S); Inertia (I); Required Torque (RT)*

5.4 Sequencing the execution

Through the design graphs in section 5.3, the sequences of calculation steps have been identified for each component. Now, assembling these sequences together defines the global sizing procedure. This assembly is done using the efficient formalism of the XDSM representation. The actuator detailed XDSM diagram is available in Appendix V. The diagram is included with a vectorial format to enable a clean zooming in if necessary. This diagram is too large to be included here.

We propose to synthetize this actuator sizing procedure by another diagram (see fig. 5.16). This diagram presents the different disciplines to go through until reaching an estimation of the actuator mass. Also, it makes a list of the sizing scenarios corresponding to each component key design driver. From these sizing scenarios, 30 constraints emerge in the optimization settings. With the objective of minimizing the actuator mass and to satisfy the constraints, the optimizer plays in a design domain of 10 variables. One of them is a technological variable (lead). The nine other ones are oversizing coefficients coming from the application of the NVH formulation.

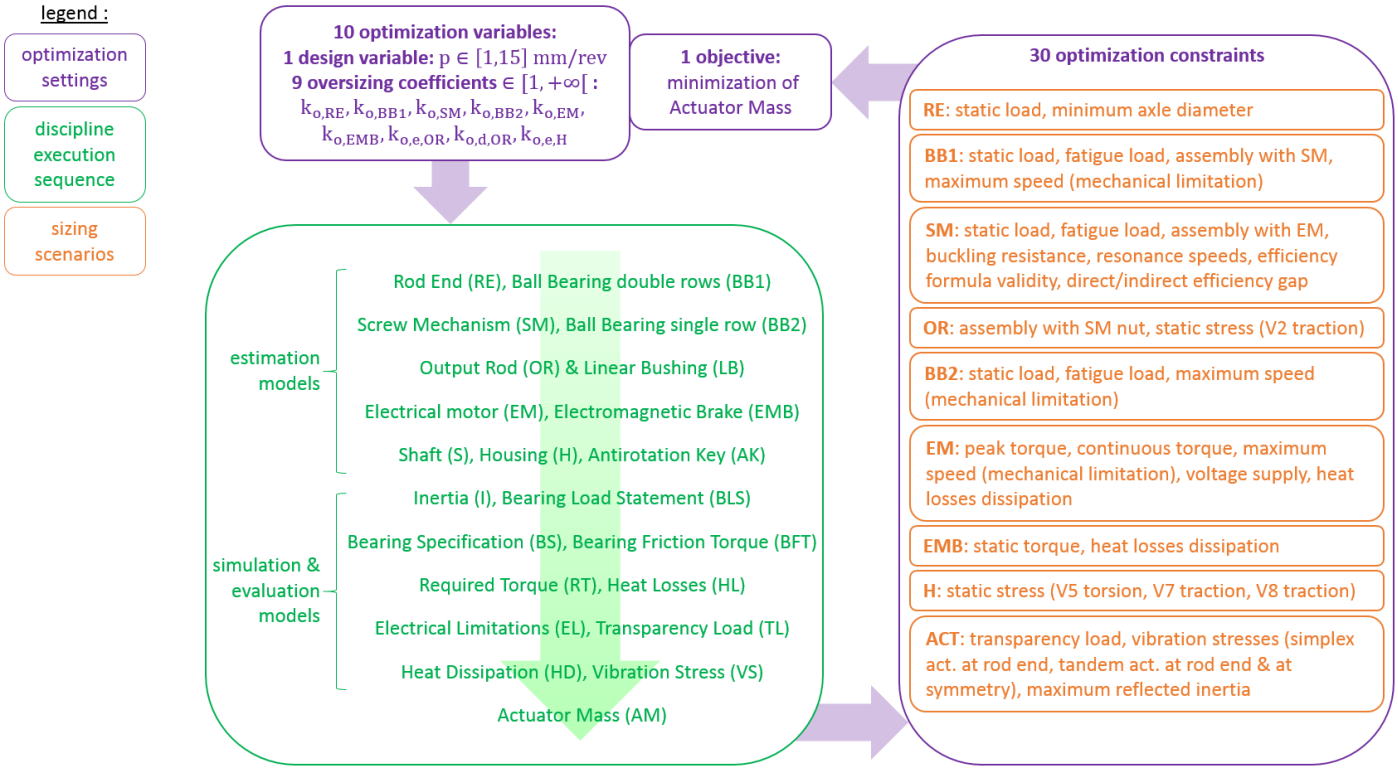

FIGURE 5.16: *Influence diagram of the actuator sizing procedure*

5.5 GUI WebApp

The previously detailed sizing procedure has been implemented into a GUI WebApp (fig. 5.17). The access to it does not require any type of installation. It only requires an internet connection, a web browser, a login and a password.

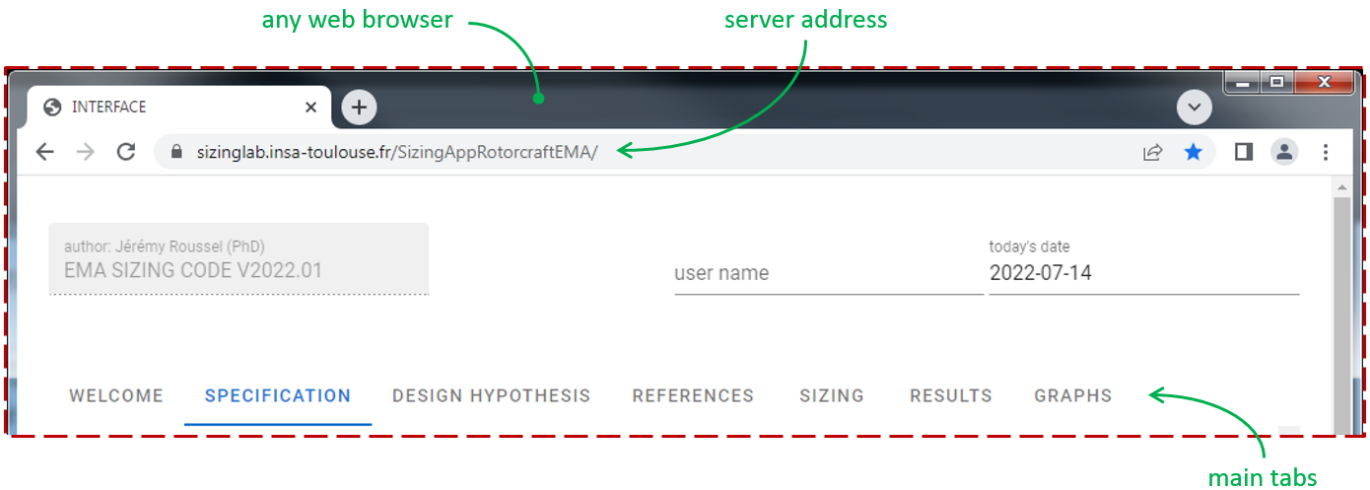

FIGURE 5.17: *GUI WebApp: upper ribbon & main tabs*

The preliminary sizing code and the GUI WebApp have been implemented using Open Source tools. The sizing code is programmed in *Python*. The GUI is based on *Jupyter Notebooks* containing *ipywidgets* and calls of *Python* scripts. The WebApp is generated using *Voilà* [Voilà, 2020]. This package creates a dashboard on top of the *Jupyter-server* ecosystem. It turns the *Jupyter notebooks* into a standalone app. This

process is implemented within a Virtual Machine structure running Ubuntu 18.04 with a SSH ability.

The GUI WebApp is shown in fig. 5.17. It contains 7 main tabs (fig. 5.17). Each tab contains the following features.

1. *WELCOME* tab: it presents with sketches the design context and gives IT technical details about the WebApp.

2. *SPECIFICATION* tab (fig. 5.18): it invites to enter the specification of the desired actuator.

3. *DESIGN HYPOTHESIS* tab: drop-down menus per component and discipline gather all safety coefficients and design hypothesis parameters. Also, with colors, it reminds the related parameter of the specification and estimate instantaneously the corresponding demand. This tab offers the user the possibility to activate more or less each actuator design criteria separetly.

4. *REFERENCES* tab: it gathers the component of reference feeding the scaling laws. A drop-down menu is dedicated to each component of reference. In each drop-down menu, a picture of the component is provided with a legend.

5. *SIZING* tab: it proposes the choice between gradient-based or gradient free optimization algorithm (SLSQP or differential evolution). A red button has to be hit to launch the sizing process.

6. *RESULTS* tab (fig. 5.19): in specific drop-down menus, this tab presents the estimated characteristics of each component and the optimization parameters.

7. *GRAPH* tab: it displays a graphical mass distribution of the actuator.

By default, the interface is ready to be launched. Indeed, the input boxes of the tabs *SPECIFICATION*, *DESIGN HYPOTHESIS* and *REFERENCES* are pre-filled with default values practiced for a real sizing use case. Each input box on the two first tabs has got its own *APPLY DEFAULT* button. When the input box value is modified by the user, hitting this button brings back the default value. In the *REFERENCES* tab, the component of reference can be renamed hitting an *APPLY DEFAULT* button. Also, the user can upload its own component of reference and save the component of reference she/he has just entered.

Furthermore, in the *DESIGN HYPOTHESIS* tab, information tips are attached to some parameters to help the user understanding the parameter or to provide orders of magnitude in practice.

A screenshot of the *SPECIFICATION* tab is presented in fig. 5.18.

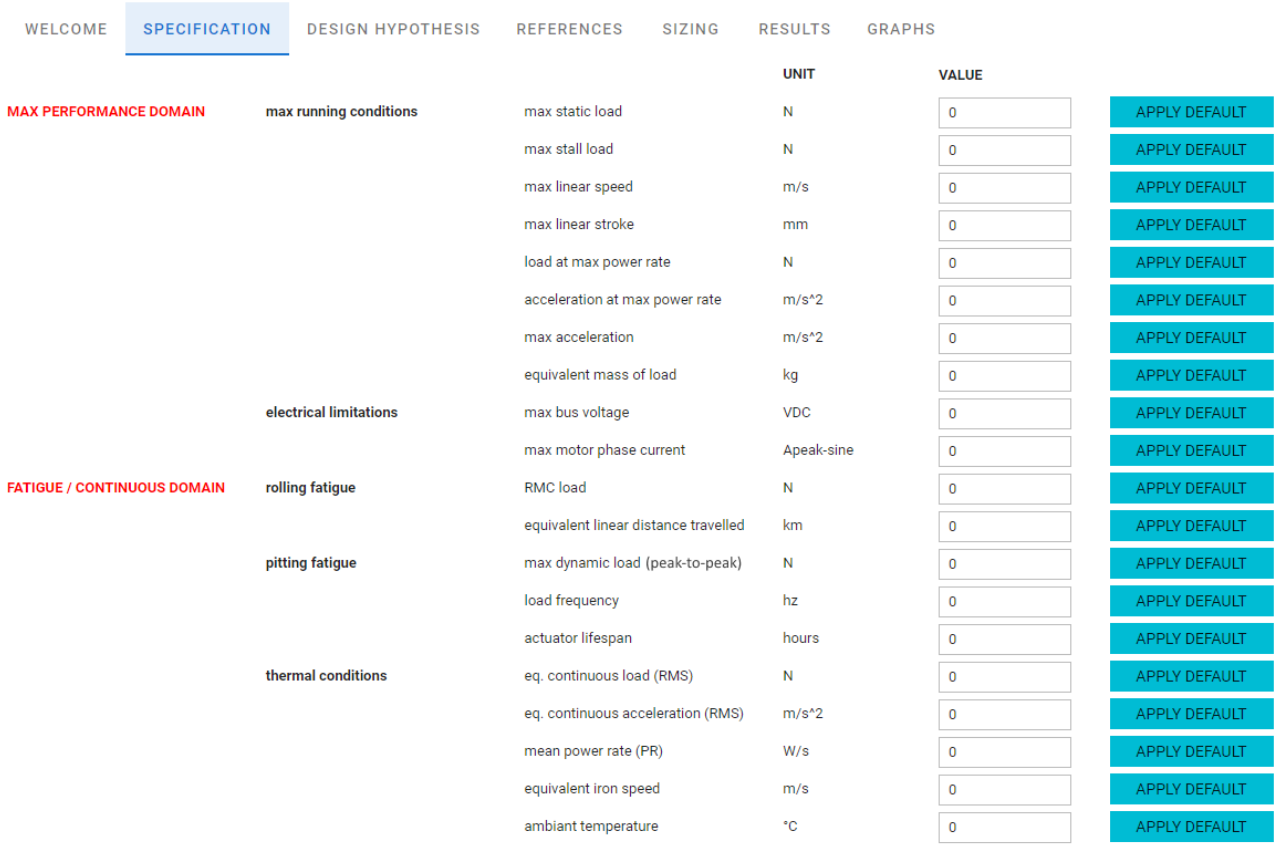

FIGURE 5.18: *GUI WebApp: SPECIFICATION tab*

The *RESULTS* tab presented in fig. 5.19 shows the different drop-down menus corresponding to each component. In each of them, the corresponding specification, design hypothesis, and effective demand are reminded above the component characteristics.

The last drop-down menu concerns the optimization parameters. It displays the optimization variables, and all the constraints. An automatic flashy background color highlights the active design drivers. A spider web representation can be another alternative to it with less constraint to display.

One asset of the NVH formulation is found here. The normalized optimization variables are implemented in the heart of the code and their value allows to monitor and understand how the algorithm processed to converge. This combined with the constraints increases the level of result interpretation.

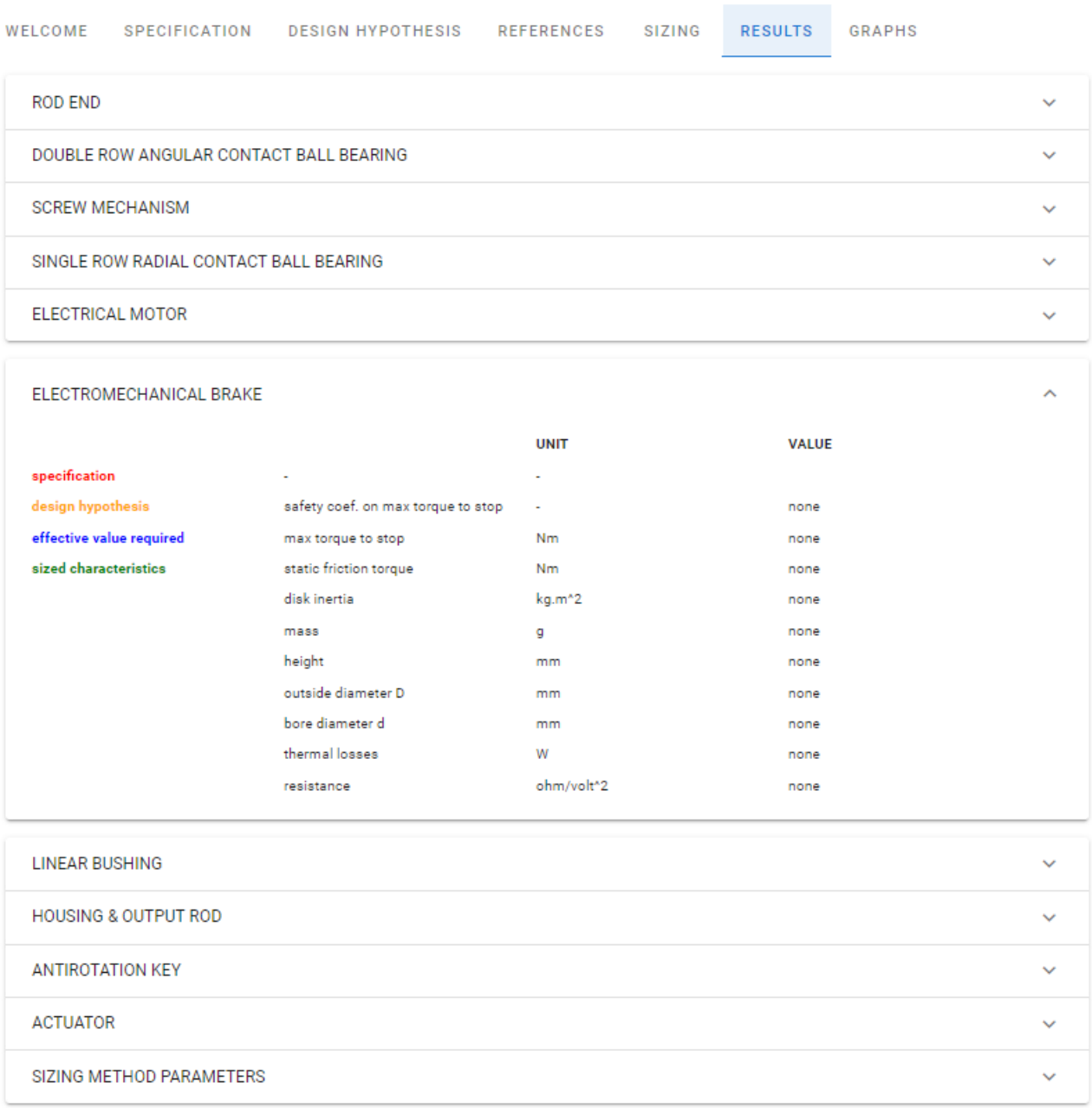

FIGURE 5.19: *GUI WebApp: RESULTS tab*

Once the optimized actuator is generated, the actuator main dimensions are exported to generate a 3D visualization. The dimensions are connected to a script where the generic geometry of the actuator is coded in *JavaScript*. The package *OpenJSCAD* [MIT, 2020] is used to compile, along with CSS style files, the HTML file of the actuator geometry. This file is opened on a new web browser page (fig. 5.20 & 5.21). The user can move the actuator in 3D. The graphical interface allows to modify the geometry manually and update the visualization instantaneously. Also, it allows to export the geometry as a STL file. This is useful if a 3D printing is needed.

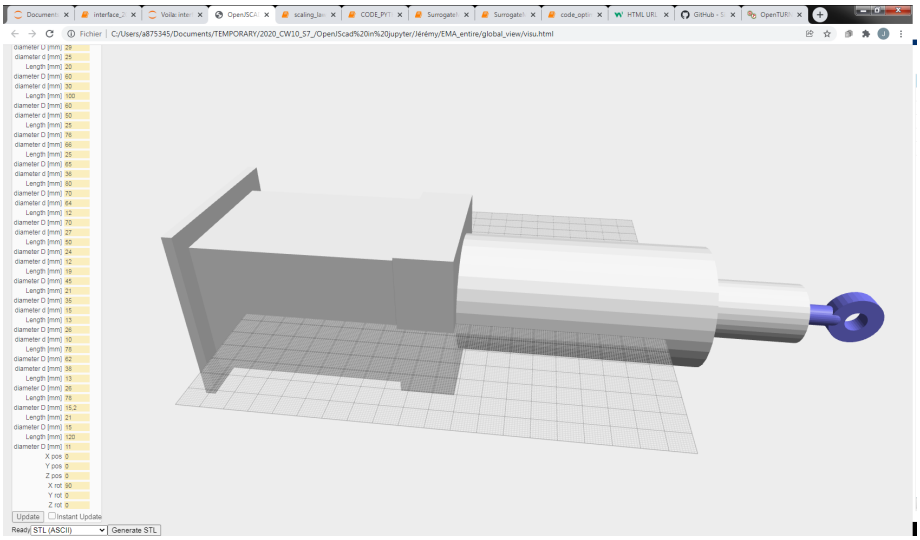

FIGURE 5.20: *GUI WebApp: 3D full view of a sizing example*

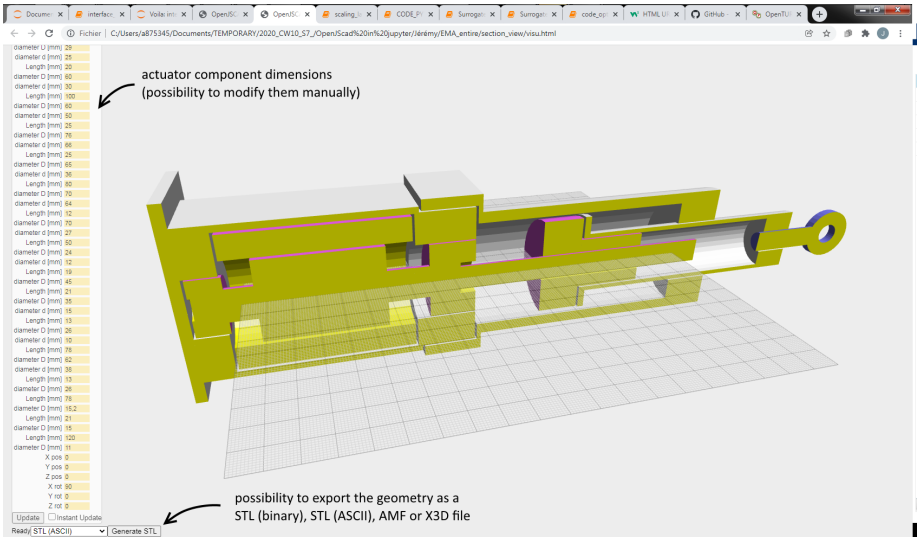

FIGURE 5.21: *GUI WebApp: 3D section view of a sizing example*

5.6 Validation

5.6.1 Basic checks

The preliminary sizing tool is checked on basic scenarios such as a pure static load & static/dynamic load, low or high running cycles, pitting consideration or not and influence of vibratory criterias.

5.6.1.1 Influence of pure static load & static/dynamic load

When not any dynamic performance are expected from the actuator, the required torque does not have the contribution of the rotating inertia. The electrical motor characteristics are not as high as they are when dynamic is taken into account. The torque to stop by the electromagnetic brake comes only from the maximum static load modified by the inverse efficiency of the screw mechanism.

The preliminary sizing verifies these statements.

5.6.1.2 Influence of low/high running cycles & pitting

The running cycles correspond to a number of fatigue cycle. The more the shaft spins, the more the mechanical components with rolling elements accumulate fatigue cycles. As supposed in Chapter 4, the pitting phenomena implies a number of fatigue cycles that corresponds to a number of running cycles. All considered, either varying the specification linked to the pitting cycles or varying the total equivalent distance travelled by the actuator, both play on the total number of fatigue cycles.

As shown by a Whöler curve, the admitted number of fatigue cycles is directly linked to the number and the amplitude of the Hertz contact pressure occuring among the rolling elements. For a given load application, the bigger the elements in contact are, the smaller the Hertz contact pressure is. Also, for important pressure amplitudes, the admitted number of cycles is low, and for smaller amplitudes, the admitted number is higher.

For a given actuator architecture and a given specified number of cycles, the component selection process varies the component sizes. When increasing the size of mechanical components, the rolling elements are bigger and/or more numerous, their fatigue capability is increased.

The preliminary sizing verifies these statements.

5.6.1.3 Influence of vibratory criterias

The surrogate model ckecks that the longer is the actuator, the lower is the resonance frequency. The generated vibratory stress induces the housing and output rod to thicken and increase in diameter.

When setting the output rod diameter as unbounded optimization variable, the increase of the output rod diameter involves the increase of the virtual nut considered in the surrogate hypothesis. Indeed, the nut, filled with the density entered as parameter, evolves with geometrical similarity hypothesis. Consequently, important output rod diameters involves important masses under vibration at nut level. In a context of mass optimization, the increase of the diameter results to have a bound up instead of being boundless. For not reaching this bound up, the diameter increase has been bounded to be smaller than 120% of the effectively sized nut diameter.

As far as the interface between the nut and the output rod is concerned, the solution to fasten the output rod onto the nut might differ depending on the output rod diameter and the nut diameter. If the output rod thickness is thin and the inner diameter matches the one of the nut, the output rod requires a flange around to be fastened. Consequently, an additional length margin should be considered in the specified stroke.

It is clear that most vibratory feedback will come from laboratory bench tests once the actuator is designed and prototyped. The vibratory problem is complex to model. As presented previously, we propose the surrogate as a simple model adapted to preliminary phases.

The leap seal located between the output rod and the housing should have a significant impact on vibratory results. When the bushing is not in contact, the lip seal provides some stiffness between the output rod and the housing along with a damping effect.

Some more information about EMA housing sizing can be found in [Budinger et al., 2015].

5.6.2 Arbitrary Sizings

We suggest presenting some preliminary sizing results from an arbitrary specification. The arbitrary specification and the associated design hypothesis are given in table 5.3. The actuator sizing results regarding the simplex topology (fig. 1.23) are available in table 5.4, in the column named *sizing A*. To show the sensitivity of the values of the static load, stroke, and acceleration (RMS), the arbitrary specification is run again three times with, every time, a modification of one indicator value. *Sizing B* includes the arbitrary static load multiplied by 2. *Sizing C* includes the arbitrary stroke multiplied by 4. *Sizing D* includes the arbitrary RMS acceleration multiplied by 2.

Specification	**Units**	**Value**	**Specification & Design Hypothesis**	**Units**	**Value**
stroke L_s	mm	50	load frequency f_{load}	hz	20
equivalent distance traveled L_{eq}	km	100	total lifespan t_{life}	$hours$	20,000
speed max v_{max}	$m \cdot s^{-1}$	0.2	bus voltage max $V_{dc,bus}$	V_{dc}	110
speed iron v_{iron}	$m \cdot s^{-1}$	0.1	motor phase current max I_{max}	$A_{peak-sine}$	10
acceleration max a_{max}	$m \cdot s^{-2}$	5	all safety coefficients	$-$	1
acceleration rms a_{rms}	$m \cdot s^{-1}$	1	housing heat-transfer coef. (convection)	$W \cdot m^{-2} \cdot K^{-1}$	5
load max F_{max}	kN	3	housing emissivity	$-$	0.4
load rms F_{rms}	kN	1	housing & output rod density	$kg \cdot m^{-3}$	7800
load rmc F_{rmc}	kN	1	housing & output rod thickness min	mm	1
load dynamic peak-to-peak $F_{pitting}$	kN	1	housing & output rod fatigue stress	MPa	500
power rate mean $\overline{PR}$	$W \cdot s^{-1}$	1	quality coefficient Q_m	$-$	30
pair $(a_{PRmax}; F_{PRmax})$	$(m \cdot s^{-2}; kN)$	(3;1.5)	vibratory acceleration a_{vib}	$m \cdot s^{-2}$	98
equivalent load mass M_{load}	kg	50	time-to-stop speed (EMB) t_{EMB}	s	0.05
ambient temperature t_{amb}	$^\circ C$	25	shaft density	$kg \cdot m^{-3}$	7800
skin temperature max $t_{max,skin}$	$^\circ C$	100			

TABLE 5.3: *Arbitrary specification and its design hypothesis*

		Value of Characteristics			
Components	**Characteristics**	**Sizing A**	**Sizing B (F_{max} X2)**	**Sizing C (s_{max} X4)**	**sizing D (a_{rms} X2)**
MECHANICAL COMPONENTS					
screw mechanism (SM)	thread lead $[mm/rev]$	3.1	3.1	3.5	3.8
SM (nut, screw), BB1, BB2, and RE (x2)	total mass $[kg]$	0.72	0.72	0.91	0.65
ELECTRICAL COMPONENTS					
electrical motor (EM)	inertia $[kg \cdot m^2]$	$7.6 \cdot 10^{-5}$	$1.1 \cdot 10^{-4}$	$4.9 \cdot 10^{-5}$	$1.1 \cdot 10^{-4}$
	external diameter $[mm]$	60	64	55	65
	motor constant K_m $[10^{-2}\ (Nm)^2/W]$	4.6	6.3	3.0	6.8
	torque constant K_t $[Nm/A_{rms-sine}]$	0.23	0.26	0.24	0.26
	mass $[kg]$	1.1	1.4	0.87	1.4
electromagnetic brake (EMB)	inertia $[kg \cdot m^2]$	$1.0 \cdot 10^{-5}$	$2.0 \cdot 10^{-5}$	$1.0 \cdot 10^{-5}$	$1.3 \cdot 10^{-5}$
	mass $[kg]$	0.72	1.1	0.73	0.83
ACTUATOR					
housing (H)	thickness $[mm]$	1.1	1.2	4.6	1.1
	mass $[kg]$	1.8	2.0	4.1	1.9
output rod (OR)	thickness $[mm]$	1.4	1.4	3.9	1.4
	mass $[kg]$	0.14	0.14	0.78	0.14
actuator (simplex)	total mass $[kg]$	4.6	5.5	7.5	5.1

TABLE 5.4: *Sizing results from the arbitrary specification*

The following lines comment the sizing results presented in table 5.4 to better understand the sizing choices performed by the optimization.

The arbitrary specification leads a design of the mechanical components mainly guided by the fatigue criteria (*sizing A*). This means that the static load criteria are satisfied with margins. Moreover, because of the low heat-transfer coefficient, the low emissivity, and the significant RMS acceleration level (see table 5.3), the electrical motor design is driven by the heat dissipated through the actuator skin, by convection and radiation.

In *sizing B*, the increase in the static load stands in the static load margin of the mechanical components; their sizing remains unchanged. However, the *Electromagnetic Brake (EMB)* must stop a higher torque. Indeed, the torque to stop in an emergency relies on two specified values: the static load converted by the indirect efficiency of the *Screw Mechanism (SM)* and the screw maximum speed to stop within the specified time t_{EMB}. Doubling the static load, the EMB requires to develop a higher braking force. It is bigger then. This involves the increase in the EMB disk inertia that sums to the total rotating inertia. Thus, a higher electrical motor performance is required. Because of the increased length of the electrical components, the housing is heavier.

Increasing the specified stroke (*sizing C*) makes the actuator longer. The ratio diameter by length is decreased. The housing and the output rod must have their thickness increased to withstand the vibratory accelerations. The screw of the SM is longer, involving an additional mass. What is more, the increased actuator length offers a more extended outer surface for dissipating the heat generated by the motor. The *Electrical Motor (EM)* can have lower performances if the thread lead is increased. The EM has a reduced mass then.

The motor heat generation is based on a continuous torque. The RMS acceleration highly contributes to this torque. Doubling the specified RMS acceleration (*sizing D*) involves an important specified continuous torque. The motor size must be increased to satisfy this specification. Increasing the lead limits the motor size increase for a reduced mass. With a bigger motor, the rotating inertia is higher and the EMB is required to be bigger. Moreover, increasing the lead reduces the fatigue phenomenon applied to the mechanical components. The mechanical components are chosen with slightly smaller fatigue capabilities. They are slightly smaller then. Moreover, the sized electrical components make the actuator longer. Thus, the *Housing (H)* is slightly heavier.

5.6.3 Real use case

The industrial context of this thesis provides an actuator prototype, named DARS, designed for the VSR700 helicopter. This provides a real use case to compare with the preliminary sizing tool results.

Three preliminary sizing cases are launched. A first one, sizing A, takes the DARS specification with its design hypothesis as inputs. A second one, sizing B, takes the same inputs but forces the screw mechanism lead to be exactly the one of the DARS. A third one, sizing C, also takes the same inputs but cancel the pitting phenomena in the specification.

The component characteristic differences between these sizing results and the DARS are compared in table 5.5.

		relative difference r_f [%] (1)		
component	**characteristic**	**sizing A**	**sizing B**	**sizing C**
MECHANICAL COMPONENTS				
screw mechanism (SM)	lead	14	0	-48
	screw diameter	8	11	-41
	nut diameter	7	7	-40
	mass	35	42	-66
ball bearing (BB1)	diameter	-3	0	-38
	heigth	0	6	-33
	mass	12	21	-70
ball bearing (BB2)	mass	20	30	-20
ELECTRICAL COMPONENTS				
electrical motor (EM)	inertia	-62	-66	-85
	resistance	22	6	-36
	external diameter	-14	-14	-28
	length	22	20	2
	motor constant *Km*	-42	-44	-62
	mass	-41	-44	-65
electromagnetic brake (EMB)	inertia	-35	-43	-75
	mass	20	10	-32
motor (EM) & brake (EMB)	mass	-22	-27	-55
ACTUATOR				
housing (H)	mass	-30	-29	-65
actuator (all included)	mass	-28	-28	-68
actuator (without accessories (2))	mass	-16	-16	-62

(1) *the relative difference is defined as* $r_f = (C_{sizing} - C_{DARS})/C_{DARS} \cdot 100$; (2) *accessories are fasteners, connectors & sensors*

TABLE 5.5: *Comparison of the preliminary sizing code results with the characteristics of a real actuator (DARS)*

In table 5.5, sizing A shows that the total actuator mass prediction is close to the one of the DARS when the accessories are removed. Indeed, the fasteners, the antirotation key, the sensors and the electrical connectors are not considered by the preliminary sizing tool. The same observation is done forcing the lead to be the one of the DARS (sizing B).

The DARS actuator has been done with off-the-shelves mechanical components. In sizing A, the tool predicts the ball bearing geometries close to the one of the DARS. Regarding the screw mechanism, the prediction is turned towards a bigger screw with a slightly bigger lead. The higher is the lead, the higher is the fatigue capability. In sizing B, the lead is forced to be lower than in sizing A, the screw mechanism size is increased to keep the same fatigue capabilities. The bearing sizes increase consequently, geometrically constrained by the screw diameter for assembly reasons. What is more, comparing sizing A & B with sizing C highlights that the pitting phenomena significantly guides the screw mechanism design.

As far as the electrical components are concerned, sizing A & B give rather a motor smaller in diameter and longer. The rotating inertia results to be lower. During any electrical supply cut-off and thanks to a smaller lead, the shaft rotation is driven by a lower torque stemming from the load application through the indirect efficiency. The brake size is smaller in sizing B then.

Among all the components, the electrical component characteristics carry the biggest relative differences. The optimized component selection contributes into

these differences. Also, the choice of the component of reference for the scaling laws can explain the differences. The DARS is equipped with a taylor-made motor and brake, both can not be found in any catalog. The sizing tool considers components of reference taken from the supplier' catalogs [PARKER, 2022] [MIKIPULLEY, 2022]. The sizing tool adapts the electrical motor winding characteristics to the specified voltage and current. Moreover, each supplier component range has its own design specificities. Furthermore, among the electrical components, the biggest relative difference is for the inertia characteristic. This characteristic determination is the most sensitive to uncertainties because of the power used in the scaling law.

Table 5.5 shows that the actuator can potentially take advantage of a mass gain regarding the electrical motor design. As reminder, the preliminary sizing is based on continuous laws associated with uncertainties. It does not provide necessarily components available in the industry. This highlights the need for a future development: a preliminary sizing based on the component selection into suppliers' catalogs.

5.6.4 Resolution performance

Thanks to the analytical content of the code (no call of external softwares), the time to solve the optimization problem is relatively quick (< 1 *min*). This level of reactivity is essential for a preliminary sizing tool.

In table 5.6, the sizing tool is run with the two available optimization algorithms. As expected, the gradient-based algorithm is faster than the gradient-free one. Both point to very close solutions. Even if the gradient-free algorithm is slower, we use it to make sure to point towards a global minimum.

	SLSQP	**Differential evolution**
tolerance or accuracy	10^{-5}	10^{-5}
relative difference between solutions	$2.2 \cdot 10^{-3}$ %	
resolution time	919 ms	50.5 s
MFE [(1)]	229	1000
gradient evaluations	18	–

[(1)] *Maximum Functional Evaluation (MFE): number of times the objective function has been evaluated*

TABLE 5.6: *Resolution performance of the sizing tool*

5.7 Application

In this section, some real application cases are brought to illustrate the applicability of such preliminary sizing methodology.

Different specifications from real application cases are executed into this sizing code and output results are presented. These specifications are linked to redundant topologies of actuation and to two different helicopter use cases: the main rotor and the tail rotor.

For confidentiality matters, inputs and results are presented as ratios of quantities. The observation of the sizing evolutions is the focus point of this section.

5.7.1 MRA vs TRA applications

Chapter 2 showed that the TRA application was distinguished from the MRA in terms of dynamism, load and especially in terms of induced motor losses. To illustrate this difference between the MRA and TRA applications (table 2.10), their specifications are executed into the sizing code. The resulting sized motor characteristics and the actuator mass distribution are displayed in fig. 5.22 & 5.23.

For confidentiality reasons, the results of the MRA and TRA sizing are normalized. The reference is taken as the actuator sizing which satisfies both applications at the same time.

Figure 5.22 globally shows that the selected motor for the TRA has reduced characteristics compared to the one selected for the MRA. The rotor inertia, which induces motor losses, is drastically lowered compared to the MRA selected motor.

Chapter 2 suggests the mean power rate $\overline{PR}$ and the RMS acceleration a_{rms} as a way to consider the induced motor losses. In fig. 5.22, the orange line shows the sizing resulting from the reference actuator specification regardless $\overline{PR}$ and a_{rms}. The losses results to be estimated at roughly 40% of what they are for the reference actuator and the continuous torque at roughly 70%. The performance difference is also seen through the actuator mass statement in fig. 5.23. It is clear that not considering the values $\overline{PR}$ and a_{rms} into the actuator specification involves a significant risk of undersizing the electrical motor of the actuator.

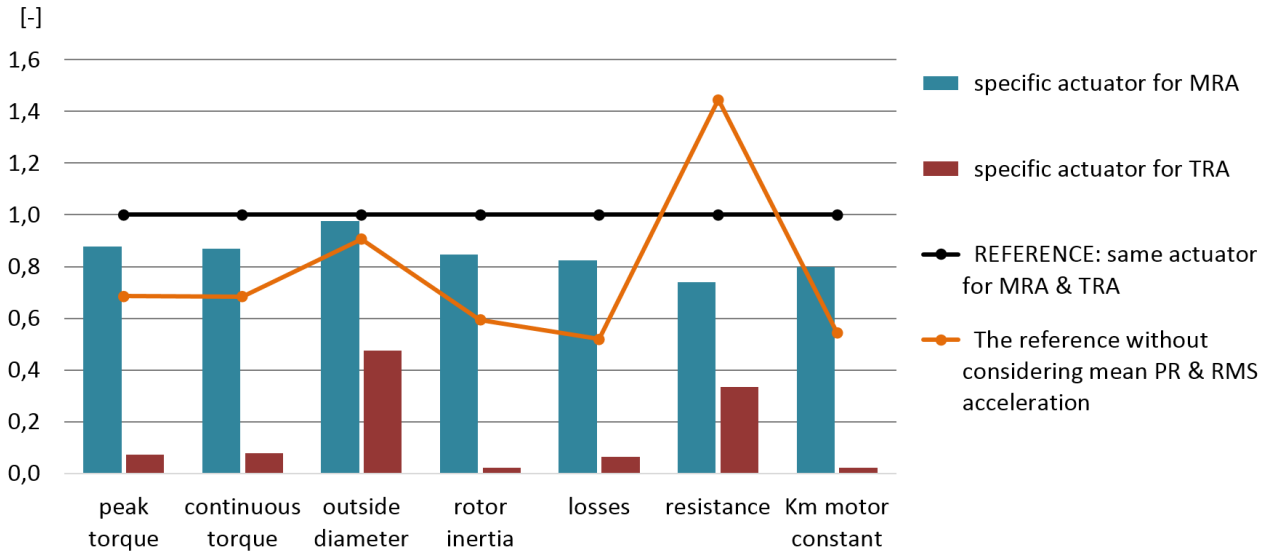

FIGURE 5.22: *Motor characteristic evolution of specific actuators for the MRA & TRA applications compared to an unique actuator for both applications (reference).*

Fig. 5.23 shows the important mass decrease among components induced by TRA application compared to MRA one. The TRA total mass shows to be 80% lower than the one of the actuator satisfying both applications.

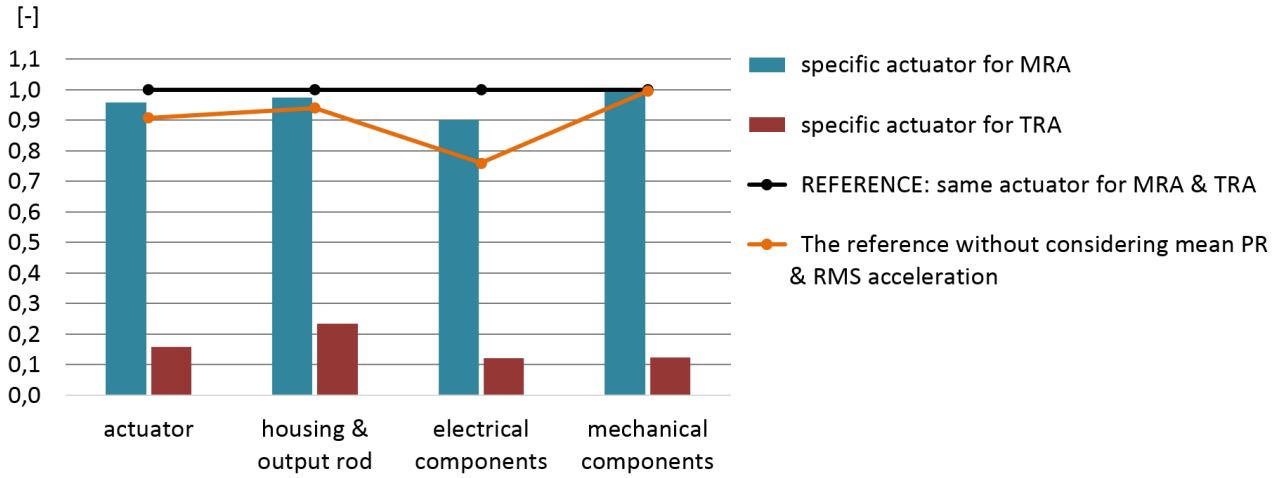

FIGURE 5.23: *Mass distribution of specific actuators for the MRA & TRA applications compared to an unique actuator for both applications.*

The MRA and TRA of the considered helicopter PFCS lead to two significantly different sizings. MRA and TRA are two applications to be distinguished. Designing a specific actuator for each application will benefit the helicopter mass and its electrical network.

5.7.2 Redundant topologies of actuation

There are mainly two redundant topologies of actuation [Maré, 2017, Naubert et al., 2016, Seemann et al., 2012]. A first one is the force summing where the failed or passive actuator shall be free in motion. In this case, the actuator must be equiped with a clutch or any breaking fuse system. A second one is the position summing where the failed or passive actuator shall be locked from motion. In this case, the actuators must be equiped with a power-off brake. The position summing topology can be seen with actuators either installed in tandem (as presented in fig. 5.24 (a)) or in parallel (fig. 5.24 (b)). The tandem configuration is the most commonly found in aeronautics (Chapter 1, table 1.5). This equips the PFCS of fighter aircrafts and helicopters, and the SFCS of comercial aircrafts (except spoiler) [Maré, 2017]. Meanwhile, the parallel configuration is far less used [Maré, 2017].

We suggest to study the impact on housing mass and output rod mass involved by the consideration of topology (b) compared to topology (a) (fig. 5.24). It is clear that topology (b) introduces potential additionnal plays and wear points compared to topology (a). However, it is important to estimate if this topology involves any mass gain that would compensate these drawbacks.

From tandem to parallel topologies, the force is halved, meanwhile the stroke, speed and acceleration are doubled. The work produced by the actuator remains the same.

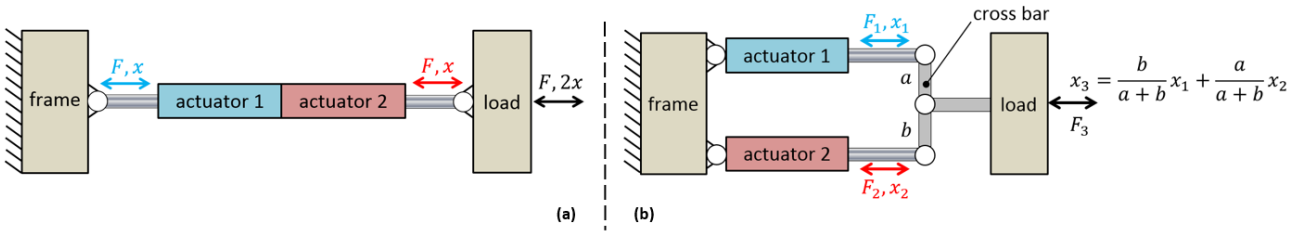

FIGURE 5.24: *Redundant topologies of actuator in position summing (passive/failed actuator shall be locked). (**a**) 1 tandem actuator, (**b**) 2 simplex actuators linked by a cross bar ($a = b$ considered, $F_1 = F_2 = F_3/2$).*

The bar chart presented in fig. 5.25 presents sizing results involved by both actuation topologies. The results are given as a ratio with the sizing results obtained for a simplex actuator not equipped with any electromagnetic brake.

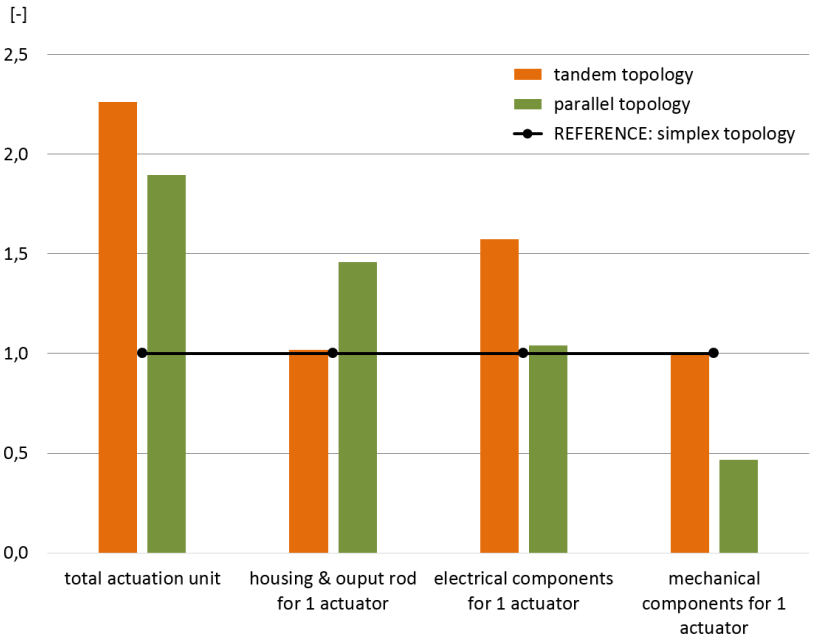

FIGURE 5.25: *Mass evolution of tandem or parallel topologies compared to simplex topology.*

As the parallel topology requires doubled stroke and half load, the actuator is longer and smaller in diameter than in the tandem topology. The thicknesses of the housing and the output rod are nearly doubled. The mass of the set (housing & rod) results to be half heavier than the one of the tandem topology. The parallel topology shows electrical components and mechanical ones with reduced characteristics and reduced masses compared to the tandem topology. Therefore, the contribution of the set (housing & rod) mass on total actuator mass is much higher for the parallel topology. Fig. 5.26 confirms it with a contribution of a third of the actuator mass concerning the tandem topology against more than half the actuator mass concerning the parallel topology.

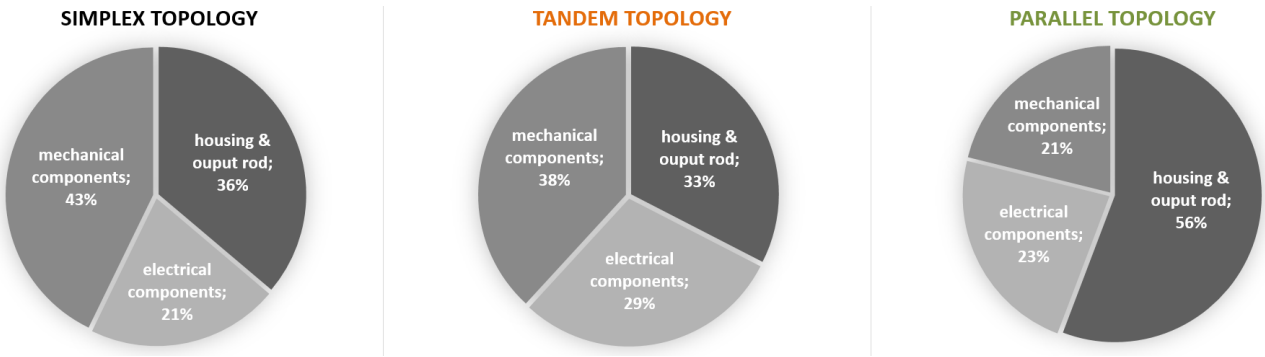

FIGURE 5.26: *Component mass distribution for one actuator.*

The parallel configuration seemed to be a relevant choice because of the load reduction. However, this finally penalizes the actuator since the load reduction involves a small actuator diameter. With the increase of the stroke, the diameter to length ratio is no longer interesting. There is not any mass gain on the housing and the output rod. The cross bar has to be considered in the mass statement too.

Finally, the total actuation mass gain involved by the parallel topology is not significant enough relatively to the potential drawbacks it introduces.

5.8 Conclusion

The MDO field mainly solves multidisciplinary couplings and singularities to create a viable workflow of equation execution with optimization. Different strategies are available: either using a distributed architecture or a monolithic one. The choice is turned towards monolithic compatible with the problem scale and the expected resolution speed. The monolithic architectures follow two different approaches in order to solve the multidisciplinary couplings. One uses numerical solvers meanwhile the second relies on an optimizer and reformulates the design problem. The second approach precisely was chosen for this thesis (i.e. the NVH architecture). The sizing procedure includes non-linearities. To make sure of a global minimum, the optimization algorithm is suggested to be a gradient-free one such as the differential evolution. The resolution time is reasonably fast.

The presentation of the design graphs per component and then, the full sizing procedure, highlight that the complexity level of a multidisciplinary problem requires some methodology. This thesis actuator preliminary sizing has a reduced number of parameters. Some graphical representations are used to settle down the problem. The design graphs and/or N^2-diagram check the interfaces between several disciplines. The XDSM representation is an efficient formalism to check out the whole MDO process of the actuator sizing problem.

What is more, this Chapter showed the implementation of the actuator preliminary sizing procedure into a GUI WebApp. This is to create a user-friendly tool escaping from any code lines to deal with or any bothers from software package installations.

Finally, the validity of the preliminary sizing prediction is compared to a real use case (VSR700 actuator prototype). Also, the applicability of the preliminary sizing tool is emphasized with two studies.

The first study compares redundant topologies of actuation. For a given specification, the first study concludes that the parallel topology was not a relevant choice compared to the tandem topology. This because of the trade-off between failure level and mass gain.

The second study compares the MRA and TRA specifications from the same helicopter (VSR700). This study backs up the conclusion of Chapter 2. Chapter 2 stated a clear dynamism and load difference between the MRA and the TRA with indicators quantifying the importance of the motor losses. These losses are induced by the mean power rate $\overline{PR}$ and especially the equivalent continuous acceleration a_{rms} of the application. The second study showed the risk of undersizing if a_{rms} and $\overline{PR}$ are not taken into account. Furthermore, it concludes that the helicopter mass could benefit from a specific sizing adapted to the MRA and the TRA. The TRA shall be designed with a rotor inertia as low as possible.

Chapter 6

Conclusion, discussion & perspectives

6.1 Conclusion & discussion

The market trend is globally facing a technological watershed towards more electrical solutions. Also, the helicopter dronization expansion generates a need for the implementation of eletrical *Primary Flight Control System (PFCS)* on already flying helicopters. The PFCS architecture involves *Electromechanical Actuators (EMAs)*. These actuators are named critical EMAs because of the harsh running conditions and the safety criterias they must comply with. The EMA is a mechatronic system including multidisciplinary components. There is a real need to support the preliminary design of critical EMAs. This need includes the formulation of an actuator specification. Thus, the added value of this thesis takes place on the downward side of the design V-cycle. This thesis brings a design methodology with models & tools to support the specification and the preliminary sizing of critical EMAs in the context of a collaborative work. This methodology can be applied to any EMA architectures. These architectures can answer diverse actuation needs, from drones to heavy vehicles.

Firstly, this thesis contributes into the specification phase through a specific analysis methodology and dedicated models. A data driven specification methodology draws a parallel between measurement data from flight tests and the EMA main design drivers using equivalent indicators. The approach enables to manage the increasing data content of flight tests. What is more, the industrial trend is to reduce the number of helicopter flight tests to shrink development costs. Consequently, the methodology must extract as much added value as possible from any available data sample. The indicators are used to express the load, the speed and the acceleration limits of the application. Furthermore, the specification methodology applied on the main rotor and the tail rotor actuation highlights the helicopter specificities. It shows a clear dynamism and load difference between the *Main Rotor Actuator (MRA)* and the *Tail Rotor Actuator (TRA)*. The indicators quantify the importance of the motor losses on the TRA compared to the MRA. These losses are induced by the mean power rate $\overline{PR}$, and especially by the equivalent continuous acceleration a_{rms}. Chapter 5 showed the risk of undersizing if a_{rms} and $\overline{PR}$ are not taken into account. In addition, it concludes that the helicopter mass could benefit from a specific sizing for the MRA and the TRA. The TRA shall be designed with a rotor inertia as low as possible.

In addition, in order to have a better understanding of the EMA load, a system level modelling of the dynamic rotor load, applied on the PFCS has been developed. The model takes basis on differential algebraic equations derived from Lagrange's equations. It allows, in particular, to represent the dynamics of the blades and the power conversion at the swashplate. This model gives access to the load application on the 3 actuators as a function of their displacements. This model highlighted several

phenomena. The hammering forces characteristic of the application are essentially due to aerodynamic force harmonics, that are difficult to represent by simple lift coefficients. This conclusion justifies the analysis of flight data in Chapter 2. The risks of instability cannot be analyzed with the approaches developed in Chapter 2 alone. The instability risk assessment gives an applicative example of the dynamic load model. Such an analysis showed an increasing instability risk with the reflected inertia of the EMA. However, this instability risk is limited, by the actuator architecture avoiding free running modes in failure scenarii, a power-off brake equips the EMA.

Secondly, this thesis contributes into a system level sizing of critical EMA through dedicated models and tools. The models are mainly based on scaling laws and the dimensional analysis. The scaling laws capture the main physical phenomena driving the component design and estimate easily the main component characteristics from a reduced number of parameters. The approach has been illustrated and validated on different components of mechanical transmission and power transmission for EMA. An extension of these scaling laws has been implemented for the EMA housing sizing. This uses a surrogate model or a *Response Surface Model (RSM)*. It is set up using dimensionless numbers (or π-numbers) based on the methodology named *Variable Power Law Metamodel (VPLM)*, already developed in the laboratory team. This thesis suggests to address the complex vibratory problem of the EMA housing by a RSM since it is adapted to preliminary studies. Indeed, it is a simple way of modelling with reduced number of parameters. The suggested model provides easily design trends for an architecture decision-making. This is illustrated in Chapter 5, where an applicative example compares actuator topologies. What is more, a tool was generated as presented with some screenshots in Chapter 5. It implements the final preliminary sizing methodology through a GUI WebApp i.e. an user-friendly interface based on Open Source solutions (Python). This tool uses only 3 inputs: a specification, some design hypothesis and components of reference (for scaling laws). After execution, it finally provides the characteristics of the actuator components complying with the specification and minimizing the total mass. This tool is available from a server and can be easily accessed by anybody equipped with a web browser only (laptop, tablet, smartphone). This facilitates the collaborative work. Also, this thesis models were developed using *Jupyter Notebooks* as a way to closely link the documentation with the models. This aims at enabling the reuse of models and the knowledge capitalization at the design office. Airbus Helicopters is already equipped with a *Jupyter Notebook* server.

6.2 Perspectives

The main perspective is to develop this thesis work further, according to three main axis: the models, the sizing tool, and the collaborative work.

Firstly, the models presented in this thesis introduce some perspective of improvment.

As far as the sizing models are concerned, the scaling prediction can be improved. A methodology based on clustering methods can be implemented to choose the best reference component, reducing the relative errors (the mean, the standard deviation). Also, the fidelity of friction models can be improved to reduce safety margins over–sizing the running motor torque. Lubrication strongly impacts friction levels. To consider lubrication, some uncertainties can be introduced. Then, for any other discipline, if more detailed models are necessary, a coupling can be introduced with FEM models using a surrogate methodology and *Functional Mock–up Interface*

(FMI). Moreover, in Chapter 5, the sizing comparison with a real actuator design highlights the interest of directly selecting components into supplier catalogs. Indeed, the optimization can be switched from a continuous design domain to a discrete one, using decision trees and machine learning methods. The idea is to size and optimize the actuator by picking up available components into supplier catalogs. The actuator design solution is directly applicable then. A PhD work on this topic is in progress at the ICA laboratory. Another perspective goes to take into account the control loop characteristics since it impacts the actuator sizing. The last section of Appendix A already introduced this perspective. It will consist in optimizing the specification according to additional specified items (actuator bandwidths). The control loop parameters entered in the mission profile filter (i.e. ξ_Ω , R_{sp}, ω_p) would be optimization parameters. The actuator bandwidths in load rejection and load pursuit would be set as constraints.

As far as the rotor dynamic load model is concerned, it requires further work on extracting the necessary parameters from CFD simulations or from an equivalent detailed dynamic model. This can be done in a way to facilitate the exchanges between the department estimating loads and the PFCS department. Another development concerns the representation of the aerodynamic load harmonics and the fine fitting onto basic running flight phases. On the long term, this model could be used in a preliminary design phase for the prediction of load levels without any flight test. Also, it could be used in an integration design phase e.g. for the validation of actuator control algorithms. Also, it could be a support to set a representative lab test bench.

Secondly, the sizing tool requires the implementation of additional features to support the architecture selection. The design methodology presented in this thesis can be applied to any other actuator architectures. Other components and actuator architectures must be introduced. For instance, the pre–constrained screw mechanism is interesting for missions alternating compression & tensile loadings. the direct-drive architecture based on a thrust ball bearing is promising in terms of loading capabilities for the helicopter PFCS. There is a real need of pre–design studies. This means to study and select, for a given application, the best architecture and the best component characteristics minimizing the actuator total mass or satisfying any other objective(s). What is more, the user might be interested in reaching the design domain close to the optimal point. The implementation of the design by shopping with parallel coordinate plots are efficient tools for decision-making in the component selection. In addition, since the actuators are critical, an analysis among different redundant topologies of actuation and a safety analysis with failure trees are important features to develop. Lastly, an actuator price assessment is a relevant and complementary feature to implement since it supports effectively the operational work of the design office.

This previous paragraph leads to a perspective of modularity regarding the sizing tool structure. We can imagine a tool interface based on the assembly of bricks, similarly to *Object–Oriented Programming (OOP)*. It would generate, on an autonomous manner and without diving into code lines, the sizing procedure, its pre–processing and post–processing according to the desired actuator architecture. The interface would enable picking up items from different libraries: one of actuator architectures, one of redundancy topologies, one of actuator components with their different physical models to tick or untick, and three other ones dealing with the optimization i.e. one of design variables, one of design objectives and one of design constraints (sizing scenarios). The interface would enable to run in parallel different sizing processes to easily compare final results and select the most suitable EMA architecture complying with a given application use case.

Furthermore, the *Multidisciplinary Design Optimization (MDO)* platforms such as the Open Source tool GEMSEO can be inspiring or resourceful in implementing the new features linked to the previously mentioned perspectives. From a single workbook where the problem is specified, this tool supports the user without getting into any code lines and until defining the whole MDO process with its *Extended Design Structure Matrix (XDSM)*. GEMSEO allows assessing miscellaneous MDO architectures and optimization algorithms. It includes interesting post-processing tools too. Also, the use of MDO frameworks is a way to manage the continuity of models and connect them to optimization algorithms with modularity.

Thirdly and lastly, to enhance the collaborative work, every tool should have its own interface available online. This is to have a portfolio of tools, enabling easily the actuator study in terms of specification, stability, and sizing for different architectures. Regarding the mission profile analysis, a GUI WebApp tool has already been started to execute the methodology presented in Chapter 2. However, on a long term basis and for unlimited capacity, the implementation should rather be on the Skywise platform developed for big data analysis. This platform implementation at Airbus Helicopters started lately in the thesis progress. It expands and some applications dealing with a broad database of helicopter components are already used by employees.

Appendix A

Command filter

A.1 Proposition

Considering the available flight data, given in Chapter 2, a tool is required to turn the position commands (sent by the FCC to the actuator) into the positions effectively performed by the actuator. We propose to set up a transfer function simulating the behavior of the actuator. This transfer function is applied as a filter over the mission profiles.

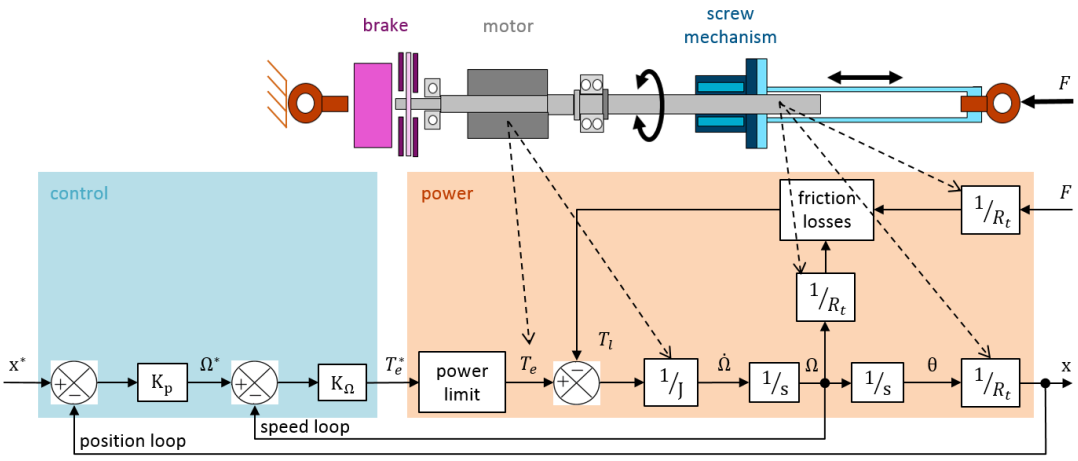

FIGURE A.1: *EMA top-level model (adapted from [Maré, 2020])*

A top-level model of EMA is proposed by [Maré, 2020] (fig. A.1). This proposition fits within a flight control use case where the EMA is position-controlled: the rod extension x must follow the position demand x^* and reject the disturbance coming from the load F. This model can be used in general basis where the motor rotor inertia dominates the natural behavior of the EMA in pursuit mode. The model has got 2 loops:

- an outer position control loop with a proportional gain K_p
- an inner speed loop controlling the motor speed Ω with pure proportional gain K_Ω

We consider a current loop as sufficiently fast (usually 1 kHz [Maré, 2020]) to be neglected regarding the position and speed loop (respectively, [1-10] Hz and [50-200] Hz in common applications [Maré, 2020]). That is why the electromagnetic torque T_e is established instantaneously and without saturation in response to the speed controller output (torque demand T_e^*).

The Power block (right of fig. A.1) gathers the mechanical transmission between the motor shaft and the output rod. For a direct-drive EMA, $R_t = 2\pi/p$ with $p\ [m/rev]$ the lead of the screw mechanism. In common aerospace applications [Maré, 2020] and in a context of preliminary study, the compliance and backlash of the mechanical transmission are sufficiently low to ignore them.

Neglecting the power limit and frictional losses (fig. A.1), [Maré, 2020] simplifies the EMA model into a pure second-order transfer function (eq. A.1).

$$x = \frac{1}{1 + \frac{2\xi}{\omega_n}s + \frac{1}{\omega_n^2}s^2} \cdot x^* - \frac{1}{K_f} \cdot \frac{1}{1 + \frac{2\xi}{\omega_n}s + \frac{1}{\omega_n^2}s^2} \cdot F \tag{A.1}$$

where w_n is the pulsation at cut-off frequency, ξ is the damping ratio and $K_f = K_p \cdot R_t \cdot K_\Omega$ the stiffness of the EMA closed-loop control with $K_p = R_t \cdot \omega_n/(2 \cdot \xi)$ and $K_\Omega = 2 \cdot J_e \cdot \xi \cdot \omega_n$.

In the context of mission profile analysis, the load rejection (right member eq. A.1) can not be considered since it involves the actuator design (transmission ratio R_t, equivalent rotor inertia J_e). However, we propose to proceed as shown at the bottom of Fig. A.2. We keep the ideal source of torque and we suppose the speed loop behaving as a second order transfer function of parameters:

$$(\xi_\Omega,\ \omega_\Omega \approx R_{sp} \cdot \omega_p)$$

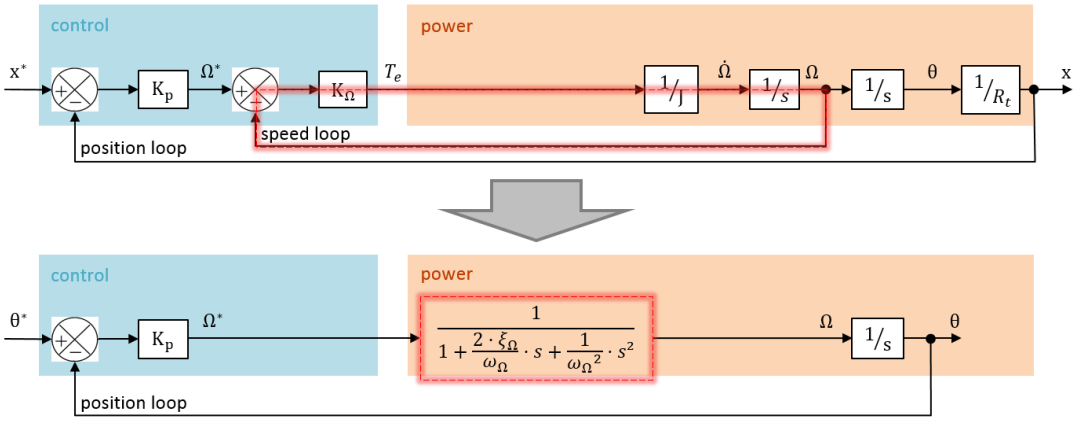

FIGURE A.2: *Block diagram: (top) actuator model from fig. A.1 with the parameters only available at preliminary phase, (bottom) proposition of considerations for filtering position data*

This leads to a third order transfer function (eq. A.2).

$$TF_{filter}(s) = \frac{x}{x^*} = \frac{\Theta}{\Theta^*} = \frac{1}{1 + \frac{1}{\omega_p}s + \frac{2\xi_\Omega}{R_{sp}\omega_p^2}s^2 + \frac{1}{R_{sp}^2\omega_p^3}s^3} \tag{A.2}$$

A.2 Parameters

In an open loop, we have:

$$TF_{OL} = \frac{\Theta^*}{\Theta} = \frac{K_p}{s} \cdot \frac{1}{1 + \frac{2\xi_\Omega}{\omega_\Omega} s + \frac{1}{\omega_\Omega^2} s^2} \tag{A.3}$$

Considering the unity gain, we easily establish the corrector K_p:

$$\lim_{s \to 0} TF_{OL} = 1 = \frac{K_p}{s} \implies \frac{K_p}{\omega_p} \approx 1 \tag{A.4}$$

$$K_p \approx \omega_p \tag{A.5}$$

Literature provides an order of magnitude of the link between the position and the speed loop (table A.1).

control loop	**bandwidth ratios from** [Maré, 2017]	**bandwidth ratios from** [Lacroux, 1985]
speed & position	$R_{sp} = \frac{\omega_s}{\omega_p} \in [2.5; 5]$	$R_{sp} = \frac{\omega_s}{\omega_p} \in [5; 10]$
current & speed	$R_{cs} = \frac{\omega_c}{\omega_s} \in [7; 10]$	$R_{cs} = \frac{\omega_c}{\omega_s} \in [5; 10]$

TABLE A.1: *EMA bandwidth ratios*

In the special use case of the VSR700 actuactors, the third order filter is set with an actuator position bandwidth f_p, a ratio $R_{sp} = 10$ and a damping coefficient $\xi_\Omega = 0.7$ as the best reduced time response (see Appendix H, fig. H.1). These parameters can be set in the mission profile analysis code. There is not any damping coefficient to be set regarding the position loop.

A.3 Validation

To validate the use of the third order transfer function (eq. A.2), an actuator model (Amesim V16, Siemens) was built to compare responses between the filters and the actuator. The model (fig. A.3) gathers a sinusoidal command or a step command, an ideal source of torque controlled by a position & speed loop with correctors, an ideal transmission and a source of load.

Two simulations have been carried out under :

1. a 5hz 1mm sinus signal input (fig. A.4)
2. a 1mm input step (fig. A.5)

They display the responses of the actuator model, considering the third and the second order filters for the same command.

It is clearly observed that simplifying the model behavior to a second order transfer function alone (member on the left of eq. A.1) has not sufficient load rejection capabilities. This is because the dynamic of the speed closed-loop is not fast enough. Taking the approach with the third order transfer function (eq. A.2) shows definitly the best representativity compared to the second order filter. Indeed, the speed

closed-loop is faster. It results in an increased closed loop control stiffness which involves a better load rejection.

Note: The 2nd order filter response is displayed with $\xi_p = 0.7$ and the specified value $\xi_p = 0.9$. A value of 0.9 ensures not any overshoot in the response. Comparing both of these displays with the third order transfer function response in terms of speed and acceleration shows important relative gaps. However, the position response to a step input shows a similar 95% response time.

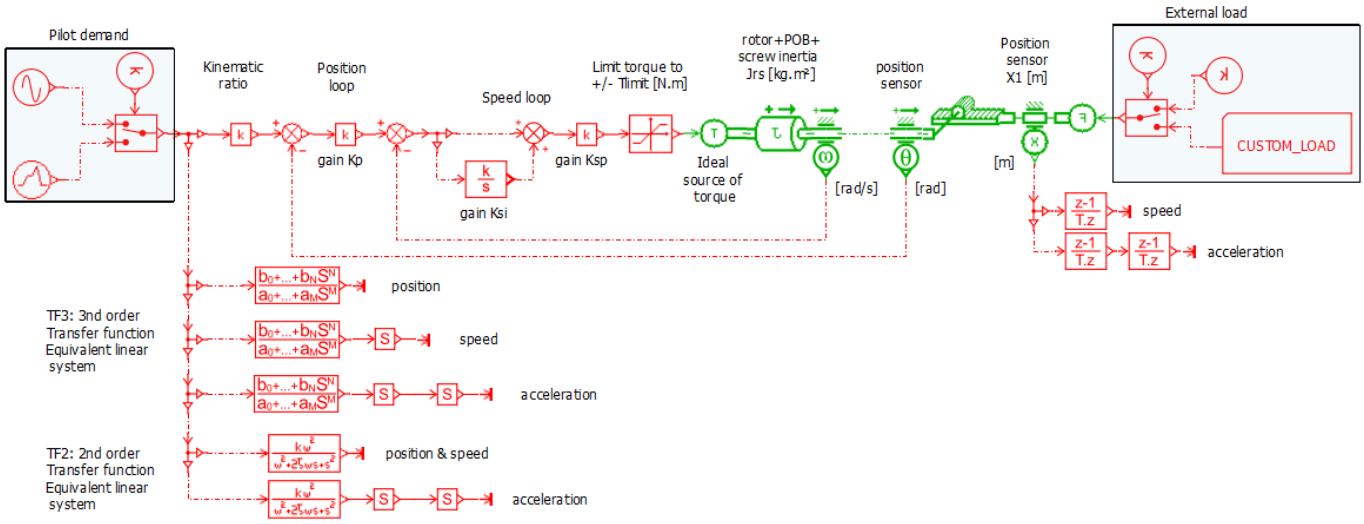

FIGURE A.3: *Actuator basic model for checking TF filter responses*

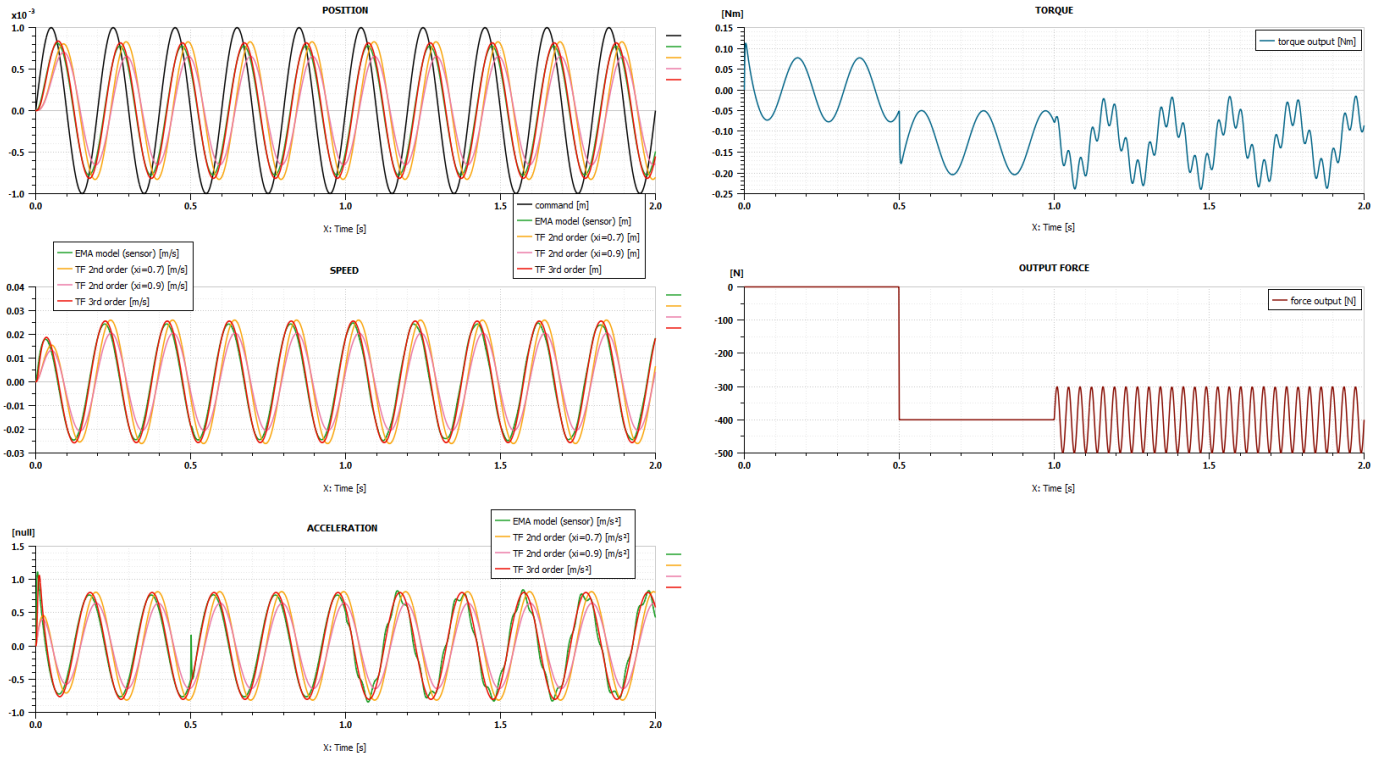

FIGURE A.4: *Comparison model vs TF filter considering 5hz sinus of 1mm amplitude (the comparison should be done with identical control loop performance)*

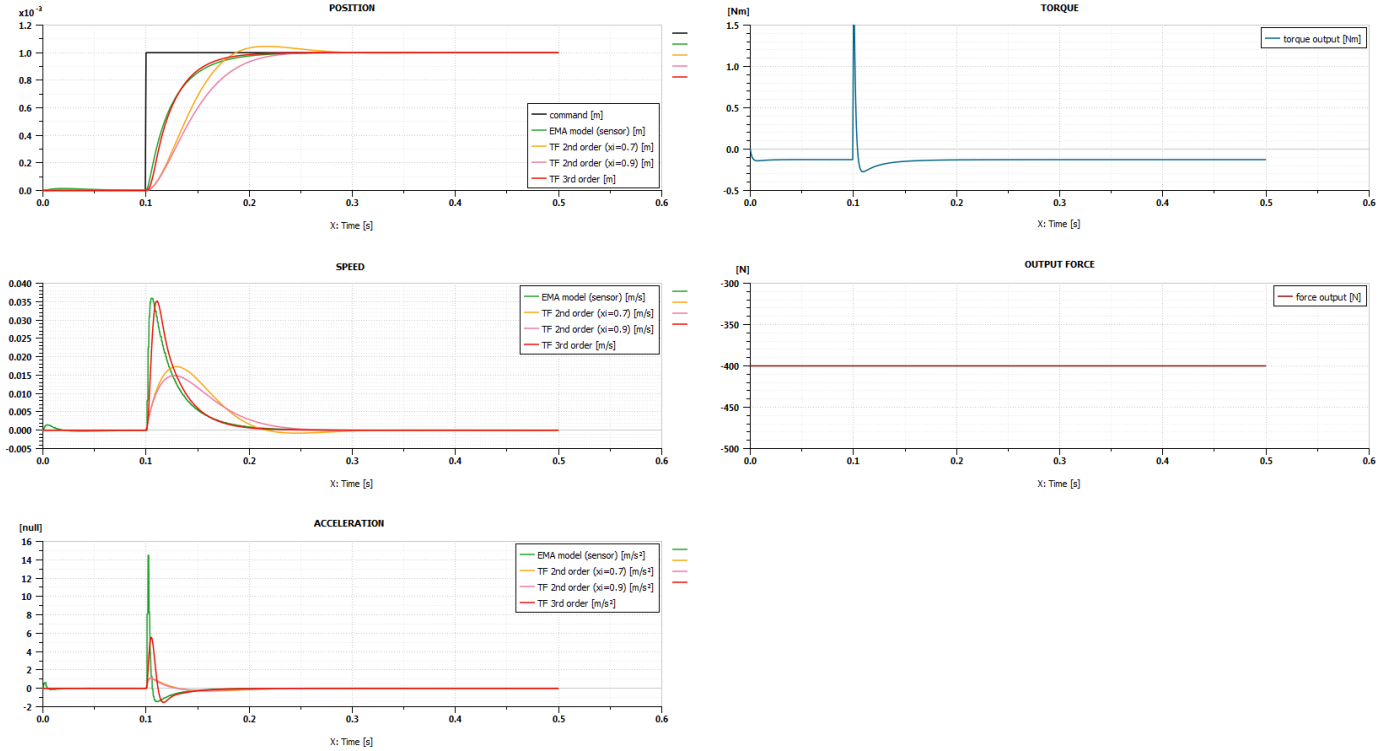

FIGURE A.5: *Comparison model vs TF filter considering 1mm input step position (the comparison should be done with identical control loop performance)*

An additional check has been done on the frequency response (fig. A.6). The third order TF filter complies with the frequency ranges expected by the automatic pilot (AFCS): fig. A.7 & A.8.

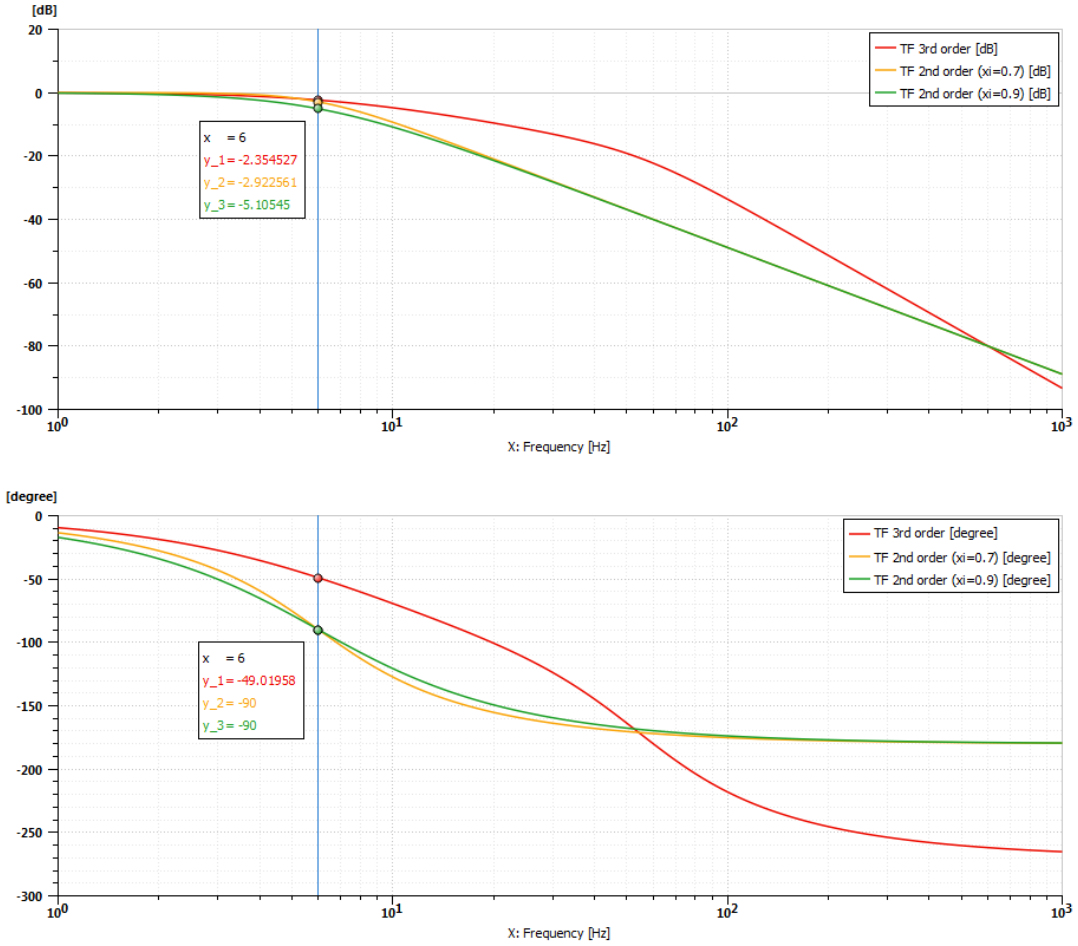

FIGURE A.6: *Bode response of TF filter*

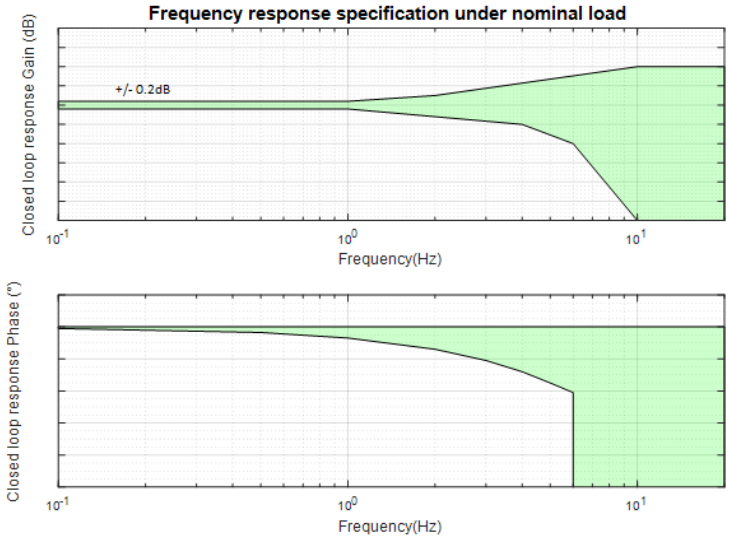

FIGURE A.7: *Bode response pattern specified under the nominal load of* $\pm 0.26 \cdot F_{max}$ *N),* F_{max} *the maximum static load*

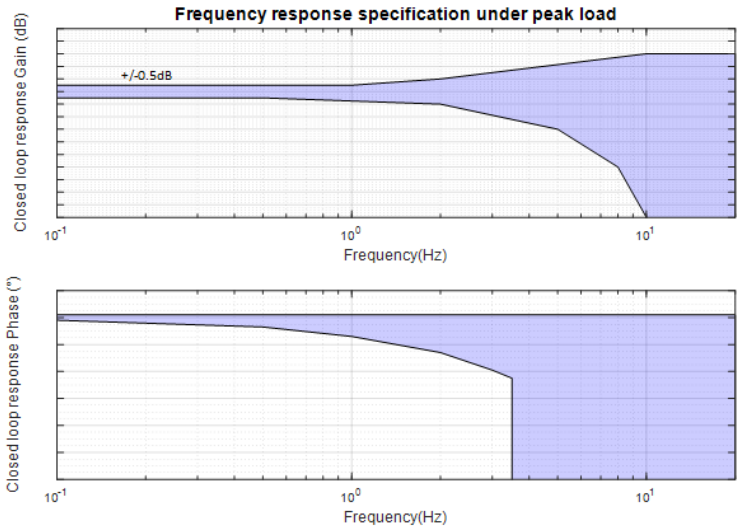

FIGURE A.8: *Bode response pattern specified under the peak load of* $\pm 0.52 \cdot F_{max}$ *N),* F_{max} *the maximum static load*

Furthermore, the TF filter has been checked with real data from VSR700 (ECU position commands & loads, 125hz records) and a more representative EMA model (same than fig. A.3 but including screw efficiencies, bearing and antirotation key frictions, see fig. A.9).

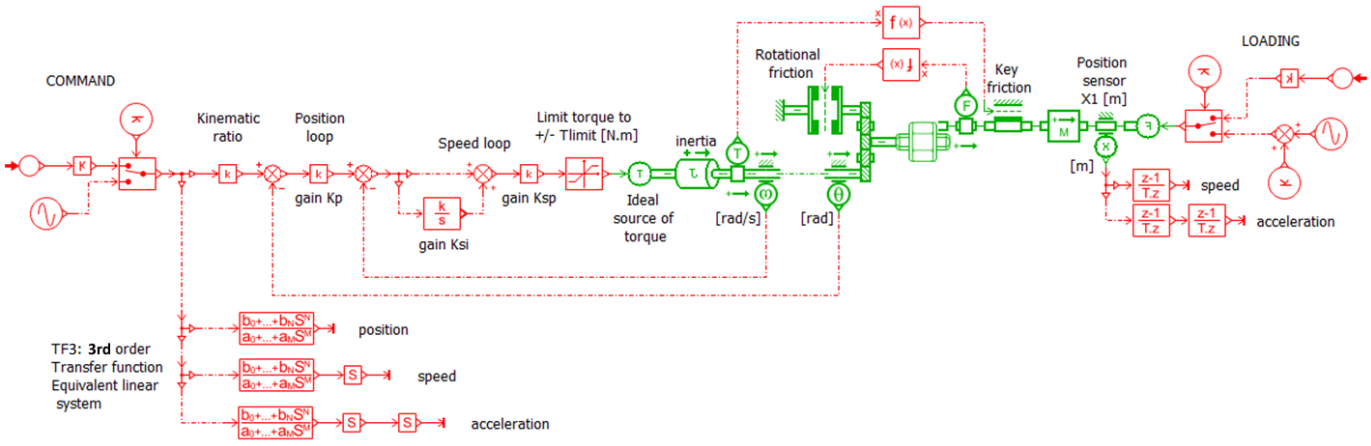

FIGURE A.9: *Actuator model for checking TF filter responses*

Fig. A.10 compares the actuator model response and the third order filter response under a sample of real positions performed during a 80knt horizontal flight test (VSR700).

In fig. A.10, the speed response from the TF filter when actuator speed gets close to a zero value is not representative. Indeed, the 3rd order filters will never simulate a friction cone (even less with stiction). Notwithstanding, this filter is considered as sufficiently representative to speed & acceleration estimations during preliminary design phases.

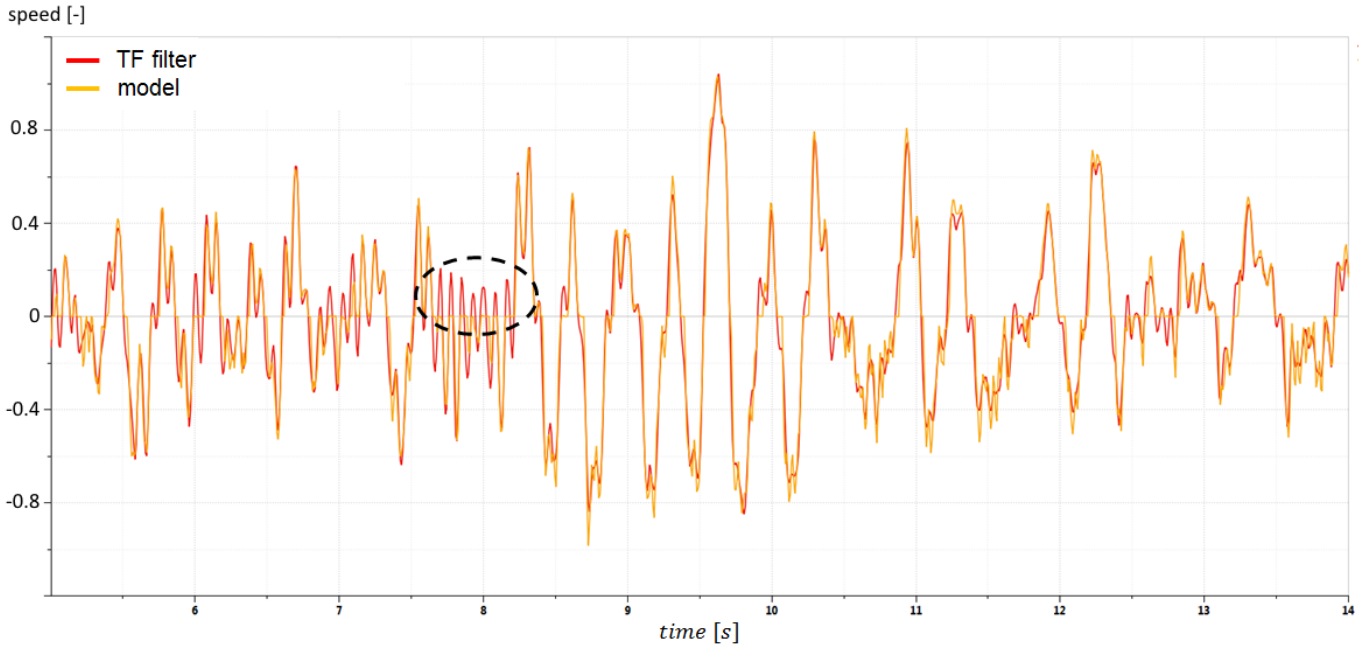

FIGURE A.10: *Comparison model VS TF filter with flight test positions, speed normalized by the maximum speed recorded*

A.4 Perspectives

The parameters of the third order filter open the way to a perspective for this thesis. The control loop characteristics impact the final actuator sizing, it is necessary to take them into account in the actuator sizing procedure. This can consist in optimizing the specification according to additional specified items (actuator bandwidths: gain margin, phase margin). The control loop parameters entered in the mission profile filter (i.e. ξ_Ω , R_{sp}, ω_p) would be optimization parameters. The actuator bandwidth in load rejection and load pursuit would be set as design constraints.

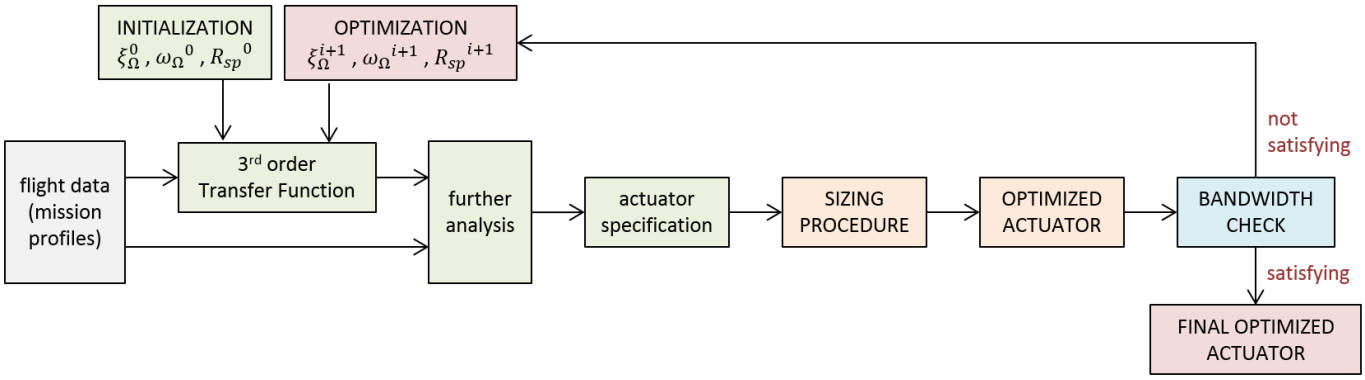

FIGURE A.11: *Perspective to consider control loop parameters in preliminary actuator sizing*

To complete this idea of perspective, the approach offered by the reference [Maré, 2022] adds key elements. Indeed, the author suggests a top-down process based on the generation and use of charts that define the optimal position gain, speed loop second–order damping factor and natural frequency with respect to the specified performance of the position loop. The author validates by simulation a design robustness stemming from the definition of these parameters. This is done using a

realistic lumped-parameter model of a flight control actuator that includes significant functional and parasitic effects.

Appendix B

Rainflow Method

B.1 Introduction

The rainflow is a method to count loading cycles.

In French, it means “methode de la goutte d’eau”. [Struzik and Celli,] says the name comes from the counting method which can be seen as water drops sliding along the temporal signal to analyze. If we consider the herebelow uniaxial variable amplitude loading history, the water drop method applied aside reveals 5 cycles.

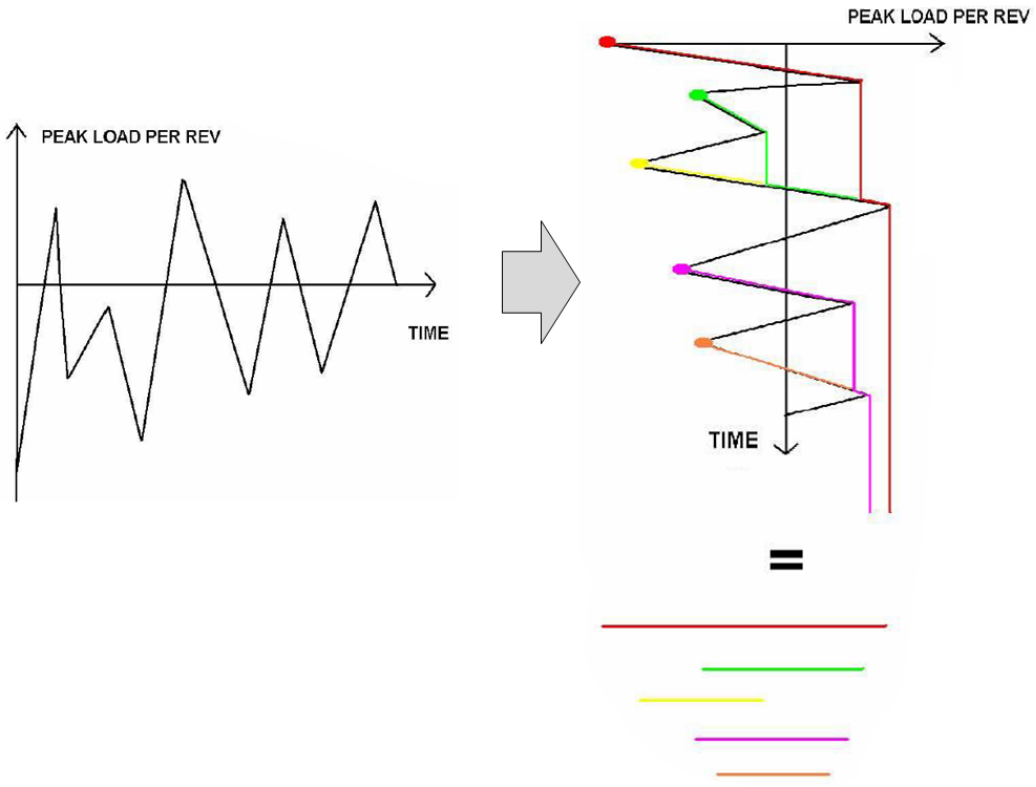

FIGURE B.1: *Rainflow method: a visual explanation*

B.2 Loading cycles

The loading cycle is important to know to understand the rainflow method.

A loading cycle needs a varying stress or load. A good way to observe a loading cycle is through a strain – stress diagram [Barkey, 2018a] [Barkey, 2018b]. We can easily draw this diagram as we go along a stress temporal curve (see fig. B.2).

A full loading cycle is identified when a hysteresis loop is drawn closed. The cycle is defined by the extreme values of this hysteresis. On the same way, if we consider a more variable stress vs time signal, the diagram can reveal cycles or half cycles. In fig. B.2, we clearly identify an half cycle ΔS_{14} and a cycle ΔS_{23}.

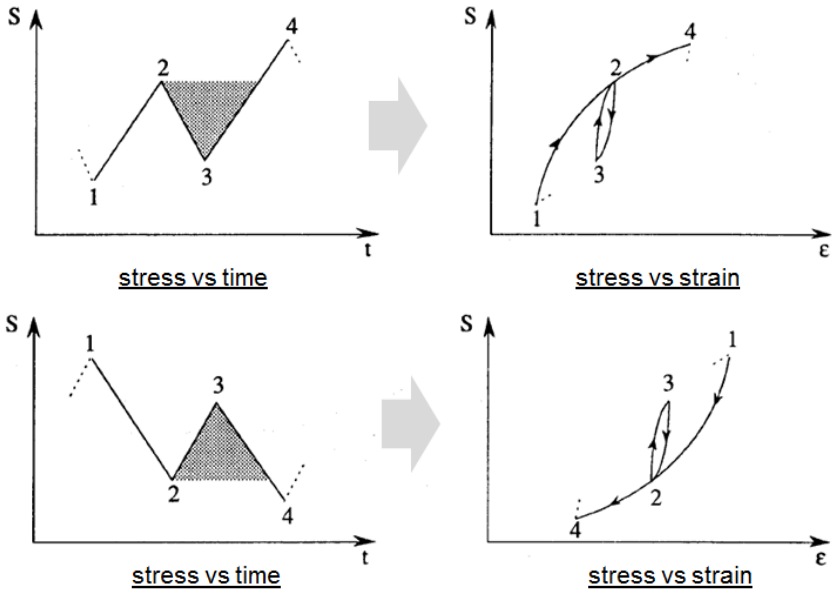

FIGURE B.2: *Example of loading cycle [Amzallag et al., 1993]*

B.3 Rainflow algorithm

The rainflow algorithm extracts loading cycles out of the input signal. The algorithm basically follows the steps below [Amzallag et al., 1993] [Jaafar, 2011]:

- **STEP 1:** identification of local extrema (simply by sign variation of first derivative), quantification (definition of representative class levels for these extrema) and centering of these extrema onto the closest class. Here, a time varying signal expressed in % is considered.

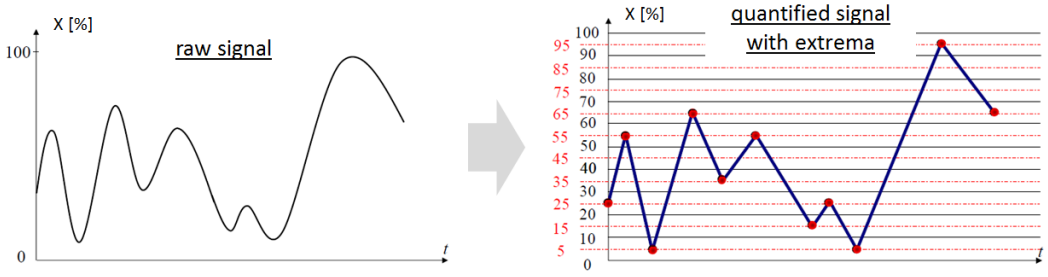

FIGURE B.3: *Rainflow algorithm: STEP 1*

- **STEP 2:** extraction of cycles based on 3 relative ranges taken among 4 successive extrema named $(E_i, E_{i+1}, E_{i+2}, E_{i+3})$ $[s]$. The relative gaps are defined as:

$$\begin{aligned} \Delta E_i &= |X(E_i) - X(E_{i+1})| \\ \Delta E_{i+1} &= |X(E_{i+1}) - X(E_{i+2})| \\ \Delta E_{i+2} &= |X(E_{i+2}) - X(E_{i+3})| \end{aligned}$$

If $\Delta E_{i+1} \leq \Delta E_i$ and $\Delta E_{i+1} \leq \Delta E_{i+2}$, then:

- the cycle ΔE_{i+1} is extracted
- the extrema E_{i+1} and E_{i+2} are removed from the signal
- the signal is linked again.

Otherwise, we slide the 4 considered extrema one step on the right (i.e. the index i is incremented by 1) and the previous test is applied again. The process goes from left to right sliding up the 4 extrema until the last signal point. The remaining points are called the residue.

Fig. B.4, Fig. B.5 and Fig. B.6 give an example in practice of the necesary iterations over a basic input signal until reaching a residue.

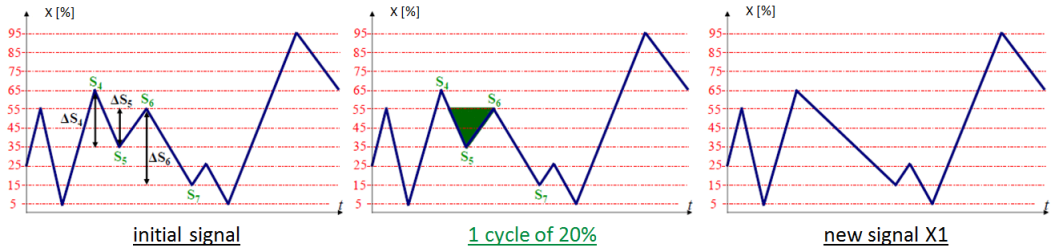

FIGURE B.4: *Rainflow algorithm: iteration 1*

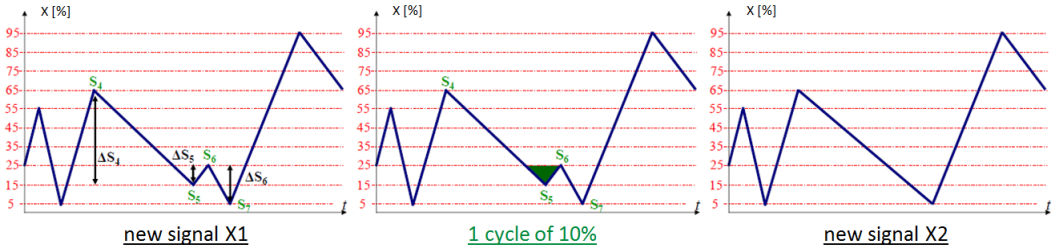

FIGURE B.5: *Rainflow algorithm: iteration 2*

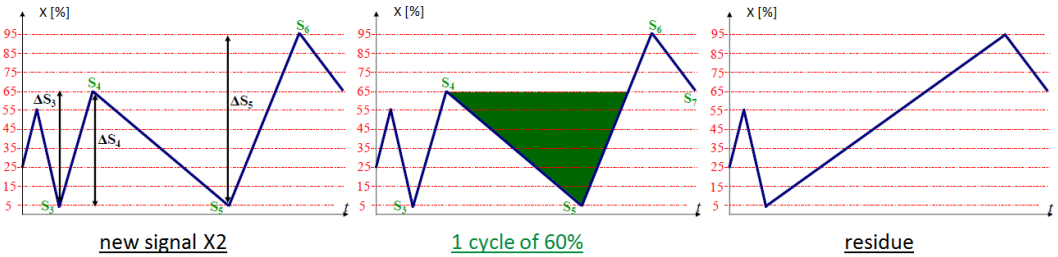

FIGURE B.6: *Rainflow algorithm: iteration 3*

- **STEP 3:** since the method can not extract any cycle out of the residue, the method duplicates the residue, carefully links the duplicate after the initial one and applies the Rainflow method. The initial residue is obtained after the extraction of the cycles which corresponds to the cycle of the initial residue.

  Fig. B.7, Fig. B.8 and Fig. B.9 give an example in practice of the necesary process from the residue got in fig. B.6 to the end of process.

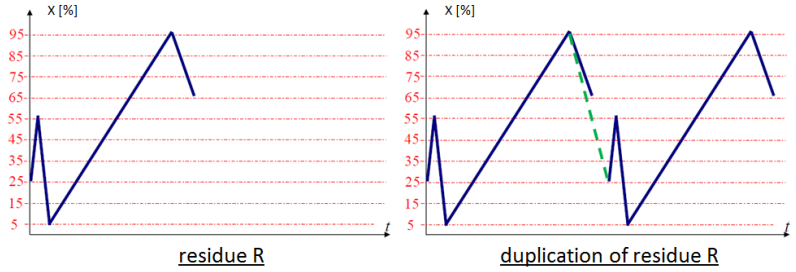

FIGURE B.7: *Rainflow algorithm: STEP 3*

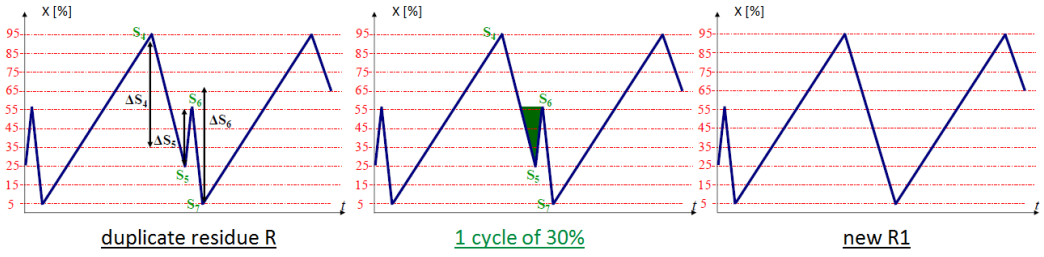

FIGURE B.8: *Rainflow algorithm: residue, iteration 1*

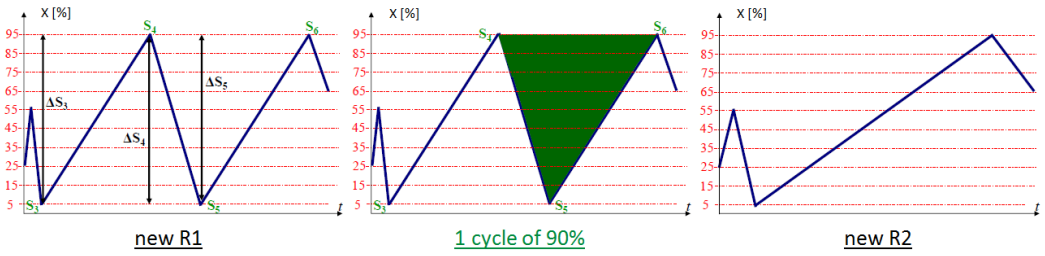

FIGURE B.9: *Rainflow algorithm: residue, iteration 2*

- **STEP 4:** conclusion: in the input signal, there are 5 cycles in total with depths of 20%, 10%, 60%, 30% and 90%.

B.4 Rainflow matrix

The outputs of the rainflow algorithm can be presented into two different ways:
- either raw as the algorithm runs (a line per cycle extraction) into a text file
- or sorted out into matrices.
There are three different possible matrices:

- **FROM-TO MATRIX:** each identified cycle is classified regarding its starting and ending stress values. Note: this matrix can be called “starting class – ending class matrix” [Amzallag et al., 1993]

- **MAX-MIN MATRIX:** each identified cycle is classified regarding its maximum and minimum stress values. Also, it can be called in French: “matrice des pics – vallées”

- **RANGE-MEAN MATRIX:** each identified cycle is classified regarding its mean and amplitude stress values. In the sense of signal treatment (see fig. B.10), the RANGE – MEAN matrix can also be called a DYNAMIC – STATIC matrix. A concrete example of it is shown in fig. B.11. In addition, the matrix can also be visualize as a "heatmap" (see fig. B.12 (left)) and a 3D or "load mountain" (see fig. B.12 (right)).

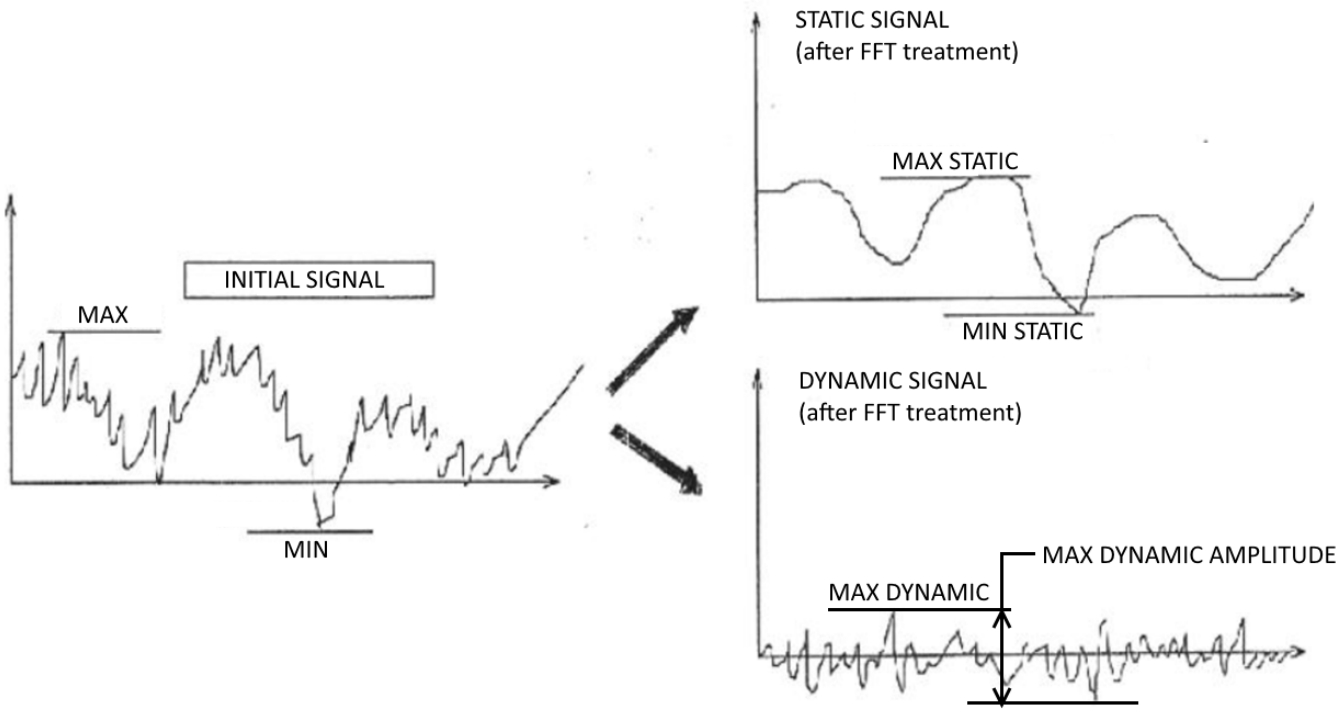

FIGURE B.10: *Decomposition of a signal into its static and dynamic components*

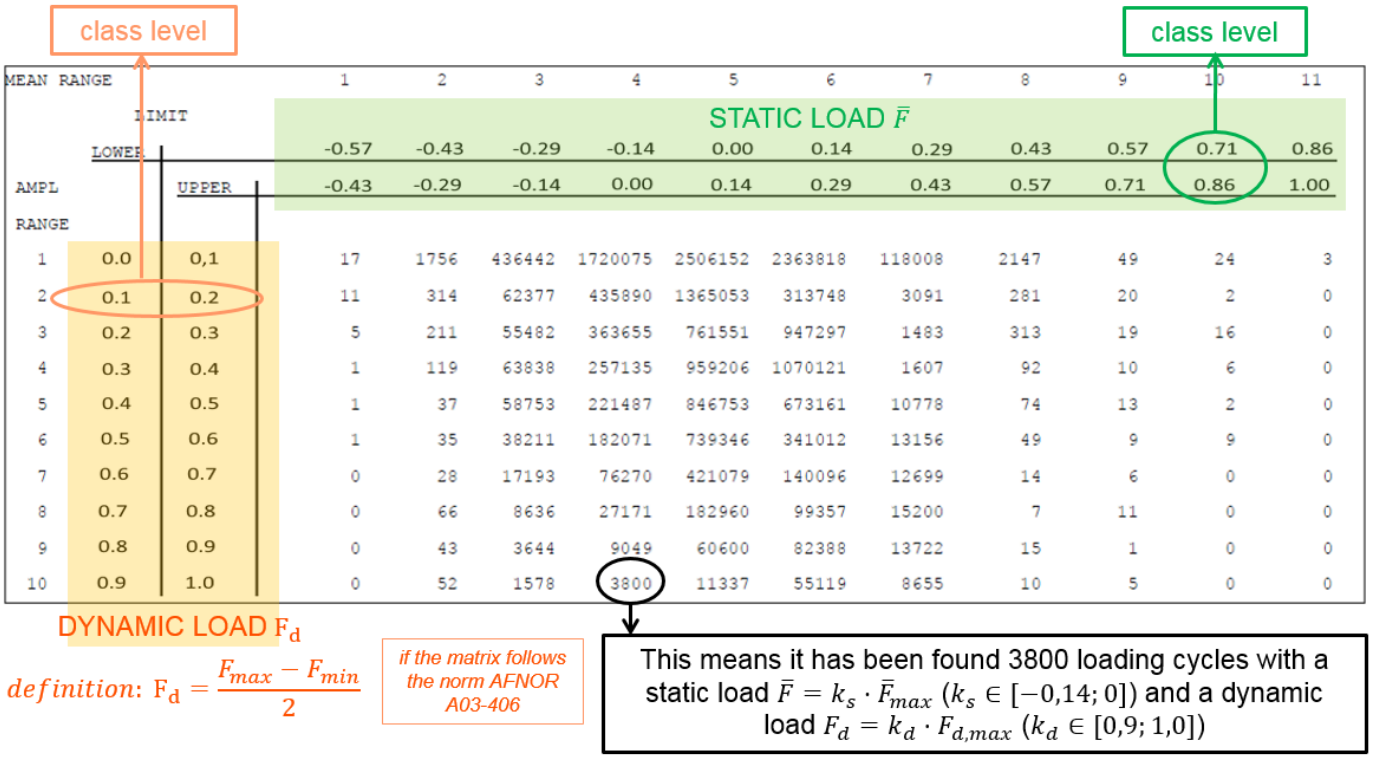

			1	2	3	4	5	6	7	8	9	10	11
			-0.57	-0.43	-0.29	-0.14	0.00	0.14	0.29	0.43	0.57	0.71	0.86
			-0.43	-0.29	-0.14	0.00	0.14	0.29	0.43	0.57	0.71	0.86	1.00
1	0.0	0,1	17	1756	436442	1720075	2506152	2363818	118008	2147	49	24	3
2	0.1	0.2	11	314	62377	435890	1365053	313748	3091	281	20	2	0
3	0.2	0.3	5	211	55482	363655	761551	947297	1483	313	19	16	0
4	0.3	0.4	1	119	63838	257135	959206	1070121	1607	92	10	6	0
5	0.4	0.5	1	37	58753	221487	846753	673161	10778	74	13	2	0
6	0.5	0.6	1	35	38211	182071	739346	341012	13156	49	9	9	0
7	0.6	0.7	0	28	17193	76270	421079	140096	12699	14	6	0	0
8	0.7	0.8	0	66	8636	27171	182960	99357	15200	7	11	0	0
9	0.8	0.9	0	43	3644	9049	60600	82388	13722	15	1	0	0
10	0.9	1.0	0	52	1578	3800	11337	55119	8655	10	5	0	0

FIGURE B.11: *Rainflow matrix sample from the H145 helicopter, axis normalized by their respective maximum*

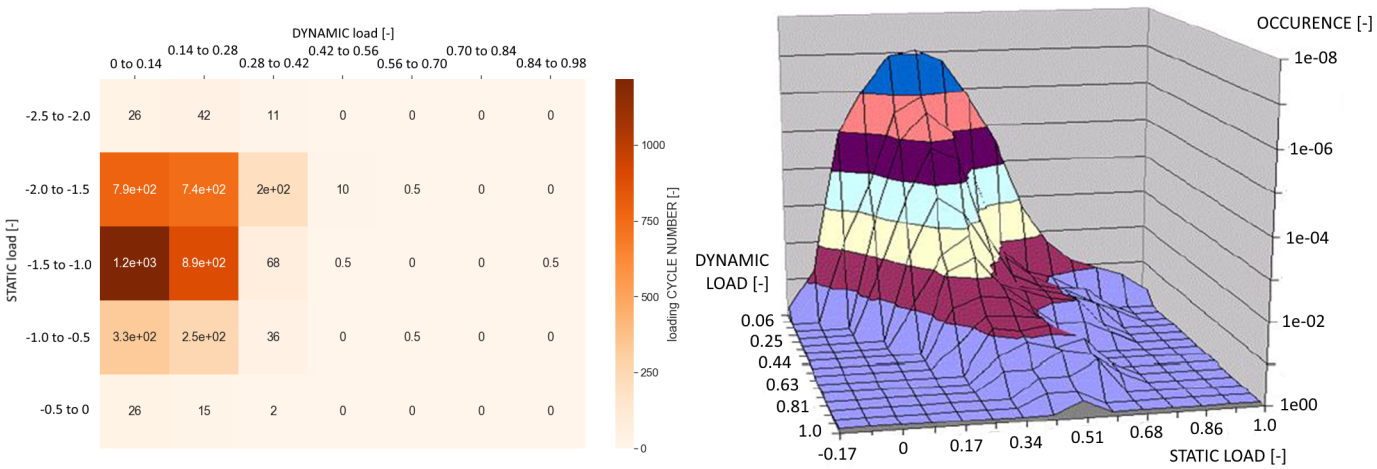

FIGURE B.12: *Rainflow matrix: examples of 3D representation, left: "heatmap", right: "load mountain", graph axis normalized by their respective maximum*

Appendix C

Mission profile analysis: cruise flight phase

C.1 CRUISE flight phase overview

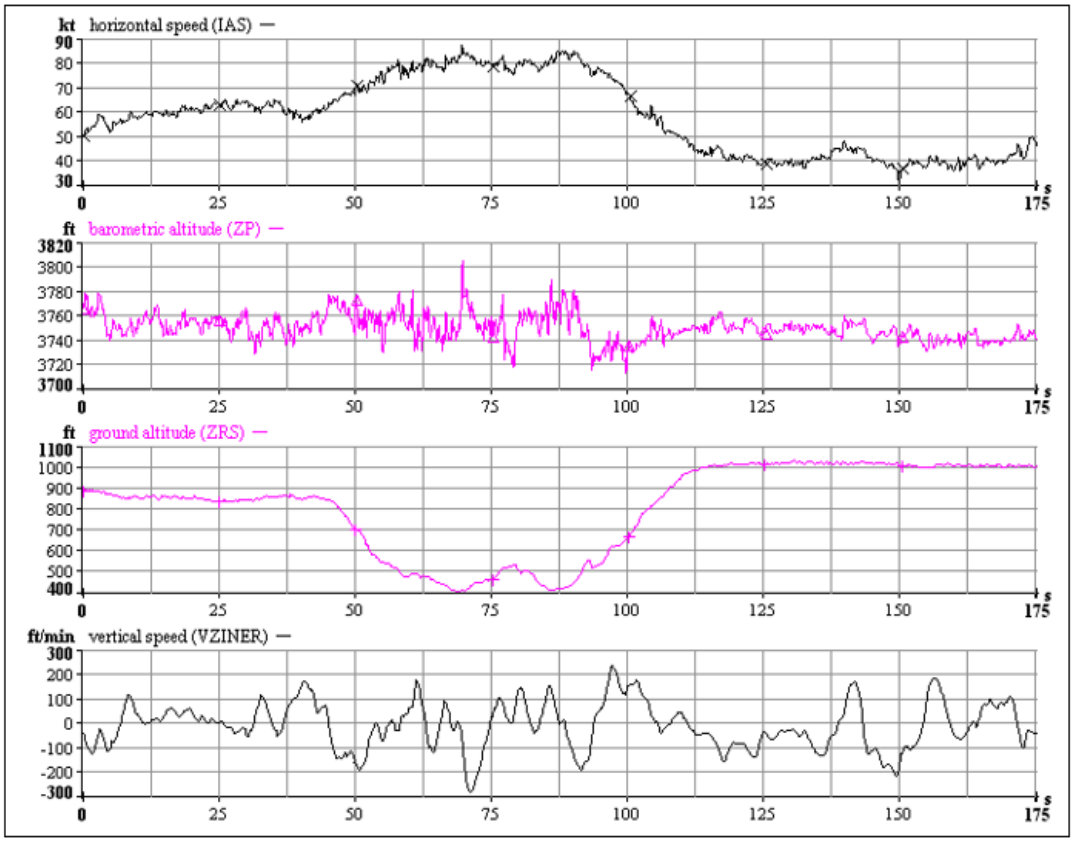

FIGURE C.1: *Considered CRUISE flight phase overview, helicopter parameters, speed: (60, 80, 40) kt, altitudes: (900, 450, 1000) ft, helicopter rotor speed: 100% of nominal rotor speed*

Appendix D

Precaution in data manipulation

D.1 Noisy data & variable product

Multiplying two noisy variables involves risks of bringing down the noise at a very low frequency. Such frequency is called the pulsation of flutter (*pulsation de battement* in french).

Here below is a simple example considering two signals such as $x_1(t)$ and $x_2(t)$.

$$x_1(t) = X_1 \cdot sin(w_1 t) \tag{D.1}$$
$$x_2(t) = X_2 \cdot sin(w_2 t) \tag{D.2}$$
$$x_1(t) \cdot x_2(t) = X_1 X_2 \cdot sin(w_1 t) sin(w_2 t) \tag{D.3}$$

Applying arc addition rule $cos(a+b) = cos(a)cos(b) - sin(a)sin(b)$:

$$x_1(t) \cdot x_2(t) = \frac{1}{2} \cdot X_1 X_2 \cdot \left[cos((w_1 - w_2)t) - cos((w_1 + w_2)t)\right] \tag{D.4}$$

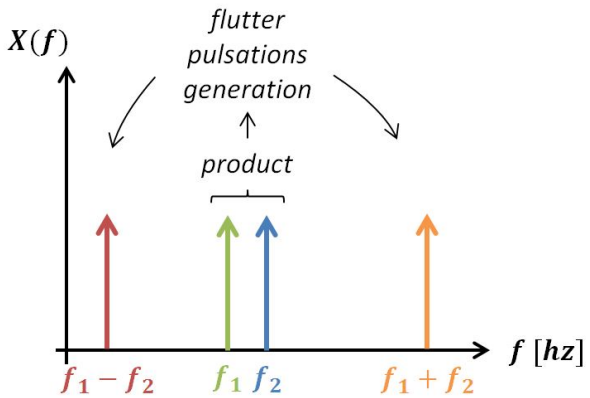

FIGURE D.1: *Consequences of product of noisy variables: flutter pulsations generation*

Appendix E

Lagrange equations

This appendix reminds what the Lagrange equations are and their assests.

E.1 Definition

The Lagrange's approach is a mathematical formulation based on the kinetic energy and the potential energy expressed within the generalized coordinates. It describes the state of a dynamic system according to its positions and time derivatives.

E.2 Comparison with Newton's approach

We propose to compare the application of the Lagrangian approach to the Newton approach on the basic example of a mass-spring system. This system characteristics are presented in fig. E.1.

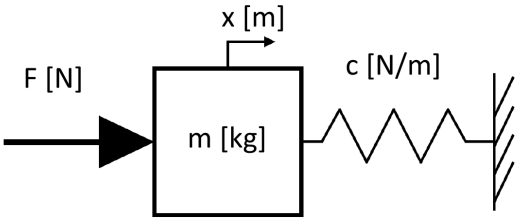

FIGURE E.1: *Mass–spring system*

E.2.1 Application of Newton's approach

The definition of Newton's second law is:

$$\sum \overrightarrow{F_{ext}} = m \cdot \overrightarrow{\ddot{x}} \tag{E.1}$$

Projecting horizontally, the differential equation describing the system is:

$$m \cdot \ddot{x} = F - c \cdot x \tag{E.2}$$

E.2.2 Application of Lagrange's approach

The Lagrange's approach is based on the derivatives of the Lagrangian $\mathscr{L}$ determined by the kinetic energy $\mathscr{E}_c$ and the potential energy $\mathscr{E}_p$:

$$\mathscr{L} = \mathscr{E}_c - \mathscr{E}_p \qquad \frac{\partial}{\partial t}(\frac{\partial \mathscr{L}}{\partial \dot{x}}) - \frac{\partial \mathscr{L}}{\partial x} = \frac{\partial \mathscr{W}}{\partial x} \tag{E.3}$$

where $\mathscr{W}$ is the work produced by the system.

The kinetic energy and the potential energy of the system are defined by:

$$\mathscr{E}_c = \frac{1}{2} \cdot m \cdot \dot{x}^2 \qquad \mathscr{E}_p = \frac{1}{2} \cdot c \cdot x^2 \tag{E.4}$$

The Lagrangian becomes:

$$\mathscr{L} = \frac{1}{2} \cdot m \cdot \dot{x}^2 - \frac{1}{2} \cdot c \cdot x^2 \tag{E.5}$$

By substitution:

$$\frac{\partial \mathscr{L}}{\partial x} = -c \cdot x \tag{E.6}$$

$$\frac{\partial \mathscr{L}}{\partial \dot{x}} = m \cdot \dot{x} \Rightarrow \frac{\partial}{\partial t}(\frac{\partial \mathscr{L}}{\partial \dot{x}}) = m \cdot \ddot{x} \tag{E.7}$$

$$\frac{\partial \mathscr{W}}{\partial x} = F \tag{E.8}$$

The final equation of motion is determined then:

$$m \cdot \ddot{x} = F - c \cdot x \tag{E.9}$$

E.2.3 Conclusion

Both approaches lead to the same differential equation (eq. E.2 & E.9) describing the dynamic behavior of the mass-spring system.

E.3 Interest of the Lagrange's approach use

On one hand, Newton's approach requires explicit expression of forces and is best suited for Cartesian coordinates. Newton's approach can include non-conservative forces such as friction forces.

On the other hand, the Lagrange's approach, is more mathematically sophisticated at first sight but it gets rid of the explicit expression of forces. The Lagrange's mechanics is ideal for systems with conservative forces and for bypassing constraint forces in any coordinate system [Hrabovsky and Susskind, 2020]. It is widely used to solve mechanical dynamic problems and when the Newton's formulation of classical mechanics is not convenient [Hrabovsky and Susskind, 2020]. It clearly facilitates the modeling of a system by avoiding its mechanical decomposition into solid objects.

Appendix F

Aerodynamic coefficients

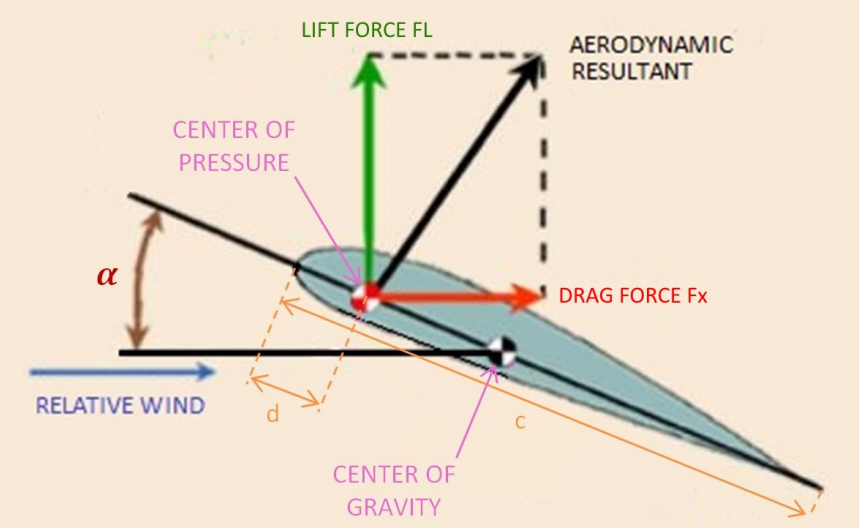

FIGURE F.1: *Airfoil profile sketch of principle ($d = 0.25 \cdot c$ for symmetric profiles)*

The lifting force F_L is dependent on 5 parameters:

$$F_L = f_1(V_{air}, c, \rho_{air}, \alpha) \tag{F.1}$$

with $V_{air}(x_i)$ the incident velocity $[m/s]$ depending on x_i the blade radius $[m]$, c the chord $[m]$, ρ_{air} the air density $[kg/m^3]$, and α the angle of attack $[rad]$.

We show by dimensional analysis that there are 2 π-groups:

$$\pi_1 = \frac{F_L}{\rho_{air} \cdot V_{air}^2 \cdot c^2} = \frac{1}{2} \cdot C_L \tag{F.2}$$

$$\pi_2 = \alpha \tag{F.3}$$

and C_L the conventional lift coefficient $[-]$. This can be reformulated as C_L depending on π_2 such as:

$$C_L = f_2(\alpha) \tag{F.4}$$

On airfoil database [Air, 2020], the characteristics of the 2 airfoil types close to the Cabri G2 blades are checked.

In fig. F.2 & F.3, the lift coefficient C_L is displayed with respect to α. A linearity is noticed on a first approximation.

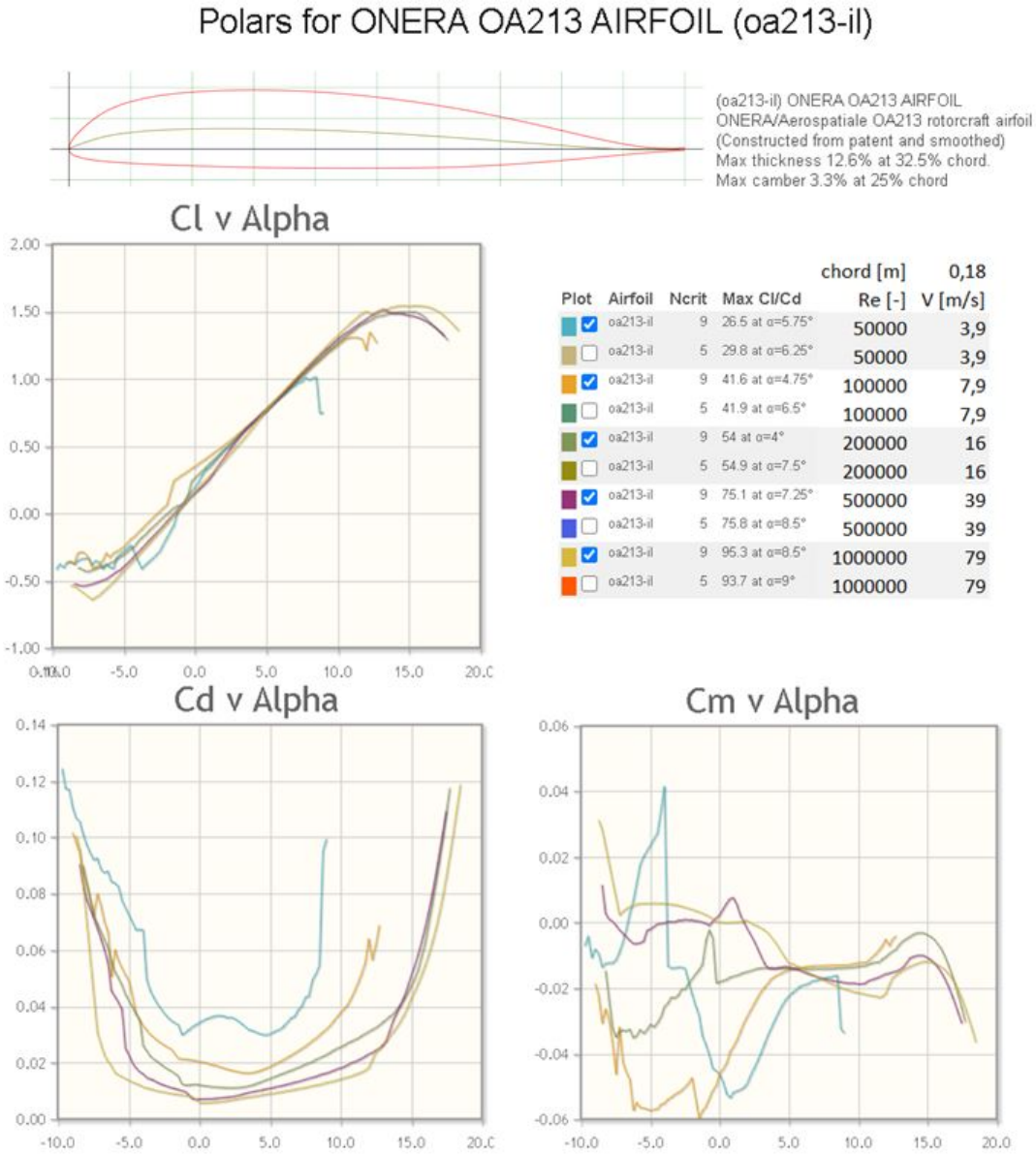

note: considered kinematic viscosity: $1.4207 \cdot 10^{-5}\ m^2/s$

FIGURE F.2: *Airfoil OA213 polars (from [Air, 2020])*

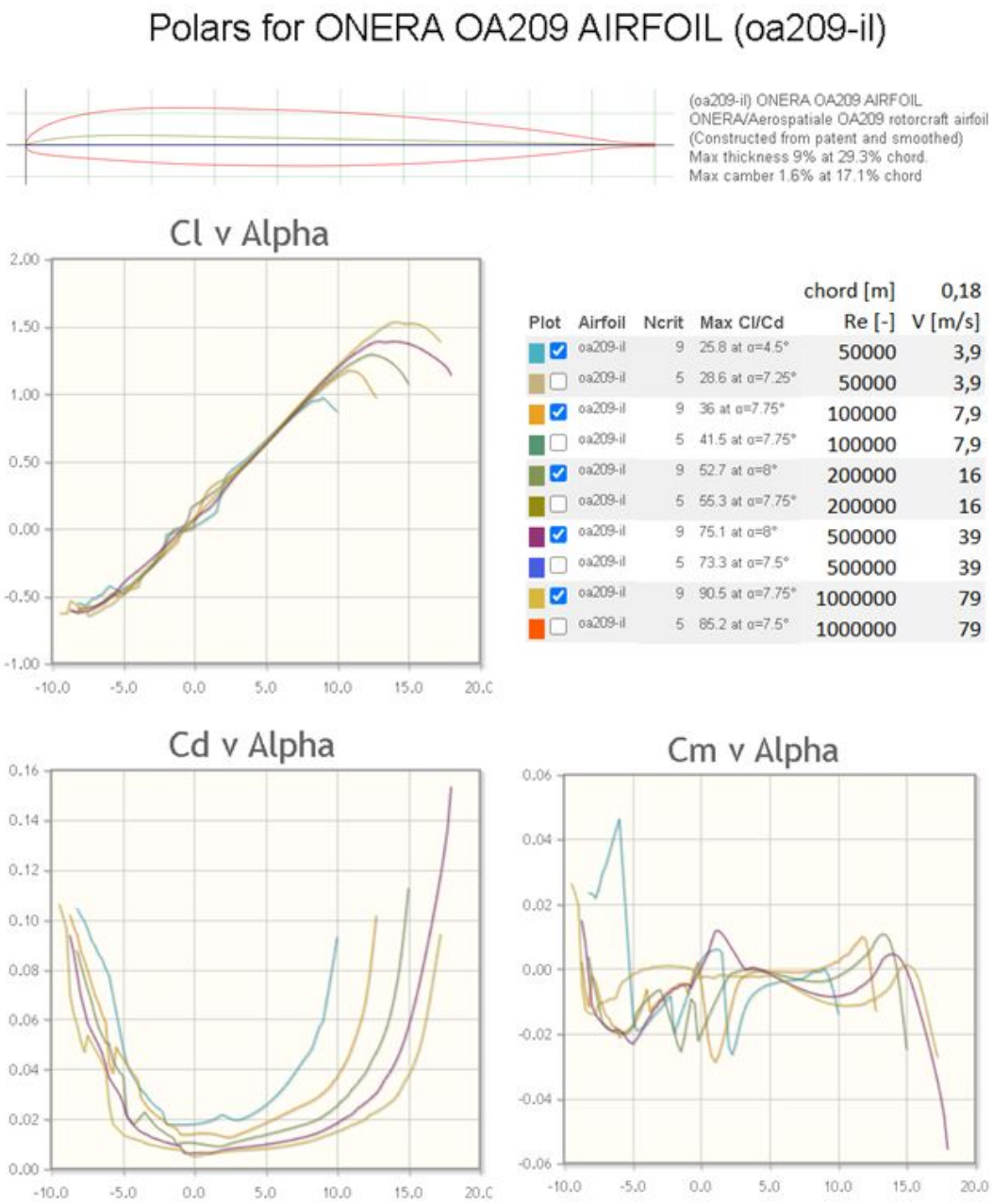

note: considered kinematic viscosity: $1.4207 \cdot 10^{-5}\ m^2/s$

FIGURE F.3: *Airfoil OA209 polars (from [Air, 2020])*

From this analysis, it is clear that the aerodynamic force estimation necessary in Chapter 3 can not rely on C_m values since not any data fitting can be suggested. What's more, the statement formulated by [Krysinski and Malburet, 2007a] is verified: "*We assume that the lift coefficient C_L is, within the usage interval, a linear function of the angle of attack α*".

Appendix G

Rotor load model

G.1 Expression of coefficients linked to mass

Considering the following variable range: $r \in [0, R]$ and $h \in [-3/4 \cdot b, b/4]$, coefficients are defined:

$$I_p = \int_{blade} r^2 dm \tag{G.1}$$

$$m_s = \int_{blade} r dm \tag{G.2}$$

$$m_p = \int_{blade} dm \tag{G.3}$$

$$I_\theta = \int_{blade} h^2 dm \tag{G.4}$$

$$m_{s,\theta} = \int_{blade} h dm \tag{G.5}$$

$$\alpha = \int_{blade} hr dm \tag{G.6}$$

G.2 Flapping, drag & pitch equations

Considering the approach with three degrees of freedom, the expressions of the kinetic energy, the flapping equation, the drag equation and the pitch equation are hereafter.

The following equation gives the kinetic energy $\mathscr{E}_c$:

$$\begin{aligned}
\mathscr{E}_c = \frac{1}{2}\Big[& m_p e^2\Omega^2 + I_p(\dot{\delta}+\Omega)^2\cos^2(\beta) + I_p\dot{\beta}^2 + m_p h^2(\dot{\delta}+\Omega)^2\cos^2(\theta) \\
& + m_p h^2(\dot{\delta}+\Omega)^2\sin^2(\theta)\sin^2(\beta) + m_p h^2\dot{\beta}^2\sin^2(\theta) + m_p h^2\dot{\theta}^2\Big] \\
& + m_s e\Omega(\dot{\delta}+\Omega)\cos(\beta)\cos(\delta) - m_s e\Omega\dot{\beta}\sin(\beta)\sin(\delta) - m_p eh\Omega(\Omega+\dot{\delta})\cos(\theta)\sin(\delta) \\
& + m_p e\Omega h(\Omega+\dot{\delta})\sin(\theta)\sin(\beta)\cos(\delta) + m_p e\Omega h\dot{\beta}\sin(\theta)\cos(\beta)\sin(\delta) \\
& - m_p e\Omega h\dot{\theta}\sin(\theta)\cos(\delta) + m_p eh\Omega\dot{\theta}\cos(\theta)\sin(\beta)\sin(\delta) \\
& + m_s h(\dot{\delta}+\Omega)^2\sin(\theta)\cos(\beta)\sin(\beta) - m_s h\dot{\theta}(\dot{\delta}+\Omega)\cos(\beta)\sin(\theta) \\
& + m_s h\dot{\beta}(\Omega+\dot{\delta})\cos(\theta)\sin(\beta) - m_s\dot{\beta}h\dot{\theta}\cos(\theta) \\
& - m_p h^2\dot{\beta}(\Omega+\dot{\delta})\cos(\theta)\sin(\theta)\cos(\beta) - m_p h^2\dot{\theta}(\dot{\delta}+\Omega)\sin(\beta)
\end{aligned} \tag{G.7}$$

The following equation describes the flapping motion (β):

$$I_\theta\Omega\theta^2\dot{\theta} + I_\theta\theta^2\dot{\delta}\dot{\theta} + 2I_\theta\theta\dot{\beta}\dot{\theta} - I_\theta\theta\ddot{\delta} + I_p\Omega^2\beta + 2I_p\Omega\beta\dot{\delta} + I_p\beta\dot{\delta}^2 + I_p\ddot{\beta} + K_\beta\beta + \Omega^2\alpha\beta^2\theta - \Omega^2\alpha\theta + \Omega^2 em_s\beta - \Omega^2 em_{s,\theta}\theta + 2\Omega\alpha\beta^2\theta\dot{\delta} - 2\Omega\alpha\beta\theta\dot{\theta} - 2\Omega\alpha\theta\dot{\delta} - rgm_p/2 + \alpha\beta^2\theta\dot{\delta}^2 - 2\alpha\beta\theta\dot{\delta}\dot{\theta} + \alpha\beta\ddot{\delta} - \alpha\theta\dot{\delta}^2 + \alpha\theta\dot{\theta}^2 - \alpha\ddot{\theta} + bgm_p\beta\theta/4 = M_{mot,\beta} - \lambda_\beta\dot{\beta} + \frac{\gamma I_p\Omega^2}{8}((-\theta) - \frac{\dot{\beta}}{\Omega}) \quad \text{(G.8)}$$

The following equation describes the drag motion (δ):

$$-2I_\theta\Omega\theta\dot{\theta} + I_\theta\beta\theta\dot{\beta}^2 - I_\theta\beta\ddot{\theta} + I_\theta\theta^2\dot{\beta}\dot{\theta} - I_\theta\theta\ddot{\beta} - 2I_\theta\theta\dot{\delta}\dot{\theta} - K_\delta\delta_0 - 2I_\theta\dot{\beta}\dot{\theta} + I_\theta\ddot{\delta} - 2I_p\Omega\beta\dot{\beta} - 2I_p\beta\dot{\beta}\dot{\delta} + I_p\ddot{\delta} + K_\delta\delta + \Omega^2 em_{s,\delta} + \Omega^2 em_{s,\theta}\beta\delta\theta + \Omega^2 em_{s,\theta} - 2\Omega\alpha\beta^2\theta\dot{\beta} + 2\Omega\alpha\beta\dot{\theta} + 2\Omega\alpha\theta\dot{\beta} - 2\alpha\beta^2\theta\dot{\beta}\dot{\delta} + 2\alpha\beta\theta\ddot{\delta} + \alpha\beta\ddot{\beta} + 2\alpha\beta\dot{\delta}\dot{\theta} + 2\alpha\theta\dot{\beta}\dot{\delta} - \alpha\theta\ddot{\theta} + \alpha\dot{\beta}^2 - \alpha\dot{\theta}^2 = \frac{-\dot{\beta}}{\Omega}(\frac{\gamma I_p\Omega^2}{8})(\theta - \frac{\dot{\beta}}{\Omega}) - \lambda_\delta\dot{\delta} \quad \text{(G.9)}$$

The following equation describes the pitch motion (θ):

$$I_\theta\Omega^2\theta - I_\theta\Omega\theta^2\dot{\beta} + 2I_\theta\Omega\theta\dot{\delta} - I_\theta\beta\ddot{\delta} - I_\theta\theta^2\dot{\beta}\dot{\delta} - I_\theta\theta\dot{\beta}^2 + I_\theta\theta\dot{\delta}^2 + I_\theta\ddot{\theta} - K_\theta\theta_0 + K_\theta\theta - \Omega^2\alpha\beta - \Omega^2 em_{s,\theta}\beta - \Omega^2 em_{s,\theta}\delta\theta + 2\Omega\alpha\beta\theta\dot{\beta} - 2\Omega\alpha\beta\dot{\delta} + 2\alpha\beta\theta\dot{\beta}\dot{\delta} - \alpha\beta\dot{\delta}^2 - \alpha\theta\ddot{\delta} - \alpha\ddot{\beta} - bgm_p/4 = M_{mot,\theta} - \lambda_\theta\dot{\theta} \quad \text{(G.10)}$$

Appendix H

Damping coefficient

This Appendix presents in fig. H.1 & H.2 the damping coefficient involved for a second order transfer function such as:

$$T(s) = \frac{A_0}{1 + \frac{2 \cdot m}{\omega_0} \cdot s + \frac{s^2}{\omega_0^2}} \tag{H.1}$$

where A_0 $[SI]$ is a static amplification, m $[-]$ the damping and ω_0 $[hz]$ the natural frequency.

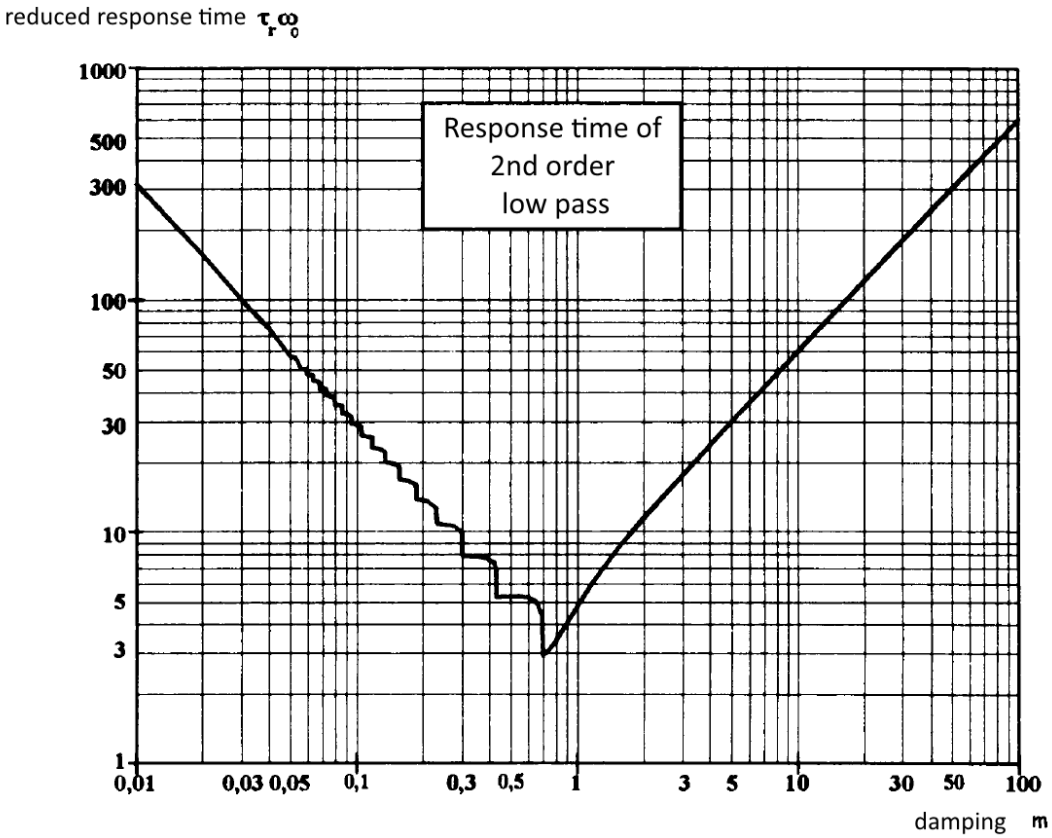

FIGURE H.1: *Damping coefficient with respect to reduced response time [Muller, 2008]*

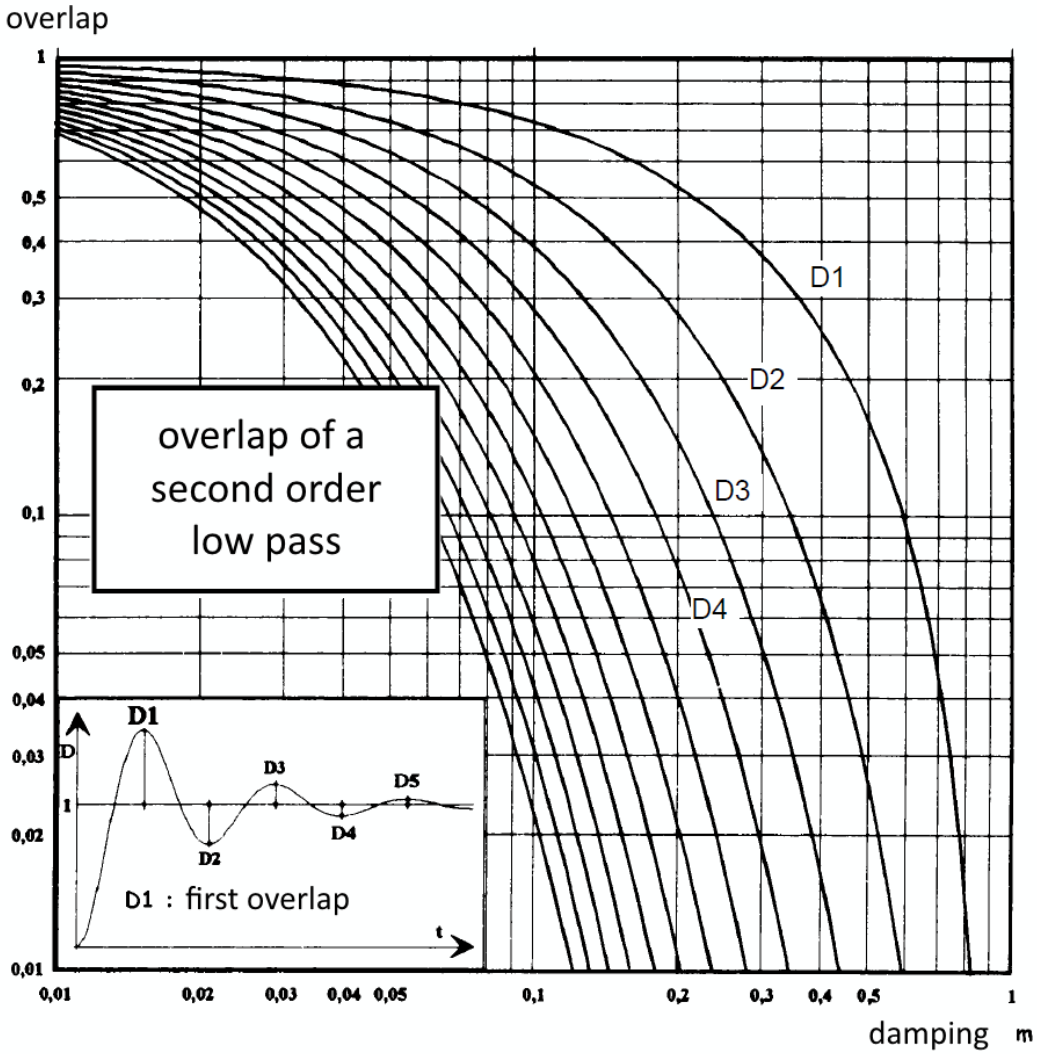

FIGURE H.2: *Overlap with respect to damping [Muller, 2008]*

Appendix I

RMS expression

Basically, the RMS (Root Mean Square) expression of any time varying signal $y(t)$ over a time period of duration t_T $[s]$ is defined as:

$$y_{RMS} = \sqrt{\frac{1}{t_T} \cdot \int_0^{t_T} y(t)^2 \, dt} \tag{I.1}$$

This appendix proposes to derive the RMS expression of a signal $y(t)$. Firstly, a signal $y(t)$ combining two members of any time varying functions will be considered. Secondly, the particular case of a signal $y(t)$ combining different sinusoidal function will be considered.

I.1 Global case

In this section, it is considered a signal y(t) such as:

$$y(t) = k_1 \cdot f_1(t) + k_2 \cdot f_2(t) \tag{I.2}$$

where k_1, k_2 are real constants; f_1, f_2 are any time varying functions. The following steps get to the RMS expression of $y(t)$.

$$\begin{aligned} y^2(t) &= k_1^2 \cdot f_1^2(t) + 2 \cdot k_1 \cdot k_2 \cdot f_1(t) \cdot f_2(t) + k_2^2 \cdot f_2^2(t) \\ y_{RMS}^2 &= \frac{k_1^2}{t_T} \cdot \int_0^{t_T} f_1^2(t) \, dt + \frac{2 \cdot k_1 \cdot k_2}{t_T} \cdot \int_0^{t_T} f_1(t) \cdot f_2(t) \, dt + \frac{k_2^2}{t_T} \cdot \int_0^{t_T} f_2^2(t) \, dt \\ &= k_1^2 \cdot f_{1,RMS}^2 + 2 \cdot k_1 \cdot k_2 \cdot < f_1(t) \cdot f_2(t) > + k_2^2 \cdot f_{2,RMS}^2 \end{aligned} \tag{I.3}$$

Thus,

$$\begin{aligned} &\text{If } y(t) = k_1 \cdot f_1(t) + k_2 \cdot f_2(t), \text{ then :} \\ &y_{RMS} = \sqrt{k_1^2 \cdot f_{1,RMS}^2 + 2 \cdot k_1 \cdot k_2 \cdot < f_1(t) \cdot f_2(t) > + k_2^2 \cdot f_{2,RMS}^2} \end{aligned} \tag{I.4}$$

I.2 Particular case

In this section, it is considered a signal y(t) combining different sinusoidal members such as:

$$y(t) = s_0 + d_i \cdot sin(\omega_i \cdot t + \phi_i) + d_j \cdot sin(\omega_j \cdot t + \phi_j) \tag{I.5}$$

where s_0, d_i, d_j are any real constants; ω_i, ω_j are any rotative frequencies; ϕ_i, ϕ_j are any phaseshifts.

The RMS value of $y(t)$ is developped as it follows.

$$\begin{aligned} y_{RMS}^2 =& \frac{1}{t_T} \cdot \int_0^{t_T} \Big[\big(s_0 + d_i \cdot sin(\omega_i \cdot t + \phi_i)\big)^2 \\ &+2 \cdot \big(s_0 + d_i \cdot sin(\omega_i \cdot t + \phi_i)\big) \cdot d_j \cdot sin(\omega_j \cdot t + \phi_j) \\ &+d_j^2 \cdot sin^2(\omega_j \cdot t + \phi_j) \Big] \, dt \\ =& M_1 + M_2 + M_3 \end{aligned} \tag{I.6}$$

The three following equations have to be developped beforehand as prerequisite results for later:

$$\int_0^{t_T} sin(\omega \cdot t + \phi) \, dt = 0 \tag{I.7}$$

$$\int_0^{t_T} sin^2(\omega \cdot t + \phi) \, dt = \int_0^{t_T} \frac{1 - cos(2 \cdot \omega \cdot t + 2 \cdot \phi)}{2} \, dt = \frac{t_T}{2} \tag{I.8}$$

$$\begin{aligned} \int_0^{t_T} sin(\omega_i \cdot t + \phi_i) \cdot sin(\omega_j \cdot t + \phi_j) \, dt =& \int_0^{t_T} -\frac{1}{2} \cdot cos\big((\omega_i + \omega_j) \cdot t + (\phi_i + \phi_j)\big) \\ &+\frac{1}{2} \cdot cos\big((\omega_i - \omega_j) \cdot t + (\phi_i - \phi_j)\big) \, dt \\ =& 0 \end{aligned} \tag{I.9}$$

Using these prerequisites, the expressions of M_1, M_2 and M_3 are developed.

$$\begin{aligned} M_3 &= \frac{d_j^2}{t_T} \cdot \int_0^{t_T} sin^2(\omega_j \cdot t + \phi_j) \, dt = \frac{d_j^2}{T} \cdot \frac{t_T}{2} = \frac{d_j^2}{2} \\ M_1 &= \frac{1}{t_T} \cdot \int_0^{t_T} \big(s_0 + d_i \cdot sin(\omega_i \cdot t + \phi_i)\big)^2 \, dt \\ &= \frac{1}{t_T} \cdot \int_0^{t_T} \big(s_0^2 + 2 \cdot s_0 \cdot d_i \cdot sin(\omega_i \cdot t + \phi_i) + d_i^2 \cdot sin^2(\omega_i \cdot t + \phi_i)\big) \, dt \\ &= \frac{s_0^2}{t_T} \cdot \int_0^{t_T} dt + \frac{d_i^2}{t_T} \cdot \int_0^{t_T} sin^2(\omega_i \cdot t + \phi_i) \, dt \\ &= s_0^2 + \frac{d_i^2}{2} \\ M_2 &= \frac{2 \cdot d_j}{t_T} \cdot \int_0^{t_T} \big(s_0 + d_i \cdot sin(\omega_i \cdot t + \phi_i)\big) \cdot sin(\omega_j \cdot t + \phi_j)\big) \, dt \\ &= \frac{2 \cdot d_j}{t_T} \cdot d_i \cdot \int_0^{t_T} sin(\omega_i \cdot t + \phi_i) \cdot sin(\omega_j \cdot t + \phi_j) \, dt \\ &+ \frac{2 \cdot d_j}{t_T} \cdot s_0 \cdot \int_0^{t_T} sin(\omega_j \cdot t + \phi_j) \, dt \\ &= 0 \end{aligned} \tag{I.10}$$

Finally, gathering the previous results into the eq. I.6:

$$y_{RMS}^2 = M_1 + M_2 + M_3 = s_0^2 + \frac{d_i^2}{2} + \frac{d_j^2}{2} \tag{I.11}$$

To conclude,

$$\text{If } y(t) = \sum_i s_i + \sum_j \left(d_j \cdot sin(\omega_j t + \phi_j)\right), \text{ then :}$$
$$y_{RMS} = \sqrt{(\sum_i s_i)^2 + \sum_j \frac{d_j^2}{2}} \tag{I.12}$$

The particular case of Parseval's theorem validates this result (bibmath.parseval).

Appendix J

Scaling law derivation: mechanical components

J.1 Spherical bearing

In this section, the scaling laws concerning the spherical bearings (or rod ends) are theoretically derived. The laws are finally validated by a comparison with supplier catalog data.

J.1.1 Theory

J.1.1.1 Dimensions

The main design constraint used for modelling any mechanical component is a constant mechanical stress $\sigma^* = 1$. This stress is due to the applied maximum static load C_0 corresponding to the maximal Hertz contact pressure [Palmgren, 1967] obtained by a plastic strain of 0.01% of the rolling elements and their races (ISO standard). Supposing geometrical similarities ($d^* = l^*$), the following can be stated:

$$\frac{C_0^*}{S^*} = 1 \implies C_0^* = S^* = l^{*2} \tag{J.1}$$

Thus,

$$\boxed{l^* = C_0^{*1/2}} \tag{J.2}$$

J.1.1.2 Mass

When considering the component as a volume V with an equivalent density ρ_{eq}:

$$M = \rho_{eq} \cdot V \implies M^* = \rho_{eq}^* \cdot V^* \implies M^* = l^{*3} \tag{J.3}$$

Thus,

$$\boxed{M^* = C_0^{*3/2}} \tag{J.4}$$

J.1.1.3 Dynamic load

Among a given product range, supposing that the maximum permissible stress in material remain constant ($\sigma_{static,max}^* = 1$), it becomes consistent stating that maximum permissible fatigue stress $\sigma_{dynamic,max}$ remains constant. Thus,

$$\sigma_{static,max}^* = \sigma_{dynamic,max}^* = 1 \tag{J.5}$$

$$\frac{C_0^*}{S^*} = \frac{C_d^*}{S^*} \tag{J.6}$$

$$\boxed{C_d^* = C_0^* = l^{*2}} \tag{J.7}$$

J.1.2 Validation

A validation has been performed with SKF catalog.

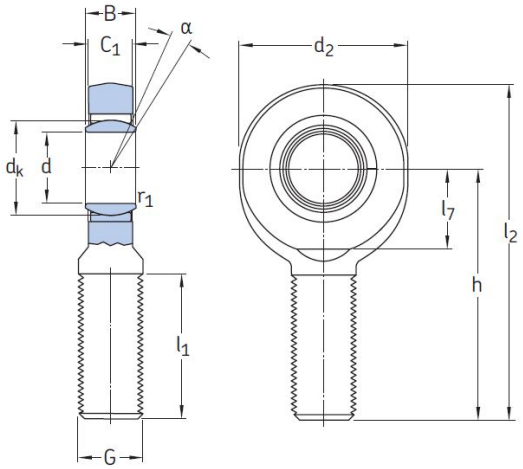

FIGURE J.1: *Rod end SKF catalog*

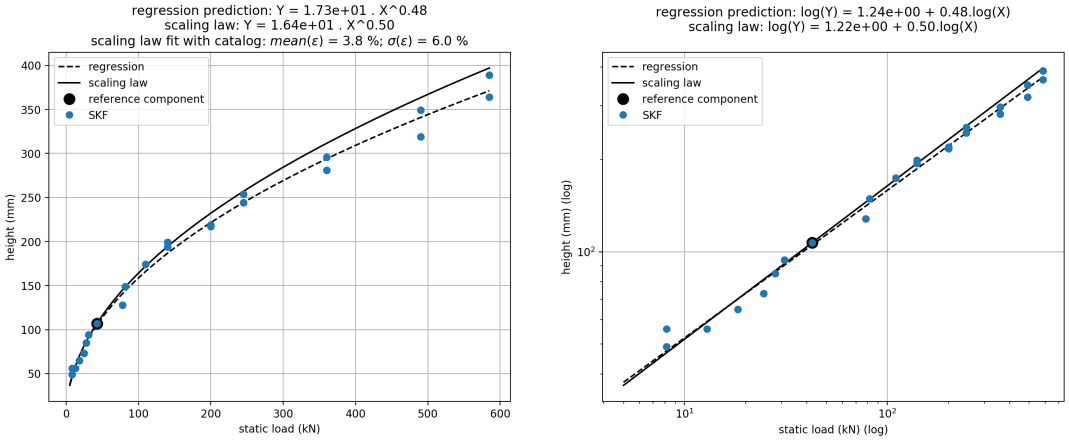

FIGURE J.2: *Validation scaling law, spherical bearing, height (SKF catalog)*

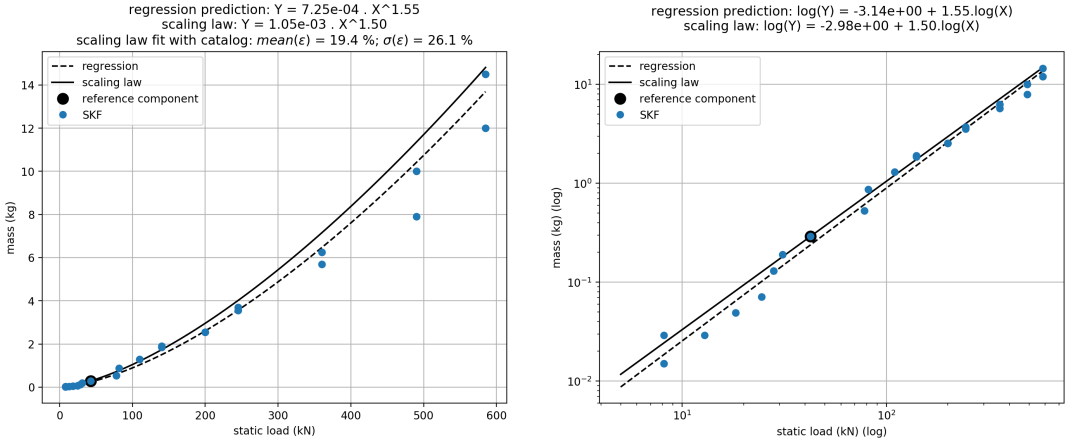

FIGURE J.3: *Validation scaling law, spherical bearing, mass (SKF catalog)*

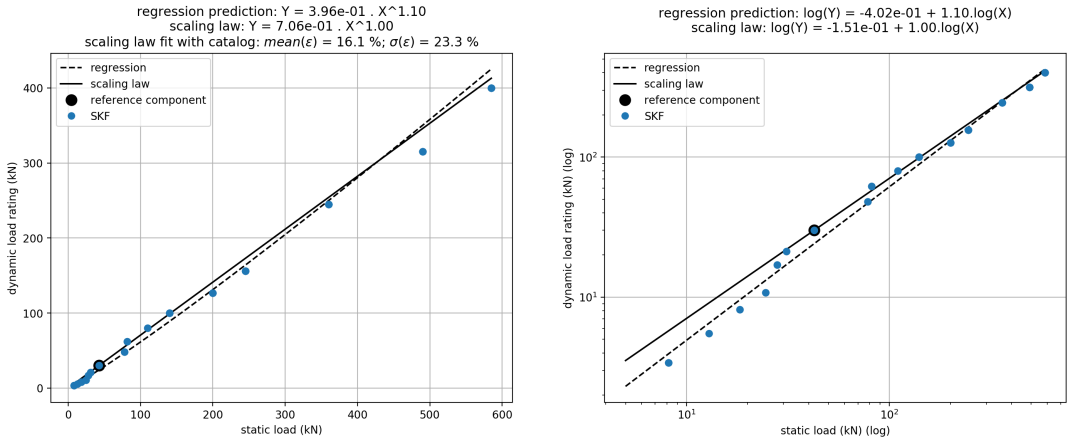

FIGURE J.4: *Validation scaling law, bearing, dynamic load (SKF catalog)*

J.2 Ball bearing

J.2.1 Theory

J.2.1.1 Design hypothesis & rolling elements

For manufacturing cost reduction and modularity, bearings are components which are standardized and organized in series. What is more, to simplify manufacturing and assembly methodologies, manufacturers define for their series a constant filling ratio which can be expressed by a ball radius with respect to the shaft diameter. This constant ratio means the number of rolling elements is constant i.e. :

$$N^*_{ball} = 1 \tag{J.8}$$

The supplier product catalog [SKF, 2018a] confirms it.

This choice can be easily understood. Since the increase of a ball diameter reduces the Hertz' contact stress (Appendix L), there is an interest of using big balls. Also, this choice allows Hertz' contact stress to remain constant throughout a product range.

Finally, for a given product range, it will be possible to consider that the different parts of the bearing follow the geometrical similarity hypothesis ($d^*_i = l^*_i$).

J.2.1.2 Dimension & mass

The main design constraint used for the modelling of any mechanical component is a constant mechanical stress $\sigma^* = 1$. This stress is due to the maximum static load C_0 corresponding to the maximal Hertz contact pressure [Palmgren, 1967] obtained by a plastic strain of 0.01% of the rolling elements and their races (ISO standard). For bearings, this maximum static load depends on the curvature radius of races, the geometry and number of rolling elements, and the material with its thermal/chimical treatments. Regarding the geometrical similarity hypothesis as mentioned before, a relation between dimensions and this maximum static load C_0 can be stated as:

$$\frac{C^*_0}{S^*} = 1 \implies C^*_0 = S^* = l^{*2} \tag{J.9}$$

$$\boxed{l^* = C^{*1/2}_0} \tag{J.10}$$

When considering the component as a volume V with an equivalent density ρ_{eq}, the component mass is easily obtained:

$$M = \rho_{eq} \cdot V \implies M^* = \rho_{eq}^* \cdot V^* \implies M^* = l^{*3} \tag{J.11}$$

Considering the relation dimension - load (eq. J.10), the following concludes:

$$\boxed{M^* = C_0^{*3/2}} \tag{J.12}$$

J.2.1.3 Dynamic load

According to geometrical and material property similarities (esp. $\sigma_{max}^* = \sigma_{fatigue}^* = 1$), the dynamique load evolution should be proportional to d_b^2, with d_b the ball diameter. However, the laboratory tests performed by Palmgren & Lundberg [Palmgren, 1967] showed that dynamic load capacity was proportional to $d_b^{1.8}$ for $d_b \leq 25.4\ mm$ and $d_b^{1.4}$ for $d_b \geq 25.4\ mm$.

Thus,

$$\boxed{C_d^* = C_0^{*1.8/2} \text{ with } d_b \leq 25.4\ mm} \tag{J.13}$$

The exponent of the law depends on the contact type considered (punctual for ball, linear for roller) since it results in a different stress state. More information can be found in [Budinger et al., 2013], [Sadeghi et al., 2009], [Halme and Andersson, 2010], and [Zaretsky, 2010].

J.2.1.4 Speeds

SKF manufacturer provides two speed ratings on its bearings:

- a reference speed, which is based on thermal conditions
- a limiting speed, which is based on mechanical limits.

According to SKF, the speed capability of a bearing is normally determined by the bearing operating temperature. However, for certain bearing types and arrangements, the mechanical limits of bearing components may have a significant influence.

For each speed, a scaling law study is applied.

J.2.1.4.1 Limiting speed The limiting speed (or maximum mechanical speed) is limited by a mechanical stress induced by a centrifugal force or by axial or transverse vibrations. Basically, the centrifugal force is defined by:

$$F_{centrifugal} = m \cdot w^2 \cdot R \implies F_{centrifugal}^* = w^{*2} \cdot l^{*4} \tag{J.14}$$

By deduction, it follows:

$$\sigma_{centrifugal}^* = w^{*2} \cdot l^{*2} \tag{J.15}$$

The problem is dependent on 4 parameters: a speed w $[rad.s^{-1}]$, a dimension l $[m]$, the Young modulus E $[kg.m^{-1}.s^{-2}]$, a density ρ $[kg.m^{-3}]$. There exists a function F such that $F(w, l, E, \rho) = 0$. The application of the dimensional analysis and Buckingham's theorem synthesized the problem into a constant single dimensionless number π_y:

$$\pi_y = \frac{E}{\rho \cdot w^2 \cdot l^2} = C^{st} \implies \pi_y^* = 1 \implies w^* = f^* = \frac{1}{l^*} \cdot \sqrt{\frac{E^*}{\rho^*}} \tag{J.16}$$

with f the resonance frequency.

Supposing material similarities ($\sigma^*_{centrifugal} = E^* = \rho^* = 1$) and considering the relation dimension - load (eq. J.10):

$$\boxed{w^*_{max,mecha} = l^{*-1} = C_0^{*-1/2}} \tag{J.17}$$

J.2.1.4.2 Reference speed The reference speed (or max thermal speed) supposes a constant heating and a convective thermal exchange. The heat considered is the heat released externally $\mathscr{P}_{diss} = h \cdot S \cdot \Delta\theta$ and the heat generated by the mechanical friction $\mathscr{P}_{mech}$. bearingtips defines basically the bearing frictional torque as:

$$T_{friction} = F \cdot \mu \cdot R \tag{J.18}$$

with F the static load applied on bearing, μ the coefficient of friction and R the bearing radius. The mechanical loss is deduced:

$$\mathscr{P}_{mech} = F \cdot \mu \cdot R \cdot w \tag{J.19}$$

Whatever the bearing size of a given product range is, the dissipated heat $\mathscr{P}_{diss}$ and the generated losses $\mathscr{P}_{mech}$ are supposed to balance. In addition, the maximum temperature variation, the convection heat transfer coefficient and the friction coefficient are supposed to follow the material properties similarities: $\Delta\theta^* = h^* = \mu^* = 1$

$$\mathscr{P}^*_{diss} = \mathscr{P}^*_{mech} \implies S^* = F^* \cdot R^* \cdot w^* \tag{J.20}$$

The surface of dissipation and the radius follow the geometrical similarities. They are expressed by $S^* = l^{*2}$ and $R^* = l^*$.

Considering the relation load - dimension from eq. J.10, the maximum speed defined by thermal limitations is expressed by:

$$\boxed{w^*_{max,thermal} = l^{*-1} = C_0^{*-1/2}} \tag{J.21}$$

J.2.2 Validation

A validation has been performed with the SKF product catalog [SKF, 2018a]. The tendency given by the scaling laws is very representative of manufacturer products. It is interesting to note the broad product range covered by the scaling law.

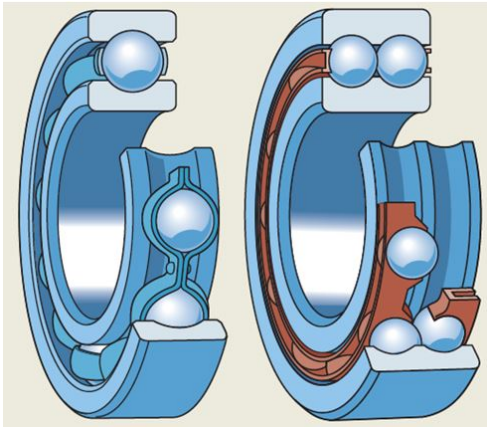

FIGURE J.5: *SKF ball bearing 3D view*

J.2.2.1 Deep groove ball bearing

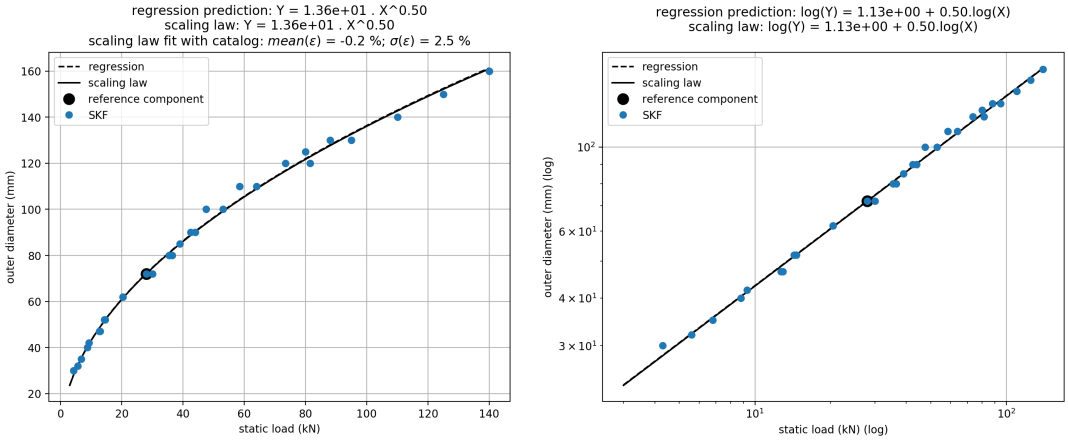

FIGURE J.6: *Validation scaling law, deep groove ball bearing, diameter (SKF)*

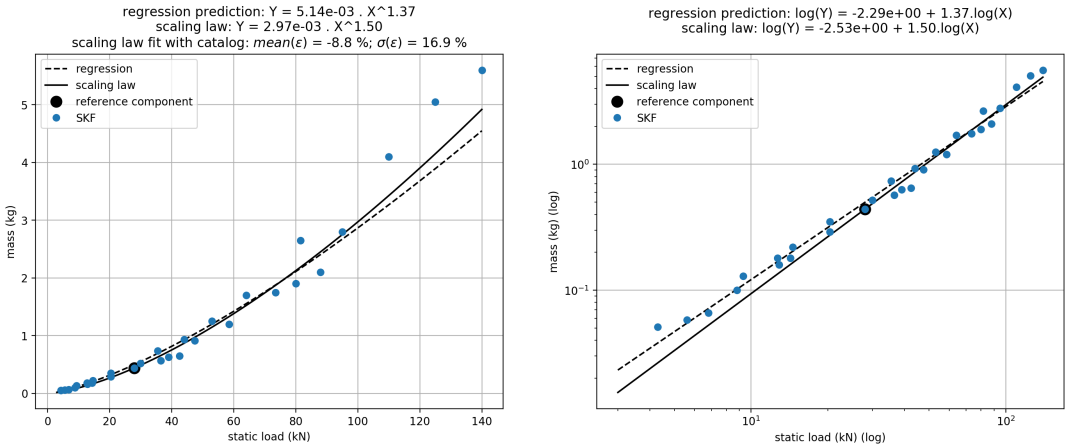

FIGURE J.7: *Validation scaling law, deep groove ball bearing, mass (SKF)*

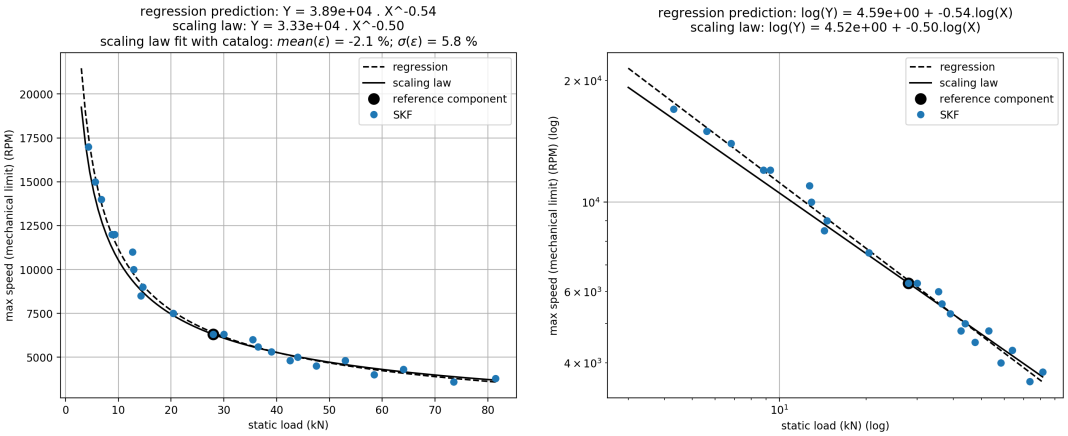

FIGURE J.8: *Validation scaling law, deep groove ball bearing, limiting speed (SKF)*

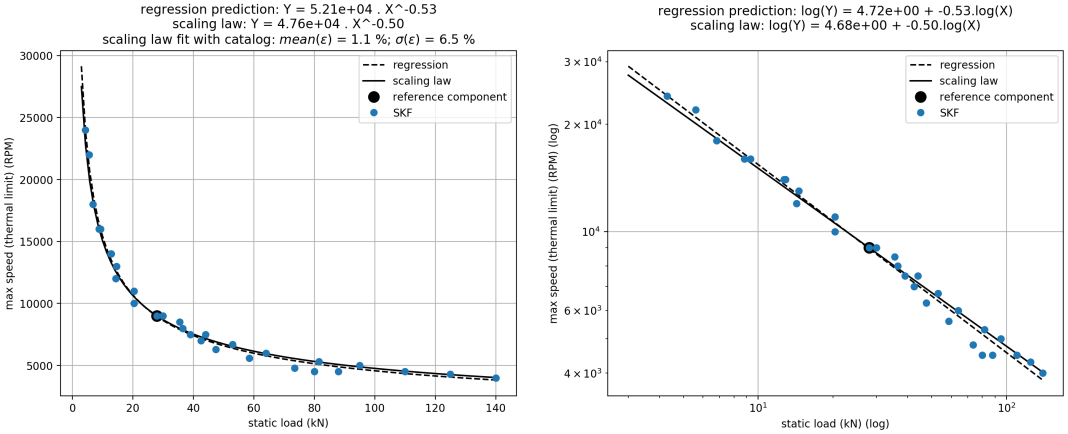

FIGURE J.9: *Validation scaling law, deep groove ball bearing, reference speed (SKF)*

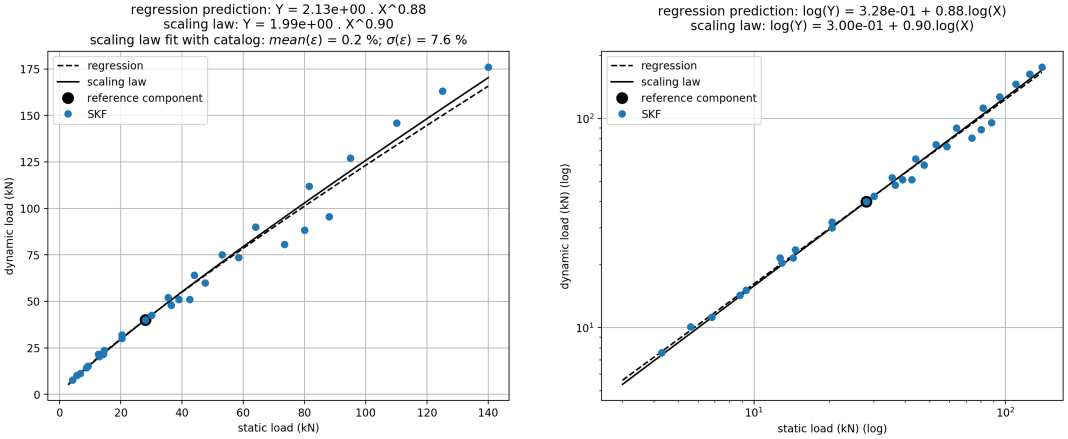

FIGURE J.10: *Validation scaling law, deep groove ball bearing, dynamic load (SKF)*

J.2.2.2 Double row angular contact ball bearing

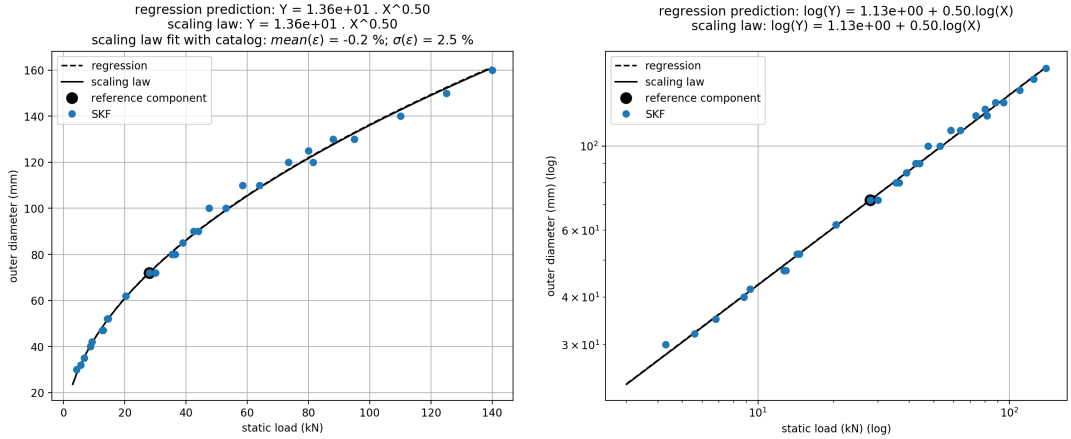

FIGURE J.11: *Validation scaling law, double row angular contact ball bearing, diameter (SKF)*

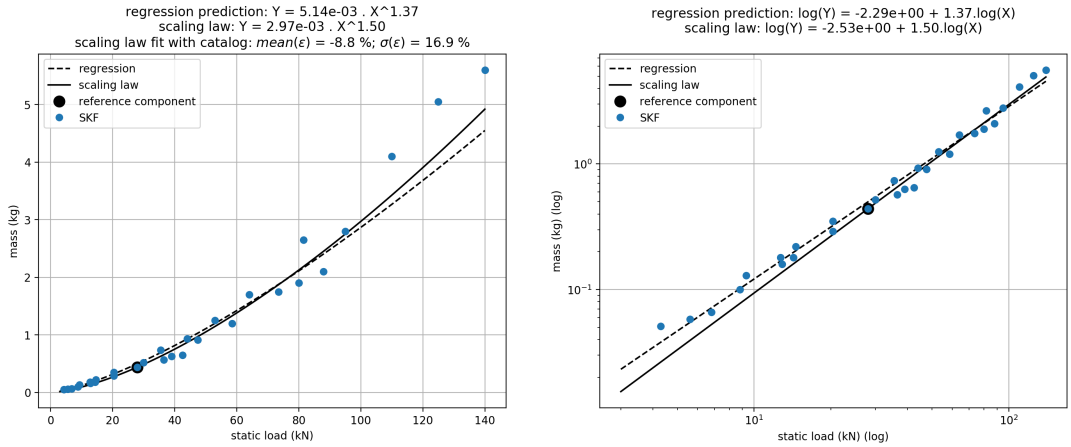

FIGURE J.12: *Validation scaling law, double row angular contact ball bearing, mass (SKF)*

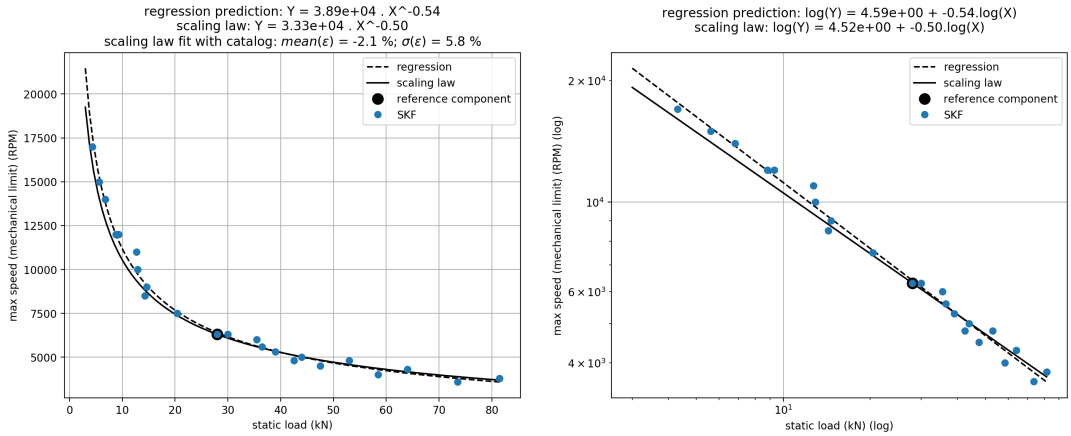

FIGURE J.13: *Validation scaling law, double row angular contact ball bearing, limiting speed (SKF)*

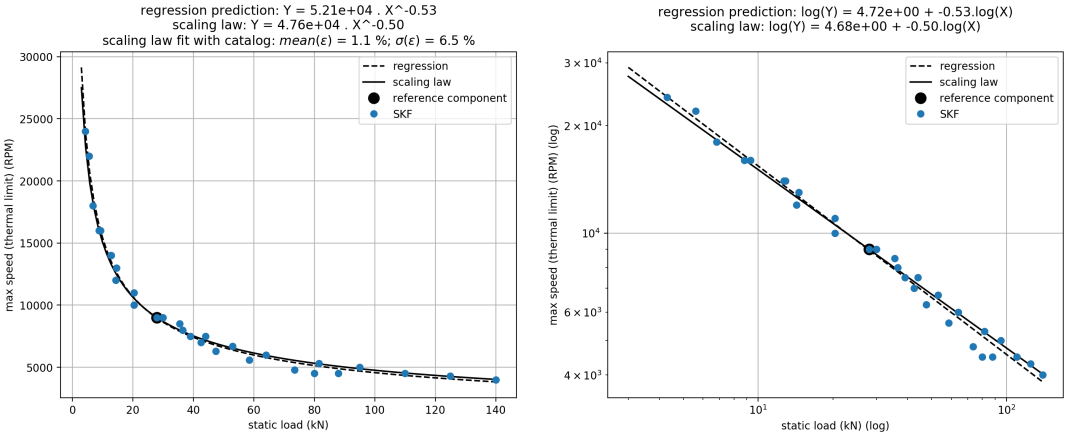

FIGURE J.14: *Validation scaling law, double row angular contact ball bearing, reference speed (SKF)*

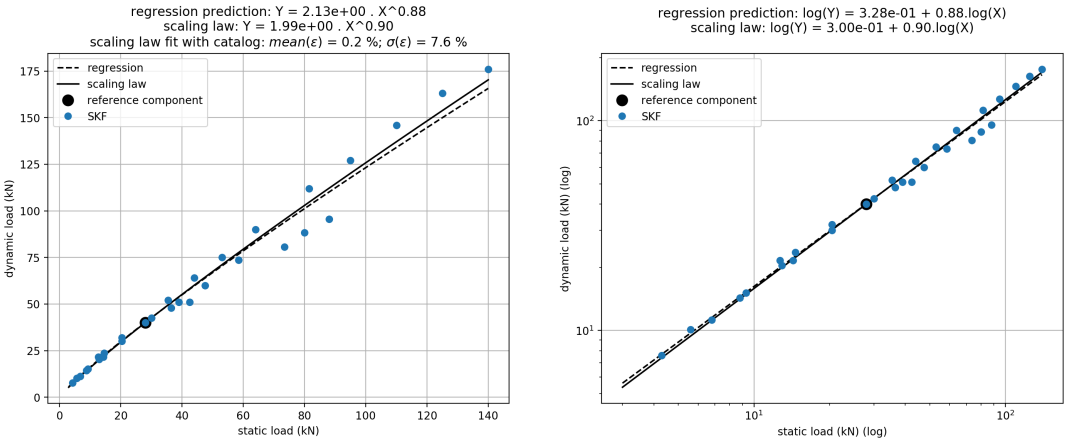

FIGURE J.15: *Validation scaling law, double row angular contact ball bearing, dynamic load (SKF)*

J.3 Screw mechanism

The screw mechanism turns a mechanical power of rotation into a mechanical power of translation. This appendix is focused on the standard and inverted PRS technologies (fig. J.16). It is made out of a screw, a nut containing the rolling elements (the rollers) and a set of bearings. Sizing a screw mechanism actually requires to select these three mechanical sets in parallel.

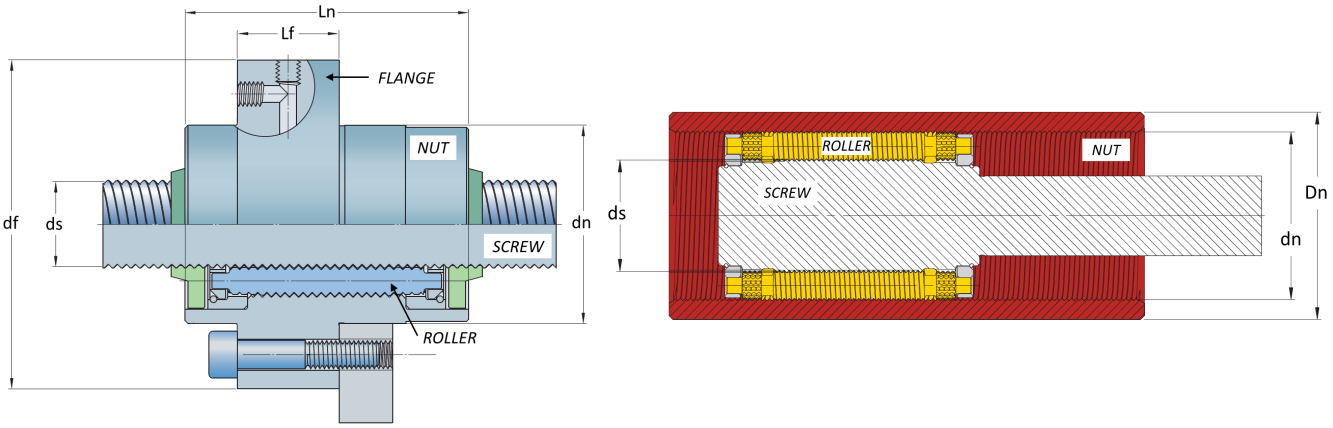

FIGURE J.16: *PRS section view with dimensions: (**left**) standard PRS from [SKF, 2014], (**right**) inverted PRS from [ROLLVIS, 2019]*

J.3.1 Theory

J.3.1.1 Design hypothesis

As any mechanical components, the roller screw mechanism sizing is based on a constant maximum mechanical stress induced by the maximum static load C_0. The correlation study confirms it (subsection J.3.2). However, this criteria differs for the nut sizing where a fatigue criteria leads to scaling laws describing better dimensions and mass evolutions.

J.3.1.2 Screw

This subsection concerns the screw of the standard PRS and the inverted PRS.

Supposing the geometrical similarities in the screw ($d^* = l^*$), the constant maximum mechanical stress provides the following relation:

$$\sigma = 1 \implies \frac{C_0^*}{S^*} = 1 \implies C_0^* = S^* = d^{*2} \tag{J.22}$$

Thus, the evolution of the screw diameter is given by:

$$\boxed{d^* = C_0^{*1/2}} \tag{J.23}$$

When considering the component as a volume V with an equivalent density $\rho_{eq,l}$ per unit of length, the component mass is easily obtained:

$$M = \rho_{eq} \cdot V \implies M_l^* = \rho_{eq,l}^* \cdot S^* \implies M_l^* = d^{*2} \tag{J.24}$$

Considering the relation dimension - load (eq. J.23), the following concludes:

$$M_l^* = C_0^* \tag{J.25}$$

The inertia considers the screw as a basic cylinder of a radius r $[m]$, a length l $[m]$, and an equivalent density ρ_{eq} $[kg.m^{-3}]$:

$$\mathscr{I} = \int r^2\, dm \quad \text{with} \quad dm = 2\pi \cdot \rho_{eq} \cdot r \cdot l \cdot dr \tag{J.26}$$

The inertia per unit of length is given by:

$$\mathscr{I}_l = 2\pi \cdot \rho \cdot \frac{r^4}{4} \implies \mathscr{I}_l^* = d^{*4} \tag{J.27}$$

Considering the relation dimension - load (eq. J.23), the following concludes:

$$J_l^* = C_0^{*2} \tag{J.28}$$

J.3.1.3 Nut

The nut of the standard PRS follows scaling laws detailed in the thesis core (section 4.2.3.1). The nut of the inverted PRS follows the relations stated for the screw of the standard PRS i.e. eq. J.23, J.25 & J.28.

J.3.1.4 Operational limit

The scaling law derivation regarding the nominal dynamic load capabilities has been detailed in the thesis core (section 4.2.3.1). A single scaling law describes this aspect for both PRS: the standard PRS and the inverted one.

J.3.2 Correlation matrix

To study dependencies between parameters, the correlation matrix is a relevant tool.

The correlation matrix of the standard roller screw from [SKF, 2014] & [ROLLVIS, 2019] is given in section 4.2.3.1 (fig. 4.8). The correlation matrix of the inverted roller screw from [SKF, 2014] & [ROLLVIS, 2019] is given in fig. J.17.

In both technologies, the static load C_0 is the parameter the most correlated to dimension parameters.

	d0_mm	d00_mm	D1_mm	lead_mm	Ca_N	C0a_N	eta_d	Mn_kgbym	Ms_kgbym
d0_mm	1.000000	0.994977	0.996574	0.751834	0.973165	0.983551	0.116298	0.976243	1.000000
d00_mm	0.994977	1.000000	0.997803	0.714574	0.987011	0.994295	0.081534	0.965755	0.994977
D1_mm	0.996574	0.997803	1.000000	0.731040	0.982238	0.990327	0.101054	0.980666	0.996574
lead_mm	0.751834	0.714574	0.731040	1.000000	0.719722	0.701872	0.709953	0.762291	0.751834
Ca_N	0.973165	0.987011	0.982238	0.719722	1.000000	0.991890	0.127755	0.943625	0.973165
C0a_N	0.983551	0.994295	0.990327	0.701872	0.991890	1.000000	0.084714	0.953700	0.983551
eta_d	0.116298	0.081534	0.101054	0.709953	0.127755	0.084714	1.000000	0.158233	0.116298
Mn_kgbym	0.976243	0.965755	0.980666	0.762291	0.943625	0.953700	0.158233	1.000000	0.976243
Ms_kgbym	1.000000	0.994977	0.996574	0.751834	0.973165	0.983551	0.116298	0.976243	1.000000

FIGURE J.17: *Correlation matrix of standard roller screw from ROLLVIS & SKF catalogs*

J.3.3 Validation

A validation has been performed with two suppliers catalogs: [SKF, 2014] and [ROLLVIS, 2019] (fig. J.16, fig. 4.7). Part of the validation graphs is presented in the thesis core (section 4.2.3.1). Some more are presented herebelow. All figures have been generated with the same components of reference.

In fig. J.18, the screw diameter scaling law is validated.

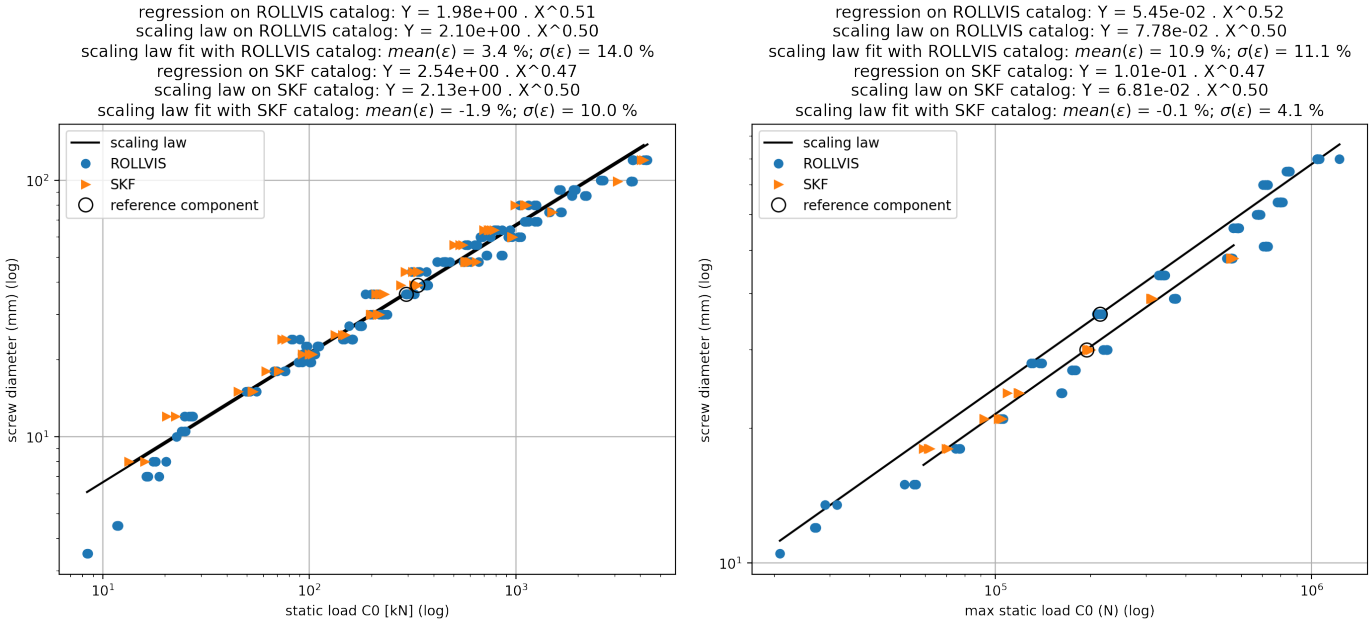

FIGURE J.18: *Screw diameter with respect to static load C_0. (**left**) standard roller screw, (**right**) inverted roller screw; scaling law prediction (eq. 4.14); data from [SKF, 2014] and [ROLLVIS, 2019]*

In fig. J.19, the scaling laws describing the mass and the inertia of the screw are validated. Since the catalog [ROLLVIS, 2019] does not provide any mass or inertia, fig. J.19 only presents data from the catalog [SKF, 2014].

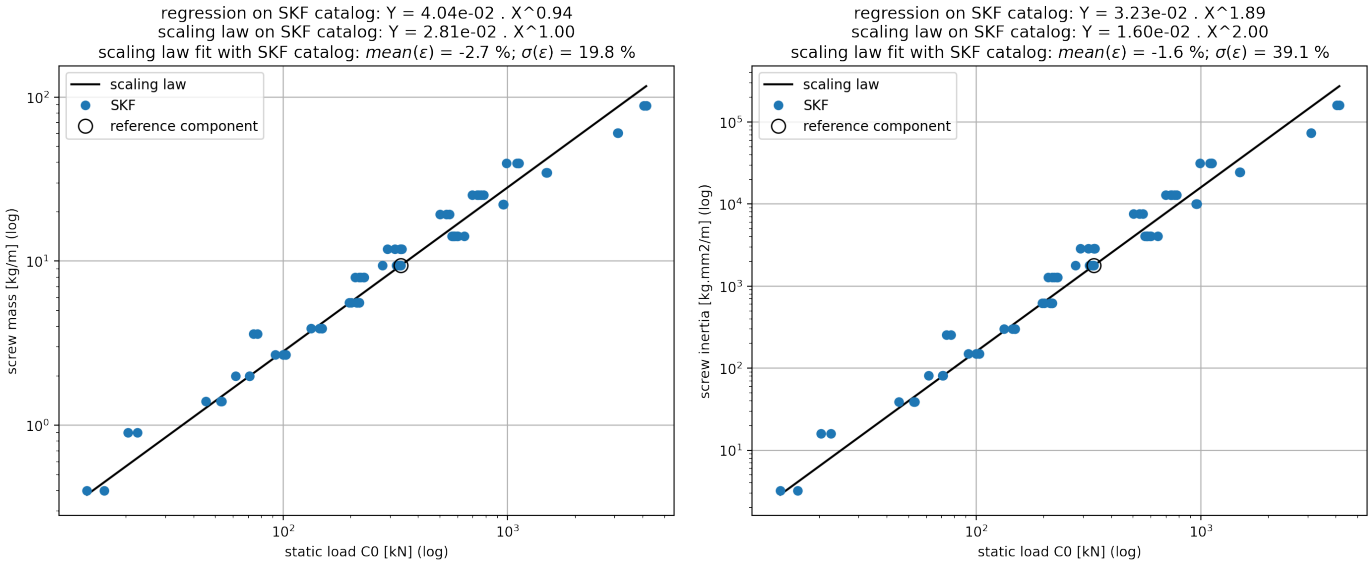

FIGURE J.19: *Mass & inertia of the screw with respect to static load C_0: (**left**) screw mass, (**right**) screw inertia; scaling law prediction (eq. 4.14); standard PRS, data from [SKF, 2014]*

In fig. J.20, the scaling laws of the nut flange dimensions are validated.

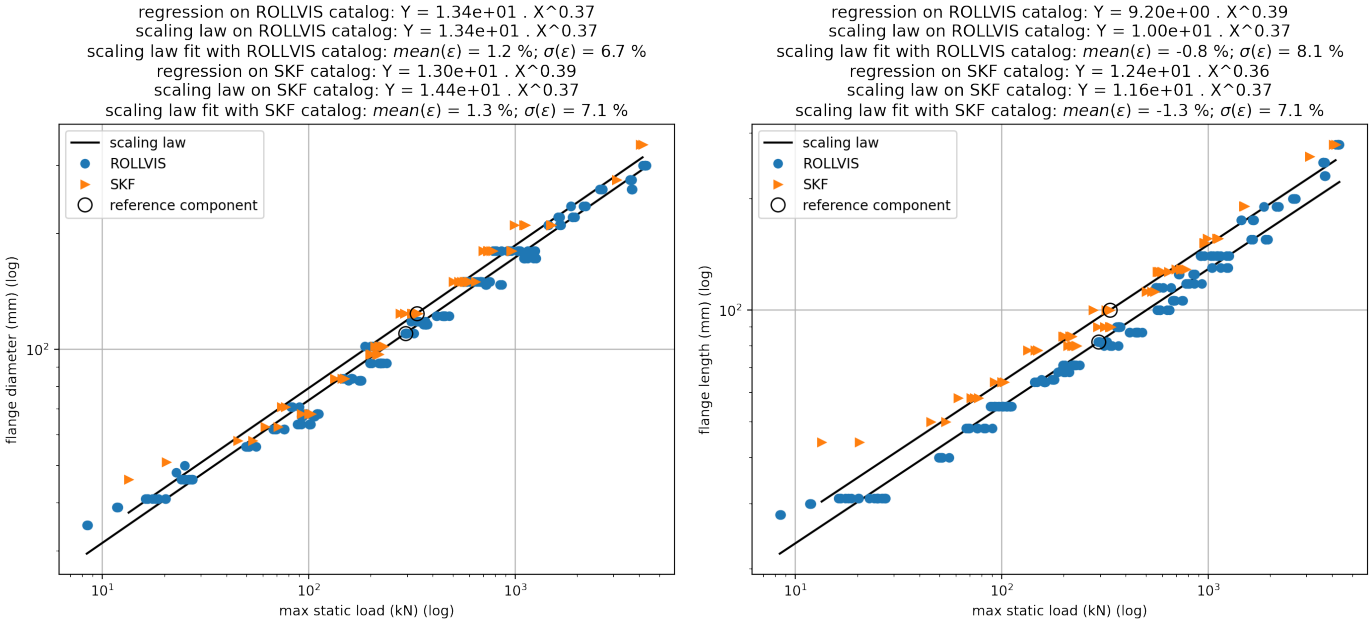

FIGURE J.20: *Nut flange dimensions with respect to static load C_0, standard roller screw, scaling law prediction (eq. 4.15; (**left**) flange diameter, (**right**) flange length; data from [SKF, 2014] and [ROLLVIS, 2019]*

In fig. J.21, the scaling laws of the nut inner diameter are validated.

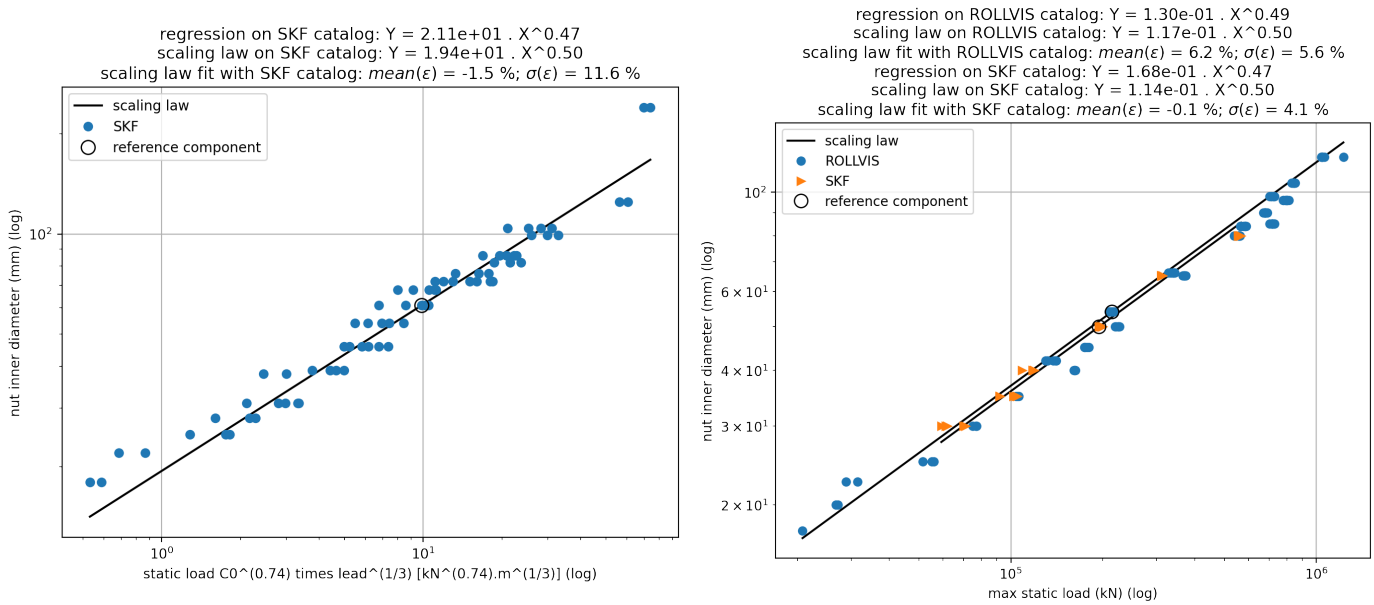

FIGURE J.21: *Nut inner diameter d with respect to: (**left**) $C_0^{0.74} \cdot lead^{1/3}$ for standard roller screw, (**right**) C_0 for inverted roller screw; scaling law prediction (eq. 4.14 and 4.17); data from [SKF, 2014] and [ROLLVIS, 2019]*

Appendix K

Scaling law derivation: electrical components

K.1 Cylindrical motor

The section focuses on spinning motors with self-piloted synchronous characteristics (electronic commutation) and permanent magnets. They are commonly called *brushless motors*. There are two types: cylindrical and annular motors. This section is dedicated to the first motor type characterised by a cylindrical shape and a shaft sticking out. The section K.2 is dedicated to the second motor type.

K.1.1 Hypothesis

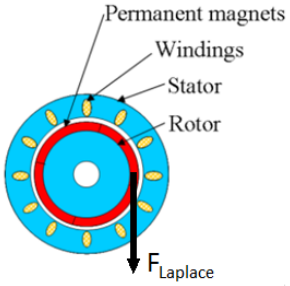

FIGURE K.1: *Cylindrical motor sketch*

The laws developed for cylindrical brushless motors are based on 3 hypothesis.

1. The physical properties P_i remain the same among a considered product range: $P_i^* = 1$
2. The number of pole pairs is constant whatever the diameter is: $n_{poles}^* = 1$
3. All the dimensions follow a homothetic evolution: $d^* = l^*$

It might happen that the hypothesis 3 can not be checked on manufacturers' catalogs. Or, this hypothesis is checked but the formulated motor laws do not fit catalog data. In this situation, the scaling laws must distinguish the motor length from its diameter. Therefore, in the following sections, the scaling laws are everytime developed according to hypothesis 3 and regardless the hypothesis 3.

K.1.2 Current density J

To state the current density expression, Joules' effect is supposed to be the main contributor in motor heat losses. Also, these losses are assumed to be dissipated by a convection phenomena on the outer motor surface. At steady state, the losses and dissipation balance:

$$Joules' \ losses \ \mathscr{P}_J = \ dissipated \ power \ \mathscr{P}_{dis} \tag{K.1}$$

- Joules losses formulation:

The resistance $\mathscr{R}$ $[Ohm]$ is defined with a winding copper resistivity ρ_{copper} $[Ohm.m]$, a wire length l_{wire} $[m]$ and a wire section S_{wire} $[m^2]$:

$$\mathscr{R} = \rho_{copper} \cdot \frac{l_{wire}}{S_{wire}} \tag{K.2}$$

The current flow $I\ [A]$ is defined by a current density $J\ [A/m^2]$:

$$J = \frac{I}{S_{wire}} \implies I = J \cdot S_{wire} \tag{K.3}$$

Joules' losses are then developed such as:

$$\mathscr{P}_J = \mathscr{R} \cdot I^2 = \rho_{copper} \cdot l_{wire} \cdot J^2 \cdot S_{wire} = \rho_{copper} \cdot V_{copper} \cdot J^2 \tag{K.4}$$

Finally, considering hypothesis 1, $\rho^*_{copper} = 1$ and Joules' losses become:

- if geometrical similarity considered ($d^* = l^*$):

$$\mathscr{P}^*_J = d^{*3} \cdot J^{*2} \tag{K.5}$$

- if no geometrical similarity considered ($d^* \neq l^*$):

$$\mathscr{P}^*_J = d^{*2} \cdot l^* \cdot J^{*2} \tag{K.6}$$

- Dissipated power formulation: The power dissipated by convection is expressed such as:

$$\mathscr{P}_{dis} = h_{convection} \cdot S_{motor} \cdot \Delta\theta$$

where $h_{convection}\ [W/m^2/K]$ the convection heat exchange coefficient, S_{motor} the motor skin surface and $\Delta\theta$ the temperature gradient between the motor skin and the ambient temperature. The current density is limited by the maximum insulation temperature of wires (to ensure a given life span to insulators), and by the means of cooling. Among a given product range, the same insulations and cooling means are considered. The temperature gradient is constant: $\Delta\theta^* = 1$. The hypothesis 1 states $h^*_{convection} = 1$. As a result, the power dissipated is reduced to a dependency regarding only the motor surface:

$$\mathscr{P}^*_{dis} = S^*_{motor} \tag{K.7}$$

- Current density formulation: Finally, gathering results from eq. K.5 & K.6 & K.7 into eq. K.1, the current density is expressed:

- if geometrical similarity considered ($d^* = l^*$):

$$\mathscr{P}^*_J = \mathscr{P}^*_{dis} \implies d^{*3} \cdot J^{*2}_{cont} = d^{*2}$$

$$\boxed{J^*_{cont} = d^{*-1/2} = l^{*-1/2}} \tag{K.8}$$

- if no geometrical similarity considered ($d^* \neq l^*$):

$$\mathscr{P}^*_J = \mathscr{P}^*_{dis} \implies d^{*2} \cdot l^* \cdot J^{*2}_{cont} = d^* \cdot l^*$$

$$\boxed{J^*_{cont} = d^{*-1/2}} \tag{K.9}$$

K.1.3 Torque & Dimension

Laplace's force is defined by:

$$\overrightarrow{dF_{laplace}} = n_{turns} \cdot I \cdot \overrightarrow{dl} \wedge \overrightarrow{B} \tag{K.10}$$

where $I\ [A]$ is the current flowing into the winding, n_{turns} the number of winding turns, and $d\overrightarrow{l}\ [m]$ the portion of winding oriented in the sense of current flow, and $\overrightarrow{B}$ the magnetic field ($[T]$ or $[kg \cdot s^{-2} \cdot A^{-1}]$) in the air gap due to permanent magnets.

The current density $J\ [A.m^{-2}]$ is defined by:

$$J = \frac{I}{S_{wire}} = \frac{I}{S_{notch}} \cdot \frac{1}{k_w} \cdot n_{turns}$$

with $S_{notch} \cdot k_w = S_{wire} \cdot n_{turns}$ the surface of copper contained in a notch section and $k_w < 1[-]$ a notch filling factor since the notch is not completely full of copper. Locating differently the equation members, the following relation comes up:

$$n_{turns} \cdot I = J \cdot S_{notch} \cdot k_w \tag{K.11}$$

Taking back the eq. K.10:

$$F_{Laplace} = J \cdot S_{notch} \cdot k_w \cdot l_{notch} \cdot B$$

The hypothesis 1 states $B^* = 1$, the induction created by the permanent magnets in the air gap is constant whatever the motor scale is. Also, the product range is assumed to follow the same design concept, thus $k_w^* = 1$. It results in:

$$F_{Laplace}^* = J^* \cdot S_{notch}^* \cdot l_{notch}^* \tag{K.12}$$

The torque results from Laplace's force applied to a given radius $r^* = d^*$:

$$T^* = F_{Laplace}^* \cdot r^* \tag{K.13}$$

If the geometrical similarities are considered (hypothesis 3, $d^* = l^*$), Laplace's force and torque become:

$$F_{Laplace}^* = J^* \cdot d^{*3} \tag{K.14}$$

$$T^* = J^* \cdot d^{*4} \tag{K.15}$$

Applying a previous result from eq. K.8, the continuous motor torque is:

$$\boxed{T_{cont}^* = d^{*3.5}} \tag{K.16}$$

Also,

$$\boxed{d^* = T_{cont}^{*1/3.5} \approx T_{cont}^{*0.3}} \tag{K.17}$$

If the geometrical similarities are not considered ($d^* \neq l^*$):

$$F_{Laplace}^* = J^* \cdot d^{*2} \cdot l^* \tag{K.18}$$

$$T^* = J^* \cdot d^{*3} \cdot l^* \tag{K.19}$$

Applying a previous result from eq. K.9, the continuous motor torque is:

$$\boxed{T_{cont}^* = d^{*2.5} \cdot l^*} \tag{K.20}$$

Also,

$$\boxed{d^* = \left(\frac{T^*_{cont}}{l^*}\right)^{1/2.5} = \left(\frac{T^*_{cont}}{l^*}\right)^{0.4}} \tag{K.21}$$

K.1.4 Peak torque T_p

The peak torque can follow different definitions according to supplier design choices. Please, see section 4.2.3.2 of the thesis core for these aspects.

K.1.5 Mass $\mathscr{M}$

The motor mass considers a basic cylinder of volume V with an equivalent density ρ_{eq}:

The motor mass is considered as the mass of a basic cylinder of volume V with an equivalent density ρ_{eq}. Applying the hypothesis 1 ($\rho^*_{eq} = 1$), the mass results in the following relations:

$$\mathscr{M} = \rho_{eq} \cdot V \rightarrow \mathscr{M}^* = V^* \tag{K.22}$$

If the geometrical similarities are considered ($d^* = l^*$):

$$\mathscr{M}^* = d^{*3} \tag{K.23}$$

Using a previous result from eq. K.17, the mass is:

$$\boxed{\mathscr{M}^* = T^{*3/3.5}_{cont} \approx T^{*0.86}_{cont}} \tag{K.24}$$

If the geometrical similarities are not considered ($d^* \neq l^*$):

$$\mathscr{M}^* = d^{*2} \cdot l^* \tag{K.25}$$

Using a previous result from eq. K.21, the mass is:

$$\boxed{\frac{\mathscr{M}^*}{l^*} = \left(\frac{T^*_{cont}}{l^*}\right)^{2/2.5} \approx \left(\frac{T^*_{cont}}{l^*}\right)^{0.8}} \tag{K.26}$$

K.1.6 Inertia $\mathscr{I}$

The motor inertia comes from the motor rotor mass rotating:

$$\mathscr{I} = \int r^2 \, dm \propto l \cdot r^4 \tag{K.27}$$

If the geometrical similarities are considered ($d^* = l^*$):

$$\mathscr{I}^* = d^{*5} \tag{K.28}$$

Using a previous result from eq. K.17, the rotor inertia is:

$$\boxed{\mathscr{I}^* = T^{*5/3.5}_{cont} \approx T^{*1.4}_{cont}} \tag{K.29}$$

If the geometrical similarities are not considered ($d^* \neq l^*$):

$$\mathscr{I}^* = d^{*4} \cdot l^* \tag{K.30}$$

Using a previous result from eq. K.21, the rotor inertia is:

$$\boxed{\frac{\mathscr{I}^*}{l^*} = \left(\frac{T^*_{cont}}{l^*}\right)^{4/2.5} = \left(\frac{T^*_{cont}}{l^*}\right)^{1.6}} \tag{K.31}$$

K.1.7 Joules' losses $\mathscr{P}_{Joules}$

All conductors with current flow generates heat by Joules' effect. This heat generation is named copper or Joules' losses. The continuous Joules' losses are formulated using previous results.

If the geometrical similarities are considered (hypothesis 3, $d^* = l^*$), Joules' losses are already formulated in eq. K.5. Introducing the continuous current density (eq. K.8) and the relation of continuous torque K.17, Joules' losses are:

$$\boxed{\mathscr{P}^*_J = d^{*2} = T^{*2/3.5}_{cont} \approx T^{*0.6}_{cont}} \tag{K.32}$$

If the geometrical similarities are not considered ($d^* \neq l^*$), Joules' losses are already formulated in eq. K.6. Introducing the continuous current density (eq. K.9) and the relation of continuous torque K.21, Joules' losses are:

$$\boxed{\frac{\mathscr{P}^*_J}{l^*} = d^* = \left(\frac{T^*_{cont}}{l^*}\right)^{1/2.5} \approx \left(\frac{T^*_{cont}}{l^*}\right)^{0.4}} \tag{K.33}$$

K.1.8 Maximum speeds

K.1.8.1 Mechanical limitation

The maximum mechanical speed is supposed to be based only on the rotor resistance to centrifugal force. The centrifugal force is defined by the rotor mass m, its radius r and its tangential speed v or rotative speed Ω.

$$F_{centrifugal} = m \cdot \frac{v^2}{r} = m \cdot \Omega^2 \cdot r \tag{K.34}$$

The generated stress is determined by the ratio of the centrifugal force with a rotor surface S.

$$\sigma_{centrifugal} = \frac{F_{centrifugal}}{S} \tag{K.35}$$

Assuming the geometrical similarities (hypothesis 3, $d^* = l^*$) and applying a previous result from eq. K.24, the stress generated by the centrifugal force is:

$$\sigma^*_{centrifugal} = \frac{d^{*3} \cdot \Omega^{*2} \cdot d^*}{d^{*2}} = d^{*2} \cdot \Omega^{*2} \tag{K.36}$$

Without considering the geometrical similarities ($d^* \neq l^*$) and applying a previous result from eq. K.26, the stress generated by the centrifugal force is::

$$\sigma^*_{centrifugal} = \frac{d^{*2} \cdot l^* \cdot \Omega^{*2} \cdot d^*}{d^* \cdot l^*} = d^{*2} \cdot \Omega^{*2} \tag{K.37}$$

The hypothesis 1 states that, over a full product range, the centrifugal stress remains the same: $\sigma^*_{centrifugal,max} = 1$. Thus, the maximum mechanical speed is:

$$\boxed{\Omega^*_{mecha,max} = d^{*-1} = T^{*-1/3.5}_{cont}} \tag{K.38}$$

K.1.8.2 Electrical limitation

The electrical speed can be expressed with the mechanical speed and the number of pole pair such as:

$$f_{elect,max} = n_{poles} \cdot \Omega_{mecha,max} \tag{K.39}$$

Applying the hypothesis 2 ($n^*_{poles} = 1$) and a previous result from eq. K.38, the maximum electrical speed limited by mechanical stress is:

$$\boxed{f^*_{elect,max} = \Omega^*_{mecha,max} = d^{*-1}} \tag{K.40}$$

K.1.8.3 Thermal limitation

The previous maximum speed is defined by the risk of rotor magnet detachment. Another maximum speed can be defined by the risk of motor overheat. Indeed, the continuous operation domain is limited by the heat generation (fig. 2.4). In this domain and at maximum speed, the iron losses are the only source of heat generation.

[Grellet, 1989] gives a global formulation of iron losses which provides the following evolution:

$$\mathscr{P}^*_{iron} = f^{*b}_{elect} \cdot \mathscr{M}^*_{cond} \tag{K.41}$$

where f_{elect} is the electrical frequency going through the conductors, b an experimental value and $\mathscr{M}_{cond}$ the mass of conductors. [Grellet, 1989] specifies for b a mean value of 1.5.

The continuous operation domain is bounded by two points. The first one is for a nul speed and maximum continuous torque. At this point, there is no iron losses. Joules' losses generate the total motor heat. The second point is at maximum speed and for nul torque. At this point, the copper losses vanish. The iron losses generate the total motor heat. For a given admissible motor heating, the losses occuring at the two points mentioned before are equal:

$$\mathscr{P}^*_{iron}(\Omega = \Omega_{max,iron}) = \mathscr{P}^*_{J}(\Omega = 0) \tag{K.42}$$

From the eq. K.41, the maximum electrical frequency, limited by iron losses $f_{elect,max,iron}$ can be expressed. On one hand, the geometrical similarities (hypothesis 3, $l^* = d^*$) gives $\mathscr{M}^*_{cond} = d^{*3}$ and Joules' losses relation from eq. K.32 is used. On a second hand, no geometrical similarities ($l^* \neq d^*$) are considered, so $\mathscr{M}^*_{cond} = d^{*2} \cdot l^*$ and Joules' losses relation from eq. K.33 is used. Both hypothetical scenarios give the same expression of the electrical frequency:

$$\boxed{f^*_{elect,max,iron} = d^{*-1/b}} \tag{K.43}$$

The electrical frequency is linked to motor speed by the number of pole pair (eq. K.39). The hypothesis 2 states the evolution of pole number $n^*_{poles} = 1$.

Thus, the expression of the maximum motor speed limited by iron losses is expressed by a single relation considering or not hypothesis 3:

$$\boxed{\Omega^*_{max,iron} = d^{*-1/b} = T^{*-1/(3.5 \cdot b)}_{cont}} \tag{K.44}$$

K.1.9 Copper & iron losses coefficients α & β

As mentioned by [Grellet, 1989] and [Jufer, 1996], the copper and iron losses bound the motor continuous operation domain. At steady state, the total heat generated by the electrical motor is the sum of Joules' losses and iron losses such as:

$$Q_{th} = Q_{Joules} + Q_{iron} = \alpha \cdot T^2 + \beta \cdot f^b_{elect} \tag{K.45}$$

where α and β are respectively Joules' coefficient and the iron losses coefficient.

As mentioned in paragraph K.1.8.3 with eq. K.42, for a given admissible motor heating, Joules' losses and iron losses even up. The copper and iron losses coefficients are obtained by the following ratios:

$$\alpha = \frac{\mathscr{P}_J}{T^2_{cont}} \tag{K.46}$$

$$\beta = \frac{\alpha \cdot T^2_{cont}}{f^b_{elect,max,iron}} \tag{K.47}$$

When considering the geometrical similarities (hypothesis 3, $d^* = l^*$), the previous results from eq. K.16 and K.32 give the following expression of α:

$$\boxed{\alpha^* = d^{*-5} = T^{*-5/3.5}_{cont}} \tag{K.48}$$

Also, the previous results from eq. K.16, K.43 and K.48 give the following expression of β:

$$\boxed{\beta^* = d^{*3} = T^{*3/3.5}_{cont}} \tag{K.49}$$

When not considering the geometrical similarities ($d^* \neq l^*$), the previous results from eq. K.20 and K.33 give the following expression of α:

$$\boxed{\alpha^* = d^{*-4} \cdot l^{*-1} = T^{*-4/2.5}_{cont} \cdot l^{*3/5}} \tag{K.50}$$

Also, the previous results from eq. K.20, K.43 and K.50 give the following expression of β:

$$\boxed{\frac{\beta^*}{l^*} = d^{*2} = \left(\frac{T^*_{cont}}{l^*}\right)^{2/2.5}} \tag{K.51}$$

Notes: α and β are usually not provided by manufacturer datasheets. Their value has to be estimated by hand, at least for the component of reference of the scaling law.

The definition of current or torque might be unclear. Another way to estimate α is using the winding parameters such as:

$$Q_{th}(\Omega \approx 0) = 3 \cdot \mathscr{R} \cdot I^2_{sr} = \alpha \cdot T^2_{sr} \implies \alpha = 3 \cdot \frac{\mathscr{R}}{K^2_t} \tag{K.52}$$

for a 3-phased motor where $\mathscr{R}$ $[ohm]$ the single phase resistance, I_{sr} $[A_{RMS}]$ and T_{sr} $[Nm]$ the current and torque at slow rotation, K_t $[Nm/A_{RMS}]$ the torque constant.

For β estimation, the running point when the motor spins at full speed with a low torque is usually not specified. Two other ways can be undertaken according to available data. A first way is to estimate the running point graphically, by hand, extrapolating the manufacturer torque-speed diagram. A second way is to use an intermediate running point which can be called the rated point:

$$\beta = \frac{Q_{th}(\Omega \approx 0) - \alpha \cdot T_{rated}^2}{\Omega_{rated}^{1.5}} \tag{K.53}$$

Kollmorgen defines it as the running point where the motor provides the maximum continuous power output based on a 130°C temperature rise and a standard aluminum heat sink. The definition might be different with other manufacturers. Also, the maximum continuous power output can change while considering different heat sinks or additional means of cooling.

K.1.10 Voltage $\mathscr{U}$ and motor constant $\mathscr{K}$

According to Lenz-Faraday's law, an electrical circuit under a time varying magnetic flux ϕ (induced by a time-varying magnetic field $\vec{B}$) produces an electromotive force e such as:

$$e = -\frac{d\phi}{dt} \tag{K.54}$$

In the particular case of a solenoid,

$$\phi = n_{turn} \cdot \iint_S \vec{B} \cdot \vec{n}\, dS \tag{K.55}$$

where n_{turn} is the number of turns, S the cross-section and $\vec{n}$ the unitary normal vector of the elementary surface dS oriented according to Maxwell's corkscrew rule. The total motor voltage is :

$$\mathscr{U} = n_{turn} \cdot \omega_{elect} \cdot B \cdot S \tag{K.56}$$

The hypothesis 1 states $B^* = 1$. The previous result from eq. K.40 is introduced.

If the geometrical similarities are considered (hypothesis 3, $d^* = l^*$), the motor voltage is:

$$\boxed{\mathscr{U}^* = n_{turn}^* \cdot \Omega_{mecha}^* \cdot d^{*2}} \tag{K.57}$$

The ratio $\mathscr{U}/\Omega_{mecha}$ provides the speed constant $\mathscr{K}_e$ and, indirectly, the torque constant $\mathscr{K}_t$:

$$\boxed{\mathscr{K}_e^* = n_{turn}^* \cdot d^{*2} = \mathscr{K}_t^* = \mathscr{K}^*} \tag{K.58}$$

If the geometrical similarities are not considered ($d^* \neq l^*$) :

$$\boxed{\mathscr{U}^* = n_{turn}^* \cdot \Omega_{mecha}^* \cdot d^* \cdot l^*} \tag{K.59}$$

The ratio $\mathscr{U}/\Omega_{mecha}$ provides the speed constant $\mathscr{K}_e$ and, indirectly, the torque constant $\mathscr{K}_t$:

$$\boxed{\mathscr{K}_e^* = n_{turn}^* \cdot d^* \cdot l^* = \mathscr{K}_t^* = \mathscr{K}^*} \tag{K.60}$$

K.1.11 Resistance $\mathscr{R}$

The resistance, already defined in eq. K.2 can be expressed such as:

$$\mathscr{R} = \rho_{copper} \cdot \frac{l_{wire}}{S_{wire}} = \rho_{copper} \cdot \frac{n_{turn} \cdot l_{turn}}{\frac{S_{notch}}{n_{turn}} \cdot k_w} = \rho_{copper} \cdot n_{turn}^2 \cdot \frac{l_{turn}}{S_{notch} \cdot k_w} \tag{K.61}$$

where n_{turn} $[-]$ and l_{turn} $[m]$ are the number and length of turn of the winding. S_{notch} $[m^2]$ is the notch section. $k_w < 1$ $[-]$ is a notch filling factor since the notch is not completely full of copper. The hypothesis 1 states that k_w and ρ_{copper} remain constant among a given product range. This results in $k_w^* = 1$ and $\rho_{copper}^* = 1$ and the resistance is:

$$\mathscr{R}^* = n_{turn}^{*2} \cdot \frac{l_{turn}^*}{S_{notch}^*} \tag{K.62}$$

If the geometrical similarities are considered (hypothesis 3, $d^* = l^*$), $l_{turn}^* = d^*$ and $S_{notch}^* = d^{*2}$. An intermediate expression of the resistance is:

$$\mathscr{R}^* = n_{turn}^{*2} \cdot d^{*-1} \tag{K.63}$$

Applying the previous results from eq. K.58:

$$n_{turn}^* = \mathscr{K}^* \cdot d^{*-2} \tag{K.64}$$

and eq. K.17, the resistance is deduced to be:

$$\boxed{\frac{\mathscr{R}^*}{\mathscr{K}^{*2}} = d^{*-5} = T_{cont}^{*-5/3.5} \approx T_{cont}^{*-1.4}} \tag{K.65}$$

If the geometrical similarities are not considered ($d^* \neq l^*$), $l_{turn}^* = l^*$ and $S_{notch}^* = d^{*2}$. An intermediate expression of the resistance is:

$$\mathscr{R}^* = n_{turn}^{*2} \cdot \frac{l^*}{d^{*2}} \tag{K.66}$$

Applying the previous results from eq. K.60:

$$n_{turn}^* = \mathscr{K}^* \cdot d^{*-1} \cdot l^{*-1} \tag{K.67}$$

and eq. K.21, the resistance is deduced to be:

$$\boxed{\frac{\mathscr{R}^* \cdot l^*}{\mathscr{K}^{*2}} = d^{*-4} = \left(\frac{T_{cont}^*}{l^*}\right)^{-4/2.5} \approx T_{cont}^{*-1.6}} \tag{K.68}$$

K.1.12 Inductance $\mathscr{L}$

The motor magnetic problem is associated to fig. K.2. A current I $[A]$ in a coil generates a magnetic flux in a circuit including ferromagnetic material and air gaps.

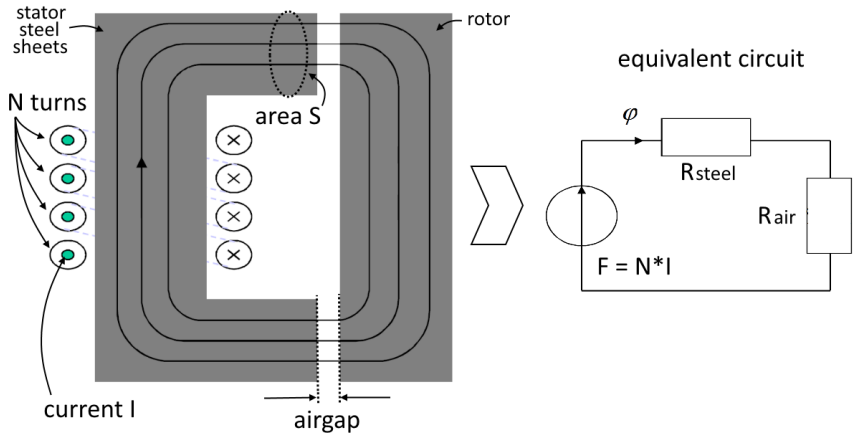

FIGURE K.2: *Electromagnetic circuit basics*

The inductance is usually defined by the inverse of the reluctance R $[H^{-1}]$ of the magnetic circuit such as:

$$\mathscr{L} = \frac{n_{turn}^2}{R} \tag{K.69}$$

with n_{turn} $[-]$ the number of spires of the winding.

For the equivalent circuit presented in fig. K.2, the reluctance R is determined by the sum of the reluctance in series.

$$R = R_{steel} + R_{air} = \frac{1}{S} \cdot \left(\frac{2 \cdot l_{airgap}}{\mu_{air} \cdot \mu_0} + \frac{l_{steel}}{\mu_{steel} \cdot \mu_0} \right) \approx \frac{2 \cdot l_{airgap}}{\mu_0 \cdot S} \tag{K.70}$$

where l_{airgap} $[m]$ is the thickness of the airgap, $\mu_0 = 4.10^{-7}$ $H \cdot m^{-1}$ the magnetic constant (or vacuum permeability), $\mu_{air} \approx 1$ $[-]$ the relative permeability of air, $\mu_{steel} \in [500 - 1000]$ $[-]$ the relative permeability of steel, and S the airgap cross-section through which the magnetic circuit flows ([Pérez et al., 2020]). The ratio l_{airgap}/μ_{air} can be considered as very high compared to l_{steel}/μ_{steel}. The reluctance of the circuit is closely equal to the reluctance of the airgap.

If the geometrical similarities are considered (hypothesis 3, $d^* = l^*$), it assumes that the winding turn length evolves with global dimensions. As a result, $l_{airgap}^* = d^*$ and $S^* = d^{*2}$. The reluctance is $R^* = d^{*-1}$ and an intermediate expression of the total inductance is deduced:

$$\mathscr{L}^* = n_{turn}^{*2} \cdot d^* \tag{K.71}$$

A previous result from eq. K.58 gives an expression of n_{turn}:

$$n_{turn}^* = \mathscr{K}^* \cdot d^{*-2} \tag{K.72}$$

Applying it with the relation from eq. K.17, the inductance is finally expressed:

$$\boxed{\frac{\mathscr{L}^*}{\mathscr{K}^{*2}} = d^{*-3} = T_{cont}^{*-3/3.5} \approx T_{cont}^{*-0.86}} \tag{K.73}$$

If the geometrical similarities are not considered ($d^* \neq l^*$), the surface evolves with diameters and lengths $S^* = d^* \cdot l^*$. The airgap distance still evolves with the diameters $l_{airgap}^* = d^*$. The reluctance is $R^* = l^{*-1}$ and an intermediate expression of

the total inductance is deduced:

$$\mathscr{L}^* = n_{turn}^{*2} \cdot l^* \tag{K.74}$$

A previous result from eq. K.60 gives an expression of n_{turn}:

$$n_{turn}^* = \mathscr{K}^* \cdot d^{*-1} \cdot l^{*-1} \tag{K.75}$$

Applying it with another result from eq. K.21, the inductance is finally expressed:

$$\boxed{\frac{\mathscr{L}^* \cdot l^*}{\mathscr{K}^{*2}} = d^{*-2} = \left(\frac{T_{cont}^*}{l^*}\right)^{*-2/2.5} = T_{cont}^{*-0.8}} \tag{K.76}$$

Some manufacturer might design their motors with a constant winding turn length over their product range. As a result, $x_{airgap}^* = 1$, $S_{turn}^* = 1$ and the reluctance becomes $R^* = 1$. An intermediate result of inductance is:

$$\mathscr{L}^* = n_{turn}^{*2} \tag{K.77}$$

If the geometrical similarities are considered (hypothesis 3, $d^* = l^*$), the relations from eq. K.72 and K.17 are applied. The inductance becomes:

$$\boxed{\frac{\mathscr{L}^*}{\mathscr{K}^{*2}} = d^{*-4} = T_{cont}^{*-4/3.5} \approx T_{cont}^{*-1.1}} \tag{K.78}$$

If the geometrical similarities are not considered ($d^* \neq l^*$), the relations from eq. K.75 and K.21 are applied. The inductance becomes:

$$\boxed{\frac{\mathscr{L}^* \cdot l^{*2}}{\mathscr{K}^{*2}} = d^{*-2} = \left(\frac{T_{cont}^*}{l^*}\right)^{*-2/2.5} = T_{cont}^{*-0.8}} \tag{K.79}$$

Usually, in manufacturer catalog, the winding turn length is a data not available. Its evolution over a product range can not be checked. The choice among all of the inductance formulations developed previously shall be done by comparison with catalogue data. The formulation fitting the most shall be selected.

K.1.13 Motor constant K_m

The motor constant K_m $[(Nm)^2/W]$ is a way to estimate heat losses avoiding the motor winding characteristics and a way to compare motor technologies. Please, see section 4.2.3.3 of the thesis core for these aspects.

K.1.14 Mechanical power $\mathscr{P}_{mechanical}$

The mechanical power can be expressed thanks to the K_m motor constant.

At steady state, the motor voltage can be written as:

$$U = \mathscr{R} \cdot I + K_T \cdot \omega \tag{K.80}$$

where $I = T/K_T$ and $K_T = K_m \cdot \sqrt{R}$.

The total power becomes:

$$\mathscr{P}_{total} = U \cdot I = \underbrace{\left(\frac{T}{K_m}\right)^2}_{Joules} + \underbrace{T \cdot \omega}_{mechanical} \tag{K.81}$$

Section K.1.7 and K.1.13 provide the expression of $\mathscr{P}_{Joules}$ according to K_m. Using the torque and speed scaling laws introduced in section K.1.3 and K.1.8.1, the mechanical power is expressed such as:

$$\text{cylindrical } l^* = d^* \qquad \mathscr{P}^*_{mechanical} = T^* \cdot \omega^* = K_m^{*1/2} \tag{K.82}$$

$$\text{cylindrical } l^* \neq d^* \qquad \frac{\mathscr{P}^*_{mechanical}}{l^*} = \frac{T^*}{l^*} \cdot \omega^* = \left(\frac{K_m^*}{l^*}\right)^{*3/8} \tag{K.83}$$

The ratio $\mathscr{P}_{Joules}/\mathscr{P}_{mechanical}$ finds an interest in a motor sizing loop as a design driver. Thus, it can limit the increase of the K_m value by the optimization algorithm. In addition, the rotor inertia might act beforehand as an upper limitation of the K_m value because of the higher power of its scaling law ($\mathscr{I}^* = K_m^*$) and its direct impact on the motor torque.

K.1.15 Validation

The validation is based on two catalogs: Parvex NK (fig. K.3, [PARKER, 2022]) and KOLLMORGEN RBE (fig. K.11, [KOLLMORGEN, 2003]). In Parvex NK catalog, a 10 poles motor range $T_{cont} \in [2; 41]\ Nm$) and a component of reference of $T_{cont} = 12\ Nm$ have been chosen. This product range follows the laws with the geometrical similarities ($d^* = l^*$). In Kollmorgen RBE catalog, a 12 poles motor range ($T \in [0.5; 38.4]\ Nm$) has been chosen with a component of reference $T_{cont} = 1.67\ Nm$. This motor range follows the scaling laws based on geometrical dissimilarity ($d^* \neq l^*$). However, the validation shows that the peak torque and the copper coefficient are best described by the scaling laws based on geometrical similarity ($d^* = l^*$).

Both product range are interesting since they include a significant number of components to be representative (respectively 9 and 95). Also, they cover two decades in terms of continuous torque.

We remind that the sections 4.2.3.2 and 4.2.3.3 of Chapter 4 complete the validation presented in the following two subsections.

K.1.15.1 PARVEX

FIGURE K.3: *Cylindrical frameless permanent magnet motors (Parvex NK)*

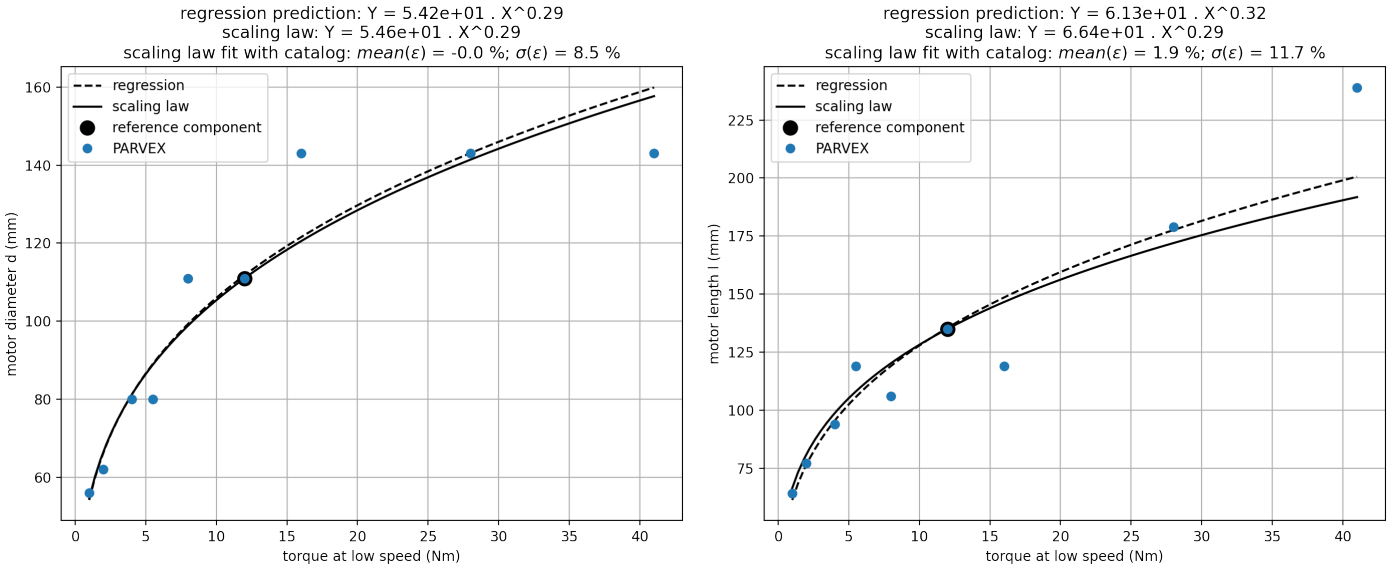

FIGURE K.4: *Validation scaling law, cylindrical motor, diameter and length (Parvex NK)*

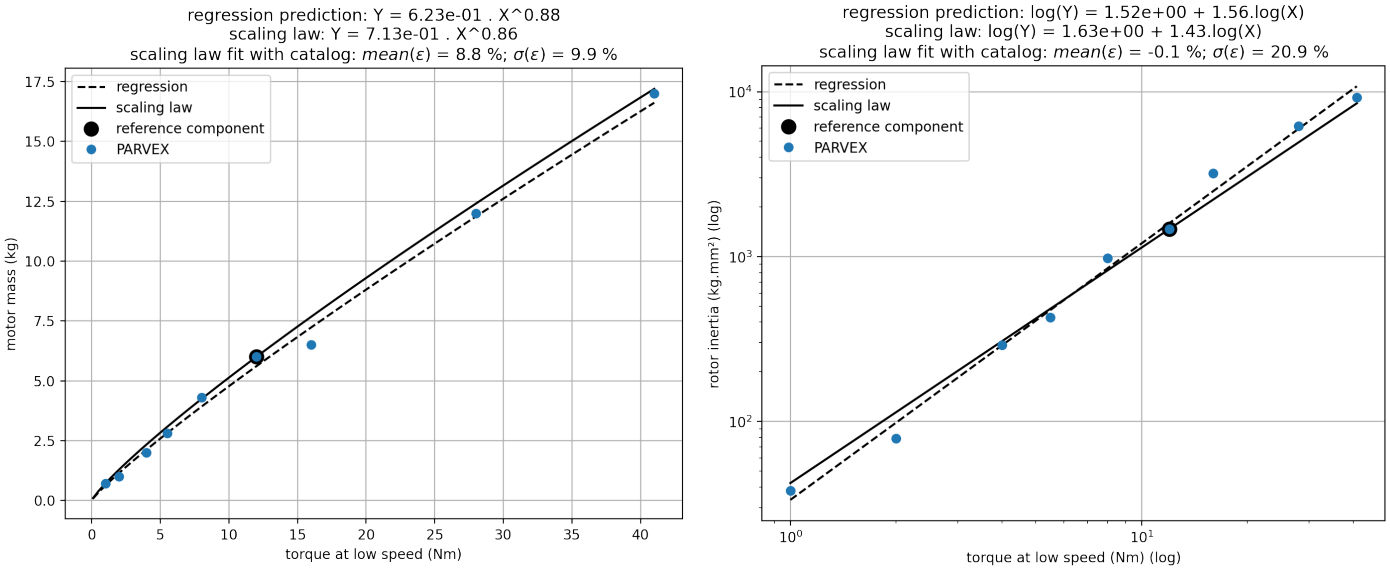

FIGURE K.5: *Validation scaling law, cylindrical motor, mass and inertia (Parvex NK)*

In the three following figures, the component of reference of $T_{cont} = 5.5\ Nm$ is used.

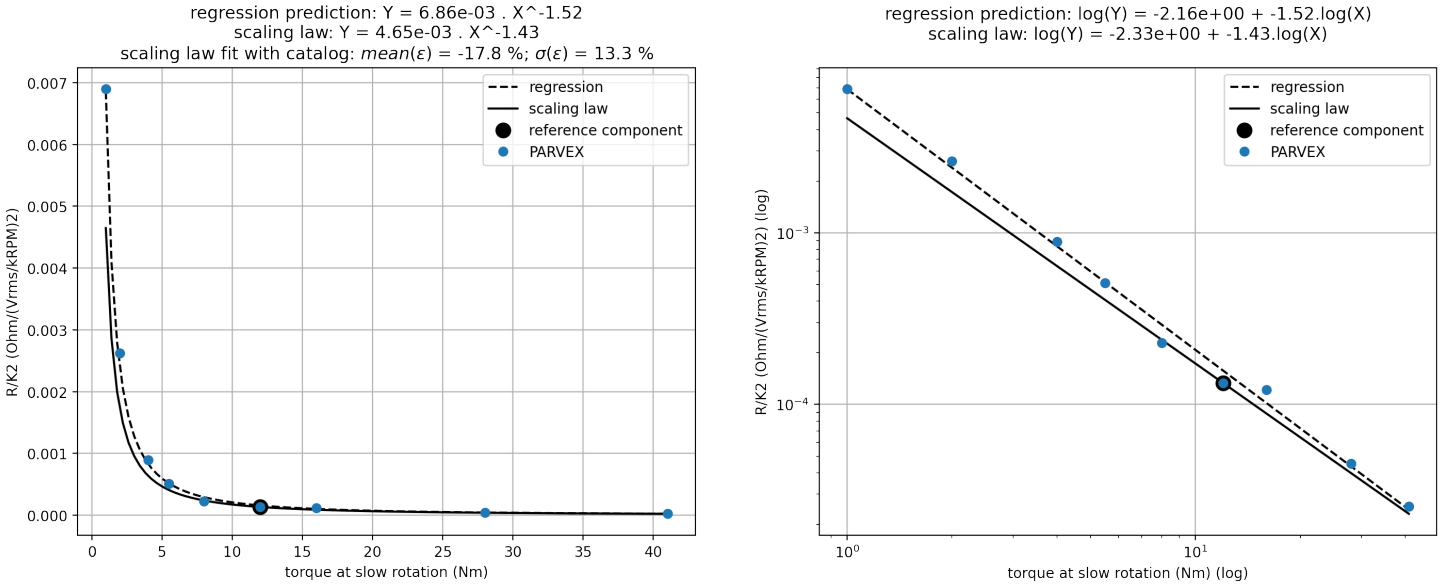

FIGURE K.6: *Validation scaling law, cylindrical motor, resistance (Parvex NK)*

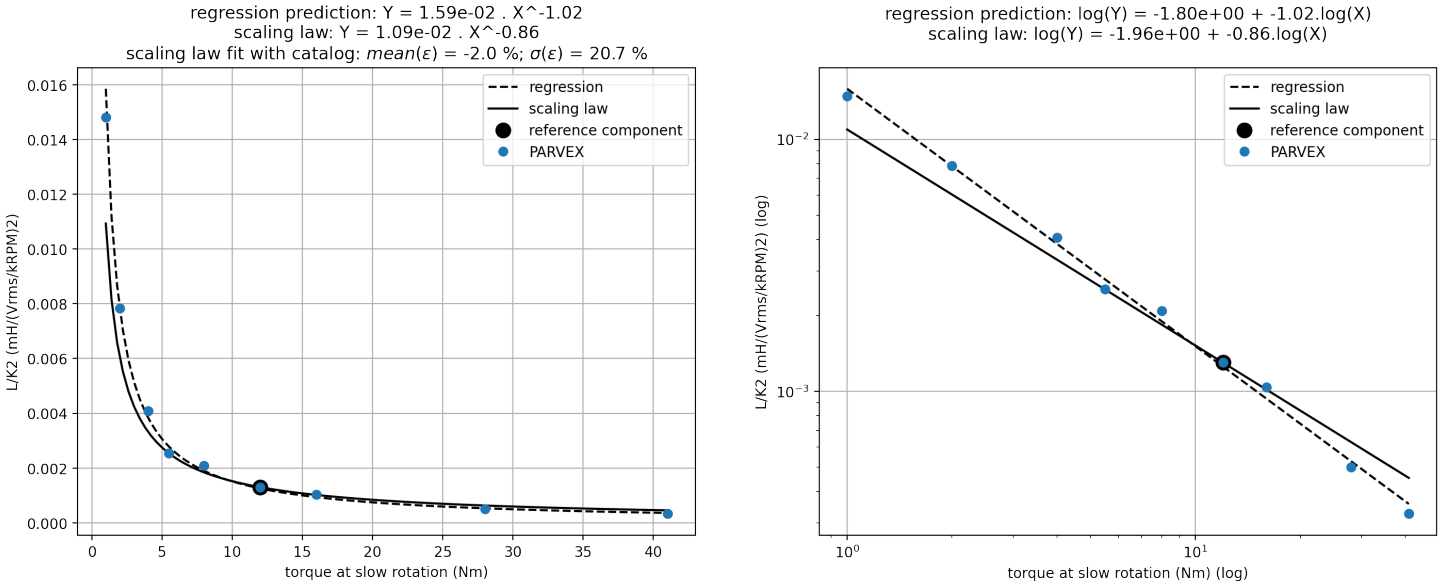

FIGURE K.7: *Validation scaling law, cylindrical motor, inductance (Parvex NK)*

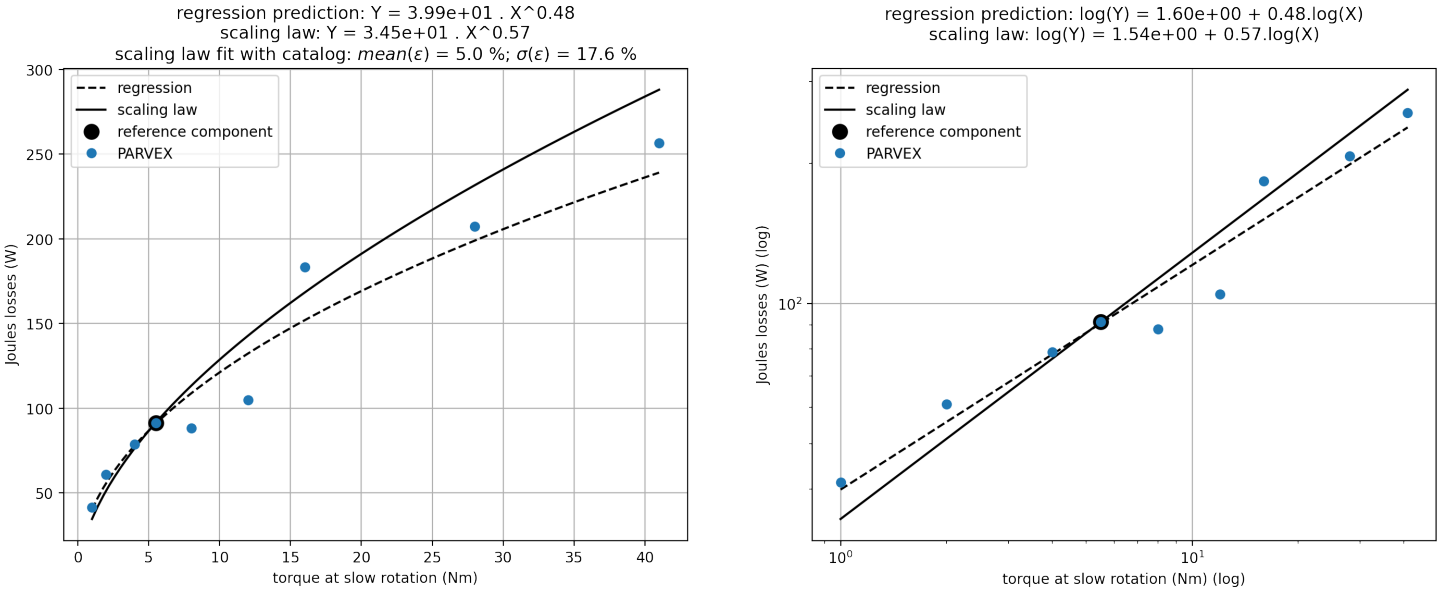

FIGURE K.8: *Validation scaling law, cylindrical motor, Joules' losses (Parvex NK)*

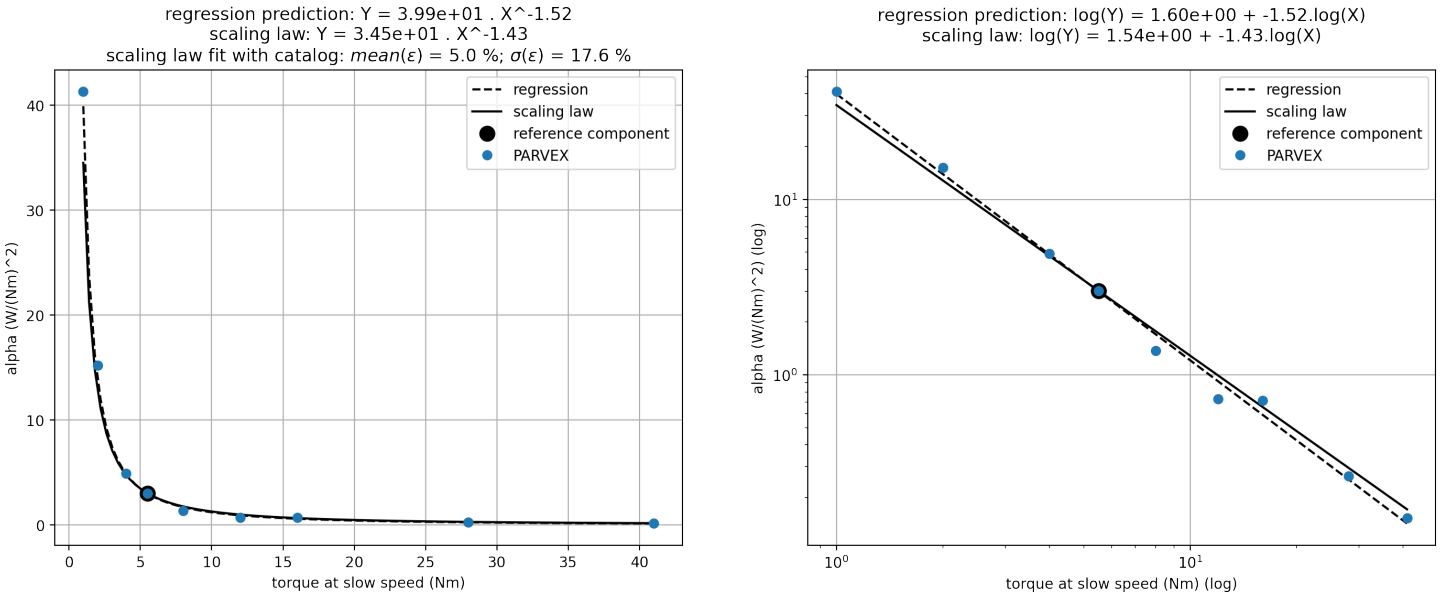

FIGURE K.9: *Validation scaling law, cylindrical motor, copper losses coef. α (Parvex NK)*

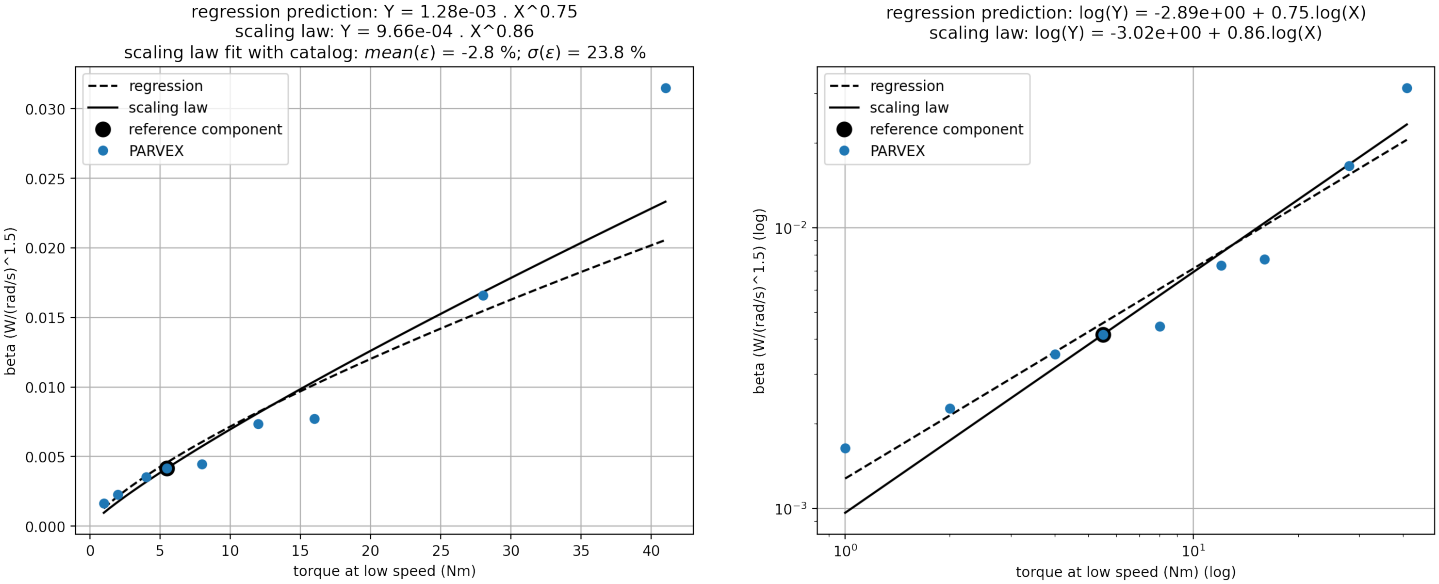

FIGURE K.10: *Validation scaling law, cylindrical motor, iron losses coef. β (Parvex NK)*

K.1.15.2 KOLLMORGEN

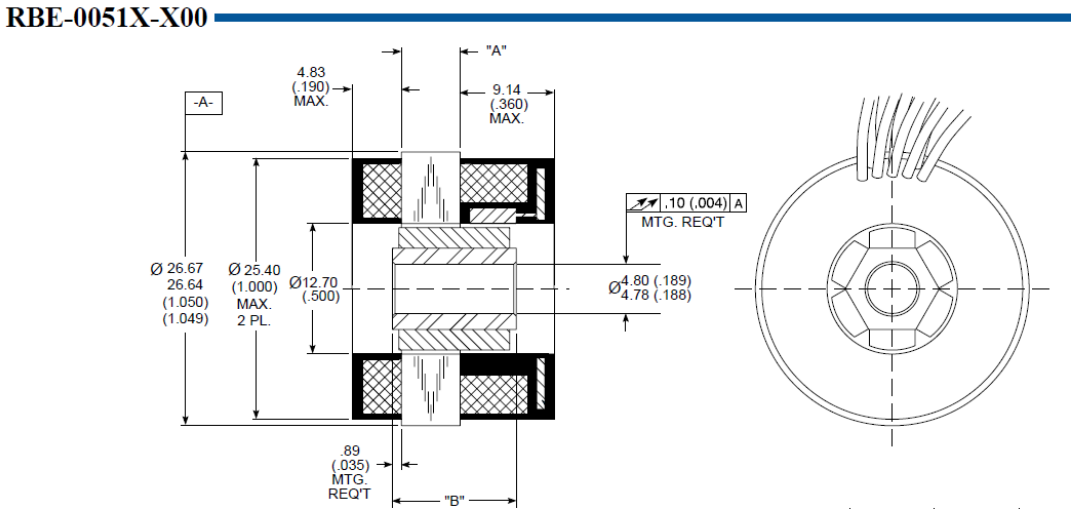

FIGURE K.11: *Cylindrical permanent magnet motor (Kollmorgen RBE)*

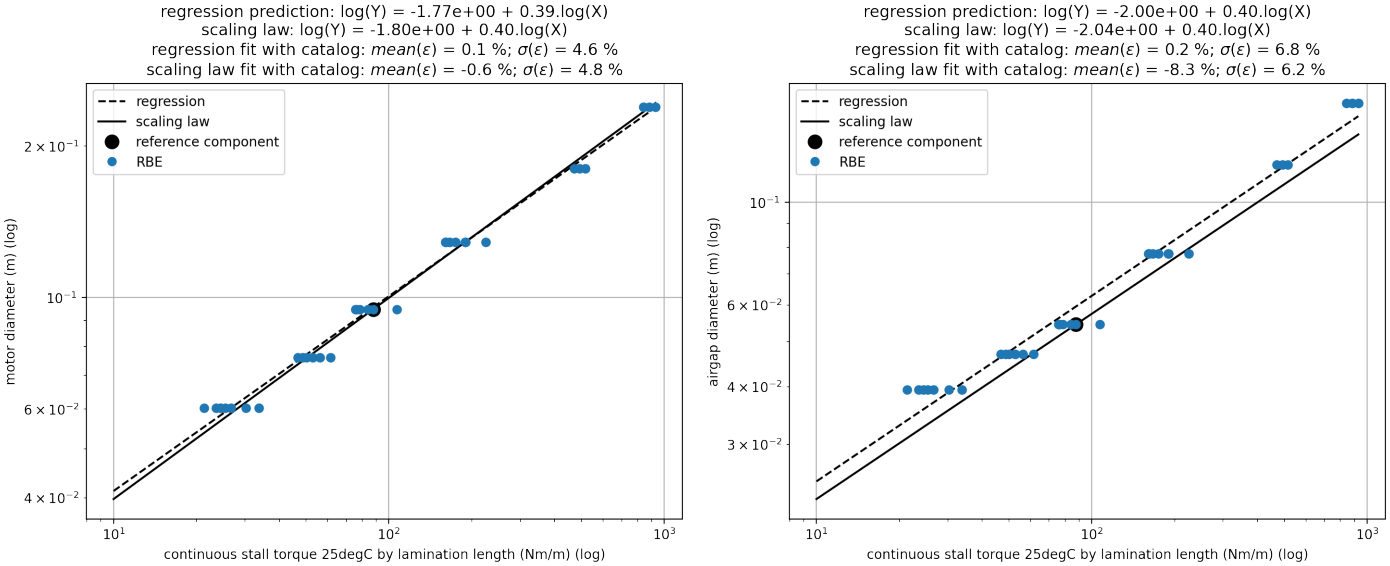

FIGURE K.12: *Validation scaling law, cylindrical motor (Kollmorgen RBE): (left) motor diameter, (right) motor airgap diameter*

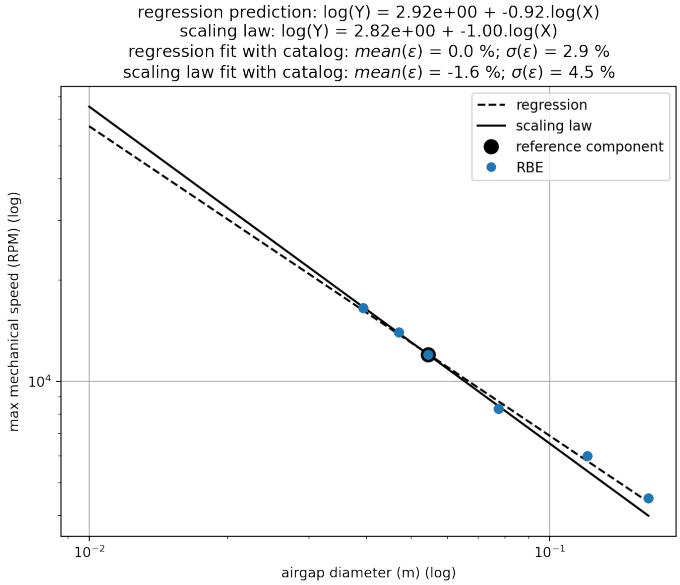

FIGURE K.13: *Validation scaling law, cylindrical motor (Kollmorgen RBE): maximum mechanical speed Ω_{max}*

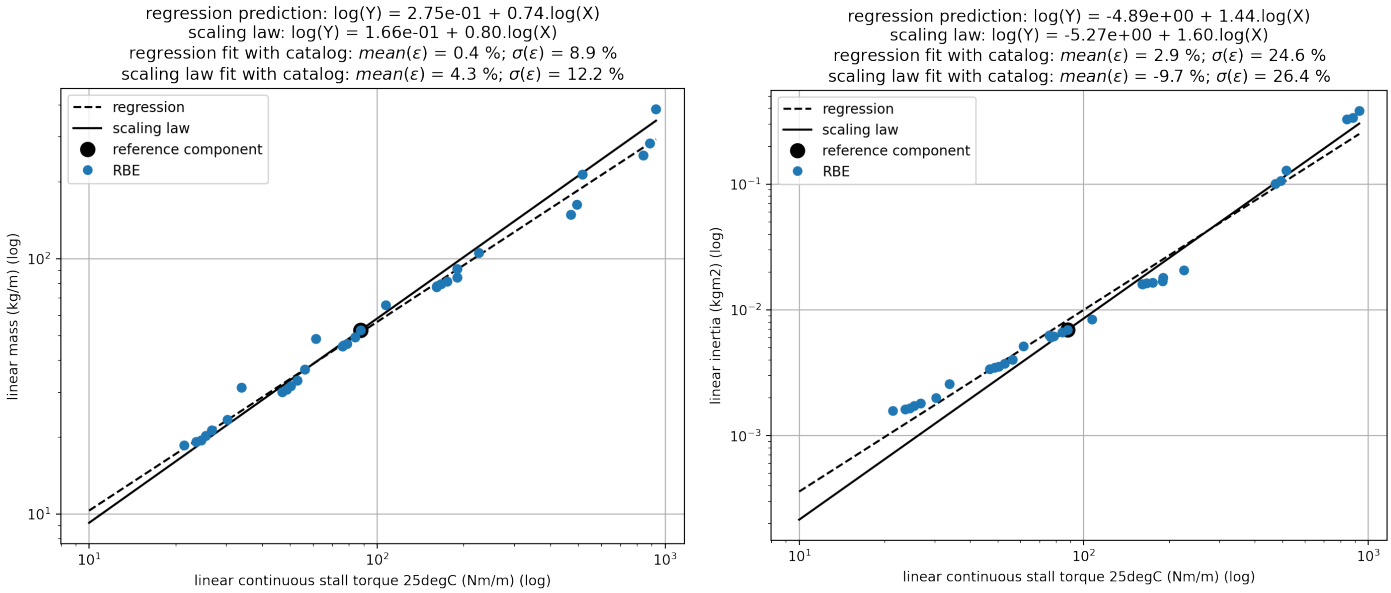

FIGURE K.14: *Validation scaling law, cylindrical motor, (Kollmorgen RBE): (left) motor linear mass, (right) motor linear inertia*

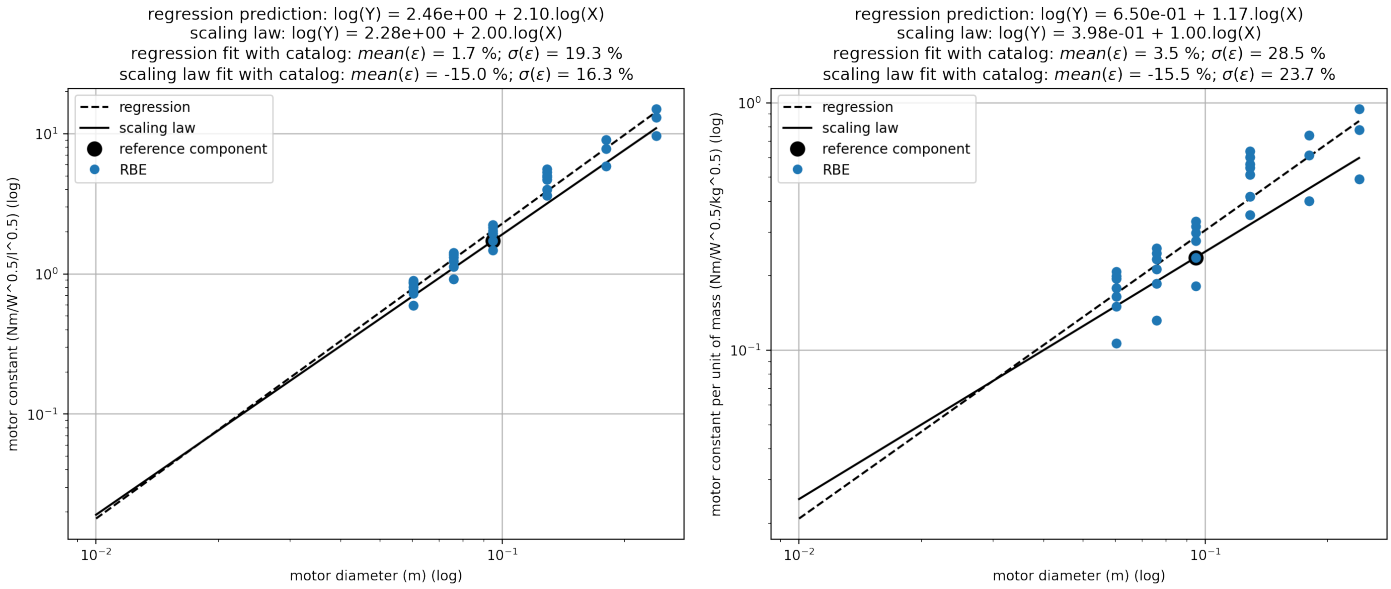

FIGURE K.15: *Validation scaling law, cylindrical motor, (Kollmorgen RBE): (left) motor constant K_m, (right) motor constant K_m per unit of mass*

The length to diameter ratios state that the RBE product range does not satisfy the geometrical similarity hypothesis ($d^* \neq l^*$). However, we observe that the peak torque scaling law based on geometrical similarity hypothesis better fits data from the RBE catalog. Fig. K.16 displays the comparison between the law based on geometrical similarity and the one based on geometrical dissimilarity.

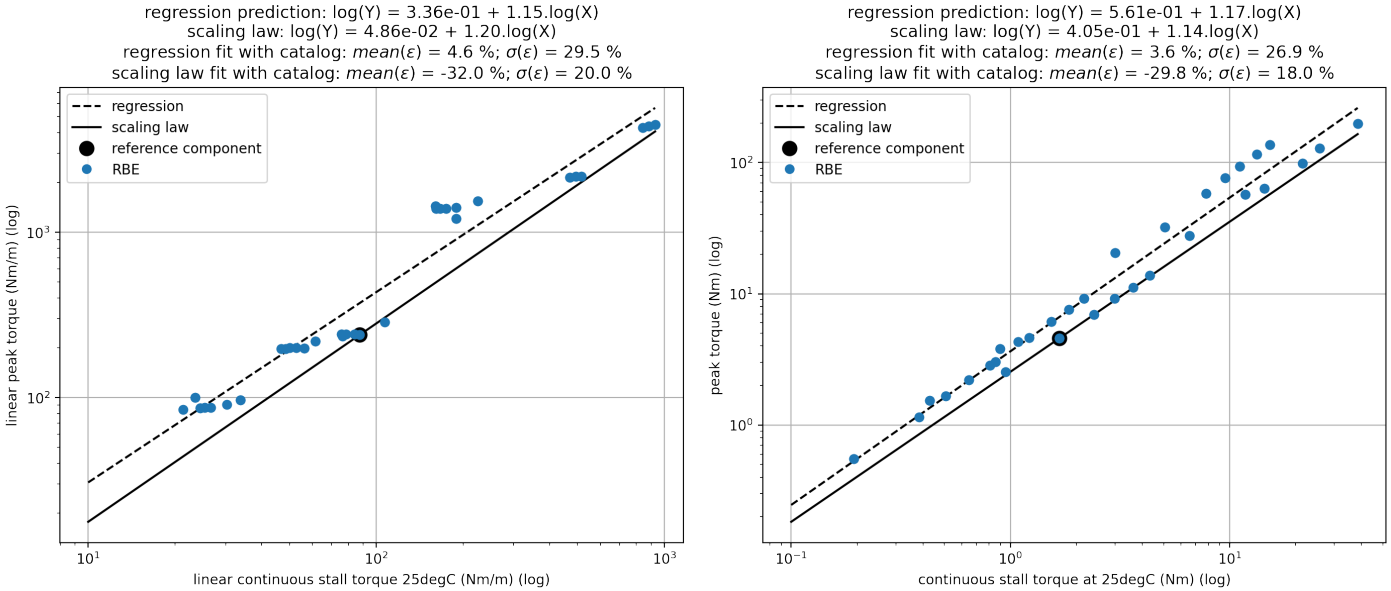

FIGURE K.16: *Validation scaling law, cylindrical motor, peak torque based on thermal criteria (Kollmorgen RBE): (left) linear peak torque T_p/l, (right) peak torque T_p*

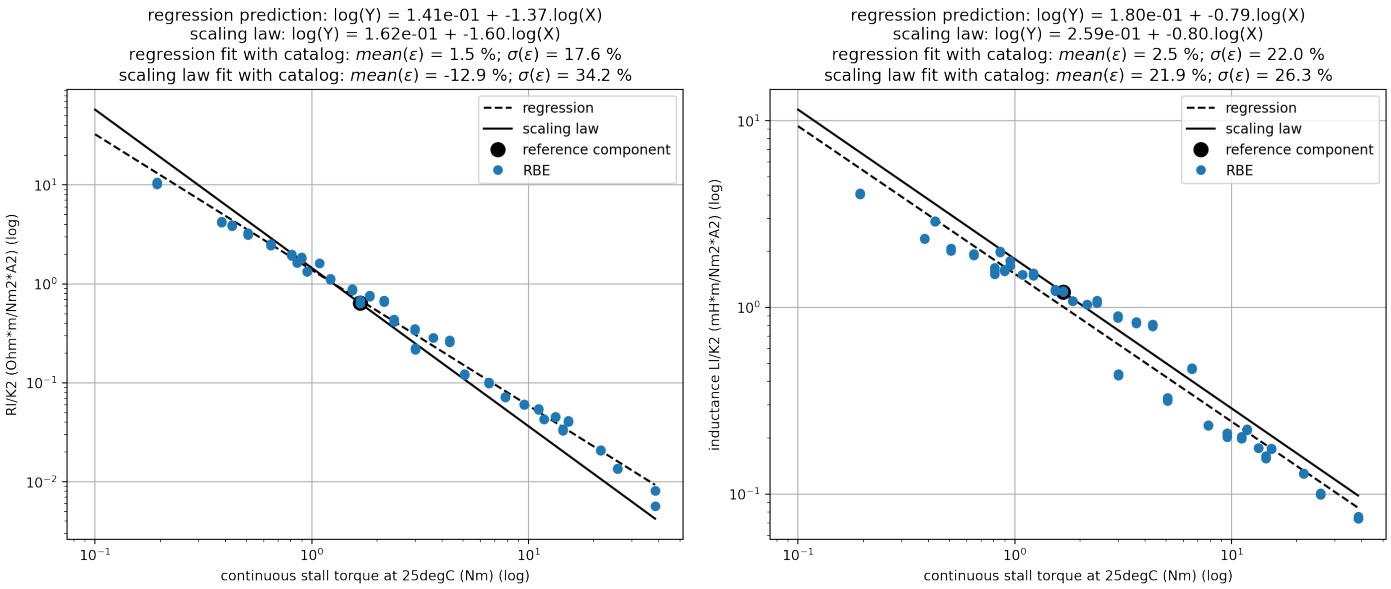

FIGURE K.17: *Validation scaling law, cylindrical motor, winding characteristics (Kollmorgen RBE): (left) resistance, (right) inductance*

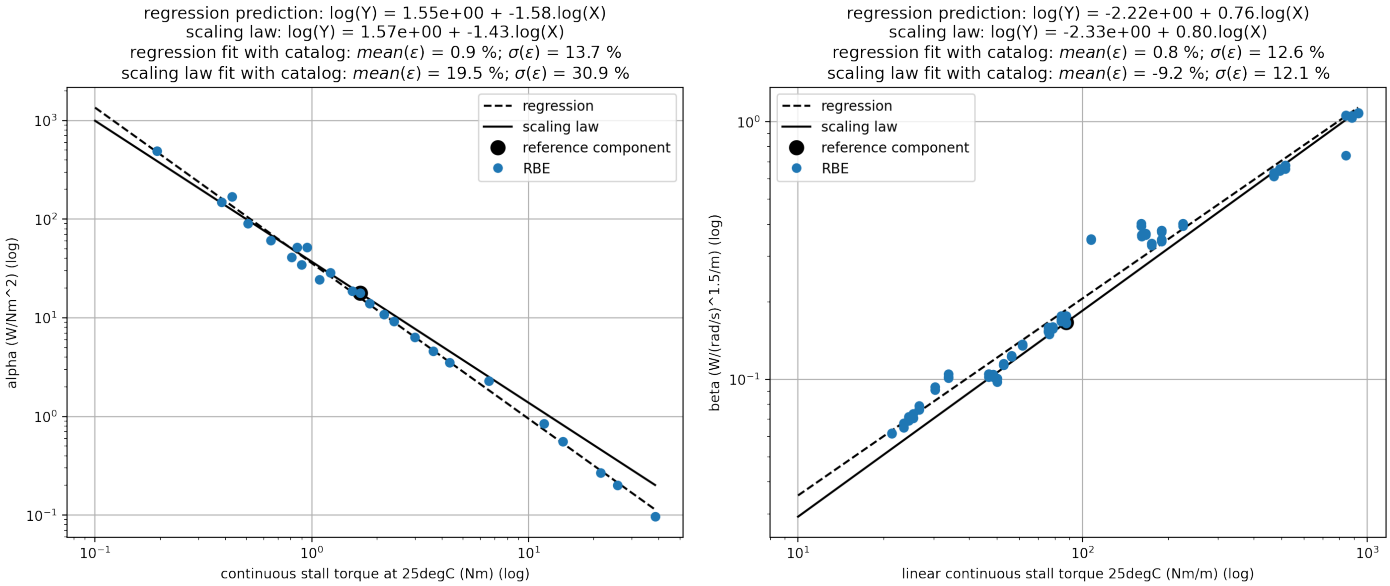

FIGURE K.18: *Validation scaling law, cylindrical motor, heat coefficients (Kollmorgen RBE): (left) copper coefficient, (right) iron coefficient*

Similarly to the peak torque, the copper coefficient α is better described with a scaling law based on geometrical similarity.

K.2 Annular motor

Further to the section K.1, this section focuses on the second type of brushless motors: the annular motors. Also, they are called *torque motors*. They are characterised by a hollowed rotor, similar to a ring. This technology provides motors of high torque density.

K.2.1 Hypothesis

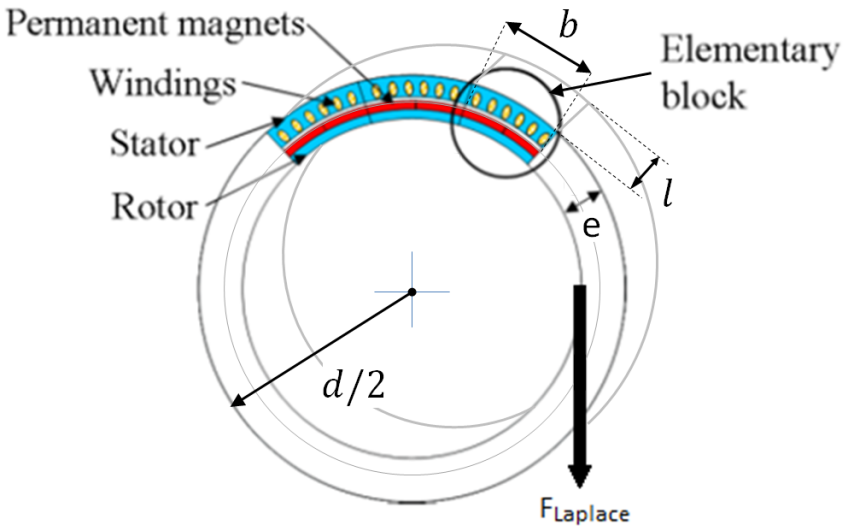

FIGURE K.19: *Annular motor sketch*

The laws developed for annular brushless motors are based on 2 hypothesis.

1. The physical properties P_i remain the same among a considered product range: $P_i^* = 1$
2. The motor is made by an assembly of the same elementary blocks (fig. K.19) with one pair of poles. This involves a pole pair number n_{poles} evolving with the motor diameter d: $n_{poles}^* = d^*$. Also, it involves a constant ring thickness and an air gap.
3. All the lengths follow a homothetic evolution: $l_i^* = l_j^* = l^*$.

Based on these hypothesis, the scaling laws are derived theoretically in the following subsections. The last subsection compares scaling law predictions with manufacturer catalog data.

K.2.2 Current density J

To state the current density expression, Joules' effect is supposed to be the main contributor in motor heat losses. Also, these losses are assumed to be dissipated by a convection phenomena on the outer motor surface. At steady state, the losses and dissipation balance:

$$Joules' \ losses \ \mathscr{P}_J = \ dissipated \ power \ \mathscr{P}_{dis} \tag{K.84}$$

- Joules' losses formulation:
The total motor resistance $\mathscr{R}$ $[Ohm]$ is the sum of the resistance of all the elementary units.

$$\mathscr{R} = n_{poles} \cdot \mathscr{R}_{unit} \tag{K.85}$$

The resistance is defined with a winding copper resistivity ρ_{copper} $[Ohm.m]$:

$$\mathscr{R}_{unit} = \rho_{copper} \cdot \frac{l_{wire}}{S_{wire}} = \rho_{copper} \cdot \frac{l_{turn} \cdot n_{turn}}{\frac{S_{notch}}{n_{turn}} \cdot k_w} \tag{K.86}$$

The current flow I $[A]$ defines a current density J $[A/m^2]$:

$$I = J \cdot S_{wire} = J \cdot \frac{S_{notch}}{n_{turn}} \cdot k_w \tag{K.87}$$

and $k_w < 1[-]$ a notch filling factor since the notch is not completely full of copper. Joules' losses are then developed such as:

$$\mathscr{P}_J = \mathscr{R} \cdot I^2 = n_{poles} \cdot \rho_{copper} \cdot l_{turn} \cdot J^2 \cdot S_{notch} \cdot k_w$$

This expression is turned into a scaling law. It gets simplified by the application of the hypothesis. The hypothesis 1 states $\rho^*_{copper} = 1$. The hypothesis 2 states $n^*_{poles} = d^*$, $S^*_{notch} = 1$ and $k^*_w = 1$. The hypothesis 3 states $l^*_{turn} = l^*_{motor} = l^*$. Joules' losses are:

$$\mathscr{P}^*_J = d^* \cdot l^* \cdot J^{*2} \tag{K.88}$$

with the resistance expressed as:

$$\mathscr{R}^* = n^{*2}_{turn} \cdot d^* \cdot l^* \tag{K.89}$$

- Dissipated power formulation: The power, dissipated by convection, is expressed such as:

$$\mathscr{P}_{dis} = h_{convection} \cdot S_{motor} \cdot \Delta\theta$$

where $h_{convection}$ $[W/m^2/K]$ is the heat exchange coefficient in convection, S_{motor} is the motor skin surface and $\Delta\theta$ is the temperature gradient between motor skin and ambient temperature. The current density is limited by the maximum insulation temperature of wires (to ensure a given life span to insulators), and by the means of cooling. Among a given product range, the same insulations and cooling means are considered. The temperature gradient is constant: $\Delta\theta^* = 1$. The hypothesis 1 states $h^*_{convection} = 1$. As a result, the power dissipated is reduced to a dependency regarding the motor surface only:

$$\mathscr{P}^*_{dis} = S^*_{motor} \tag{K.90}$$

- Current density formulation: Finally, gathering results from eq. K.88 & K.90 into eq. K.84, the continuous current density is expressed:

$$\mathscr{P}^*_J = \mathscr{P}^*_{dis} \implies d^* \cdot l^* \cdot J^{*2}_{cont} = l^* \cdot d^*$$

$$\boxed{J^*_{cont} = 1} \tag{K.91}$$

K.2.3 Torque & Dimension

The Laplace force is defined by:

$$\overrightarrow{dF_{laplace}} = n_{turns} \cdot I \cdot \overrightarrow{dl} \wedge \overrightarrow{B} \tag{K.92}$$

where I $[A]$ is the current flowing into the winding, n_{turns} the number of winding turns, and $\overrightarrow{dl}$ $[m]$ the portion of winding oriented in the sense of current flow, and $\overrightarrow{B}$ the magnetic field ($[T]$ or $[kg \cdot s^{-2} \cdot A^{-1}]$) in the air gap due to permanent magnets.
The current density is introduced thanks to eq. K.87: $n_{turns} \cdot I = J \cdot S_{notch} \cdot k_w$
Then, the Laplace force is:

$$F_{laplace} = J \cdot S_{notch} \cdot k_w \cdot l \cdot B \tag{K.93}$$

The hypothesis 1 states $B^* = 1$, the induction created by the permanent magnets in the air gap is constant whatever the motor scale is. The hypothesis 2 states $S^*_{notch} = 1$ and $k^*_w = 1$. It results in:

$$F^*_{laplace} = J^* \cdot l^* \tag{K.94}$$

The motor torque is made by Laplace's force provided by each elementary unit at a radius r from the motor rotor axis of rotation. Applying the hypothesis 2:

$$T^* = n^*_{poles} \cdot F^*_{laplace} \cdot r^* = d^{*2} \cdot F^*_{laplace} \tag{K.95}$$

and

$$T^* = d^{*2} \cdot J^* \cdot l^* \tag{K.96}$$

Applying the previous result from eq. K.91, the continuous torque is defined by:

$$\boxed{T^*_{cont} = d^{*2} \cdot l^*} \tag{K.97}$$

Also,

$$\boxed{d^* = \left(\frac{T^*_{cont}}{l^*} \right)^{1/2}} \tag{K.98}$$

K.2.4 Peak torque T_p

The peak torque can follow different definitions according to supplier design choices. Please, see section 4.2.3.2 of the thesis core for these aspects.

K.2.5 Mass $\mathscr{M}$

The motor mass is the total mass of the p elementary units. Each elementary unit is defined by a linear mass ρ_{unit} $[kg.m^{-1}]$. Applying the hypothesis 1 ($\rho^*_{unit} = 1$), 2 ($n^*_{poles} = d^*$), and 3 ($l^*_{motor} = l^*$), the mass results in the following relations:

$$\mathscr{M} = n_{poles} \cdot \rho_{unit} \cdot l_{motor} \rightarrow \mathscr{M}^* = d^* \cdot l^*$$

$$\boxed{\frac{\mathscr{M}^*}{l^*} = d^*} \tag{K.99}$$

Also, applying a previous results from eq. K.98, the mass is:

$$\boxed{\frac{\mathscr{M}^*}{l^*} = \left(\frac{T^*_{cont}}{l^*}\right)^{1/2}} \tag{K.100}$$

K.2.6 Inertia $\mathscr{I}$

Basically, the inertia is defined as:

$$\mathscr{I} = \int r^2\, dm \text{ where } dm = 2\pi \cdot \rho \cdot r \cdot l \cdot dr \tag{K.101}$$

Introducing an equivalent density ρ_{rotor} $[kg.m^{-3}]$, the motor rotor inertia is defined by:

$$\mathscr{I} = 2\pi \cdot \rho_{rotor} \cdot l_{rotor} \cdot \int r^3_{rotor}\, dr = 2\pi \cdot \rho_{rotor} \cdot l_{rotor} \frac{r^4_{rotor}}{4} \tag{K.102}$$

Thanks to the hypothesis 1 & 3, the following scaling law is deduced:

$$\frac{\mathscr{I}^*}{l^*} = d^{*4} \tag{K.103}$$

Using a previous result from eq. K.98, the rotor inertia is:

$$\boxed{\frac{\mathscr{I}^*}{l^*} = \left(\frac{T^*_{cont}}{l^*}\right)^{2}} \tag{K.104}$$

K.2.7 Joules' losses $\mathscr{P}_{Joules}$

The eq. K.88 provides the expression of the Joules' losses. Using the previous results from the current density (eq. K.91), the linear torque (eq. K.98), and the motor constant (section K.2.13), the Joules' losses are expressed such as:

$$\boxed{\mathscr{P}^*_J = d^* \cdot l^* = T^{*1/2} \cdot l^{*1/2} = K^{*1/3}_m \cdot l^{*2/3}} \tag{K.105}$$

K.2.8 Maximum speed

K.2.8.1 Mechanical limitation

The maximum mechanical speed is supposed to be based only on the rotor resistance to centrifugal force. The centrifugal force is defined by the rotor mass m, its radius r and its tangential speed v or rotative speed Ω:

$$F_{centrifugal} = m \cdot \frac{v^2}{r} = m \cdot \Omega^2 \cdot r \tag{K.106}$$

Applying a previous result from eq. K.100, the stress generated by the centrifugal force is expressed:

$$\sigma^*_{centrifugal} = \frac{F^*_{centrifugal}}{S^*} = \frac{d^* \cdot l^* \cdot \Omega^{*2} \cdot d^*}{d^* \cdot l^*} = d^* \cdot \Omega^{*2} \tag{K.107}$$

The hypothesis 1 states that $\sigma^*_{centrifugal,max} = 1$. Thus, the maximum mechanical speed is:

$$\boxed{\Omega^*_{mecha,max} = d^{*-1/2}} \tag{K.108}$$

K.2.8.2 Electrical limitation

The electrical speed can be expressed with the mechanical speed such as:

$$\omega_{elect,max} = n_{poles} \cdot \Omega_{mecha,max} \tag{K.109}$$

Applying the hypothesis 2 and a previous result from eq. K.108, the maximum electrical speed is:

$$\boxed{\omega^*_{elect,max} = d^{*1/2}} \tag{K.110}$$

K.2.8.3 Thermal limitation

Following the same development steps than the ones detailed for the cylindrical motor in section K.1.8.3, the electrical frequency for the annular motor is given by:

$$\boxed{f^*_{elect,max,iron} = d^{*-1/b}} \tag{K.111}$$

K.2.9 Copper & iron losses coefficients α & β

Following the same development steps than the ones detailed for the cylindrical motor in section K.1.9 and using the previous results developed for the annular motor, the expressions of the copper and iron coefficients are easily derived:

$$\boxed{\alpha^* \cdot l^* = d^{*-3} = T^{*-3/2}_{cont} \cdot l^{*-3/2}} \tag{K.112}$$

$$\boxed{\frac{\beta^*}{l^*} = d^{*2} = \frac{T^*_{cont}}{l^*}} \tag{K.113}$$

K.2.10 Voltage $\mathscr{U}$ & constant $\mathscr{K}$

The total motor voltage $\mathscr{U}$ is the sum of the individual voltage $\mathscr{U}_{unit}$ given by each elementary unit (hypothesis 2).

$$\mathscr{U} = n_{poles} \cdot \mathscr{U}_{unit} \tag{K.114}$$

Each elementary unit has got its own winding. According to Lenz-Faraday's law, an electrical circuit under a time varying magnetic flux ϕ (induced by a time-varying magnetic field $\vec{B}$) produces an electromotive force e such as:

$$e = -\frac{d\phi}{dt} \tag{K.115}$$

In the particular case of a solenoid,

$$\phi = n_{turn} \cdot \iint_S \vec{B} \cdot \vec{n}\, dS \tag{K.116}$$

where n_{turn} is the number of turns, S the cross-section and $\vec{n}$ the unitary normal vector of the elementary surface dS oriented according to Maxwell corkscrew rule.

The voltage at each motor elementary unit is:

$$\mathscr{U}_{unit} = n_{turn} \cdot \omega_{elect} \cdot B \cdot S \tag{K.117}$$

The hypothesis 1 ($B^* = 1$) and 2 ($p^* = d^*$) are applied. The surface is assumed to be $S = b \cdot l$ (fig. K.19) with $b = \pi d / n_{poles}$. The scaling law of S is:

$$b^* = \frac{d^*}{n^*_{poles}} = \frac{d^*}{d^*} = 1 \implies S^* = l^* \tag{K.118}$$

The electrical speed introduces the mechanical speed. The elementary unit voltage becomes:

$$\mathscr{U}^*_{unit} = n^*_{turn} \cdot d^* \cdot l^* \cdot \Omega^*_{mecha} \tag{K.119}$$

The total motor voltage is then:

$$\boxed{\mathscr{U}^* = n^*_{turn} \cdot d^{*2} \cdot l^* \cdot \Omega^*_{mecha}} \tag{K.120}$$

The ratio $\mathscr{U}^* / \Omega^*_{mecha}$ provides the voltage constant $\mathscr{K}_e^*$ and, indirectly, the torque constant $\mathscr{K}_t^*$:

$$\boxed{\mathscr{K}_e^* = n^*_{turn} \cdot d^{*2} \cdot l^* = \mathscr{K}_t^* = \mathscr{K}^*} \tag{K.121}$$

K.2.11 Resistance $\mathscr{R}$

The subsection K.2.2 derives the scaling law of the resistance (eq. K.89) which is

$$\mathscr{R}^* = n^{*2}_{turn} \cdot d^* \cdot l^*$$

From a previous result (eq. K.121), the following ratio can be written :

$$n^*_{turn} = \frac{\mathscr{K}^*}{d^{*2} \cdot l^*}$$

The resistance then is deduced:

$$\boxed{\frac{\mathscr{R}^*}{\mathscr{K}^{*2}} = d^{*-3} \cdot l^{*-1}} \tag{K.122}$$

Using eq. K.98, the resistance is:

$$\boxed{\frac{\mathscr{R}^*}{\mathscr{K}^{*2} \cdot l^{*1/2}} = T^{*-3/2}_{cont}} \tag{K.123}$$

K.2.12 Inductance $\mathscr{L}$

The total motor inductance $\mathscr{L}$ is the sum of the individual inductance $\mathscr{L}_{unit}$ given by each elementary unit (hypothesis 2).

$$\mathscr{L} = n_{poles} \cdot \mathscr{L}_{unit} \tag{K.124}$$

The inductance is usually defined by the inverse of the reluctance such as:

$$\mathscr{L}_{unit} = \frac{n^2_{turn}}{R} \tag{K.125}$$

with n_{turn} the number of spires of the winding. The problem is reduced to a magnetic circuit as presented in fig. K.2. The reluctance is already shown in eq. K.70:

$$R = \frac{2 \cdot l_{airgap}}{\mu_0 \cdot S} \tag{K.126}$$

where l_{airgap} $[m]$ is the thickness of the airgap, $\mu_0 = 4.10^{-7}$ $H \cdot m^{-1}$ the magnetic constant (or vacuum permeability), and S the airgap cross-section. The eq. K.118 already shows that $S^* = l^*$. The hypothesis 2 states that the airgap remains the same through a given product range $l^*_{airgap} = 1$. The reluctance becomes:

$$R^* = \frac{1}{l^*} \tag{K.127}$$

An intermediate expression of the total inductance is deduced:

$$\mathscr{L}^* = n^{*2}_{turn} \cdot d^* \cdot l^* \tag{K.128}$$

From a previous result (eq. K.121), the following ratio can be written :

$$n^*_{turn} = \frac{\mathscr{K}^*}{d^{*2} \cdot l^*} \tag{K.129}$$

Finally, the total inductance is deduced:

$$\boxed{\frac{\mathscr{L}^*}{\mathscr{K}^{*2}} = d^{*-3} \cdot l^{*-1}} \tag{K.130}$$

Using eq. K.98, the inductance is also:

$$\boxed{\frac{\mathscr{L}^*}{\mathscr{K}^{*2} \cdot l^{*1/2}} = T^{*-3/2}_{cont}} \tag{K.131}$$

K.2.13 Motor constant K_m

The motor constant K_m $[(Nm)^2/W]$ is a way to estimate heat losses avoiding the motor winding characteristics and a way to compare motor technologies. Please, see section 4.2.3.3 of the thesis core for these aspects.

K.2.14 Mechanical power $\mathscr{P}_{mechanical}$

The mechanical power can be expressed thanks to the K_m motor constant.

At steady state, the motor voltage can be expressed as:

$$U = \mathscr{R} \cdot I + K_T \cdot \omega \tag{K.132}$$

where $I = T/K_T$ and $K_T = K_m \cdot \sqrt{R}$.

The total power becomes:

$$\mathscr{P}_{total} = U \cdot I = \underbrace{\left(\frac{T}{K_m}\right)^2}_{Joules} + \underbrace{T \cdot \omega}_{mechanical} \tag{K.133}$$

Section K.2.7 provides the expression of $\mathscr{P}_{Joules}$ according to K_m. Using the torque and speed scaling laws introduced in section K.2.3 and K.2.8, the mechanical power is expressed such as:

$$\text{annular} \qquad \frac{\mathscr{P}^*_{mechanical}}{l^*} = \frac{T^*}{l^*} \cdot \omega^* = \left(\frac{K^*_m}{l^*}\right)^{*1/2} \tag{K.134}$$

The ratio $\mathscr{P}_{Joules}/\mathscr{P}_{mechanical}$ finds an interest in a motor sizing loop as a design driver. Thus, it can limit the increase of the K_m value by the optimization algorithm. In addition, the rotor inertia might act beforehand as an upper limitation of the K_m value because of the higher power of its scaling law ($\mathscr{I}^* = K^*_m$) and its direct impact on the motor torque.

K.2.15 Validation

The validation is based on the manufacturer catalog of TECNOTION. [TECNOTION, 2019].

FIGURE K.20: *Tecnotion: annular permanent magnet motors*

First of all, the hypothesis 2 must be checked. The display of the motor outside diameter with respect to the number of magnets (fig. K.21) shows 2 product ranges with different design concepts. On fig. K.21, the bottom data set corresponds to motors with a continuous torque within $[0.3; 36]\ Nm$. The top data set corresponds to motors with a continuous torque $[60; 331]\ Nm$.

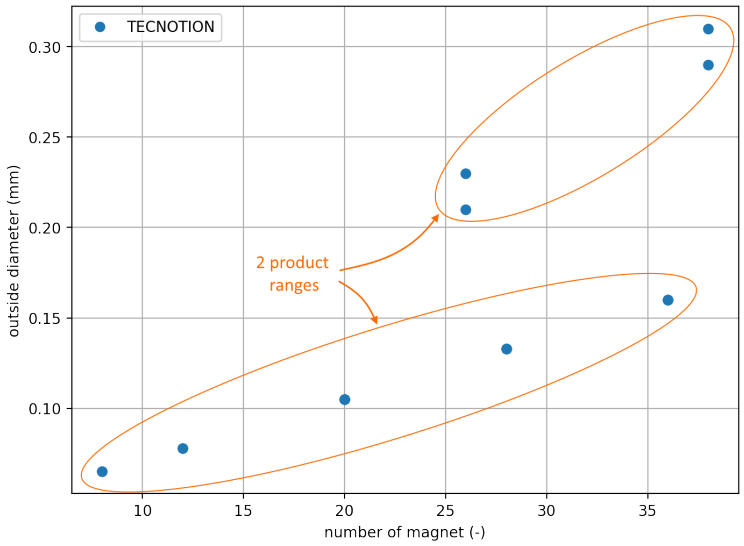

FIGURE K.21: *Annular motor, diameter vs pole number (TECNOTION)*

The bottom product range is kept for the following displays. A single component of reference is used for all the following displays. Its characterisitics are: peak torque $T_p = 3.9\ Nm$, continuous torque $T_c = 3.2\ Nm$, motor constant $K_m = 0.02\ Nm^2/W$ and stator outside diameter $d = 105\ mm$.

Since the annular motor laws are based on an assembly of elementary modules hyp. 2, the ouside motor diameter and inside motor diameter are expressed as a function of the airgap diameter with an offset:

$$d_{in,rotor} = a \cdot d_{airgap} + t_{rotor} \qquad d_{out,stator} = b \cdot d_{airgap} + t_{stator} \tag{K.135}$$

where $t_{rotor}\ [m]$ and $t_{stator}\ [m]$ are the thicknesses supposed as constant for the considered product range. This assumption is verified by the linear regressions presented in fig. K.22. The rotor and stator thicknesses are given by the value at Y-axis when the linear regression crosses it. For scaling law validation, any offset must be removed. The validation is displayed regarding the airgap diameter.

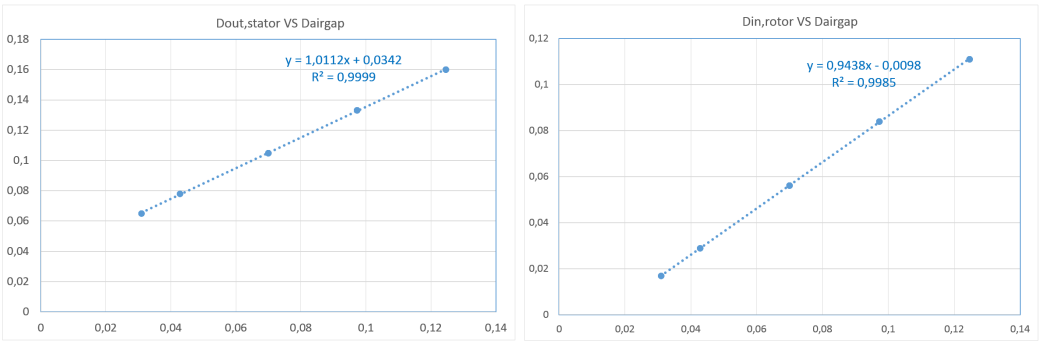

FIGURE K.22: *Annular motor (TECNOTION), left: stator thickness, right: rotor thickness*

The following displays validates the laws established for the annular motor.

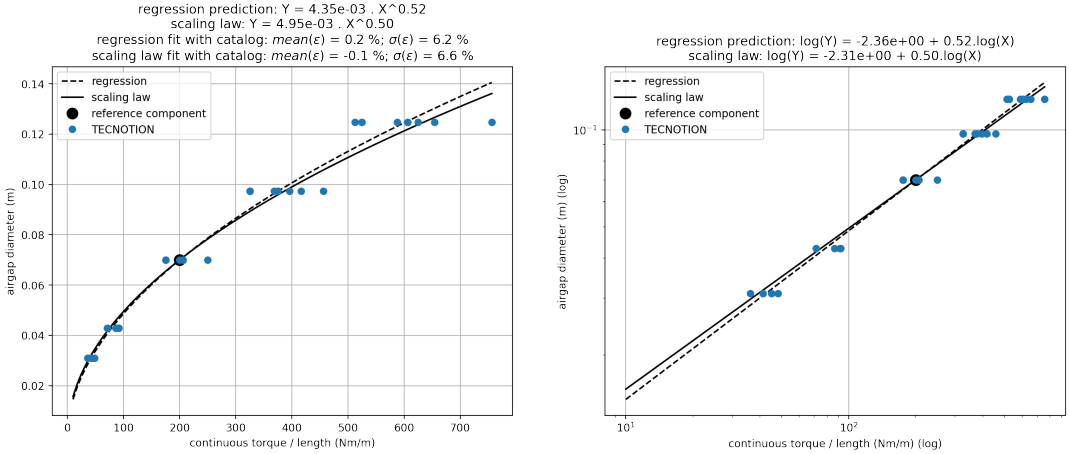

FIGURE K.23: *Validation scaling law, annular motor, airgap diameter (TECNOTION)*

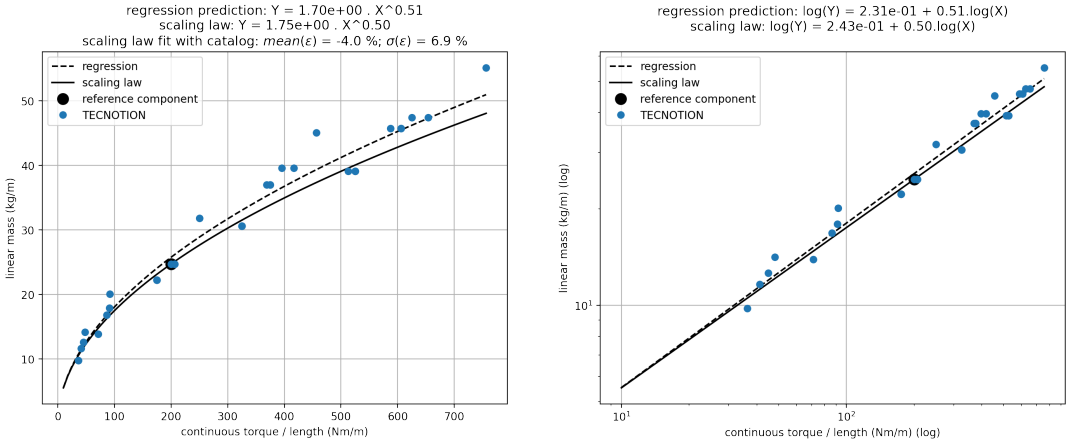

FIGURE K.24: *Validation scaling law, annular motor, linear mass (TECNOTION)*

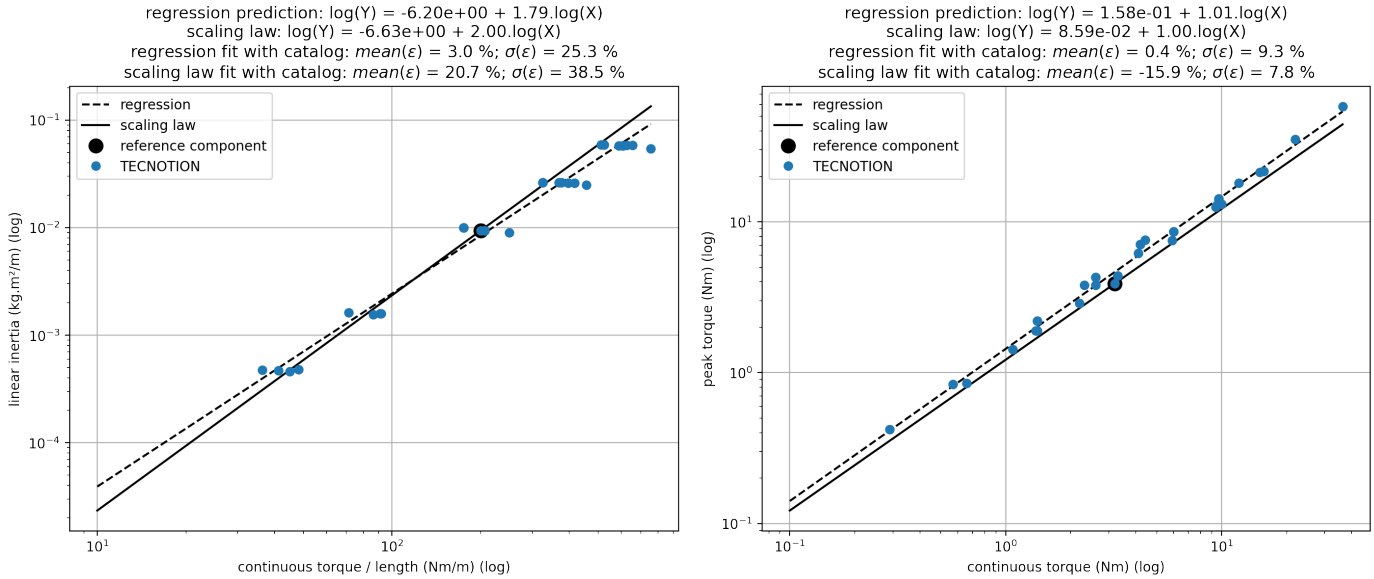

FIGURE K.25: *Validation scaling law, annular motor, linear inertia & peak torque (TECNOTION): (left) linear inertia vs linear continuous torque, (right) peak torque vs continuous torque*

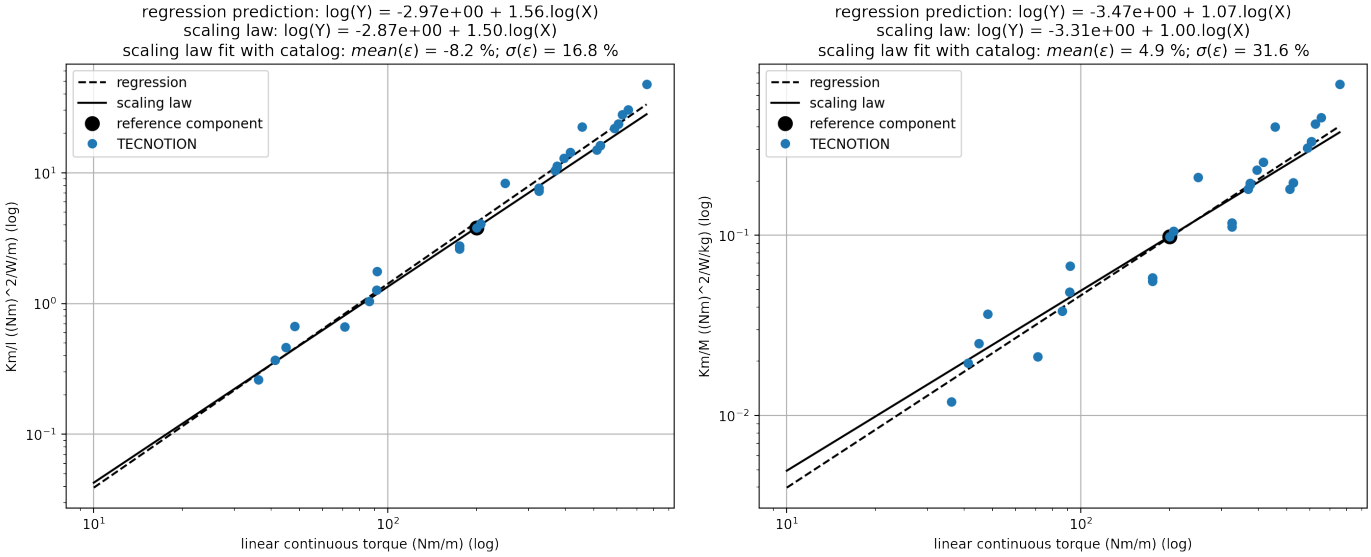

FIGURE K.26: *Validation scaling law, annular motor, motor constant vs linear torque (TECNOTION): (left) K_m, (right) K_m per unit of mass*

The following displays deals with electrical parameters linked to winding types. The data set is filtered according to a single winding type (the winding named *N* by the manufacturer is chosen since it covers the broadest product range).

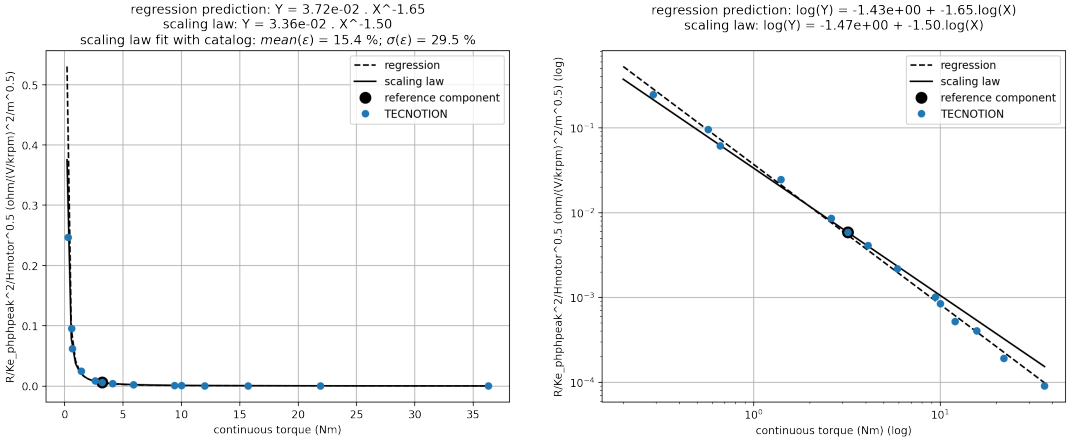

FIGURE K.27: *Validation scaling law, annular motor, resistance (TECNOTION)*

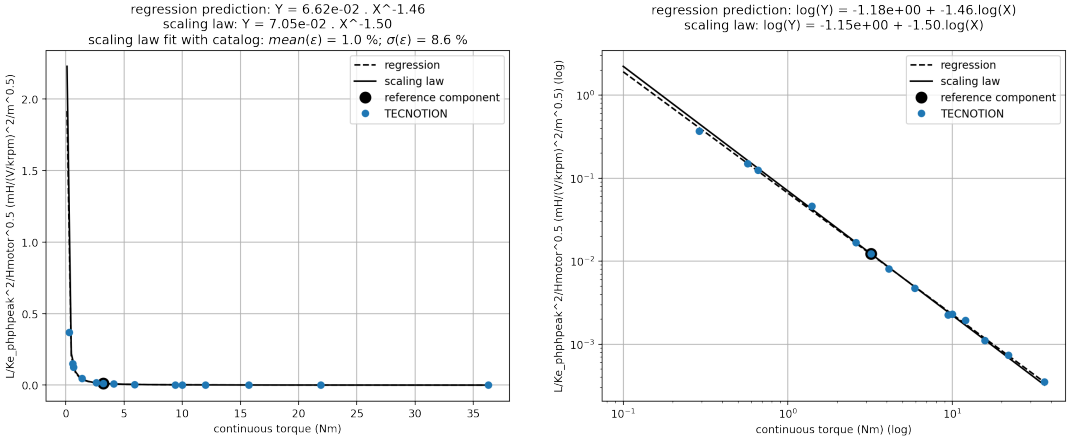

FIGURE K.28: *Validation scaling law, annular motor, inductance (TECNOTION)*

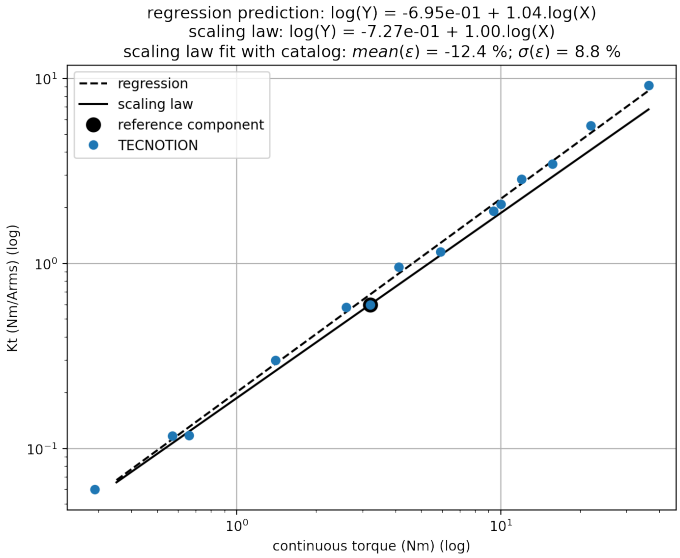

FIGURE K.29: *Validation scaling law, annular motor, torque constant K_t (TECNOTION)*

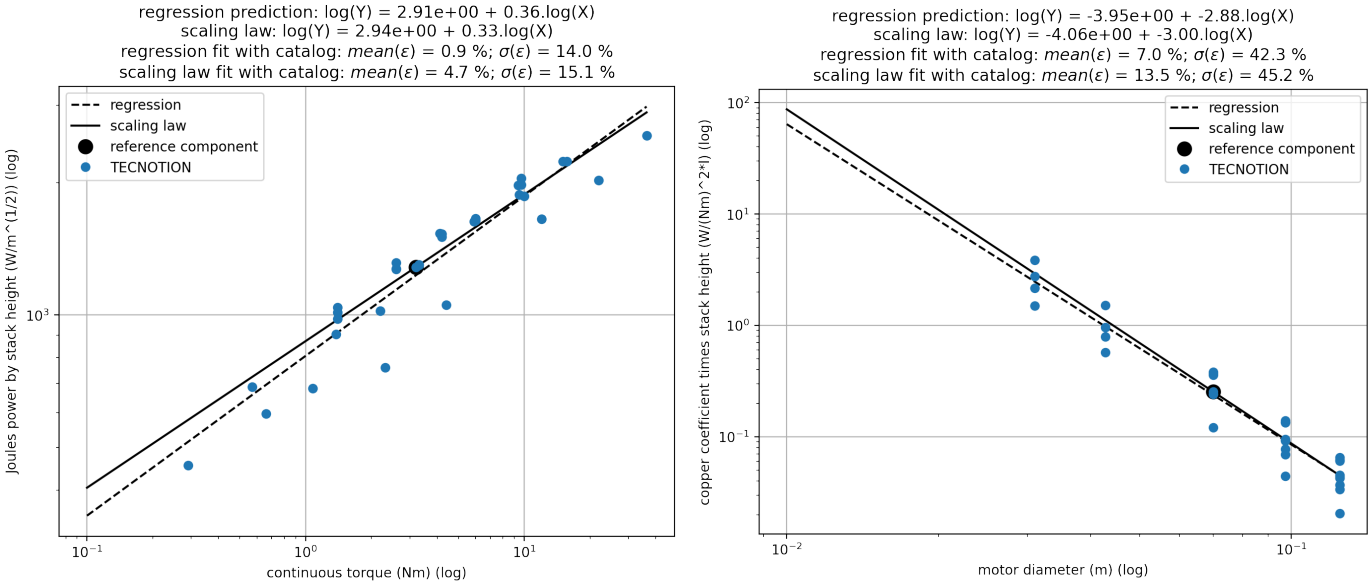

FIGURE K.30: *Validation scaling law, annular motor, copper losses (TECNOTION): (left) copper losses, (right) copper coefficient*

K.3 Electromagnetic brake

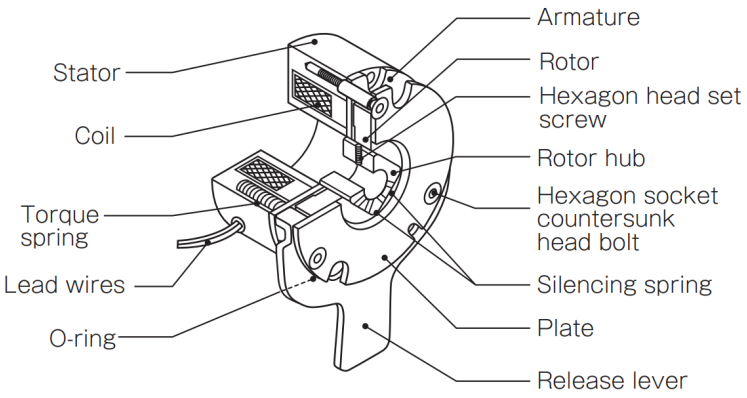

FIGURE K.31: *Electromagnetic brake sketch mikipulley.co.jp*

For electromagnetic brake, it is supposed:

- homothetic evolution of dimensions:

$$d^* = l^* \tag{K.136}$$

K.3.1 Torque & Dimensions

Amper's law gives:

$$\int_{\mathscr{C}} \vec{B} \cdot \vec{dl} = \mu_0 \cdot n_{turn} \cdot I \implies B = \mu_0 \cdot \frac{n_{turn}}{l_{airgap}} \cdot I \tag{K.137}$$

with $\mathscr{C}$ the closed contour of the considered circuit, $\vec{B}$ the magnetic field $[T]$, $\vec{dl}$ the infinitesimal element $[m]$ of $\mathscr{C}$, $\mu_0 = 4\pi \cdot 10^{-7}$ $[T \cdot m/A]$ the magnetic permeability of empty and I $[A]$ the current involved by the circuit.

For a solenoid coil, the force is given by:

$$F = \frac{B^2}{2 \cdot \mu_0} \cdot S \tag{K.138}$$

with S $[m^2]$ the copper surface of the motor transverse section.

The current lays as:

$$I = S_{wire} \cdot J \tag{K.139}$$

with the wire section S_{wire} $[m^2]$ and the current density J $[A/m^2]$. The eq. K.137 becomes:

$$B = \mu_0 \cdot \frac{n_{turn} \cdot S_{wire} \cdot J}{l_{airgap}} = \frac{S \cdot J}{k_w \cdot l_{airgap}} \tag{K.140}$$

with k_w a winding filling ratio.

Applying scaling law approach, k_w and μ_0 are supposed to be constant among the considered product range ($k_w^* = 1$, $\mu_0^* = 1$):

$$B^* = \frac{S^* \cdot J^*}{l_{airgap}^*} \tag{K.141}$$

We propose to suppose $l_{airgap}^* = d^*$. This hypothesis is verified since later it is observed that the obtained scaling law ($d^* = f(T^*)$) fits catalog data. In addition, the

current density follows $J^* = d^{*-1/2}$ (already proved relation, refer to eq. K.8). As a result:

$$B^* = \frac{d^{*2} \cdot d^{*-1/2}}{d^*} = d^{*1/2} \tag{K.142}$$

Also, the current I can be defined. I^* is expressed for later use in the derivation:

$$I = S_{wire} \cdot J = \frac{S_{winding}}{n_{turn}} \cdot k_w \cdot J \implies I^* = \frac{d^{*2}}{n^*_{turn}} \cdot d^{*-1/2} = \frac{d^{*3/2}}{n^*_{turn}} \tag{K.143}$$

With eq. K.138, the force is:

$$F^* = B^{*2} \cdot S^* = d^* \cdot d^{*2} = d^{*3} \tag{K.144}$$

Finally, the torque is a force applied at a given radius r and $r^* = d^*$:

$$T^* = d^{*4} \tag{K.145}$$

Hence

$$\boxed{d^* = l^* = T^{*1/4}} \tag{K.146}$$

K.3.2 Mass $\mathscr{M}$

Basically, the mass is defined as:

$$\mathscr{M} = \rho \cdot V = \rho \cdot \frac{\pi \cdot d^2}{4} \cdot l \implies \mathscr{M}^* = d^{*2} \cdot l^* = d^{*3} \tag{K.147}$$

considering the hypothesis (eq. K.136). Thus,

$$\boxed{\mathscr{M}^* = T^{*3/4}} \tag{K.148}$$

K.3.3 Inertia $\mathscr{J}$

Basically, the inertia is defined as:

$$\mathscr{J} = \int r^2 dm \implies \mathscr{J}^* = d^{*2} \cdot \mathscr{M}^* = d^{*5} \tag{K.149}$$

considering the hypothesis (eq. K.136). Thus,

$$\boxed{\mathscr{J}^* = T^{*5/4}} \tag{K.150}$$

K.3.4 Resistance $\mathscr{R}$

Basically, the resistance is defined as:

$$\mathscr{R} = \rho_{copper} \cdot \frac{l_{wire}}{S_{wire}} = \rho_{copper} \cdot \frac{n_{turn} \cdot l_{turn}}{S / n_{turn} \cdot k_w} \implies \mathscr{R}^* = \frac{n^{*2}_{turn} \cdot d^*}{d^{*2}}$$

$$\mathscr{R}^* = n^{*2}_{turn} \cdot d^{*-1} \tag{K.151}$$

With eq. K.143 and K.151, the voltage $\mathscr{U}$ can be defined easily:

$$\mathscr{U} = \mathscr{R} \cdot I \implies \mathscr{U}^* = \mathscr{R}^* \cdot I^* = n_{turn}^{*2} \cdot d^{*-1} \cdot \frac{d^{*3/2}}{n_{turn}^*}$$

$$\mathscr{U}^* = n_{turn}^* \cdot d^{*1/2} \tag{K.152}$$

With the voltage (eq. K.152), the resistance is easily re-defined such as:

$$\boxed{\mathscr{R} = \mathscr{U}^{*2} \cdot T^{*-1/2}} \tag{K.153}$$

K.3.5 Inductance $\mathscr{L}$

Basically, the inductance is defined as:

$$\mathscr{L} = \mu_0 \cdot \frac{n_{turn}^2 \cdot S}{l_{airgap}} \implies \mathscr{L}^* = \frac{n_{turn}^{*2} \cdot d^{*2}}{d^*}$$

$$\mathscr{L}^* = n_{turn}^{*2} \cdot d^* \tag{K.154}$$

With the voltage (eq. K.152), the inductance is easily re-defined such as:

$$\boxed{\mathscr{L} = \mathscr{U}^{*2}} \tag{K.155}$$

K.3.6 Thermal losses $\mathscr{P}_J$

Basically, the thermal losses are mainly due to Joules effect. Using eq. K.143 combined with eq. K.152, the thermal losses are defined such as:

$$\mathscr{P}_J = \mathscr{R} \cdot I^2 \implies \mathscr{P}_J^* = n_{turn}^* \cdot d^{*1/2} \cdot \frac{d^{*3/2}}{n_{turn}^*}$$

$$\mathscr{P}_J^* = d^{*2} \tag{K.156}$$

Thus,

$$\boxed{\mathscr{P}_J = T^{*1/2}} \tag{K.157}$$

K.3.7 Validation

The validation is based on 3 manufacturer catalogs (RS, MIKIPULLEY, KENDRION).

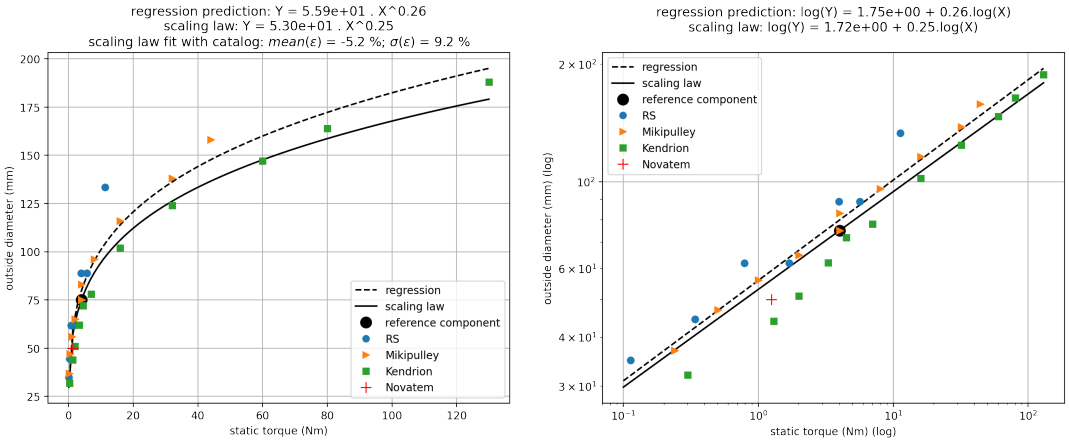

FIGURE K.32: *Validation scaling law, eletromagnetic brake, dimension*

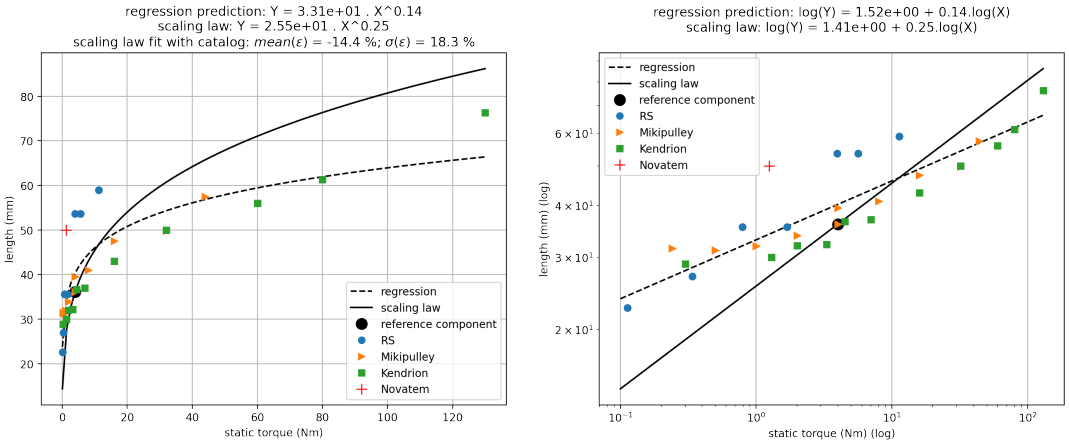

FIGURE K.33: *Validation scaling law, eletromagnetic brake, length*

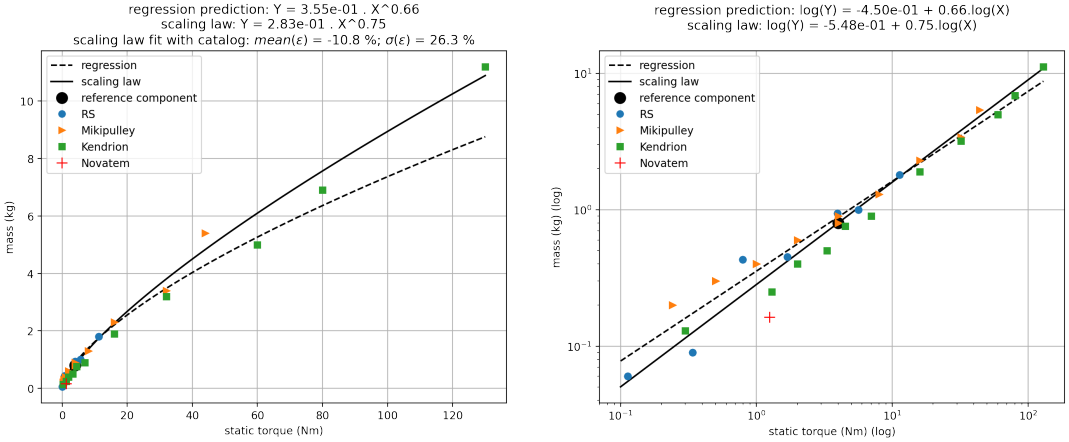

FIGURE K.34: *Validation scaling law, eletromagnetic brake, mass*

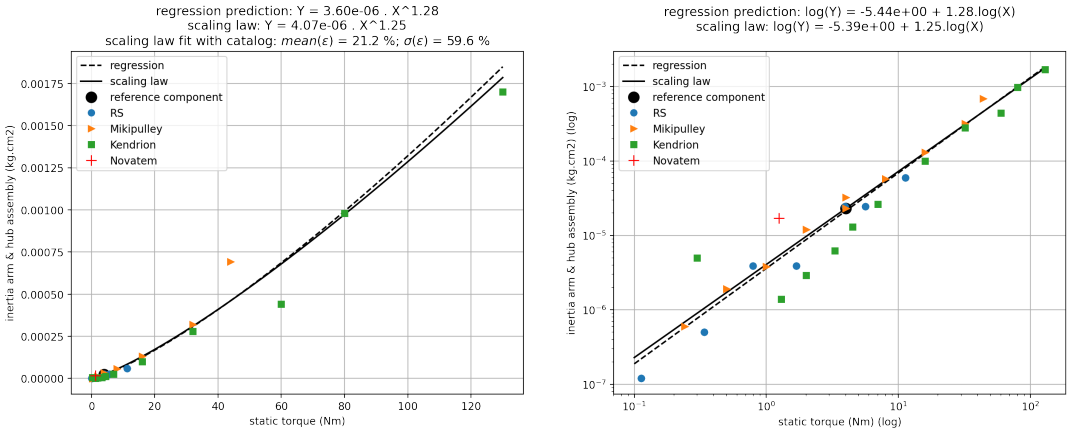

FIGURE K.35: *Validation scaling law, eletromagnetic brake, disk inertia*

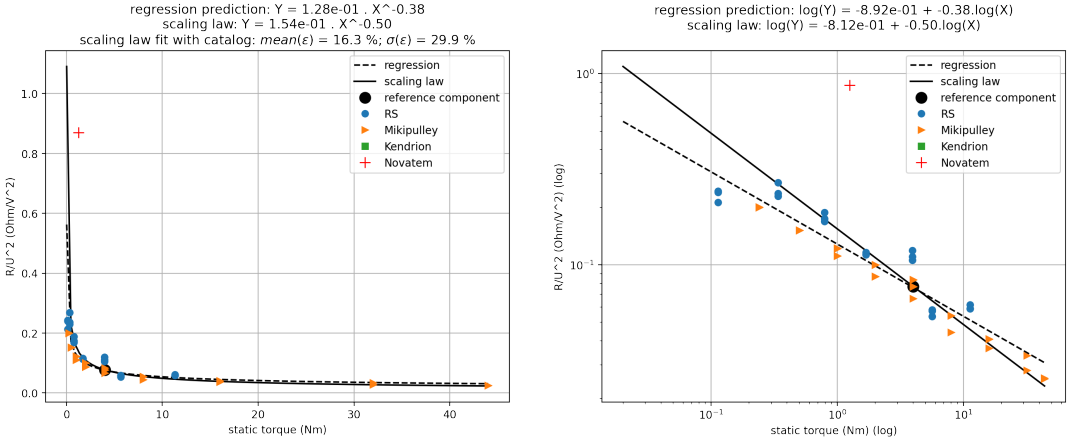

FIGURE K.36: *Validation scaling law, eletromagnetic brake, coil resistance*

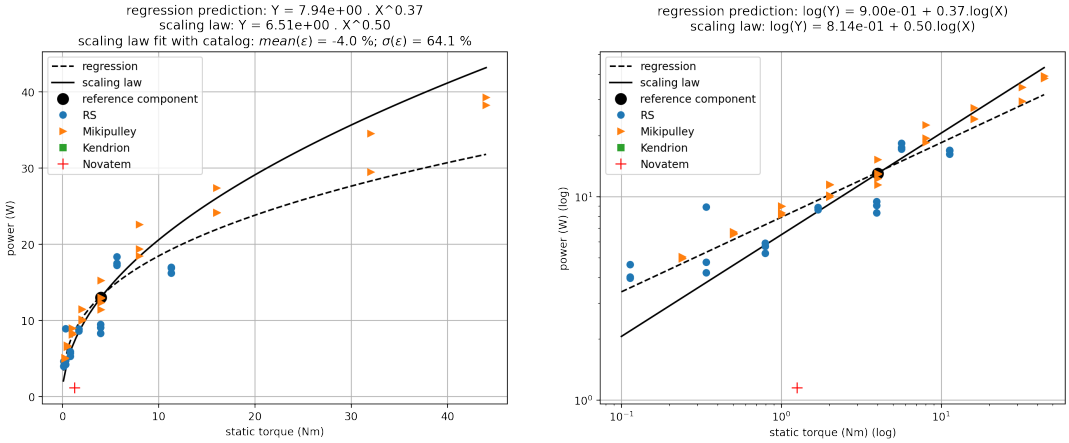

FIGURE K.37: *Validation scaling law, eletromagnetic brake, Joules' losses*

K.4 Important notes

To study scaling laws, this thesis experience feedbacks some advice:

- Avoid as much as possible scaling laws mixing too many variables. The higher the number of parameter is, the lower the prediction quality is. For instance, it is prefered using R/K^2 instead of R/U^2 since $U = K \cdot \omega$.
- Before undertaking any validation step, always analyze the raw data from a catalog. In this way, it can be possible to point out components with heterogenous characteristics due to a different design criteria, a different feature installed (e.g. air versus water cooling) and/or a typing mistake in the datasheet.
- It is important to check the scaling laws hypothesis. For instance, the proportionality between a diameter d and the number of pole ($n^*_{poles} = d^*$) in the case of annular motors, or in the case of cylindrical motor, the ratio between lengths and diameters. The mean and the standard deviation of the ratio of variables is useful to perform quickly such checks: $\sigma/\bar{x} < 15\%$, σ the standard deviation and $\bar{x}$ the mean of the considered data set.

Appendix L

Hertz contact scaling laws

This appendix proposes a scaling law study around the Hertz contact to extract potentially interesting scaling laws about different contacts: roller, ball, and thread.

The theory presented in the three following sections is based on Hertz assumptions. They are reminded herebelow:

- The bodies are elastic, linear, isotropic and homogeneous with continuous surface.
- The load application is normal to the considered contact point.
- The surfaces of bodies in motion are perfectly smooth (no friction consideration).
- The area of contact is far smaller than the body dimensions.

L.1 Cylindrical contact

For cylindrical contacts, as found in thrust bearings, a stress estimation is presented theoretically in fig. L.1. The theory comes from [Shigley, 2006].

$$b = \sqrt{\frac{2F}{\pi l}\frac{\left(1-\nu_1^2\right)/E_1 + \left(1-\nu_2^2\right)/E_2}{1/d_1 + 1/d_2}}$$

$$p_{\max} = \frac{2F}{\pi b l}$$

E : Young's modulus
ν : Poisson's coefficient

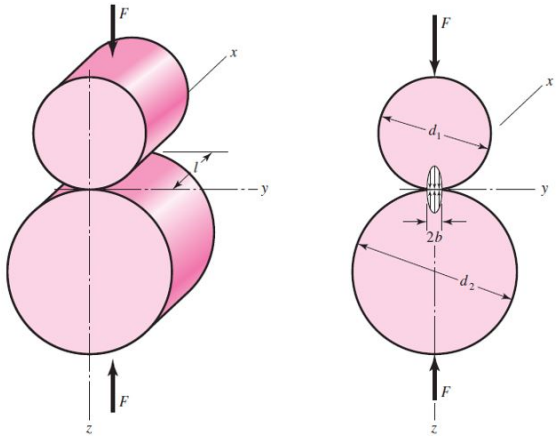

FIGURE L.1: *Spherical hertz contact theory ([Shigley, 2006], p.118)*

Assuming geometrical and material properties similarities, it is possible to state that all diameters evolves the same as a rolling element diameter d_r, Poisson's coefficient and Young's modulus do not change whatever the dimensions are. The rolling element length l_r remains independent.

$$\text{diameters: } d_1^* = d_2^* = d_r^* \tag{L.1}$$

$$\text{Poisson's coef. and Young's modulus: } \nu_i^* = E_i^* = 1 \tag{L.2}$$

Given these hypothesis, the scaling law of the contact stress is obtained as a function of the load and the roller dimensions:

$$\sigma^* = \frac{F^{*1/2}}{d_r^{*1/2} \cdot l_r^{*1/2}} \tag{L.3}$$

L.2 Spherical contact

For spherical contacts as found in ball screws, a stress estimation is presented theoretically in fig. L.2. The theory comes from [Shigley, 2006].

$$a = \sqrt[3]{\frac{3F}{8}\frac{\left(1-\nu_1^2\right)/E_1 + \left(1-\nu_2^2\right)/E_2}{1/d_1 + 1/d_2}}$$

$$p_{\max} = \frac{3F}{2\pi a^2}$$

E: Young's modulus
ν: Poisson's coefficient

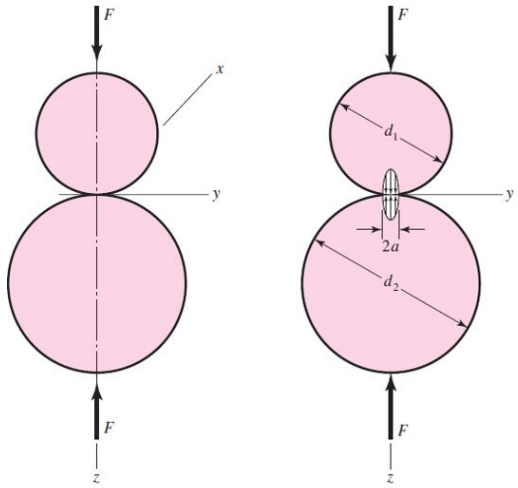

FIGURE L.2: *Spherical hertz contact theory ([Shigley, 2006], p.117)*

Assuming geometrical and material properties similarities, it is possible to state that all the dimensions evolve in the same way as the screw diameter d_s, Poisson's coef and Young's modulus do not change whatever the dimensions are:

$$\text{dimensions: } d_1^* = d_2^* = d_s^* \tag{L.4}$$

$$\text{Poisson's coef. and Young's modulus: } \nu_i^* = E_i^* = 1 \tag{L.5}$$

Given these hypothesis, the scaling law of the contact stress is obtained as a function of the load and the screw diameter:

$$\sigma^* = \frac{F^{*1/3}}{d_s^{*2/3}} \tag{L.6}$$

L.3 Elliptical contact

For elliptical contacts as found in roller screws ([Kossi Abevi, 2013], [Sandu, 2018], [Lisowski, 2015]), a stress estimation is presented theoretically in fig. L.3. The theory comes from [Barber, 2018].

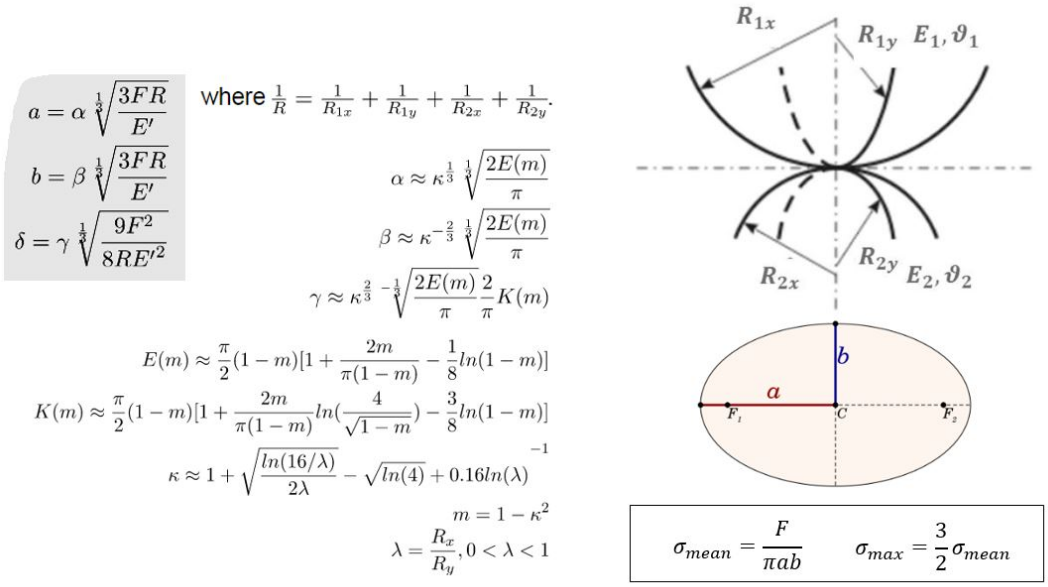

FIGURE L.3: *Elliptical hertz contact theory ([Tri, 2022])*

[Tri, 2022] shares online Matlab codes which apply this theory.

Assuming geometrical and material properties similarities, it is possible to state that the curvature radius evolves in the same way as all the dimensions, such as the screw diameter d_s, Poisson's coefficient and Young's modulus do not change whatever the dimensions are:

$$\text{curvature radius and dimensions: } R^*_{1x} = R^*_{2x} = R^*_{1y} = R^*_{2y} = d^*_s \tag{L.7}$$

$$\text{Poisson's coef. and Young's modulus: } v^*_i = E^*_i = 1 \tag{L.8}$$

Given these hypothesis, the scaling law of the contact stress is obtained as a function of the load and the screw diameter:

$$\sigma^* = \frac{F^{*1/3}}{d^{*2/3}_s} \tag{L.9}$$

In fig. L.4, the scaling law (eq. L.9) is applied on supplier catalog data from Rollvis. The reference component is taken with a stress of $\sigma_{ref} = 3600\ MPa$ as specified by the supplier. Over the full product range, it is observed that the stresses estimated by the scaling law are within $[3000; 3800]\ MPa$. The biggest gap represents 16% of the referenced value. This validates the scaling law.

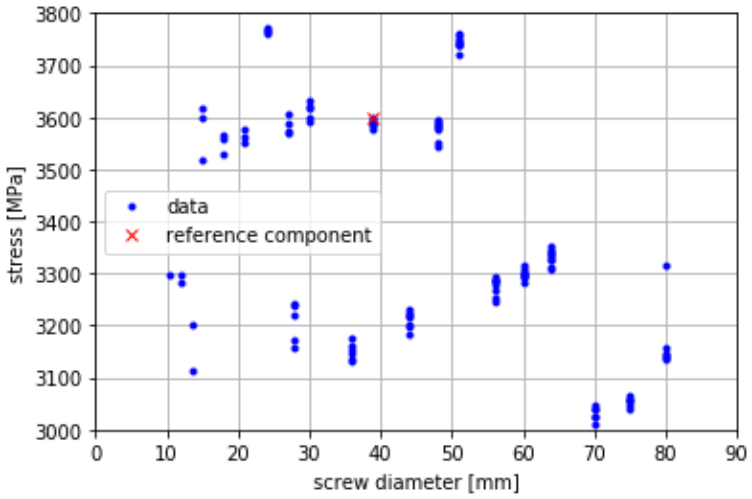

FIGURE L.4: *Stress estimation with Rollvis' catalog (inverted roller screw)*

Appendix M

Simulation & evaluation models

In this Appendix, the simulation & evaluation models are gathered in detail per discipline reminding the key design drivers, the associated equations and scenarios.

The tables are read from left to right. A colour coding has been set to improve reading comfort.

- The cyan color is dedicated to the technological variable (lead $[m/rad]$) and the optimization variables (oversizing coef. k_o).
- The red color is dedicated to the variables developping the actuator specification (the inputs of the sizing problem).
- The bleu color is dedicated to the variables set as the design hypothesis of the sizing problem.
- The orange color is dedicated to the sizing scenarios setting the link between either the specification and the component characteristics or the interactions between components.
- The green color is dedicated to the equations written in the sizing code script.

TABLE M.1: *Simulation & evaluation models for Rod End (RE) & Output Rod (OR)*

Component	KDD	Specification	Design hypothesis	Sizing scenario	Equations	Units
OUTPUT ROD (OR)	*geometry*	-	min diameter (linked to min standard nut diameter) $d_{in,V2,min}$ [m]	$d_{in,V2} \geq d_{out,nut,SM}$	$d_{out,nut,SM} = f_{SL}(C_{0,SM})$ $d_{in,V2} = d_{in,V2,min} \cdot k_{o,d,OR}$	m
	stress	max static load F_{max} [N]	min thickness $e_{min,OR}$ [m] fatigue stress of chosen material $\sigma_{fatigue}$ [Pa] safety fatigue stress coef. k_s [-]	$\sigma_{traction,V2} \leq \sigma_{fatigue} \cdot k_s$	volume V2: *thickness*: $e_{V2} = e_{min,OR} \cdot k_{o,e,OR}$ $d_{out,V2} = d_{in,V2} + 2 \cdot e_{V2}$	m
					$S_{V2} = \frac{\pi}{4} \cdot \left({d_{out,V2}}^2 - {d_{in,V2}}^2 \right)$	m²
					$\sigma_{traction,V2} = \frac{F_{max}}{S_{V2}}$	Pa
ROD END (RE)	*max stress*	max static load F_{max} [N]	safety coef. k_s [-]	$C_0 \geq F_{max} \cdot k_s$	$C_0 = F_{max} \cdot k_s \cdot k_{o,RE}$	N
	geometry	-	minimum standard axle diameter $d_{axle,min}$ [m]	$d_{axle} \geq d_{axle,min}$	$d_{axle} = f_{SL}(C_0)$	m

TABLE M.2: *Simulation & evaluation models for double row angular contact Ball Bearing (BB1)*

Component	KDD	Specification	Design hypothesis	Sizing scenario	Equations	Units
BALL BEARING BB1 (angular contact double row)	*max stress*	max static load F_{max} [N]	safety coef. k_s [-]	$C_0 \geq F_{max} \cdot k_s$	$C_0 = F_{max} \cdot k_s \cdot k_{o,BB1}$	N
		max linear speed v_{max} [m/s]	safety coef. $k_{s,w}$ [-]	$\Omega_{max,mech} \geq \Omega_{max,spec} \cdot k_{s,w}$	*max speed (mechanical limits):* $\Omega_{max,mech} = f_{SL}(C_0)$	RPM
					$\Omega_{max,spec} = \frac{v_{max}}{p} \cdot \frac{60}{2\pi}$	RPM
	fatigue	max pitting load $F_{max,p}$ [N] eq. fatigue load F_{rmc} [N] load frequency f_{load} [hz] lifespan t_{life} [hours] equivalent dist. travelled L_{eq} [km]	safety coef. $k_{s,f}$ [-] reliability factor for survival probability upper than 90% k_{rf} [-]	$C_d \geq C_{d,spec} \cdot k_{s,f}$	$C_d, n_{ball} = f_{SL}(C_0)$	N
					$N_{eq,rolling} = \frac{L_{eq}}{p} \cdot \frac{10^3}{2\pi}$	rev
					$D_{rolling} = {F_{RMC}}^3 \cdot N_{eq,rolling}$	$N^3 rev$
					$N_{c,pitting} = f_{load} \cdot t_{life}$; $N_{eq,pitting} = N_{c,pitting} \cdot k_{cycle}$; $k_{cycle} = \frac{1}{0.5 \cdot n_{ball}}$	cycle; rev; -
					$D_{pitting} = {F_{max,p}}^3 \cdot N_{eq,pitting}$	$N^3 rev$
					$\sum F^3 \cdot N_{eq} = {C_{d,spec}}^3 \cdot 10^6 = D_{rolling} + D_{pitting} = D_{total}$	$N^3 rev$
					$C_{d,spec} = \left(\frac{D_{total}}{10^6 \cdot k_{rf}}\right)^{1/3}$	N
	geometry	-	-	$d_{in} \geq d_{screw,SM}$	$d_{in} = f_{SL}(C_0)$	m
	rotational inertia	-	equivalent ring density $\rho_{eq,ring}$ [kg.m²]	-	*dimensions:* $d_{in}, d_{out}, l = f_{SL}(C_0)$; $d_{mean} = 0.5 \cdot (d_{in} + d_{out})$	m
					$J_{ring} = \frac{M_{ring}}{2} \cdot \left[\left(\frac{d_{mean}}{2}\right)^2 + \left(\frac{d_{in}}{2}\right)^2\right]$; $M_{ring} = \frac{\pi}{4}\left(d_{mean}^2 - d_{in}^2\right) \cdot l \cdot \rho_{eq,ring}$	kg.m² ; kg
	friction torque	max static load F_{max} [N] max linear speed v_{max} [m/s]	safety coef. $k_{s,Tfs}$ [-] safety coef. $k_{s,Tfl}$ [-] kinematic viscosity v_{grease} [mm²/s] radial load as a ratio of axial load k_{radial} [-]	see T_f in (EM)	*loading hypothesis:* *axial load:* $R_a = F_{max}$ *radial load:* $R_t = k_{radial} \cdot F_{max}$	N
					speed dependent friction: *if* $v_{grease} \cdot \Omega_{max,spec} \geq 2000$ *then:* $T_{fs} = 2.3 \cdot 10^{-7} \cdot \left(v_{grease} \cdot \Omega_{max,spec}\right)^{2/3} \cdot {d_{mean}}^3$ *else:* $T_{fs} = 368 \cdot 10^{-7} \cdot {d_{mean}}^3$	Nmm
					load dependent friction: $P_0 = R_t + 0.76 \cdot R_a$ $[N]$ *eq. load for contact angle* 25° $f_1 = 0.001 \cdot \left(\frac{P_0}{C_0}\right)^{0.33}$ $[-]$ *friction coefficient* $P_1 = \lvert 1.4 \cdot R_a - 0.1 \cdot R_t \rvert$ $[N]$ *deterministic load* $T_{fl} = f_1 \cdot P_1 \cdot d_{mean}$ *[Nmm]*	
					$T_f = \left(k_{s,Tfs} \cdot T_{fs} + k_{s,Tfl} \cdot T_{fl}\right) \cdot 10^{-3}$	Nm

TABLE M.3: *Simulation & evaluation models for single row deep groove Ball Bearing (BB2)*

Component	KDD	Specification	Design hypothesis	Sizing scenario	Equations	Units
BALL BEARING BB2 (deep groove single row)	*max stress*	max static load F_{max} [N]	safety coef. k_s [-] radial load as a ratio of axial load k_{radial} [-]	$C_0 \geq F_{max} \cdot k_{radial}$	-	N
		max linear speed v_{max} [m/s]	safety coef. $k_{s,w}$ [-]	$\Omega_{max,mech} \geq \Omega_{max,spec} \cdot k_{s,w}$	*max speed (mechanical limits):* $\Omega_{max,mech} = f_{SL}(C_0)$	RPM
					$\Omega_{max,spec} = \frac{v_{max}}{p} \cdot \frac{60}{2\pi}$	RPM
	fatigue	max pitting load $F_{max,p}$ [N] eq. fatigue load F_{rmc} [N] load frequency f_{load} [hz] lifespan t_{life} [hours] equivalent dist. travelled L_{eq} [km]	safety coef. $k_{s,f}$ [-] reliability factor for survival probability upper than 90% k_{rf} [-] radial load as a ratio of axial load k_{radial} [-]	$C_d \geq C_{d,spec} \cdot k_{s,f}$	$C_d = f_{SL}(C_0)$	N
					$D_{rolling} = (F_{RMC} \cdot k_{radial})^3 \cdot N_{eq,rolling}$; $N_{eq,rolling} = \frac{L_{eq}}{p} \cdot \frac{10^3}{2\pi}$	$N^3 rev$; rev
					$C_{d,spec} = \left(\frac{D_{rolling}}{10^6 \cdot k_{rf}}\right)^{1/3}$	N
	geometry	-	-	-	$d_{in} = d_{screw,SM}$	m
					$C_0 = f_{SL}(d_{in})$	N
	rotational inertia	-	equivalent ring density $\rho_{eq,ring}$ [kg.m²]	-	dimensions: $d_{out} = f_{SL}(C_0)$; $l = f_{SL}(C_0)$; $d_{mean} = 0.5 \cdot (d_{in} + d_{out})$	m
					$J_{ring} = \frac{M_{ring}}{2} \cdot \left[\left(\frac{d_{mean}}{2}\right)^2 + \left(\frac{d_{in}}{2}\right)^2\right]$; $M_{ring} = \frac{\pi}{4}(d_{mean}^2 - d_{in}^2) \cdot l \cdot \rho_{eq,ring}$	kg.m² ; kg
	friction torque	max static load F_{max} [N] max linear speed v_{max} [m/s]	safety coef. $k_{s,Tfs}$ [-] safety coef. $k_{s,Tfl}$ [-] kinematic viscosity v_{grease} [mm²/s] radial load as a ratio of axial load k_{radial} [-]	see T_f in (EM)	<u>loading hypothesis:</u> *axial load:* $R_a = 0$ *radial load:* $R_t = k_{radial} \cdot F_{max}$	N
					<u>speed dependent friction:</u> $if\ v_{grease} \cdot \Omega_{max,spec} \geq 2000\ then$: $T_{fs} = 1.3 \cdot 10^{-7} \cdot (v_{grease} \cdot \Omega_{max,spec})^{2/3} \cdot {d_{mean}}^3$ $else$: $T_{fs} = 208 \cdot 10^{-7} \cdot {d_{mean}}^3$	Nmm
					<u>load dependent friction:</u> $if\ R_a/R_t \leq 0.8\ then\ P_0 = R_t\ [N]\ eq.load$ $else$: $P_0 = 0.6 \cdot R_t + 0.5 \cdot R_a\ [N]\ eq.load$ $f_1 = 0.0007 \cdot \left(\frac{P_0}{C_0}\right)^{0.5}\ [-]\ friction\ coefficient$ $P_1 = \lvert 3.3 \cdot R_a - 0.1 \cdot R_t \rvert\ [N]\ deterministic\ load$ $T_{fl} = f_1 \cdot P_1 \cdot d_{mean}\ [Nmm]$	
					$T_f = (k_{s,Tfs} \cdot T_{fs} + k_{s,Tfl} \cdot T_{fl}) \cdot 10^{-3}$	Nm

TABLE M.4: *Simulation & evaluation models for Housing (H)*

Component	KDD	Specification	Design hypothesis	Sizing scenario	Equations	Units
HOUSING (H)	*geometry*	max linear stroke L_s [m]	height output rod sealing l_{seal} [m]	*housing volumes ≥ components outside dimensions*	-	m
	stress	max static load F_{max} [N]	min thickness $e_{min,H}$ [m] fatigue stress of chosen material $\sigma_{fatigue}$ [Pa] safety fatigue stress coef. k_s [-]	$\sigma_{traction,V7} \leq \sigma_{fatigue} \cdot k_s$	volume V7: *thickness*: $e_{V7} = e_{min,H} \cdot k_{o,e,H}$ $d_{in,V7} = d_{out,BB1}$ $d_{out,V7} = d_{in,V7} + 2 \cdot e_{V7}$ *or* $d_{in,V5}$ *or* $d_{out,V8}$ (if condition)	m
					$S_{V7} = \frac{\pi}{4} \cdot \left(d_{out,V7}{}^2 - d_{in,V7}{}^2\right)$	m²
					$\sigma_{traction,V7} = \frac{F_{max}}{S_{V7}}$	Pa
				$\sigma_{torsion,V5} \leq \sigma_{fatigue} \cdot k_s$	volume V5: $e_{V5} = e_{min,H} \cdot k_{o,e,H}$ if $(d_{out\_V3} \geq d_{out,V2})$ then: $d_{in,V5} = d_{out,V3}$ else: $d_{in,V5} = d_{out,V2}$ $d_{out,V5} = d_{in,V5} + 2 * e_{V5}$	m
					torsion moment: $M_{max,V5} = T_{max,EM,rated}$	Nm
					quadratic moment: $I_{0,V5} = \pi/32 \cdot \left(d_{out,V5}{}^4 - d_{in,V5}{}^4\right)$	m^4
					torsion stress: $\sigma_{torsion,V5} = \frac{M_{max,V5}}{\frac{I_{0,V5}}{d_{out,V5}}}$	Pa
				$\sigma_{traction,V8} \leq \sigma_{fatigue} \cdot k_s$	volume V8: *thickness*: $e_{V8} = e_{min,H} \cdot k_{o,e,H}$ $d_{in,V8} = d_{out,EM}$ $d_{out,V8} = d_{in,V8} + 2 \cdot e_{V8}$	m
					$S_{V8} = \frac{\pi}{4} \cdot \left(d_{out,V8}{}^2 - d_{in,V8}{}^2\right)$	m²
					$\sigma_{traction,V8} = \frac{F_{max}}{S_{V8}}$	Pa
	heat dissipation	ambient temp. θ_{amb} [°C]	min thickness $e_{min,H}$ [m] convection heat transfer coef. h_{conv} [W/m^2/K] emissivity ϵ_{rad} [-] maximum skin temperature $\theta_{max,skin}$ [°C]	$Q_{dissipation} \geq Q_{Joules,EM} + Q_{iron,EM} + Q_{EMB}$	equivalent geometry of dissipation: $l_{diss} = l_{stroke} + l_{V7} + l_{V8} + l_{V9} + l_{V10}$	m
					$D_{diss} = d_{out,EM} + 2 \cdot e_{min,H}$	m
					$S_{diss} = \pi \cdot D_{diss} \cdot l_{diss} + 2 \cdot \pi \cdot D_{diss}^2/4$	m²
					$Q_{convection} = \left(\theta_{max,skin} - \theta_{amb}\right) \cdot h_{conv} \cdot S_{diss}$	W
					$Q_{radiation} = \epsilon_{rad} \cdot \sigma_{SB} \cdot S_{diss} \cdot \left[\left(\theta_{max,skin} + 273\right)^4 - \left(\theta_{amb} + 273\right)^4\right]$	W

TABLE M.5: *Simulation & evaluation models for Screw Mechanism (SM)*

Component	KDD	Specification	Design hypothesis	Sizing scenario	Equations	Units
SCREW MECHANISM (SM)	*max stress*	max static load F_{max} [N]	safety coef. k_s [-]	$C_0 \geq F_{max} \cdot k_s$	$C_0 = F_{max} \cdot k_s \cdot k_{o,SM}$	N
		max linear speed v_{max} [m/s] max linear stroke L_s [m]	safety coef. $k_{s,w}$ [-]	$\Omega_{r,0l} \geq \Omega_{max,spec} \cdot \mathrm{k_{s,w}}$ $\Omega_{r,l} \geq \Omega_{max,spec} \cdot \mathrm{k_{s,w}}$	$\Omega_{max,spec} = \frac{v_{max}}{p} \cdot \frac{60}{2\pi}$	RPM
					$dimensions$: $d_{screw}, l_{nut} = f_{SL}(C_0)$	m
					permissible critical speed under 0 N axial load: $\Omega_{r,0l} = 34.56 \cdot 10^6 \cdot \frac{(d_{screw} \cdot 1000)}{((L_s + l_{nut}) \cdot 1000)^2}$	RPM
					permissible critical speed under axial load: $\Omega_{r,l} = 160000/(d_{screw} \cdot 1000)$	RPM
		max static load F_{max} [N] max linear stroke L_s [m]	safety coef. k_s [-]	$F_{buckling} \geq F_{max} \cdot k_s$	$F_{buckling} = 21220 \cdot \frac{(d_{screw} \cdot 1000)^4}{((L_s + l_{nut}) \cdot 1000)^2}$	N
	geometry	-	-	$d_{out,rotor,EM} \geq d_{screw}$	$d_s = f_{SL}(C_0)$	m
	fatigue	max pitting load $F_{max,p}$ [N] eq. fatigue load F_{rmc} [N] load frequency f_{load} [hz] lifespan t_{life} [hours] equivalent dist. travelled L_{eq} [km]	safety coef. $k_{s,f}$ [-] reliability factor for survival probability upper than 90% k_{rf} [-]	$C_d \geq C_{d,spec} \cdot k_{s,f}$	$C_d, d_{in,nut}, n_{roller} = f_{SL}(C_0)$; $d_{roller} = 0.5 \cdot (d_{in,nut} - d_s)$	N, m, -, m
					$N_{eq,rolling} = \frac{L_{eq}}{p} \cdot \frac{10^3}{2\pi}$; $k_{cycle} = f(d_{roller}, d_{in,nut}, n_{roller})$	rev, -
					$N_{eq,pitting} = N_{c,pitting} \cdot k_{cycle}$; $N_{c,pitting} = f_{load} \cdot t_{life}$	rev, cycle
					$D_{rolling} = {F_{RMC}}^3 \cdot N_{eq,rolling}$	$N^3 rev$
					$D_{pitting} = {F_{max,p}}^3 \cdot N_{eq,pitting}$	$N^3 rev$
					$\sum F^3 \cdot N_{eq} = {C_{d,spec}}^3 \cdot 10^6 = D_{rolling} + D_{pitting} = D_{total}$	$N^3 rev$
					$C_{d,spec} = \left(\frac{D_{total}}{10^6 \cdot k_{rf}}\right)^{1/3}$	N
	efficiency	-	safety coef. on efficiency $k_{s,\eta}$ [-]	$\eta_{validity} \geq 0$ $\eta_i \geq 0.9 \cdot \eta_d$	$helix\ angle$: $\phi = atan\left(\frac{p \cdot 2\pi}{d_{screw} \cdot \pi}\right) \cdot \frac{180}{\pi}$	°
					friction coefficient: $\mu_{dyn} = 10^{-5} \cdot \phi^3 + 2 \cdot 10^{-5} \cdot \phi^2 + 0.0007 \cdot \phi + 0.0088$	-
					$dyn.\,direct\ efficiency$ [3]: $\eta_d = \frac{1}{\left(1 + 0.5 \cdot d_{screw} \cdot \frac{\mu_{dyn}}{p}\right)} \cdot k_{s,\eta}$	-
					$dyn.\,indirect\ efficiency$: $\eta_i = \frac{1}{\left(2 - \frac{1}{\eta_d}\right)}$	-
					validity criteria for use of SKF efficiency formula: $\eta_{validity} = \frac{d_{screw}}{p \cdot 2\pi} - \frac{\sqrt{10}}{\pi}$	-

TABLE M.6: *Simulation & evaluation models for Antirotation Key (AK), Linear Bushing (LB), and actuator (ACT)*

Component	KDD	Specification	Design hypothesis	Sizing scenario	Equations	Units
ANTIROTATION KEY (AK)	-	-	friction coef. along its surface in contact with output rod or nut flange μ_{AK} [-]	see T_f in (EM)	normal load applied on key: $F_n = \frac{T_{max,EM,rated}}{d_{in,V5}/2}$	N
					linear force created by friction on antirotation key: $F_l = \mu_{AK} \cdot F_n$	N
					induced friction torque at motor level: $T_f = \frac{F_l \cdot p}{\eta_{d,SM}}$	Nm
LINEAR BUSHING (LB)	-	max linear speed v_{max} [m/s]	friction coef. of linear bushing μ_{LB} [-] normal load seen by linear bushing $F_{n,LB}$ [N] ratio of bush length out of bush diameter $k_{rld,LB}$ [-]	see T_f in (EM) A sizing scenario should be put onto pU factor (pU < 1.8 N/mm²*m/s)	linear force generated by friction: $F_l = \mu_{LB} \cdot F_{n,LB}$	N
					linear friction force converted into torque at motor level: $T_f = \frac{F_l \cdot p}{\eta_{d,SM}}$	Nm
					bushing length: $l = k_{rld,LB} \cdot d_{out,V2}$	m
					bushing surface of contact with output rod: $S = \pi \cdot d_{out,V2} \cdot l$	m²
					bushing specific pressure: $p = \frac{F_{n,LB}}{S}$	N/m²
					bushing pU factor: $pU = p \cdot v_{max}$	N/m²*m/s
ACTUATOR (ACT)	*transparency load*	max static load F_{max} [N]	safety coef. k_s [-]	$F_{transparency} \geq F_{max} \cdot k_s$	$F_{transparency} = T_{max,EM,derated} \cdot \frac{\eta_{i,SM}}{p}$	N
	reflected inertia	-	max reflected inertia allowed by the application $M_{max,reflected,J}$ [kg]	$M_{reflected,Jtotal} \leq M_{max,reflected,J}$	total inertia reflected to the linear reference: $M_{reflected,Jtotal} = \frac{J_{total}}{p^2}$	kg
	vibration stress	-	safety coef. k_s [-] quality factor Q_m [-] vibration acceleration G_{vib} [m/s²] fatigue stress of output rod & housing material $\sigma_{fatigue}$ [Pa] output rod & housing material density ρ_{vib} [kg/m³]		single actuator length without rod end at basement: $L_{max,ACT} = h_{RE} + l_{V2} + l_{V5} + l_{V7} + l_{V8} + l_{V9} + l_{V10} + l_{V11}$	m
				$\sigma_{vib,SA} \leq \sigma_{fatigue} \cdot k_s$	maximum stress during vibration of SINGLE ACTUATOR: $\sigma_{vib,SA} = f_{SA}(d_{in,V2};\ L_{max,ACT};\ e_{V2};\ e_{V5};\ Q_m;\ \rho_{vib};\ G_{vib})$ surrogate function	Pa
				$\sigma_{vib,DA,r} \leq \sigma_{fatigue} \cdot k_s$	maximum stress during vibration of DOUBLED ACTUATOR: $\sigma_{vib,DA,r} = f_{DA,r}(d_{in,V2};\ L_{max,ACT};\ e_{V2};\ e_{V5};\ Q_m;\ \rho_{vib};\ G_{vib})$ surrogate function, stress taken on rod	Pa
				$\sigma_{vib,DA,s} \leq \sigma_{fatigue} \cdot k_s$	maximum stress during vibration of DOUBLED ACTUATOR: $\sigma_{vib,DA,s} = f_{DA,s}(d_{in,V2};\ L_{max,ACT};\ e_{V2};\ e_{V5};\ Q_m;\ \rho_{vib};\ G_{vib})$ surrogate function, stress taken between actuators	Pa

TABLE M.7: *Simulation & evaluation models for Electrical Motor (EM)*

KDD	Specification	Design hypothesis	Sizing scenario	Equations	Units
motor magnetic saturation	max static load F_{max} [N] max stall load $F_{max,eps}$ [N] max load at max PR F_{PRmax} [N] max acceleration at max PR a_{PRmax} [m/s²] max acceleration a_{max} [m/s²] max linear speed v_{max} [m/s] ambient temperature θ_{amb} [°C]	safety coef. k_s [-] max winding temperature $\theta_{max,winding}$ [°C] exponent of speed for iron losses b_{iron} [-]	$T_{max,EM,derated} \geq T_{max,spec} \cdot k_s + T_{iron,max} + T_{f,BB1} + T_{f,BB2} + T_{f,AK} + T_{f,LB}$ T_f *the friction torques*	$T_{stall} = \frac{F_{max,eps} \cdot p}{\eta_{d,SM}}$; $T_{a,max} = J_{total} \cdot \frac{a_{max}}{p}$	Nm
				$T_{PR} = \frac{F_{PRmax} \cdot p}{\eta_{d,SM}} + J_{total} \cdot \frac{a_{PRmax}}{p}$	Nm
				$T_{max,spec} = \max(T_{stall}; T_{a,max}; T_{PR})$	Nm
				$T_{max,EM,rated} = T_{initial} \cdot k_{o,EM}$; $T_{initial} = \frac{F_{max} \cdot p}{\eta_{i,SM}}$	Nm
				$k_{derating} = \sqrt{\frac{\theta_{max,winding} - \theta_{amb}}{\theta_{max,winding} - \theta_{rated,EM,ref}}}$	-
				$T_{max,EM,derated} = T_{max,EM,rated} \cdot k_{derating}$	Nm
				$T_{iron,max} = \beta_{EM} \cdot \left(\frac{v_{max}}{p}\right)^{(b_{iron}-1)}$; $\beta_{EM} = f_{SL}(T_{max,EM,rated})$	Nm ; W/(rad/s)^1.5
continuous motor temperature	eq. continuous load F_{RMS} [N] eq. continuous acceleration a_{RMS} [m/s²] mean power rate $\overline{PR}$ [W/s] iron speed v_{iron} [m/s] ambient temp. θ_{amb} [°C]	safety coef. k_s [-] max winding temperature $\theta_{max,winding}$ [°C] exponent of speed for iron losses b_{iron} [-]	$T_{rms,EM,derated} \geq T_{rms,spec} \cdot k_s + T_{iron,mean} + T_{f,BB1} + T_{f,BB2} + T_{f,AK} + T_{f,LB}$ T_f *the friction torques*	$T_{rms,spec} = \sqrt{\left(\frac{F_{rms} \cdot p}{\eta_{d,SM}}\right)^2 + 2 \cdot \frac{J_{total}}{\eta_{d,SM}} \cdot \overline{PR} + \left(J_{total} \cdot \frac{a_{rms}}{p}\right)^2}$	Nm
				$T_{rms,EM,rated} = f_{SL}(T_{max,EM,rated})$ $T_{rms,EM,derated} = T_{rms,EM,rated} \cdot k_{derating}$	Nm
				$T_{iron,mean} = \beta_{EM} \cdot \left(\frac{v_{iron}}{p}\right)^{(b_{iron}-1)}$	Nm
	iron speed v_{iron} [m/s]	exponent of speed for iron losses b_{iron} [-]	$Q_{Joules} + Q_{iron} \leq Q_H - Q_{EMB}$	*Joules loss:* $Q_{Joules} = \alpha \cdot {T_{rms,spec}}^2$; $\alpha_{EM} = f_{SL}(T_{max,EM,rated})$	W
				iron loss: $Q_{iron} = \beta_{EM} \cdot \left(\frac{v_{iron}}{p}\right)^{b_{iron}}$	W
rotor magnet stress	max linear speed v_{max} [m/s]	safety coef. $k_{s,w}$ [-]	$\Omega_{max,EM} \geq \Omega_{max,spec} \cdot k_{s,w}$	$\Omega_{\max,\mathrm{spec}} = \frac{v_{max}}{p} \cdot \frac{60}{2\pi}$	RPM
				$\Omega_{max,EM} = f_{SL}(T_{max,EM,rated})$ *(for mechanical limits)*	RPM
supply limitations	max bus voltage $V_{dc,bus}$ [volts] max phase current I_{max} [Apeak-sine]	-	$\mathrm{V_{dc,bus}} \geq V_{dc,EM}$	$K_t = K_{t,i} \cdot \sqrt{2}$; $K_{t,i} = \frac{T_{max,spec}}{I_{max}}$	Nm/Arms-sine ; Nm/Apeak-sine
				$K_e = K_{e,i} \cdot \sqrt{\frac{3}{2}} \cdot \frac{2\pi}{60} \cdot 1000$; $K_{e,i} = \frac{2}{3} \cdot K_{t,i}$	Urms/kRPM PtP ; Nm/Apeak or Vpeak/(rad/s) PN
				$R = f_{SL}(K_t; T_{max,EM,rated})$; $L = f_{SL}(K_t; T_{max,EM,rated})$	Ohm PtP; H PtP
				$n_{poles} = f_{SL}()$	pole pair nbr
				$V_{BEMF} = \frac{K_e}{1000 \cdot \sqrt{3}} \cdot \Omega_{max,spec}$; $V_R = \frac{R}{2} \cdot \frac{I_{max}}{\sqrt{2}}$	V_{rms} *PN*
				$V_L = \frac{L}{2} \cdot \frac{I_{max}}{\sqrt{2}} \cdot n_{poles} \cdot \Omega_{\max,\mathrm{spec}} \cdot \frac{2\pi}{60}$	V_{rms} *PN*
				$V_{dc,EM} = V_{EM} \cdot \frac{2\sqrt{2}}{1.15}$; $V_{EM} = \sqrt{(V_{BEMF} + V_R)^2 + {V_L}^2}$	V_{dc} ; V_{rms} *PN*

KDD	Specification	Design hypothesis	Sizing scenario	Equations	Units
continuous holding pressure	max static load F_{max} [N] max linear speed v_{max} [m/s] mass of load M_{load} [kg]	time until max rotating speed shall be cancelled t_{EMB} [s] safety coef. k_s [-]	$T_{EMB} \geq T_{max,EMB,spec}$	$\Omega_{max,spec} = \frac{v_{max}}{p} \cdot \frac{60}{2\pi}$	RPM
				$J_{reflected,mass} = \left(M_{load} + M_{n,SM} + M_{RE} + M_{output,rod}\right) \cdot p^2$	kg.m²
				$J_{total,int} = J_{ring,BB1} + J_{ring,BB2} + J_{s,SM} + J_{EM} + J_{reflected,mass}$	kg.m²
				$T_{EMB} = \left(\frac{F_{max} \cdot p}{\eta_{i,SM}} + J_{total,int} \cdot \frac{\Omega_{max,spec}}{t_{EMB}}\right) \cdot k_{o,EMB}$	Nm
				$J_{total} = J_{total,int} + J_{EMB}$; $J_{EMB} = f_{SL}(T_{EMB})$	kg.m²
				$T_{max,EMB,spec} = \frac{F_{max} \cdot p}{\eta_{i,SM}} + J_{total} \cdot \frac{\Omega_{max,spec}}{t_{EMB}}$	Nm
continuous temperature	-	-	$Q_{EMB} \leq Q_{dissipation,H} - Q_{Joules,EM} - Q_{iron,EM}$	$Q_{EMB} = f_{SL}(T_{EMB})$	W

Appendix N

Motor derating coefficient

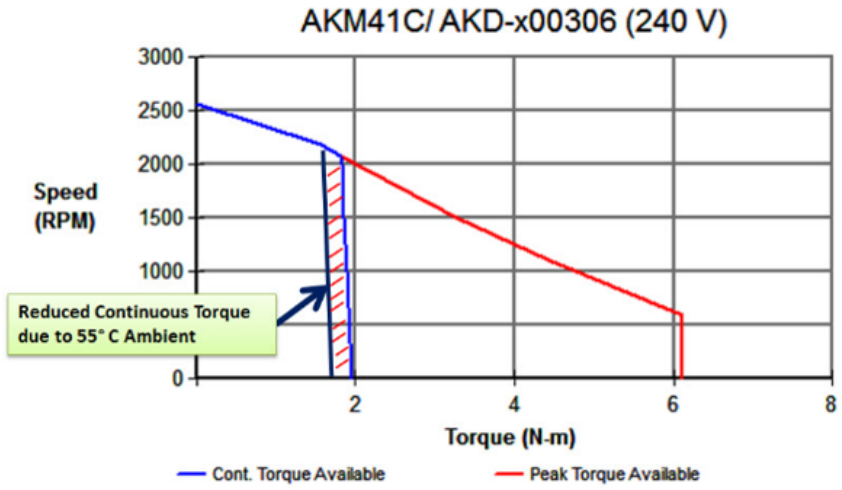

FIGURE N.1: *Motor derating example (from Kollmorgen)*

Most of motor manufacturers supply datasheet for a given ambient temperature. Kollmorgen specifies an ambient temperature of $t_r = 25\,°\text{C}$. For higher ambient temperature conditions, electrical motors decrease performance. To take into account another temperature environment, a derating coefficient must be applied on the motor torque (fig. N.1). The relation is:

$$T_{derated(t_d°\text{C})} = T_{rated(t_r°\text{C})} \cdot \sqrt{\frac{t_{max} - t_d}{t_{max} - t_r}} \tag{N.1}$$

with t_{max} $[°C]$ the maximum winding temperature, t_r $[°C]$ the manufacturer rated temperature, and t_d $[°C]$ the derated temperature i.e the application ambient temperature (from Kollmorgen>Derating).

As for example, a motor with a maximum winding temperature of $t_{max} = 155\,°\text{C}$ and a rated temperature of $t_r = 25°C$ is considered. Its application in an environment with an ambient temperature of $70\,°\text{C}$ shows torque such as:

$$T_{derated(70\,°\text{C})} = T_{rated(40\,°\text{C})} \cdot \sqrt{\frac{155 - 70}{155 - 25}} \approx T_{rated(40\,°\text{C})} \cdot 0.81 \tag{N.2}$$

The derating coefficient can be justified using Joules' losses and the thermal resistance at steady state (continuous torque):

$$\mathscr{P}_J = R_{th} \cdot \Delta\theta \tag{N.3}$$

where $\Delta\theta = t_{max,winding} - t_{ambient}$. Joules' losses are proportional to the squared motor torque T^2. Turning the equation into a scaling law, $R^*_{th} = 1$ since the same motor is considered. The derrated torque comes out:

$$T^{*2} = \Delta\theta^* \implies \frac{T_{derated}}{T_{rated}} = \sqrt{\frac{\Delta\theta_{derated}}{\Delta\theta_{rated}}} \tag{N.4}$$

At transient state (peak torque), a thermal capacity is considered such that:

$$\mathscr{P}_J = C_{th} \cdot \frac{\Delta\theta}{\Delta t} \tag{N.5}$$

where $C^*_{th} = \Delta t^* = 1$ since the same motor is considered. Developing on the same way, the relation N.4 is found again.

Appendix O

Behn-Eschenburg's model

The model of Behn-Eschenburg proposes to model the electrical motor as an equivalent circuit (fig. O.1) with a voltage supply V_s $[V]$, a resistance $\mathscr{R}$ $[Ohm]$, an inductance $\mathscr{L}$ $[H]$, and an electromotive force E_b $[V]$ [Multon, 2010]. $\mathscr{L}$ is the cyclic inductance if the sum of the motor phase current is nul. This is the case of a three phased motor with a star connection.

In addition, the model assumes a constant air gap (rotor with smooth surface) and no magnetic saturation. This means that the flux due to the magnetic reaction of the armature is independent of the rotor position and is proportional to the current in the inductor.

What is more, it assumes that the electromotive force E has, as first approximation, a sinus shape which amplitude is proportional to the motor speed and the inductor flux. The inductor flux is constant for parmanent magnet rotors.

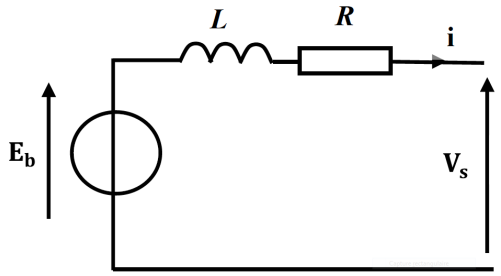

FIGURE O.1: *Equivalent circuit for electrical motor: Behn-Eschenburg's model [Multon, 2010]*

Appendix P

Power architecture conversions

In fig. P.1, [Maré, 2017] presents the generic architecture of the electrical power path of a PbW actuator. Fig. P.1 shows the elements in charge of power control (dynamic brake chopper, inverter) and electrical conditioning (filters, rectifier). The protection functions are not explicitly mentioned.

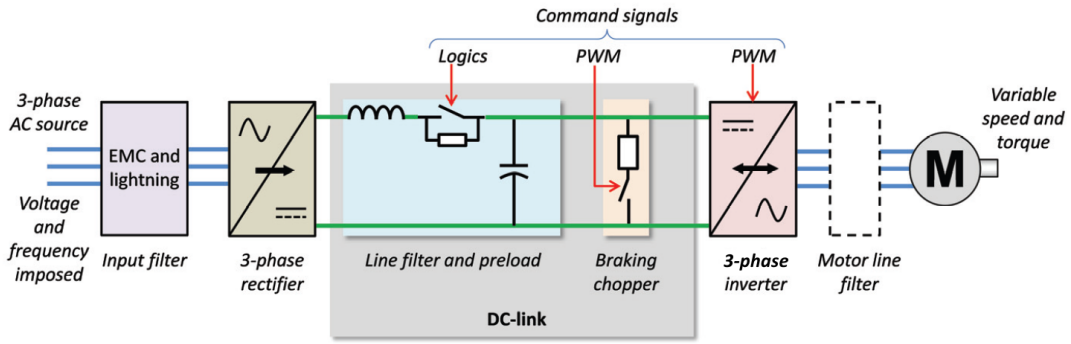

FIGURE P.1: *Generic architecture of the electrical power path of a PbW actuator [Maré, 2017]*

The table P.1 sums up the main voltage conversions to perform on the way from the power source to the motor phases or the other way round.

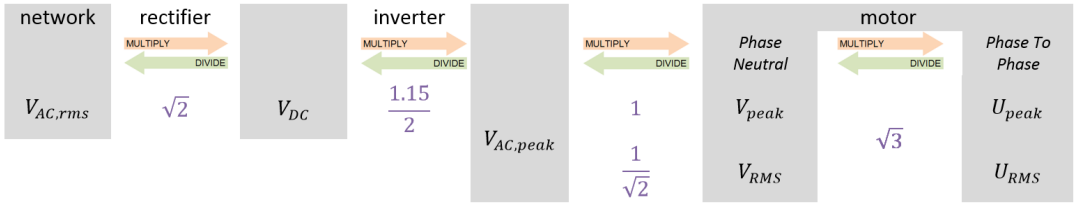

TABLE P.1: *Conversion table of generic power architecture*

[Feld, 2000b] [Feld, 2000a] shows that there is an harmonic 3 in the voltage command which increases the amplitude of an inverter output voltage by a factor of $f_{h3} = 2/\sqrt{3} \approx 1.15$. As a result, the inverter provides a voltage with a maximum amplitude of:

$$V_{AC,peak} = \frac{V_{DC}}{2} \cdot f_{h3} \tag{P.1}$$

Reminder on voltage notations: U (phase to phase), V (phase neutral)

Appendix Q

Bearing lubricant viscosity

The oils used for lubrication of bearings are usually from mineral oil with viscosity index of roughly 90 cSt at 40 $°C$ [SNR, 2000].

The evolution of viscosity with respect of bearing dimensions and running speed is displayed in fig. Q.1.

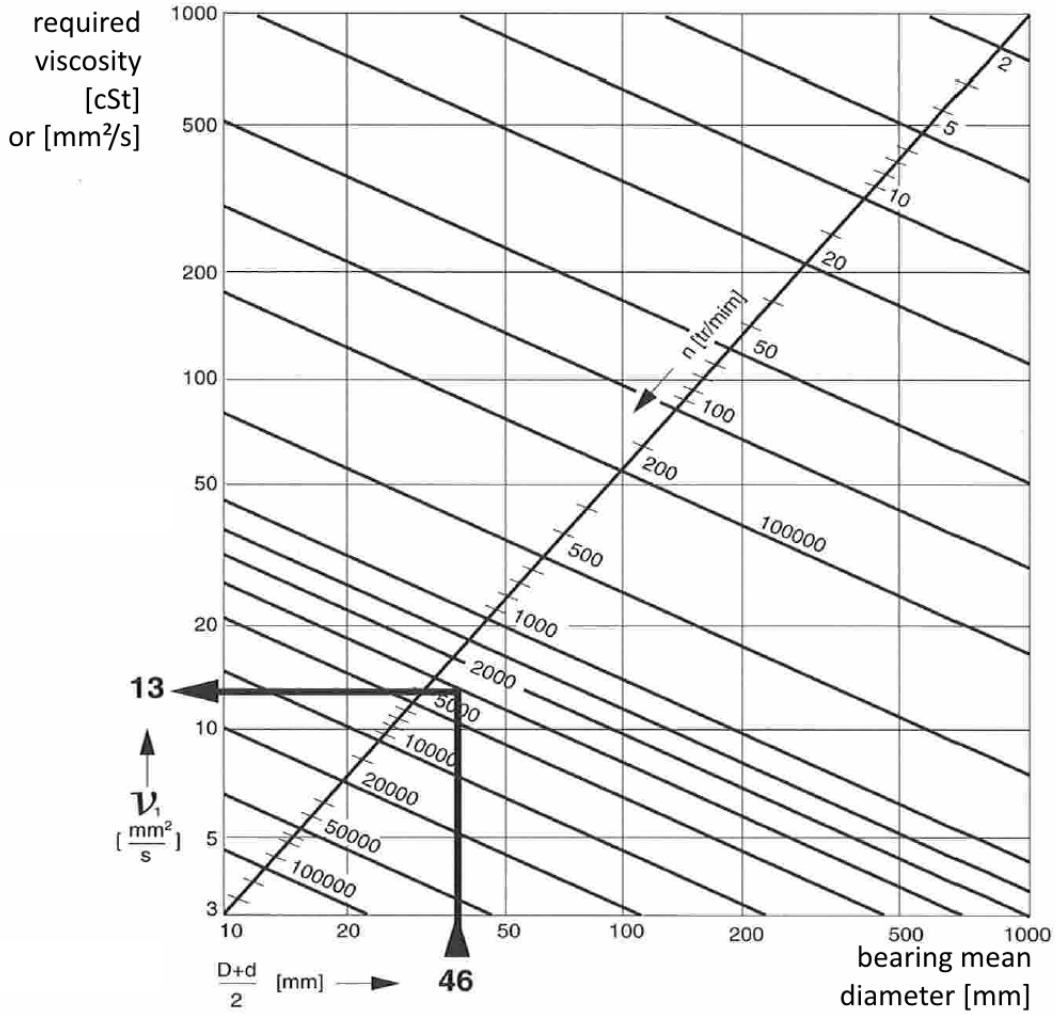

FIGURE Q.1: *Generic viscosity-diameter diagram for bearings [SNR, 2000]*

To estimate the viscosity evolution with respect to temperature, the suppliers of lubricants give the precise characteristics of their products and especially the diagram viscosity versus temperature. In preliminary design, this diagram is missing, [SNR, 2000] proposes the use of the generic diagram presented in fig. Q.2.

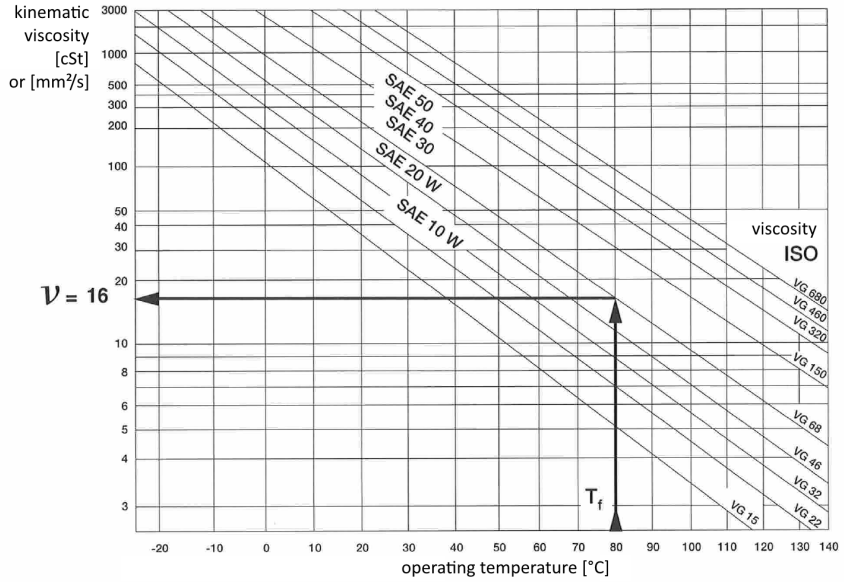

FIGURE Q.2: *Generic viscosity-temperature diagram for bearings [SNR, 2000]*

To make the use of this diagram easier, we propose the mathematical formulation of the drawn lines fitted on the line VG68.

$$\nu = \nu_{ref} \cdot e^{k \cdot \left(\frac{1}{T} - \frac{1}{T_{ref}} \right)} \tag{Q.1}$$

where $\nu_{ref} = 500\ [mm^2/s]$ is a viscosity at a temperature $T_{ref} = 283\ [K] = 10\ [C]$, and $k = 4912\ [K]$ is a fitting constant.

Appendix R

Convection heat transfer coefficient

For the choice of the convection heat transfer coefficient, this appendix provides two references offering an order of magnitude.

A first reference developping the fundamentals of heat transfer provides the values in fig. R.1.

Process	h ($W/m^2 \cdot K$)
Free convection	
Gases	2–25
Liquids	50–1000
Forced convection	
Gases	25–250
Liquids	100–20,000
Convection with phase change	
Boiling or condensation	2500–100,000

FIGURE R.1: *Convection heat transfer values for different fluids [Incropera et al., 2007]*

A second reference [Multon, 2006] provides, in the electrical and actuator design fields, the values presented in fig. R.2.

NATURAL CONVECTION for T = 10 to 50 °K

fluid	air 1bar	air 10 bar	air 25°C	silicon oil 25°C	hydrogen 1 bar 25°C
α W/m²/K	4-7	15-26	450-780	50-90	12-19

SINGLE-PHASED FORCED CONVECTION with 1 or 2 m/s

fluid m/s	air 1bar 0,24-1,2	air 1bar 30	air 25-100°C 0,5-2,5	silicon oil 25-100°C	hydrogen 1 bar 25°C 0,49-4,7
α W/m²/K	7,8-23	135	2900-20000	380-1200	43-130

FIGURE R.2: *Convection heat transfer values for different fluids [Multon, 2006]*

Appendix S

Friction coefficient

This appendix presents in fig. S.1 some generic values of friction coefficients between well known materials in contact.

Matériaux en contact	Nature du frottement	μ	Matériaux en contact	Nature du frottement	μ
Acier / Fonte Acier / Bronze	Sec	0,19	Garniture de frein / Fonte pression de contact 0,2 à 0,6 MPa	Sec Température 140 °C max.	0,35 à 0,40
	Gras	0,16			
	Bon graissage	0,10	Plastique / Plastique	Bon graissage	0,02 à 0,08
Acier / Antifriction	Bon graissage	0,05	PA 6/6 / Acier	Sec	0,32 à 0,42
Fonte / Bronze Fonte / Fonte	Sec	0,21	PA 11 / Acier	Sec	0,32 à 0,38
	Gras	0,15	PC / Acier	Sec	0,52 à 0,58
	Bon graissage	0,05 à 0,10	PE / Acier	Sec	0,24 à 0,28
Acier trempé / Bronze	Graissage moyen	0,10	PS / Acier	Sec	0,35 à 0,5
	Graissage sous pression	0,05	PTFE / Acier	Sec	0,22
Acier trempé / Acier trempé	Graissage moyen	0,10	Pneus / Route goudronnée	Sec	0,60 à 0,70
	Bon graissage	0,07		Mouillé	0,35 à 0,60
	Graissage sous pression	0,05		Verglacé	0,10

FIGURE S.1: *Generic values of friction coefficients [Chevalier, 2004]*

Appendix T

Pitting fatigue workflow

T.1 Pitting fatigue consideration

To address the pitting fatigue more precisely, we propose the process presented in fig. T.1 as a workflow. It is described briefly as it follows:

1. The mission profile analysis provides dynamic loads F_d, static loads F_s classified with occurences N
2. A set of relations (scaling laws), dependent on the actuator component technologies, makes the conversion from loads to stresses.
3. Haigh's diagram ensures transfering all dynamic stresses into equivalent dynamic stresses $\sigma_{d,eq}$ at null static stress.
4. Since [Marcoux, 1987] states that stresses smaller than the limit fatigue are not damaging the material, we remove them from the loop.
5. The top level specification provides the actuator lifespan. With the mission profile length, the number of occurence N_{ij} is re-adapted to the actuator lifespan $N_{T,ij}$.
6. At this step, the amount of damage D_T is worked out and a value of equivalent stress σ_{eq} can be estimated supposing an equivalent number of cycles N_{eq} based on endurance curve (number of cycles where the curve starts flattening).
7. σ_{eq} is compared to the infinite fatigue limit σ_∞ (table **??**) of the material lowered by a safety margin k_3 whose definition comes from intern return experience [Struzik and Celli,] [Marcoux, 1987].

Notes: The admissible damage D_{adm} can be estimated using the equivalent dynamic stresses $\sigma_{d,eq,ij}$ and the endurance curve (fig. T.4) which provides the corresponding number of cycles $N_{adm,ij}$.

$$D_{adm} = \sum \sigma_{d,eq,ij}^{k} \cdot N_{adm,ij} \tag{T.1}$$

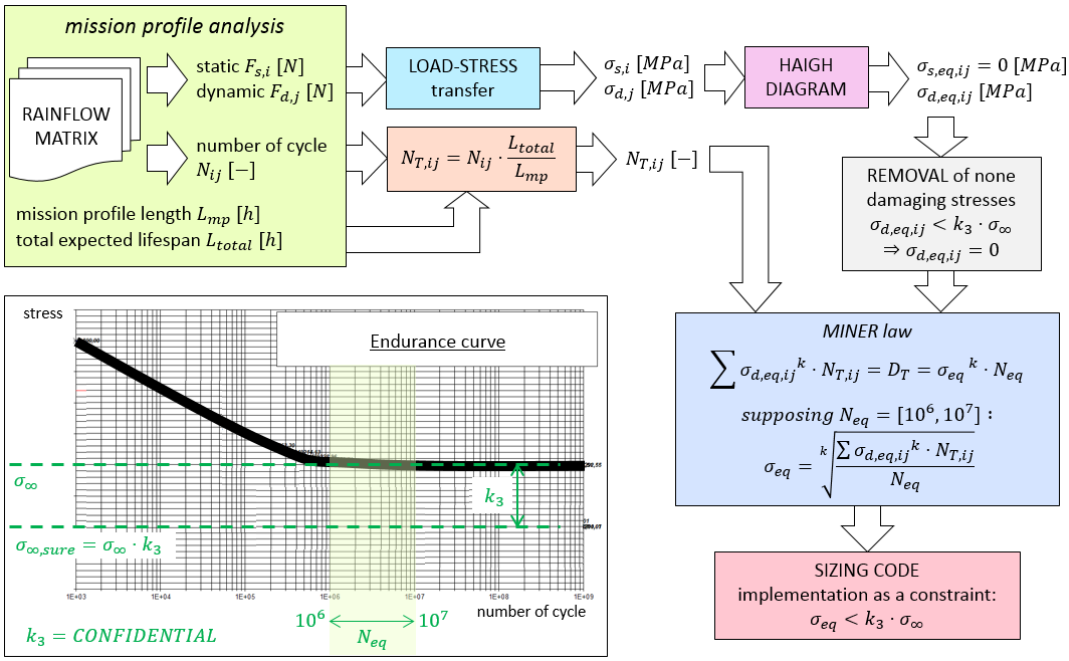

FIGURE T.1: *Pitting fatigue*

T.1.1 Rainflow matrix

Refer to section 2.4.2.

T.1.2 Load-stress transfer

To make the link between the load available on the mission profile and the stress needed to go through the fatigue study, we propose the following relations:

$$load - stress\ link : \begin{cases} structure & linear\ contact & \sigma = F/S \\ ball - screw & spherical\ contact & \sigma^* = F^{*1/3}/d^{*2/3} \\ roller - screw & elliptical\ contact & \sigma^* = F^{*1/3}/d^{*2/3} \end{cases} \quad \text{(T.2)}$$

In T.2, the ball and roller-screw relations comes from the scaling law theory applied onto a spherical and elliptical contact state of the art (theory & validation in Appendix L).

In the case of a roller-screw, the most critical contact surface is the first flange (or thread). The considered load is rescaled regarding the load distribution proposed by [Kossi Abevi, 2013] (p151, 154) (shown in fig. T.2). We propose to take 12% of the load from mission profile. Since the rollers are located in parallel on the load chain and knowing than the minimum roller number is 3 for kinematical aspect, the load has to be divided by 3.

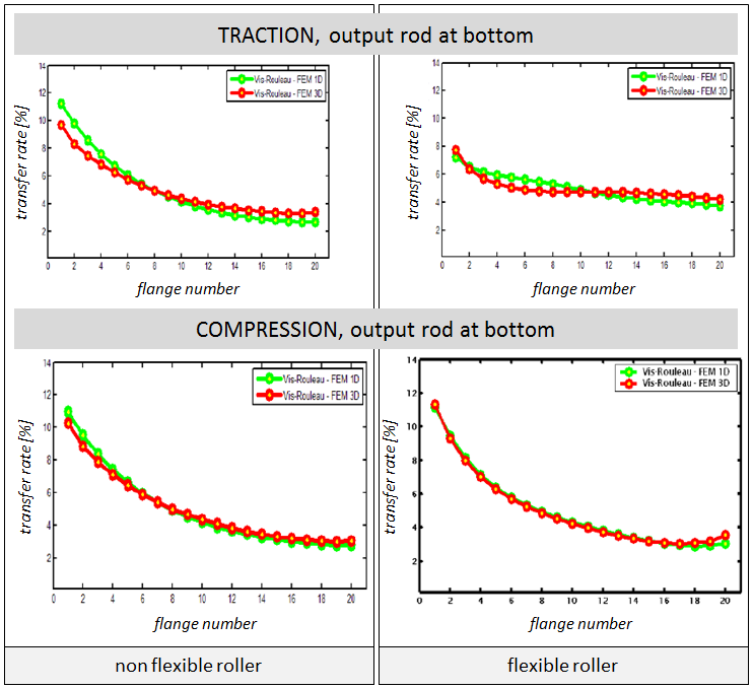

FIGURE T.2: *Load distribution on roller flanges of a roller-screw (results from simulation, [Kossi Abevi, 2013])*

T.1.3 Haigh diagram

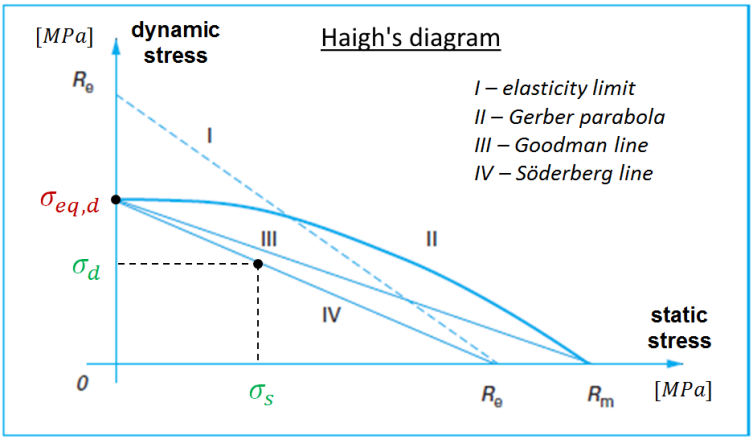

FIGURE T.3: *Haigh's diagram*

Since endurance or Wöhler's curve are based on dynamic loads with null static loads, the dynamic load at a given static load has to be converted into an equivalent dynamic load at null static load. Haigh's diagram is a tool to make this transfer [GALTIER et al., 2019].

The equivalent stress for null static stress is defined as:

$$\sigma_{eq} = \frac{\sigma_d}{1 - \left(\frac{\sigma_s}{k_t \cdot R_i}\right)^{\delta}} \tag{T.3}$$

with k_t the coefficient of stress concentration, R_i the resistance to failure (R_m) or the elastic resistance (R_e) and δ such as:

- steel material: Gerber's parabola ($\delta = 2$, $R_i = R_m$)
- aluminium, magnesium, Ti10.2.3 material: Goodman's line ($\delta = 1$, $R_i = R_m$), Söderberg's line ($\delta = 1$, $R_i = R_e$)
- TA6V material: concave curve ($\delta < 1$, $R_i = R_e$)

T.1.4 Endurance curve

The endurance curve gives the admissible number of cycle out of a given stress value.

The Stromeyer's model [GALTIER et al., 2019] is used (fig. T.4). The link between Stromeyer's curve and the y-axis belongs to Airbus internal. The parameters to apply the relation are not provided for confidentiality reasons.

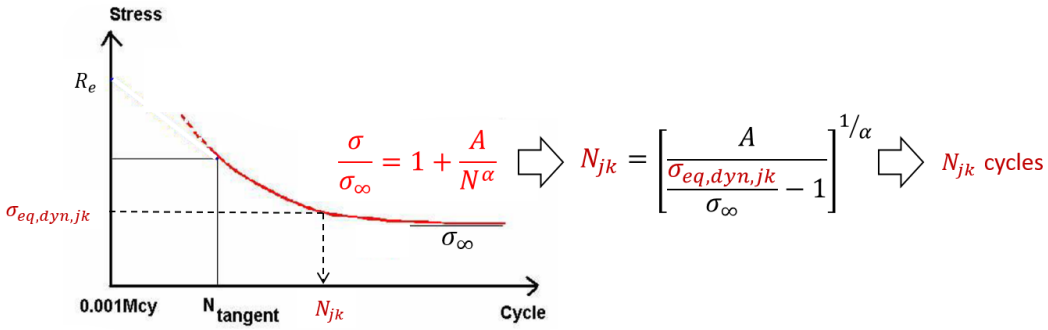

FIGURE T.4: *Endurance curve theory [Struzik and Celli,] [GALTIER et al., 2019]*

Appendix U

Design graphs

This appendix gathers the design graphs absent in the thesis core. Some abbreviations are used to simplify the representation, they are detailed in table U.1. The color legend is in fig. 5.12.

RE	Rod End	SM	Screw Mechanism
BB1	Ball Bearing 1 (double rows)	BB2	Ball Bearing 2 (single row)
OR	Output Rod	LB	Linear Bushing
EM	Electrical Motor	EMB	Electromagnetic Brake
S	Shaft	I	Inertia
BLS	Bearing Load Statement	BS	Bearing Specification
BFT	Bearing Friction Torque	RT	Required Torque
HL	Heat Losses	EL	Electrical Limitation
TL	Transparency Load	H	Housing
HD	Heat Dissipation	AK	Antirotation Key
VS	Vibration Stress	AM	Actuator Mass

TABLE U.1: *List of abbreviations (components & disciplines)*

U.1 Ball bearing 1

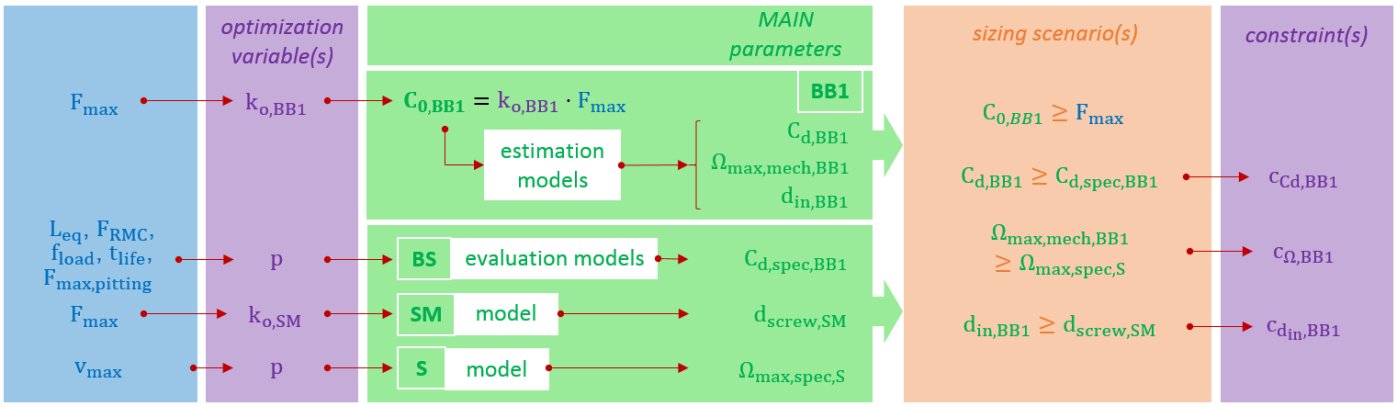

FIGURE U.1: *Design graph of component Ball Bearing (BB1)*

U.2 Ball bearing 2

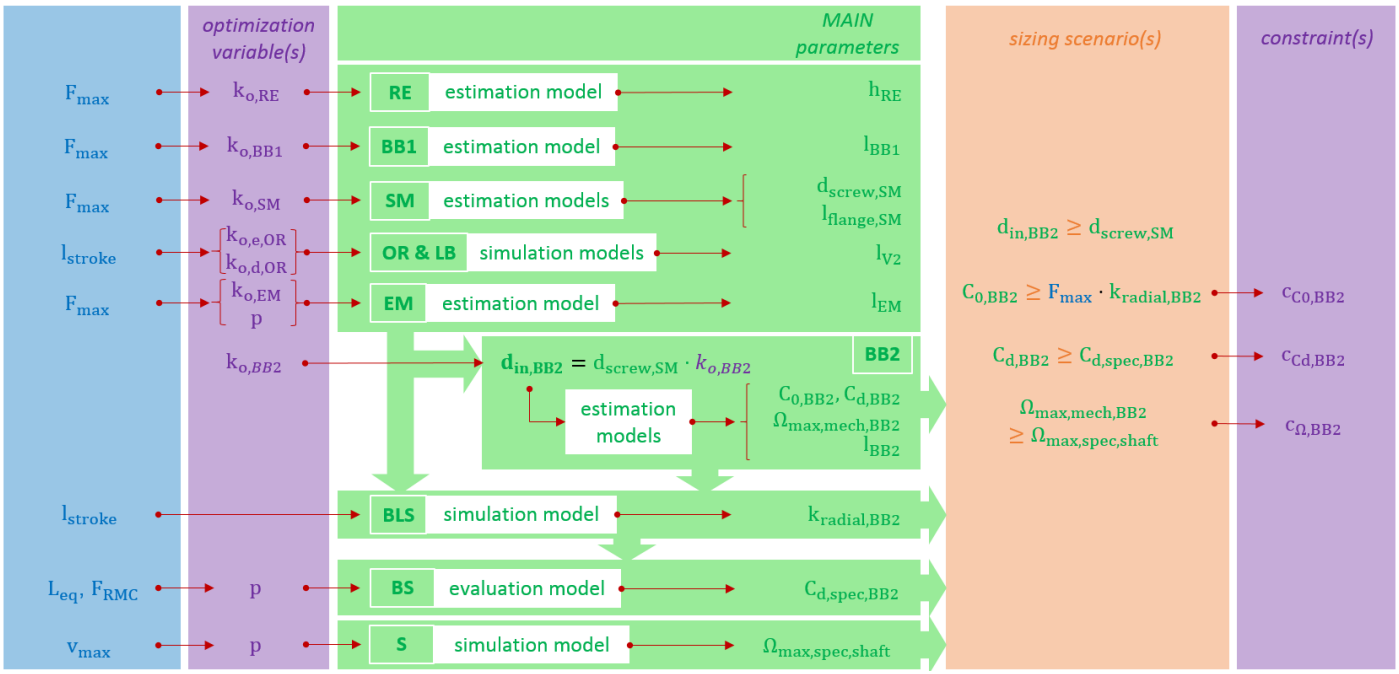

FIGURE U.2: *Design graph of component Ball Bearing (BB2)*

U.3 Electrical motor

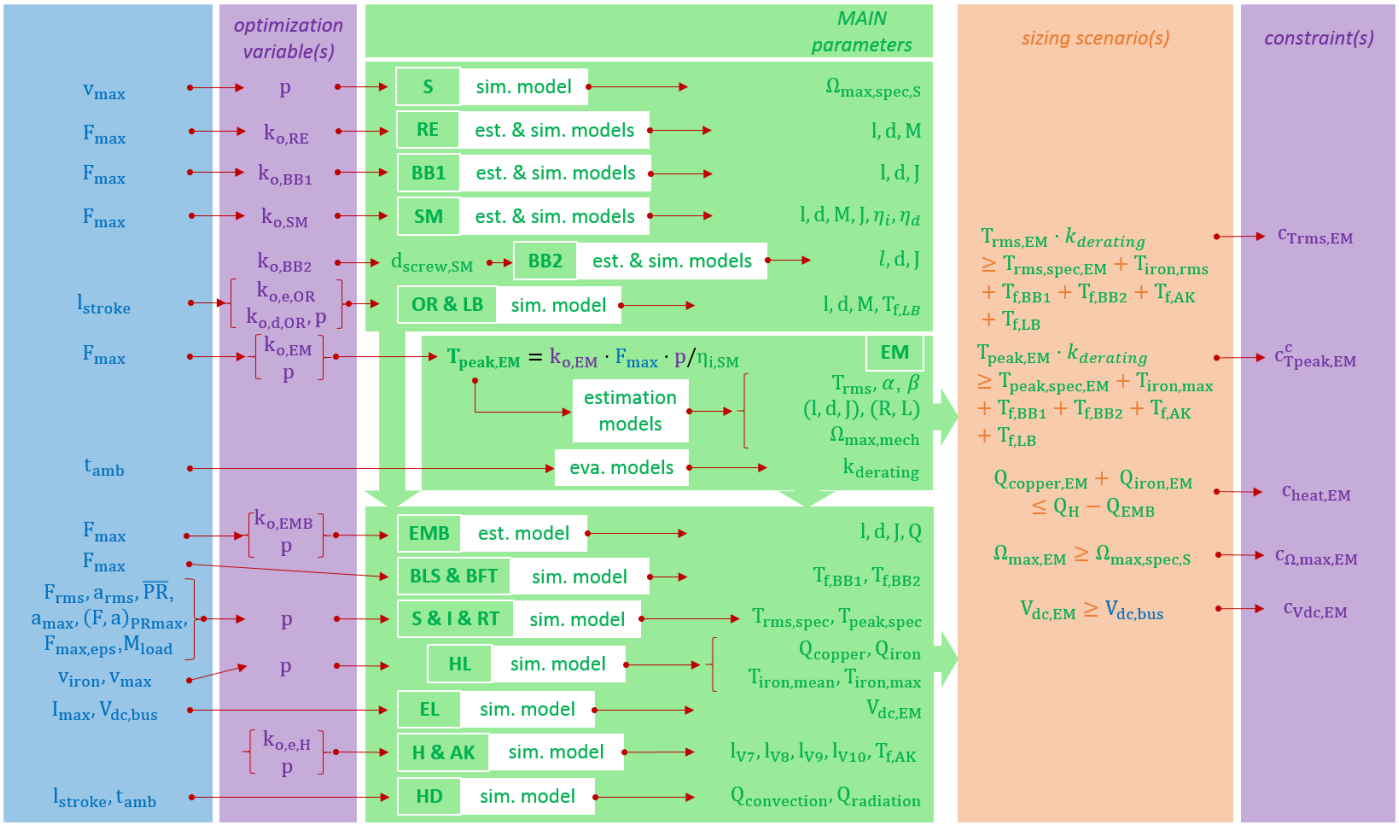

FIGURE U.3: *Design graph of component Electrical Motor (EM)*

U.4 Output rod & Linear bushing

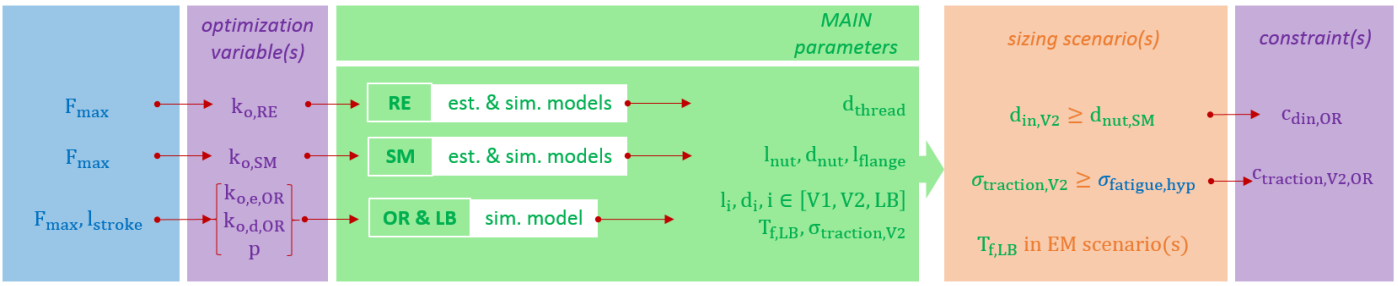

FIGURE U.4: *Design graph of components Output Rod (OR) & Linear Bushing (LB)*

U.5 Housing

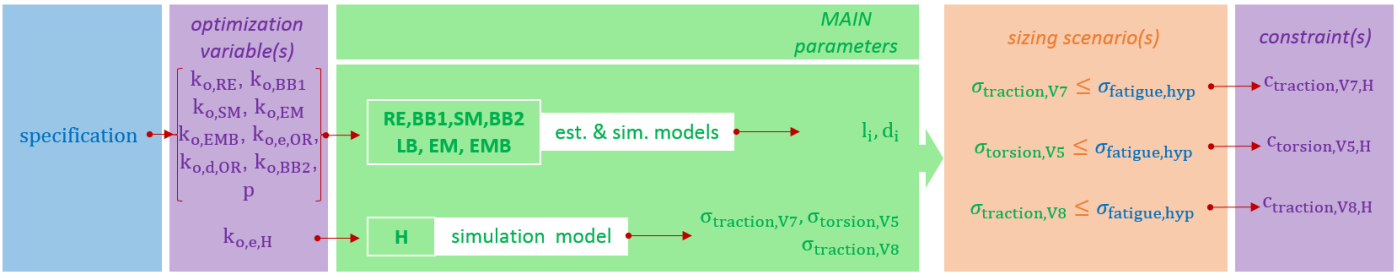

FIGURE U.5: *Design graph of component Housing (H)*

U.6 Antirotation key

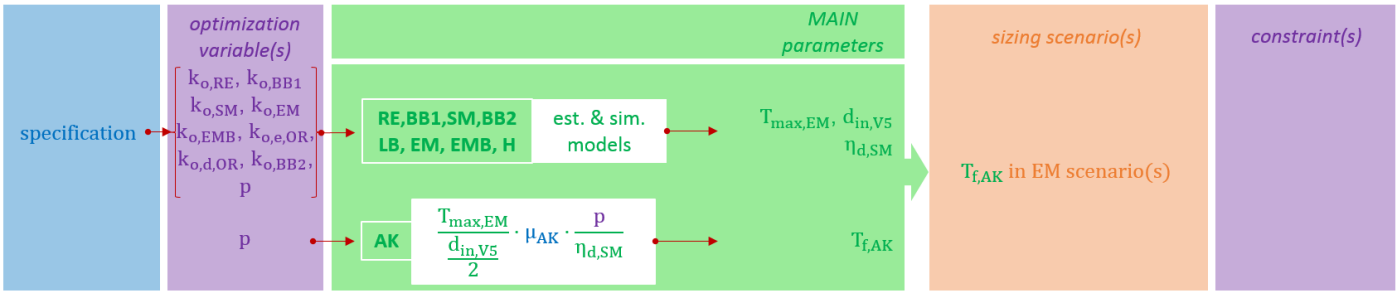

FIGURE U.6: *Design graph of component Antirotation Key (AK)*

U.7 Actuator

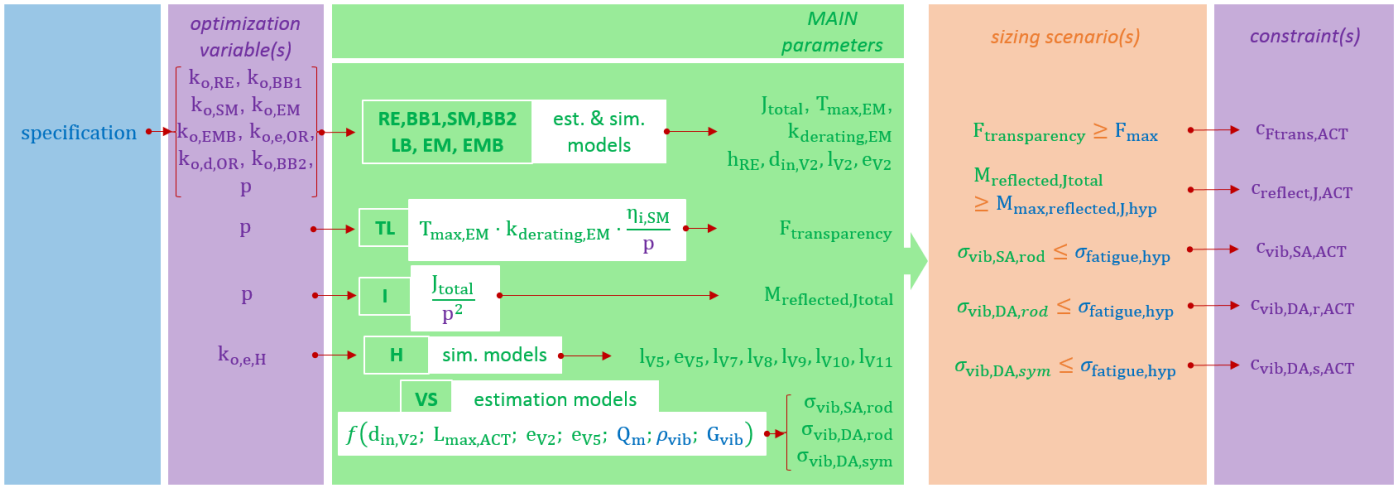

FIGURE U.7: *Design graph of component Actuator (ACT)*

Appendix V

Actuator global sizing procedure

Fig. V.1 presents, with the *Extended Design Structure Matrix (XDSM)* conventions (fig. 5.2, [Lambe and Martins, 2012]), the global procedure applied for the preliminary sizing of the EMA architecture taken as this thesis work base (see section 1.5.6).

Fig. V.1 has a vectorial format allowing zooming in. A comfortable reading of fig. V.1 is guaranteed on the digital version of this manuscript.

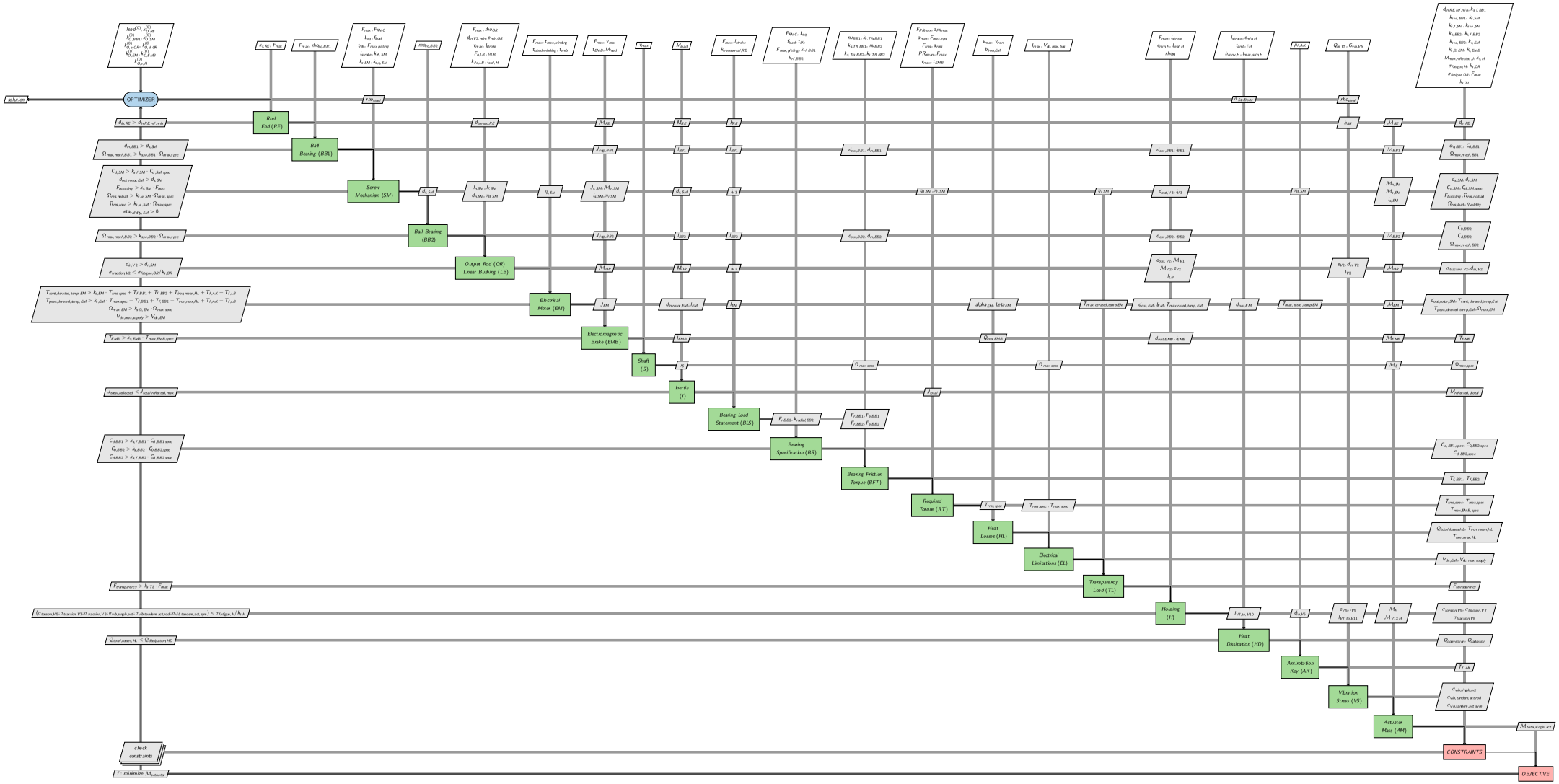

FIGURE V.1: *Actuator global sizing procedure: XDSM representation*

List of Symbols

Symbol	Unit	Name
		Chapter 1
λ	FH^{-1}	failure rate in flight hour
		Chapters 2 & 4
a	$m \cdot s^{-2}$	amplitude of sinusoidal vibratory acceleration
α	$m^{-2} \cdot N^{-2} \cdot W$	copper losses coefficient
a_{max}	$m \cdot s^{-2}$	max acceleration
a_{rms}	$m \cdot s^{-2}$	equivalent continuous acceleration
a_{PRmax}	$m \cdot s^{-2}$	acceleration at maximum power rate
b	$-$	constant of iron losses
β, β'	$rad^{-1.5} \cdot s^{1.5} \cdot W$	iron losses coefficient
B	T or $kg \cdot s^{-2} \cdot A^{-1}$	magnetic field
c	$-$	scaling law power
C_0	N	max static load capability
C_d	N	max fatigue load capability
C_{eq}	$N \cdot m^{-1} \cdot s$	equivalent damping
C_{th}	$J \cdot K^{-1}$	thermal capacity
d	m	dimension or diameter
d_0	m	nominal screw diameter (see table 4.9)
d_{rs}	m	roller-screw nut diameter
D	Pa^{k_2} or $m \cdot N^3$	quantity of cumulated damage (90% reliability)
e	m	thickness
e_1	m	housing thickness
e_2	m	output rod thickness
η_{air}	$kg \cdot m^{-1} \cdot s^{-1}$	dynamic viscosity of air
η_B	$-$	efficiency of screw with $\mathscr{B}$oolean logic
η_d	$-$	direct efficiency of screw
η_i	$-$	indirect efficiency of screw
η_{oil}	$kg \cdot m^{-1} \cdot s^{-1}$	dynamic viscosity of oil
ϵ	$-$	slip ratio
ϵ'	$-$	slip ratio for ideal running condition
ϵ_e	$-$	error
ϵ_r	%	mean of relative errors
ϵ_{rad}	$-$	emissivity of radiation
$\mathscr{E}_c$	$kg \cdot m^2 \cdot s^{-2}$	kinetic energy
E	Pa	Young's modulus
E_b	V	back electromotive force
$f()$	–	*function of* or *dependent on*

f_{load}	hz	load frequency
f_r	hz	first resonance mode frequency
$f_{SL}()$	–	scaling law application
F	N	load
F	–	Front actuator attachment (fig. 3.7)
$F(t)$	N	load on mission profiles
F_a	N	axial load
$F_{dyn,ptp}$	N	dynamic component (peak-to-peak) of pitting load
F_e	N	excitation load applied on M_{eq}
F_{max}	N	max load
F_{PRmax}	N	load at maximum power rate
F_r	N	radial or transverse load
F_{rmc}	N	rolling fatigue load
F_{rms}	N	equivalent continuous load
F_{static}	N	static component of pitting load
Γ	$-$	gear or overdrive ratio
G_{vib}	$m \cdot s^{-2}$	vibratory acceleration
h_{conv}	$W \cdot m^{-2} \cdot K^{-1}$	convection heat transfer coefficient
J	$kg \cdot m^2$	rotating inertia
$k_{derating}$	$-$	derating coefficient (considers temperature environment)
k_{rf}	$-$	reliability factor
k_s	$-$	safety coefficient
k_2	$-$	empirical constant (see section 2.4.1)
K_e	$N \cdot m \cdot rad^{-1} \cdot s$	speed constant
K_{eq}	$N \cdot m^{-1}$	equivalent stiffness
K_m	$m^2 \cdot N^2 \cdot W^{-1}$	motor constant
K_t	$A^{-1} \cdot m \cdot N$	torque constant
l	m	length
λ	rad	helix angle
λ'	deg	helix angle
$\mathscr{L}$	H	motor winding inductance
L	–	Left actuator attachment (fig. 3.7)
L_a	m	actuator total length
L_{eq}	m	total equivalent distance travelled
L_{rs}	m	roller-screw nut length
L_s	m	stroke
μ	$[\mu]$	mean value (Gauss' law, section 2.6.2)
μ	$-$	friction coefficient
μ_0	$T \cdot m \cdot A^{-1}$	magnetic permeability of empty
$M, \mathscr{M}$	kg	mass
M_{eq}	kg	equivalent mass
n_i	–	number of "i"
n_{turn}	$-$	number of winding turns (electrical motor)
ν	$m^2 \cdot s^{-1}$	kinematic viscosity
N	rev	life rating in number of cycles
N_{10}	$10^6\ rev$	life rating in 10^6 revolutions
ω	$rad \cdot s^{-1}$	angular speed
ω_e	$rad \cdot s^{-1}$	electrical speed
Ω	RPM	angular speed
p	$m \cdot rad^{-1}$	screw thread lead
p'	$m \cdot rad^{-1}$	screw thread pitch (see table 4.9)

pU	$Pa \cdot m \cdot s^{-1}$	bushing pressure–speed factor
P	$[P]$, Pa	material property or pressure
$\mathscr{P}$	W	power
π_i	-	π-number from dimensional analysis
PR	$N \cdot m \cdot s^{-2}$	power rate
$\overline{PR}$	$N \cdot m \cdot s^{-2}$	mean power rate
Q	W	heat
Q_m	$-$	quality factor
r	m	radius
ρ	$kg \cdot m^{-3}$	density
$\mathscr{R}$	Ohm	motor winding resistance
R	$-$	reduction ratio
R_i	%	ratio of specification indicators
R	–	Right actuator attachment (fig. 3.7)
Ra	m	surface roughness
R_{th}	$m^2 \cdot K \cdot W^{-1}$	thermal resistance
s	$-$	Sommerfeld's number (lubrication quality parameter)
$sec()$	–	secant function
σ	Pa	mechanical stress
σ	$[\sigma]$	standard deviation (Gauss' law, section 2.6.2)
σ_r	%	standard deviation of relative errors
σ_{SB}	$m^{-2} \cdot K^{-4} \cdot W$	Stefan-Boltzmann's constant
S	m^2	surface
SN	$-$	service number
t	s	time
τ_{th}	s	thermal time constant
t_{EMB}	s	time for brake to stop shaft
θ	$^\circ C$	temperature
t_{life}	s	total actuator lifespan
t_T	s	total duration of mission
T	$m \cdot N$	torque
T	–	actuator attachment point on tail rotor swashplate
T_0	$m \cdot N$	ideal torque (no friction)
T_p	$m \cdot N$	peak torque
U	m	displacement of M_{eq}
u	m	actuator deflection
v	$m \cdot s^{-1}$	speed
v_a	$m \cdot s^{-1}$	actuator deflection speed
φ	rad	half thread angle
v_{iron}	m	speed representative of iron losses
v_m	$m \cdot s^{-1}$	speed of M_{eq}
v_{max}	$m \cdot s^{-1}$	max speed
$\mathscr{V}$	m^3	volume
V	V	voltage
V_s	V	voltage supply
V1,...,V12	–	actuator volumes identified in fig. 4.38
x	m	vibratory displacement amplitude
ξ	$-$	equivalent damping coefficient
$x(t)$	m	position on mission profiles
$\dot{x}(t)$	$m \cdot s^{-1}$	speed from mission profiles
$\ddot{x}(t)$	$m \cdot s^{-2}$	acceleration from mission profiles

$X(t)$	$[X]$	any time-varying variable
y^*	$-$	scaling ratio y/y_{ref}
y_{ref}	$[y]$	characteristic of component of reference used in scaling law
Y_0	$[Y]$	value of Y at first resonance mode

Chapter 3

a	m	blade chord
A	N	empirical constant
$\alpha_F, \alpha_L, \alpha_R$	rad	actuator angular position on swashplate (fig. 3.7)
α_x, α_y	rad	rotating degree of freedom of swashplate (fig. 3.7)
B	N	empirical constant
B	–	attachment point between pitch rod and pitch horn
b	m	blade equivalent width
β	rad	flap angle $(\overrightarrow{X_2}; \overrightarrow{X_3})$ (fig. 3.1 & 3.6)
c	$N \cdot m \cdot rad^{-1}$	spring constant
c_{vf}	$N \cdot m^{-1} \cdot s$	viscous friction coefficient
C_m	$-$	coefficient of moment
C_p	$-$	lift coefficient
C_{zp}	$-$	local lift coefficient
d	$N \cdot m \cdot s \cdot rad^{-1}$	damping constant
δ	rad	drag angle $(\overrightarrow{X_1}; \overrightarrow{X_2})$ (fig. 3.1 & 3.6)
δ_0	rad	neutral drag angle
e	m	blade eccentricity (OA distance, fig. 3.6)
η	$-$	loss factor
$\mathscr{E}_c$	$kg \cdot m^2 \cdot s^{-2}$	kinetic energy
F	N	load
F	–	Front actuator attachment (fig. 3.7)
F_P	N	lifting load
F_T	N	dragging load
g	$m \cdot s^{-2}$	hearth gravity acceleration
γ	$-$	Lock number*
i	rad	blade incidence
I_p	$kg \cdot m^2$	blade inertia in flap and drag
I_θ	$kg \cdot m^2$	blade inertia in rotation around its longitudinal axis
l	m	blade equivalent thickness
λ	$-$	ratio $\gamma/16$
l_{arm}	m	drag damper lever arm
L	–	Left actuator attachment (fig. 3.7)
$\mathscr{L}$	$kg \cdot m^2 \cdot s^{-2}$	Lagrange's quantity
λ_β	$N \cdot m \cdot rad^{-1}$	coefficient of viscous pitch moment of bearing
λ_δ	$N \cdot m \cdot rad^{-1}$	coefficient of viscous drag moment from damper
λ_θ	$N \cdot m \cdot rad^{-1}$	coefficient of viscous flap moment of bearing
k_h	$-$	harmonic number used in test model
K'	$N \cdot m^{-1}$	storage modulus
K''	$N \cdot m^{-1}$	loss modulus
K_β	$N \cdot m \cdot rad^{-1}$	stiffness in flapping
K_c	$N \cdot m^{-1}$	complex stiffness
K_δ	$N \cdot m \cdot rad^{-1}$	stiffness in drag
K_{hyd}	$N \cdot m^{-1}$	equivalent hydraulic stiffness

K_θ	$N \cdot m \cdot rad^{-1}$	stiffness in pitch
l_i	m	length
m	kg	mass
m_p	kg	blade mass
m_s	$kg \cdot m$	static moment
M	$-$	Mach number
M_i	$N \cdot m$	moment
M_{rJ}	kg	reflected inertia
ω	$rad \cdot s^{-1}$	angular speed
ω_0	$rad \cdot s^{-1}$	eigenfrequency
ω_λ	$rad \cdot s^{-1}$	drag eigenfrequency
Ω	$rad \cdot s^{-1}$	$= \dot{\psi}$, rotor mast speed
ϕ	rad	slope
ϕ_i	rad	loading phaseshift of blade i
ψ	rad	rotor mast rotation angle $(\overrightarrow{X_0}; \overrightarrow{X_1})$ (fig. 3.1 & 3.6)
$\dot{\psi}$	$rad \cdot s^{-1}$	rotor mast speed
r	m	blade length (AM distance, fig. 3.6)
ρ_{air}	$kg \cdot m^{-3}$	air density
ρ_b	$kg \cdot m^{-3}$	blade equivalent density
$\mathscr{R}_i$	–	sketches of reference ($i \in [g, 1, 2, 3, 4]$, see section 3.2.3.2)
R	m	rotor radius at blade tip
R	–	Right actuator attachment (fig. 3.7)
R_s	m	swashplate radius
θ	rad	pitch angle $(\overrightarrow{Z_3}; \overrightarrow{Z_4})$ (fig. 3.1 & 3.6)
θ_0	rad	neutral pitch angle
$x_d d$	m	drag damper strain during a motion of δ
ξ	$-$	damping coefficient
φ	rad	pitch horn phaseshift from flap axis on blade plane (fig. 3.16)
v, V	$m \cdot s^{-1}$	speed
V_x	$m \cdot s^{-1}$	helicopter advancing speed
$\overrightarrow{X_i}$	–	reference vector (see section 3.2.3.2)
$\overrightarrow{Y_i}$	–	reference vector (see section 3.2.3.2)
z	m	height
z_0	m	lowest height of swashplate orthogonal to rotor mast
z_G	m	height at gravity center
$\overrightarrow{Z_i}$	–	reference vector (see section 3.2.3.2)
$\mathscr{W}$	$kg \cdot m^2 \cdot s^{-2}$	work

Chapter 5

A	$[A]$	scaling law constant from components of reference
B	$-$	scaling law power
c_i	$[c_i]$	constraint i
c_i^c	$[c_i]$	consistency constraint i
$f_{scen}()$	–	motor peak torque scenarios (see section 4.3.2.1.2)
f_{obj}, f	$[f]$	objective function
$\mathcal{H}_f$	$[f]$	(nxn) Hessian's matrix of $f(x_1, ..., x_n)$
k_o	$-$	oversizing coefficient $\subset [1; +\inf[$
k_u	$-$	undersizing coefficient $\subset [1; +\inf[$
p_{SM}	$m \cdot rad^{-1}$	screw mechanism thread lead

x	$[x]$	any design variable or optimization variable
x_1, x_2, x_3	$[x_1]$, $[x_2]$, $[x_3]$	arbitrary variables to illustrate the *Sellar problem*
X_i^t	$[X_i]$	coupling variable X_i
y_1, y_2	$[y_1]$, $[y_2]$	arbitrary variables to illustrate the *Sellar problem*

For all other symbols in this Chapter, please see the symbol list of Chapters 2 & 4

Bibliography

[AFNOR, 2006] AFNOR. *Ball screw norm. Part 5: Static and dynamic axial load ratings and operational lifetime.* French norm, NF ISO 3408-5 E 22-201-5, **2006**.

[Air, 2020] *Airfoil database.* Online tool available at http://airfoiltools.com/airfoil/details?airfoil=naca001234-il (accessed on 3 September 2020).

[Airbus, 2021] Airbus, News. *Airbus helicopters starts flight tests with engine back-up system.* **2021**. Available at www.airbus.com/en/newsroom/press-releases (accessed on September 2021).

[Airbus, 2022a] Airbus, News. *First helicopter flight powered solely by sustainable aviation fuel.* **2022**. Available at www.airbus.com/en/newsroom/press-releases (accessed on June 2022).

[Airbus, 2022b] Airbus, Products. *H160 helicopter*. **2022**. Available at https://www.airbus.com/en/products-services/helicopters/civil-helicopters/h160 (accessed on June 2022).

[Airbus, 2022c] Airbus, Products & Services. *Helicopters*. **2022**. Available at https://www.airbus.com/en/products-services/helicopters (accessed on June 2022).

[Airbus, 2022d] Airbus, Products. *Vahana: single-seat evtol demonstrator*. **2022**. Available at https://www.airbus.com/en/urbanairmobility/cityairbus-nextgen/vahana (accessed on June 2022).

[Airbus, 2022e] Airbus, Products. *VSR700: the multi-mission naval UAS*. **2022**. Available at https://www.airbus.com/en/products-services/defence/uas/vsr700 (accessed on June 2022).

[Airbus et al., 2022] Airbus, EDF, IMACS, ONERA, and Phimeca. *Openturns, an open source initiative for the treatment of uncertainties*. **2022**. Available at https://openturns.github.io/openturns/latest/index.html (accessed on June 2022).

[Alexandrov and Lewis, 2000] Alexandrov, N. and Lewis, R. Algorithmic perspectives on problem formulations in MDO. In *Proceedings of 8th symposium on multidisciplinary analysis and optimization*, Long Beach, CA, U.S.A., 6–8 September 2000, p. 4719.

[Amzallag et al., 1993] Amzallag, B., Bignonnet, C., Flavenot, F., Gerey, M., and Olagnon, R. (1993). *Fatigue sous sollicitations d'amplitude variable – méthode rainflow de comptage des cycles*, french norm, AFNOR 03-406. Technical report, **1993**.

[Anderson et al., 2022] Anderson, M., Chanthavane, S., Broshkevitch, A., Braden, P., Bassford, C., Kim, M., Fantini, M., Konig, S., Owens, T., and Sorensen, C. A survey of web-based tools for collaborative engineering design. *Journal of Mechanical Design*, **2022**, volume 144.

[Andersson et al., 1998] Andersson, J.; Krus, P.; Nilsson, K. Optimization as a support for selection and design of aircraft actuation systems. In *Proceedings of 7th AIAA/USAF/NASA/ISSMO Symposium on Multidisciplinary Analysis and Optimization*, St. Louis, MO, USA, 2–4 September 1998; pp. 4887.

[Arpiany and Michon, 2021] Arpiany, P. and Michon, T. Ecopulse: a distributed propulsion hybrid aircraft demonstrator. In *Proceedings of MEA2021, More Electric Aircraft conference*, Bordeaux, France, 20–21 October 2021.

[Avi, 2020] L'Avionnaire. *Aerodynamique, centre de poussée et foyer d'une aile.* Online resource available at https://www.lavionnaire.fr/AerodynCPFoyer.php (accessed on 3 September 2020).

[Barber, 2018] Barber, J.R. *Contact mechanics*; Springer International Publishing: Berlin, Germany. 2018.

[Barkey, 2018a] Barkey, M. *Rainflow cycle counting part 1/3–introduction*. Mechanics video channel. 2018. Online resource available at https://www.youtube.com/watch?v=3Ak-zkbBuOQ (accessed on June 2021).

[Barkey, 2018b] Barkey, M. *Rainflow cycle counting part 2/3–algorithm development*. Mechanics video channel. 2018. Online resource available at https://www.youtube.com/watch?v=CZOSbW89F1o (accessed on June 2021).

[Bazzani, 2018] Bazzani, M. *Guimbal Cabri G2*. 2018. Online resource available at https://www.heli-archive.ch/en/helicopters/in-depth-articles/guimbal-cabri-g2?L=0 (accessed on 15 June 2022).

[Boeing, 2022] Boeing. V-22 osprey: Unlike any aircraft in the world. 2022. Online resource available at https://www.boeing.com/defense/v-22-osprey/ (accessed on June 2022).

[Botten et al., 2000] Botten, S.L., Whitley, C.R., and King, A.D. Flight control actuation technology for next-generation all-electric aircraft. *Technology Review Journal*, **2000**, volume 8, pp. 55–68.

[Boudon, 2014] Boudon, B. *Méthodologie de modélisation des systèmes mécatroniques complexes à partir du multi-bond graph : application à la liaison BTP-fuselage d'un hélicoptère*. Ph.D. Thesis, Ecole nationale supérieure d'arts et métiers - ENSAM, Paris, France, 2014.

[Boukamel, 2006] Boukamel, A. *Modélisation mécaniques et numériques des matériaux et structures en élastomères*. Ph.D. thesis, Université de la Méditerranée-Aix-Marseille II, Aix-en-Provence, Marseille, France, 2006.

[Browning, 2001] Browning, T.R. Applying the design structure matrix to system decomposition and integration problems: a review and new directions. *IEEE Transactions on Engineering management*, **2001**, volume 48, pp. 292–306.

[Budinger, 2014] Budinger, M. *Preliminary design and sizing of actuation systems*. HDR (Accreditation to Direct Research), University of Paul Sabatier UPS, Toulouse, France, 2014. pp. 30, 32, 56-57. Available at https://hal.archives-ouvertes.fr/tel-01112448/file/HDR_Budinger_global_final_72dpi.pdf.

[Budinger, 2020] Budinger, M. *Electromagnetic actuator magnetic field and magnetic force calculations*. Engineering course at INSA Toulouse, Toulouse, France, 2020, pp. 103.

[Budinger, 2021] Budinger, M. *Dimensionnement des chaines d'énergie*. Course of System Engineering (I5ISCM21 group), INSA Toulouse, Toulouse, France, 2021.

[Budinger et al., 2012a] Budinger, M., Liscouët, J., Hospital, F., and Maré, J. Estimation models for the preliminary design of electromechanical actuators. *Proceedings of the Institution of Mechanical Engineers, Part G: Journal of Aerospace Engineering*, **2012**, volume 226: pp. 243–259.

[Budinger et al., 2012b] Budinger, M., Liscouet, J., Hospital, F., and Multon, B. *TI Techniques de l'Ingénieur—tri152—Mise en place des modèles d'estimation pour la conception préliminaire*; Editions des Techniques de l'Ingénieur: Saint-Denis, France, 2012.

[Budinger et al., 2013] Budinger, M., Hospital, F., Liscouet, J., Multon, B., Mare, J.-C., and Reysset, A. *TI Techniques de l'Ingénieur—bm8026—Chaîne de transmission de puissance mécatroniques – Modèles d'estimation*; Editions des Techniques de l'Ingénieur: Saint-Denis, France, 2013.

[Budinger et al., 2014] Budinger, M.; Reysset, A.; Halabi, T.E.; Vasiliu, C.; Maré, J.C. Optimal preliminary design of electromechanical actuators. *Proceedings of the Institution of Mechanical Engineers, Part G: Journal of Aerospace Engineering*, **2014**, volume 228, pp. 1598–1616.

[Budinger et al., 2015] Budinger, M.; Reysset, A.; Maré, J.C. Preliminary design of aerospace linear actuator housings. *Aircraft Engineering and Aerospace Technology: An International Journal*, **2015**, volume 87, pp. 224–237.

[Budinger et al., 2019] Budinger, M., Hazyuk, I., and Coïc, C. *Multi-physics Modeling of Technological Systems*; John Wiley & Sons: Hoboken, USA; ISTE: London, UK. 2019. ISBN: 978-1-78630-378-3.

[Budinger et al., 2020] Budinger, M.; Reysset, A.; Ochotorena, A.; Delbecq, S. Scaling laws and similarity models for the preliminary design of multirotor drones. *Aerospace Science and Technology*, **2020**, *98*, 105658.

[Budynas et al., 2008] Budynas, R.G., Nisbett, J.K., et al. *Shigley's mechanical engineering design*; McGraw-Hill: New York, USA. 2008.

[Bui, 2011] Bui, A.T. *Caractérisation et modélisation du comportement des matériaux magnétiques doux sous contrainte thermique*. Ph.D. thesis, Université Claude Bernard-Lyon I, Lyon, France, 2011, pp. 24.

[Chellil, 2008] Chellil, A. *Identification et modélisation par éléments finis des charges dynamiques du rotor principale d'hélicoptère*. Ph.D. thesis, Université M'hamed Bougara. Faculté des sciences de l'ingenieur, Boumerdès, Algeria, 2008. Also, resource available as a printed book (ISBN: 978-613-1-53467-6)

[Chen, 1987] Chen, Robert T.N. Flap-lag equations of motion of rigid, articulated rotor blades with three hinge sequences. Technical report No. NASA-TM-100023. 1987.

[Chevalier, 2004] Chevalier, A. *Guide du dessinateur industriel: pour maîtriser la communication technique*; Hachette Technique: Paris, France, 2004. ISBN: 2.01.16.8831.0

[Cochoy et al., 2007] Cochoy, O., Carl, U. B., and Thielecke, F. Integration and control of electromechanical and electrohydraulic actuators in a hybrid primary flight control architecture. In *International Conference on Recent Advances in Aerospace Actuation Systems and Components (R3ASC)*, Toulouse, France, 13–15 June 2007; INSA Toulouse, France; pp. 1–8.

[Cooper, 1968] Cooper, D. *Tables of hertzian contact-stress coefficients*. Coordinated Science Laboratory Report no. R-387, 1968.

[Cros and Viarouge, 2002] Cros, J. and Viarouge, P. *Synthesis of high performance pm motors with concentrated windings*. IEEE Transactions on Energy Conversion, **2002**, volume 17, pp. 248–253.

[Dareck et al., 2011] Dareck, M., Edelstenn, C., and Ender, T. *Flightpath 2050 Europe's vision for aviation*. Technical report. 2011. Available at https://ec.europa.eu/transport/sites/transport/files/modes/air/doc/flightpath2050.pdf (accessed on 5 September 2020).

[Darren, 2022] Darren, J. *Deploy your Python script on the web with Flask*. Realpython course. 2022. Online resource available at https://realpython.com/courses/deploy-python-script-web-flask/ (accessed on June 2022).

[De and White, 2001] De, S.K. and White, J.R. *Rubber technologist's handbook*, volume 1; Smithers Rapra Publishing: Akron, USA, 2001.

[Defoort et al., 2012] Defoort, S., Balesdent, M., Klotz, P., Schmollgruber, P., Morio, J., Hermetz, J., Blondeau, C., Carrier, G., and Bérend, N. Multidisciplinary aerospace system design: Principles, issues and ONERA experience. *Aerospace Lab*, 2012, no. 4, pp. 1–15.

[Delbecq, 2018] Delbecq, S. *Knowledge-based multidisciplinary sizing and optimization of embedded mechatronic systems-application to aerospace electro-mechanical actuation systems*. Ph.D. Thesis, INSA, Toulouse, France, 2018.

[Delbecq et al., 2020a] Delbecq, S.; Budinger, M.; Reysset, A. Benchmarking of monolithic MDO formulations and derivative computation techniques using OpenMDAO. *Structural and Multidisciplinary Optimization*, **2020**, volume 62, pp. 645–666.

[Delbecq et al., 2020b] Delbecq, S.; Budinger, M.; Ochotorena, A.; Reysset, A.; Defaÿ, F. Efficient sizing and optimization of multirotor drones based on scaling laws and similarity models. *Aerospace Science and Technology*, **2020**, volume 102, 105873.

[Doat, 2016] Doat, G. *Le pilotage des helicoptères*, Manuel de vol; Editions JPO: Levallois-Perret, France, 2016. ISBN: 978-2-37301-043-5

[DPS, 2022] DPS. *Karren, le seul outil collaboratif pour la conception de produits complexes*. 2022. Online resource available at https://www.dps-fr.com/karren (accessed on June 2022).

[Duprat, 1997] Duprat, D. *TI Techniques de l'Ingénieur—bm5052v1—Fatigue et mécanique de la rupture des pièces en alliage léger*; Editions des Techniques de l'Ingénieur: Saint-Denis, France, 1997, pp. 7.

[EASA, 2007] European Union Aviation Safety Agency (EASA). *Certification Specifications and Acceptable Means of Compliance for Large Aeroplanes CS-25 Amendment 4*; EASA: Cologne, Germany, 2007.

[Electropaedia, 2005] Electropaedia. *Electric drives – Brushless DC/AC and reluctance motors description & applications*. 2005. Online resource available at https://www.mpoweruk.com/motorsbrushless.htm (accessed on April 2020).

[Estival, 2015] Estival, P. *Concept Innovant d 'Actionneur Electromécanique pour la Commande de Vol d'Hélicoptère de Nouvelle Génération*. Ph.D. thesis, Université Paris-Saclay (ComUE), Paris, France, 2015.

[ETEL, 2013] ETEL (manufacturer). *Torque motors TMM*. Product range data sheets. 2013.

[ETEL, 2022] ETEL (manufacturer). *Torque motors TMB+*. Product range data sheets. 2022. Available at https://www.etel.ch/torque-motors/tmb/specifications/ (accessed on May 2022).

[Eynard et al., 2005] Eynard, B., Liénard, S., Charles, S., and Odinot, A. Web-based collaborative engineering support system: applications in mechanical design and structural analysis. *Concurrent engineering*, **2005**, volume 13, no. 2, pp. 145–153.

[FAA, 2014] Federal Aviation Administration (FAA). *System safety handbook.* Appendix A: Glossary. Technical report. 2014.

[FAA, 2019] Federal Aviation Administration (FAA). *Helicopter Flying Handbook*; US Department of Transportation, 2019. Available at https://www.faa.gov/sites/faa.gov/files/regulations_policies/handbooks_manuals/aviation/helicopter_flying_handbook/helicopter_flying_handbook.pdf (accessed on 30 July 2022).

[Feld, 2000a] Feld, G. *Modélisation de la machine synchrone*. Lecture. 2000.

[Feld, 2000b] Feld, G. Modélisation de l'onduleur. In [Feld, 2000a], 2000, pp. 22–24.

[Ferry, 1980] Ferry, J.D. *Viscoelastic properties of polymers*; John Willey & Sons: New York, USA, 1980.

[Flankl et al., 2017] Flankl, M., Tüysüz, A., and Kolar, J.W. Cogging torque shape optimization of an integrated generator for electromechanical energy harvesting. *IEEE Transactions on Industrial Electronics*, **2017**, volume 64, no. 12, pp. 9806–9814.

[Fuerst and Neuheuser, 2007] Fuerst, D. and Neuheuser, T. (2007). Development, prototype production and testing of an electromechanical actuator for a swash-plateless primary and individual helicopter blade control system. In *Proceedings of the 1st International Workshop on Aircraft System Technologies (AST)*, Hamburg, Germany, 29–30 March 2007; pp. 7–19.

[Gallard et al., 2018] Gallard, F., Vanaret, C., Guénot, D., Gachelin, V., Lafage, R., Pauwels, B., Barjhoux, P.-J., and Gazaix, A. GEMS: A Python library for automation of multidisciplinary design optimization process generation. In *Proceedings of AIAA/ASCE/AHS/ASC Structures, Structural Dynamics, and Materials Conference*, Kissimmee, Florida, USA, 8–12 January 2018. eISBN: 978-1-62410-532-6

[Gallard et al., 2022] Gallard, F., Vanaret, C., Guénot, D., Gachelin, V., Lafage, R., Pauwels, B., Barjhoux, P.-J., and Gazaix, A. *GEMSEO: A generic engine for multidisciplinary scenarios, exploration and optimization*. 2022. Online resource available at https://gemseo.readthedocs.io/en/stable/index.html (accessed on June 2022).

[GALTIER et al., 2019] GALTIER, A., MUNIER, R., PHILIPPOT, A., and WEBER, B. *TI Techniques de l'Ingénieur—m4170—Essais de fatigue – Domaine des grands nombres de cycles*; Editions des Techniques de l'Ingénieur: Saint-Denis, France, 2019.

[Gazaix et al., 2017] Gazaix, A., Gallard, F., Gachelin, V., Druot, T., Grihon, S., Ambert, V., Guénot, D., Lafage, R., Vanaret, C., Pauwels, B., et al. Towards the industrialization of new mdo methodologies and tools for aircraft design. In *Proceedings of 18th AIAA/ISSMO Multidisciplinary Analysis and Optimization Conference*, Denver, Colorado, USA, 5–9 June 2017, pp. 3149. eISBN: 978-1-62410-507-4

[GGB, 2015] GGB (manufacturer). *High performance bushings*. Product range data sheets. 2015.

[Gill et al., 2005] Gill, P.E., Murray, W., and Saunders, M.A. SNOPT: An SQP algorithm for large-scale constrained optimization. *SIAM review*, **2005**, volume 47, no. 1, pp. 99–131.

[Gray et al., 2010] Gray, J., Moore, K., and Naylor, B. (2010). OpenMDAO: An open source framework for multidisciplinary analysis and optimization. In *Proceedings of 13th AIAA/ISSMO Multidisciplinary Analysis Optimization Conference*, Fort Worth, Texas, USA, 13–15 September 2010, pp. 9101. eISBN: 978-1-60086-954-9

[Gray et al., 2019] Gray, J.S., Hwang, J.T., Martins, J.R., Moore, K.T., and Naylor, B.A. OpenMDAO: An open-source framework for multidisciplinary design, analysis, and optimization. *Structural and Multidisciplinary Optimization*, **2019**, volume 59, no. 4, pp. 1075–1104.

[Gray et al., 2022] Gray, J.S., Hwang, J.T., Martins, J.R., Moore, K.T., and Naylor, B.A. OpenMDAO: an open-source framework for efficient multidisciplinary optimization. Online resource available at `https://openmdao.org/` (accessed on June 2022).

[Grellet, 1989] Grellet, G. *TI Techniques de l'Ingénieur—d3450v1—Pertes dans les machines tournantes*; Editions des Techniques de l'Ingénieur: Saint-Denis, France, 1989.

[Guidi et al., 2021] Guidi, G., Amokrane, M., Borgarelli, N., and Malleret, F. (2021). Benefits and challenges of electro-mechanical actuation on aircraft landing and braking systems. In *Proceedings of MEA2021 More Electric Aircraft conference*, Bordeaux, France, 20–21 October 2021.

[Guimbal, 2022] Guimbal Industries. Cabri G2. Online resource available at `https://www.guimbal.com/` (accessed on June 2022).

[Hagberg et al., 2008] Hagberg, A., Swart, P., and S Chult, D. *Exploring network structure, dynamics, and function using networkx*. Technical report, Los Alamos National Lab (LANL), Los Alamos, NM (USA), 2008, no. LA-UR-08-05495; no. LA-UR-08-5495.

[Halme and Andersson, 2010] Halme, J. and Andersson, P. Rolling contact fatigue and wear fundamentals for rolling bearing diagnostics-state of the art. In *Proceedings of the Institution of Mechanical Engineers, Part J: Journal of Engineering Tribology*, UK, April 2010, volume 224, no. 4, pp. 377–393.

[Hansen, 2006] Hansen, N. The CMA evolution strategy: a comparing review. *Towards a new evolutionary computation*, **2006**, pp. 75–102.

[Hehenberger et al., 2010] Hehenberger, P.; Poltschak, F.; Zeman, K.; Amrhein, W. Hierarchical design models in the mechatronic product development process of synchronous machines. *Mechatronics*, **2010**, Special Issue on Theories and Methodologies for Mechatronics Design, volume 20, pp. 864–875. Available at https://doi.org/10.1016/j.mechatronics.2010.04.003.

[Holmes, 2019] Holmes, M.H. Chapter: Dimensional Analysis. In *Introduction to the Foundations of Applied Mathematics*; Springer: Berlin/Heidelberg, Germany, 2019; pp. 1–47.

[Hrabovsky and Susskind, 2020] Hrabovsky, G. and Susskind, L. *Classical mechanics: the theoretical minimum*; Penguin Books UK: London, UK, 2020.

[Incropera et al., 2007] Incropera, F.P., Lavine, A.S., Bergman, T.L., and DeWitt, D.P. *Fundamentals of heat and mass transfer*; Wiley: New York, USA, 2007.

[Inglebert and Lemaire Caron, 2012] Inglebert, Geneviève; Da Silva Botelho, T. and Lemaire Caron, I. *TI Techniques de l'Ingénieur—tri200—Théorie du contact de hertz – contacts ponctuels ou linéiques*; Editions des Techniques de l'Ingénieur: Saint-Denis, France, 2012.

[Iordanidis and Dellac, 2010] Iordanidis, G. and Dellac, S. DRESS: Distributed and Redundant Electro-mechanical nose wheel Steering System. *SAE International Journal of Aerospace*, **2010**, volume 2, no. 1, pp. 46.

[Jaafar, 2011] Jaafar, A. Analysis of Mission Profiles and Environment Variables for Integration into the Systemic Design Processus. Ph.D. Thesis, INP, Toulouse, France, 2011.

[Jenkins Jr, 1967] Jenkins Jr, J.L. *A numerical method for studying the transient blade motions of a rotor with flapping and lead-lag degrees of freedom*. Technical report, no. NASA-TN-D-4195, 1967.

[Jensen et al., 2000] Jensen, S.C., Jenney, G.D., and Dawson, D. Flight test experience with an electro-mechanical actuator on the F-18 systems research aircraft. In *Proceedings of 19th Digital Avionics Systems Conference (DASC)*, Philadelphia, PA, USA, 7–13 October 2000. IEEE publisher, 2000, volume 1, cat. no. 00CH37126, pp. 2E3/1–2E310. Available at https://www.nasa.gov/centers/dryden/pdf/88699main_H-2425.pdf.

[Jiao et al., 2019] Jiao, Z.; Yu, B.; Wu, S.; Shang, Y.; Huang, H.; Tang, Z.; Wei, R.; Li, C. An intelligent design method for actuation system architecture optimization for more electrical aircraft. *Aerospace Science and Technology*, **2019**, *93*, 105079.

[Jrad, 2014] Jrad, H. *Etude du comportement dynamique non linéaire des composants viscoélastiques: Caractérisation, modélisation et identification*. Ph.D. thesis, Ecole Centrale Paris; Paris, France, École nationale d'ingénieurs de Sfax, Sfax, Tunisia, 2014.

[Jufer, 1996] Jufer, M. Design and losses-scaling law approach. In Proceedings of the Nordic Research Symposium Energy Efficient Electric Motors and Drives, Skagen, Denmark, 12–16. August 1996; pp. 21–25. Available at https://www.researchgate.net/profile/Marcel-Jufer/publication/288811698_Design_and_Losses-Scaling_Law_Approach/links/6146d76e3c6cb310697a4154/Design-and-Losses-Scaling-Law-Approach.pdf (accessed on 24 August 2022).

[Karam, 2007] Karam, W. *Générateurs de forces statiques et dynamiques à haute puissance en technologie électromécanique*. Ph.D. thesis, Institut National des Sciences Appliquées de Toulouse (INSA), Toulouse, France, 2007.

[KOLLMORGEN, 2003] KOLLMORGEN (manufacturer). *RBE, Series Brushless Motors for Frameless DDR (Direct Drive Rotary) Motor Applications*, Product range data sheets, 2003. Available at http://www.kollmorgen.com/ (accessed on 30 July 2022).

[Kossi Abevi, 2013] Kossi Abevi, F. *Développement d'un outil d'assistance pour le prédimensionnement d'une vis à rouleaux satellites soumise à des sollicitations complexes*. Ph.D. thesis, Institut National des Sciences Appliquées de Toulouse (INSA), Toulouse, France, 2013.

[Kraft et al., 1988] Kraft, D. et al. (1988). A software package for sequential quadratic programming. Research Report. *German Research and Testing Institute for Aeronautics and Astronautics*, 1988.

[Krysinski and Malburet, 2007a] Krysinski, T. and Malburet, F. Chapter 3: Dynamics of a rotor, section 3.2. In [Krysinski and Malburet, 2007b], pp. 75–85.

[Krysinski and Malburet, 2007b] Krysinski, T. and Malburet, F. *Mechanical vibrations: Active and passive control*; ISTE: London, UK, Newport Beach, USA, 2007. ISBN: 978-1-905209-29-3

[Kuhn, 2014] Kuhn, H.W. Non-linear programming: a historical view. In *Traces and emergence of non-linear programming*; Birkhäuser: Basel, Switzerland, 2014, pp. 393–414.

[Lacey and Steele, 2006] Lacey, D.; Steele, C. The use of dimensional analysis to augment design of experiments for optimization and robustification. *Journal of Engineering Design*, **2006**, volume 17, pp. 55–73.

[Lacroux, 1985] Lacroux, G. *Les actionneurs électriques pour la robotique et les asservissements*, 2nd éditions; Technique et Documentation Lavoisier: Paris, France, 1994.

[Lagarde and Orlandini, 2019] Lagarde, P. and Orlandini, F. Safran: Hybrid turboshaft engine for helicopter eco-mode operation. In *Proceedings of MEA2019 More Electric Aircraft conference*, Toulouse, France, 6–7 February 2019.

[Lambe and Martins, 2012] Lambe, A.B. and Martins, J.R.R.A. Extensions to the design structure matrix for the description of multidisciplinary design, analysis, and optimization processes. *Structural and Multidisciplinary Optimization*, **2012**, volume 46, no. 2, pp. 273–284.

[Lasdon, 1970] Lasdon, L.S. Chapter 3. In *Optimization Theory for Large Systems*; Macmillan: New York, USA, 1970.

[Lebel, 2012] Lebel, G. *Prévision des charges aéromécaniques des rotors d'hélicoptère: Application aux pales à double flèche*. Ph.D. thesis, Institut National des Sciences Appliquées de Lyon (INSA), Lyon, France, 2012.

[Liscouet, 2010] Liscouet, J. *Conception préliminaire des actionneurs électromécaniques: Approche hybride, directe/inverse*. Ph.D. thesis, Institut National des Sciences Appliquées de Toulouse (INSA), Toulouse, France, 2010.

[Liscouët et al., 2012] Liscouët, J.; Maré, J.C.; Budinger, M. An integrated methodology for the preliminary design of highly reliable electromechanical actuators: Search for architecture solutions. *Aerospace Science and Technology*, **2012**, volume 22, pp. 9–18. Available at https://scholar.google.fr/citations?view_op=view_citation&hl=fr&user=nkGEGZgAAAAJ&citation_for_view=nkGEGZgAAAAJ:ufrVoPGSRksC (accessed on 30 July 2022).

[Liscouet-Hanke, 2008] Liscouet-Hanke, S. A Model-Based Methodology for Integrated Preliminary Sizing and Analysis of Aircraft Power System Architectures. Ph.D. Thesis, Institut National des Sciences Appliquées de Toulouse, Toulouse, France, 2008.

[Lisowski, 2015] Lisowski, F. Numerical computation of stresses and deformations in the planetary roller screw components. *Czasopismo Techniczne*, **2015**.

[Long, 2005] Long, A.H.K. *Analyse du comportement dynamique d'un élastomère: Modélisation et identification*. Ph.D. thesis, Ecole des Ponts ParisTech, Paris, France, 2005.

[Luenberger et al., 1984] Luenberger, D.G., Ye, Y., et al. *Linear and non-linear programming*, volume 2; Addison-Wesley: Boston, USA, 1984; Springer Nature Switzerland AG: Switzerland, 2022.

[Ma et al., 2012] Ma, S., Liu, G., Tong, R., and Zhang, X. A new study on the parameter relationships of planetary roller screws. *Mathematical Problems in Engineering*, **2012**, volume 2012.

[Ma et al., 2015] Ma, S., Zhang, T., Liu, G., Tong, R., and Fu, X. Kinematics of planetary roller screw mechanism considering helical directions of screw and roller threads. *Mathematical Problems in Engineering*, **2015**, volume 2015.

[Marcoux, 1987] Marcoux, C. *Principe de justification des pièces mécaniques*, Airbus Internal Documentation, 1987, ref: CAL30.007 (accessed on March 2021).

[Maré, 2015] Maré, J.C. Friction modelling and simulation at system level: Considerations to load and temperature effects. In *Proceedings of the Institution of Mechanical Engineers, Part I: Journal of Systems and Control Engineering*, **2015**, volume 229, no. 1, pp. 27–48.

[Maré, 2016] Maré, J.C. *Aerospace Actuators 1: needs, reliability and hydraulic power solutions*; ISTE Group: London, UK, 2016.

[Maré, 2017] Maré, J.C. *Aerospace Actuators 2: Signal-by-Wire and Power-by-Wire*; ISTE Group: London, UK, 2017.

[Maré, 2020] Maré, J.C. Practical considerations in the modelling and simulation of electromechanical actuators. In *Actuators*, MDPI (Multidisciplinary Digital Publishing Institute), **2020**, volume 9, no. 4, pp. 94.

[Maré, 2022] Maré, J.C. A preliminary top-down parametric design electromechanical actuator position control. In *Aerospace*, MDPI (Multidisciplinary Digital Publishing Institute), **2022**, volume 9, no. 6, pp. 314.

[Martins, 2012] Martins, J.R.R.A. A short course on multidisciplinary design optimization. *Lecture Notes for AEROSP*, 2012, volume 588. Available at http://adl.stanford.edu and https://pdfslide.net.

[Martins et al., 2009] Martins, J.R.R.A., Marriage, C., and Tedford, N. pyMDO: An object-oriented framework for multidisciplinary design optimization. *ACM Transactions on Mathematical Software (TOMS)*, **2009**, volume 36, no. 4, pp. 1–25.

[Martins and Lambe, 2013] Martins, J.R.R.A.; Lambe, A.B. Multidisciplinary design optimization: a survey of architectures. *AIAA Journal*, **2013**, volume 51, pp. 2049–2075.

[Massachusetts, 2022] Massachusetts, Institute of Technology (MIT) Thermodynamic and Propulsion—Aircraft Engine Performance— Performance of Propellers. 2022. Online resource available at https://web.mit.edu/16.unified/www/FALL/thermodynamics/notes/node86.html (accessed on 30 July 2022).

[Mazzoleni et al., 2021] Mazzoleni, M.; Di Rito, G.; Previdi, F. *Electro-Mechanical Actuators for the More Electric Aircraft*; Springer: Berlin/Heidelberg, Germany, 2021.

[McCormick et al., 1979] McCormick, B.W.; Aljabri, A.S.; Jumper, S.J.; Martinovic, Z.N. The Analysis of Propellers Including Interaction Effects. *NASA Scientific and Technical Information Facility*. **1979**. Available at https://www.researchgate.net/publication/23913137_The_Analysis_of_Propellers_Including_Interaction_Effects (accessed on 30 July 2022).

[Mermoz and FFG, 2022] Institut Aéronautique Jean Mermoz, FFG (Fédération Française de Giraviation) and EASA. *Manuel du pilote privé d'helicoptère*, manuel PPL théorique, épreuves communes, 2022.

[MIKIPULLEY, 2022] MIKIPULLEY (manufacturer). *Emergency braking in power outages, long holds of stopped positions*. Product range data sheets. 2022. Available at https://www.mikipulley.co.jp/EN/Products/ElectoromagneticClutchesAndBrakes/SpringActuatedTypeBrakes/BXW/index.html (accessed on April 2022).

[MIT, 2020] Massachusetts, Institute of Technology (MIT). *OpenJSCAD*. Open Source Solution for 3D display. 2020. Online resource available at https://openjscad.com/, package at https://github.com/jscad/OpenJSCAD.org (accessed on June 2020).

[Moës, 2011] Moës, N. *Continuum and Discrete Mechanics*. Lecture, Ecole Centrale de Nantes, France, 2011. Available at https://cel.archives-ouvertes.fr/cel-00612360v1/document (accessed on 30 July 2022).

[MOOG, 2020a] MOOG (manufacturer). *Motor information & application*. Product range data sheets. 2020. Available at https://www.moog.com/content/dam/moog/literature/MCG/moapp.pdf (accessed on January 2022).

[MOOG, 2020b] MOOG (manufacturer) Roller screw catalog. Product range data sheets. 2020. Available at https://www.moog.com/content/dam/moog/literature/ICD/planetaryrollerscrews.pdf (accessed on May 2022).

[MOOG, 2022] MOOG (manufacturer). *Ball screws, planetary and inverted roller screws*. Product range data sheets. 2022. Available at http://www.moogscrews.com/landing-page-1448FH-40185K.html (accessed on May 2022).

[Muljadi and Green, 2009] Muljadi, E. and Green, J. Cogging torque reduction in a permanent magnet wind turbine generator. In *Wind Energy Symposium of American*

Society of Mechanical Engineers Digital Collection (ASME), **2009**, volume 7476, pp. 340–342.

[Muller, 2008] Muller, J.-P. *Réponse d'un système linéaire — Physique appliquée*, Lecture for BS2EL, Cachan, France, 2008.

[Multon, 2006] Multon, B. Conception et optimisation de systèmes électromagnétiques, conception d'actionneurs spéciaux. Ph.D. thesis, STITS & EDSP, Paris, France, 2006. pp. 41,94.

[Multon, 2010] Multon, B. *Les machines synchrones autopilotées*, Lecture. ENS, Cachan, France, 2010. pp. 10.

[Multon et al., 2005] Multon, B., Ahmed, H. B., Ruellan, M., and Robin, G. Comparaison du couple massique de diverses architectures de machines synchrones à aimants. In *Electrotechnique du Futur 2005*, **2005**, pp. 8.

[Nancy-Metz, 2021] Nancy-Metz Academy. *Viscosité cinématique et dynamique*. Online resource available at https://www4.ac-nancy-metz.fr/physique/ancien_site/Tp-phys/Term/TP-fluid/visco-eau.htm (accessed on 01 December 2021).

[NASA, 2019] National Aeronautics and Space Administration (NASA). *Aeronautics strategic implementation plan: 2019 update.* Technical Report, NP-2017-01-2352-HQ, **2019**.

[Naubert et al., 2016] Naubert, A.; Bachmann, M.; Binz, H.; Christmann, M.; Perni, F.; Toro, S. Disconnect device design options for jam-tolerant EMAs. In *Proceedings of the International Conference on Recent Advances in Aerospace Actuation Systems and Components (R3ASC)*, Toulouse, France, 16–17 March 2016; INSA Toulouse: Toulouse, France, 2016; pp. 187–192.

[Nocedal and Wright, 2006] Nocedal, J. and Wright, S.J. Quadratic programming. *Numerical optimization*, **2006**, pp. 448–492.

[NOESIS, 2022] NOESIS company. *ID8 solution: unleash the power of your engineering data*. 2022. Online resource available at https://www.noesissolutions.com/our-products/id8 (accessed on June 2022).

[NSK, 2013] NSK Motion & Control. *Starting and running torques for bearings*. Technical report. 2013. Available at https://www.bearing.co.il/img/tech1/PDF/nsk_cat_e728g_7.pdf

[Palmgren, 1967] Palmgren, A. *Les Roulements: description, théorie, applications*, 2e édition. SKF, France, 1967.

[Papalambros and Wilde, 2000] Papalambros, P.Y.; Wilde, D.J. *Principles of Optimal Design: Modeling and Computation*, 2nd ed.; Cambridge University Press: Cambridge, UK; New York, NY, USA; 2000.

[Papalambros and Wilde, 2017] Papalambros, P.Y. and Wilde, D.J. *Principles of Optimal Design: Modeling and Computation*, 3rd ed.; Cambridge University Press: Cambridge, UK; New York, NY, USA; 2017.

[PARKER, 2022] PARKER (manufacturer). *Frameless Low Cogging Servo Motors—NK Series*. Product range data sheets. 2022. Available at https://ph.parker.com/us/en/frameless-low-cogging-servo-motors-nk-series/nk630esrr1000 (accessed on 30 July 2022).

[PARKER, 2022b] PARKER (manufacturer). *Low Cogging Brushless Servo Motors—NX Series*. Product range data sheets. 2022. Available at https://ph.parker.com/us/en/nx-series-low-cogging-brushless-servo-motors (accessed on 30 July 2022).

[Pate et al., 2014] Pate, D.J., Gray, J., and German, B.J. A graph theoretic approach to problem formulation for multidisciplinary design analysis and optimization. *Structural and Multidisciplinary Optimization*, **2014**, volume 49, no. 5, pp. 743–760.

[Penas et al., 2013] Penas, O., Plateaux, R., Choley, J.Y., Kadima, H., Soriano, T., Combastel, C., and Riviere, A. *TI Techniques de l'Ingénieur—bm8020—Conception mécatronique: vers un processus continu de conception mécatronique intégrée*; Editions des Techniques de l'Ingénieur: Saint-Denis, France, 2013.

[Pérez et al., 2020] Pérez, J.-P., Carles, R., Fleckinger, R., and Lagoute, R. *Electromagnétisme: fondements et applications avec 300 exercices et problèmes résolus*, 4ème édition. Dunod: Malakoff, France, 2020.

[Pfennig et al., 2010] Pfennig, M.; Carl, U.B.; Thielecke, F. Recent advances towards an integrated and optimized design of high lift actuation systems. *SAE International Journal of Aerospace*, **2010**, volume 3, pp. 55.

[Piaton, 2010] Piaton, J. *Electric motor for rotoline actuator*. Patent. Reference no.: FR2940549A1. Published on 25 June 2010. Holder: SAGEM Defense Securité, Paris, France. Available at https://patents.google.com/patent/FR2940549A1 (accessed on June 2022).

[Plateaux et al., 2009] Plateaux, R., Choley, J., Penas, O., and Riviere, A. Towards an integrated mechatronic design process. In *Proceedings of IEEE International Conference on Mechatronics*, 14–17 April 2009, pp. 1–6. DOI: 10.1109/ICM13388.2009.

[Qiao et al., 2018] Qiao, G., Liu, G., Shi, Z., Wang, Y., Ma, S., and Lim, T.C. A review of electromechanical actuators for more/all electric aircraft systems. *Proceedings of the Institution of Mechanical Engineers, Part C: Journal of Mechanical Engineering Science*, **2018**, volume 232, pp. 4128–4151.

[Raletz, 2010] Raletz, R. *Basic Theory of the Helicopter*; CEPADUES: Toulouse, France, 2010. ISBN: 9782854289374.

[Raymer, 2012] Raymer, D. *Aircraft Design: A Conceptual Approach*; American Institute of Aeronautics and Astronautics (AIAA), Inc.: Reston, VA, USA, 2012.

[Reysset, 2015] Reysset, A. Conception préliminaire d'actionneurs électromécaniques—outils d'aide à la spécification et à la génération de procédures de dimensionnement pour l'optimisation. Ph.D. Thesis, INSA, Toulouse, France, 2015.

[Reysset et al., 2015] Reysset, A.; Budinger, M.; Maré, J.C. Computer-aided definition of sizing procedures and optimization problems of mechatronic systems. *Concurrent Engineering*, **2015**, volume 23, pp. 320–332.

[ROLLVIS, 2019] ROLLVIS (manufacturer). *Satellite roller screws*. Product range data sheets. 2019. Available at http://rollvis.com/swiss/products/?lang=en.

[Romanowicz and Szybiński, 2019] Romanowicz, P.J. and Szybiński, B. Fatigue life assessment of rolling bearings made from AISI 52100 bearing steel. *Materials*, **2019**, volume 12, no. 3, pp. 371.

[Roos, 2005] Roos, F. On Design Methods for Mechatronics: Servo Motor and Gearhead. Ph.D. Thesis, Royal Institute of Technology, Stockholm, Sweden, 2005. Available at https://www.diva-portal.org/smash/record.jsf?pid=diva2 (accessed on 30 July 2022).

[Roos et al., 2006] Roos, F.; Johansson, H. and Wikander, J. Optimal selection of motor and gearhead in mechatronic applications. *Mechatronics*, **2006**, volume 16, pp. 63–72. Available at https://www.diva-portal.org/smash/record.jsf?pid=diva2 (accessed on 30 July 2022).

[Roussel et al., 2022] Roussel, J.; Budinger, M.; Ruet, L. Unmanned helicopter flight control actuator specification through mission profile analysis. In *Proceedings of IOP Conference Series: Materials Science and Engineering*; IOP Publishing: Bristol, UK, 2022, volume 1226; pp. 012100. Available at https://iopscience.iop.org/article/10.1088/1757-899X/1226/1/012100/meta (accessed on 24 August 2022).

[RTCA, 2005] RTCA. *Environmental Conditions and Test Procedures for Airborne Equipment, DO-160E, EUROCAE ED-14E*; RTCA: Washington, DC, USA, 2005.

[Sadeghi et al., 2009] Sadeghi, F., Jalalahmadi, B., Slack, T.S., Raje, N., and Arakere, N.K. A review of rolling contact fatigue. In *Journal of Tribology & Tribology division of ASME*, **2009**, volume 131, no. 041403, pp. 1–15. DOI: 10.1115/1.3209132.

[Saerens et al., 2019] Saerens, E.; Crispel, S.; Garcia, P.L.; Verstraten, T.; Ducastel, V.; Vanderborght, B.; Lefeber, D. Scaling laws for robotic transmissions. *Mechanism and Machine Theory*, **2019**, volume 140, pp. 601–621.

[Sanchez et al., 2017] Sanchez, F.; Budinger, M.; Hazyuk, I. Dimensional analysis and surrogate models for the thermal modeling of Multiphysics systems. *Applied Thermal Engineering*, **2017**, volume 110, pp. 758–771.

[Sandu, 2018] Sandu, S. *Developing a power dissipation model for planetary roller screws*. Ph.D. thesis, Lyon, France, 2018.

[Savitzky and Golay, 1964] Savitzky, A. and Golay, M.J. Smoothing and differentiation of data by simplified least squares procedures. *Analytical chemistry*, **1964**, volume 36, no. 8, pp. 1627–1639.

[ScheafflerKG, 2009] Scheaffler (manufacturer). *Bearing catalog*. Product range data sheets. Scheaffler Group Industrial, Haguenau; Châtillon, France, 2009.

[SciPy, 2022] SciPy. *scipy.optimize: functions for minimizing (or maximizing) objective functions, possibly subject to constraints*. 2022. Online resource available at https://docs.scipy.org/doc/scipy/reference/optimize.html (accessed on June 2022).

[Seemann et al., 2012] Seemann, S.; Christmann, M.; and Jänker, P. Control and monitoring concept for a fault-tolerant electromechanical actuation system, EADS Innovation Work. In *Proceedings of International Conference on Recent Advances in Aerospace Actuation Systems and Components (R3ASC)*, Toulouse, France, 13–14 June 2012; INSA Toulouse: Toulouse, France, 2012; pp. 39–43.

[Sellar and Batill, 1996] Sellar, R. and Batill, S. Concurrent subspace optimization using gradient-enhanced neural network approximations. In *Proceedings of 6th Symposium on Multidisciplinary Analysis and Optimization*, Bellevue, WA, USA, 04–06 September 1996, pp. 4019.

[Sellar et al., 1996] Sellar, R., Batill, S., and Renaud, J. Response surface based, concurrent subspace optimization for multidisciplinary system design. In *Proceedings of 34th Aerospace Sciences Meeting & Exhibit*, Reno, NV, USA, 15–18 January 1996, pp. 714.

[Shigley, 2006] Shigley, J. *Mechanical engineering design*, 8th edition. McGraw-Hill: USA, 2006. ISBN: 0-390-76487-6.

[Shishko and Aster, 1995] Shishko, R. and Aster, R. *NASA systems engineering handbook. NASA Special Publication*, no. 6105, 1995.

[SIEMENS, 2022] SIEMENS. *Simcenter system architect & analyst*. Software solutions. 2022. Online resource available at https://www.plm.automation.siemens.com/global/es/products/simcenter/simcenter-system-architect.html and https://www.plm.automation.siemens.com/global/es/products/simcenter/system-analyst.html (accessed on June 2022).

[Singleton and Yeager Jr, 2000] Singleton, J.D. and Yeager Jr, W.T. Important scaling parameters for testing model-scale helicopter rotors. *Journal of Aircraft*, **2000**, volume 37, no. 3, pp. 396–402.

[SKF, 2005] SKF (manufacturer). *Roller screws*. Product range data sheets. 2005. Resource not available anymore, stopped activity.

[SKF, 2008] SKF (manufacturer). *Ball screws*. Product range data sheets. 2008.

[SKF, 2010] SKF (manufacturer). *Bushings, thrust washers and strips catalog*. Product range data sheets. 2010.

[SKF, 2011] SKF (manufacturer). *Spherical plain bearings and rod ends*. Product range data sheets. 2011.

[SKF, 2014] SKF (manufacturer). *Roller screws*. Product range data sheets. 2014. Resource not available anymore, stopped activity.

[SKF, 2018a] SKF (manufacturer). *Rolling bearings*. Product range data sheets. 2018. Resource available at https://www.skf.com/binaries/pub12/Images/0901d196802809de-Rolling-bearings---17000_1-EN_tcm_12-121486.pdf.

[SKF, 2018b] SKF (manufacturer). *SKF rating life*. In [SKF, 2018a], pp. 90. Resource available at https://www.skf.com/binaries/pub12/Images/0901d196802809de-Rolling-bearings---17000_1-EN_tcm_12-121486.pdf.

[SNR, 2000] SNR (manufacturer). *Technologie du roulement, produits standards et documentation*. Product range data sheets. SNR: Annecy, France, 2000.

[Sobieszczanski-Sobieski et al., 1998] Sobieszczanski-Sobieski, J., Agte, J., and Sandusky, Jr, R. (1998). Bi-level integrated system synthesis (bliss). In *7th AIAA/USAF/NASA/ISSMO Symposium on Multidisciplinary Analysis and Optimization*, page 4916.

[Spencer, 2004] Spencer, A.J.M. *Continuum Mechanics*; Courier Corporation, North Chelmsford, MA, USA, 2004; ISBN-13: 978-0486435947.

[Storn and Price, 1997] Storn, R. and Price, K. Differential evolution–a simple and efficient heuristic for global optimization over continuous spaces. *Journal of global optimization*, **1997**, volume 11, no. 4, pp. 341–359.

[Struzik and Celli,] Struzik, A. and Celli, M.-A. *RDLP Stress & Fatigue Analysis basics*. Lecture. Airbus Helicopters internal training (accessed on April 2021).

[Surjanovic and Bingham, 2013] Surjanovic, S. and Bingham, D. *Virtual library of simulation experiments, test functions and datasets, eggholder function*. Simon Fraser University, 2013. Online resource available at https://www.sfu.ca/~ssurjano/egg.html (accessed on May 2022).

[Sympy, 2021] Sympy. *Sympy, a Python library for symbolic mathematics*. 2021. Online resource available at https://www.sympy.org/ (accessed on June 2022).

[Tamer et al., 2019] Tamer, A., Muscarello, V., Masarati, P., and Quaranta, G. Evaluation of vibration reduction devices for helicopter ride quality improvement. *Aerospace Science and Technology*, **2019**, volume 95, pp. 105456.

[TECNOTION, 2019] TECNOTION (manufacturer). *Frameless torque motor series*. Product range data sheets. 2019. Available at https://www.tecnotion.com/downloads/ (accessed on May 2022).

[Thareja and Haftka, 1986] Thareja, R. and Haftka, R. Numerical difficulties associated with using equality constraints toachieve multi-level decomposition in structural optimization. In *Proceedings of 27th structures, structural dynamics and materials conference*, San Antonio, TX, USA, 21 May 1986, pp. 854.

[Timoshenko and Goodier, 1951] Timoshenko, S. and Goodier, J. *Theory of Elasticity*, 2nd edition. McGraw-Hill Book Company: USA, 1951. Available at https://books.google.fr/books?id=ialLYAAACAAJ.

[Todeschi, 2012] Todeschi, M. Airbus – EMAs for Flight Control Actuation Systems – 2012 status and perspectives. In *Proceedings of 5th International Conference on Recent Advances in Aerospace Actuation Systems and Components (R3ASC)*, Toulouse, France, 13-14 June 2012.

[Todeschi M, 2014] Todeschi, M. and Baxerres, L. Airbus-health monitoring for the flight control emas: 2014 status and perspectives. In *Proceedings of 6th International Conference on Recent Advances in Aerospace Actuation Systems and Components (R3ASC)*, Toulouse, France, 2–3 April 2014, pp. 73–83.

[Tri, 2022] Tribolonet. *Hertzian contact equations for elliptical, spherical and cylindrical contacts.* Online resource available at https://www.tribonet.org/wiki/hertz-equations-for-elliptical-spherical-and-cylindrical-contacts/ (accessed on January 2022).

[Van Groesen and Molenaar, 2007] Van Groesen, E.; Molenaar, J. *Continuum Modeling in the Physical Sciences*; SIAM: Bangkok, Thailand, 2007. Volume 13; pp. 1–29.

[Vanaret et al., 2017] Vanaret, C., Gallard, F., and Martins, J.R. On the consequences of the "no free lunch" theorem for optimization on the choice of an appropriate

MDO architecture. In *Proceedings of 18th AIAA/ISSMO Multidisciplinary Analysis and Optimization Conference*, Denver, Colorado, USA, 5–9 June 2017, pp. 3148. eISBN: 978-1-62410-507-4

[Vanthuyne, 2009] Vanthuyne, T. An electrical thrust vector control system for the VEGA launcher. In *Proceedings of 13th European Space Mechanisms And Tribology Symposium (ESMATS)*, Vienna, Austria, 23–25 September 2009, volume 670.

[Velinsky et al., 2009] Velinsky, S.A., Chu, B., and Lasky, T.A. Kinematics and efficiency analysis of the planetary roller screw mechanism. *American Society of Mechanical Engineers (ASME), Part: Journal of Mechanical Design*, **2009**, volume 131, no. 1.

[Voilà, 2020] Voilà. *Using voilà*. 2020. Online resource available at https://voila.readthedocs.io/en/stable/using.html, package available at: https://github.com/voila-dashboards/voila (accessed on June 2020).

[Wikipedia, 2021] Wikipedia. *Propriété de l'air*. Online resource available at websiteathttps://fr.wikipedia.org/wiki/Air (accessed on 01 December 2021).

[Wikipedia, 2022] Wikipedia. *Dynamic Mechanical Analysis (DMA)*. Online resource available at https://fr.wikipedia.org/wiki/analyse_mecanique_dynamique (accessed on June 2022).

[Wolpert and Macready, 1997] Wolpert, D.H. and Macready, W.G. No free lunch theorems for optimization. *IEEE transactions on evolutionary computation*, **1997**, volume 1, no. 1, pp. 67–82.

[Wu et al., 2017] Wu, S.; Yu, B.; Jiao, Z.; Shang, Y.; Luk, P. Preliminary design and multi-objective optimization of electro-hydrostatic actuator. In *Proceedings of the Institution of Mechanical Engineers, Part G: Journal of Aerospace Engineering*, **2017**, volume 231, pp. 1258–1268.

[Zaporozhets et al., 2021] Zaporozhets, O., Isaienko, V., and Synylo, K. PARE preliminary analysis of ACARE flightpath 2050 environmental impact goals. *CEAS Aeronautical Journal*, **2021**, volume 12, no. 3, pp. 653–667.

[Zaretsky, 2010] Zaretsky, E.V. In search of a fatigue limit: A critique of ISO standard 281: 2007. *Tribology & lubrication technology*, **2010**, volume 66, no. 8.

[Zhang et al., 2012] Zhang, X.C., Liu, G., Ma, S.J., Tong, R.T., and Luo, H. Study on axial contact deformation of planetary roller screw. *Applied Mechanics and Materials*, **2012**, volume 155, pp. 779–783.